DETECTION OF FAULTS IN A SCALED DOWN DOUBLY-FED INDUCTION GENERATOR USING ADVANCED SIGNAL PROCESSING TECHNIQUES

Prepared by:

Name: **Ester Hamatwi**

Student Number: **HMTEST001**

Supervisor: **Prof Paul Barendse**

Thesis submitted to the Department of Electrical Engineering, University of Cape Town, in complete fulfilment of the requirements for the degree of Doctor of Philosophy

December 2022

Department of Electrical Engineering

Faculty of Engineering and the Built Environment

University of Cape Town

University of Cape Town

The copyright of this thesis vests in the author. No quotation from it or information derived from it is to be published without full acknowledgement of the source. The thesis is to be used for private study or non-commercial research purposes only.

Published by the University of Cape Town (UCT) in terms of the non-exclusive license granted to UCT by the author.

University of Cape Town

DECLARATION

This dissertation is submitted to the Department of Electrical Engineering, University of Cape Town, in complete fulfilment of the requirements for the degree of Doctor of Philosophy. It has not been submitted before for any degree or examination at this or any other university. The author confirms that this thesis is based on her own work, save for which is duly referenced. Portions of this work have been published in peer-reviewed journals and at referred international conference proceedings.

In appreciation of the invaluable support, encouragement, and motivation, I dedicate this work to my late father: Petrus Nghilalulwa Hamatwi, my beloved mother; Ester Sakeus, my inspiring siblings and my adorable son, Nikko.

ACKNOWLEDGEMENTS

Firstly, I would like to thank the Almighty God for His consistent guidance, and for giving me the courage and faith that I needed to successfully complete this project.

Moreover, I would like to appreciate the following people who made an enormous contribution towards the execution and completion of this project:

- Prof Paul S. Barendse, my supervisor, for his vital professional and career-advancing advice, excellent guidance, and his patience throughout the development of my research project and the tedious implementation of the experimental test rig.

- Mr. Maysam Soltanian, the Chief Technical Officer, for his continued technical support, precise guidance, and assistance in the Machines Laboratory throughout the implementation of the experimental test rig.

- Prof Azeem Khan, for his guidance and assistance with the acquisition of some of the equipment used to develop the experimental test rig.

- Ms. S. Sabodien, for overseeing the administrative work, smoothly.

- The lab technicians, Mr. Hoosain Salie, and Mr. Riyaad Jakobs, for continuously assisting in the development of the test rig.

- My fellow postgraduates in the Advanced Machines and Energy Systems (AMES) Research group; Akinola Ajai-Obe, Chigozie Boniface and John Mushenya, from whom I have acquired some knowledge which helped me to develop my research and experimental test rig.

- My loving family and friends, who gave me support and encouragement throughout the duration of my studies.

- My Employer, UNAM, for believing in me and granting me the opportunity to pursue this PhD degree under the Staff Development Fellowship program.

ABSTRACT

The study ventures into the development of a micro-based doubly fed induction generator (DFIG) test rig for fault studies. The 5kW wound rotor induction machine (WRIM) that was used in the test rig was based on a scaled-down version of a 2.5MW doubly fed induction generator (DFIG). The micromachine has been customized to make provision for implementing stator inter-turn short-circuit faults (ITSCF), rotor ITSCF and static eccentricity (SE) faults in the laboratory environment. The micromachine has been assessed under the healthy and faulty states, both before and after incorporating a converter into the rotor circuit of the machine. In each scenario, the fault signatures have been characterised by analyzing the stator current, rotor current, and the DFIG controller signals using the motor current signature analysis (MCSA) and discrete wavelet transform (DWT) analysis techniques to detect the dominant frequency components which are indicative of these faults. The purpose of the study is to evaluate and identify the most suitable combination of signals and techniques for the detection of each fault under steady-state and transient operating conditions.

The analyses of the results presented in this study have indicated that characterizing the fault indicators independent of the converter system ensured clarity in the fault diagnosis process and enabled the development of a systematic fault diagnosis approach that can be applied to a controlled DFIG. It has been demonstrated that the occurrence of the ITSCFs and the SE fault in the micro-WRIM intensifies specific frequency components in the spectral plots of the stator current, rotor current, and the DFIG controller signals, which may then serve as the dominant fault indicators. These dominant components may be used as fault markers for classification and have been used for pattern recognition under the transient condition. In this case, the DWT and spectrogram plots effectively illustrated characteristic patterns of the dominant fault indicators, which were observed to evolve uniquely and more distinguishable in the rotor current signal compared to the stator current signal, before incorporating the converter in the rotor circuit. Therefore, by observing the trends portrayed in the decomposition bands and the spectrogram plots, it is deemed a reliable method of diagnosing and possibly quantifying the intensity of the faults in the machine. Once the power electronic converter was incorporated into the rotor circuit, the DFIG controller signals have been observed to be best suited for diagnosing faults in the micro-DFIG under the steady-state operating condition, as opposed to using the terminal stator or rotor current signals.

The study also assessed the impact of undervoltage conditions at the point of common coupling (PCC) on the behaviour of the micro-DFIG. In this investigation, a significant rise in the faulted currents was observed for the undervoltage condition in comparison to the faulty cases under the rated grid voltage conditions. In this regard, it could be detrimental to the operation of the micro-DFIG, particularly the faulted phase windings, and the power electronic converter, should the currents exceed the rated values for extended periods.

TABLE OF CONTENTS

LIST OF FIGURES

LIST OF TABLES

LIST OF ABBREVIATIONS

2L:	Two Level
3L:	Three Level
A:	Ampere
AC:	Alternating Current
CMFD:	Condition Monitoring and Fault Diagnosis
CWT:	Continuous Wavelet Transform
DAQ:	Data Acquisition
DC:	Direct Current
DFIG:	Doubly Fed Induction Generator
DWT:	Discrete Wavelet Transform
EMF:	Electromotive Force
FC:	Flying Capacitor
FEA:	Finite Element Analysis
FFT:	Fast Fourier Transform
FPGA:	Field-Programmable Gate Array
GSC:	Grid-side Converter
GUI:	Graphical User Interface
GW:	Giga Watts
HHT:	Hilbert Huang Transform
IGBT:	Insulated Gate Bipolar Transistors
IM:	Induction Machine / Induction Motor
IMC:	Internal Model Control
ITSCF:	Inter-turn Short-circuit Fault
LabVIEW:	Laboratory Virtual Instruments Engineering Workbench
MCSA:	Motor Current Signature Analysis
MPPT:	Maximum Power Point Tracking
MW:	Mega Watt
NI:	National Instruments
NPC:	Neutral-point-clamped
NSC:	Negative Sequence Component
NTV:	Nearest Three Vectors

PCB: Printed Circuit Board

PCC: Point of Common Coupling

PCI: Peripheral Component Interconnect

PE: Power Electronics

PI: Proportional Integral

PLL: Phase-Locked Loop

PSH: Principal Slot Harmonic

PWM: Pulse Width Modulation

PXI: PCI Extensions for Instrumentation

PXIe: PCI Express Extensions for Instrumentation

RE: Renewable Energy

RITSCF: Rotor Inter-turn Short-circuit Fault

RMS: Root Mean Square

RPM: Revolutions per Minute

RSC: Rotor-side Converter

RT: Real-Time

SCB: Shielded Connector Boards

SE: Static Eccentricity

SEDC: Separately Excited DC

SPWM: Sinusoidal Pulse Width Modulation

SVPWM: Space Vector Pulse Width Modulation

TCR: Time Constant Regulators

VA: Volt Ampere

VAR: Volt Ampere Reactive

VSC: Voltage Source Converter

W: Watt

WECS: Wind Energy Conversion System

WRIM: Wound Rotor Induction Machine

WT: Wind Turbine

ZSC: Zero Sequence Component

LIST OF SYMBOLS

Cp:	Power Coefficient
T_a:	Aerodynamic Torque [Nm]
T_e:	Electromagnetic Torque [Nm]
J_r:	Total shaft inertia [kgm/s]
D_r:	Damping Coefficient
$\vec{V}_s, \vec{V}_r$:	Stator and rotor supply voltage [V]
$\vec{E}_s, \vec{E}_r$:	Stator and rotor induced voltage [V]
$\vec{I}_s, \vec{I}_r$:	Stator and rotor induced current [A]
R_s, R_r:	Stator and rotor resistance [Ω]
$L_{\sigma s}, L_{\sigma r}$:	Stator and rotor leakage inductance [H]
L_m:	Magnetizing inductance [H]
L_s, L_r:	Stator and Rotor inductances [H]
ω_s:	Stator voltage and current electrical angular frequency [rad/s]
ω_m:	Rotor mechanical angular speed [rad/s]
ω_r:	Rotor electrical angular speed [rad/s]
ω_{slip}:	Rotor voltage and current electrical angular frequency [rad/s]
s:	Slip
P_p:	Machine pole pairs
f_r:	Rotor Electrical Frequency [Hz]
f_s:	Fundamental / Supply Electrical Frequency [Hz]
K_s, K_r:	Stator and rotor winding factor
N_s, N_r:	Number of turns on the stator and rotor windings,
f_s, f_r:	Stator and rotor electrical frequency [Hz]
$\underline{\emptyset}_m$:	Magnetizing flux [Wb]
$\vec{\phi}_s$:	Stator flux [Wb]
n:	Effective turns-ratio
P_{cu_s}, P_{cu_r}:	Active power losses in the Stator and Rotor winding [W]
P_s, P_r:	Stator and Rotor active powers [W]
Q_s, Q_r:	Stator and Rotor reactive powers [VAR]

$\boldsymbol{P_{mech}}$: Mechanical power [W]

$\boldsymbol{\theta_g}$: Grid voltage angle

$\boldsymbol{\theta_s}$: Angle of the synchronous frame with respect to the stationary frame

$\boldsymbol{\theta_r}$: Angle of the rotor frame with respect to the stationary frame

$\boldsymbol{\theta_{slip}} = \theta_s - \theta_r$: Angle of the rotor frame with respect to the synchronous frame

$\boldsymbol{V_{dc}}$: DC-Link Voltage [V]

$\boldsymbol{R_g}$, $\boldsymbol{L_g}$: Resistance [Ω] and inductance [H] of the grid filter

$\vec{\boldsymbol{V}}_{\boldsymbol{ag}}, \vec{\boldsymbol{V}}_{\boldsymbol{bg}}, \vec{\boldsymbol{V}}_{\boldsymbol{cg}}$: Grid voltages [V]

$\vec{\boldsymbol{I}}_{\boldsymbol{ag}}, \vec{\boldsymbol{I}}_{\boldsymbol{bg}}, \vec{\boldsymbol{I}}_{\boldsymbol{cg}}$: Current [A] flowing through the grid filter

$\vec{\boldsymbol{E}}_{\boldsymbol{ag}}, \vec{\boldsymbol{E}}_{\boldsymbol{bg}}, \vec{\boldsymbol{E}}_{\boldsymbol{cg}}$: Converter output voltages [V]

$\boldsymbol{S}$: Real power [VA]

$\boldsymbol{P_g}$: Grid Active Power [W]

$\boldsymbol{Q_g}$: Grid Reactive Power [VAR]

$\boldsymbol{\omega_g}$: Grid angular frequency [rad/s]

$\boldsymbol{W_{dc}}$: Energy stored in the DC-link capacitor [J]

$\boldsymbol{C_{dc}}$: DC-link capacitance [C]

$\vec{\boldsymbol{V}}_{\boldsymbol{ref}}$: Reference Voltage Vector [V]

$\boldsymbol{T_s}$: Sampling Period [s]

$\boldsymbol{F_s}$: Sampling frequency [samples/second (Hz)]

$\boldsymbol{T_1}$, $\boldsymbol{T_2}$ and $\boldsymbol{T_0}$: Dwell Times [s]

$\boldsymbol{m}$: Modulation Index

$\vec{\boldsymbol{x}}_{\boldsymbol{1}}, \vec{\boldsymbol{x}}_{\boldsymbol{2}}$: Scalar magnitudes of the vector projections

$\boldsymbol{d_a}, \boldsymbol{d_b}, \boldsymbol{d_c}$: Duty cycles

$\boldsymbol{d}$: Direct-axis component

$\boldsymbol{q}$: Quadrature-axis component

$\boldsymbol{F(s)}$: Controller Transfer Function

$\boldsymbol{G(s)}$: Plant Transfer Function

$\boldsymbol{H(s)}$: Feedback Transfer Function

$\boldsymbol{R(s)}$: Reference / set-point

$\boldsymbol{E(s)}$: Feedback Error

$\boldsymbol{U(s)}$: Plant Input

$\boldsymbol{D(s)}$: System Disturbance

$\boldsymbol{Y(s)}$: Plant Output

ω_n: Natural Frequency [rad/s]

ζ: Damping ratio

t: Time [s]

t_s: Settling time [s]

t_r: Rise time [s]

t_p: Peak time [s]

K_P , K_I : Proportional and Integral gains of the PI compensator

α_r: Closed loop bandwidth of the normal rotor current controller

$\alpha_{r_{soft}}$: Closed loop bandwidth of the soft synchronization rotor current controller

α_ω: Closed loop bandwidth of the speed controller

α_g: Closed loop bandwidth of the grid current controller

α_{dc}: Closed loop bandwidth of the DC-link voltage controller

G_a, R_a, B_a & R_c: Gain constants

R_{NL}: No load resistance [Ω]

X_{NL}: No load reactance [Ω]

R_{BL}: Blocked rotor resistance [Ω]

X_{BL}: Blocked rotor reactance [Ω]

$\psi(t)$: Mother wavelet

$x(n)$: Sampled signal

N: Number of samples

d_j: Detail coefficient

a_n: Approximation coefficient

n_f: Number of decomposition levels

E_j^a: Energy of the approximation coefficients

E_j^d: Energy of the detail coefficients

E_{Total}^d: Total energy of the n_f detail coefficients

D: Internal stator diameter [mm]

L: Core length [mm]

h_s: Slot depth [mm]

J: Current Density [A/mm^2]

B: Flux Density [T]

b_{ss}: Slot width [mm]

δ: Air gap [mm]

γ: Slot width scaling factor

v & μ: Stator and Rotor air-gap field pole numbers

f_{Is}^{H}:	Frequency components in the stator current signal of a healthy machine
f_{Ir}^{H}:	Frequency components in the rotor current signal of a healthy machine
$f_{I_s}^{asy}$:	Inherent asymmetry-related frequency components in the stator current signal
$f_{I_r}^{asy}$:	Inherent asymmetry-related frequency components in the rotor current signal
j:	Supply time harmonic
$f_{I_s}^{SITSCF}$:	Frequency components in the stator current signal due to the stator inter-turn fault
$f_{I_s}^{RITSCF}$:	Frequency components in the stator current signal due to the rotor inter-turn fault
$f_{I_r}^{SITSCF}$:	Frequency components in the rotor current signal due to the stator inter-turn fault
$f_{I_r}^{RITSCF}$:	Frequency components in the rotor current signal due to the rotor inter-turn fault
f_{C}^{RITSCF}:	Frequency components in the DFIG controller signals due to the rotor inter-turn fault
$f_{ecc_{LF}}$:	Low harmonic frequencies due to eccentricity faults
M_{Faulty}:	Magnitude of Frequency components in a faulty machine [dB]
$M_{Healthy}$:	Magnitude of Frequency components in a healthy machine [dB]
I_P:	Positive-sequence current component
I_N:	Negative-sequence current component

Chapter 1: Introduction

1.1 Orientation of Study

The wind energy sector has gone through a rapid growth over the last decade. The global cumulative wind energy capacity reached 792GW by the end of 2020 [1] (*see Fig. 1.1*).

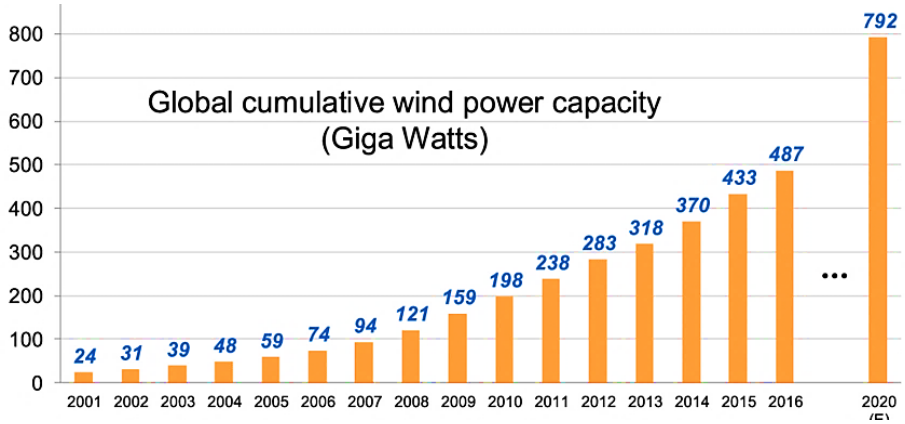

Figure 1. 1: Global Cumulative Installed Wind Power Capacity (2001-2020) [2]

The doubly-fed induction generator (DFIG) is the most common topology used in MW sized wind turbines (WTs) owing to their advantages such as high efficiency, good controllability, a wide range of speed operation, low converter rating, and low cost of operation and maintenance when compared to the synchronous generators used for the same purpose [3-8]. Compared with conventional power plants, WTs are usually located in harsher environments and, therefore, have relatively higher failure rates [5, 7]. Figure 1.2 presents the failure rate of the components in a typical wind turbine.

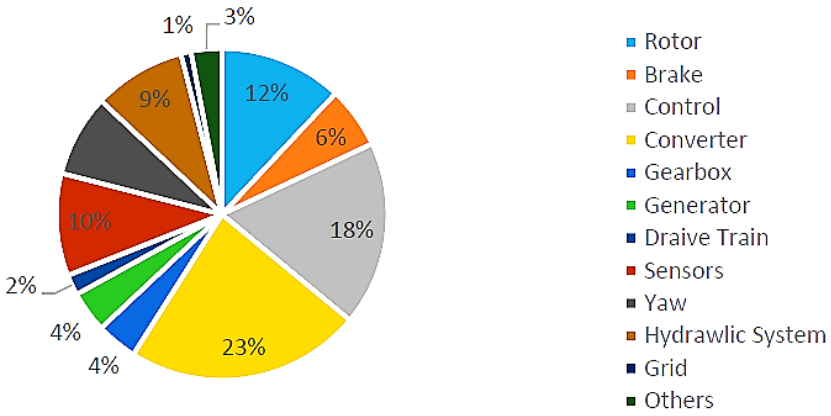

Figure 1. 2: Failure rate of wind turbine components [7]

In general, about half of the wind turbine failures are due to electronic components and the control system, but these failures have low downtimes [5]. Second to this is the failure of the generator and the gearbox, which are less frequent but have longer downtimes [5, 7]. The WT generators are prone to electrical and mechanical faults, which gradually degrades their operation [9, 10].

Figure 1.3 presents the common failure modes in induction machines [7, 11].

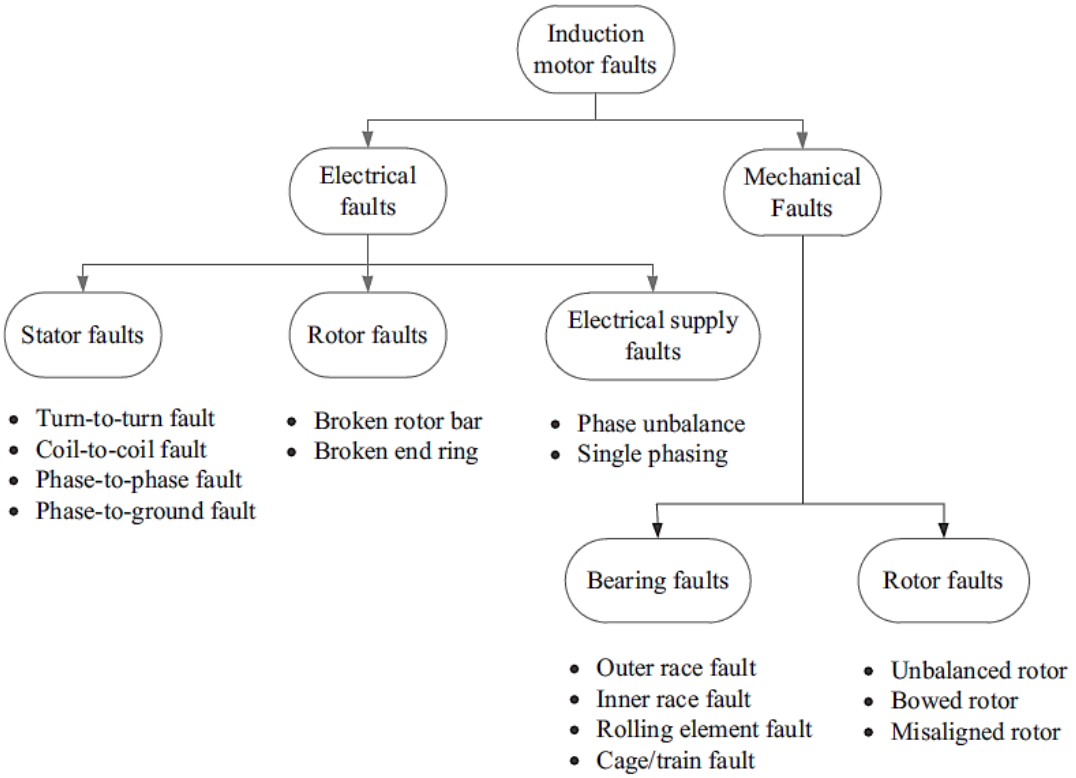

Figure 1. 3: Types of Faults in Induction Machines [12]

The common electrical faults that occur in DFIGs are the inter-turn short-circuit winding faults in the rotor and stator windings, making up 10% and 35% of the total faults, respectively, as shown in Fig. 1.4 [13, 14]. In addition, air gap eccentricities are considered the most prominent mechanical faults within the DFIG [15-17]. If these faults are not detected and rectified soon enough, they propagate quickly and become catastrophic leading to unexpected outages which are associated with high operating and maintenance costs [12].

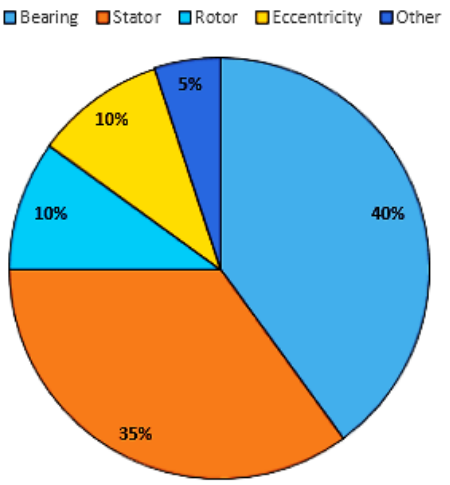

Figure 1. 4: Summary of types of faults commonly associated with induction machines [5]

The stator and rotor winding faults can be classified as follows: open-circuit, turn-to-turn, coil-to-coil, phase-to-ground, and phase-to-phase, as illustrated in Fig. 1.5 [5, 12].

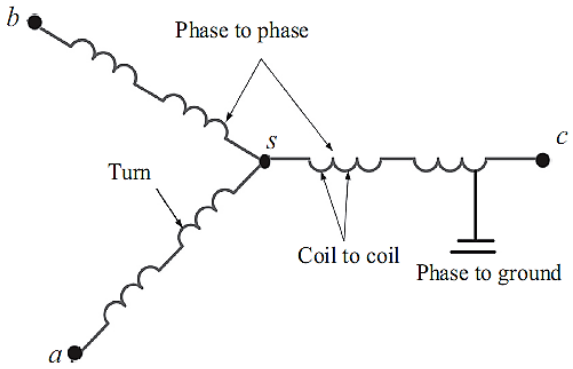

Figure 1. 5: Stator and rotor winding faults in an induction machine [12]

From the failure modes presented in Fig. 1.5, turn-to-turn faults are the most catastrophic since the other types of winding faults originate from them [5, 14, 18, 19]. Fundamentally, an inter-turn winding fault emanates from the deterioration of the insulation between individual coils which results in short-circuiting of the phase windings [14, 20]. Whereas air-gap eccentricity is characterized by the existence of a non-uniform air gap between the stator and rotor, which can either be static, dynamic, or even co-exist at times, resulting in mixed eccentricities [20-23]. These faults introduce frequency components in the stator and rotor current signals, which are tracked to diagnose the corresponding faults [20].

Over a typical 20-year lifespan of a WT, the cost of unscheduled maintenance accounts for 30% - 60% of the total operation & Maintenance (O&M) costs, and it generally increases over time as a wind turbine ages [5, 24]. There has been an increasing focus on reducing the O&M costs associated with unscheduled maintenance due to unexpected failures of wind turbine components [25]. According to the literature, the most effective way to prevent unexpected shutdowns and reduce O&M costs is by implementing a preventive-centered maintenance strategy. This strategy involves implementing a cost-effective and reliable technique to detect a fault in advance and assess its severity to begin the maintenance process thereby minimizing the economic implications resulting from a catastrophic failure [26, 27]. Figure 1.6 illustrates the trend in costs depending on the type of maintenance strategy.

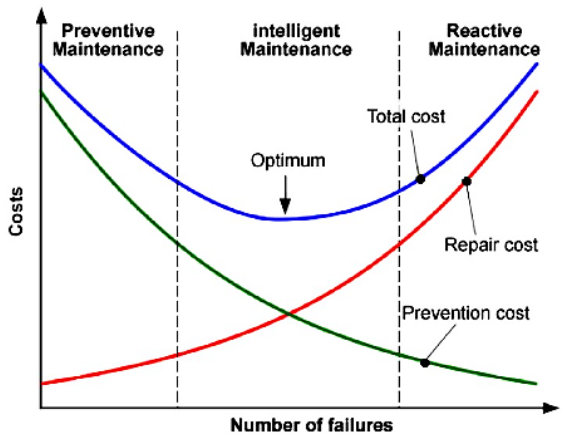

Figure 1. 6: The trend in costs for each maintenance strategy [28]

The growth in the installation of WTs based on DFIGs and moving to less accessible offshore environments prompts a need to develop effective condition monitoring and fault detection strategies to detect, locate and mitigate these faults at their incipient stages before a complete breakdown occurs [20]. This, in turn, minimizes the downtime of the WT thereby maximizing the WT productivity [29, 30]. Figure 1.7 shows a typical WT CMFD system, which consists of several functional modules [31].

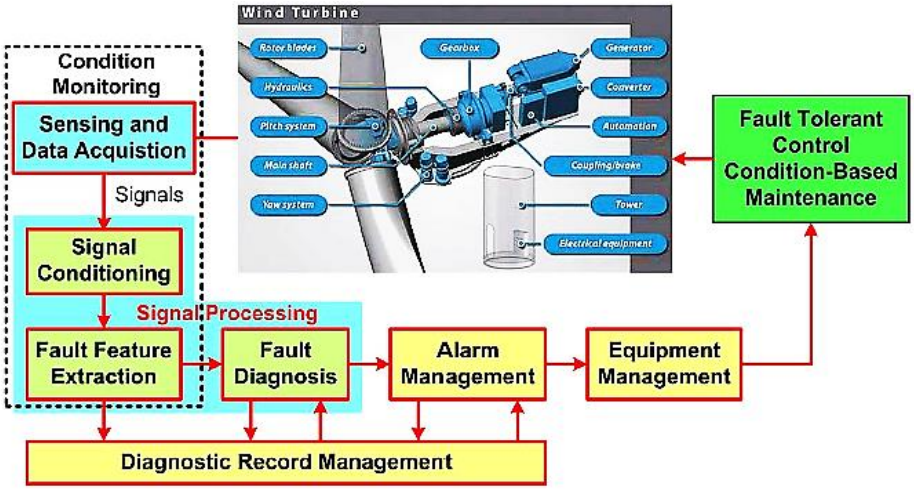

Figure 1. 7: Typical CMFD systems for WTs [31]

The signals and signal processing methods are the most important components of the WT CMFD. An effective CMFD technique should be able to detect the inception of the fault, its location and its severity at a fast rate [5]. The following factors are identified as the points of reference in developing appropriate CMFD strategies for rotary machines [5, 32, 33]:

- ✓ Applicability is based on the fault type and applications where the machine is deployed.
- ✓ Reliability of sensors, instrumentation, and data acquisition system.
- ✓ Cost competitiveness and invasiveness: i.e., the technique should be less invasive.
- ✓ Accurate and reliable fault diagnosis and quantification of the severity of the fault.
- ✓ Computational intensity and accuracy of the signal processing techniques

1.2 Problem Statement

Prior to the present time, the studies which were proposed to develop techniques for improving the performance of wind energy systems were based on numerical modelling and the simulation of these systems. However, the complexity and sometimes, the inaccuracy of the simulation models reduce the quality of these simulation-based investigations, hence, highly accurate investigations can be achieved through experimental analysis. Therefore, in most investigations, researchers have adopted the use of standard small-scale off-the-shelf IMs ranging in sizes from 4 – 50kW to develop experimental test rigs to perform several laboratory-based studies. However, despite the popularity of using these IMs in laboratory-based test rigs to conduct fault studies, there are no reports in literature validating their applicability in comparison to using the actual machines. Given the advancement in CMFD, there is an increasing need to explore and develop novel techniques for processing both steady-state and transient signals, which would require rigorous testing in laboratory environments before these techniques can be standardized and applied to large-scale machines in the industry. Therefore, it is crucial to be strategic in selecting a small-scale machine that would ensure that the experimental results obtained from laboratory-based studies are an accurate reflection of what is expected in a large-scale machine. This is especially relevant in the case of conducting fault studies in wind turbine systems, given their non-linear and nonstationary behavior. From this perspective, the current research investigation uses a micromachine to develop a test rig for fault studies in a DFIG-based WECS. Micromachines are scaled-down versions of large-scale machines, and are designed to mimic specific dynamic responses, which is ensured through dimensional analysis techniques.

Under the concept of CMFD, the motor current signature analysis (MCSA) technique has been widely used for fault diagnosis, particularly for machines operating under steady-state conditions, owing to its cost-effectiveness, ease of implementation and non-invasiveness. However, the MCSA method falls short when the speed or the load torque is not constant because this leads to variations in the machine slip. Consequently, it becomes difficult to trace the fault signatures which are slip dependent and spread out on a bandwidth proportional to the speed range. Considering that the operation of wind turbine generators is predominantly transient, this prompts the search for non-stationary fault detection techniques. In this regard, advanced time-frequency decomposition tools such as the discrete wavelet transform (DWT), and Hilbert Huang Transform (HHT) have been explored to diagnose faults in the IMs under the transient regimes. These techniques have been proven to effectively extract the characteristic patterns of the harmonic components resulting from the occurrence of faults, thereby making it the most preferred technique for analyzing non-stationary signals.

On fault detection in induction machines, the diagnosis of stator inter-turn short-circuit faults (ITSCFs) in wound rotor induction machines (WRIMs) has been researched broadly as opposed to the rotor ITSCF. This is attributed to the ease with which the stator inter-turn faults may be implemented & studied, which is not the case for the rotor ITSCF conditions.

This is mainly because there is difficulty in practically implementing the rotor ITSCFs and locating the harmonic components associated with these faults because of the low frequency in the rotor circuit. Furthermore, the rotor-side converter diminishes the fault signatures in the electrical signals which complicates the fault detection process. However, detecting the rotor ITSCFs is also essential due to the catastrophic nature of this fault, i.e., the rotor coils may dislodge while the machine is rotating which could damage the stator core and windings beyond repair, hence, it is an area that has been considered in this study.

Regarding the signals that can be analyzed to diagnose faults in IMs, it has been observed from literature, that the past investigations on the detection of faults in IMs have primarily emphasized using the MCSA of the stator current signal for diagnosis and less emphasis has been put on using the rotor current signal to detect the same faults. This has been observed for investigations that focus on the steady-state conditions and in studies that have looked at using the start-up stator current signal to track the evolution of the dominant fault indicators during the starting transient operating condition. Overall, it has been observed that the rotor current signal has rarely been explored in the literature to diagnose faults in WRIMs, under both steady-state and transient operating conditions, although it may also provide substantial fault features and hence, it is of particular interest in this study.

There have also been studies on the diagnosis of faults in WRIMs, which primarily focus on DFIGs which are controlled through a closed-loop system. However, the converter's switching harmonics and the dynamics of the control loops in such a system suppress the fault signatures in the terminal current signals thereby compromising the DFIG fault diagnosis process. Consequently, the fault-related harmonics are masked by these switching harmonics thereby making their detectability complicated. Therefore, to have a better understanding of the inherent fault signatures associated with WRIMs, it is crucial to investigate the diagnosis of these faults before connecting a converter in the rotor circuit of the WRIM. This is an area that has not been explored in literature, and thus remains of considerable interest, hence, it has been explored in this study. This exercise enables the fault signatures to be characterized independent of the harmonics which result from the switching mechanism of the converter switches thus ensuring clarity in the fault diagnosis process. Moreover, it enables the development of a systematic fault diagnosis approach that would be applied to a controlled DFIG.

Therefore, this study ventures into the implementation and diagnosis of the stator and rotor ITSCFs on a 5kW WRIM that was prototyped in the university laboratory as a scaled-down version of a 2.5MW DFIG. The 5kW micromachine/micro-WRIM has been customized to make provision for implementing both the stator ITSCF and rotor ITSCFs at different severity levels in the lab environment. Moreover, the machine has been customized to enable the implementation of a static eccentricity (SE) fault, which has not been widely explored in DFIGs, thus contributing to the novelty of this research study.

To develop an effective method(s) of assessing the micromachine under a healthy and faulty state, experimental investigations have been conducted on the developed test rig before, and after connecting the power electronic converter system in the rotor circuit of the micro-WRIM. In each scenario, the MCSA, HHT and DWT signal processing techniques have been used to analyze both the stator and rotor current signals, as well as the DFIG controller signals for fault-feature extraction and fault diagnosis under the steady-state and the starting transient / speed-varying conditions, respectively.

1.3 Aims and Objectives

The main objective of this project is to develop a robust fault detection technique for a scaled down double-fed induction generator used in a typical wind energy conversion system (WECS). To facilitate the experimental validation of the developed technique(s), a test rig that enables the practical implementation of stator and rotor inter-turn short-circuit faults (ITSCFs) and static eccentricity (SE) fault in a laboratory environment has been built in the Machines Laboratory. The test rig is based on a 5kW micromachine/micro-WRIM.

To achieve the main objective, the sub-objectives of the proposed project are as follows:

- Customize the micromachine/micro-WRIM to implement the stator inter-turn, rotor inter-turn and static eccentricity faults.
- Identify the appropriate signal processing and fault-feature extraction techniques to detect the winding inter-turn and static eccentricity faults in the micromachine under the steady-state and transient operating conditions.
- Develop a test rig whereby the micromachine operates in motor mode, i.e., a test rig without a converter system connected to the rotor circuit of the micromachine/micro-WRIM.
- Diagnose the stator ITSCFs, rotor ITSCFs and SE fault in the micro-WRIM in complete isolation of the converter system
- For the micromachine operating in motor mode, compare the use of the stator and rotor current to identify which current signal is best suited for diagnosing the ITSCFs and the SE fault, when there is no converter connected in the rotor circuit of the micro-WRIM.
- Upgrade the initial test rig by synchronizing the micromachine to the utility grid to operate in generator mode, i.e., a test rig with a power electronic converter system incorporated in the rotor circuit of the micromachine.
- Diagnose the stator ITSCFs, rotor ITSCFs and static eccentricity in the micro-WRIM in the presence of the converter system
- For the micromachine operating in generator mode, compare the use of the stator current, rotor current and the DFIG controller signals, to identify which signal is best suited for diagnosing the ITSCFs and static eccentricity fault when there is a converter incorporated in the rotor circuit of the micromachine.

- For the micromachine operating in generator mode, perform experiments when there is a low voltage level at the point of common coupling (PCC) and examine the impact of an undervoltage condition on the operation of the micro-DFIG that is in its healthy state.
- Evaluate the unbalance/asymmetry that occurs in the stator and rotor of the micro-DFIG due to the occurrence of the inter-turn winding faults in this machine under both rated and low grid voltage conditions.

1.4 Research Questions

This project is formulated with the following research questions:

- What is the significance of using the micro-WRIM as opposed to the standard off-the-shelf smaller-sized WRIMs, to develop a test rig for condition monitoring and fault studies?
- How can the micro-WRIM be modified to implement the stator inter-turn and rotor inter-turn winding faults as well as the static eccentricity (SE) fault?
- What are the appropriate signal processing and fault-feature extraction techniques that can be used for inter-turn winding and SE fault diagnosis during steady-state and transient operating conditions?
- What is the importance of investigating the diagnosis of faults in WRIMs before connecting a converter to the rotor circuit?
- What are the dominant fault-related frequency components introduced in the stator current, rotor current and the DFIG controller signals due to the presence of the stator ITSCF, rotor ITSCF and the SE fault in the micromachine under the steady-state operating condition?
- How do the resultant dominant fault-related frequency components evolve within the decomposition bands and spectrogram plots of the captured current signals during the start-up transient or speed-varying operating condition of the micromachine?
- Which current signal, between the stator and rotor current, is best suited for diagnosing the ITSCFs and the SE fault under the steady-state and transient operating conditions when there is no converter incorporated in the rotor circuit of the micromachine?
- Which signal, between the stator current, rotor current and the DFIG controller signals, is best suited for diagnosing the ITSCFs and the SE fault under the steady-state and transient operating conditions when there is a converter incorporated in the rotor circuit of the micromachine?
- How does having a low voltage at the point of common coupling (PCC) affect the operation and root-mean-square currents of a micro-DFIG in its healthy state?
- How does an undervoltage at the PCC in combination with the inter-turn fault conditions influence the operation and symmetry of the stator and rotor of the micro-DFIG?

1.5 Scope of Study

This study focuses on the development of a DFIG-based test rig that enables the implementation of the stator inter-turn, rotor inter-turn and the static eccentricity (SE) faults in a laboratory environment. The test rig enables experimental fault studies to be conducted to develop a robust technique aimed at diagnosing faults in the micromachine. The overview of a DFIG-based WECS and its components has been thoroughly discussed. The overall system's control architecture has initially been modelled in MATLAB/Simulink and assessed via simulations, and later, modelled/implemented in LabVIEW FPGA and experimentally evaluated in the laboratory.

The micromachine has been customized by modifying the stator and rotor windings to achieve inter-turn faults at different severity levels. The machine has also been customized to enable the emulation of a static eccentricity fault. The test rig which is primarily used for conducting fault studies has been developed and built in the Machines Laboratory at the University of Cape Town. The micromachine has initially been assessed under the healthy and faulty states before incorporating a converter in the rotor circuit of the machine. Thereafter, fault investigations have been conducted on the complete DFIG-based WECS, i.e., after the converter has been incorporated into the rotor circuit. In both investigations, both the stator and rotor current signals have been extracted and analyzed to diagnose the stator inter-turn, rotor inter-turn and SE faults in a micro-WRIM, while operating under the steady-state and transient/ speed-varying conditions.

In this research investigation, four signal processing techniques have been explored for fault diagnosis. Firstly, the MCSA technique has been used to perform the spectral analysis on the stator and rotor current signals during the steady-state condition, to detect the dominant frequency components corresponding to the different fault conditions. Secondly, time-frequency analysis techniques have been explored to analyze the current signals under the transient operating condition. In this regard, the Hilbert transform technique is first applied to the start-up stator and rotor current signals to suppress the fundamental frequency that masks the evolution of fault indicators. Thereafter, the DWT technique is applied to the resultant Hilbert modulus to extract the characteristic patterns of the fault indicators in the decomposition bands. The spectrogram plots of the rotor current signal have also been presented to illustrate the evolution of the fault indicator(s) during the starting transient. In all the analyses, the study evaluates the use of the stator current, rotor current and the DFIG controller signals to detect the ITSCF and SE fault conditions with the main aim of identifying which signal is best suited for diagnosing these faults. This comparison offers additional flexibility to the diagnostic capability of the micromachine.

Another scenario has been explored to assess the impact of a low voltage level at the point of common coupling (PCC) on the behaviour of the micro-DFIG that is in its healthy state. This has been realized by observing the root-mean-square (RMS) values of the stator and rotor currents as the voltage at the PCC changes from the rated grid voltage (380 V_{LL}) to 85% of the rated voltage. Secondly, an investigation has been conducted to evaluate the asymmetry that occurs in the stator and rotor currents due to the occurrence of the inter-turn faults, under both rated and low grid voltage conditions. This is realized by determining the negative sequence component of the stator and rotor currents and observing how this component is affected when the inter-turn short circuit faults occur in the stator and rotor windings, at different severity levels. In this aspect, the ratio of the negative-sequence to the positive-sequence component for each current signal also referred to as the current unbalance factor, has been determined and used to quantify the unbalance as the inter-turn fault severity level is increased. Moreover, the impact of the combination of scenarios, i.e., the inter-turn fault and the low grid voltage condition, on the operation of the micro-DFIG has been presented, taking into consideration the changes observed in the rms currents of the faulted phase winding as well as the negative-sequence current component as the fault severity level is increased.

1.6 Research Output and List of Publications

The research output, and the list of the peer-reviewed conference (C) and journal (J) publications are as follows:

- A developed micro-DFIG -based test rig for fault studies

C1: E. Hamatwi and P. Barendse, "Condition Monitoring and Fault Diagnosis of Stator and Rotor Inter-turn Winding Faults in a DFIG-based Wind Turbine System: A Review", 28th South African Universities Power Engineering Conference, Cape Town, South Africa, Jan 2020.

C2: E. Hamatwi, P. Barendse and A. Khan, "Development of a Test Rig for Fault Studies on a Scaled-down DFIG", IEEE Energy Conversion Congress and Exposition", Vancouver, Canada, Oct 2021.

C3: E. Hamatwi, P. Barendse and A. Khan, "An Investigation into the Diagnosis of Inter-turn Winding Faults in a Scaled-down DFIG using the MCSA and DWT of the Stator and Rotor Current", Vancouver, Canada, Oct 2021.

J1: (*Undergoing Review*) E. Hamatwi, P. Barendse and A. Khan, "A Case for Micromachines in Laboratory-Based DFIG Wind Turbine Systems" submitted to *IEEE Transactions on Industry Applications* (*March 2022*)

J2: (*Undergoing Review*) E. Hamatwi, P. Barendse and A. Khan, "Diagnosis of Eccentricity and Inter-turn Winding Faults in a micro-WRIM using the Transient and Steady-state Stator and Rotor Current Signals" submitted to *IEEE Transactions on Industry Applications (May 2022)*

1.7 Scientific Contributions and Outline of the Thesis

This project proposes an approach to developing a robust condition monitoring and fault diagnosis (CMFD) technique for the DFIG-based wind energy conversion system (WECS) while in operation. This is achieved through the development of a DFIG-based test rig that enables the implementation of stator inter-turn, rotor inter-turn, and the static eccentricity faults in a laboratory environment. This investigation aims to provide clarity on the emergence and movement of the fault harmonics, which are specific to DFIGs used in the wind energy field and develop advanced CMFD techniques for such faults.

A novel contribution of this work lies in the use of a scaled-down wound rotor induction micromachine (WRIM) to accurately represent the actual DFIG. Therefore, the experimental results obtained from a test rig, made up of this micromachine would be more representative of what is expected in actual systems, in this case, the wind energy field, because scaled-down/micromachines are designed to mimic specific dynamic responses as thoroughly presented by Dehnavifard *et al* in [34], as opposed to off-the-shelf smaller-sized machines. This is achieved through the dimensional analysis techniques which relate the key design specifications and parameters of the actual machine to those of the micromachine. Specific to this study, the focus is on ensuring that there is a correlation between the integer combinations for fault harmonics/indicators in the large-scale DFIG and those of its micromachine counterpart. This correlation forms a foundation for other aspects that are being investigated on the laboratory-based test rig, thereby assisting in the development of condition monitoring strategies which are closely suited to the actual system.

Another novel contribution of this work is tied to the exercise of firstly assessing the micro-WRIM before connecting a converter in the rotor circuit of the machine to diagnose the inter-turn winding and the static eccentricity faults. It is crucial to investigate the diagnosis of these faults in isolation of the converter, to have a better understanding of the inherent fault signatures associated with WRIMs. Considering that this is an area that has not been explored in literature, particularly in the diagnosis of inter-turn and air-gap eccentricity faults, it gives this work a level of novelty, thus giving it an edge in the body of knowledge. Therefore, this study aims to plug a gap in the literature by taking a more fundamental approach to identify fault-related components, but more importantly, stressing the factors that need to be considered when conducting fault diagnosis at a system level, especially when using harmonics under transient operating conditions. Therefore, it has been deduced that this exercise would enable the fault signatures to be characterized independent of the harmonics which result from the switching mechanism of the converter switches thus ensuring clarity in the fault diagnosis process before moving on to complicated closed-loop controlled DFIGs. In this regard, it enables the development of a systematic fault diagnosis approach that would be applied to a controlled DFIG, as it has been done in several research studies for the inverter-fed squirrel cage induction motors (SCIMs).

Moreover, the study has not only focused on using the stator current signal for analysis, as is frequent practice in detecting faults in induction machines but has also proposed and explored the use of the rotor current signal to detect the stator ITSCF, rotor ITSCF and static eccentricity fault. Additionally, the paper presents a comparison of using the stator and rotor current signals to identify which signal is best suited for diagnosing the faults in the micro-WRIM in isolation of the converter, which constitutes a fundamental approach that is new and has not been explored in literature. This has been done by investigating, identifying, and comparing the more dominant fault frequency components in the rotor and stator current signals, to propose fault markers for classification before the use of the converter. Subsequently, this is then used for pattern recognition when considering the transient analysis of the current signals, which would make provision for a more robust means of fault detection based on its non-stationary operation as it pertains to the variability of the wind resource.

This thesis is organized as follows, discussing all the key concepts, presenting the system models, assessing these models and, conducting fault studies on the developed test rig to diagnose the faults considered in this study using different signal processing and fault-feature extraction techniques:

CHAPTER 1: Introduction

This chapter focused on the sections that form the foundation of this thesis. These are the orientation of the study, the problem statement, the aims and objectives of this study, the research questions that ought to be answered in this study, the scope of the study as well as scientific contributions of the study.

CHAPTER 2: Conceptualization of the Study: Overview of the DFIG-based WECS and Review of the Condition Monitoring and Fault Diagnosis in Induction Machines

a) The DFIG-Based Wind Energy Conversion System

This subsection presents an overview of the operating principles of the components associated with the Doubly fed Induction Generator (DFIG)-based wind energy conversion system (WECS). It also sheds light on the dynamic modelling of DFIG.

b) The Back-To-Back Power Electronic Conversion System

This subsection presents an overview of the power electronic converter system with specific emphasis on the two-level and three-level neutral-point-clamped (NPC) voltage source converter (VSC) topologies. The section also covers the operating principles and mathematical modelling of these power electronic converters, the DC-link, and the grid-filter components. It concludes with an overview of the pulse width modulation (PWM) techniques of these VSCs with emphasis on the Space Vector PWM which is the modulation technique implemented in this research.

c) Control System of a DFIG-Based Wind Energy Conversion System

This subsection presents the aspects of designing and implementing the control system for a DFIG-based wind energy conversion system. In this regard, an overview of a general controller design based on the pole placement method and the internal model control turning technique has been presented. The objectives of the rotor-side converter (RSC) and grid-side converter (GSC) controllers have been outlined and the transfer functions of the respective controllers have been derived.

d) Condition Monitoring and Fault Diagnosis of a DFIG-Based WECS

This subsection presents an overview of the principle of condition monitoring and fault diagnosis in a DFIG-based WECS. The failure modes associated with a DFIG-based WECS have been discussed, with emphasis on the stator and rotor inter-turn and the air-gap eccentricity fault conditions. The section goes on to give an overview of the signals and the signal processing methods used to diagnose and characterize the fault features associated with the respective machine faults.

CHAPTER 3: DFIG's Control System Implementation and Performance Analysis Through Simulations

This chapter focuses on the modelling and implementation of the components associated with the DFIG-based WECS in MATLAB/Simulink. This step ensures that the operating principles of the different components are thoroughly understood before implementing the DFIG system in the laboratory. The desired controller specifications have been determined and the dynamic operation and testing of the complete DFIG-based WECS have been conducted. The simulation results presented in this chapter serve as a means of validating the experimental results.

CHAPTER 4: Development of the DFIG-Based Test Rig and Experimental Validation of the DFIG's Control System

a) Development of the DFIG-Based Test Rig for Fault Studies

This subsection focuses on the development of the DFIG-based WECS test rig for fault studies in the laboratory environment. The hardware and software components of the test rig have been discussed with emphasis put on their operating principles. The section also covers a detailed experimental determination of the WRIM equivalent circuit parameters which are needed for the design of a robust controller system.

b) Experimental Validation and Performance Analysis of the DFIG's Control System

This subsection presents the practical implementation of the DFIG's control system in LabVIEW FPGA. Experimental tests have been performed on the DFIG-based laboratory Test Rig setup. The experimental results have been compared to the simulation results presented in *Chapter 3* to validate the performance of the control system's subcomponents. Moreover, the dynamic performance of the overall DFIG system has been presented in this chapter.

CHAPTER 5: A Case for Micromachines in Laboratory-based Test Rigs and Customization of the Scaled-down WRIM for Fault Implementation

a) A Case for Micromachines in Laboratory-based DFIG Wind Turbine Systems

This subsection presented a comprehensive study on the correlation in the dimensional parameters, winding factors, and the evolution of specific electrical asymmetry indicators for an in-service large-scale DFIG, its micromachine/scaled-down version and in a standard small-scale off-the-shelf WRIM. This is done to explore whether there is a need for micromachines in the context of studying faults in laboratory-based test rigs, or whether standard small-scale off-the-shelf IMs would suffice.

b) Customization of the micro-WRIM to Implement the SE, and Stator & Rotor ITSCFs

This subsection presented the customization of the micromachine to enable the practical implementation of the stator inter-turn, rotor inter-turn and the static eccentricity (SE) fault conditions in the laboratory environment. The scaled-down WRIM machine that is used in this work has been designed and built in the university laboratory by Dehnavifard using Berchten's scaling methodology.

c) Signal Processing Techniques for Fault Feature Extraction and Fault Diagnosis in the micro-WRIM

This subsection sheds light on the signal processing techniques which are explored in this study to detect the inter-turn winding faults in the rotor and stator of the WRIM, as well as the SE fault during steady-state and transient operating conditions.

CHAPTER 6: Detection of the Inter-turn Winding and Static Eccentricity Faults in the micro-WRIM in Isolation of the Power Electronic Converter System

This chapter presents the analysis of the stator and rotor current signals to detect the inter-turn and SE fault conditions in a 5kW micro-WRIM operating in the motoring mode, i.e., in the absence of the power electronic converter system. The MCSA and DWT signal processing techniques have been used to analyze the captured current signals for fault-feature extraction and fault diagnosis during steady-state and transient operating conditions. A comparative study of using the stator and rotor current signals for fault detection has been presented in this chapter, to identify which current signal is best suited for diagnosing the inter-turn winding and static eccentricity faults.

CHAPTER 7: Detection of the Inter-turn and Static Eccentricity Faults in the micro-WRIM in the presence of the Power Electronic Converter System

This chapter focuses on the diagnosis of the stator ITSCF, rotor ITSCF and the SE faults in the scaled-down WRIM in the presence of the power electronic (PE) converter system. Likewise, the MCSA and DWT signal processing techniques have been used to analyze the captured stator current, rotor current and the DFIG controller signals for fault-feature extraction and fault diagnosis during the steady-state and transient operating conditions.

CHAPTER 8: Assessing the Behaviour of the Micro-DFIG due to Undervoltage Conditions and Inter-turn Short-Circuit Faults

This chapter focuses on assessing the behavior of a healthy micro-DFIG due to a low voltage level at the point of common coupling (PCC). The chapter goes on to evaluate the unbalance/asymmetry that occurs in the stator and rotor of the micro-DFIG when an inter-turn fault occurs at different severities under the rated and low grid voltage conditions. Moreover, the impact of the combination of scenarios, i.e., the inter-turn fault and the low grid voltage condition, on the operation of the micro-DFIG has been presented. The chapter concludes with an assessment as to which fault condition, between the stator inter-turn and rotor inter-turn fault, is more detrimental to the grid, considering the level of unbalance or negative-sequence injection into the grid resulting from these fault conditions.

CHAPTER 9: Conclusions and Recommendations

This chapter concludes the thesis by summarizing the main findings of this study and drawing recommendations for future research investigations.

Chapter 2: Conceptualization of the Study: Overview of the DFIG-based WECS and Condition Monitoring and Fault Diagnosis in Induction Machines

2.1 Introduction

The operating principles of the components which constitute the Doubly fed Induction Generator (DFIG)-based wind energy conversion system (WECS) have been discussed in this chapter. In this case, the steady-state and dynamic modeling of the DFIG has been presented. The chapter also covers an overview of the power electronic converter system with specific emphasis on the two-level and three-level three-phase voltage source converter (VSC) topologies, which are used in the developed test rig in this study. The pulse width modulation (PWM) techniques of the VSCs have also been presented with emphasis on the Space Vector PWM which is the modulation technique to be implemented in this research. The aspects of designing and implementing a control system for the DFIG-based WECS have also been presented. The transfer functions of the rotor side converter (RSC) controller, grid-side converter (GSC) controller, and phase-locked loop have been derived, according to the dynamic models of the DFIG and the converter system. The RSC and GSC controllers' objectives have been outlined and the design specifications to be achieved in this project have been determined. Lastly, the chapter presents an overview of the principle of condition monitoring and fault diagnosis in a DFIG-based WECS. Whereby specific failure modes associated with induction machines have been presented. The chapter goes on to present an overview of the signals and the signal processing methods used to diagnose and characterize the fault features associated with the faults.

2.2 The DFIG-based Wind Energy Conversion System (WECS)

Figure 2.1 presents a schematic diagram of a typical DFIG-based Wind Energy Conversion System (WECS).

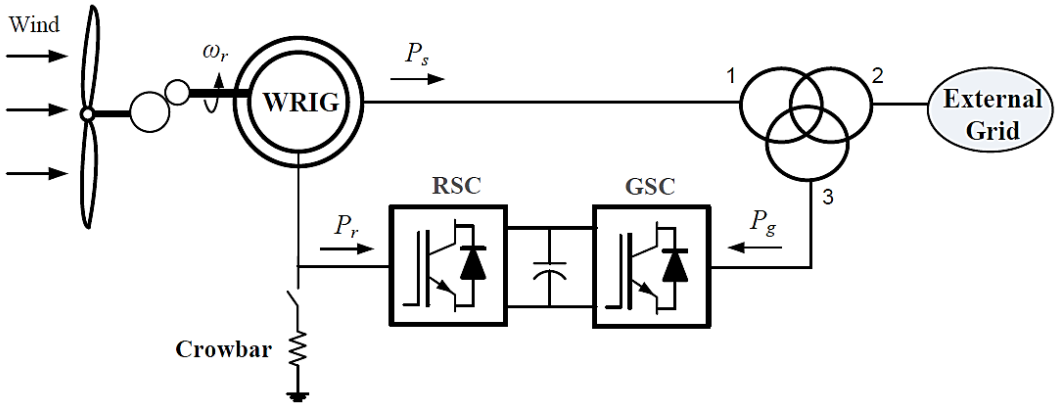

Figure 2. 1: Schematic diagram of a typical DFIG-based WECS [35]

2.2.1 Mechanical System

The mechanical system of a DFIG-based WECS comprises of the turbine blades, the turbine shaft, and the pitch angle control system [36]. The shaft system is represented by a drive train model that describes its rotational dynamics [8]. The turbine blades capture the aerodynamic torque from the wind resource, which is then transferred to the generator through the turbine shaft [35]. The conversion of the mechanical energy from the turbine to electrical energy is carried out by the generator [8].

2.2.2 Generator System

The stator winding of the DFIG are directly connected to the grid, while the rotor winding is connected to the grid via a partially scaled back-to-back power electronic converter system [5]. Consequently, the rating of the power electronic converter is only 30% of the generator capacity, which makes this concept attractive and popular from an economic point of view [5, 37]. The converter system exchanges the slip power between the rotor and the grid, for variable speed operation as shown in Fig. 2.2. The power flows into the rotor and flows out of the stator when the DFIG is operating below the synchronous speed, i.e., sub-synchronous speed (slip $s > 0$) [5]. On the other hand, the power flows out of both the stator and rotor when the DFIG is operating above the synchronous speed, i.e., super-synchronous speed (slip $s < 0$), which is split in the ratio of 70% and 30%, respectively, at maximum power [5, 38].

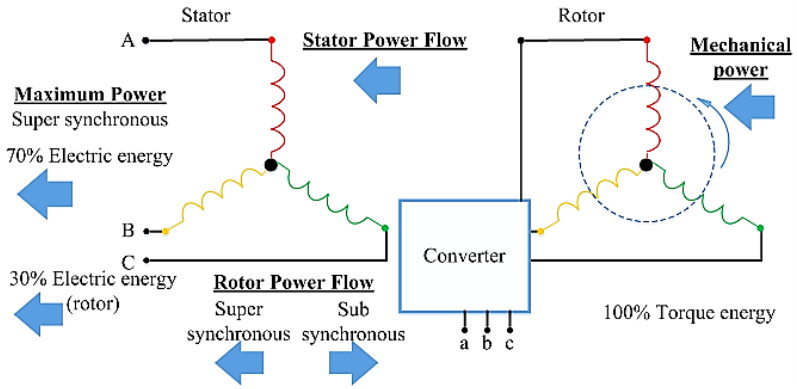

Figure 2. 2: Power Flow in a DFIG-based WECS

2.2.3 Power Electronic Converter System

The power electronic (PE) converter system consists of a rotor-side converter (RSC) and a grid-side converter (GSC). The converters are pulse width modulation controlled voltage source converters (VSCs) that use power electronic switches to synthesize an AC voltage from a DC source [39, 40]. The converters are connected to a DC bus that serves as an energy storage system and smoothens the power flow [35]. A coupling filter for attenuating the switching frequency harmonics connects the GSC to the grid. Generally, the RSC is responsible for regulating the generator speed to control the machine electric torque (stator power) and regulating the reactive power produced from the

generator while the GSC is mainly responsible for maintaining a constant dc-link voltage for continuous power flow between the rotor circuit and the grid and to control the reactive power to achieve a unity power factor [35].

2.2.4 Transformer System

The stator windings are commonly designed for low voltage levels (typically 400, 690, 900V for 50Hz systems) [41]. Therefore, a transformer is necessary to connect the stator to distribution grids that have medium voltage levels. The interfacing transformers can be connected in several ways, depending on the voltage rating of the stator and the converter. One transformer connection type is as shown in Fig. 2.1. Two more connections are shown in Fig. 2.3. In the configuration in Fig. 2.3 (a), the stator and the GSC's terminal voltages are the same. Whereas in the configuration in Fig. 2.3 (b), the voltage rating of the stator is the same as the grid voltage while the voltage rating of the transformer is the same as that of the GSC.

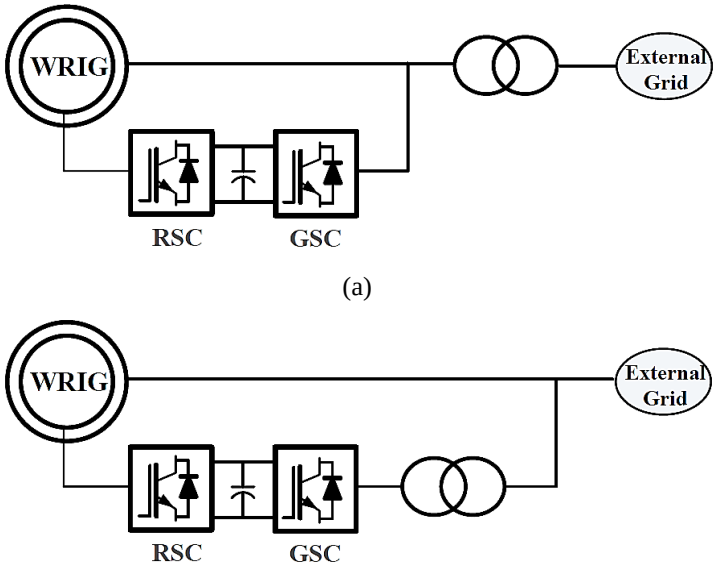

Figure 2. 3: Different Transformer Connections [35]

2.3 DFIG Mechanical and Electrical Models

2.3.1 Turbine Aerodynamic Model

The turbine mechanical torque T_a, wind speed V_w and the blade pitch angle β are related by (2.1) [8, 35, 42]:

$$T_a = \frac{\rho}{2}\pi r^3 \left(\frac{C_p(\lambda,\beta)}{\lambda}\right) {V_w}^2 \tag{2.1}$$

The mechanical power extracted from the wind resource is given by (2.2) [43]:

$$P_a = \frac{\rho}{2}\pi r^2 C_p(\lambda,\beta) {V_w}^3 \tag{2.2}$$

Where the variables ρ, r, C_p, λ, and β represent the air density which is equal to 1.225kg/m^3 at sea level, turbine blade radius, maximum power coefficient, tip speed ratio, and blade pitch angle, respectively [43].

The power coefficient C_p is a function of the tip speed ratio λ and the pitch angle β. The C_p is determined by aerodynamic laws and thus can vary for different turbines [39]. C_p can be approximated for a three-bladed wind turbine using (2.3) [42]:

$$C_p(\lambda,\beta) = 0.22\left(\frac{166}{\lambda_i} - 0.4\beta - 5\right)e^{-\frac{12.5}{\lambda_i}} \tag{2.3}$$

Where,

$$\lambda_i = \frac{1}{\frac{1}{\lambda+0.08\beta} - \frac{0.035}{\beta^3}} \tag{2.4}$$

The ratio of the blade circumferential speed to the wind velocity is referred to as the tip speed ratio λ, given by (2.5) [42]:

$$\lambda = \frac{\omega_m r}{V_w} \tag{2.5}$$

Where ω_m is the rotor angular speed [rad/s].

In a real wind turbine, the blade angle changes constantly due to wind variations to maintain an optimum angle and achieve maximum power extraction from the wind resource as shown in Fig. 2.4.

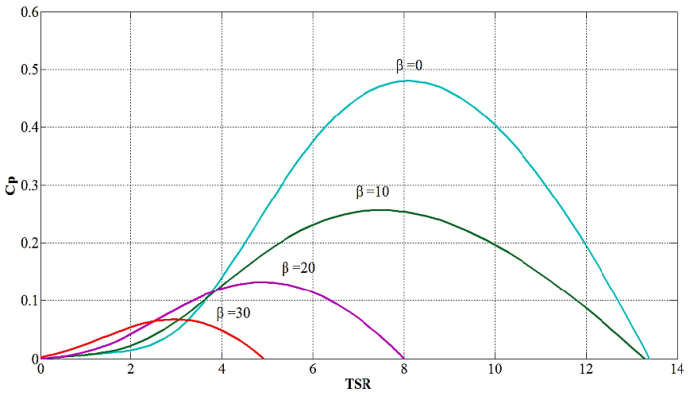

Figure 2. 4: C_p vs λ for varying pitch angle β [8]

Under low wind speeds, the effect of the varying wind on the pitch angle is minimal and hence, zero degrees is sufficient to represent the optimum pitch angle [8].

2.3.2 Turbine Shaft Model

A turbine shaft model, also known as the drive-train model transfers the aerodynamic torque from the low-speed shaft to the high-speed shaft [44]. The four types of drive-train models have been discussed in [45], which are six-, three-, two- and one-mass (lumped mass) models. In general, higher-order drive-train models are used for transient stability analysis, which is not required for the

controller design [8]. Therefore, the lumped mass model for the mechanical drive train is considered in this study. The lumped-mass model is expressed by (2.6) [35]:

$$J_r \frac{d\omega_m}{dt} = T_a - T_e - D_r \omega_m \tag{2.6}$$

Where the variables J_r, ω_m, T_a, T_e, and D_r represent the total shaft inertia, shaft angular mechanical speed, aerodynamic torque defined in (2.1), electromagnetic torque produced by the machine, and damping coefficient of the rotational system, respectively.

2.3.3 DFIG Steady State Model

2.3.3.1 DFIG Steady-State Equivalent Electric Circuit

The steady-state electrical circuit of a DFIG is presented in Fig. 2.5.

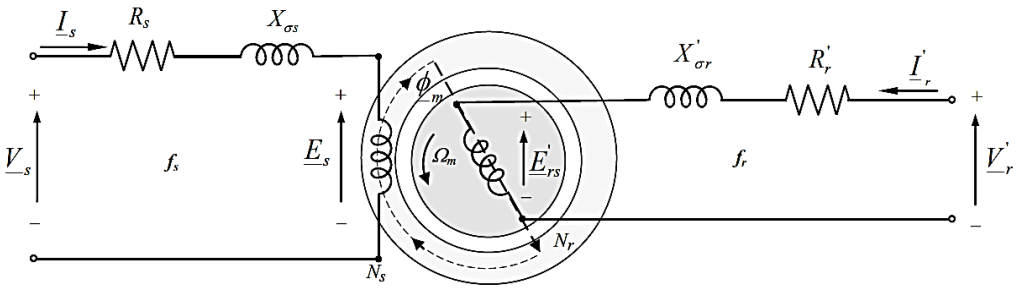

Figure 2. 5: The steady-state equivalent circuit of a DFIG [41]

The parameters shown in Fig. 2.5 are defined as follow, using the phasor theory [8, 41]:

- $\vec{V_s}, \vec{V_r}$: the stator and rotor supply voltages [V]
- $\vec{E_s}, \vec{E_r}$: the stator and rotor induced voltages [V]
- $\vec{I_s}, \vec{I_r}$: the stator and rotor induced currents [A]
- R_s, R_r: the stator and rotor resistances [Ω]
- $L_{\sigma s}$, $L_{\sigma r}$: the stator and rotor leakage inductances [H]
- ω_s: the stator voltage and current electrical angular frequencies [rad/s]
- ω_m: the rotor mechanical angular speed [rad/s]
- ω_r: the rotor electrical angular speed [rad/s] given by (2.7)

$$\omega_r = \omega_m P_p \tag{2.7}$$

where P_p: pole pairs of the machine.

- ω_{slip}: the electrical angular frequencies of the rotor voltage and current [rad/s] given by (2.8)

$$\omega_{slip} = \omega_s - \omega_r \tag{2.8}$$

- s: machine slip, given by (2.9)

$$s = \frac{\omega_s - \omega_r}{\omega_s} \tag{2.9}$$

The rotor electrical angular frequency ω_{slip} is related to stator electrical angular frequency ω_s and slip s by (2.10)

$$\omega_{slip} = s\omega_s \tag{2.10}$$

The relationship between slip and the frequencies is given by (2.11)

$$f_r = sf_s \tag{2.11}$$

Depending on the sign of the slip, the three operating modes of the machine are as follow [41]:

$$\omega_r < \omega_s \Rightarrow \omega_r > 0 \Rightarrow \boldsymbol{s > 0} \Rightarrow Sub - synchronous\ operation$$

$$\omega_r > \omega_s \Rightarrow \omega_r < 0 \Rightarrow \boldsymbol{s < 0} \Rightarrow Super - synchronous\ operation$$

$$\omega_r = \omega_s \Rightarrow \omega_r = 0 \Rightarrow \boldsymbol{s = 0} \Rightarrow Synchronous\ operation$$

2.3.3.2 Referring the Rotor Circuit to the Stator

The voltages induced in the stator and rotor windings of the machine depend on the flux ∅ and the number of turns N [41]. These voltages are expressed by (2.12) and (2.13), respectively [41]:

$$\vec{E}_s = \sqrt{2}\pi K_s N_s f_s \underline{\emptyset}_m (V_{s_{rms}}) \tag{2.12}$$

$$\vec{E}_r = \sqrt{2}\pi K_r N_r f_r \underline{\emptyset}_m (V_{r_{rms}}) \tag{2.13}$$

$$\vec{E}_{rs} = \sqrt{2}\pi K_r N_r s f_s \underline{\emptyset}_m (V_{r_{rms}}) \tag{2.14}$$

Where;

- K_s, K_r: Stator and rotor winding factor
- N_s, N_r: the number of turns on the stator and rotor windings, respectively
- f_s, f_r: the stator and rotor electrical frequencies [Hz]
- $\underline{\emptyset}_m$: Magnetizing flux [Wb]

Considering a machine at standstill, it can be approximated that $K_s = K_r$. Equating (2.12) and (2.13), the effective turns-ratio is obtained using (2.15) [8]:

$$n = \frac{\vec{E}_s}{\vec{E}_r} = \frac{N_s}{N_r} \tag{2.15}$$

The voltages, currents and parameters of the rotor are referred to the stator, using the effective turns ratio as shown in the following expressions [41]:

$$\vec{E}'_{rs} = \frac{\vec{E}_{rs}}{n} \tag{2.16}$$

$$\overrightarrow{V'}_r = \frac{\vec{V}_r}{n} \tag{2.17}$$

$$R'_r = \frac{R_r}{n^2} \tag{2.18}$$

$$L'_{\sigma r} = \frac{L_{\sigma r}}{n^2} \tag{2.19}$$

$$\vec{I}'_r = n\vec{I}_r \tag{2.20}$$

The resulting single-phase steady-state equivalent circuit of the DFIG, with the rotor referred to the stator, is shown in Fig. 2.6.

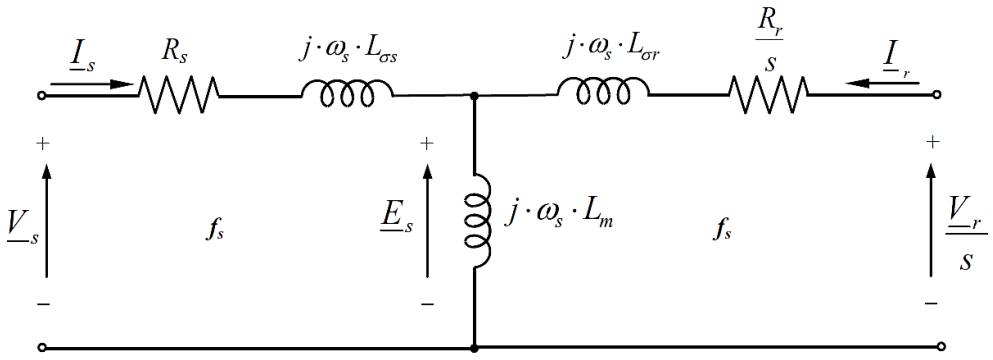

Figure 2. 6: The steady-state equivalent circuit of the DFIG referred to the stator [41]

The steady-state model equations of the stator and rotor windings can be derived from the equivalent circuit in Fig. 2.6 [36]. The model equation for the stator winding is expressed by (2.21) [41]:

$$\vec{V}_s - \vec{E}_s = (R_s + j\omega_s L_{\sigma s})\vec{I}_s \tag{2.21}$$

The model equation for the rotor winding is expressed by (2.22):

$$\vec{V}_r - \vec{E}_{rs} = (R_r + js\omega_s L_{\sigma r})\vec{I}_r \tag{2.22}$$

Substituting the relation between the stator and rotor *emf* from (2.14) [41]:

$$\vec{V}_r - s\vec{E}_s = (R_r + js\omega_s L_{\sigma r})\vec{I}_r \tag{2.23}$$

To transform (2.23) to stator frequency, (2.23) should be divided by the slip s as shown in (2.24):

$$\frac{\vec{V}_r}{s} - \vec{E}_s = (\frac{R_r}{s} + j\omega_s L_{\sigma r})\vec{I}_r \tag{2.24}$$

Combining (2.21) and (2.24) yields (2.25):

$$\vec{V}_s - \frac{\vec{V}_r}{s} - (R_s + j\omega_s L_{\sigma s})\vec{I}_s + (\frac{R_r}{s} + j\omega_s L_{\sigma r})\vec{I}_r \tag{2.25}$$

The stator induced emf is expressed by,

$$\vec{E}_s = j\omega_s L_m(\vec{I}_s + \vec{I}_r) \tag{2.26}$$

Where L_m is the magnetizing inductance [41].

The fluxes of the stator and rotor are obtained using expression (2.27) and (2.28), respectively [41]:

$$\vec{\psi}_s = L_m(\vec{I}_s + \vec{I}_r) + L_{\sigma s}\vec{I}_s = L_s\vec{I}_s + L_m\vec{I}_r \tag{2.27}$$

$$\vec{\psi}_r = L_m(\vec{I}_s + \vec{I}_r) + L_{\sigma r}\vec{I}_r = L_m\vec{I}_s + L_r\vec{I}_r \tag{2.28}$$

Where L_s and L_r are the stator and rotor inductances given by (2.29) and (2.30), respectively [41]:

$$L_s = L_m + L_{\sigma s} \tag{2.29}$$

$$L_r = L_m + L_{\sigma r} \tag{2.30}$$

2.3.3.3 DFIG Operating Modes and Power Flow

To study the different operating modes of the DFIG, it is vital to analyze the power relations of the machine [41]. The active power losses in the DFIG's stator and rotor windings are given by (2.31) and (2.32), respectively [41]:

$$P_{cu\_s} = 3R_s\vec{I}_s^{\,2} \tag{2.31}$$

$$P_{cu\_r} = 3R_r\vec{I}_r^{\,2} \tag{2.32}$$

The directions of the power flow in the machine can then be represented graphically as shown in Fig. 2.7.

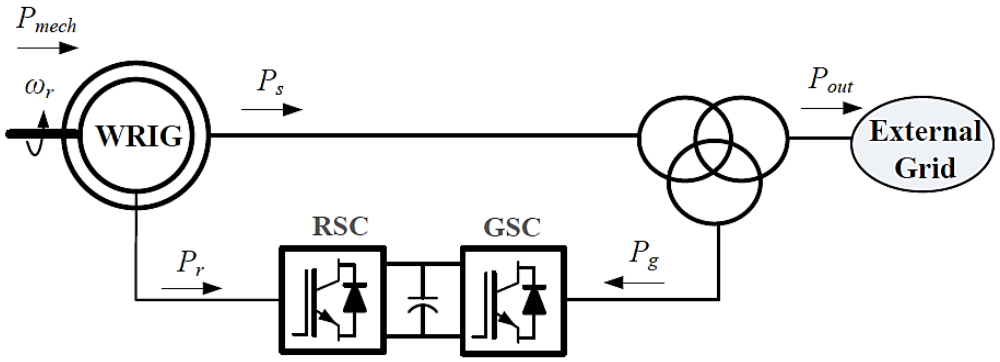

Figure 2. 7: Directions of the power flow in the DFIM model [35]

The active power balance can be mathematically expressed by (2.33):

$$P_s + P_r = P_{cu\_s} + P_{cu\_r} + P_{mech} \tag{2.33}$$

Where P_s is the stator active power expressed by (2.34) [41]:

$$P_s = 3Re\{\vec{V}_s\vec{I}^*_s\} = 3|\vec{V}_s| \cdot |\vec{I}_s|\cos(\theta_v - \theta_i) \tag{2.34}$$

P_r is the rotor active power expressed by (2.35) [41]:

$$P_r = 3Re\{\vec{V}_r\vec{I}^*_r\} = 3|\vec{V}_r| \cdot |\vec{I}_r|\cos(\theta_v - \theta_i) \quad (2.35)$$

P_{mech} is the mechanical power transmitted through the electrical circuit to the shaft. The sign of P_{mech} indicates the operation of the machine,

- If $P_{mech} > 0$, the machine is delivering power through the shaft: $Motoring\ Mode$
- If $P_{mech} < 0$, the machine is receiving power through the stator: $Generating\ Mode$

The mechanical power is related to the electromagnetic torque T_e by (2.36):

$$P_{mech} = T_e\omega_m = T_e\frac{\omega_r}{p_p} \quad (2.36)$$

The electromagnetic torque is related to the stator power by (2.37):

$$P_s = T_e\frac{\omega_s}{p_p} \quad (2.37)$$

The electromagnetic torque is related to the rotor power by (2.38):

$$P_r = T_e\frac{\omega_{slip}}{p_p} \quad (2.38)$$

If the power loss in the machine windings is neglected, expression (2.33) becomes [35]:

$$P_{mech} = P_s + P_r \quad (2.39)$$

$$P_r \cong -sP_s \quad (2.40)$$

Substituting (2.40) into (2.39) gives,

$$P_{mec} \cong P_s - sP_s = (1-s)P_s \quad (2.41)$$

2.3.4 DFIG Dynamic Model

2.3.4.1 *Reference Frame Transformations*

The concept of stationary and synchronous reference frame transformation is used to illustrate the characteristics of the machine under transient operating conditions and formulate its dynamic model [8]. This concept is termed as *space vector representation* and it involves representing time-dependent three-phase quantities with a rotating space vector in an arbitrary reference frame [8]. Figure 2.8 presents the schematic diagram of the reference frames of the DFIG.

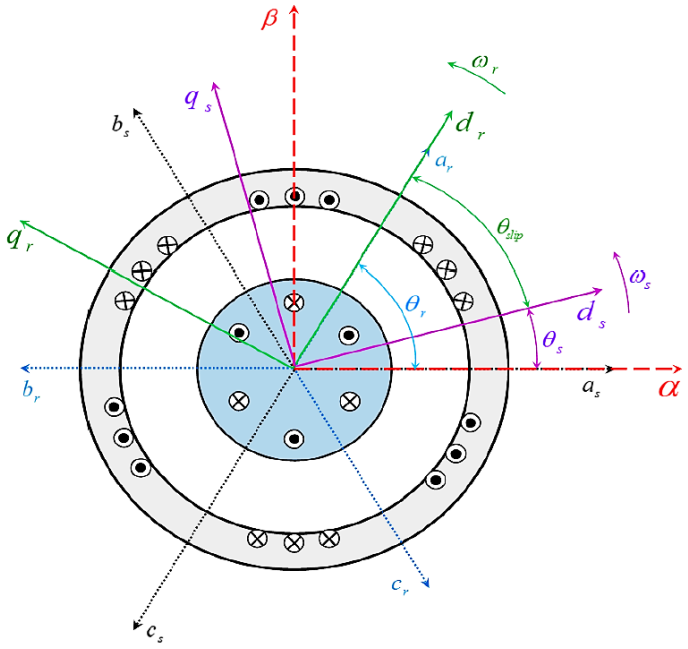

Figure 2. 8: Reference frames of the DFIG [8]

The rotor and stator windings are distributed in space by 120° and are assumed to have one pole pair [8]. The relative positions of the orthogonal rotating reference frames to the stationary reference frame d_s, q_s are represented by the following angles:

- θ_s: the angle of the synchronous reference frame relative to the stationary reference frame.
- θ_r: the angle of the rotor reference frame relative to the stationary reference frame.
- $\theta_{slip} = \theta_s - \theta_r$: angle of the rotor reference frame relative to the synchronous reference frame.

2.3.4.2 Dynamic Model

The dynamic model equations of the DFIG are presented by (2.42), in the synchronous reference frame [8, 35, 41]:

$$\begin{aligned} \vec{V}_s^{\,e} &= R_s \vec{I}_s^{\,e} + \frac{d\vec{\psi}_s^{\,e}}{dt} + j\omega_s \vec{\psi}_s^{\,e} \\ \vec{V}_r^{\,e} &= R_r \vec{I}_r^{\,e} + \frac{d\vec{\psi}_r^{\,e}}{dt} + j\omega_{slip} \vec{\psi}_r^{\,e} \\ \vec{\psi}_s^{\,e} &= L_s \vec{I}_s^{\,e} + L_m \vec{I}_r^{\,e} \\ \vec{\psi}_r^{\,e} &= L_m \vec{I}_s^{\,e} + L_r \vec{I}_r^{\,e} \end{aligned} \tag{2.42}$$

The superscript "*e*" denotes space vectors referred to the synchronous reference frame [8].

The electromagnetic torque generated by the DFIG is given by (2.43) [8, 41]:

$$T_e = \frac{3}{2} p_p \frac{L_m}{L_s} Im\left\{\vec{\psi}_s^{\,e} \vec{I}_r^{\,e}\right\} = \frac{3}{2} p_p \frac{L_m}{L_s} (\psi_{qs} I_{dr} - \psi_{ds} I_{qr}) \quad (2.43)$$

The active & reactive powers in the synchronous reference frame are expressed by (2.44) – (2.47) [41, 46]:

$$P_s = \frac{3}{2} Re\left\{\vec{V}_s^{\,e} \vec{I}_s^{\,e^*}\right\} = \frac{3}{2} (V_{ds} I_{ds} + V_{qs} I_{qs}) \quad (2.44)$$

$$P_r = \frac{3}{2} Re\left\{\vec{V}_r^{\,e} \vec{I}_r^{\,e^*}\right\} = \frac{3}{2} (V_{dr} I_{dr} + V_{qr} I_{qr}) \quad (2.45)$$

$$Q_s = \frac{3}{2} Im\left\{\vec{V}_s^{\,e} \vec{I}_s^{\,e^*}\right\} = \frac{3}{2} (V_{qs} I_{ds} - V_{ds} I_{qs}) \quad (2.46)$$

$$Q_r = \frac{3}{2} Im\left\{\vec{V}_r^{\,e} \vec{I}_r^{\,e^*}\right\} = \frac{3}{2} (V_{qr} I_{dr} - V_{dr} I_{qr}) \quad (2.47)$$

2.4 The Back-to-Back Power Electronic Converter System

2.4.1 The Power Electronic Converter Topologies

Voltage source converters (VSCs) are self-commutated converters controlled by IGBTs or Gate Turn-off Transistors (GTOs) semiconductor devices. A VSC can be categorized as either a two-level or a multi-level converter topology, depending on the arrangement of the semiconductor switches of the converter [44, 47]. Two-level VSC topologies are robust, have a simple configuration, and have a reliable performance. However, they are associated with high switching losses and poor waveform quality, hence, they require extra filtering elements [44, 48]. On the other hand, multi-level converters can handle higher voltages and synthesize voltages with better waveform quality compared to the 2-level converter topologies [44, 48]. Moreover, multilevel converters are associated with lower harmonic distortion, lower switching losses, higher overall efficiency, and a reduction in the size and number of filter elements [44]. However, they also have shortcomings such as higher conduction losses due to the high number of semiconductor devices in the conduction path, control circuit complexity, voltage imbalance across the upper and lower DC-link capacitors, and unequal current stress on the semiconductor switches [44, 48, 49].

The multilevel VSC topologies are the neutral-point-clamped (NPC), flying capacitor (FC), the cascaded H-bridge (CHB), and the modular multilevel converter (MMC) [44, 50]. The NPC uses clamping diodes joined to the center point of the DC-link to split the DC-link voltage into several voltage levels [44, 48]. The FC converter topology employs the same operating technique as the NPC [44]. However, the FC uses floating capacitors instead of the diodes used in the NPC.

The CHB consists of series-connected full-bridge converter modules whereby each module is fed by a separate DC capacitor [44]. A modular multilevel converter (MMC) is made up of several submodules (SM) which comprises of a half-bridge made up of 2 bidirectional switches connected in parallel with a capacitor [44, 50-52]. A converter arm is formed by connecting a number of these SMs in series with an inductor. Comparative studies of the NPC, FC, CHB, and MMC multilevel converter topologies have been carried out in the literature highlighting their strengths and weaknesses [44, 48-50, 53].

Multilevel converter topologies have gained momentum in large wind turbine applications. The power electronic conversion system considered in this project consists of a 2-Level (2L) VSC which is used for the rotor-side converter (RSC) and a 3-Level neutral-point-clamped (NPC) VSC which is used for the grid-side converter (GSC). Therefore, their operation, modulation, and control are discussed in more detail in the following sections.

2.4.1.1 Two-Level Voltage Source Converter Topology

Figure 2.9 presents the schematic diagram of a 2 Level 3-phase VSC, which has three legs, i.e., one leg for each phase. There are two switches per leg. The converter outputs two voltage levels, i.e., V_{dc} and 0, at the output phases '*a*', '*b*', and '*c*' relative to the negative point of the DC bus '*o*' [41, 54].

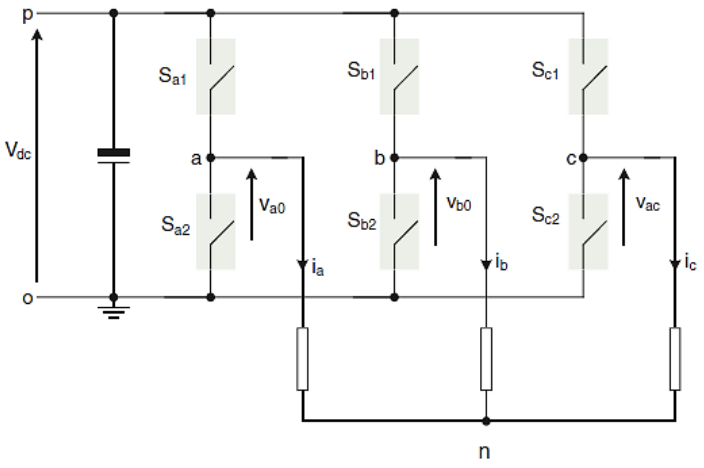

Figure 2. 9: Two-level Voltage Source Converter [54]

The two switches on each leg of a 2-level VSC operate as a complementary pair, to avoid a DC-bus short circuit [8]. Meaning, if the first switch of phase *a* (S_{a1}) is turned *on*, i.e., S_{a1}=1, then the second switch of phase *a* (S_{a2}) must be *off*, i.e., S_{a2}=*0*, and the same applies to phases *b* and *c* [44, 50]. Equation (2.48) expresses the converter's output phase voltage with respect to the load neutral '*n*' as a function of the DC-link voltage V_{dc} [8]:

$$\begin{bmatrix} V_{an} \\ V_{bn} \\ V_{cn} \end{bmatrix} = \frac{V_{dc}}{3} \begin{bmatrix} 2 & -1 & -1 \\ -1 & 2 & -1 \\ -1 & -1 & 2 \end{bmatrix} \begin{bmatrix} s_{a1} \\ s_{b1} \\ s_{c1} \end{bmatrix} \quad (2.48)$$

For a 2-level VSC, there are $2^3 = 8$ eight permutations, giving eight different combinations of output voltages. Table 2.1 shows the output voltage combinations of the 2L-VSC [41].

Table 2. 1: Different Output Voltage Combinations of a 2L-VSC [41]

s_{a1}	s_{b1}	s_{c1}	v_{a0}	v_{bo}	v_{co}	v_{an}	v_{bn}	v_{cn}
0	0	0	0	0	0	0	0	0
0	0	1	0	0	V_{dc}	$-V_{dc}/3$	$-V_{dc}/3$	$2V_{dc}/3$
0	1	0	0	V_{dc}	0	$-V_{dc}/3$	$2V_{dc}/3$	$-V_{dc}/3$
0	1	1	0	V_{dc}	V_{dc}	$-2V_{dc}/3$	$V_{dc}/3$	$V_{dc}/3$
1	0	0	V_{dc}	0	0	$2V_{dc}/3$	$-V_{dc}/3$	$-V_{dc}/3$
1	0	1	V_{dc}	0	V_{dc}	$V_{dc}/3$	$-2V_{dc}/3$	$V_{dc}/3$
1	1	0	V_{dc}	V_{dc}	0	$V_{dc}/3$	$V_{dc}/3$	$-2V_{dc}/3$
1	1	1	V_{dc}	V_{dc}	V_{dc}	$-V_{dc}/3$	$-V_{dc}/3$	$-V_{dc}/3$

2.4.1.2 Three-Level Neutral Point Clamped Voltage Source Converter Topology

Figure 2.10 shows a schematic diagram of a 3-Level 3-phase NPC VSC.

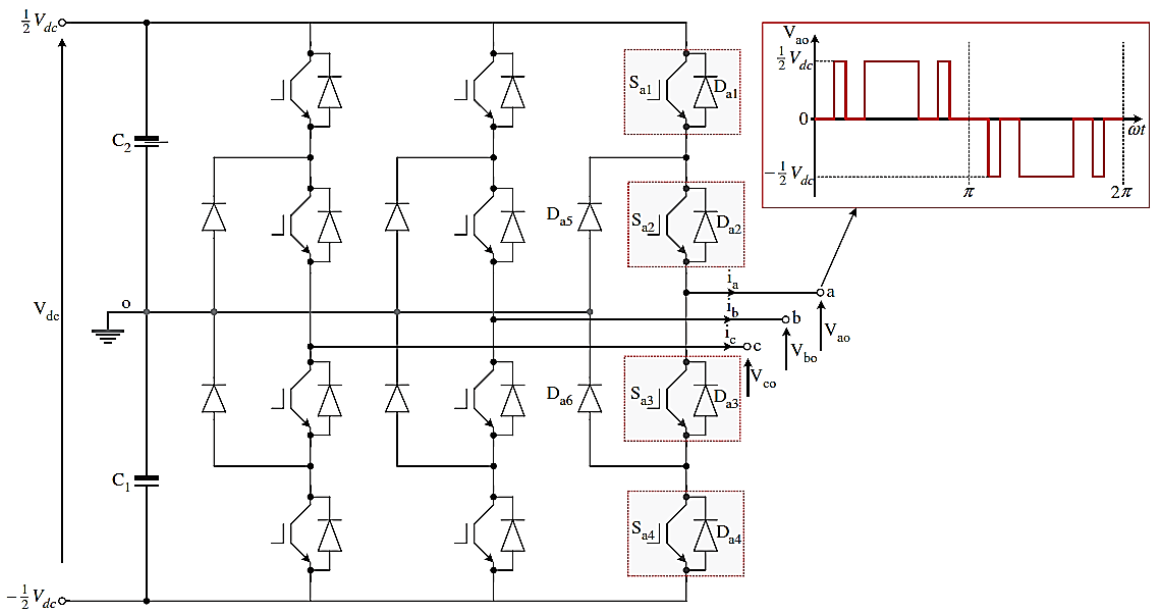

Figure 2. 10: Three-level NPC VSC [54]

There are four switches per phase in a 3-level NPC VSC. The converter generates phase voltage waveforms comprising of three levels ($\frac{V_{dc}}{2}, 0\ and\ -\frac{V_{dc}}{2}$) relative to the supply mid-point '*o*'. In this converter topology, switches (S_{a1}, S_{a3}) and (S_{a2}, S_{a4}) of phase *a* represent a complementary pair [41, 44]. Meaning, when S_{a1} is *on*, S_{a3} will be *off*, and if S_{a2} is *on*, then S_{a4} will be *off*, and the same

applies to phases *b* and *c* [50]. Two consecutive switches of each leg should be ON at any time to connect a voltage level from the series capacitors to the output. Table 2.2 presents the switch states that generate different voltage levels for phase *a* and the corresponding conduction paths [54].

Table 2. 2: Switch states that generate different voltage levels in the 3L NPC VSC and the conduction paths [54]

	Switch States				**Conduction path**	
Voltage level	s_{a1}	s_{a2}	s_{a3}	s_{a4}	$i_a > 0$	$i_a < 0$
$\frac{V_{dc}}{2}$	ON	ON	OFF	OFF	$s_{a1} and\ s_{a2}$	$D_{a1} and\ D_{a2}$
0	OFF	ON	ON	OFF	$s_{a2} and\ D_{a5}$	$s_{a3} and\ D_{a6}$
$-\frac{V_{dc}}{2}$	OFF	OFF	ON	ON	$D_{a3} and\ D_{a4}$	$s_{a3} and\ s_{a4}$

To guarantee proper operation of the 3L NPC VSC, the dc voltages across the DC-link capacitors should be balanced and kept at $\frac{V_{dc}}{2}$ across each capacitor.

2.4.2 The Grid-filter Model

Figure 2.11 presents the circuit diagram of a grid filter. A line filter is normally placed at the output of the GSC to attenuate the switching frequency harmonics.

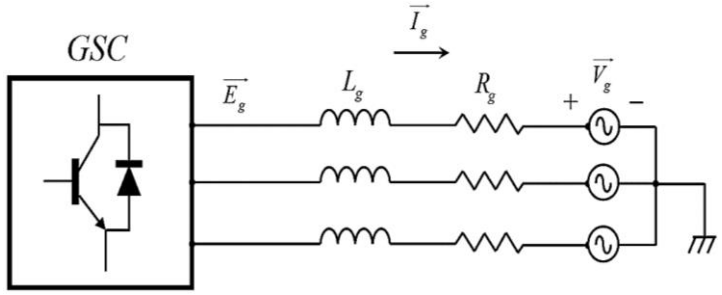

Figure 2. 11: Grid filter circuit [8]

The common filter types are the *L-type* [55] and *LCL-type* [56]. The *LCL-type* has better attenuation properties in the higher frequency range, which reduces the size of the required inductors [8]. According to [8], the *L-type* filter is sufficient for the DFIG system since the converters only need to handle 30% of the system's power. The grid is modeled as an ideal three-phase balanced voltage source. From Fig. 2.11, the three-phase equations of the grid-side circuit are expressed by (2.49) – (2.51), in the grid natural reference frame [41]:

$$\vec{E}_{ag} = \vec{I}_{ag}R_g + L_g\frac{d\vec{I}_{ag}}{dt} + \vec{V}_{ag} \tag{2.49}$$

$$\vec{E}_{bg} = \vec{I}_{bg}R_g + L_g\frac{d\vec{I}_{bg}}{dt} + \vec{V}_{bg} \tag{2.50}$$

$$\vec{E}_{cg} = \vec{I}_{cg}R_g + L_g\frac{d\vec{I}_{cg}}{dt} + \vec{V}_{cg} \tag{2.51}$$

Where;

- R_g, L_g represents the resistive part (Ω) and inductance (H) of the grid filter, respectively.
- $\vec{V}_{ag}, \vec{V}_{bg}, \vec{V}_{cg}$ represent the grid voltages (V), with ω_s as the electric angular speed (rad/s)
- $\vec{I}_{ag}, \vec{I}_{bg}, and\ \vec{I}_{cg}$ represent the current (A) flowing through the grid filter.
- $\vec{E}_{ag}, \vec{E}_{bg}, \vec{E}_{cg}$ represent the converter output voltages (V)

Transforming (2.49) – (2.51) to the synchronous rotating frame, the *d- and q*-components of the grid filter model are expressed by (2.52) and (2.53), respectively [50]:

$$\vec{E}_{gd} = \vec{I}_{gd}R_g + L_g\frac{d\vec{I}_{gd}}{dt} + \vec{V}_{gd} - \omega_s L_g I_{gq} \tag{2.52}$$

$$\vec{E}_{gq} = \vec{I}_{gq}R_g + L_g\frac{d\vec{I}_{gq}}{dt} + \vec{V}_{gq} + \omega_s L_g I_{gd} \tag{2.53}$$

The grid active and reactive powers are given by (2.54), respectively:

$$\left.\begin{aligned} P_g &= \frac{3}{2}(V_{gd}I_{gd} + V_{gq}I_{gq}) \\ Q_g &= \tfrac{3}{2}(V_{gq}I_{gd} - V_{gd}I_{gq}) \end{aligned}\right\} \tag{2.54}$$

2.4.3 The DC-Link Model

The DC-link which is common to the VSCs serves as an energy storage system and smoothens the power flow [35]. Figure 2.12 presents the schematic diagram of a DC-link connected between the RSC and GSC, where P_r and P_g represent the machine and grid power flow, respectively [8].

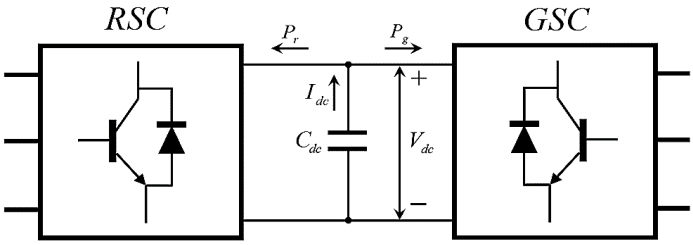

Figure 2. 12: DC-Link [8]

The energy that is stored in the DC-link capacitor is expressed by (2.55):

$$W_{dc} = \frac{1}{2}C_{dc}V^2{}_{dc} \tag{2.55}$$

Where the variables W_{dc}, C_{dc}, and V_{dc} represent the energy that is stored in the DC-link capacitor, the DC-link capacitance, and the DC-link voltage, respectively.

Considering the converter losses to be negligible, the power balance between the GSC and RSC to the energy stored is expressed by (2.56):

$$\frac{dW_{dc}}{dt} = V_{dc}C_{dc}\frac{dV_{dc}}{dt} = P_r + P_g \tag{2.56}$$

In practical operations, the DC-link voltage is normally controlled by the GSC, and hence, P_r from (2.56) can be regarded as a disturbance. Substituting the expression of P_g from (2.54) into (2.56) gives,

$$V_{dc}C_{dc}\frac{dV_{dc}}{dt} = P_r + \frac{3}{2}(V_{gd}I_{gd} + V_{gq}I_{gq}) \tag{2.57}$$

From (2.57), it is evident that V_{dc} remains constant when the power balance is met between the RSC and GSC, that is, $P_g = -P_r$.

2.5 Power Electronic Converter Modulation Techniques

2.5.1 Overview of the Converter Modulation Techniques

The commutation of switches in the VSCs is realized by synthesizing a sinusoidal signal that turns them *on* and *off* various times per fundamental period T_s [44]. This is done to control the magnitude of the fundamental components of the output voltages and to reduce the harmonic content in voltage and current waveforms [54]. Some of the well-developed modulation strategies include selective harmonic elimination (SHE), sinusoidal pulse width modulation (SPWM), and space vector pulse width modulation (SVPWM) [50, 54]. The SPWM is a modulation technique that has widely been used to control both single-phase and three-phase VSCs. The gating pulses are generated by comparing a low-frequency reference signal to a high-frequency carrier signal [44, 50]. SVPWM generates the AC output converter voltages based on the space vector representation of voltage in the α-β plane [41]. SVPWM uses the reference voltage space-vector to calculate the optimum switching pattern of the converter switches to achieve the desired space-vector voltage [57]. SVPWM has gained popularity in industrial applications in recent years because it achieves the best performance among other PWM techniques [58]. SVPWM is associated with optimized switching that reduces the switching losses, reduces harmonic distortions, and increases the DC-link voltage utilization [59]. Therefore, SVPWM is adopted in this research, and it will be discussed in more detail concerning its application in the modulation of 2L VSC and 3L NPC VSC switches.

2.5.2 Space Vector Pulse Width Modulation technique for a 2-Level VSC

2.5.2.1 Overview of the 2L SVPWM

SVPWM uses a space vector as a reference representing the Clarke transformation of the sinusoidal reference 3-phase voltages in the α-β plane [59]. The converter output voltages are transformed using (2.58) which is derived based on the vector alignments shown in Fig. 2.13 [57-59].

$$\begin{bmatrix} v_\alpha \\ v_\beta \end{bmatrix} = \frac{2}{3}\begin{bmatrix} 1 & -\frac{1}{2} & -\frac{1}{2} \\ 0 & \frac{\sqrt{3}}{2} & -\frac{\sqrt{3}}{2} \end{bmatrix}\begin{bmatrix} v_a \\ v_b \\ v_c \end{bmatrix} \tag{2.58}$$

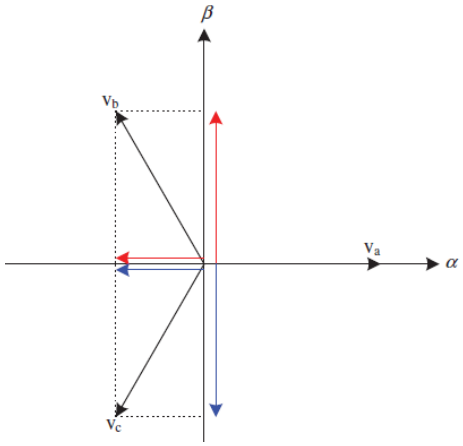

Figure 2. 13: Representation of the three-phase *abc* variables into the αβ plane [54]

The possible switch combinations of a 2L-VSC (8 permutations), corresponding output phase voltages, the resultant voltage vectors in the α-β plane, and their angular positions are given in Table 2.3.

Table 2. 3: Switching combinations, output phase voltages, voltage vectors, and their angular positions [54]

S_{a1}	S_{b1}	S_{c1}	V_{ao}	V_{bo}	V_{co}	v_α	v_β	$\lvert\vec{V}\rvert = \sqrt{v_\alpha^2 + v_\beta^2}$	$\theta = \tan^{-1}\frac{v_\beta}{v_\alpha}$	Vector
0	0	0	0	0	0	0	0	0	0°	V_0
0	0	1	0	0	V_{dc}	$-V_{dc}/3$	$-\sqrt{3}V_{dc}/3$	$2\,V_{dc}/3$	240°	V_5
0	1	0	0	V_{dc}	0	$-V_{dc}/3$	$\sqrt{3}V_{dc}/3$	$2\,V_{dc}/3$	120°	V_3
0	1	1	0	V_{dc}	V_{dc}	$-2V_{dc}/3$	0	$2\,V_{dc}/3$	180°	V_4
1	0	0	V_{dc}	0	0	$2V_{dc}/3$	0	$2\,V_{dc}/3$	0°	V_1
1	0	1	V_{dc}	0	V_{dc}	$V_{dc}/3$	$-\sqrt{3}V_{dc}/3$	$2\,V_{dc}/3$	300°	V_6
1	1	0	V_{dc}	V_{dc}	0	$V_{dc}/3$	$\sqrt{3}V_{dc}/3$	$2\,V_{dc}/3$	60°	V_2
1	1	1	V_{dc}	V_{dc}	V_{dc}	0	0	0	0°	V_7

From Table 2.3, the space vector diagram of the 2L-VSC is as shown in Fig. 2.14.

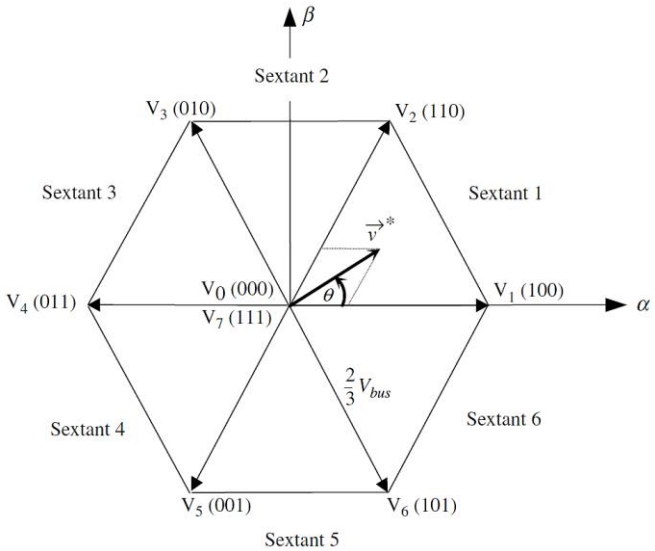

Figure 2. 14: The Space Vector Diagram of a 2-Level VSC [41]

The space vector diagram in Fig. 2.14 represents the eight output voltage combinations. The diagram has six sectors, separated by the six active vectors ($\vec{V}_{100}$, $\vec{V}_{110}$, $\vec{V}_{010}$, $\vec{V}_{011}$, $\vec{V}_{001}$, $\vec{V}_{101}$) which are 60° apart, and two zero vectors ($\vec{V}_{000}$, $\vec{V}_{111}$) in the center.

2.5.2.2 Implementation of the SVPWM for a 2-Level VSC

a) Sector Identification

The sector under which the reference vector is located is identified by the angle θ of the rotating reference voltage vector $\vec{V}_{ref}$ as shown in Table 2.4 [59].

Table 2. 4: Sector Identification [59]

Angle θ	Sector
$0 < \theta < \pi/3$	1
$\pi/3 < \theta < 2\pi/3$	2
$2\pi/3 < \theta < \pi$	3
$\pi < \theta < 4\pi/3$	4
$4\pi/3 < \theta < 5\pi/3$	5
$5\pi/3 < \theta < 2\pi$	6

b) Selection of the NTVs

SVPWM uses the Volt/Second balancing principle to approximate the reference vector $\vec{V}_{ref}$ in Fig. 2.15 as it rotates across all six sectors.

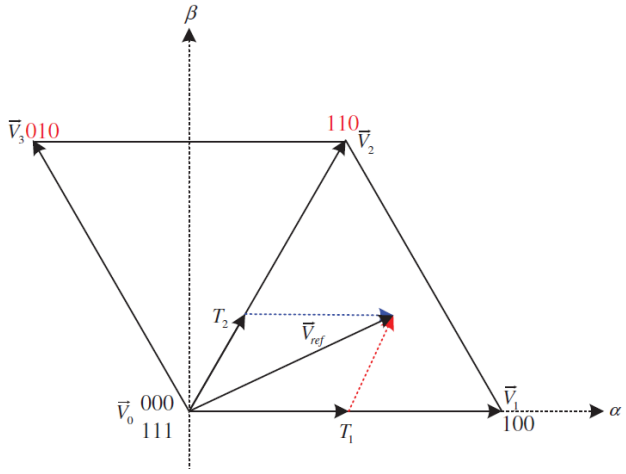

Figure 2. 15: Illustration of reference vector and dwell times calculations in sector 1 [54]

The reference vector in each sector is approximated by its nearest three vectors (NTVs) and their respective dwell times of the switch states over one switching period [60]., Two of these 3 NTVs are different, determined by the sector in which the reference vector is located [41], however, the *3rd* vector is always a zero vector V_o or V_7 [41]. Considering a reference vector in *Sector 1*, the required output voltage is synthesized using (2.59) [8, 50, 54]:

$$T_s\vec{V}_{ref} = T_1\vec{V}_1 + T_2\vec{V}_2 + T_0\vec{V}_0 \tag{2.59}$$

Where T_1, T_2, and T_0 represent the dwell times which should sum up to the switching period T_s.

c) Dwell Times Calculation

From Table 2.3, the voltage vectors $\vec{V}_1, \vec{V}_2 \; and \; \vec{V}_0$ can be expressed by (2.60):

$$\vec{V}_0 = 0$$
$$\vec{V}_1 = \frac{2}{3}V_{dc}\angle 0° = \frac{2}{3}V_{dc} \tag{2.60}$$
$$\vec{V}_2 = \frac{2}{3}V_{dc}\angle 60° = \frac{2}{3}V_{dc}(\cos 60° + j \sin 60°) = \frac{2}{3}V_{dc}\left(\frac{1}{2} + \frac{j\sqrt{3}}{2}\right)$$

$$\vec{V}_{ref} = V_{ref}\angle\theta = V_{ref}(\cos\theta + j \sin\theta)$$

Substituting (2.60) into (2.59) and equating the real and imaginary elements, gives these expressions:

$$\frac{2}{3}V_{dc}T_1 + \frac{1}{3}V_{dc}T_2 = T_s V_{ref} cos\theta \tag{2.61}$$

$$T_2 = \sqrt{3}T_s\frac{V_{ref}}{V_{dc}}sin\theta = mT_s sin\theta \; 0 < \theta < \frac{\pi}{3} \tag{2.62}$$

Where $m = \frac{\sqrt{3}V_{ref}}{V_{dc}}$ is the modulation index.

Substituting (2.62) into (2.61),

$$T_1 = T_s\frac{\vec{V}_{ref}}{V_{dc}}cos\theta - \frac{1}{3}mT_s sin\theta = mT_s \sin(\frac{\pi}{3} - \theta) \tag{2.63}$$

The dwell time of zero vectors is calculated using (2.64):

$$T_0 = T_s - T_1 - T_2 \tag{2.64}$$

The general expressions for calculating the dwell times T_1 and T_2 in other sectors are given by (2.65)[59]

$$\left.\begin{aligned} T_1 &= mT_s \sin(\frac{n}{3}\pi - \theta) \\ T_2 &= mT_s \sin(\theta - \frac{n-1}{3}\pi) \end{aligned}\right\} \tag{2.65}$$

Where *n* represents the sector number.

The linear converter modulation range is determined by the largest circle that can be contained within the space vector diagram given in Fig. 2.15 [8]. The maximum output voltage that can be achieved within the linear modulation range is given by (2.66) [8], corresponding to the amplitude shown in Fig. 2.16.

$$V_{max} = \frac{V_{dc}}{\sqrt{3}} \tag{2.66}$$

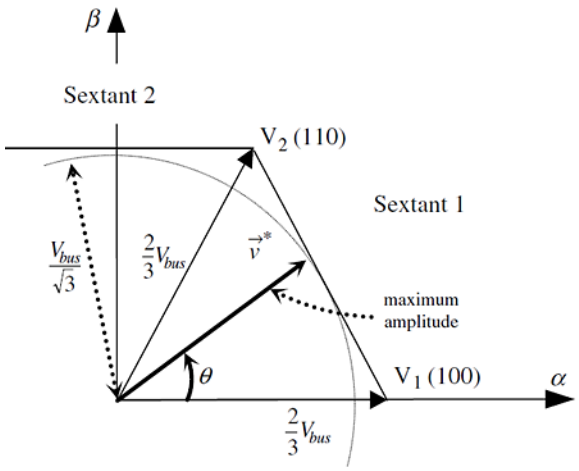

Figure 2. 16: maximum fundamental component amplitude with SVM [41]

d) Duty cycle calculation

The duty cycles of the converter switches are determined using the dwell times obtained in (2.64) and (2.65), based on the sector in which the reference voltage is located [59]. Seven (7) switching states in each sector start and end with a zero vector [61]. Considering a reference vector located in sector one (1), this corresponds to these switching states *000 – 100 – 110 – 111 – 110 – 100 – 000* which can be graphically represented as shown in Fig. 2.17. Diving the period T_s among these switching states gives (2.67) [61]:

$$T_s = \frac{T_0}{4} + \frac{T_1}{2} + \frac{T_2}{2} + \frac{T_0}{2} + \frac{T_2}{2} + \frac{T_1}{2} + \frac{T_0}{4} \tag{2.67}$$

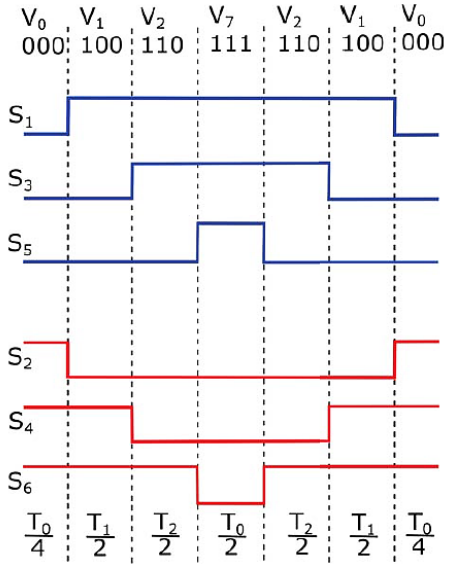

Figure 2. 17: Representation of sector one's switching states [59]

From the representation illustrated in Fig. 2.17, the duty cycles of the upper switches can be presented in terms of the dwell times using (2.68) [59]:

$$S_{a1} = T_1 + T_2 + \frac{T_0}{2}; \qquad S_{b1} = T_2 + \frac{T_0}{2}; \qquad S_{c1} = \frac{T_0}{2} \tag{2.68}$$

The duty cycles of the upper switches in different sectors can be determined by interchanging the expressions in (2.68) as shown in Table 2.5 [41].

Table 2. 5: Duty Cycle Calculation for each sector as per changes in phases [41]

SECTOR					
1	2	3	4	5	6
$S_{a1} \rightarrow S_{a1}$	$S_{a1} \rightarrow S_{b1}$	$S_{a1} \rightarrow S_{c1}$	$S_{a1} \rightarrow S_{c1}$	$S_{a1} \rightarrow S_{b1}$	$S_{a1} \rightarrow S_{a1}$
$S_{b1} \rightarrow S_{b1}$	$S_{b1} \rightarrow S_{a1}$	$S_{b1} \rightarrow S_{a1}$	$S_{b1} \rightarrow S_{b1}$	$S_{b1} \rightarrow S_{c1}$	$S_{b1} \rightarrow S_{c1}$
$S_{c1} \rightarrow S_{c1}$	$S_{c1} \rightarrow S_{c1}$	$S_{c1} \rightarrow S_{b1}$	$S_{c1} \rightarrow S_{a1}$	$S_{c1} \rightarrow S_{a1}$	$S_{c1} \rightarrow S_{b1}$

Therefore, the duty cycles of the three upper switches under different sectors are calculated from the dwell times as shown in Table 2.6 [59].

Table 2. 6: Duty Cycles for Upper Switches for different Sectors

Sector	**Duty Cycles for Upper Switches**
1	$S_{a1} = T_1 + T_2 + \frac{T_0}{2};\ S_{b1} = T_2 + \frac{T_0}{2};\ S_{c1} = \frac{T_0}{2}$
2	$S_{a1} = T_1 + \frac{T_0}{2};\ S_{b1} = T_1 + T_2 + \frac{T_0}{2};\ S_{c1} = \frac{T_0}{2}$
3	$S_{a1} = \frac{T_0}{2};\ S_{b1} = T_1 + T_2 + \frac{T_0}{2};\ S_{c1} = T_2 + \frac{T_0}{2}$
4	$S_{a1} = \frac{T_0}{2};\ S_{b1} = T_1 + \frac{T_0}{2};\ S_{c1} = T_1 + T_2 + \frac{T_0}{2}$
5	$S_{a1} = T_2 + \frac{T_0}{2};\ S_{b1} = \frac{T_0}{2};\ S_{c1} = T_1 + T_2 + \frac{T_0}{2}$
6	$S_{a1} = T_1 + T_2 + \frac{T_0}{2};\ S_{b1} = \frac{T_0}{2};\ S_{c1} = T_1 + \frac{T_0}{2}$

e) Deadtime addition and PWM generation

After calculating the duty cycles, the *ON* and *OFF* switching times of each switch can be computed to generate the corresponding pulses of the switches [59]. This is realized by comparing a repeated ramp signal to the duty cycles as illustrated in Fig. 2.18 to provide the PWM signals of the switches [59]. A dead time is added between the *ON* states of the upper and lower switches to avoid short-circuiting the converter legs [59].

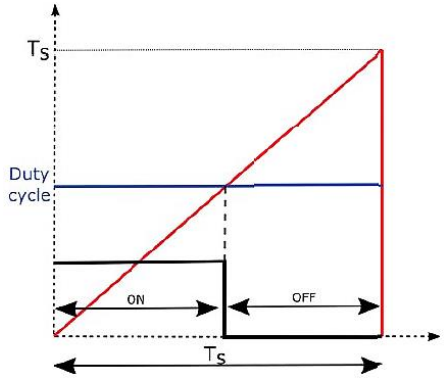

Figure 2. 18: Ramp Vs Duty cycle comparison [59]

2.5.3 Space Vector Pulse Width Modulation technique for a 3-Level NPC VSC

2.5.3.1 Overview of the 3-Level SVPWM

One major drawback in the operation of a 3L NPC VSC is the unbalance of the DC-link neutral point voltage which causes current to flow in the neutral line, and if not controlled, this results in completely discharging one of the DC-link capacitors [8]. In three-level NPC VSCs, proper modulation is required to maintain the voltage across each dc-link capacitor at half the value of the total dc-link voltage, i.e., $\frac{1}{2}V_{dc}$. SVPWM incorporates an algorithm to balance the voltage across the DC–link capacitors [41, 62]. The 3-Level NPC VSC gives 3^3=27 switching states as shown in Fig. 2.19 [41].

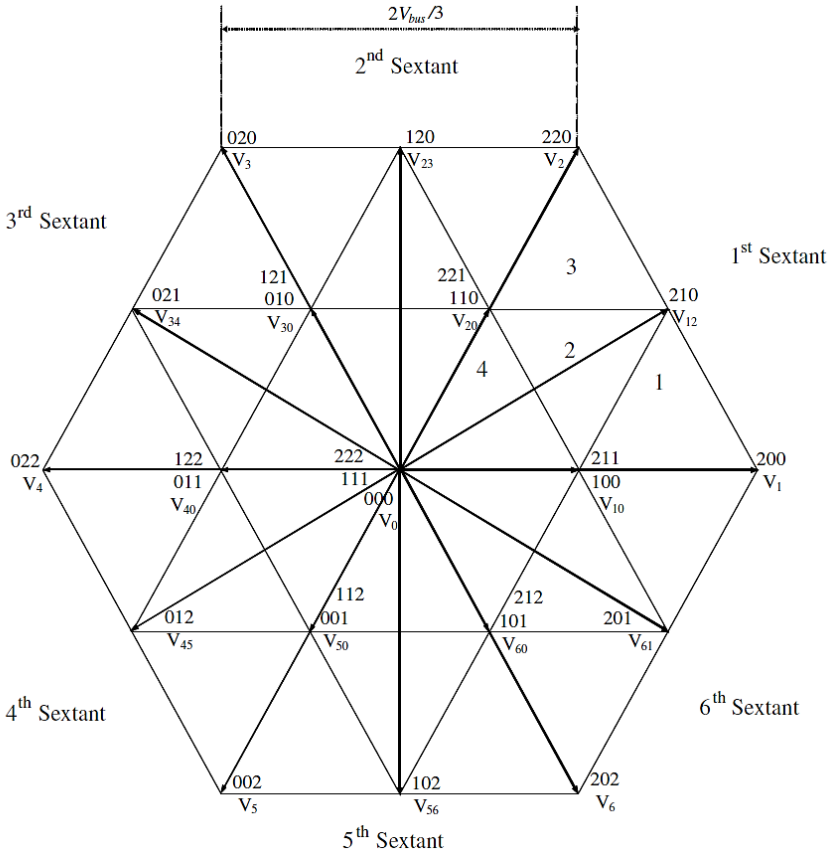

Figure 2. 19: 3-Level VSC SVPWM Diagram [41]

The 3-Level (3L) SVPWM diagram in Fig. 2.19 is divided into *six sectors*, whereby each sector is partitioned into *four regions*. The 3-level switching vectors are placed into six groups which are described as follows [8]:

- ***Large vectors*** [$\vec{V}_{200}$, $\vec{V}_{220}$, $\vec{V}_{020}$, $\vec{V}_{022}$, $\vec{V}_{002}$, $\vec{V}_{202}$]: vectors with the highest amplitudes, connecting the phase output voltages to either positive or negative terminals of the DC-bus [8]. They do not contribute to the charging and discharging of the DC-link capacitors.
- ***Medium vectors*** [$\vec{V}_{210}$, $\vec{V}_{120}$, $\vec{V}_{021}$, $\vec{V}_{012}$, $\vec{V}_{102}$, $\vec{V}_{201}$]: The amplitude of these vectors defines the maximum output voltage that can be achieved in the linear modulation range [41].

Medium vectors connect phase output voltages to a neutral point thereby charging or discharging the DC-link capacitors.

- ***Short vectors*** [$\vec{V}_{100/211}$, $\vec{V}_{110/221}$, $\vec{V}_{010/121}$, $\vec{V}_{011/122}$, $\vec{V}_{001/112}$, $\vec{V}_{101/212}$]: their amplitudes are half those of the large vectors and they connect two-phase output voltages to a single point on the DC-bus [8]. For short vectors, two different switching combinations produce the same phase output voltage, hence, they are vector pairs.
- ***Zero vectors*** [$\vec{V}_{000}$, $\vec{V}_{111}$, $\vec{V}_{222}$]: they connect all phase output voltages to a single point on the DC-bus [8], thus producing zero voltages and currents through the neutral point.

The same Volt/Second balancing principle implemented for the 2L VSC in the previous subsections can be equally applied to the 3L NPC VSC's SVPWM as outlined in [61]. The dwell times for each vector of the NTVs can be calculated based on trigonometric relations between $\vec{V}_{ref}$ and θ [8]. For the 3L NPC VSC, NTVs are chosen depending on the sector and the region in which $\vec{V}_{ref}$ is in Fig. 2.19. This leads to complex and time-consuming computations with the involvement of trigonometric equations. Therefore, a novel dwell time calculation technique discussed in [63] is implemented in this thesis as outlined in the following subsections to carry out all SVPWM computations.

2.5.3.2 Duty Cycle Calculations using Projections

From the Volt/Second balancing principle, a set of three vectors in an $\alpha\beta$ plane can generate a reference vector $\vec{V}_{ref}$ in this plane by averaging the expression given by (2.59) [63]. The reference vector $\vec{V}_{ref}$ is required to be in the triangular region given by the three vectors as shown in Fig. 2.20 [8].

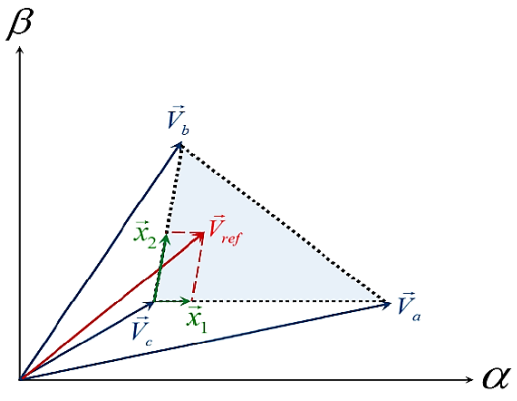

Figure 2. 20: Limiting area for $\vec{V}_{ref}$ [8]

The reference vector $\vec{V}_{ref}$ is projected onto the triangular boundary by $\vec{x}_1$ and $\vec{x}_2$, which are the scalar magnitudes of the vector projections that join the extremes of $\vec{V}_c$ to $\vec{V}_b$ and $\vec{V}_c$ to $\vec{V}_a$, respectively. Thus, $\vec{V}_{ref}$ is presented as [8, 63]:

$$\vec{V}_{ref} = \vec{V}_c + \vec{x}_1 + \vec{x}_2 \tag{2.69}$$

$$\vec{V}_{ref} = \vec{V}_c + x_1 \frac{\vec{V}_a - \vec{V}_c}{l_1} + x_2 \frac{\vec{V}_b - \vec{V}_c}{l_2} \tag{6.70}$$

Where l_1 and l_2 represents the lengths of vectors $\vec{V}_a - \vec{V}_c$ and $\vec{V}_b - \vec{V}_c$, respectively.

The expression in (2.70) can be rearranged to (2.71) as follow:

$$\vec{V}_{ref} = \frac{x_1}{l_1}\vec{V}_a + \frac{x_2}{l_2}\vec{V}_b + (1 - \frac{x_1}{l_1} - \frac{x_2}{l_2})\vec{V}_c \tag{2.71}$$

The coefficients,

$$\frac{x_1}{l_1}, \frac{x_2}{l_2} \text{ and } 1 - \frac{x_1}{l_1} - \frac{x_2}{l_2} \tag{2.72}$$

represents duty cycles when (2.71) is compared to (2.59).

Normalizing the vector diagram in Fig. 2.19 to obtain equilateral triangles with lengths $l_1 = l_2 = l$, the duty cycles are expressed as follow [8, 41, 63]:

$$d_a = x_1; \qquad d_b = x_2; \qquad d_c = 1 - x_1 - x_2 \tag{2.73}$$

Considering a reference vector to be in region four of the first sector of the 3L SV diagram as shown in Fig. 2.21.

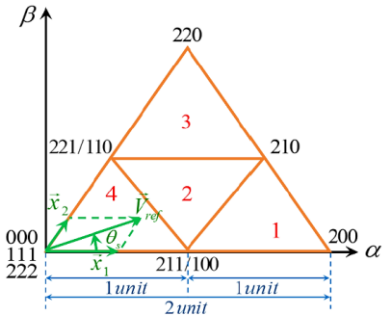

Figure 2. 21: Sector one of the SV diagram with $\vec{V}_{ref}$ in region four [8]

The NTVs of $\vec{V}_{ref}$ in Fig. 2.21 are $\vec{V}_a = \vec{V}_{211/100}, \vec{V}_b = \vec{V}_{221/110}, and\ \vec{V}_c = \vec{V}_{111}$. The vector projections coincide with the regional boundary, hence, the corresponding duty cycles for the NTVs are to be computed using (2.73) [8]. Figure 2.22 shows the cases when $\vec{V}_{ref}$ is located in the first, second and third region, respectively [8].

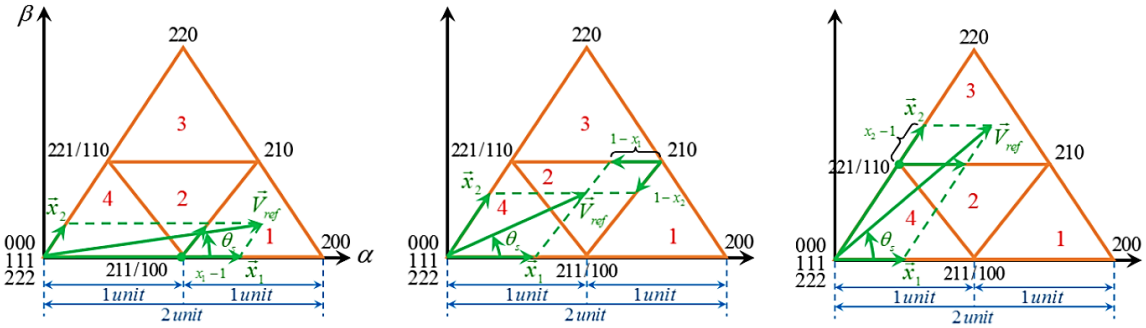

Figure 2. 22: Instances when $\vec{V}_{ref}$ is in the first, second & third region of sector 1 in the 3L SV diagram [8]

Table 2.7 shows the summary of duty cycle calculations and NTV selections in all regions of the first sector. Th duty cycles and the region where the voltage vectors are located are determined concurrently.

Table 2. 7: Duty cycle calculations in the four regions of sector one [8, 41]

Case	Region	NTVs	Duty Cycles
$x_1 > 1$	1	$\vec{V}_a = \vec{V}_{200}$ $\vec{V}_b = \vec{V}_{210}$ $\vec{V}_c = \vec{V}_{100/211}$	$d_a = x_1 - 1$ $d_b = x_2$ $d_c = 1 - d_a - d_b$
$x_1 \leq 1$ $x_2 \leq 1$ $x_1 + x_2 > 1$	2	$\vec{V}_a = \vec{V}_{100/211}$ $\vec{V}_b = \vec{V}_{110/221}$ $\vec{V}_c = \vec{V}_{210}$	$d_a = 1 - x_2$ $d_b = 1 - x_1$ $d_c = 1 - d_a - d_b$
$x_2 > 1$	3	$\vec{V}_a = \vec{V}_{210}$ $\vec{V}_b = \vec{V}_{220}$ $\vec{V}_c = \vec{V}_{110/221}$	$d_a = x_1$ $d_b = x_2 - 1$ $d_c = 1 - d_a - d_b$
$x_1 \leq 1$ $x_2 \leq 1$ $x_1 + x_2 \leq 1$	4	$\vec{V}_a = \vec{V}_{100/211}$ $\vec{V}_b = \vec{V}_{110/221}$ $\vec{V}_c = \vec{V}_{111}$	$d_a = x_1$ $d_b = x_2$ $d_c = 1 - d_a - d_b$

2.5.3.3 Sector One Reference Vector Equivalence

Considering the symmetry of the SV diagram, the vector equivalent to that of the first sector can be determined when $\vec{V}_{ref}$ lies in any of the other sectors. The equivalent transformation can be implemented by interchanging the a, b, and c variables [8]. Table 2.8 summarizes the equivalent variable interchanges of $\vec{V}_{ref}$ in sectors one to six.

Table 2. 8: Variable interchanges for sector one equivalent $\vec{V}_{ref}$ [8, 63]

SECTOR					
1	**2**	**3**	**4**	**5**	**6**
a	$a \rightarrow b$	$a \rightarrow c$	$a \rightarrow c$	$a \rightarrow b$	a
b	$b \rightarrow a$	$b \rightarrow a$	b	$b \rightarrow c$	$b \rightarrow c$
c	c	$c \rightarrow b$	$c \rightarrow a$	$c \rightarrow a$	$c \rightarrow b$

2.5.3.4 Sector selection and reference vector projections' (x_1 and x_2) determination

To compute the duty cycles for NTVs, the vector projections x_1 and x_2 are to be determined accordingly. The authors in [64] introduced a novel algorithm that is computationally efficient for multilevel converter SVM and easily executable in real-time processors such as the Field-Programmable Gate Array (FPGA). The algorithm is based on expressing $\vec{V}_{ref}$ on the *gh* reference frame, whereby the *g* and *h* axes are 60°, coinciding with the boundaries of the first sector as shown in Fig. 2.23 [64].

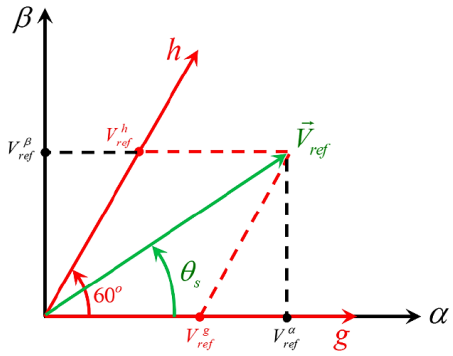

Figure 2. 23: Graphical representation of the *gh* reference frame [8]

The vector projections x_1 and x_2 are denoted by $V_{ref}^{g}\ and\ V_{ref}^{h}$, respectively on the *gh* coordinates. Since the controller provides the voltage vector $\vec{V}_{ref}$ in the synchronous reference frame, its *dq* components should be transformed onto the *gh* reference frame by (2.74), as graphically illustrated in Fig. 2.24 [8].

$$\begin{bmatrix} g \\ h \end{bmatrix} = \frac{2}{V_{dc}} \begin{bmatrix} \sin\left(\theta_e + \frac{2\pi}{3}\right) & \cos\left(\theta_e + \frac{2\pi}{3}\right) \\ \sin\theta_e & \cos\theta_e \end{bmatrix} \begin{bmatrix} d \\ q \end{bmatrix} \tag{2.74}$$

Variable $\frac{2}{V_{dc}}$ normalizes the reference voltage $\vec{V}_{ref}$ to a two-per-unit SV diagram. If $\vec{V}_{ref}$ is aligned with the synchronous d-axis, the transformation angle $\theta_e = \theta_s$, which is usually the case when grid voltage orientation is adopted.

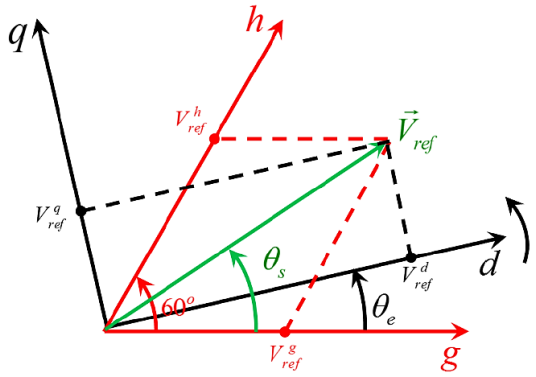

Figure 2. 24: Graphical representation of the *dq-gh* transformation [8]

Once the *gh* vector projection $V_{ref}^{g}\ and\ V_{ref}^{h}$ have been obtained, the sector in which the reference vector $\vec{V}_{ref}$ is located and the corresponding vector projections x_1 and x_2 can be determined. Table 2.9 summarizes the sector selection and equivalent vector projections in each sector based on the *gh* vector projections [8, 63].

Table 2. 9: Sector selection and corresponding vector projections based on $V_{ref}^{g}\ and\ V_{ref}^{h}$ [8]

***gh* Component**	**Sector**	**Equivalent x_1 and x_2**
$V_{ref}^{g} \geq 0, \quad V_{ref}^{h} \geq 0$	1	$x_1 = V_{ref}^{g}, \quad x_2 = V_{ref}^{h}$

$V_{ref}^{g} < 0, V_{ref}^{h} \geq 0, \quad (V_{ref}^{g} + V_{ref}^{h}) \geq 0$	2	$x_1 = -V_{ref}^{g}, \quad x_2 = V_{ref}^{g} + V_{ref}^{h}$
$V_{ref}^{g} < 0, V_{ref}^{h} \geq 0, \quad (V_{ref}^{g} + V_{ref}^{h}) < 0$	3	$x_1 = V_{ref}^{h}, \quad x_2 = -V_{ref}^{g} - V_{ref}^{h}$
$V_{ref}^{g} < 0, \quad V_{ref}^{h} < 0$	4	$x_1 = -V_{ref}^{h}, \quad x_2 = -V_{ref}^{g}$
$V_{ref}^{g} \geq 0, V_{ref}^{h} < 0, \quad (V_{ref}^{g} + V_{ref}^{h}) < 0$	5	$x_1 = -V_{ref}^{g} - V_{ref}^{h}, \quad x_2 = V_{ref}^{g}$
$V_{ref}^{g} \geq 0, V_{ref}^{h} < 0, \quad (V_{ref}^{g} + V_{ref}^{h}) \geq 0$	6	$x_1 = V_{ref}^{g} + V_{ref}^{h}, \quad x_2 = -V_{ref}^{h}$

2.5.3.5 Balancing the Voltage Across the DC-link Capacitors

As discussed previously, the unbalance in the voltage across the DC-link capacitors is one of the major challenges associated with the 3L NPC VSC. The neutral-point voltage can be achieved by exploiting the property of short vectors, which are double vectors that produce the same VSC output voltage [8]. The graphical illustration in Fig. 2.25 demonstrates how selecting the appropriate short vector influence the balancing of the neutral point [8] .

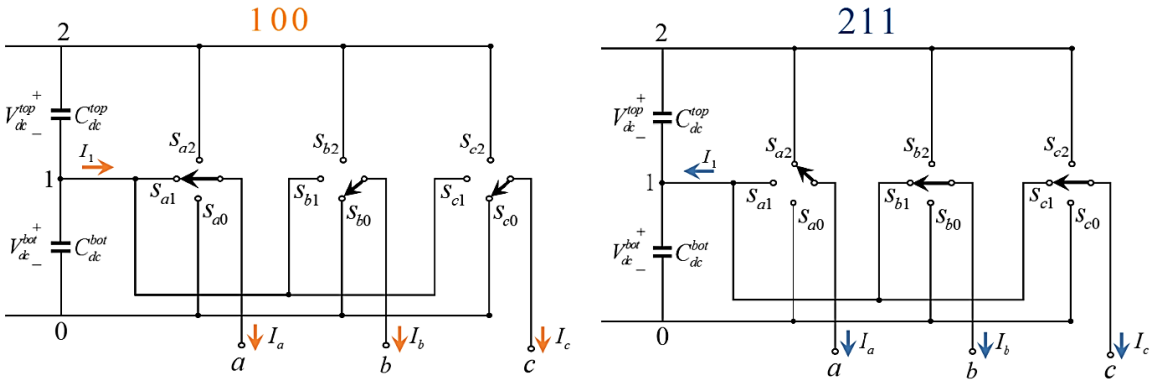

Figure 2. 25: The effect of selecting $\vec{V}_{100/211}$ on balancing the DC-link neutral point voltage [8]

The short vectors provoke different neutral current (I_1) flow directions, given that the load currents I_a, I_b, *and* I_c are non-zero. In the case that vector $\vec{V}_{100}$ is applied and the load current is positive, output *a* is connected to the mid-point, and thus $I_1 = I_a$. Therefore, the bottom capacitor C_{dc}^{bot} will discharge due to the positive I_1, and V_{dc}^{bot} will be reduced. On the other hand, the top capacitor C_{dc}^{top} will be charged given its polarity relating to the neutral point, hence, there will be no change in the total V_{dc} [8]. Alternatively, if vector $\vec{V}_{211}$ is applied, output *b* and *c* are connected to the mid-point, and thus $I_1 = I_b + I_c = -I_a$. Therefore, the bottom capacitor C_{dc}^{bot} will charge due to the negative I_1 and V_{dc}^{bot} will increase [8]. Checking the voltages of the capacitors V_{dc}^{top} and V_{dc}^{bot}, and the sign of the currents I_a *and* I_c, the short vectors are selected to equalize the capacitor voltages as outlined in Table 2.10. The currents I'_a *and* I'_c represent the equivalent phase currents for I_a *and* I_c which are interchanged according to Table 2.11 considering the sector where the voltage reference vector is situated.

Table 2. 10: Short vector selection based on capacitor voltage and current direction [41]

Selection for $\vec{V}_{100/211}$			**Selection for $\vec{V}_{110/221}$**		
$V_{dc}^{bot} > V_{dc}^{top}$	$I'_a > 0$	**Vector**	$V_{dc}^{bot} > V_{dc}^{top}$	$I'_c > 0$	**Vector**
0	0	$\vec{V}_{100}$	0	0	$\vec{V}_{221}$
0	1	$\vec{V}_{211}$	0	1	$\vec{V}_{110}$
1	0	$\vec{V}_{211}$	1	0	$\vec{V}_{110}$
1	1	$\vec{V}_{100}$	1	1	$\vec{V}_{221}$

Table 2. 11: Current Interchanges for Capacitor Voltage Balancing [41]

Equivalent Current	**SECTOR**					
	1	2	3	4	5	6
I'_a	I_a	I_b	I_b	I_c	I_c	I_a
I'_c	I_c	I_c	I_a	I_a	I_b	I_b

2.5.3.6 Vector Sequencing

Once the short vectors have been selected based on the capacitor voltages and the direction of resultant currents, the sequence of NTVs can be defined. Table 2.12 presents the sequence of NTVs for approximating $\vec{V}_{ref}$ in the first sector.

Table 2. 12: NTV Sequences for the first sector [41]

Region	**Short Vectors**	**NTV Sequence**	**State Transitions**
1	$\vec{V}_{100}$	$\vec{V}_{100} - \vec{V}_{200} - \vec{V}_{210} // \vec{V}_{210} - \vec{V}_{200} - \vec{V}_{100}$	2//2
	$\vec{V}_{211}$	$\vec{V}_{200} - \vec{V}_{210} - \vec{V}_{211} // \vec{V}_{211} - \vec{V}_{210} - \vec{V}_{200}$	2//2
2	$\vec{V}_{100} - \vec{V}_{110}$	$\vec{V}_{100} - \vec{V}_{110} - \vec{V}_{210} // \vec{V}_{210} - \vec{V}_{110} - \vec{V}_{100}$	2//2
	$\vec{V}_{100} - \vec{V}_{221}$	$\vec{V}_{100} - \vec{V}_{210} - \vec{V}_{221} // \vec{V}_{221} - \vec{V}_{210} - \vec{V}_{100}$	4//4
	$\vec{V}_{211} - \vec{V}_{110}$	$\vec{V}_{110} - \vec{V}_{210} - \vec{V}_{211} // \vec{V}_{211} - \vec{V}_{210} - \vec{V}_{110}$	2//2
	$\vec{V}_{211} - \vec{V}_{221}$	$\vec{V}_{210} - \vec{V}_{211} - \vec{V}_{221} // \vec{V}_{221} - \vec{V}_{211} - \vec{V}_{210}$	2//2
3	$\vec{V}_{110}$	$\vec{V}_{110} - \vec{V}_{210} - \vec{V}_{220} // \vec{V}_{220} - \vec{V}_{210} - \vec{V}_{110}$	2//2
	$\vec{V}_{221}$	$\vec{V}_{210} - \vec{V}_{220} - \vec{V}_{221} // \vec{V}_{221} - \vec{V}_{220} - \vec{V}_{210}$	2//2
4	$\vec{V}_{100} - \vec{V}_{110}$	$\vec{V}_{100} - \vec{V}_{110} - \vec{V}_{111} // \vec{V}_{111} - \vec{V}_{110} - \vec{V}_{100}$	2//2
	$\vec{V}_{100} - \vec{V}_{221}$	$\vec{V}_{100} - \vec{V}_{111} - \vec{V}_{221} // \vec{V}_{221} - \vec{V}_{111} - \vec{V}_{100}$	4//4
	$\vec{V}_{211} - \vec{V}_{110}$	$\vec{V}_{110} - \vec{V}_{111} - \vec{V}_{211} // \vec{V}_{211} - \vec{V}_{111} - \vec{V}_{110}$	2//2
	$\vec{V}_{211} - \vec{V}_{221}$	$\vec{V}_{111} - \vec{V}_{211} - \vec{V}_{221} // \vec{V}_{221} - \vec{V}_{211} - \vec{V}_{111}$	2//2

After selecting the NTVs and defining the optimal sequence, the next step is to link the duty cycles calculated from Table 2.7 to the corresponding NTVs. The phase interchanges outlined in Table 2.8 are utilized to determine the real sector where $\vec{V}_{ref}$ is located.

2.6 Control System of the DFIG-Based WECS

2.6.1 Overall Control System

The control of a DFIG generator is paramount to the operation of a WECS. The fundamental control strategy of a typical DFIG-based WECS can be subdivided into three levels as shown in Fig. 2.26: (1) DFIG control, (2) Wind turbine control, (3) Grid integration and wind farm control. The functionalities of these control levels are discussed in more detail by Lei *et al* in [35].

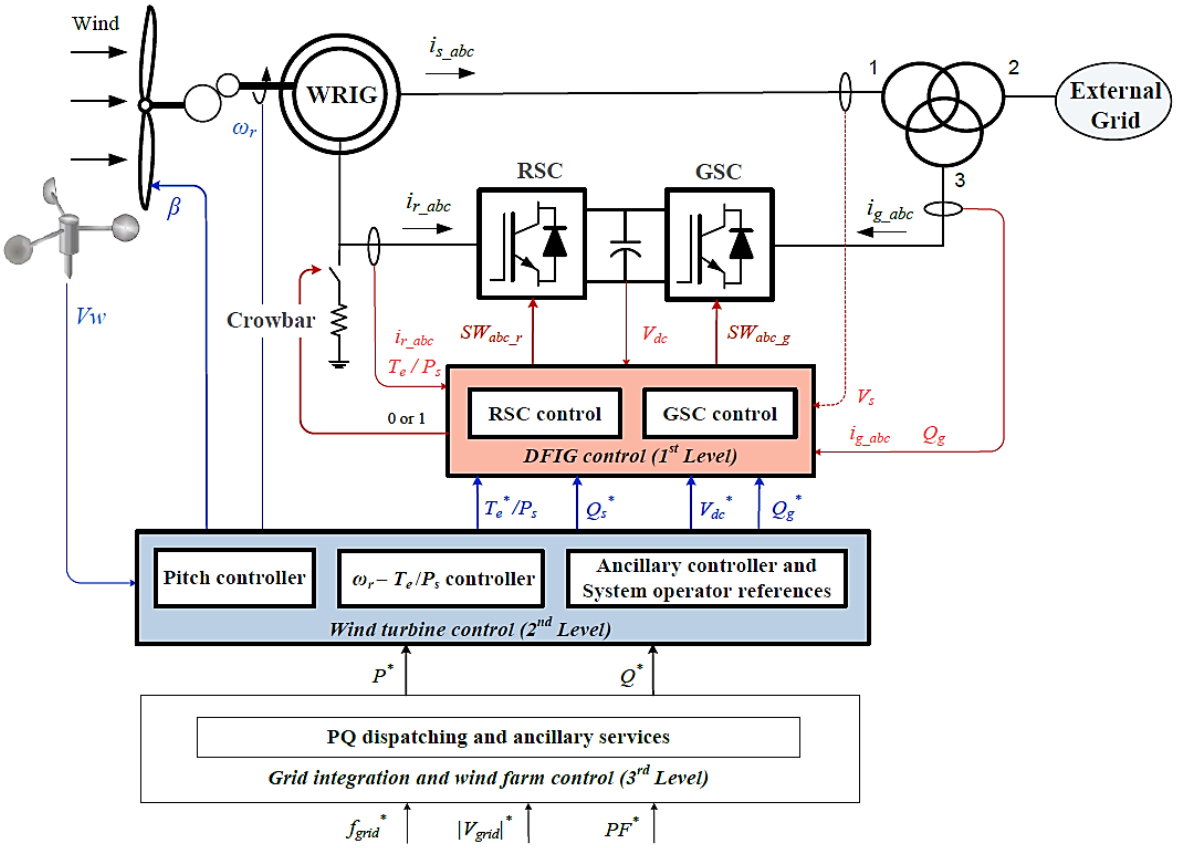

Figure 2. 26: Overall Control Structure of a DFIG-based WECS [35, 41]

2.6.2 General Controller Design based on the Vector Control Technique

According to [41, 65, 66], the vector control architecture is an industry control standard for variable speed drive systems such as DFIGs owing to its robust closed-loop performance. The DFIG control level presented in Fig. 2.26 can be expanded as shown in Fig. 2.27 to demonstrate the generic vector control architecture of a typical DFIG-based WECS. The vector control technique regulates the active and reactive power independently in the *dq* reference frame [44]. The synchronous reference frame transformations in the RSC and GSC controllers are enabled by the grid voltage and rotor slip angles, respectively. The grid angle is normally obtained using the phase-locked loop while the rotor slip angle can be obtained using an incremental encoder [8].

The RSC and GSC controllers have a dual control loop structure made up of an inner current control loop and an outer control loop [44]. The outer control loops are generally used to control the DC-link voltage, the AC voltage, and the active and reactive power [44]. The reference currents fed into the inner current control loops are obtained from the outer control loops. Fundamentally, the response time of inner current control loops needs to be shorter than that of the outer control loops to ensure a robust control system [44]. The vector controllers apply a feedforward compensation algorithm to decouple the dynamics of the *d* and *q* axes.

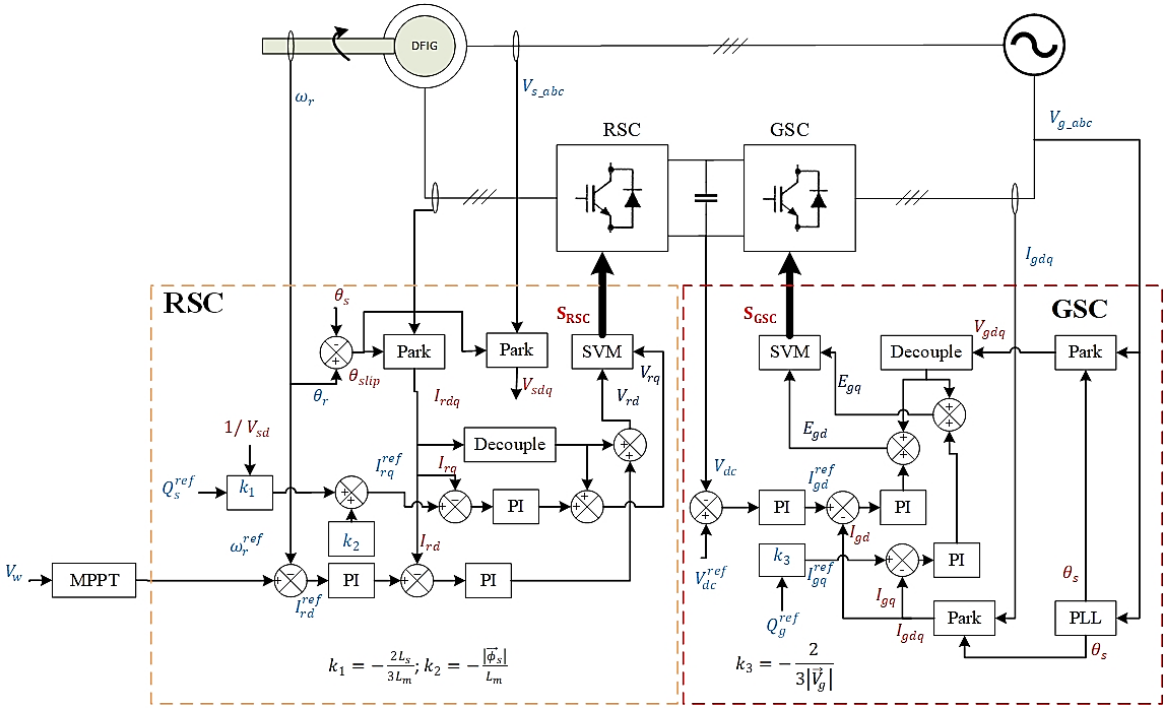

Figure 2. 27: Vector Control Implementation of a DFIG-based WECS [8]

2.6.2.1 Pole Placement Method

Most industrial control applications have adopted the "classical" feedback control system given in Fig. 2.28, which is an individual loop structure of a dual loop controller representing the Laplace transform of a time-domain system.

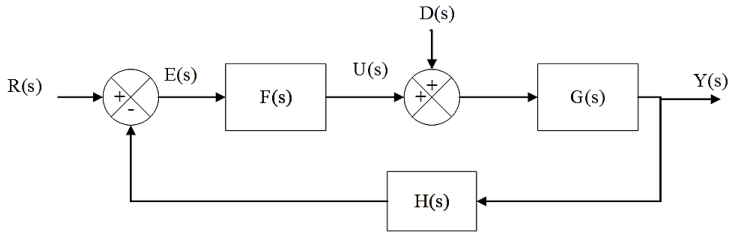

Figure 2. 28: Classical Feedback control structure [67]

The functions in Fig. 2.28 are defined as follow [8]:

- ***F(s), G(s), H(s)***: the transfer functions of the controller, plant process, and feedback filter.
- ***R(s), E(s), U(s), D(s), Y(s)****:* system signals representing the reference, feedback error, plant input, system disturbance, and plant output.

According to [8], the pole placement method involves matching the poles of a closed-loop system to a characteristic equation of a second-order system presented by (2.75) [67]:

$$G(s) = \frac{\omega_n^2}{s^2+2\zeta\omega_n s+\omega_n^2} \tag{2.75}$$

Where the variables ω_n and ζ represent the natural frequency of an undamped system and damping ratio, respectively. When these two values are changed, there will be changes in the transient response of the system relating to the settling time t_s, rise time t_r, peak time t_p, and percentage overshoot *%OS* of the system's step response [8]. Equation (2.76) relate the setting time, peak time and percentage overshoot to the natural frequency ω_n and damping ratio ζ as follows [67]:

$$t_s = -\frac{ln(0.02\sqrt{1-\zeta^2})}{\zeta\omega_n}$$

$$t_p = \frac{\pi}{\omega_n\sqrt{1-\zeta^2}} \tag{2.76}$$

$$\%OS = e^{\frac{-\zeta\pi}{\sqrt{1-\zeta^2}}} \times 100$$

Settling time is defined as the time it takes for the transient oscillations to reach and stay within ±2% of its steady-state value [44]. Whereas the peak time is defined as the time taken for the damped oscillation to reach the maximum peak [8], and percentage overshoot refers to the amount that the waveform overshoots the steady-state value at peak time [8, 67]. Rise time refers to the time required for the waveform to rise from 0.1 to 0.9 of the final value. The rise time generally increases with increasing damping ratio ζ [8]. Designing a controller using a pole placement method requires that the expected values of these design specifications be known, and compromises are made for the less imperative requirements. Consider a general transfer function of a first-order system presented in (2.77):

$$G_{1st}(s) = \frac{1}{As+B} \tag{2.77}$$

Assuming unity feedback and no disturbance in the classical feedback control structure presented in Fig. 2.28, that is, $H(s) = 1\ and\ D(s) = 0$, with the process plant represented by the first-order system in (2.76), the controller's transfer function *F(s)* can be implemented as a proportional-integral (PI) controller given by (2.78) [67]:

$$F(s) = PI(s) = K_P + \frac{K_I}{s} \tag{2.78}$$

Where K_P and K_I represent the proportional and integral gains of the PI controller, respectively. The open-loop system's transfer function can be derived by substituting (2.77) and (2.78) into the control structure in Fig. 2.28 and following the subsystem reduction procedure outlined in [67]:

$$G_{open}(s) = G_{1st}(s)PI(s) = \frac{1}{As+B} \times \left(K_P + \frac{K_I}{s}\right) = \frac{K_p s+K_I}{As^2+Bs} \tag{2.79}$$

The closed-loop system's transfer function can be derived from (2.79) as follow:

$$G_{cl}(s) = \frac{Y(s)}{R(s)} = \frac{G_{open}(s)}{1+G_{open}(s)} = \frac{\frac{K_P}{A}s+\frac{K_I}{A}}{s^2+\frac{B+K_P}{A}s+\frac{K_I}{A}} \tag{2.80}$$

Expression (2.80) is a transfer function of a second-order system, which is the same as expression (2.75). From (2.80), the numerator indicates that there is a real zero at $s = -\frac{K_I}{K_p}$, however, the dynamics due to the closed-loop zero can be neglected considering that these zeros are located away from the dominant pole pair of a second-order system [8, 67]. Therefore, the first term in the numerator of expression (2.80) can be neglected to ensure that (2.80) resembles expression (2.75). Therefore,

$$G_{cl}(s) = \frac{\frac{K_I}{A}}{s^2+\frac{B+K_P}{A}s+\frac{K_I}{A}}$$

$$G_{cl}(s) \approx G_{2nd}(s) \tag{2.81}$$

$$\therefore \frac{\frac{K_I}{A}}{s^2+\frac{B+K_P}{A}s+\frac{K_I}{A}} = \frac{\omega_n^2}{s^2+2\zeta\omega_n s+\omega_n^2}$$

Therefore, for a first-order plant model, equating the numerator and denominator coefficients in (2.81), the K_P *and* K_I gains of a compensator are derived and expressed by (2.82):

$$\left.\begin{aligned} K_I &= \omega_n^2 A \\ K_P &= 2\zeta\omega_n A - B \end{aligned}\right\} \tag{2.82}$$

To ensure that there is an accurate approximation between $G_{cl}(s)$ and $G_{2nd}(s)$, pole placement tuning requires a simulation to be conducted to tune the PI gains and ensure that the closed-loop response is as desired [8, 66]. The tools commonly used to validate the controller performance are such as the Root Locus and Nyquist chart [8, 67].

2.6.2.2 Internal Model Control Technique

The internal model control (IMC) technique was initially developed for chemical engineering applications [8, 68]. However, its application has been extended to AC machine control as discussed in [8, 69]. Figure 2.29 presents the IMC structure.

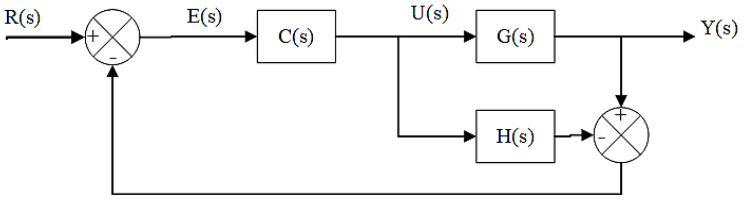

Figure 2. 29: IMC Structure [69]

The IMC structure comprises of an internal model $\hat{G}(s)$ in parallel with the process plant *G(s)* and the control loop is augmented by the control block *C(s)* [70].

If $\hat{G}(s) = G(s)$, then there will be no feedback in Fig. 2.29 [69]. Therefore, the closed-loop transfer function will match the open-loop dynamics as expressed by (2.83) [8]:

$$G_{cl}(s) = G_{open}(s) = C(s)G(s) \tag{2.83}$$

Therefore, the closed-loop system stabilizes if and only if *G(s)* and *C(s)* are both stable [69] [70]. From (2.83), if we let $C(s) = G^{-1}(s)$, the plant dynamics will be canceled, resulting in an output signal *Y(s)* equal to the set-point *R(s)*. However, this is not accomplishable since both *C(s)* and *G(s)* must be individually stable. *C(s)* becomes unstable if *G(s)* contains zeros in the right-half plane or has a denominator with a higher order. In this regard, the controller will not be suitable [8]. Furthermore, cancelling the plant dynamics results in large magnitudes of the control signals [69]. However, with some modifications, the idea can be explored by separating *G(s)* into two components and detuning the optimal controller with a low-pass filter as expressed in (2.84) [8, 69];

$$\left.\begin{aligned} G(s) &= G_A(s)G_M(s) \\ C(s) &= G^{-1}(s)L(s), where\ L(s) = \frac{\alpha^n}{(s+\alpha)^n} \end{aligned}\right\} \tag{2.84}$$

$G_A(s)$ contains all the right-half plane zeros and time delays for *G(s)*. The order of the low pass filter represented by a positive integer *n* should be chosen large enough to ensure that *C(s)* becomes proper, i.e. order of the denominator higher than the order of the numerator [69]. The system bandwidth α is made smaller to make the closed-loop system arbitrarily robust. The classical feedback control system in Fig. 2.28 can be rearranged to incorporate the IMC structure as presented in Fig. 2.30.

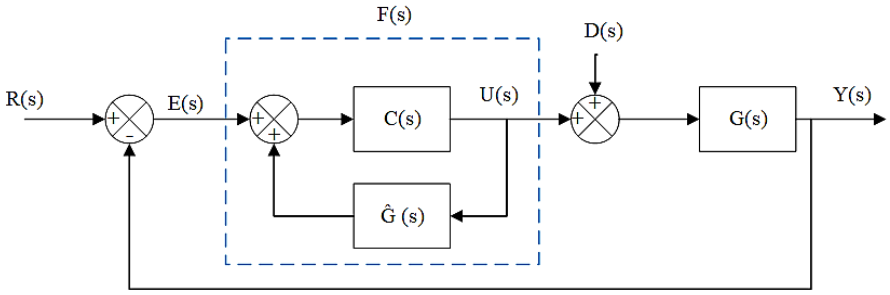

Figure 2. 30: Classical IMC Structure

From Fig. 2.30, it is observed that the classical controller *F(s)* has been replaced by the internal model $\hat{G}(s)$ and the IMC controller *C(s)*. This relationship is expressed by (2.85):

$$F(s) = \frac{C(s)}{1-\hat{G}(s)\,C(s)} \tag{2.85}$$

To demonstrate the steps of designing the controller based on the IMC, the same process presented in subsection 2.6.2.1 (pole placement method) is adopted. Considering a first order system from (2.77) and substituting the internal model controller *C(s)*'s transfer function from (2.84) into (2.85),

the suitable first-order system's transfer function can be expressed by (2.86), choosing a first-order low pass filter *L(s)*, i.e., *n = 1*:

$$\left.\begin{aligned} C(s) &= G^{-1}(s)\frac{\alpha}{s+\alpha} \\ \therefore F(s) &= G^{-1}(s)\frac{\alpha}{s} = A\alpha + \frac{B\alpha}{s} \end{aligned}\right\} \quad (2.86)$$

Comparing expression (2.86) to expressing (2.78), the K_P *and* K_I gains are expressed by (2.87):

$$\left.\begin{aligned} A\alpha + \frac{B\alpha}{s} &= K_P + \frac{K_I}{s} \\ \therefore K_P = A\alpha \text{ and } K_I &= B\alpha \end{aligned}\right\} \quad (2.87)$$

Considering the classical controller function from (2.86) the open-loop transfer function of the system in Fig. 2.30 is expressed by (2.88), assuming *D(s)* = 0:

$$G_{open}(s) = F(s) \times G(s) = G^{-1}(s)\frac{\alpha}{s} \times G(s) = \frac{\alpha}{s} \quad (2.88)$$

The closed loop transfer function is formulated from (2.88) and is expressed by (2.89):

$$G_{cl}(s) = \frac{Y(s)}{R(s)} = \frac{G_{open}(s)}{1+G_{open}(s)} = \frac{\alpha}{s+\alpha} \quad (2.89)$$

For the first order system, the closed loop system bandwidth α is related to the 2% settling time t_s and 10% - 90% rise time t_r by expression (2.90) [8, 67]:

$$t_s = \frac{4}{\alpha}\ ;\ t_r = \frac{\ln(9)}{\alpha} \quad (2.90)$$

Therefore, unlike the pole placement method which is associated with the challenge of adjusting two parameters; i.e., the PI gains, the IMC design technique entirely depends on the desired closed-loop bandwidth, which is related to the desired system response presented in (2.90) [8].

2.6.2.3 Practical Controller Implementation Issues

2.6.2.3.1 Active Damping

One of the drawbacks of the IMC is that the resulting control structure may reject the load disturbances poorly [71]. To investigate the disturbance rejection in a first-order system, consider the transfer function from the load disturbance *D(s)* to output signal *Y(s)* in (2.91) [36]:

$$\frac{Y(s)}{D(s)} = G_{DY}(s) = \frac{G(s)}{1+G(s)F(s)} \quad (2.91)$$

Substituting $G_{1st}(s)$ from (2.77) and *F(s)* from (2.86) into (2.91), the disturbance to the output transfer function can be expressed by (2.92) [8]:

$$G_{DY}(s) = \frac{s}{(s+\alpha)(As+B)} \quad (2.92)$$

If all parameters are known and the dynamics of *G(s)* are faster than the dynamics of the closed-loop system, the load disturbance rejection should be enough. However, the dynamics of the process plant *G(s)* are normally much slower compared to those of the closed-loop system, that is, the plant time constant $(-\frac{A}{B})$ is bigger than the closed-loop time constant $(-\frac{1}{\alpha})$. Therefore, the disturbance rejection is largely determined by the process plant and hence the disturbance rejection is very poor [35, 71]. The research studies in [8, 65, 71, 72] have discussed a method that is implemented to speed up the disturbance rejection for the IMC. The method is known as *active damping* which is based on introducing an inner-feedback loop with a gain G_a as depicted in Fig. 2.31, to introduce an additional degree of freedom.

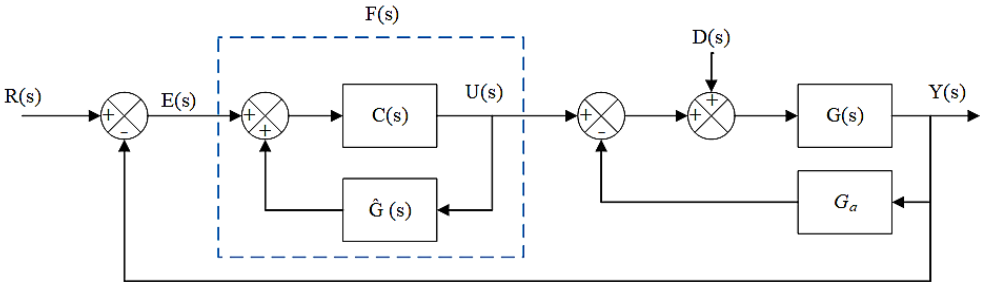

Figure 2. 31: Classical IMC structure with Active Damping

The gain can either be dynamic or static (constant). A constant gain is considered in this thesis which solely provides additional damping of the disturbance to ensure that the dynamics of the plant match those of the controller. In this regard, the transfer function in (2.92) becomes (2.93), with inclusion of the inner-feedback loop constant G_a [36]:

$$G_{DY}(s) = \frac{s}{(s+\alpha)(As+B+G_a)} \tag{2.93}$$

For the first-order system, it is possible to choose $G_a = \alpha A - B$, so that expression (2.93) reduces to (2.94):

$$G_{DY}(s) = \frac{s}{A(s+\alpha)^2} \tag{2.94}$$

The transfer function in (2.94) demonstrates that the output response due to the disturbance will be damped with the closed-loop time constant [8]. To ensure that the system does not become unstable, the inner-feedback loop constant must be greater than zero and the closed-loop bandwidth should have a minimum value given by (2.95) [8]:

$$\alpha_{min} > \frac{B}{A} \tag{2.95}$$

With the inclusion of active damping in the IMC structure, the expressions for computing the PI gains given by (2.87) change to (2.96):

$$\left.\begin{aligned} K_P &= A\alpha \\ K_I &= \alpha(B + G_a) \end{aligned}\right\} \tag{2.96}$$

2.6.2.3.2 Saturation and Integrator Anti-Windup

When implementing practical controllers, the control signals need to be limited/saturated to cater for the physical limitations of hardware equipment. For instance, for the proposed DFIG system, the outputs of the current and speed controllers should be kept within appropriate levels to avoid unfavorable DFIG operating conditions [8]. When the controller is saturated, an integral part of the PI controller accumulates the error between the feedback and the set-point value, this phenomena is referred to as integrator-windup. The integrator-windup appears as overshoots in the step response of the output signal when the controller returns to normal conditions after a saturated step response [8, 35, 71]. The integrator-windup challenge is overcome by implementing a simple and effective technique known as the *back-calculation method* [35, 71] which is based on modifying the reference value to ensure that the ideal controller output signal does not exceed the maximum value. Considering a classical feedback control structure shown in Fig. 2.28, where *F(s) = PI(s)* and the controller output is *U(s)* which is expressed by (2.97) [8]:

$$\left.\begin{aligned} U(s) &= k_p E(s) + k_I I(s) \\ where\ I(s) &= \frac{E(s)}{s} \end{aligned}\right\} \tag{2.97}$$

If the controller is to be saturated to $\bar{U}(s)$ as expressed in (2.98) due to a large change in the reference *R(s)*, the error *E(s)* should be modified to $E^*(s)$ to ensure that the output signal in (2.97) does not accumulate all the error due to the integral component $k_I I(s)$ [8]. In this case, $U(s) = \bar{U}(s)$ as depicted in (2.98):

$$\left.\begin{aligned} \bar{U}(s) &= U(s)|_{min}^{max} \\ \bar{U}(s) &= k_p E^*(s) + k_I I(s) \end{aligned}\right\} \tag{2.98}$$

Subtracting *U(s)* in (2.97) from $\bar{U}(s)$ in (2.98) and making $E^*(s)$ the subject of the formulae:

$$E^*(s) = \frac{1}{k_P}[\bar{U}(s) - U(s) + k_P E(s)] = E(s) + \frac{1}{k_P}[\bar{U}(s) - U(s)] \tag{2.99}$$

Therefore, the resulting controller's output signal with integrator anti-windup implemented is expressed by (2.100):

$$U(s) = k_p E(s) + \frac{k_I}{s} E^*(s) \tag{2.100}$$

It is evident from (2.100) that the proportional component used the original error signal whereas the integrator component uses the modified error to overcome the integrator windup challenge. Figure 2.32 shows the PI controller structures without and with the integrator anti-windup.

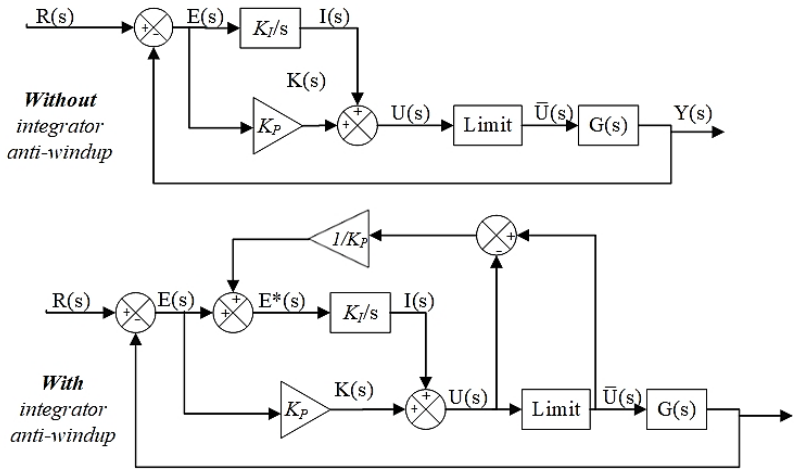

Figure 2. 32: PI Controllers without and with integrator anti-windup

2.6.2.3.3 Discretization

Majority of the modern control systems are developed using digital electronics that convert analog signals to discrete data, sampled at constant time intervals T_s [8]. The analog to digital conversion process is associated with signal delays that depend on the sampling frequency $F_s = 1/T_s$ [8]. For large sampling intervals, the delays cannot be neglected, and hence the system model needs to be discretized. For this investigation, the controller design is implemented on the FPGA, a digital electronic component that can achieve a high processing speed, which is limited by its onboard clock at 40 MHz. The integral component of the PI compensator is implemented digitally by using shift registers in LabVIEW FPGA, according to the expression in (2.101):

$$k_I I(k) = k_I[E^*(k) + E^*(k-1)] \tag{2.101}$$

Where *I(k)*, $E^*(k)$ and $E^*(k-1)$ represent the current sample of the integral component, the current sample of the modified error, and the previous sample of the modified error, respectively. The digital implementation of the integrator term $\frac{k_I}{s}$ from Fig. 2.32 is as shown in Fig. 2.33.

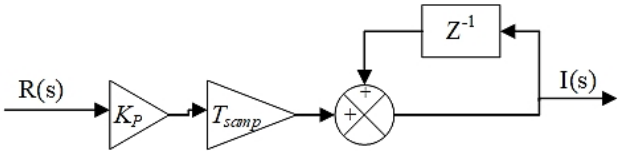

Figure 2. 33: Digital implementation of the integrator

2.6.2.3.4 Command Voltage Limiting

As mentioned previously, the vector control strategy consists of two control loops: the inner current control loop and the outer control loop. As discussed earlier, the outputs from the controllers in these loops need to be limited/saturated to certain values due to the physical limitations of the hardware equipment. Since the outer control loops provide the reference/set-point values for the inner loops on only one of the *dq* components, the controller outputs in the outer loops can be limited by saturating their numerical value.

This is done to ensure that the reference currents do not exceed the maximum current permitted for the machine and the converters. However, the inner loops provide both the *dq* components of the voltage control references which are used to generate the PWM signals for the converters, and hence these voltage references cannot be limited by numerical saturations. Instead, these control voltages must be saturated by limiting the modulus of their *dq* components [8]. The condition for saturating the inner current outputs, i.e., the control voltage references, can be expressed by (2.102) [8]:

$$\left.\begin{aligned} |\vec{V}_{com}| &\geq \frac{V_{dc}}{\sqrt{3}} \\ |\vec{V}_{com}| &= \sqrt{(V_{com}^{d})^2 + (V_{com}^{q})^2} \end{aligned}\right\} \quad (2.102)$$

Where $\vec{V}_{com}$, V_{com}^{d}, and V_{com}^{q} are the output control voltage vector and its dq components, respectively. The expression $\frac{V_{dc}}{\sqrt{3}}$ relates to the maximum voltage than can be achieved within the linear modulation range for SVPWM (eq. 2.66) presented in subsection 2.5 which covers the detailed discussion of the converter modulation schemes. The overmodulation range is beyond the scope of this project and hence these scenarios are not considered. Provided that the condition in (2.102) has been met, the actual voltage command saturation is expressed by (2.103):

$$|\vec{V}_{com}|_{max} = \frac{V_{dc}}{\sqrt{3}} \times \frac{|\vec{V}_{com}|}{|\vec{V}_{com}|} = \frac{V_{dc}}{\sqrt{3}} \times \frac{\sqrt{(V_{com}^{d})^2+(V_{com}^{q})^2}}{\sqrt{(V_{com}^{d})^2+(V_{com}^{q})^2}} \quad (2.103)$$

Expression (2.103) illustrates that the voltage saturation occurs at the limit of the converter's linear modulation range since $\frac{|\vec{V}_{com}|}{|\vec{V}_{com}|} = 1$ enforces a unity modulation index [8].

2.6.3 Phase-Locked Loop (PLL)

A PLL is commonly used to obtain the phase angle and frequency from the grid voltages [44]. The commonly implemented PLL is a synchronous PI PLL depicted in Fig. 2.34 [8, 73]:

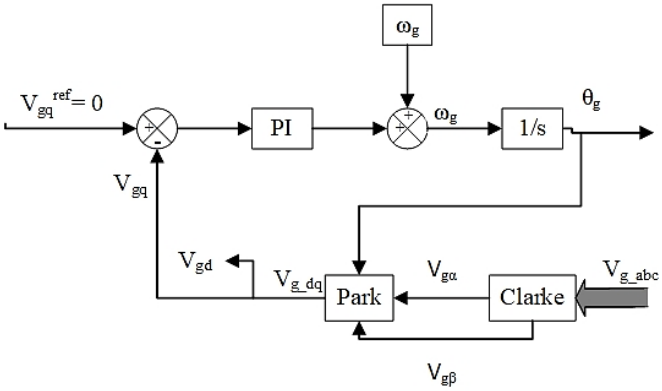

Figure 2. 34: Synchronous PI PLL

The feedback of the PLL is the grid's q-axis voltage V_{gq} whose magnitude dictates the phase angle of the converter's output current. The reference voltage V_{gq}^{ref} provides a set-point for locking the converter current onto the grid voltage at a specific phase angle [8].

The PI controller reduces the difference in the phase angles of the converter output current and grid voltage to zero. The reference grid angular frequency ω_g which acts as a feedforward term is then added to the output of the PI controller to produce the grid frequency. The integrator $\frac{1}{s}$ converts the grid frequency to the grid voltage angle θ_g which is needed to carry out the synchronous reference frame transformation. The PLL's closed-loop transfer function is expressed by (2.104):

$$G_{cl}(s) = \frac{k_P(s)+k_I}{s^2+k_p(s)+k_I} \tag{2.104}$$

Using the pole placement method, the PI gains are computed using (2.105) [8]:

$$k_P = 2\zeta\omega_n; \qquad k_I = \omega_n^2 \tag{2.105}$$

Whereby the values of the damping ratio ζ and natural frequency ω_n are to be selected based on the desired system's step response using (2.76).

2.6.4 Rotor-side Converter Control

2.6.4.1 DFIG Field alignments

The basis of the vector control strategy is to decompose the DFIG dynamic model presented in *subsection 2.3.4.2* into its *dq* components and refer the rotor currents in a synchronous reference frame, such that the *d*-axis is aligned with any stator electrical space vector [8, 41]. Two field alignments/ orientations are commonly used for the DFIG control system, namely, the grid voltage and stator flux orientation to simplify the DFIG's dynamic model. In this investigation, the grid voltage orientation is adopted, considering that it can be applied to both RSC and GSC control with ease, and hence, it has been discussed in more detail. The grid voltage orientation is based on aligning the *d*-axis d_s of the reference frame with the grid voltage space vector $\vec{V_g}$, both rotating at an angular frequency ω_s as shown in Fig. 2.35 [8]. In this regard, the stator *d*-axis voltage is constant and equal to the grid voltage vector, while the stator *q*-axis voltage is zero [74].

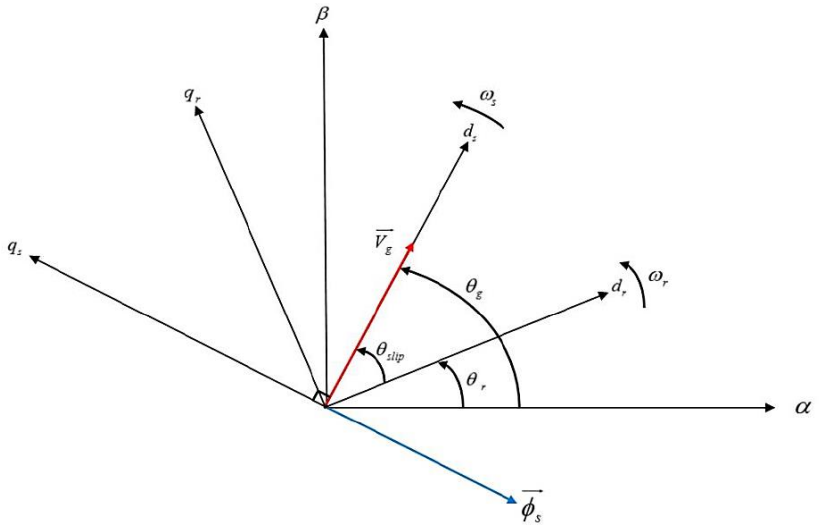

Figure 2. 35: Vector diagram of the Grid Voltage Orientation

The angle θ_g used for the gird voltage orientation is obtained from the PLL discussed in subsection 2.6.3. The angle (θ_{slip}) used to transform the rotor electrical quantities to the synchronous reference frame is given by (2.106):

$$\theta_{slip} = \theta_g - \theta_r \tag{2.106}$$

In the grid voltage orientation, the stator flux $\vec{\phi}_s$ is aligned with the quadrature component q_s of the stator voltage. In this regard, the *dq* components of the $\vec{V}_s$ and $\vec{\phi}_s$ are expressed in (2.107) [8]:

$$\begin{gathered} \vec{V}_s = \vec{V}_g \\ V_{sd} = \left|\vec{V}_g\right| \qquad V_{sq} = 0 \\ \phi_{sd} = 0 \quad \phi_{sq} = -\left|\vec{\phi}_s\right| \end{gathered} \tag{2.107}$$

Where $\left|\vec{V}_g\right|$ and $\left|\vec{\phi}_s\right|$ represent the amplitudes of the grid voltage and stator flux, respectively. Substituting the expressions in (2.107) into the DFIG dynamic model expressions derived in (2.42), the synchronous *dq* dynamic equations for the DFIG in grid voltage orientation are expressed in (2.108):

$$\begin{gathered} I_{sd} = \frac{-L_m I_{rd}}{L_s} \qquad\qquad I_{sq} = \frac{-\left|\vec{\phi}_s\right| - L_m I_{rq}}{L_s} \\ \therefore \phi_{sd} = L_\sigma I_{rd} \qquad \therefore \phi_{sq} = L_\sigma I_{rq} - \frac{-L_m}{L_s}\left|\vec{\phi}_s\right| \\ \therefore V_{rd} = R_r I_{rd} + L_\sigma \frac{dI_{rd}}{dt} - \omega_{slip} L_\sigma I_{rq} + \omega_{slip} \frac{L_m}{L_s}\left|\vec{\phi}_s\right| \\ \therefore V_{rq} = R_r I_{rq} + L_\sigma \frac{dI_{rq}}{dt} + \omega_{slip} \frac{L_m}{L_s} \frac{d\left|\vec{\phi}_s\right|}{dt} + \omega_{slip} L_\sigma I_{rd} \\ where\ L_\sigma\ is\ the\ leakage\ coefficient; \\ L_\sigma = L_r - \frac{L_m^2}{L_s} \\ V_{sd} = R_s I_{sd} + \omega_s \left|\vec{\phi}_s\right|; V_{sq} = 0 \end{gathered} \tag{2.108}$$

The stator resistance R_s is usually smaller than the reactance within the machine [8, 71]. Therefore, neglecting R_s and assuming a balanced grid (the stator is continuously excited by $\left|\vec{V}_g\right|$), then the stator flux magnitude $\left|\vec{\phi}_s\right|$ and ϕ_{sq} will be constant. The DFIG's dynamic equations in (2.108) can then be expressed by (2.109):

$$\begin{gathered} V_{rd} = R_r I_{rd} + L_\sigma \frac{dI_{rd}}{dt} - \omega_{slip} L_\sigma I_{rq} + \omega_{slip} \frac{L_m}{L_s}\left|\vec{\phi}_s\right| \\ V_{rq} = R_r I_{rq} + L_\sigma \frac{dI_{rq}}{dt} + \omega_{slip} L_\sigma I_{rd} \\ V_{sd} = \omega_s \left|\vec{\phi}_s\right| \qquad\qquad V_{sq} = 0 \end{gathered} \tag{2.109}$$

Where the term $\frac{L_m}{L_s}\left|\vec{\phi}_s\right|$ represents the *back-EMF* generated by the stator. The rotor *dq* equations in (2.109) are cross coupled which causes instabilities in the final controller design.

Good controller performance is obtained by decoupling the *d*- and *q*-axes by implementing a feed-forward compensation [71, 74], in which the cross-coupling and back-EMF terms are canceled out of the rotor *dq* equations. The *dq* output voltages are modified through the addition of the feedforward compensation terms given in (2.110) to these output voltages:

$$\begin{aligned} \boldsymbol{d-axis}: &\quad -\omega_{slip} L_\sigma I_{rq} + \omega_{slip} \frac{L_m}{L_s} \left|\vec{\phi}_s\right| \\ \boldsymbol{q-axis}: &\quad \omega_{slip} L_\sigma I_{rd} \end{aligned} \qquad (2.110)$$

After the cross-coupling terms in (2.110) have been removed from the rotor *dq* equations in (2.109), the final rotor voltage dynamic equations are expressed as:

$$\begin{aligned} V_{rd} &= R_r I_{rd} + L_\sigma \frac{dI_{rd}}{dt} \\ V_{rq} &= R_r I_{rq} + L_\sigma \frac{dI_{rq}}{dt} \end{aligned} \qquad (2.111)$$

Applying Laplace Transform to (2.111) yields (2.112):

$$\begin{aligned} V_{rd}(s) &= R_r I_{rd}(s) + sL_\sigma I_{rd}(s) \\ V_{rq}(s) &= R_r I_{rq}(s) + sL_\sigma I_{rq}(s) \end{aligned} \qquad (2.112)$$

Therefore, the rotor electrical plant model is given by (2.113), taking the rotor current as the output and the voltage as the input [8]:

$$G(s) = \frac{I_{rdq}(s)}{V_{rdq}(s)} = \frac{1}{sL_\sigma + R_r} \qquad (2.113)$$

Since R_r & L_σ are the same for V_{rd} & V_{rq}, the *dq* axis rotor current controllers are designed as the same. The expression for the developed electromagnetic torque T_e in the grid voltage orientation is derived by substituting (2.107) into (2.43) yields:

$$T_e = -\frac{3}{2} p_p \frac{L_m}{L_s} \left|\vec{\phi}_s\right| I_{rd} \qquad (2.114)$$

The expression in (2.114) shows that T_e is solely dependent on the rotor *d*-axis current I_{rd}. Substituting (2.107) and (2.108) into (2.44) – (2.47) yields the stator active and reactive powers as expressed in (2.115):

$$\begin{aligned} P_s &= -\frac{3}{2} \left|\vec{V}_g\right| \frac{L_m}{L_s} I_{rd} \\ Q_s &= -\frac{3}{2L_s} \left(\frac{\left|\vec{V}_g\right|^2}{\omega_s} + \left|\vec{V}_g\right| L_m I_{rq} \right) \end{aligned} \qquad (2.115)$$

The expression in (2.115) shows that the stator's active and reactive powers are controlled by regulating the rotor currents' I_{rd} and I_{rq} components, respectively. Depending on the application, the outer control loop can be implemented to control either the active power P_s, reactive power Q_s, or developed torque T_e. Therefore, equations (2.114) and (2.115) can be used to obtain the *d*- and *q-axis* rotor current references which are the inputs into the inner current controller loops.

2.6.4.2 RSC Controller Objective

The RSC control has a dual-loop structure whereby the outer loop is designed for speed control and the inner loop is for controlling the rotor's *dq* currents. The outer loop provides the set-points for the inner current control loop and hence the dynamics of the outer loops are much slower than those of the inner current loops [8]. The controllers are modeled using the IMC technique owing to its ease of implementation and accuracy compared to the pole placement method. Active damping has been incorporated into all controllers to improve the controllers' disturbance rejection capability.

2.6.4.3 Rotor Current Control Loop

Figure 2.36 shows the feedback control structure for the inner current control adopting a plant model given by (2.113) and including the active damping principle represented by the constant R_a.

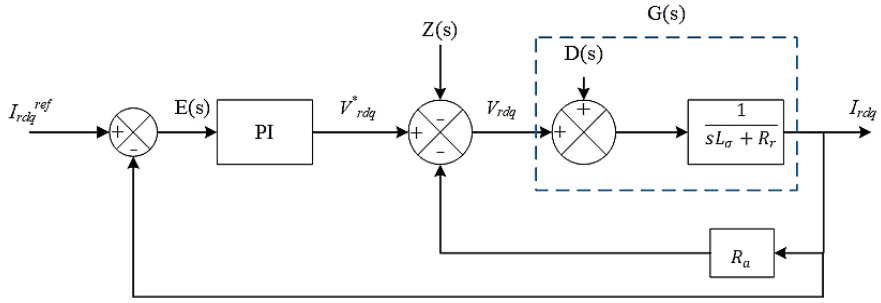

Figure 2. 36: RSC: Inner current control loop structure

From Fig. 2.36, I_{rdq}^{ref} is the rotor *dq* current set-points obtained from the outer control loop. The machine disturbance and feedforward compensation in (2.110) are represented by *D(s)* and *Z(s)*, respectively. The PI controller output V_{rdq}^* is altered by applying the active damping and feedforward compensation terms, resulting in the actual control voltage V_{rdq} which is an input into the plant model *G(s)*. Assuming the perfect decoupling (i.e., *Z(s) = D(s)*), the k_P and k_I gains of the PI controller are obtained from the rotor electrical plant model $\frac{1}{sL_\sigma + R_r}$, following the design procedure discussed in *subsection 2.6.2.2*. Therefore, the PI controller gains and the value of R_a are computed using (2.116) [8]:

$$k_P = \alpha_r L_\sigma; \qquad k_I = \alpha_r (R_r + R_a); \qquad R_a = \alpha_r L_\sigma - R_r \tag{2.116}$$

Where α_r represents the closed-loop bandwidth for the rotor current controller and has a minimum value given by [8]:

$$\alpha_{r_{min}} > \frac{R_r}{L_\sigma} \tag{2.117}$$

The numerical value of $\alpha_r$can be obtained by using its relationship with the system settling time given by (2.118) [8]:

$$t_s = \frac{4}{\alpha_r} \tag{2.118}$$

2.6.4.4 Outer Control Loops

2.6.4.4.1 Speed Control Loop

The speed control loop provides the *d*-component of the rotor's reference current [44]. The DFIG speed controller is designed using the machine's mechanical dynamics of a lumped mass model described by (2.6). Therefore, the plant model's transfer function is expressed by (2.119):

$$G(s) = \frac{\omega_m}{T_e} = \frac{1}{J_r s + D_r} \tag{2.119}$$

Figure 2.37 illustrates the speed control loop structure, including the active damping principle represented by the constant B_a.

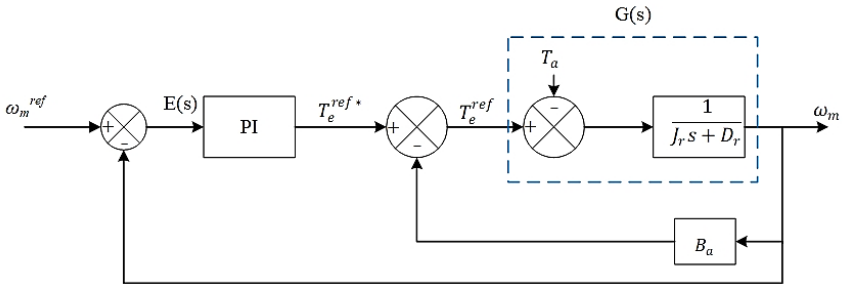

Figure 2. 37: RSC: Speed Control Loop structure

The desired machine speed is compared to the measured machine speed. The aerodynamic torque T_a acts as a disturbance. The speed controller output T_e^{ref*} is altered by the application of active damping to give the actual controller output T_e^{ref}, a torque reference from which the *d* component of the rotor reference current is computed by rearranging (2.114):

$$I_{rd}^{ref} = -\frac{2}{3}\frac{L_s}{L_m}\frac{T_e^{ref}}{p_p|\vec{\phi}_s|} \tag{2.120}$$

Considering the plant model in (2.119), the k_P and k_I gains of the PI controller and the value of B_a are computed using (2.121):

$$k_P = \alpha_\omega J_r; \qquad k_I = \alpha_\omega (D_r + B_a); \qquad B_a = \alpha_\omega J_r - D_r \tag{2.121}$$

Where α_ω represents the closed-loop bandwidth for the speed control loop which should be chosen to ensure that the dynamics of the outer loop are slower than those of the inner current control loop. For most applications, the outer loop's control bandwidth should at least be ten times slower than that of the inner loop [35]. Therefore:

$$\alpha_\omega \leq \frac{\alpha_r}{10} \tag{2.122}$$

2.6.4.4.2 Reactive Power Control Loop

Considering the grid voltage orientation, the reactive power control loop provides the *q*-component of the rotor's reference current [44]. The I_{rq}^{ref} is selected to ensure that the reactive power at the stator terminals is kept at zero. Simplifying the stator reactive power expression given in (2.115) yields (2.123):

$$Q_s = -\frac{3}{2L_s}\left(\frac{|\vec{V}_g|^2}{\omega_s} + |\vec{V}_g|L_m I_{rq}\right) = -\frac{3}{2L_s}\left(\frac{V_{sd}^2}{\omega_s} + V_{sd}L_m I_{rq}\right)$$

$$= -\frac{3}{2L_s}\left(V_{sd}|\vec{\phi}_s| + V_{sd}L_m I_{rq}\right) = -\frac{3L_m}{2L_s}V_{sd}\left(I_{rq} + \frac{|\vec{\phi}_s|}{L_m}\right) \quad (2.123)$$

$$I_{rq} = I_{rq}^{ref} = -\frac{2L_s}{3L_m V_{sd}}Q_s - \frac{|\vec{\phi}_s|}{L_m}$$

2.6.5 DFIG Grid Soft-Synchronization Dynamics

2.6.5.1 DFIG Open Stator Dynamics

To enable soft synchronization of the DFIG to the grid, it is a standard requirement that the initial voltage at the open stator terminals should be the same as the grid voltage, in terms of magnitude, frequency, and phase [8]. Therefore, the DFIG dynamic model derived in (2.45) should be modified in accordance with the dynamics of an open stator to enable a soft synchronization controller design. It is worth noting that, during open stator dynamics, there will be no current flowing in the stator winding and hence the DFIG dynamic model equations in (2.45) are modified as follow:

$$\vec{\psi}_s = L_m\vec{I}_r; \qquad \vec{\psi}_r = L_r\vec{I}_r$$

$$\vec{V}_s = L_m\frac{d\vec{I}_r}{dt} + j\omega_s L_m\vec{I}_r \quad (2.124)$$

$$\vec{V}_r = R_r\vec{I}_r + L_r\frac{d\vec{I}_r}{dt} + j\omega_{slip}L_r\vec{I}_r$$

From (2.124), it is observed that during open stator conditions, the magnetization of the DFIM only depends on the rotor currents, and the stator and rotor flux components, $\vec{\psi}_s$ and $\vec{\psi}_r$ are collinear with the rotor current $\vec{I}_r$. Therefore, when the machine is in the steady-state condition, i.e., $\frac{d\vec{I}_r}{dt} = 0$, a quadrature component of the stator voltage is induced in the stator winding. The space vector diagram that represents the open-stator dynamics of the DFIG is given in Fig. 2.38.

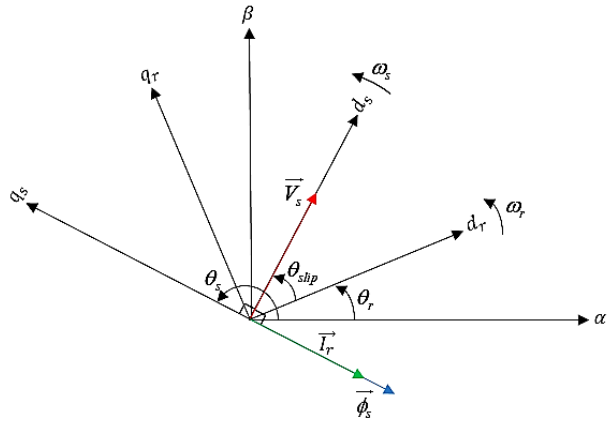

Figure 2. 38: Open Stator Vector Diagram

To achieve a soft synchronization of the stator to the grid, the following condition must be met:

$$\vec{V}_s = \vec{V}_g \quad (2.125)$$

It is reasonable to assume that before the DFIG is connected to the grid, the machine is operating in a steady-state and hence by considering (2.107), (2.124), and (2.125), the rotor currents required to induce the stator voltage should satisfy the conditions given by (2.126) [75, 76]:

$$I_{rd} = 0 \text{ and } I_{rq} = -\frac{|\vec{V}_g|}{\omega_s L_m} \tag{2.126}$$

The objective of the soft synchronization procedure is to avoid having high current spikes in the stator of the machine at the instant of connecting the machine to the grid. It is noted that substituting (2.126) into (2.115) equates the stator's active and reactive powers to zero if the condition in (2.126) is met which ensures that there is no power exchange between the stator and grid after synchronization. The rotor dynamic equation in (2.124) can be expressed in its *dq* components as follow:

$$\left.\begin{aligned} V_{rd} &= R_r I_{rd} + L_r \frac{dI_{rd}}{dt} - \omega_{slip} L_r I_{rq} \\ V_{rq} &= R_r I_{rq} + L_r \frac{dI_{rq}}{dt} + \omega_{slip} L_r I_{rd} \end{aligned}\right\} \tag{2.127}$$

As discussed previously, the controller's *dq* output voltages need to be decoupled for optimized controller performance. The feedforward compensation terms under the soft synchronization are given in (2.128):

$$\left.\begin{aligned} \boldsymbol{d-axis}&: \quad -\omega_{slip} L_r I_{rq} \\ \boldsymbol{q-axis}&: \quad +\omega_{slip} L_r I_{rd} \end{aligned}\right\} \tag{2.128}$$

The corresponding rotor electrical plant model is given by (2.129), taking the rotor current as the output and the voltage as the input:

$$G(s) = \frac{I_{rdq}(s)}{V_{rdq}(s)} = \frac{1}{sL_r + R_r} \tag{2.129}$$

2.6.5.2 Rotor Current Controller for Soft Synchronization

From (2.109) and (2.127), it is evident that the rotor electrical dynamics are different during the normal DFIG operation and the soft synchronization operation. It is observed that the time constant for normal operation is $\frac{L_\sigma}{R_r}$ and it changes to $\frac{L_r}{R_r}$ during synchronization. Moreover, the *d*-axis back-EMF component $\omega_{slip}\frac{L_m}{L_s}\left|\vec{\phi}_s\right|$ does not exist when the stator is open [75]. Since $L_\sigma \ll L_r$, the open-loop dynamics of the rotor circuit are faster when the DFIG is in normal operation with its stator connected to the grid and hence, this condition requires a shorter settling time [75]. Therefore, it is necessary to design a separate controller for synchronizing operations based on the plant model given in (2.129) to cater for the changing rotor electrical dynamics. The k_P and k_I gains of the PI controller for soft synchronization can be obtained from the rotor electrical plant model $\frac{1}{sL_r+R_r}$, following the design procedure discussed in *subsection 2.6.2.2*.

Therefore, the PI controller gains and the value of the active damping R_{soft} are computed using (2.130):

$$k_P = \alpha_{r_{soft}} L_r; \qquad k_I = \alpha_{r_{soft}} (R_r + R_{soft}); \qquad R_{soft} = \alpha_{r_{soft}} L_r - R_r \tag{2.130}$$

Where $\alpha_{r_{soft}}$ represents the closed-loop bandwidth for the soft synchronization rotor current controller and has a minimum value given by (2.131):

$$\alpha_{r_{soft\_min}} > \frac{R_r}{L_r} \tag{2.131}$$

2.6.5.3 Practical Implementation of the DFIG Soft Synchronization

When designing the DFIG's control system, it is vital to know the electrical position of the rotor for both soft synchronization and normal operation. In this research study, the rotor angle is obtained using an *RS58-0/1000 shaft encoder* that is coupled to the shaft of the machine set. However, the encoder used in this research only measures the position of the rotor relative to an initial resting angle $\theta_r^{initial}$. Therefore, if the rotor is not initially aligned to the stator stationary axis, i.e., $\theta_r^{initial} \neq 0$, then the measured θ_r will add an offset to θ_{slip}, which is used in the rotor current synchronous reference frame transformations. This results in a phase shift between the induced stator voltage and grid voltage before synchronization [8, 75, 76]. Therefore, before initiating the synchronization process, the initial rotor angle position needs to be identified/ estimated and from that moment, the encoder will be measuring an increment of $\Delta\theta_r$ with respect to $\theta_r^{initial}$. The $\theta_r^{initial}$ is approximated using (2.132) when the stator is open and then added to θ_{slip} to ensure that the rotor currents in the synchronous reference frame are in quadrature with the grid voltage component [8].

$$\theta_r^{initial} = \theta_g - 90° - \theta_{slip} \tag{2.132}$$

Where θ_g is the angle used for the gird voltage orientation, which is obtained from the phase locked loop. Once the stator voltage has been synchronized to the grid voltage and the grid connection has been made, the rotor current controller must be changed from the synchronization control to the normal rotor current control mode. Moreover, the grid-voltage- and stator-flux-oriented reference frames coincide once the synchronization has been achieved [75].

2.6.5.4 Smooth Controller Gain Interchange between normal and synchronization operations

As discussed earlier, the rotor electrical dynamics are different during a normal and soft synchronization operation. Therefore, the respective controller gains and feed-forward compensation terms change when switching between the two operations. It is imperative to ensure that there is a smooth transition between the two controller schemes at the point of closing the stator contactor thereby connecting the stator to the grid. A "*bumpless*" transition must be adopted whereby the control voltages V_{rd} and V_{rq} are to be kept the same for a period equivalent to the mechanical closing time of the stator contactor [8, 75].

This application ensures that the smoothness of the grid connection does not get affected by the abrupt change in parameters of the controller which may cause large bumps in the control voltages. Presuming that transitioning from one control scheme to another occurs at the sampling instant represented by the discrete variable *k*, the *bumpless* transfer operation can be mathematically expressed as follow [75]:

$$V_{rdq}(k) = V_{rdq}(k-n) \tag{2.133}$$

Where *n* is an integer increment that resets to zero if the condition in (2.134) is met [8]:

$$nT_s = T_{mech} \tag{2.134}$$

Where T_s and T_{mech} represent the rotor current sampling period and the stator contactor mechanical closing period, respectively.

2.6.5.5 Task Sequence for Soft Synchronization

The steps to be followed to carry out soft synchronization of the DFIG stator to the grid are detailed in the flow chart provided in Fig. 2.39.

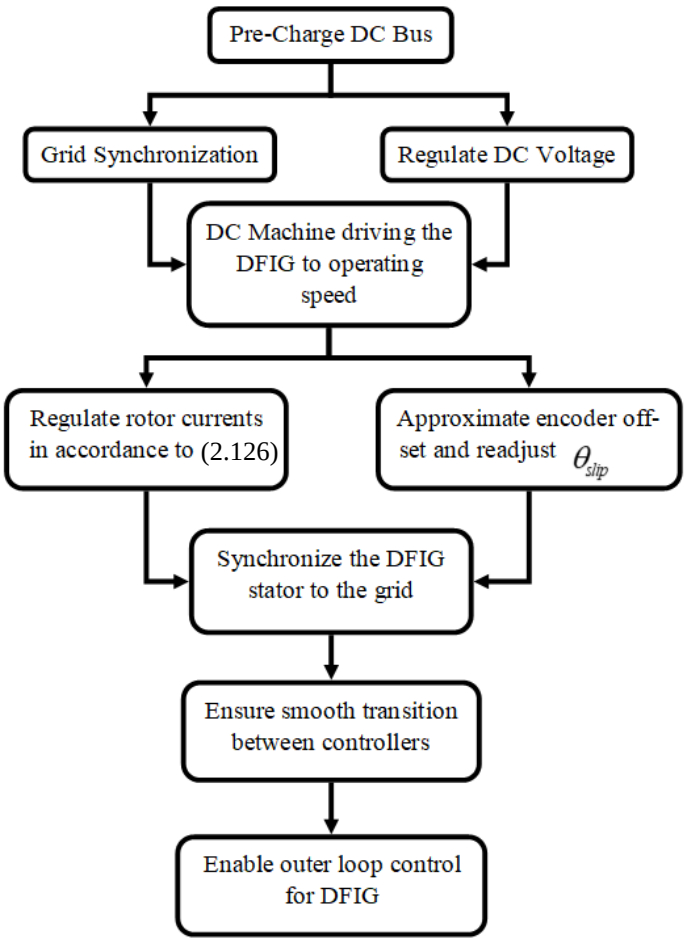

Figure 2. 39: Task Sequence for DFIG soft synchronization

2.6.6 Grid-side Converter Control

2.6.6.1 GSC Controller Objective

The GSC controller aims to stabilize the DC-link voltage to its set value to ensure a continuous flow of active power from the DFIG to the grid [44]. The dual-loop structure consists of the outer DC-link control loop and the inner loop of grid current control. The grid voltage orientation is adopted for the GSC control. The synchronous dynamic model equations of the grid filter are expressed by (2.135) as discussed earlier in *subsection 2.4.2*:

$$\begin{gathered} V_{gd} = \vec{V}_g;\ V_{gq} = 0 \\ E_{gd} = I_{gd}R_g + L_g\frac{dI_{gd}}{dt} + V_{gd} - \omega_s L_g I_{gq} \\ E_{gq} = I_{gq}R_g + L_g\frac{dI_{gq}}{dt} + \omega_s L_g I_{gd} \end{gathered} \tag{2.135}$$

The feedforward compensation must be performed to decouple the grid current controllers' *dq* output voltages. The feedforward compensation terms are expressed by (2.136):

$$\left.\begin{array}{ll} \boldsymbol{d-axis}: & +V_{gd} - \omega_s L_g I_{gq} \\ \boldsymbol{q-axis}: & +\omega_s L_g I_{rd} \end{array}\right\} \tag{2.136}$$

After the cross-coupling terms in (2.136) have been removed from the grid filter *dq* equations in (2.135), the final grid filter voltage dynamic equations are expressed as:

$$\left.\begin{array}{l} E_{gd} = I_{gd}R_g + L_g\frac{dI_{gd}}{dt} \\ E_{gq} = I_{gq}R_g + L_g\frac{dI_{gq}}{dt} \end{array}\right\} \tag{2.137}$$

Applying Laplace Transform to (2.137),

$$\left.\begin{array}{l} E_{gd}(s) = R_g I_{gd}(s) + sL_g I_{gd}(s) \\ E_{gq}(s) = R_g I_{gq}(s) + sL_g I_{gq}(s) \end{array}\right\} \tag{2.138}$$

Therefore, the grid filter plant model is given by (2.139):

$$G(s) = \frac{I_{gdq}(s)}{E_{gdq}(s)} = \frac{1}{sL_g + R_g} \tag{2.139}$$

Substituting (2.135) into (2.54) yields the grid active and reactive power as expressed in (2.140):

$$\left.\begin{array}{l} P_g = \frac{3}{2}\left|\vec{V}_g\right| I_{gd} \\ Q_g = -\frac{3}{2}\left|\vec{V}_g\right| I_{gq} \end{array}\right\} \tag{2.140}$$

The expressions in (2.140) show that the active and reactive powers are controlled by regulating the grid currents I_{gd} and I_{gq}, respectively.

2.6.6.2 Grid Current Control Loop

Figure 2.40 shows the feedback control structure for the inner current control adopting a plant model given by (2.139) and including the active damping principle represented by the constant R_c.

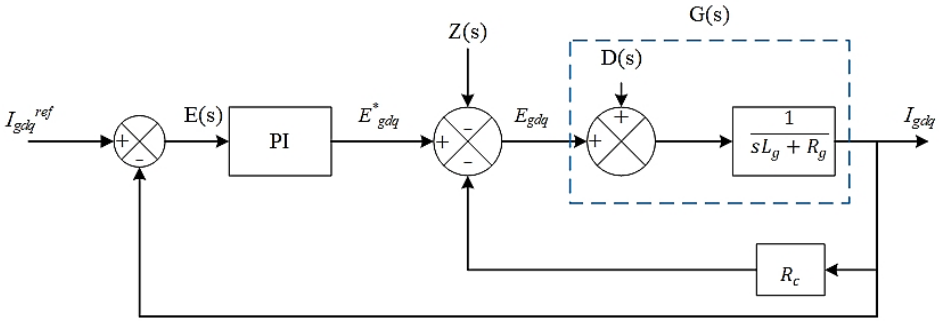

Figure 2. 40: GSC: Inner Current Control Loop Structure

From Fig. 2.40, I_{gdq}^{ref} is the grid *dq* current references obtained from the outer control loop. The grid disturbance and feedforward compensation in (2.136) are represented by *D(s)* and *Z(s)*, respectively. The PI controller output E_{rdq}^{*} is altered by applying the active damping and feedforward compensation terms, resulting in the actual control voltage E_{rdq} which is an input into the plant model *G(s)*. Assuming the perfect decoupling (i.e., *Z(s) = D(s))*, the k_P and k_I gains of the PI controller are obtained from the grid filter electrical plant model $\frac{1}{sL_g+R_g}$, following the design procedure discussed in *subsection 2.6.2.2*. Therefore, the PI controller gains, and the value of R_c is computed using (2.141):

$$k_P = \alpha_g L_g; \qquad k_I = \alpha_g (R_g + R_c); \qquad R_c = \alpha_g L_g - R_g \tag{2.141}$$

Where α_g represents the closed-loop bandwidth for the grid current controller and has a minimum value given by (2.142):

$$\alpha_{g_{min}} > \frac{R_g}{L_g} \tag{2.142}$$

The numerical value of $\alpha_g$can be obtained by using its relationship with the system settling time given by (2.143):

$$t_s = \frac{4}{\alpha_g} \tag{2.143}$$

2.6.6.3 Outer Control Loops

2.6.6.3.1 DC-Link Voltage Control Loop

The DC-link voltage controller provides the *d*-component of the grid's reference current [44]. The DC-link voltage controller is designed based on the DC-link dynamics given in (2.57). Considering a grid voltage orientation, the expression in (2.57) is simplified as:

$$V_{dc} C_{dc} \frac{dV_{dc}}{dt} = P_r + \frac{3}{2} |\vec{V}_g| I_{gd} \tag{2.144}$$

The coexistence of $V_{dc}\ and\ \frac{dV_{dc}}{dt}$ makes the expression in (2.144) to exhibit nonlinear dynamics. To perform a linear controller design and carry out a linear stability analysis of the system, the non-linear equation needs to be linearized around steady-state reference points [44]. This is achieved by introducing a new state variable [8]:

$$W = V_{dc}^2 \tag{2.145}$$

Substituting expression (2.145) into (2.144) gives (2.146) which is linear with respect to *W*:

$$\frac{1}{2}C_{dc}\frac{dW}{dt} = P_r + \frac{3}{2}|\vec{V}_g|I_{gd} \tag{2.146}$$

The corresponding plant model is expressed by (2.147)

$$G(s) = \frac{W}{I_{gd}} = \frac{3|\vec{V}_g|}{C_{dc}s} \tag{2.147}$$

Figure 2.41 illustrates the DC-link voltage control loop structure, including the active damping provided by constant G_a.

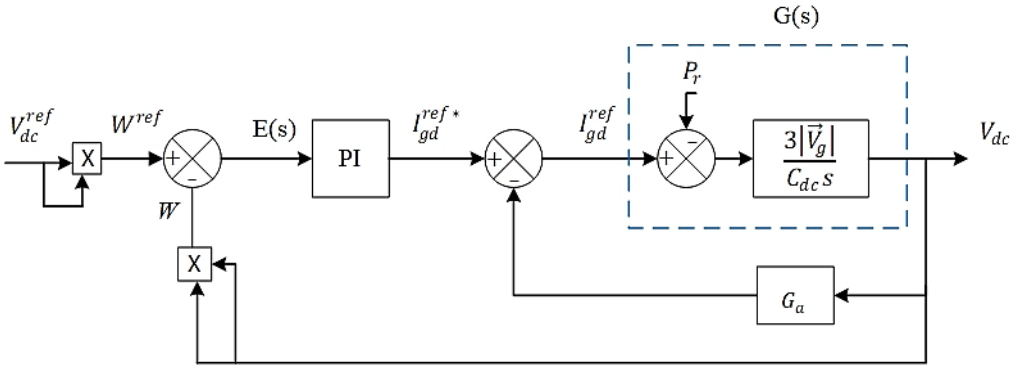

Figure 2. 41: GSC: DC-link voltage control loop structure

The controller linearization is achieved by squaring V_{dc}^{ref} and V_{dc}. The rotor active power P_r acts as a disturbance. The DC-link voltage controller output $I_{gd}^{ref*}$is altered by the application of active damping to give the actual controller output I_{gd}^{ref}. Considering the plant model in (2.147), the k_P and k_I gains of the PI controller and the value of G_a are computed using (2.148):

$$k_P = \frac{C_{dc}\alpha_{dc}}{3|\vec{V}_g|}; \qquad k_I = \alpha_{dc}G_a; \qquad G_a = k_P \tag{2.148}$$

Where α_{dc} represents the closed-loop bandwidth for the DC-link voltage control loop which should be chosen such that the outer loop's dynamics are slower than those of the inner current loop. Therefore:

$$\alpha_{dc} \leq \frac{\alpha_g}{10} \tag{2.149}$$

2.6.6.3.2 Reactive Power Control Loop

Considering the grid voltage orientation, the reactive power control loop provides the *q*-component of the grid reference current I_{gq}^{ref} [44], which is expected to be zero. Therefore, the reactive power is usually set to zero to ensure a unity power factor [44]. Therefore, I_{gq}^{ref} is obtained by rearranging (2.140) as follows:

$$I_{gq}^{ref} = -\frac{2Q_g}{3|\vec{V}_g|} \tag{2.150}$$

2.7 Condition Monitoring and Fault Diagnosis of a DFIG-Based WECS

2.7.1 Failure modes associated with a DFIG-based Wind Turbine System

As presented in *Chapter 1*, the failure modes in electrical machine can be categorized as either electrical or mechanical [7, 11, 12]. According to [77], the classification of faults associated with wound rotor induction machines is outlined in Table 2.13.

Table 2. 13: Types of faults in induction machines

Fault type	***Percentage of total fault occurrence***
Bearing	40%
Stator	35%
Rotor	10%
Eccentricity	10%
Other	5%

The stator and rotor winding faults can be classified as follows: open-circuit, turn-to-turn, coil-to-coil, phase-to-ground, phase-to-phase winding faults as illustrated in Fig. 1.5 of *Chapter 1*, where it has been discussed that the turn-to-turn faults are the most common and challenging since the other types of failures usually originate from turn-to-turn faults [5, 12, 18]. In this project, the most common rotor and stator inter-turn winding faults of the DFIG are considered. In addition, the air gap eccentricity fault is also a focal point of this study.

Air gap eccentricities are considered the most prominent mechanical faults within the induction machines and highly contributes to the outage of these machines [21]. This fault condition is characterized by the existence of a non-uniform air gap between the stator and rotor [12, 15, 20]. Eccentricity faults may lead to an accelerated wearing of bearings, unwanted vibrations, increased losses which reduces the efficiency of the machine and eventually, if not detected soon enough, will lead to rotor-stator rub which damages the stator core and windings beyond repair [78]. An airgap eccentricity fault can be classified as either being static or dynamic [21-23]. Under the static eccentricity fault, the axis of rotation coincides with the axis of the rotor, but it is displaced from the axis of the stator [12, 20, 21], as shown in Fig. 2.42 *(a)*. On the other hand, a dynamic eccentricity fault occurs when the axis of rotation coincides with the axis of the stator but it is displaced from the axis of the rotor [20, 21] as shown in Fig. 2.42 *(b)*.

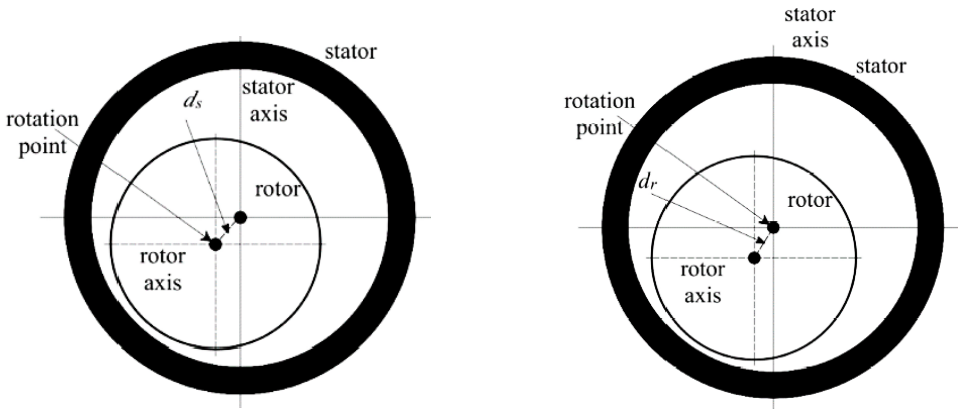

Figure 2. 42: Different Types of Eccentricity Faults, (a) Static, (b) Dynamic [15]

Under the static eccentricity condition, the position of the minimal radial air-gap length remains fixed in space whereas, for the dynamic eccentricity, the position of the minimal airgap rotates with the rotor [12, 78]. According to Nandi *et al* [79, 80], high levels of static eccentricity cause an unbalanced magnetic pull in one direction, which results in shaft flexing and ultimately lead to some degree of dynamic eccentricity. Therefore, in reality, static and dynamic eccentricities tend to coexist, resulting in mixed eccentricity faults [15, 81].

2.7.2 Inter-turn Fault Diagnosis in the Stator and Rotor Windings of a DFIG

2.7.2.1 Signals used in the diagnosis of Stator and Rotor Inter-turn Winding Faults

Generally, an online CMFD system requires the sensing and analysis of the signals that contain specific patterns which are indicators of specific fault occurrences. There are several techniques that have been developed to diagnose faults in electrical machines, however, the signal analysis technique has been widely used to perform this task and it has been considered to be the best, simple and affordable technique [82, 83]. Various signals such as vibration, temperature, torque, electrical-based and supervisory control, and data acquisition systems have previously been used for fault diagnosis in induction machines [7, 12, 23, 31]. The surveys by Qiao *et al* [31] and Hossain *et al* [7] have outlined the benefits and drawbacks of these signals. The electrical-based signals such as current, voltage and instantaneous power are commonly used for the diagnosis of electromechanical faults in induction machines (IMs) owing to their low cost, high reliability when compared to other CMFD signals and their ability to monitor both electrical and mechanical faults in IMs [31, 84]. Furthermore, electrical-signal based analysis utilizes the easily accessible IM terminal signals such as the stator currents, and hence, there is no need for additional sensing devices [9].

2.7.2.2 Signal Processing Methods

Figure 2.43 illustrates the different signal processing methods that are used to perform specific functions pertaining to CMFD: signal conditioning, fault feature extraction, fault detection, and fault prognosis [31].

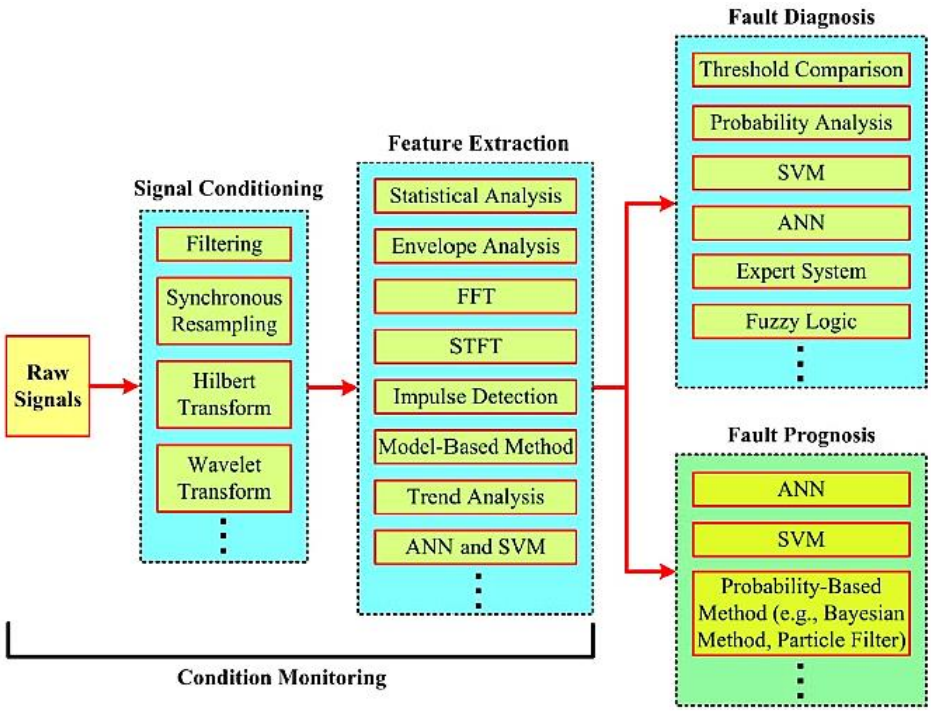

Figure 2. 43: Signal Processing Methods for the WT CMFD and Prognosis [31]

Motor current signature analysis (MCSA) is one of the widely used condition monitoring techniques, particularly in IMs operating under steady-state conditions, because it is cost effective, easy to implement and non-invasive [30, 85, 86]. MCSA is based on the Fast Fourier Transform (FFT) of the stator current signal to track the frequency components which are related to the new rotating flux components resulting from the specific faults [87]. The single-phase stator current monitoring system is commonly used [88], whereby the motor currents are sensed by the current sensors in the time domain and then passed on to a spectrum analyzer for further analysis. When a fault occurs, the frequency spectrum of the line current becomes different from that of a healthy machine; there will be additional sideband harmonic components around the supply/grid frequency, depending on the type of fault [87]. Faults in motor components modulate the air gap and produce rotating frequency harmonics in the self and mutual inductances of the machine [87, 88]. Therefore, by comparing certain parts of the analyzed signal's spectra of the faulty machine with that of the healthy machine, the faults can be identified, and their severities are accessed. The MCSA has successfully been applied to detect shorted turns in stator windings [3, 20, 30, 89], broken rotor bars [78, 86, 90], and air-gap eccentricity faults [20, 78, 90]. Although the MSCA technique is refined and its industrial application can be dated back to the 1980s [86], it has a shortfall under variable speed or load torque conditions because this results in variations in the machine slip and hence it becomes difficult to trace the fault signatures which are slip dependent and spread out on a bandwidth proportional to the speed range [20, 91-93].

As an alternative, advanced time-frequency signal processing tools such as wavelet transform, Hilbert Huang transforms and short-term Fourier transform (STFT) have been explored to diagnose faults in induction machines under the transient regimes [7, 31, 83, 94, 95]. These methods transform a one-dimensional signal *y(t)* into a two-dimensional function of time and frequency (*y: t, ω*) [83]. However, the STFT technique has a constant window: it uses a constant resolution for all frequencies which leads to a poor frequency resolution [96, 97]. On the other hand, wavelet transform analysis has a window that adjusts automatically depending on the frequency of the signal to give the appropriate resolution developed by its approximations and detailed signals [5, 20, 98, 99]. Wavelet transform allows high-frequency components to be analyzed with short-time intervals and low-frequency components to be analyzed with long-time intervals [100]. Wavelet transform is the most preferred method for analyzing non-stationary signals as it enables the extraction of the time-frequency characteristics of the signals more effectively than the other signal processing methods [5, 32]. Therefore, wavelet transform is discussed in more detail in the following sections.

2.7.2.3 Wavelet Transform Analysis

A wavelet transform is a mathematical operation that converts a time-domain signal into a family of wavelets comprising of a series of wavelet coefficients representing time and scale [5, 88, 96]. The transformation of a signal from the time domain to the time-frequency domain enables the details that usually get hidden in the frequency domain to be visible [101]. The Wavelet transform can be categorized as follows: Continuous Wavelet Transform (CWT), Discrete Wavelet Transform (DWT), and Wavelet Packet Transform (WPT) [5, 32, 88, 102, 103].

2.7.2.3.1 Continuous Wavelet Transform (CWT)

Considering a non-stationary signal $x(t)$, the CWT of $x(t)$ is a time-scale signal processing method that can be defined as the sum overall time of the signal multiplied by the shifted scale version of the wavelet function *ψ(t)* expressed by (2.151) [32, 96, 102, 104, 105]:

$$cwt(a,b) = \frac{1}{\sqrt{a}} \int_{-\infty}^{\infty} x(t) \psi^* \left(\frac{t-b}{a}\right) dt \qquad (2.151)$$

Where the parameters $\psi^*(t), a, and\ b$ represent the complex conjugate of the mother wavelet *ψ(t)*, the scale (contraction or dilation) parameter, and the shift (translation) parameter, respectively[105]. The scale parameter *a* is the reciprocal of frequency and it represents the distance between the center of the wavelet function and its crossing on the time axis, whereas the translation parameter *b* governs the movement of the wavelet function along the time axis [32, 105]. CWT suffers redundancy when reconstructing the signal, as the scale parameter *a* and translation parameter *b* are changed continuously [102]. Furthermore, CWT is associated with high computations and requires a lot of resources.

2.7.2.3.2 Discrete Wavelet Transform (DWT)

DWT is a discretization of the CWT, and it provides a flexible simultaneous analysis of the transients of different frequency components present in the same signal[5]. Furthermore, DWT is associated with low computational requirements as compared to the CWT and the WPT [5, 32, 103]. DWT is available in standard commercial software packages, hence no complex algorithms are required for its application [103]. This makes DWT the preferred technique for analyzing nonstationary signals to detect faults and hence it has been used in this research as the signal processing and fault feature extraction technique. The DWT focuses on sampling the scaling and shifted parameters, which leads to high-frequency resolution at low frequencies and high-time resolution at higher frequencies [106]. DWT is expressed by (2.152) [32, 96, 102]:

$$dwt(j,k) = \frac{1}{\sqrt{2^j}} \int_{-\infty}^{\infty} x(t)\psi^* \left(\frac{t-2^j k}{2^j}\right) dt \tag{2.152}$$

Where 2^j and $2^j k$ represent the scale and translation parameters, respectively.

The main idea that underlies the application of DWT is the dyadic bandpass filtering process (filtering & down-sampling) carried out by this transform, illustrated in Fig. 2.44 [5, 103].

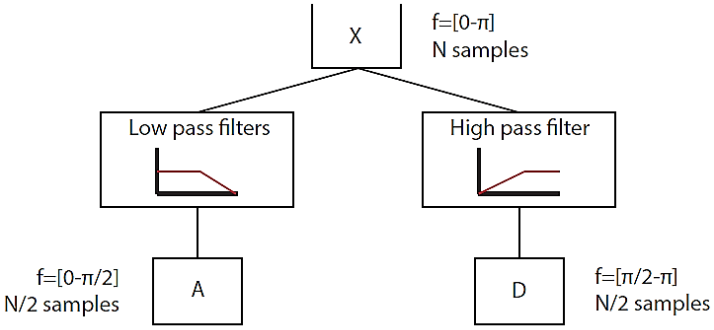

Figure 2. 44: DWT decomposition of a signal (*X*), in approximation information (*A*) and detail information (*D*) using filters [104]

Given a sampled signal $x(n)$, the DWT decomposes it onto several wavelet signals; an approximation signal a_n and n detail signals d_j [103]. The approximation coefficient, which represents the signal's low-frequency components is obtained from a low-pass filter and the detail coefficients, which represent the signal's high-frequency components, are obtained using the high-pass filter as shown in Fig. 2.44. When this filtering process is carried out on a digitized signal, the output data from the filters is doubled (i.e., if the input signal has *N* input samples, the output signals from the high-pass filter and the low-pass filter will be made up of *N* samples each, hence doubling the number of samples) [82]. To overcome this challenge, down-sampling *by two* is factored into the process to ensure that the total number of coefficients is preserved. The multiresolution analysis concept is normally used to apply the DWT on a signal repeatedly until the required decomposition level has been achieved. Under the DWT, only the approximation information can be decomposed into the different frequency bands as shown in Fig. 2.45.

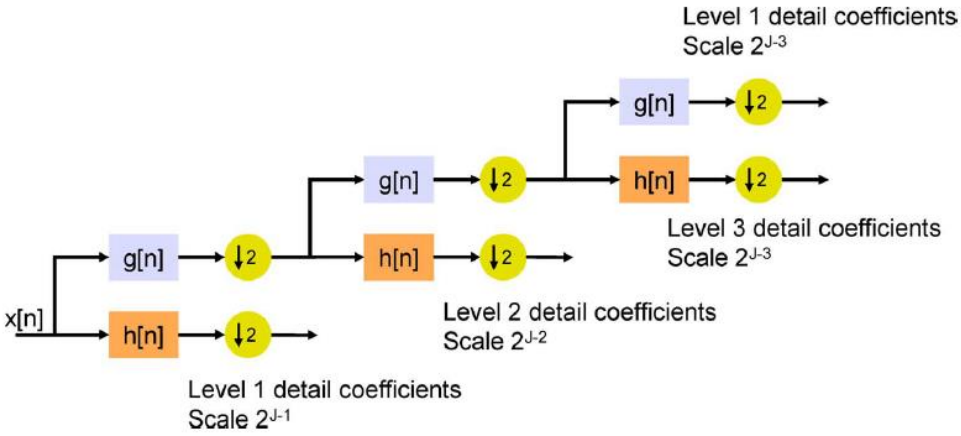

Figure 2. 45: Wavelet decomposition for three (3) levels [106]

If F_s (in *samples/second*) is the sampling frequency used to capture the signal $x(n)$, then the detail space d_j contains the information concerning the signals components whose frequencies are falling within the interval given by (2.153), where $k = 1{:}\,n_f, where\ n_f$ is the minimum number of decomposition levels given by (2.155) [5, 32, 101, 103]. The approximation space a_n includes the low frequency components of the signal which falls in the interval given by (2.154) [5, 32]:

$$f(d_j) \in [2^{-(k+1)}.f_s, 2^{-k}.f_s] \tag{2.153}$$

$$f(a_n) \in [0, 2^{-(n+1)}.f_s] \tag{2.154}$$

$$n_f = integer\left[\frac{\log\left(\frac{f_s}{f}\right)}{\log(2)}\right] \tag{2.155}$$

The decomposed components can be reconstructed to obtain the original signal without losing any information using the inverse discrete wavelet transforms (IDWT) [105]. Reconstructing the original signal involves up-sampling and filtering [32, 105]. Figure 2.46 presents the filtering process that is performed by the DWT.

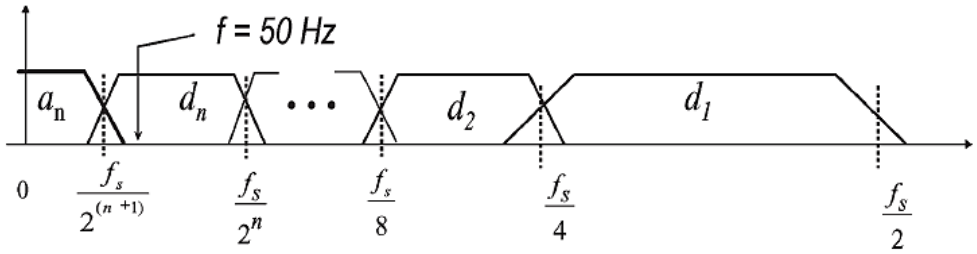

Figure 2. 46: Filtering process performed by the DWT [103]

The flowchart presented in Fig. 2.47 gives an overview of the steps of implementing the DWT. The method is classified into stages: *(1)* Data Acquisition, (2) Signal Processing and Fault Feature Extraction *(3)* Detection Algorithm and Diagnosis Conclusion [82, 83, 103].

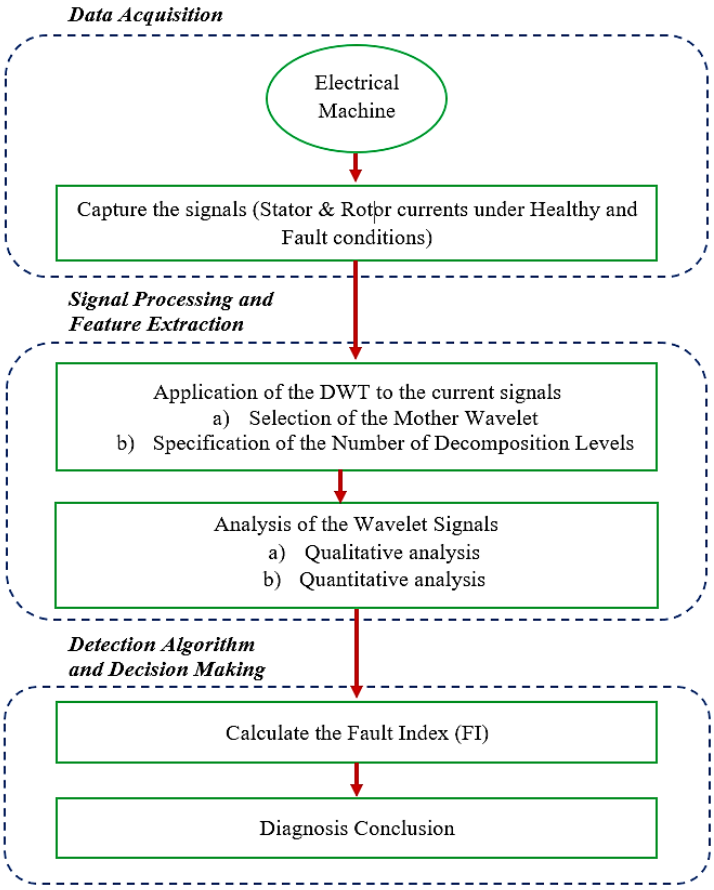

Figure 2. 47: Flow Chart of implementing the DWT for signal processing and fault diagnosis

1) Data Acquisition

When capturing the signal to be analyzed and facilitate the fault diagnosis process, the selection of the sampling frequency F_s plays a significant role. The nonideal filtering carried out by the DWT, whereby the adjacent frequency bands overlap as shown in Fig. 2.46 causes a distortion if a certain frequency component is close to the limit of a band [103]. Therefore, it is recommended to not set the limits of the wavelet band that envelopes the fundamental frequency f_s in close proximity with the sampling frequency F_s [103]. Otherwise, the fundamental component will be filtered within the adjacent bands and overshadow the evolution of other components within these bands because it has a high amplitude [12, 103]. Therefore, the sampling frequencies which are dyadic multiples of around 40 Hz (e.g., 5ksamples/s; standard in data acquisition devices) enable a good frequency resolution and hence are recommended for the application [103].

2) Feature Extraction, Signal Processing, and Fault Diagnosis

a) Application of the Discrete Wavelet Transform

Feature extraction and signal processing in an induction machine using a wavelet approach involve capturing the stator current signals, followed by the calculation of the wavelet coefficients at all possible positions and scales [82, 97]. This is made possible by selecting the appropriate Mother wavelet and determining the number of decomposition levels [20].

i) Selection of the Mother Wavelet

A wavelet function that represents a small wave with oscillating wave-like characteristics and focuses on its short time energy is required to perform the wavelet transform [102]. Several family of wavelets can be used as mother functions to produce a wavelet function that transforms the original signal using the process of translation, scaling, and multiplication [96]. These mother wavelets a grouped in two categories, i.e., infinite-supported and compact-supported, and they are briefly discussed in [96, 103]. *Daubechies* wavelets are frequently used as mother wavelets, but the effectiveness of different mother wavelets needs to be evaluated for specific applications [5, 107]. It is noted that there is a relationship between the extracted signal and the wavelet function at different scales; the more similar the signal is to the wavelet function, the better the defect-related features will be extracted [5, 102].

Once the mother wavelet is selected, it is recommended that the DWT should be carried out using a high-order mother wavelet, i.e., a wavelet associated with a filter that has many coefficients [103]. This is because a low-order mother wavelet worsens the frequency response and the overlap between adjacent frequency bands increases [12]. *Daubechies* or *Symlet* mother wavelets with orders higher than *20* and *10*, respectively, have shown satisfactory results [108]. The research by Deepak *et al* [109] investigated the use of several mother wavelets by testing different wavelet functions on simulated signals and concluded that the Daubechies wavelet 44 (*db44*) is the most suitable mother wavelet for detecting inter-turn faults in induction motors.

ii) Specification of the Number of Decomposition Levels

The number of decomposition levels n_f is determined by the low-frequency components that are to be traced [103]. The number of decomposition levels is computed using (2.155). After the number of decomposition levels has been obtained, the frequency bands associated with each approximation and detail coefficient at the different decomposition levels can then be computed using (2.154) and (2.153), respectively.

b) Analysis of the Wavelet Signals

i) Qualitative Analysis

This analysis is carried out to detect the presence of fault-related patterns in the wavelet signals. This analysis has three steps, i.e., physical analysis, determination of the frequency bands, and determination of the type of fault [103].

ii) Quantitative Analysis

This analysis is carried out to assess the fault severity by computing the quantification parameters defined for the corresponding faults. Generally, the evolution of faults in the wavelet signals is depicted by oscillations which increase the energy of the wavelet signals [103]. This feature is used as a basis for determining the parameters that are used to quantify the severity of the fault.

Ideally, the fault severity quantifying parameter, also known as the fault severity factor (FSF)/ fault index is obtained by evaluating the energy content of the detail coefficient in which the fault-related frequencies evolve [109]. The energies of the approximation E_j^a and detail coefficients E_j^d are calculated using Parseval's theorem as expressed in (2.156) [109, 110].

$$E_j^a = \sqrt{\frac{\sum_{i=1}^{N}(A_j)^2}{N}}, E_j^d = \sqrt{\frac{\sum_{i=1}^{N}(D_j)^2}{N}} \quad (2.156)$$

Where $j = 1 \ldots \ldots n_f$ $(decomposition\ levels)$ and *N* number of samples of the sampled signal.

3) <u>Diagnosis Conclusion</u>

Once the qualitative analysis has been conducted to detect the presence of the fault-related patterns in the wavelet signals, and the severity of these faults has been quantified using the fault index, the conclusion regarding the condition of the machine can be reached [82, 103].

2.7.2.3.3 Wavelet Packets Transform

The wavelet packet transform (WPT) is a multi-stage filtering method that decomposes the detail and approximation information of the signal further until the desired level. The WPT overcomes the limitation of the multiresolution analysis (MRA); its incapability to further decompose both the approximation and detail information in high-frequency bands. Figure 2.48 illustrates the WPT decomposition until level 3. The term $W(k,j)$ represents the coefficients obtained for a packet, where *k* is the decomposition level and *j* is the position of the packet within the decomposition level. The WPT has been studied by many researchers for condition monitoring and detecting incipient faults in rotating machines and it has been proven to be reliable and accurate [111, 112]. However, WPT faces the same challenge of high computational requirements as CWT.

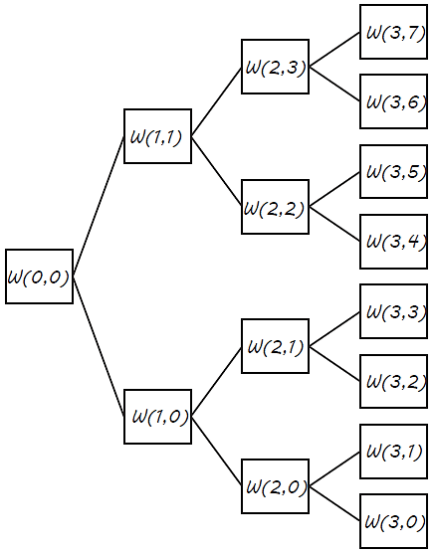

Figure 2. 48: WPT decomposition for three levels [104]

2.8 Chapter Summary

2.8.1 The DFIG-based Wind Energy Conversion System

The main components of a DFIG-based WECS have been presented. The DFIG's electrical models have been presented, whereby the detailed derivation of the DFIG's steady-state model has been carried out and presented in an equivalent circuit. The dynamic equations of the DFIG and its different operating modes have been presented, through the analysis of the power flow diagram.

2.8.2 The back-to-back Power Electronic Converter System

An overview of the power electronic converter system has been presented, with specific emphasis on the two-level and three-level VSC topologies: the 2 Level VSC was chosen to be used as the rotor-side converter (RSC) and the 3 Level NPC VSC was chosen to be used as the grid-side converter (GSC) to maximize the utilization of the DC-link voltage. The space vector pulse width modulation technique was chosen to be adopted in this study, owing to its increased popularity in industrial applications, it's optimized switching that reduces the switching losses, and ability to increase the DC-link voltage utilization. The flow chart in Fig. 2.49, and 2.50 presents the implementation procedures of the 3-level and 2-level SVPWM techniques, respectively.

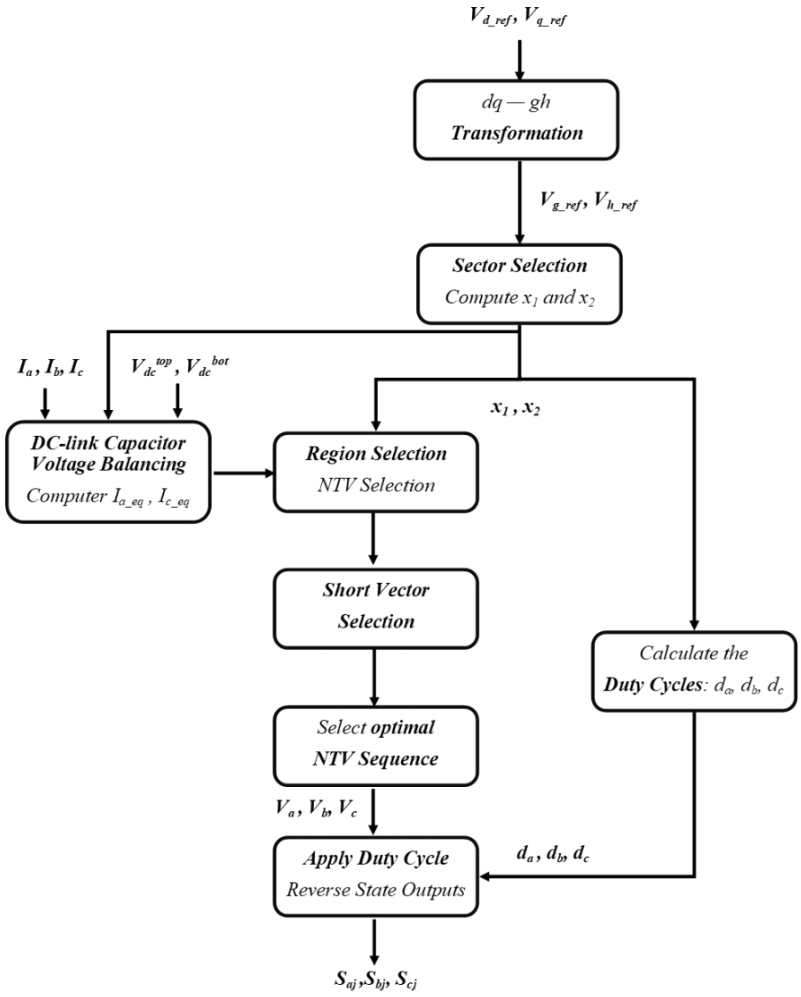

Figure 2. 49: Summary of Implementing the 3L SVPWM

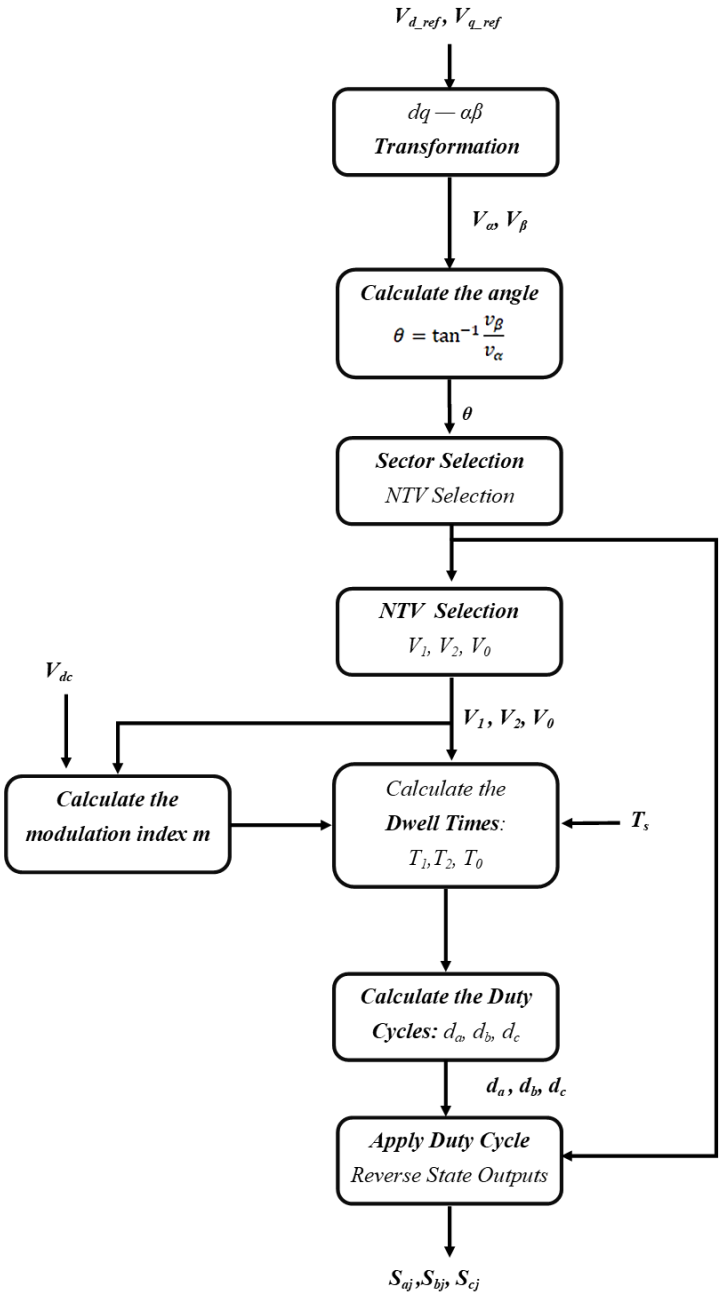

Figure 2. 50: Summary of Implementing the 2L SVPWM

2.8.3 Control of the DFIG-based WECS

The fundamental concepts of designing and implementing a control system for a DFIG-based WECS have been presented in this section. The vector control strategy, which consists of a dual control loop structure has been adopted for the DFIG control, owing to its robust closed-loop performance. The grid voltage orientation is adopted in this study owing to its ease of implementation for both RSC and GSC control. The internal model control turning technique has been considered, taking into consideration the practical controller implementation issues and how the controllers can be optimally designed to overcome these implementation issues.

The controller objectives have been discussed and the transfer functions of the overall system's controllers have been derived accordingly. The numerical values of the *PI* controller gain, and other controller variables will be determined, and the controller responses will be implemented and tested in MATLAB/Simulink in the following chapter, i.e., Chapter 3.

2.8.4 Condition Monitoring and Fault Diagnosis of a DFIG-Based WECS

An overview of fault detection in a DFIG-based WECS has been presented, with emphasis on the signals and the signal processing techniques used to diagnose and characterize fault signatures. It has been established that the Discrete Wavelet Transform (DWT) analysis technique is the most preferred method for processing non-stationary signals associated with variable speed wind turbine systems. As a result, this technique was chosen to be used for fault feature extraction and fault diagnosis in the micro-machine during transient operating conditions, in conjunction with the Hilbert Huang Transform (HHT) technique. The motor current signature analysis (MCSA) technique was chosen to be used for fault-feature extraction and fault diagnosis under steady-state operating conditions, owing to its cost-effectiveness, ease of implementation, and non-invasiveness.

Chapter 3: Implementation and Performance Analysis of the DFIG's Control System through Simulations

3.1 Introduction

This chapter focuses on the modelling and implementation of the components associated with the DFIG-based WECS in MATLAB/Simulink. This step ensures that the operating principles of the different components are thoroughly understood before implementing the DFIG system in the laboratory. To ensure that the simulation model resembles the practical system, the model parameters used have been derived from the actual hardware parameters. In which case, some parameters have been extracted from supplier datasheets and others have been determined experimentally. The desired controller specifications that ensure a robust and accurate control system have been determined. Initially, the responses of the RSC, GSC and DFIG soft synchronization controllers have been conducted individually. Thereafter, the dynamic operation and testing of the complete DFIG-based WECS have been conducted. The simulation results presented in this chapter will serve as a means of validating the experimental results presented in the subsequent chapter, i.e., Chapter 4.

3.2 DFIG Parameters

The DFIG machine used in this research is a 5kW wound rotor induction machine (WRIM) whose parameters are given in Table 3.1.

Table 3. 1: DFIG machine parameters [20]

Parameter	**Value**
Power rating [W]	5000
Efficiency [%]	78
Stator Voltage (line to line) [V]	37
Stator Current [A]	20
Rated speed [rpm]	1500 (157 rad/s)
Rated Torque [Nm]	8.16
Number of poles	4
Stator Resistance R_s [Ω]	0.169
Stator Leakage Inductance $L_{\sigma s}$ [H]	3.73×10^{-4}
Magnetising Inductance L_m [H]	3.27×10^{-3}
Rotor Leakage Inductance $L_{\sigma r}$ [H]	1.05×10^{-3}
Rotor Resistance R_r [Ω]	0.116
Leakage coefficient L_σ [H]	1.39×10^{-3}
Inertia [kgm/s]	0.0889

3.3 Rotor-side Converter Control

Considering the grid voltage orientation, the linear relationship between the electric torque and the *d*-component of the rotor current, as well as the linear relationship between the reactive power and the *q*-component of the rotor current are employed to obtain the *d*- and *q*- axis references of the rotor currents which are the inputs into the inner current control loops. The RSC controller is implemented in MATLAB/Simulink based on the internal model control (IMC) technique. The PI controller gains are calculated using the physical system parameters given in Table 3.1.

3.3.1 Rotor Current Control

The rotor current controller is modelled based on the feedback control structure of the inner current control presented in Fig. 2.36 and adopting a plant model given by (2.113). The parameters of the WRIM that is used in the test rig result in a process bandwidth equal to $\frac{R_r}{L_\sigma} = \frac{0.116}{1.39\times10^{-3}} = 83.45$. According to (2.117), the rotor current controller's closed-loop bandwidth α_r needs to be greater than the process bandwidth. Therefore α_r is chosen to be 2.4 times the process bandwidth, resulting in $\alpha_r = 200.20$. According to (2.118), the corresponding system settling time is $t_s = \frac{4}{200.20} = 0.020s$. For the fast operation of the inner current controller to be achieved, the control sampling frequency is chosen to be ten times the closed-loop bandwidth, resulting in a sampling period of $T_s = 0.50ms$. Theoretically, the closed-loop bandwidth α_r may be set as fast as desired. However, a large closed-loop bandwidth may enforce impractical requirements for the controller sampling frequency which would make the system to become susceptible to noise [8]. Therefore, the closed-loop bandwidth should be set considering the physical limitations of the controller hardware [8]. The rotor current controller's PI gains and the active damping constant R_a are computed in (3.1) which is derived from expression (2.116):

$$\begin{aligned} k_P &= \alpha_r L_\sigma = 0.28 \\ R_a &= \alpha_r L_\sigma - R_r = 0.16 \\ k_I &= \alpha_r (R_r + R_a) = 55.74 \\ k_I T_s &= 0.028 \end{aligned} \tag{3.1}$$

The step and the open-loop frequency responses of the rotor current controller are shown in Fig. 3.1. These plots have been obtained from Matlab M-file codes which made use of the actual hardware system parameters as inputs into the controller equations given in (3.1) to determine the PI gains of each controller. The PI gains obtained are used in the open-loop and closed-loop transfer functions derived in Chapter 2. The step response plot (time based) is for the closed-loop transfer function, while the frequency response plot (bode plot) is for the open-loop transfer function. Obtaining the step and frequency response plots assist in verifying the desired controller performances.

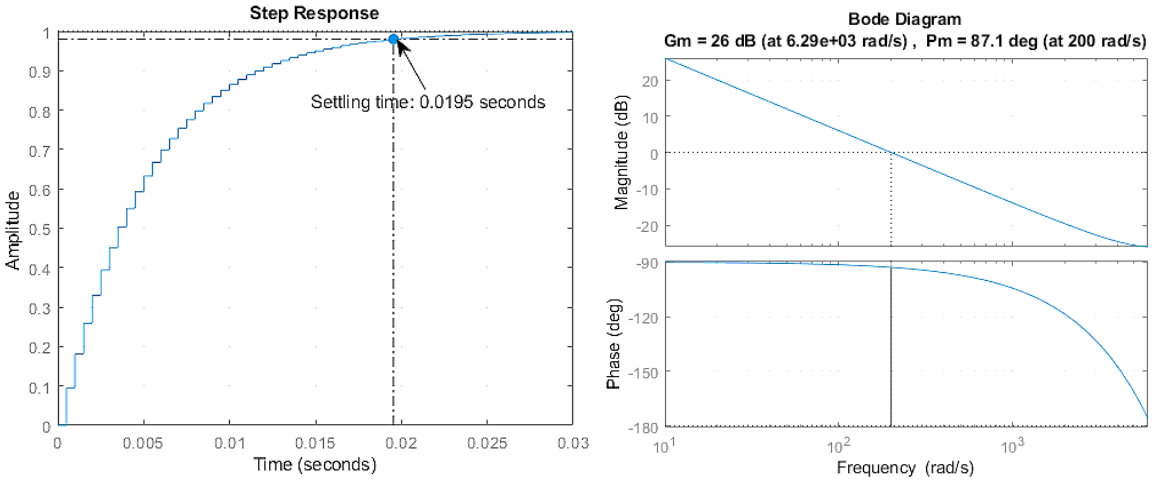

(a) (b)

Figure 3. 1: DFIG rotor current controller responses, (a) step response, (b) frequency response

The step response shows the expected behavior concerning the desired settling time of t_s = 0.020s. The frequency response has a gain margin of 26dB and a phase margin of 87.1° at the desired current control bandwidth of 200rad/s. This indicates that the controller of the closed-loop system meets the desired design specifications and the system will be stable.

3.3.2 Soft-synchronization Rotor Current Control

During soft synchronization, the DFIG stator is required to be open. As a result, the process bandwidth is $\frac{R_r}{L_r} = \frac{0.116}{4.94\times10^{-3}} = 23.48$. Since the DFIG rotor circuit has a smaller bandwidth before the machine is connected to the grid, a much more stable and moderate transient response is required and hence the synchronization controller must be designed to achieve the desired response. Since the closed-loop bandwidth α_r for the rotor current controller is required to be greater than the process bandwidth, $\alpha_{r_{soft}}$ *is* chosen to be 2.4 times the process bandwidth, resulting in $\alpha_{r_{soft}} = 56.35$. The corresponding system settling time during soft synchronization is $t_s = 0.071s$. Likewise, the fast operation of the inner current controller is ensured by selecting the control sampling frequency to be ten times the closed-loop bandwidth, resulting in a sampling period of $T_s = 1.77ms$. The synchronization rotor current controller's PI gains and the active damping constant R_{soft} are computed in (3.2):

$$\begin{aligned} k_P &= \alpha_r L_r = 0.28 \\ R_a &= \alpha_r L_\sigma - R_r = 0.16 \\ k_I &= \alpha_r (R_r + R_a) = 15.69 \\ k_I T_s &= 0.0078 \end{aligned} \tag{3.2}$$

The step and the open-loop frequency responses of the synchronization rotor current controller are shown in Fig. 3.2.

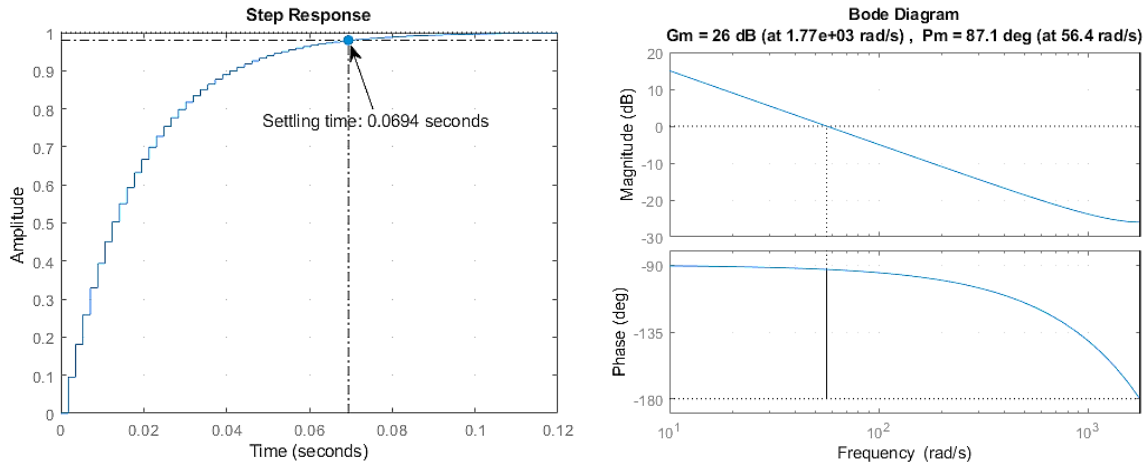

(a) (b)

Figure 3. 2: Soft synchronisation current controller responses, (a) step response, (f) frequency response

The step response shows the expected behavior for the desired settling time of ts=0.07s. The frequency response has a gain margin of 26dB and a phase margin of 87.1° at the desired current control bandwidth of 56.4rad/s.

3.3.3 Speed Control

The speed controller is modelled based on the speed control loop structure presented in Fig. 2.37. To ensure slower dynamics for the outer control loop, the closed-loop bandwidth for the speed control loop has to be chosen such that the dynamics of the outer loop is slower than the dynamics of the inner current loop [35]. Therefore, in this work, the closed-loop bandwidth of the speed controller is chosen to be sixty times slower than the rotor current controller's closed-loop bandwidth and hence, the closed-loop bandwidth is set to $\alpha_\omega = \frac{\alpha_r}{60} = \frac{200.20}{60} = 3.33$. The corresponding settling time is set to $t_s = 1.19s$. The speed control sampling frequency was chosen to be ten times less than the inner current control sampling frequency, resulting in a sampling period of $T_s = 5ms$. The speed controller's PI gains and active damping constant B_a are calculated using (3.3) which is derived from expression (2.121):

$$\begin{aligned} k_P &= \alpha_\omega J_r = 3.33 * 0.0889 = 0.294 \\ B_a &= \alpha_\omega J_r - D_r = k_P \\ k_I &= \alpha_\omega (D_r + B_a) = 3.33 * 0.294 = 0.98 \\ k_I T_s &= 0.0049 \end{aligned} \tag{3.3}$$

The step response and the corresponding frequency response of the speed controller are shown in Fig. 3.3.

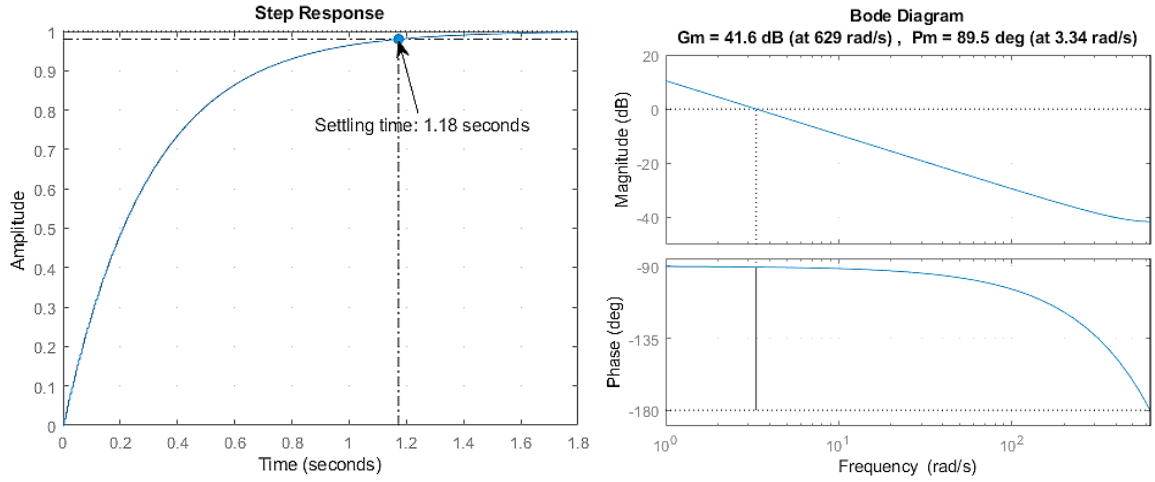

(a) (b)

Figure 3. 3: DFIG Speed controller responses, (a) Step Response, (b) Frequency response

The step response shows the expected behavior for the desired settling time of *ts=1.19s*. The frequency response has a gain margin of 26dB and a phase margin of 87.1° at the approximate desired speed control bandwidth of 3.34 rad/s.

3.4 Grid-side Converter Control

The GSC controller has also been implemented in MATLAB/Simulink based on the IMC design. For the GSC, the *d*- and *q*- axis reference currents which are the inputs into the inner current control loop are provided by the DC-link voltage outer control loop and reactive power control loop, respectively.

3.4.1 Grid Current Control

The GSC controller is modelled based on the feedback control structure for the inner current control presented in Fig. 2.40, adopting a plant model given by (2.139). The PI controller gains are calculated using the physical system parameters of the grid filter available in the university laboratory: i.e., $R_g = 0.75\Omega$ and $L_g = 47\text{mH}$. The grid filter components result in a process bandwidth of $\frac{R_g}{L_g} = \frac{0.75}{0.047} = 15.96$. Since the grid current controller's closed-loop bandwidth α_g is required to be greater than the process bandwidth, it was chosen to be thirteen times the process bandwidth, resulting in $\alpha_g = 200.26$. The corresponding system settling time is $t_s = 0.19s$. Likewise, the control sampling frequency was chosen to be ten times the closed-loop bandwidth to achieve a fast operation of the inner current controller, resulting in a sampling period of $T_s = 0.49ms$. The grid current controller's PI gains and the active damping constant R_c are computed in (3.4) which is derived from expression (2.141):

$$\left.\begin{aligned} k_P &= \alpha_g L_g = 9.41 \\ R_c &= \alpha_g L_g - R_g = 8.66 \\ k_I &= \alpha_g (R_g + R_c) = 1885 \\ k_I T_s &= 0.941 \end{aligned}\right\} \quad (3.4)$$

The step and open-loop frequency responses of the grid current controller are shown in Fig. 3.4.

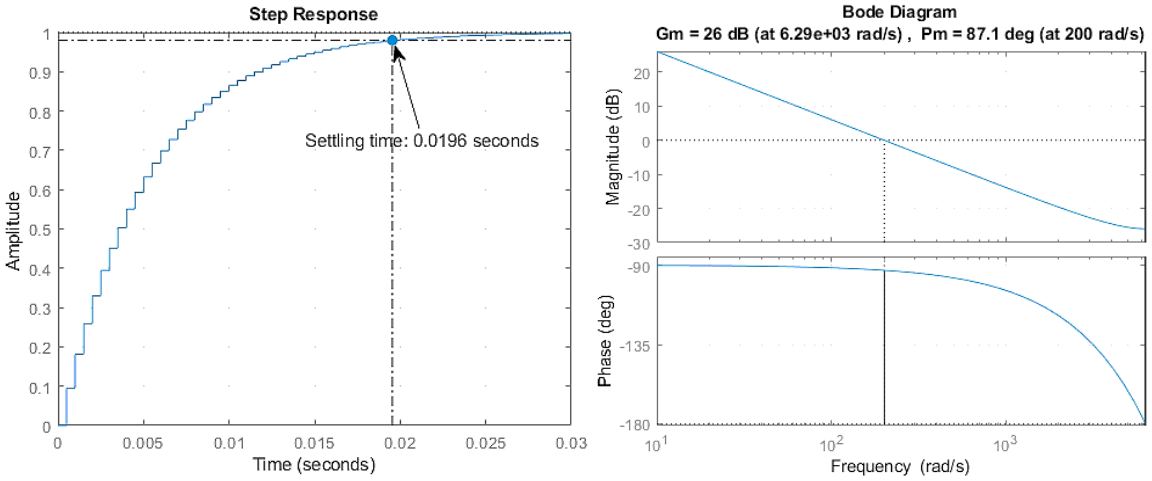

(a) (b)

Figure 3. 4: Grid current controller responses, (a) Step response, (b) Frequency response

The step response shows the expected behavior for the desired settling time of t_s=*0.019s*. The frequency response has a gain margin of 26dB and a phase margin of 87.1° at the desired grid current controller bandwidth of 200 rad/s.

3.4.2 DC-link Voltage Control

The DC-link voltage controller is modelled based on the DC-link voltage control loop structure presented in Fig. 2.41. To ensure slower dynamics for the outer control loop, the closed-loop bandwidth of the DC-link voltage controller is chosen to be thirty times slower than the grid current controller. Therefore, the closed-loop bandwidth is set to $\alpha_{dc} = \frac{\alpha_g}{30} = \frac{200.26}{30} = 6.67$. The corresponding settling time is $t_s = 0.599s$. The DC-link control sampling frequency was chosen to be ten times less than the inner current control sampling frequency, resulting in a sampling period of $T_s = 5ms$. The DC-link voltage controller's PI gains and active damping constant G_a are calculated using (3.5) which is derived from expression (2.148):

$$\left.\begin{aligned} k_P &= \frac{C_{dc}\alpha_{dc}}{3|\vec{V}_g|} = 5.98 \times 10^{-4} \\ G_a &= k_P = 5.98 \times 10^{-4} \\ k_I &= \alpha_{dc} G_a = 3.99 \times 10^{-3} \\ k_I T_s &= 1.99 \times 10^{-5} \end{aligned}\right\} \quad (3.5)$$

The step response and the corresponding frequency response of the DC-link voltage controller are shown in Fig. 3.5.

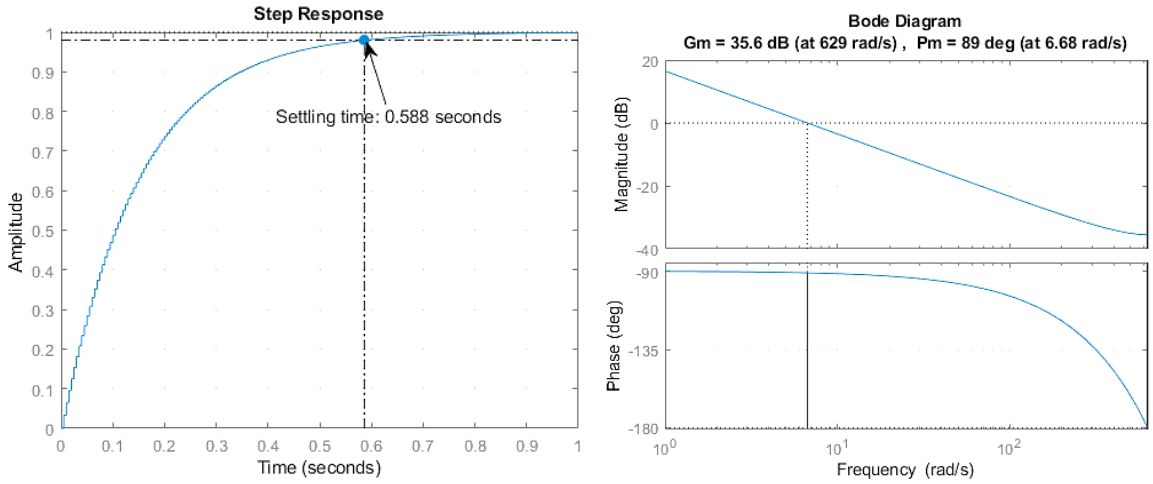

(a) (b)

Figure 3. 5: DC-link voltage controller responses, (a) Step Response, (b) Frequency Response

The step response shows the expected behavior for the desired settling time of t_s=*0.59s*. The frequency response has a gain margin of 35.6dB and a phase margin of 89° at the desired DC-link voltage controller bandwidth of 6.68 rad/s.

3.5 Phase-Locked Loop (PLL) Operation

The PLL is implemented to obtain the phase angle and frequency from the grid voltages. The PI gains of the PLL controller are obtained using (2.104) and (2.105). Considering that the grid frequency is 50Hz, the closed loop settling time is therefore set to be t_s = 0.02s. The damping ratio of a critically damped system is considered and hence $\zeta = \frac{1}{\sqrt{2}}$. Therefore, the PI gains are given as $k_P = 212.93$ and $k_I = 2267$. The PLL depicted in Fig. 2.34 is implemented in MATLAB/Simulink and the simulations for the PLL operation are shown in Fig. 3.6.

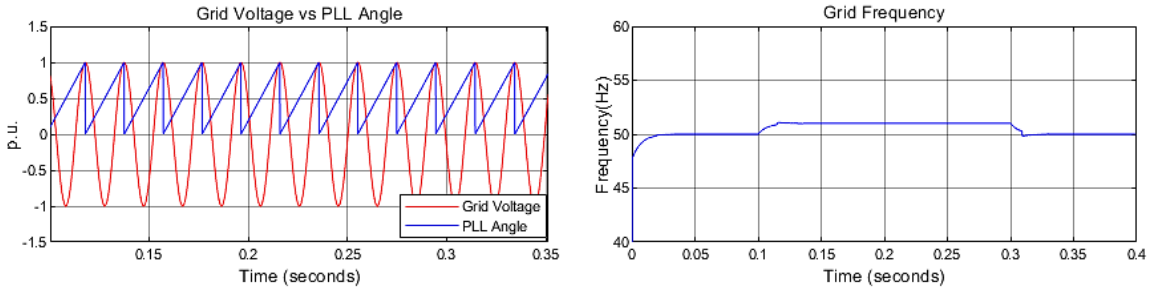

(a) (b)

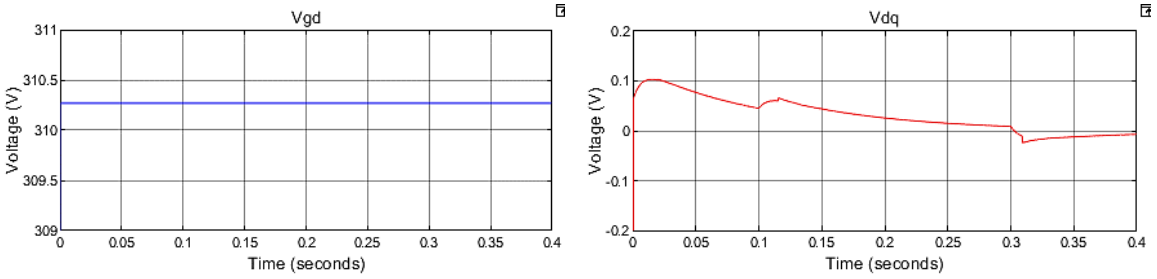

(c) (d)

Figure 3. 6: PLL Operation

The grid voltage is set to 380 V_{rms}^{LL} with a fundamental frequency of 50 *Hz*. For ease of representation, the grid voltage has been converted to the *p.u.* The reliability of the PLL has been evaluated by implementing a grid voltage frequency jump of 1 *Hz* between *t=0.1s* and *t*=0.3*s* as shown in Fig. 3.6 (b). The designed PLL produced an output angle that is still synchronized to the grid voltage despite the change in the frequency as shown in Fig. 3.6 (a). The PLL output angle has been used to transform the grid voltage from the *abc* reference to the *dq* synchronous frame. The corresponding *d*- and *q*-axis voltages are given in Fig. 3.6 (c) and (d), respectively, where the V_{gd} remains constant while V_{gq} changes for the grid frequency jump.

3.6 The Operation and Modulation of the Voltage Source Converters (VSCs)

In this investigation, the 2 Level (2L) VSC has been chosen to be used as the rotor-side converter (RSC), owing to its robustness, its simple configuration and the low modulation index operations associated with the DFIG control. Whereas the 3 Level (3L) neutral-point-clamped (NPC) VSC is chosen to be used as the grid-side converter (GSC) to maximize the utilization of the DC-link voltage. The two-level and three-level VSCs and the corresponding space vector pulse width modulation (SVPWM) switching algorithms have been modelled in MATLAB/Simulink and their operations have been assessed through simulations as presented in the following subsections.

3.6.1 Two Level VSC

The 2 level SVPWM algorithm, which has thoroughly been discussed in Chapter 2, has been implemented in MATLAB/Simulink. The output voltage from phase-A of the two-level VSC is shown in Fig. 3.7, which indicates both the PWM (*blue*) and the sinusoidal waveforms (*red*).

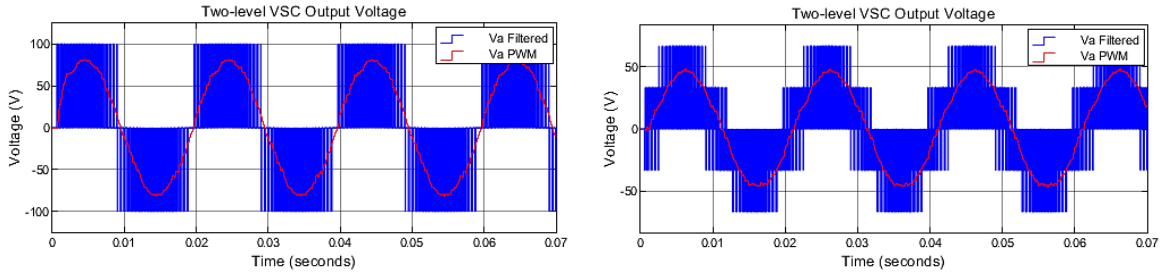

(a) (b)

Figure 3. 7: Output voltage of the two-level VSC, (a) Phase-to-phase, (b) Phase-to-ground

The DC-bus voltage has been set to 100V, while the open-loop output modulation index is 0.8, and the switching frequency of the converters has been set to 2kHz. The FFT analysis of the two-level VSC's output voltage is shown in Fig. 3.8.

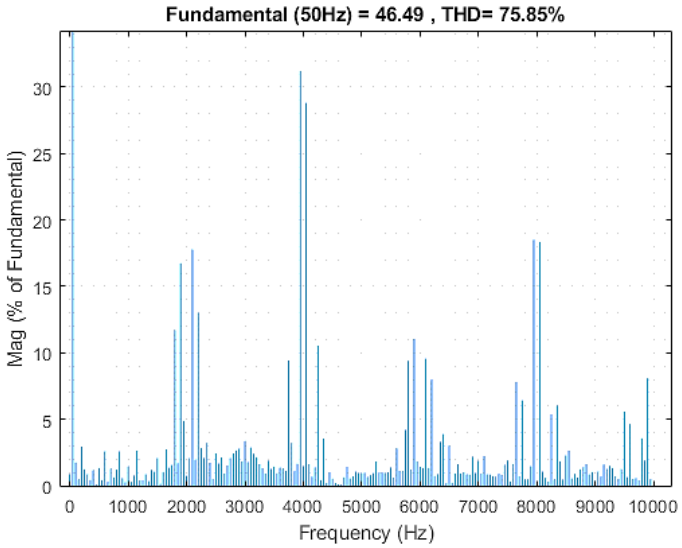

Figure 3. 8: FFT analysis of the two-level VSC output voltage

It is observed in the FFT spectrum that the harmonics are centered around the integer multiples of the switching frequency (2kHz). Furthermore, it is indicated that the fundamental frequency is about 47Hz, and the third harmonic distortion (THD) is 75.85%. A high THD in the output voltage of a 2-level VSC is expected. The simulation results presented in this subsection validate the operation of the developed two-level SVPWM switching algorithm.

3.6.2 Three Level NPC VSC

The three-level SVPWM algorithm has been implemented and simulated in MATLAB/Simulink following the procedure discussed in Chapter 2. Figure 3.9 shows the *dq* and *gh* control signals and the transformation angle. The *dq* control signals are given in per unit where the *q*-axis value is kept at zero and the *d*-axis represents the modulation index.

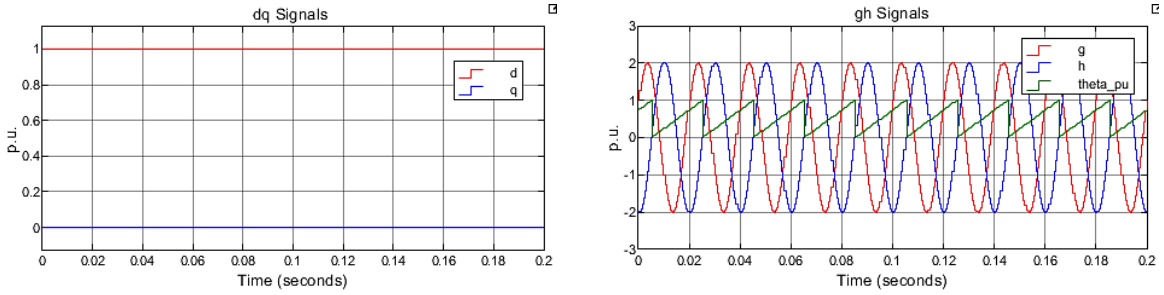

(a) (b)

Figure 3. 9: (a) *dq* control signals; (b) *gh* control signals and transformation angle per unit

According to [8], the three-level SVPWM algorithm operates in a 2-per-unit system and hence, the *gh* components given in Fig. 3.9 (b) have amplitudes of 2. It is observed that the angle of transformation and the *h*-axis component have the same zero-crossing because the reference vector $\vec{V}_{ref}$ is aligned with the *g*-axis whenever the transformation angle completes a period [8]. The selection of sectors and regions was carried out by using the logic expressions presented in Table 2.9 and Table 2.7, respectively. The normalized vector projections and the sector and region numbers are shown in Fig. 3.10.

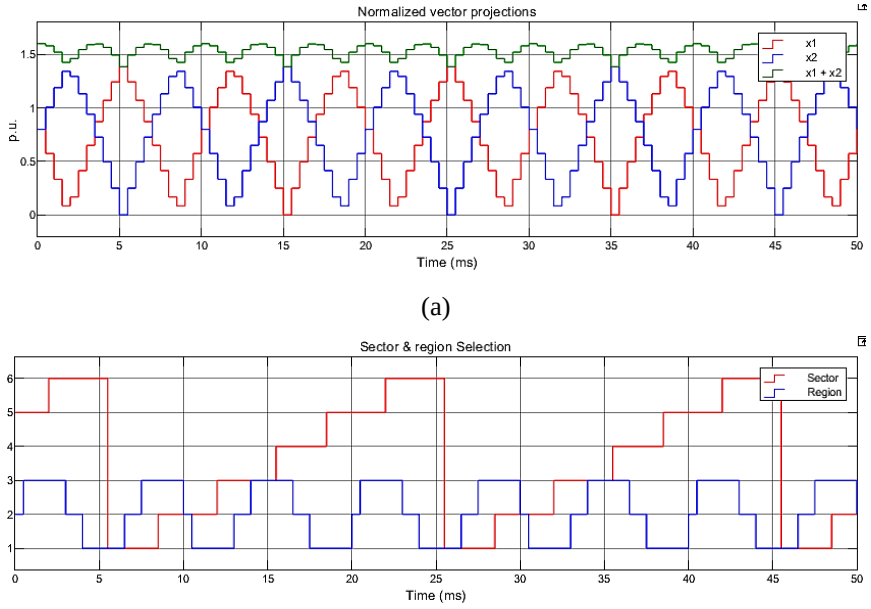

(a)

(b)

Figure 3. 10: (a) Vector projections; (b) Sector and Region numbers

The vector projections get inverted every time the reference vector $\vec{V}_{ref}$ changes the sector position. The peak values of the projections x_1 and x_2 are shown to be about 1.4, which reflects a modulation index of 0.8 in a 2-per-unit system. The three-level SVPWM has been implemented in Simulink to generate the switching pulses for the 3-level NPC VSC. The waveforms of the three-level VSC output are shown in Fig. 3.11.

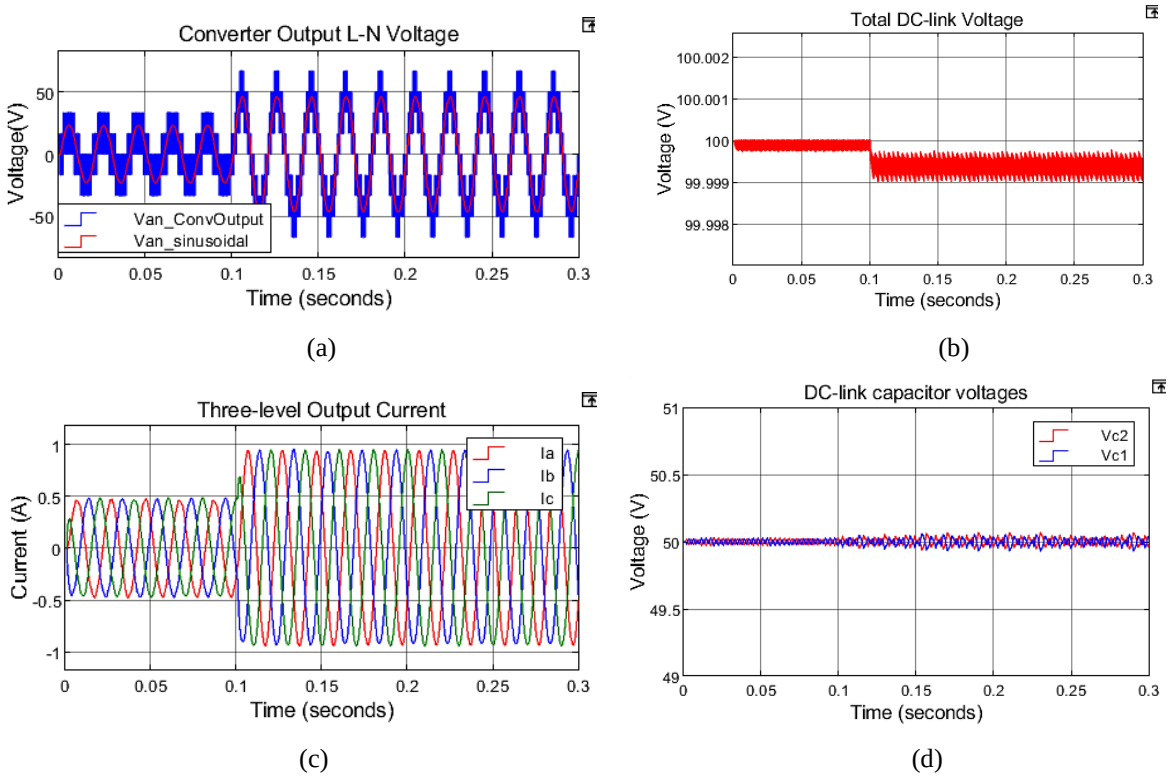

Figure 3. 11: Three-level NPC VSC operations: (a) Converter line-to-neutral output voltage, (b) Total DC-link voltage, (c) converter output current, (d) DC-link capacitor voltages

The phase-A output voltage is shown in Fig. 3.11 (a) with its fundamental waveform superimposed. The DC bus was pre-charged to 100V (Fig. 3.11 (b)), by a single-phase variac and a series-connected resistor. The switching frequency for the GSC is set to *2kHz*. The modulation index was initially set to *0.4*, and then stepped up to *0.8* at *t=0.1s*. It is observed that, for low modulation indices, the output voltage of a 3-level NPC VSC has the same form as that of a two-level VSC, meaning that the $\vec{V}_{ref}$ is only made up of short vectors and hence not all possible output states of the three-level VSC are utilized during low modulation indices. The corresponding three-phase output current waveforms are shown in Fig. 3.11 (c) and Fig. 3.11 (d) shows the voltage across the DC-link capacitors. It can be observed that the DC-link voltage is balanced, which is achieved by the charging and discharging of DC-link capacitors using the short vector selection method discussed in *subsection 2.5.3.5*. For the large modulation index scenario, i.e., between *t=0.1s* and *t=0.3s*, oscillations are observed in the DC-link capacitor voltages which is attributed to the increase in the load current, thereby producing a large DC-bus neutral current flow.

The FFT analysis has been performed on the output voltage of the three-level NPC VSC for both modulation indices of *0.4* and *0.8* and the results are illustrated in Fig. 3.12.

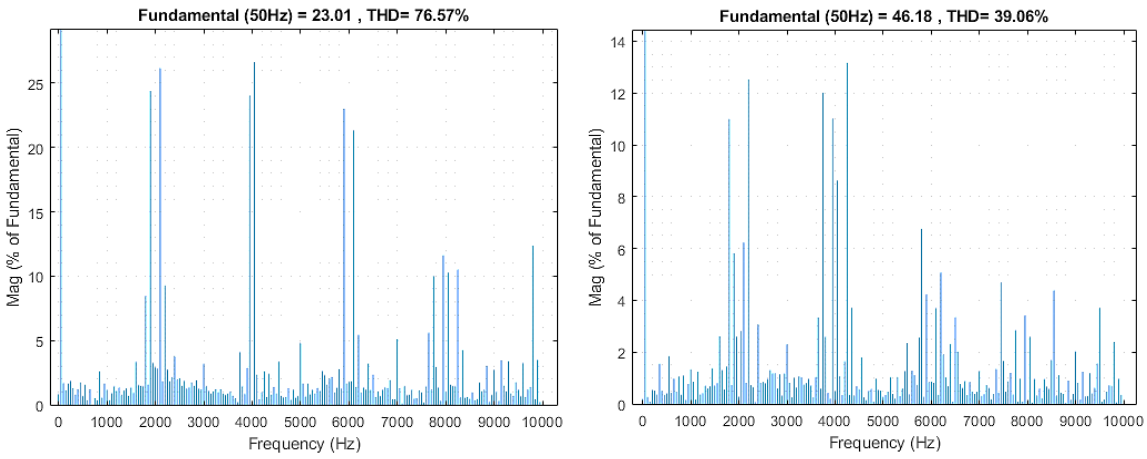

(a) (b)

Figure 3. 12: FFT of the 3-L VSC output voltage: (a) at *0.4* modulation index, (b) at *0.8* modulation index

The FFT spectrum of the output voltage validates the commanded switching frequency (i.e., *2 kHz*) because harmonics are centered on integer multiples of the switching frequency which is more evident for lower modulation indices (Fig. 3.12 (a)). For higher modulation indices, the switching frequency from the three-level SVPWM algorithm varies over time. This is evident in the FFT spectrum in Fig. 3.12 (b) where switching harmonics are scattered for larger modulation indices. However, the dominant harmonics are still observed to be centered on multiples of the switching frequency. It is further observed that the THD of the 3-level VSC output voltage is high (76.57%) at lower modulation indices (0.4 in this case). This is because, as mentioned earlier, the output voltage of the 3L VSC has the same form as that of a 2L VSC at lower modulation indices (see Fig. 3.11 (a)), meaning that the reference voltage vector $\vec{V}_{ref}$ used in the SVPWM is only made up of the short vectors and hence not all possible output states are utilized. Thus, the THD would still be high at low modulation indices because the 3L VSC is operating as a 2L VSC. However, as the modulation index is increased, all possible output states of the 3L VSC get utilized and the output voltage would be what is expected from the 3L converter, thereby reducing the THD from 76.57% to 39.08% as observed in Figure 3.12. The simulation results presented in this subsection indicate that the developed three-level SVPWM algorithm is adequate.

3.7 System Dynamic Simulations

The performance of the GSC and RSC control is evaluated individually through simulations to demonstrate their respective performance and operating dynamics. Thereafter, the operating dynamics of the complete system have also been evaluated through simulation studies.

3.7.1 DFIG Soft Synchronization dynamics

The dynamic operation of the DFIG soft synchronization has been modelled and simulated in Simulink following the procedures and flow chart presented in Fig. 2.39 in Chapter 2. The GSC was assumed to be synchronized to the grid and the DC-link voltage was regulated at 200 V.

Since the rated stator voltage of the machine under study is 37 V, the three-phase voltage source which represents the grid in the model has been set to have a grid voltage of 37 V as well. However, in the practical system implementation, a 40V/380V transformer has been used to connect the low-voltage stator winding of the machine to the high-voltage grid. The rotor current controller for the soft synchronization control presented in *subsection 2.6.5.2* has been implemented in Simulink and the simulation results are presented in Fig. 3.13.

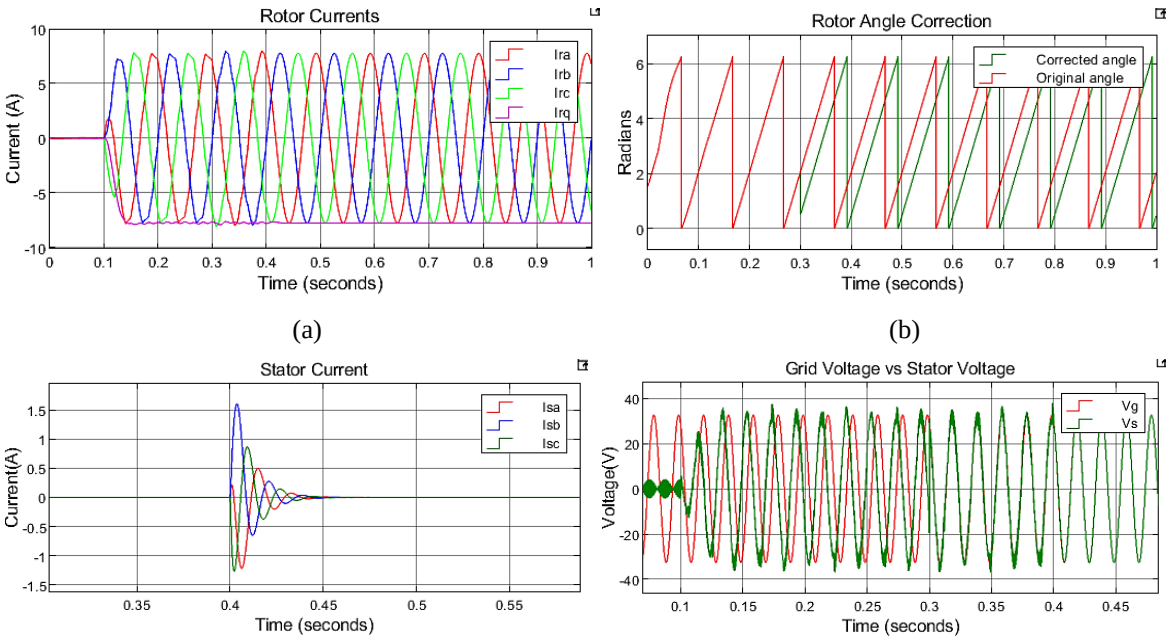

Figure 3. 13: Simulated DFIG soft synchronization dynamics

From Fig. 3.13 (a), it is observed that the rotor *d*- and *q*-axis currents were assigned to their reference values at t = 0.1s, following the condition presented in (2.126). Therefore, the rotor *d*-axis current is maintained at 0A while the *q*-axis current was stepped to -7.75 A. It is observed in Fig. 3.13 (d) that the stator voltage begins to be induced into the stator winding from $t = 0.1s$ and eventually becomes equal to the grid voltage after the transient period. However, due to the offset in the initial rotor angle position, there is a phase shift between the two voltages.

The rotor angle correction method that is given by (2.132) was implemented at $t = 0.3s$ as shown in Fig. 3.13 (b), after which the stator voltage is observed to fully synchronize with the grid voltage. After the two voltages have been synchronized, the stator contactor was then closed at $t = 0.4s$. The rated stator current amplitude of the scaled-down machine is 20 A, and it is observed in Fig. 3.13 (c) that the peak amplitude of the stator current transient during synchronization is 1.55 A which is only 7.75% of the rated current. Once the DFIG is connected to the grid, the rotor current controller can be switched over to normal operation mode ensuring a *bumpless* transfer operation [8]. The stator currents shown in Fig. 3.13 (c) return to zero after synchronization, which denotes that there is no exchange of active or reactive power between the DFIG and the grid at this point.

3.7.2 Independent DFIG control dynamics

The inner current controllers for the RSC-side converter have been modelled in Simulink and the results for various operating dynamics are presented in Fig. 3.14.

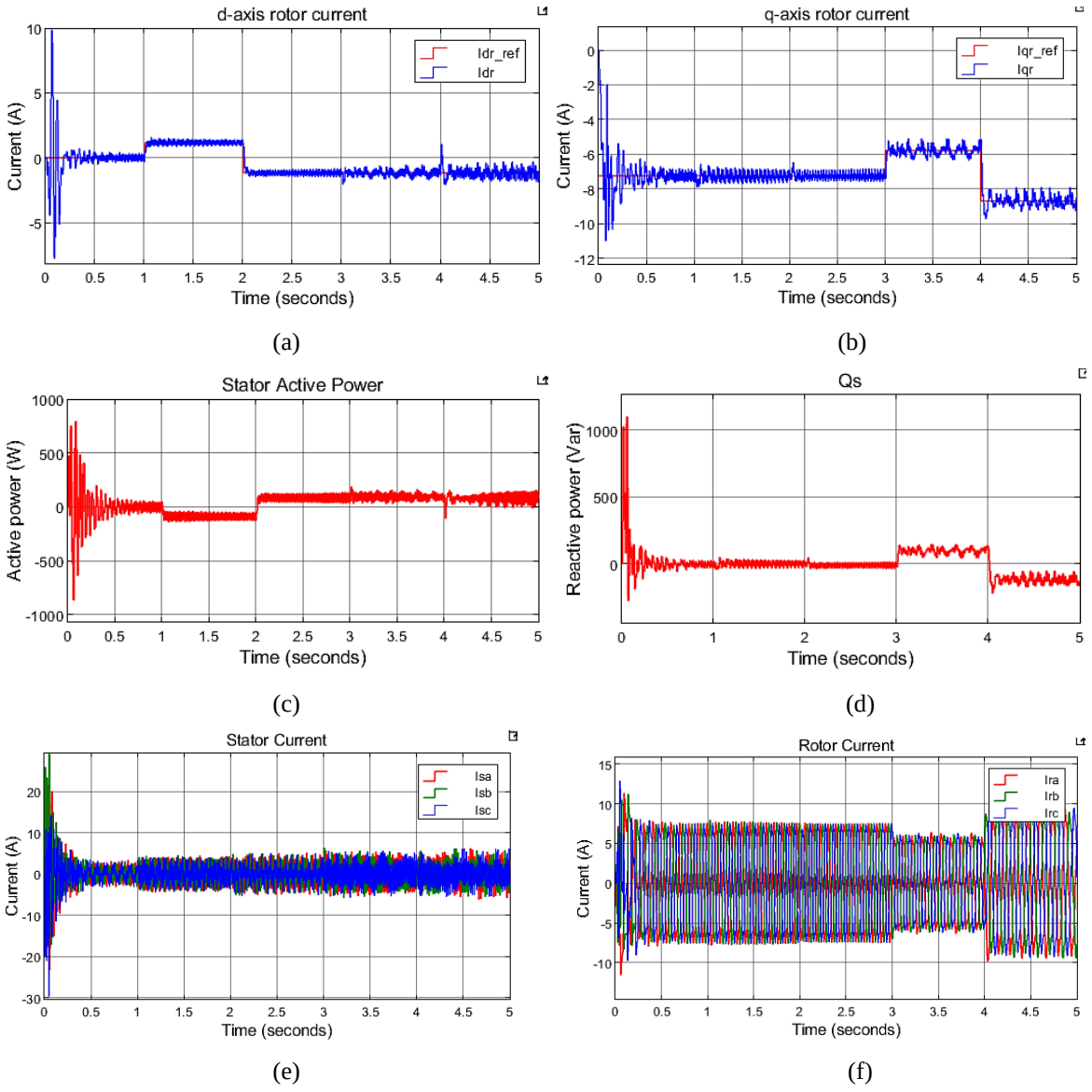

Figure 3. 14: Rotor Current Control Dynamics

For this test, the machine has been operated at a constant slip of *0.2*. The rotor *d*-axis current was first increased to 4 A at *t=1s* and dropped to -4 A at *t=1.2s* as shown in Fig. 3.14 (a). It is observed in Fig. 3.14 (c) that the stator active power has variations which are opposite those of the *d*-axis current. For the RSC control, negative power represents the current flow from the machine to the grid [8]. The rotor *q*-axis current was initially set to -7.75 A, which is the value of the magnetizing current that ensures that there is no exchange of reactive power between the stator and the grid as shown in Fig. 3.14 (d). The rotor *q*-axis current was then stepped to -6 A at *t=3s* and to -8.2 A at *t=4s*, and the stator reactive power is observed to change accordingly.

Therefore, based on the results presented above, it is deduced that the stator active and reactive powers are controlled by the rotor *d*-axis and *q*-axis currents, respectively. Examining the stator and rotor three-phase current signals presented in Fig. 3.14 (e) and (f), the stator currents are observed to operate at a frequency that is higher than that of the rotor currents. This is expected since the rotor electrical frequency is slip dependent, thus, it is much slower than the stator electrical frequency. Additionally, a large overshoot is observed in the signals in Fig. 3.14 during the starting state; this is due to the high inrush current required to overcome the inertia of the machine set. However, the waveforms stabilize once the machine reaches its steady state, fast-tracked by the controller operation.

The speed control loop of the RSC was then simulated with the rotor current controller as the inner control loop. The dynamic simulation results are presented in Fig. 3.15.

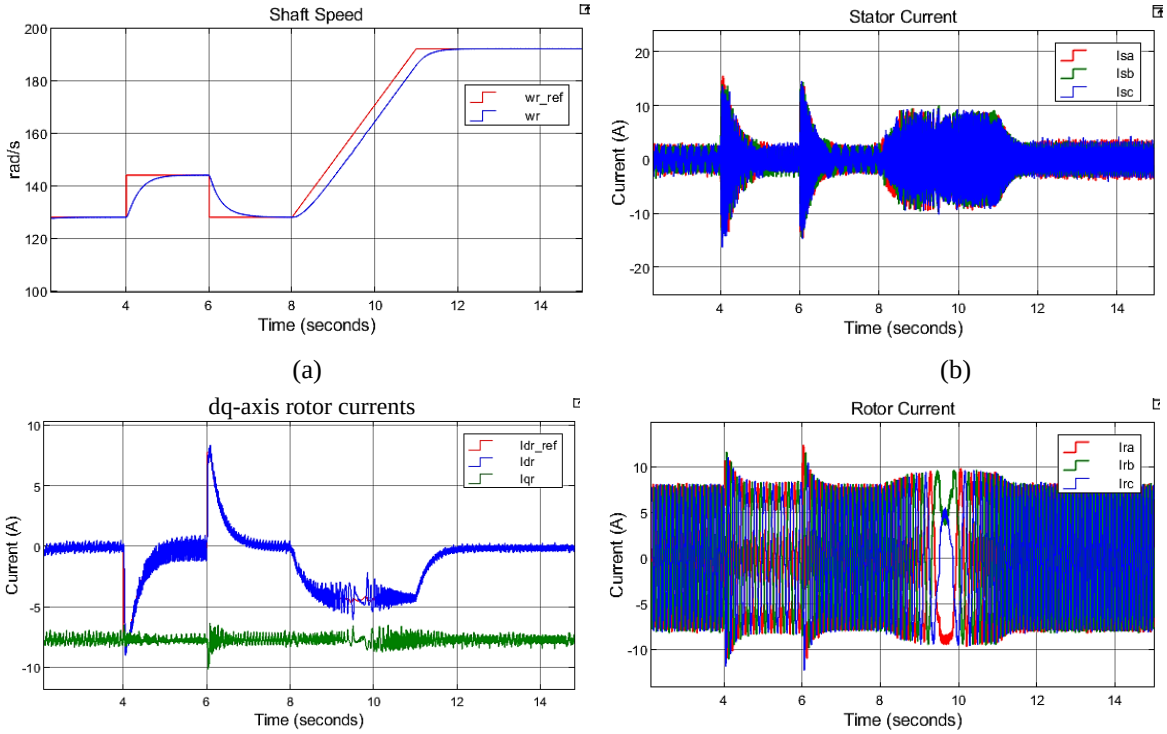

Figure 3. 15: DFIG Speed Control Dynamics

The machine was initially operated at steady state, after which the speed reference was stepped up by 18rad/s at *t=4s* and returned to the original speed at *t=6s*. It is shown in Fig. 3.15 (c) that the rotor *d*-axis current tracks the references from the speed controller instantly, and the corresponding transients in the stator current resulting from the variations are observed in Fig. 3.15 (b). For the DFIG speed control simulations, the input power to the DFIG was set to zero, and hence, the stator currents always returned to relatively small values (approximately zero) once the steady-state speed has been reached. A ramp speed reference was provided for the period between *t=8s* and *t=11s*, to accelerate the DFIG from sub-synchronous to super-synchronous speeds.

Considering that the rotor currents operate at the slip frequency of the machine, it is expected that the rotor electrical frequency will be zero at synchronous speed (i.e., slip = 0). In this regard, it is observed that the frequency became zero between *t=9s* and *t=10s*, which is illustrated by the DC state of the three-phase rotor currents waveform in Fig. 3.15 (d).

3.7.3 Independent GSC Control dynamics

The inner current control for the GSC-side system has been simulated and the results for the dynamic operation responses are shown in Fig. 3.16.

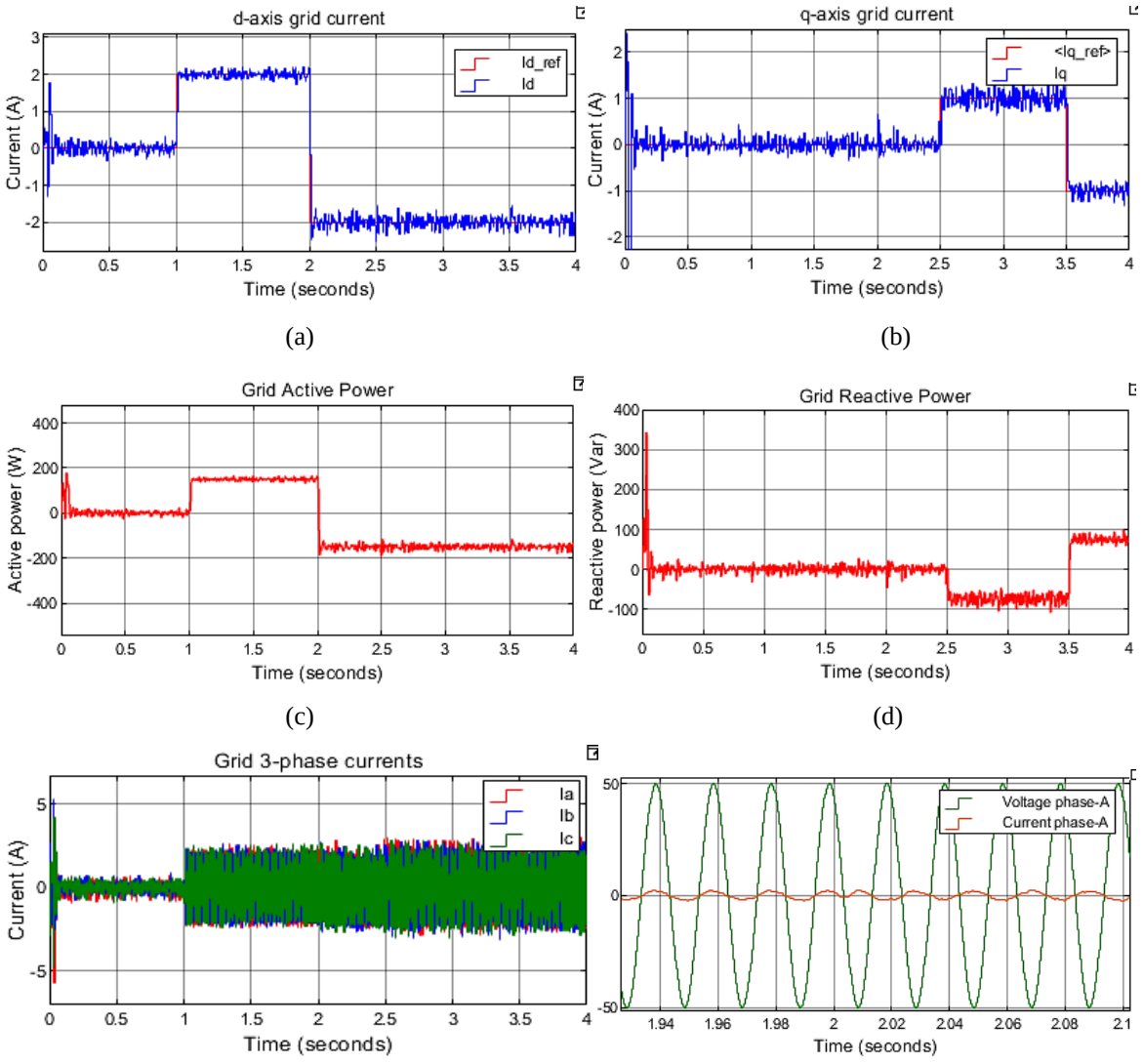

Figure 3. 16: Grid Current Control Dynamics

A constant DC-link voltage of 200 V was imposed to simulate the dynamic operations of the GSC current control. The *d*-axis current reference was stepped to 2 A at *t*=1*s* and then to -2 A at *t*=2*s*. It is observed in Fig. 3.16 (a) that the *d*-axis current tracks the reference current instantly.

The positive quantities represent a directional power flow from the converter to the grid. When the polarity of the *d*-axis current changed at *t*=2*s*, the direction of the grid active power also changed as shown in (Fig. 3.16 (c)). The effect of this polarity change is also observed in the grid phase voltage and current waveforms presented in Fig. 3.16 (f). The *0*° and *180*° phase differences between the grid current and voltage indicate that unity power factor operation is always achieved. The *q*-axis current was stepped to 1 *A* at *t=2.5s* and to -1 *A* at *t*=3.5*s* as shown in Fig. 3.16 (b), where the corresponding reactive power variations in Fig. 3.16 (d) show inverted characteristics to the *q*-axis current variations. The above results also illustrate that the grid active and reactive powers are controlled by the *d*-axis and *q*-axis currents, respectively.

The DC-link voltage control has been simulated with the grid current controller as the inner control loop. The dynamic simulation results are presented in Fig. 3.17.

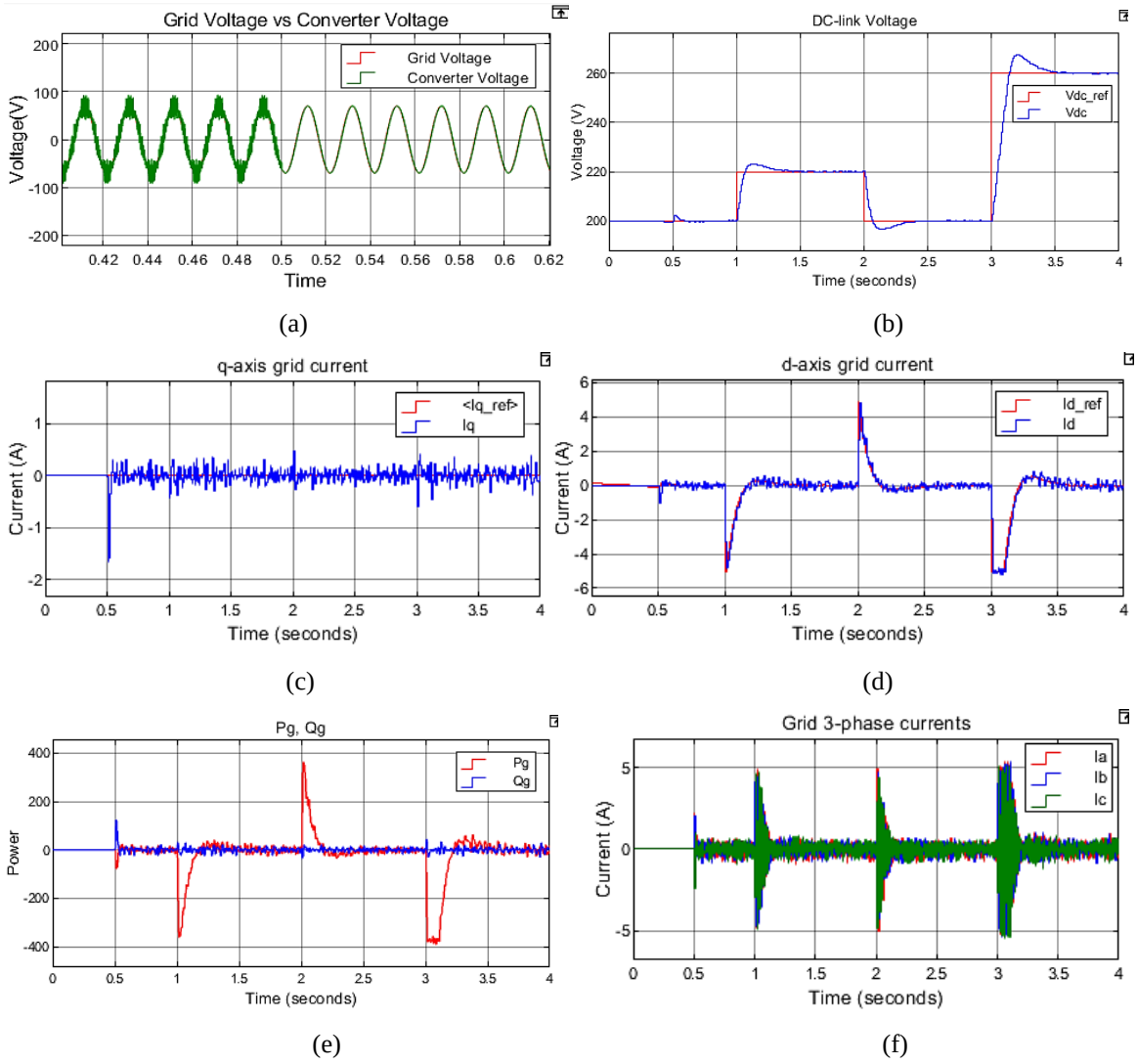

Figure 3. 17: DC-link voltage control dynamics

The process of synchronizing the GSC to the grid is observed in Fig. 3.17 (a) from *t = 0s* to *t = 0.5s*. This procedure is done before the DFIG soft synchronization as illustrated in the task sequence in Fig. 2.39. Once the grid contactor has been closed at *t = 0.5s*, DC-link voltage control can then be conducted. The DC-link voltage was first stepped from 200V to 220V at *t = 1s* and then a step of 60V was simulated at *t = 3s* as shown in Fig. 3.17 (b). The corresponding *d*-axis current reference produced by the outer control loop is shown in Fig. 3.17 (d), where the grid d-axis current follows the reference instantly. The charging and discharging of the DC-bus require the current to be drawn from or dissipated into the grid, this is demonstrated by the changes in the polarity of the grid *d*-axis current [8]. It was assumed that no input power from the DFIG was present and hence the currents in Fig. 3.17 (d) always return to zero after the DC-bus voltage has reached the steady-state. Fig. 3.17 (e) shows the corresponding grid active and reactive powers whereby the active power changes in magnitude with the change in the *d*-axis grid current while the reactive power is optimally maintained at zero to achieve a unity power factor.

3.7.4 Overall DFIG System Dynamics

The individual controller performances have thus far been validated through simulations by observing their dynamic responses to ensure that the theoretical principles presented in previous sections are accurate. To investigate the DFIG system dynamics, simulations have been carried out on the overall system considering changes in the aerodynamic torque T_a to emulate a typical wind turbine operation. The aerodynamic torque T_a serves as an input into the DFIG. Considering the basics of the power flow directions in a typical DFIG presented in Fig. 2.7, and assuming a lossless system, the following power equations are presented:

$$\begin{aligned} P_a &= P_s + P_r \approx P_{total} \\ P_r &= -P_g \qquad\qquad Q_r = -Q_g \\ \therefore P_{total} &\approx P_s + (-P_g) \\ \therefore Q_{total} &\approx Q_s + (-Q_g) \end{aligned} \tag{3.6}$$

The input mechanical power P_a from the turbine is calculated using (3.7):

$$P_a = \omega_m T_a \tag{3.7}$$

The simulation results illustrating the dynamics of the complete system are presented in Fig. 3.18.

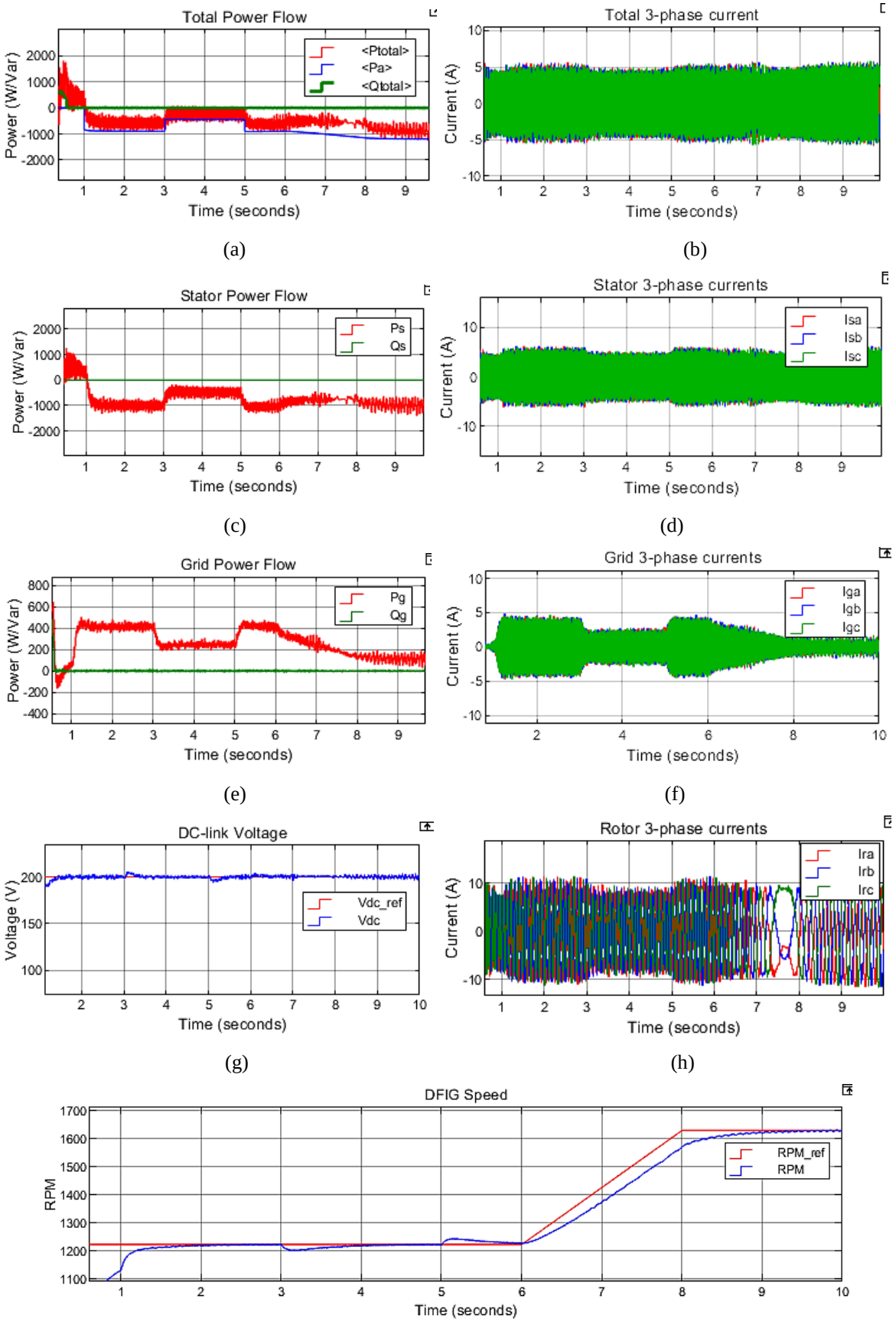

Figure 3. 18: Overall System Dynamics

The aerodynamic power P_a is initially varied by step changes in the aerodynamic torque T_a at *t= 1s*, *t=3s* and *t=5s* while the shaft speed was fixed at 20% slip. It is shown in Fig. 3.18 (a) that the total active power output P_{total} is approximately equal to the input power P_a. Since the machine is initially operating in the sub-synchronous operation, the relationship between P_s and P_g is subtractive and hence $P_{total} = P_s - P_g$. Between *t = 6s* and *t = 8s*, P_a is varied by accelerating the machine to a super synchronous slip of -20% as shown in Fig. 3.18 (i), while keeping T_a constant. During the super-synchronous operation, the relationship between P_s and P_g is additive and hence $P_{total} = P_s + P_g$. The speed control dynamics in Fig. 3.18 (i) and the DC-link voltage dynamics shown in Fig. 3.18 (g) exhibit small variations for all simulated power transients hence further validating the controller design. The reactive power of the system has been regulated to zero to ensure that unity power factor is enforced.

3.8 Chapter Summary

This chapter focused on the modelling and implementation of the components associated with the DFIG-based WECS in MATLAB/Simulink. The desired controller specifications that would ensure a robust control system have been determined. The step and frequency responses of the controllers presented in this chapter have verified that the closed-loop system of each controller meets the desired design specifications and hence, the system will be stable. The independent dynamic response analysis of the RSC, GSC and DFIG soft synchronization controllers has demonstrated that the controller objectives were met, and soft synchronization was achieved. The dynamic operation and testing of the complete DFIG-based WECS presented results which fully verify the expected system behaviors; hence, this control architecture and the corresponding controller parameters can be implemented in the laboratory for practical implementation and testing.

Chapter 4: Development of the DFIG-Based Test Rig and Experimental Validation of the DFIG's Control System

4.1 Introduction

This chapter focuses on the development of a DFIG-based WECS test rig in the laboratory. The hardware and software components of the test rig have been discussed with emphasis put on their operating principles. The chapter also covers a detailed experimental determination of the WRIM equivalent circuit parameters which are needed for the design of a robust controller system. The datasheets of the hardware components, as well as the schematic drawings, are given in *Appendix A*. The chapter also presents the practical implementation of the DFIG's control system in LabVIEW FPGA. Thereafter, experimental tests are performed on the developed DFIG-based laboratory setup. The experimental results are then compared to the simulation results presented in *Chapter 3* to validate the performance of the control system's subcomponents. Moreover, the dynamic performance of the overall DFIG-based WECS system has been presented in this chapter.

4.2 Development of the Experimental Test Rig

Figure 4.1 (a) shows the overall test rig, its hardware, software, and interface components. Whereas Fig. 4.1 (b) presents the schematic diagram that outlines the connections between the hardware components and interface components.

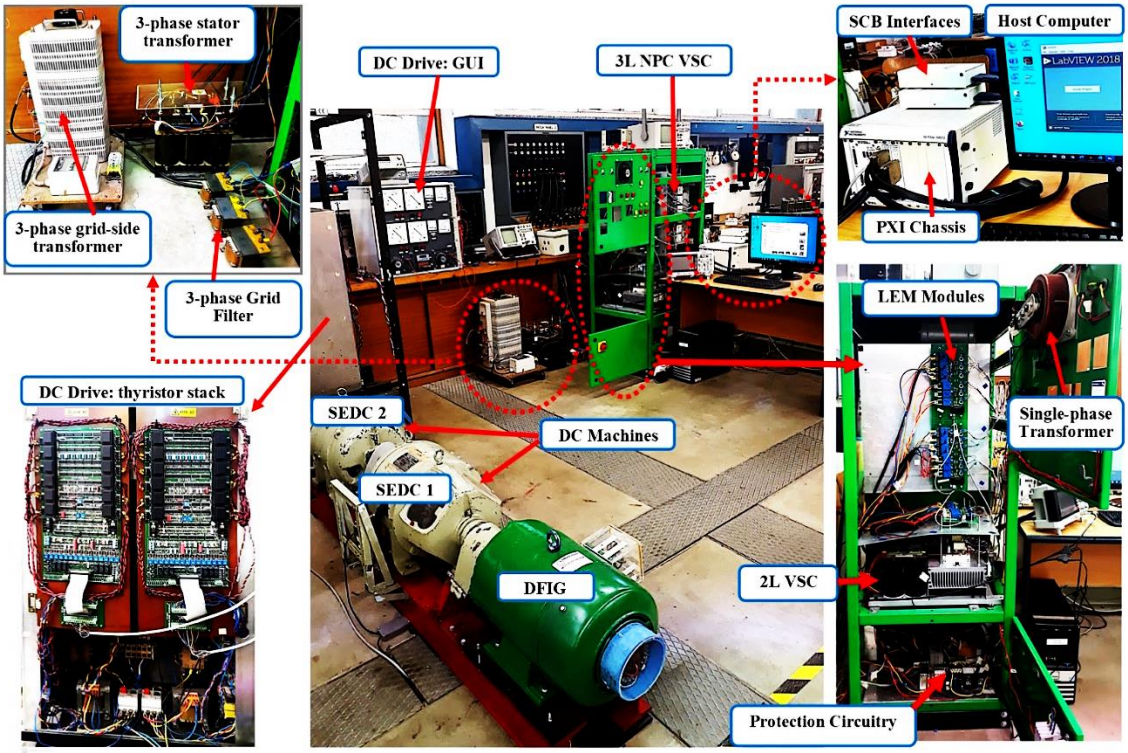

(a)

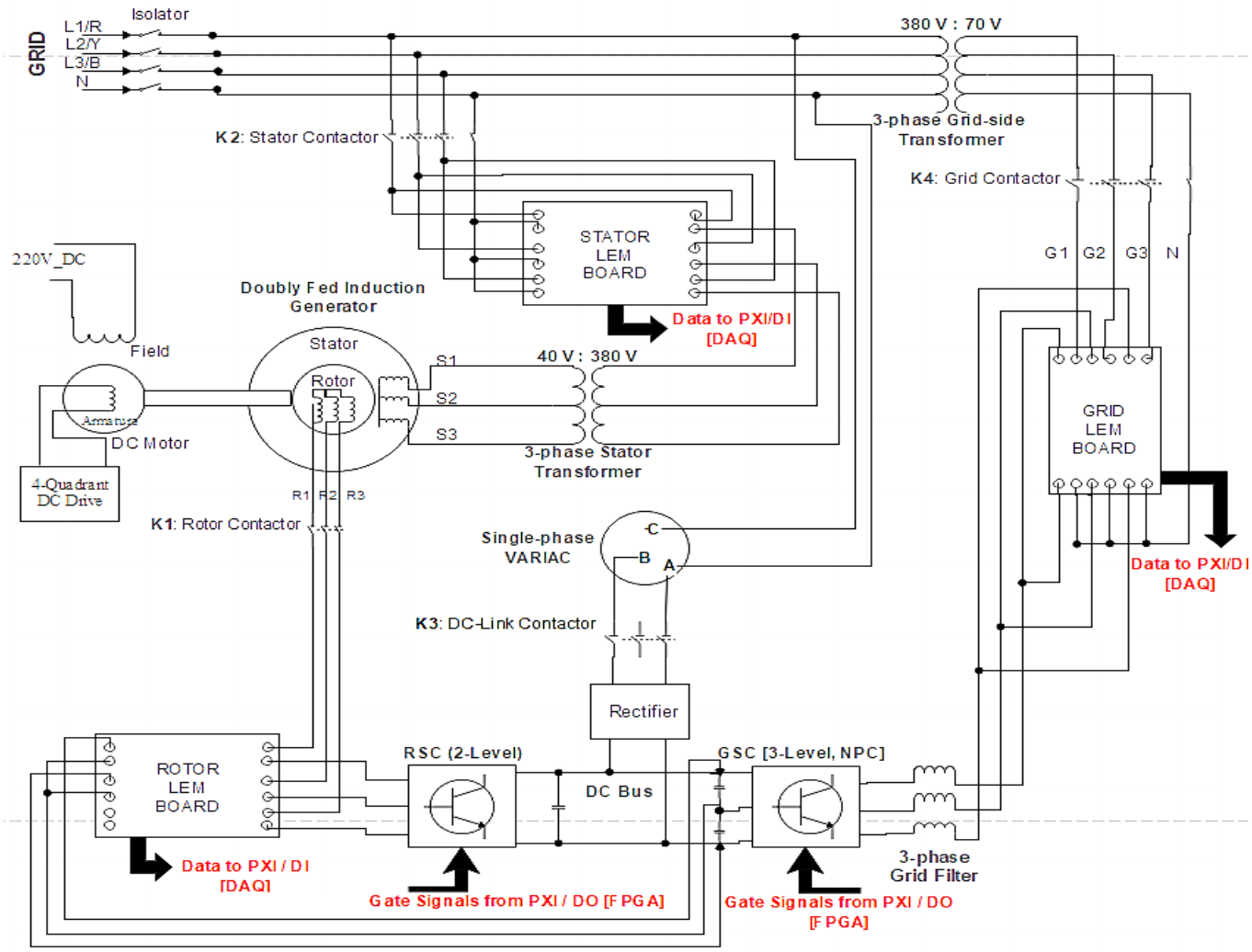

(b)

Figure 4. 1: Developed DFIG-based test rig showing the key components (a) physical hardware, software, and interface components, (b) schematic diagram of the connection between the components

The hardware and software components of the test rig and their functionalities are briefly discussed as follows:

- **A 5kW wound-rotor induction machine (WRIM) (slip-ring motor) and two 3.7kW separately excited DC (SEDC) machines**: which are directly coupled via their shafts to emulate a wind-turbine-driven DFIG.
- **An Incremental Encoder** is connected to the shaft of the machine set to obtain the instantaneous rotor angular position.
- **A back-to-back VSC system** to connect the rotor circuit of the WRIM to the grid. A 2-Level (*2L*) voltage source converter (VSC) is connected to the rotor side while a 3-level (*3L*) neutral point clamped (NPC) VSC is connected to the grid side via a 3-phase variac/transformer (380V/70V). The stator is connected to the 380V grid supply in the laboratory through a three-phase step-up transformer, i.e., *40/380V*.
- **A Single-phase Variac** to pre-charge the DC bus prior to converter operations.
- **A three-phase RL grid filter:** with a per-phase resistance of *47*Ω and per-phase inductance of *47mH*.
- **Transducers for voltage and current measurements**; there are 7 LEM modules (*LV 25-P*) for voltage measurement and 9 LEM modules (*LA 100-P*) for current measurement.
- **A relay module:** to fully isolate the low power devices from high power devices/components.
- **Four digitally controlled contactors** protect the electrical connections between the DFIG system and the grid supply through overcurrent detection.
- **NI PXI Chassis (*PXIe-1092*)**: used to implement the system control and process the system operations. The chassis comprises the field-programmable gate array (FPGA) card (*PXI-7813R*), the data acquisition (DAQ) card (*PXIe-6363*), and the processing unit card (*PXIe-8108*).
- **Shielded connector boards (*NI SCB-68A*)**: used as an interface for the signals from the PXI expansion cards (FPGA and DAQ) to the transducers and IGBT drivers.
- **LabVIEW platform** for programming the code on the host PC and sending run-time commands and signals to the PXI hardware via an Ethernet connection.

4.2.1 Hardware Equipment

The hardware components of the test rig are discussed in more detail in the following subsections.

4.2.1.1 DC Machine Drive

Figure 4.2 shows how the WRIM, SEDC machines, and incremental encoder are coupled together to form a complete machine set.

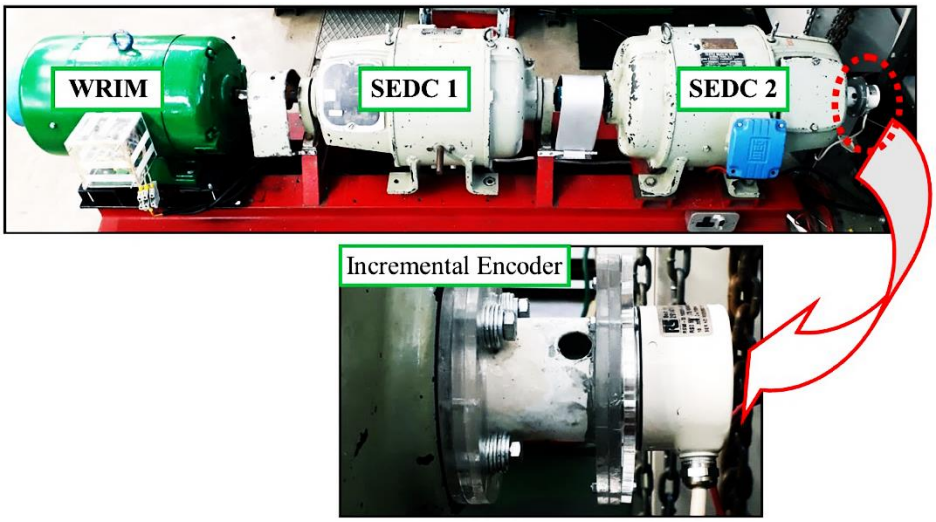

Figure 4. 2: WRIM Coupled to a SEDC Machines

The parameters of the DFIG machine under investigation have already been provided in Table 3.1. Table 4.1 presents the parameters of the SEDC machines.

Table 4. 1: Parameters of the 3.7kW SEDC Machines [13]

Parameter	**Value**
Power [kW]	3.7 (5 hp)
Voltage [V]	230
Current [A]	20
Speed [rpm]	1750

The SEDC 2 machine acts as a prime mover whose speed is directly controlled by varying the armature current using a 4-quadrant thyristor-based DC drive shown in Fig. 4.3 to emulate basic turbine torque and speed variations. While SEDC 1 was operated in generator mode to load the machine set during the initial tests, i.e., IEEE standard tests, while having the WRIM operating in motor mode. A 220V DC supply is used to excite the field of the DC machine.

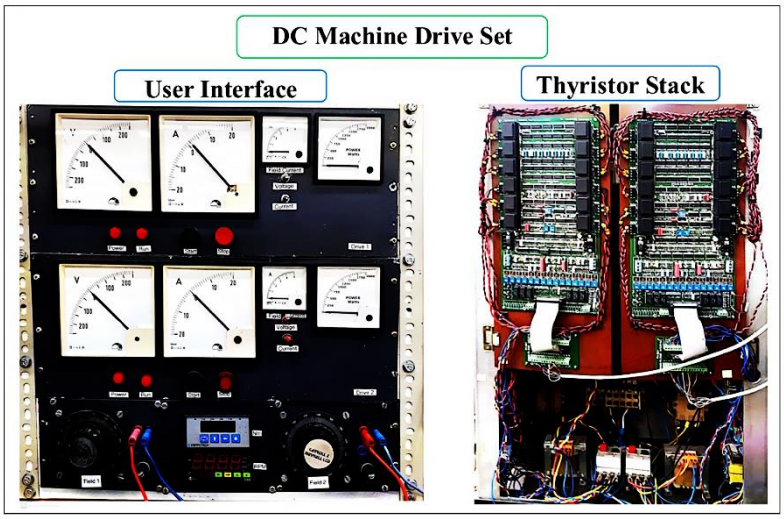

Figure 4. 3: DC Machine Drive Set

4.2.1.2 PXI multipurpose Real-Time Controller

The PXI controller is a multipurpose controller designed by National Instrument (NI) to be used in real-time control applications. This controller comprises of a chassis with multi-card slot where compatible expansion modules can be installed and synchronized to the same system clock [8]. In this research, the NI *PXIe-1062Q* chassis is adopted and it comprises the following expansion modules:

- The field-programmable gate array (FPGA) card (*PXI-7813R*),
- The data acquisition (DAQ) card (*PXIe-6363*) and
- The processing unit card (*PXIe-8108*) as shown in Fig. 4.4.

The URL links to the datasheets of the NI *PXIe-1062Q* chassis and the corresponding extension cards are provided in *Appendix A*.

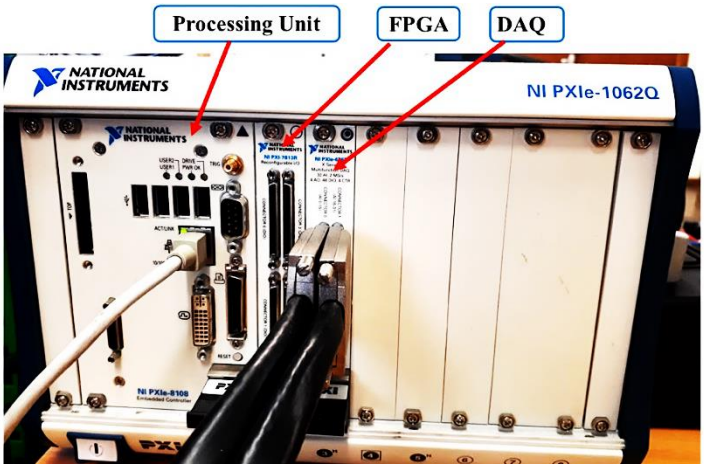

Figure 4. 4: PXI Multipurpose Controller

The PXI hardware is programmed using the LabVIEW real-time (RT) which is on the processing unit card and the user commands are generated in LabVIEW software installed on a remote host PC that communicates to the PXI controller via the Ethernet connection. The shielded connector boards (SCB) of type NI *SCB-68* in Fig. 4.5 are used as interfaces for the signals from the PXI expansion cards to other system devices such as transducers and IGBT drivers.

Figure 4. 5: Shielded Connector Boards

4.2.1.2.1 Processing Unit (*PXIe-8108*)

The PXIe-8108 is an Intel Core 2 Duo embedded controller that is mainly used for synchronizing system communication and providing a reliable user interface [8]. The processing unit is installed with the LabView RT operating system.

4.2.1.2.2 Field Programmable Gate Array (*FPGA PXI-7813R*)

The FPGA *PXI-7813R* card enclosed in the chassis has a maximum logic rate of 40MHz with 160 configurable digital lines [8]. The FPGA card can execute logical functions at high speeds up to a maximum of 25*ns* resolution, hence, it can handle parallel computing and perform numerous tasks concurrently [8]. This makes the FPGA suitable for implementing the control of the DFIG-based WECS and to perform the PWM switching operations at the same time. However, its device resources are limited, therefore the computational efficiency and memory utilization must be carefully considered when programming the FPGA card [8]. The digital lines are configured into inputs and outputs using the LabView FPGA software and they are interfaced with the external devices via the SCB connectors.

4.2.1.2.3 Data Acquisition Device (*PXIe-6363*)

A data acquisition (DAQ) card is used for analog and digital data transmission between the PXI controller and the transducers. The DAQ card (*PXIe-6363*) enclosed in the chassis has 16 differential analog input channels with a maximum sample rate of 1Ms/s, and 48 digital output channels with maximum data rates of *2.88Ms/s* and *10Ms/s*, respectively [8]. The sixteen input channels on the DAQ card are interfaced with the transducers via SCB connectors to supply the PXI controller with the measured signals of the following system quantities:

- The three-phase grid voltages
- The three-phase stator voltages
- The three-phase grid currents
- The three-phase stator currents
- The three-phase rotor currents
- The DC-link voltages across the top and bottom capacitors.

4.2.1.3 Converters and DC-link Capacitor Sizing

4.2.1.3.1 Power Electronic Converters

The power electronic conversion system that connects the rotor circuit of the WRIM to the grid supply consists of a 2-level VSC on the rotor-side connected back-to-back to a 3-level NPC VSC on the grid-side as presented in Fig. 4.6.

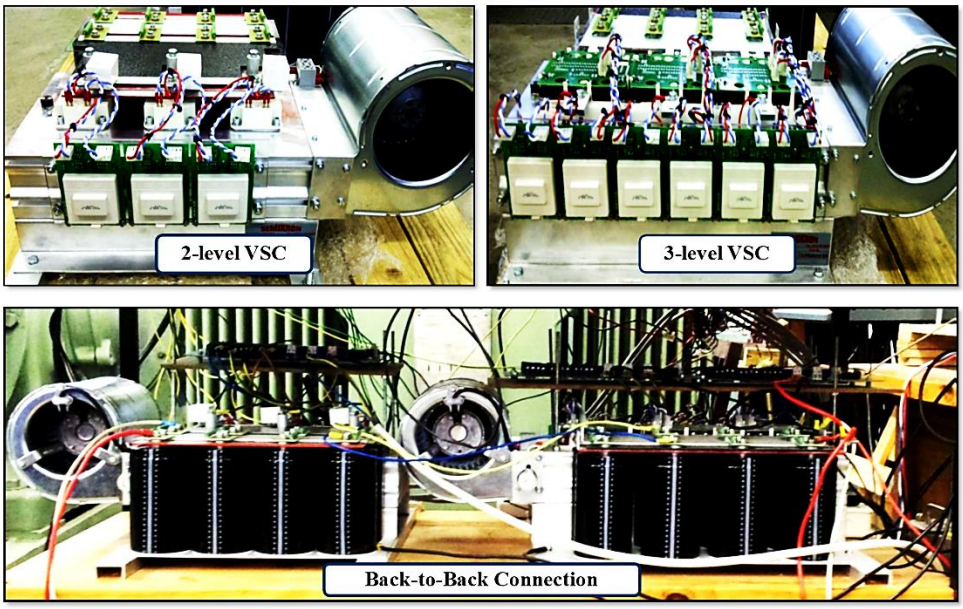

Figure 4. 6: *2L* VSC and *3L* NPC VSC connected back-to-back

The converters in Fig. 4.6 are manufactured by Semikron, with built-in DC capacitors and each VSC consists of IGBT modules, and their corresponding drivers mounted on a printed circuit board (PCB). When the converters are connected in a back-to-back configuration, the total DC-link capacitance is $18800\mu F$.

4.2.1.3.2 Insulated Gate Bipolar Transistors (IGBTs)

The two-level VSC is made up of three Semikron *SKM200GB12V* IGBT modules, one for each phase. Each module consists of two IGBTS (one for the upper leg and another one for the lower leg), whose voltage and current ratings are 1200V and 145A, respectively. Whereas the three-level VSC consists of three Semikron *SKiM201MLI12E4* IGBT modules, one for each phase. Each module consists of four IGBTS, whose voltage and current ratings are 1200V and 200A, respectively. The IGBT modules are shown in Fig. 4.7 and the links to their datasheets are provided in *Appendix A*.

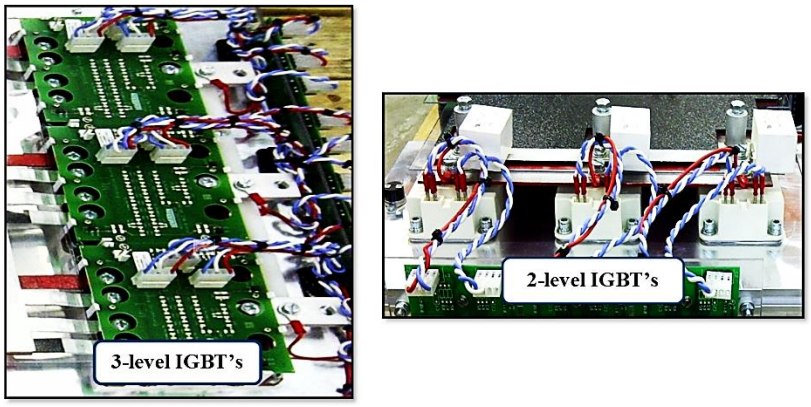

Figure 4. 7: The 3-Level and 2-Level IGBT modules

4.2.1.3.3 IGBT Gate Drivers

The Semikron *SKHI22BR* drivers shown in Fig. 4.8 are used to supply the gating signals to the IGBTs in both converters. These drivers have built-in protection measures for both the IGBTs and the external controlling circuits. The IGBT's collector-emitter voltage monitoring provides short-circuit protection while the signal transmission via optocouplers enables the isolation between the external circuits and the IGBTs [8]. The link to the datasheet of the gate driver in Fig. 4.8 is given in *Appendix A*.

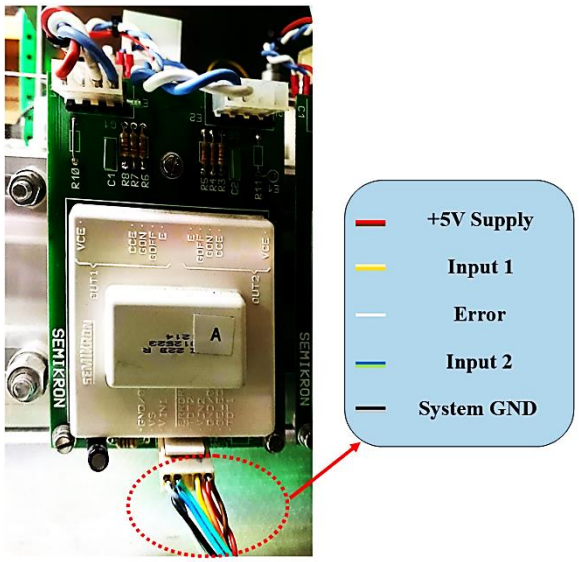

Figure 4. 8: IGBT Gate Driver and its corresponding Inputs

The inputs to the driver accept control voltages of 0V (*off*) and +5V(on) and outputs gate-emitter signals of - 7V(off) and +15V(on) for the IGBTs via the optocoupler. Additional external components can be placed on the PCB to set the output characteristics of the *SKHI22BR* drivers. The settings of these components are discussed in more detail by Hu in [8].

4.2.1.3.4 Signal Level Shifter

The switching signals obtained from the digital lines of the FPGA (PXI-7813R card) have a logic output voltage of +3.3V for a *High* and 0V for a *Low*. However, the IGBT drivers require an input voltage of +5V. Therefore, an interface circuit has been designed to shift all signals from the FPGA card to +5V by using quad two-input AND gates (*MN74HC08*). Figure 4.9 shows the printed circuit board (PCB) of the signal level shifter and its wiring in a box. The schematic diagram of the level shifter and the URL link to the datasheets of the *MN74HC08* AND gates are given in *Appendix A*.

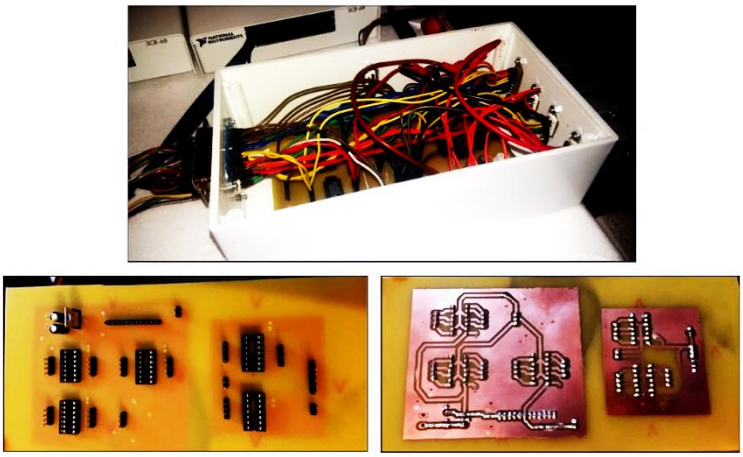

Figure 4. 9: Signal Level Shifter

4.2.1.4 Measurement Instrumentation and System Protection

4.2.1.4.1 Voltage and Current Transducers

In this project, the current and voltage signals are measured using the LEM modules. These transducers use the Hall Effect principle to provide the necessary isolation between the primary power circuit and the secondary side (the DAQ device) [8, 32]. Seven voltage LEM modules (*LV 25-P*) and nine current LEM modules (*LA 100-P*) have been used to perform the current and voltage measurements. These modules are mounted on custom PCB as shown in Fig 4.10. The schematic diagram of the LEM integrated circuit board and the URL links to the datasheets of the current and voltage transducers are given in *Appendix A*.

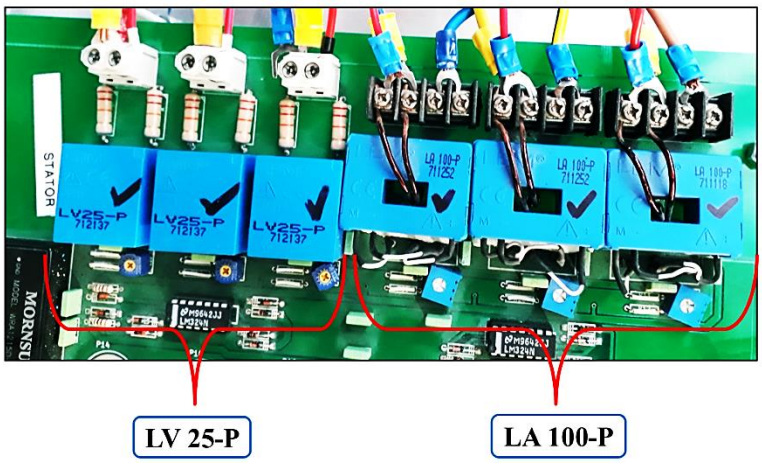

Figure 4. 10: LEM modules for voltage and current measurements

The overall system's circuit components onto which these transducers are connected need to be carefully chosen to ensure that the voltage and currents are confined within the allowable operating ranges of the transducers to avoid saturation. The current and voltage transducers and their scaling methodology to keep them within the saturation range are discussed in more detail by Hu in [8].

4.2.1.4.2 Incremental Encoder

The *RS58-0/1000* incremental encoder has been used to obtain the angular position of the rotor. The encoder is connected to the shaft of the machine set as shown in Fig. 4.2. The URL link to the datasheet of this incremental encoder is given in Appendix A. The incremental encoder has a resolution of 1000 pulses/revolution and can measure speeds up to 10000rpm. It has two output channels, *A* and *B*, which generate digital signals which are phase-shifted from each other by 90˚. The encoder obtains 4000 counts per revolution from each output channel to represent the rotor angular position. Apart from that, the encoder also generates an index pulse which is used to reset the counting of the pulses to zero after completing one revolution [8]. The rotor angular position θ_m which corresponds to the output pulse counts of the encoder is determined by using (4.1) [8]:

$$\theta_m = \frac{2\pi}{4000} count \tag{4.1}$$

The rotor angular position obtained in (6.1) represents the rotor mechanical angular position in radians. Therefore, this quantity needs to be converted to electrical radians to transform the rotor quantities to the synchronous reference frame. The LabVIEW FPGA interface can be used to decode the encoder pulse counts and obtain the rotor mechanical angular speed using the operation of shift registers to realize (4.2):

$$\omega_m = \frac{\theta_m(k-1) - \theta_m(k)}{T_s} \tag{4.2}$$

Where k and T_s represent the sampling instance and sampling period, respectively.

To shield and preserve the data that is transmitted from the encoder to the DAQ device from getting corrupted by environmental noises, the signals are converted from the TTL format to differential signals which are less prone to electrical noise pollution. This is done by passing the signals through a quad differential line driver (AM26LS31CN) and these signals are then converted back to TTL format at the receiving end by a quad differential receiver (AM26LS31ACN). The circuits of the differential driver and receiver set are presented in Fig. 4.11. The URL links to the datasheets of the differential line driver and receiver chips are given in *Appendix A*.

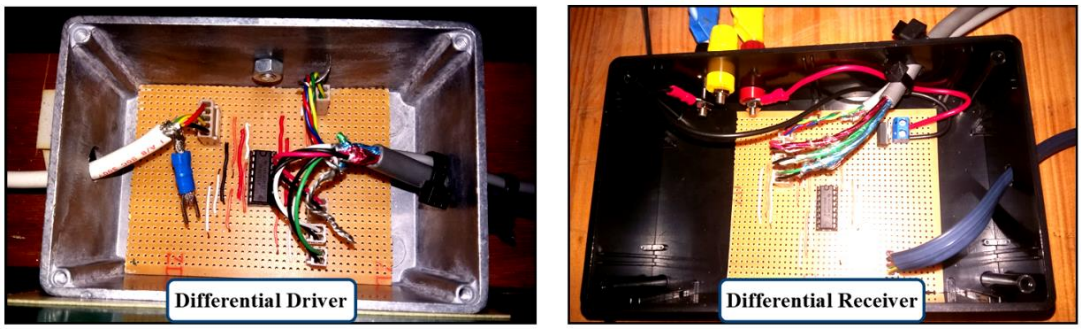

Figure 4. 11: Differential line driver and receiver set

4.2.1.5 System Protection Circuitry

Figure 4.12 shows the components that are used for the protection of the complete system. The system protection circuitry comprises the relay interface which acts as a buffer circuit, relays, contactors, and a 24V power supply which provides the voltage that is required by the relays and the buffer circuit. The schematic diagram of the protection circuitry is given in *Appendix A*.

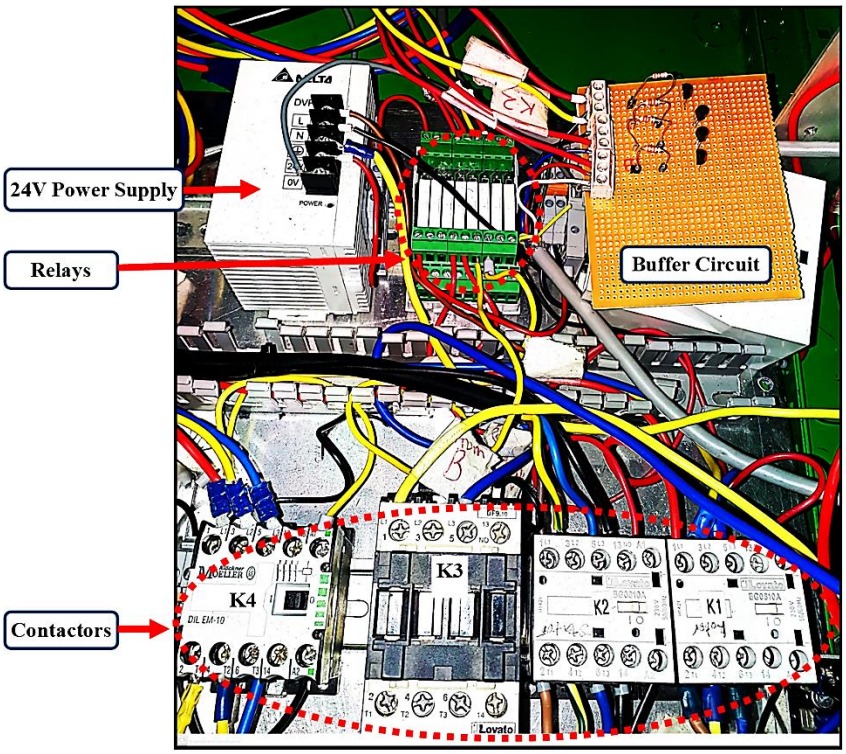

Figure 4. 12: System Protection Circuitry

The operating principle of the system protection circuitry is as follows:

The operational amplifiers in the buffer circuit are used to buffer the error signals which are generated by the converter driver boards and the controller overcurrent detection. This is done to prevent large feedback voltage to the controller I/O in the case of circuit malfunction. The output terminals of the buffer circuit are connected to the 24V relay low voltage terminals, whereas the 230V high voltage terminals of the relays are further connected to contactors where the switching commands are registered. The four contactors are labeled as follows:

- **K1**: Rotor contactor which protects the two-level RSC
- **K2**: Stator contactor for DFIG soft synchronization
- **K3**: DC-link contactor for pre-charging the DC bus
- **K4**: Grid contactor to protect the grid and the three-level NPC VSC used as the GSC.

4.2.1.6 Transformer and Grid Filter Circuit Components

4.2.1.6.1 Transformer Parameters

Since the rated voltage of the stator is lower than the grid voltage, a 40/380V 5.5kVA three-phase step-up transformer shown in Fig. 4.13 has been used to connect the stator to the grid supply in the laboratory. The parameters of the transformer are given in Table 4.2.

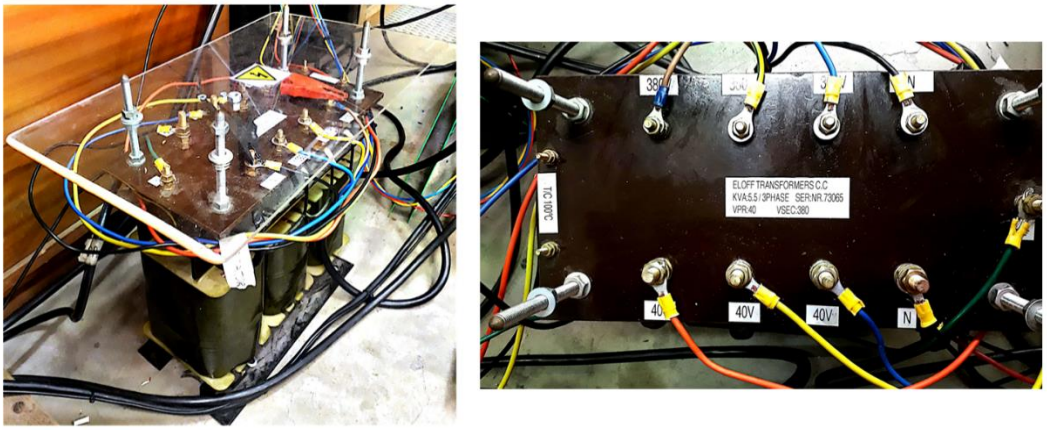

Figure 4. 13: The three-phase step-up transformer for connecting the stator to the grid supply

Table 4. 2: Three-phase Step-up Transformer Parameters [113]

Parameter	Value	Parameter	Value
Power [kVA]	5.5	Secondary Voltage [V]	380
Primary Voltage [V]	40	Secondary Current [A]	8.3
Primary Current [A]	20	Transformer ratio	0.104

4.2.1.6.2 Grid Filter Circuit Components

The three-phase grid filter shown in Fig. 4.14 has been used in the test rig. The filter comprises of three inductors whose individual inductances are 47mH, and a parasitic resistance of 0.75Ω. The current limit for each inductor is 5A. The ratings of the grid filter components are used for computing the desired parameters of the grid current controller.

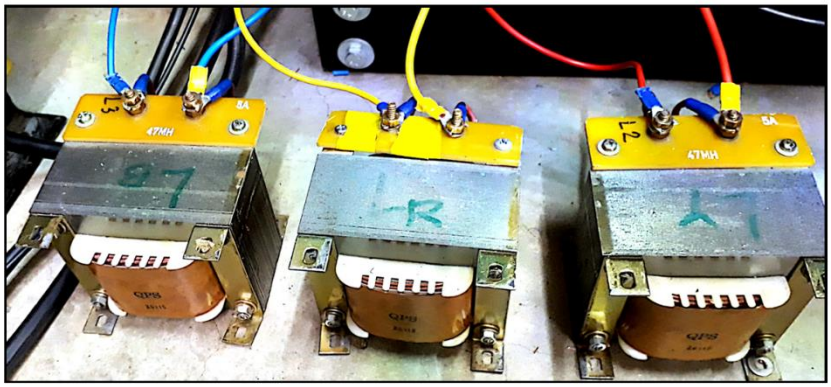

Figure 4. 14: Three-phase Grid Filter

4.2.2 Software and Hardware Interface Equipment

The software packages which are essential in the development of a DFIG-based WECS test rig are as follow:

- LabVIEW
- LabVIEW RT
- LabVIEW FPGA
- Xilinx compilation tool for FPGA

The data flow pattern between the PXI hardware and software packages is shown in Fig. 4.15.

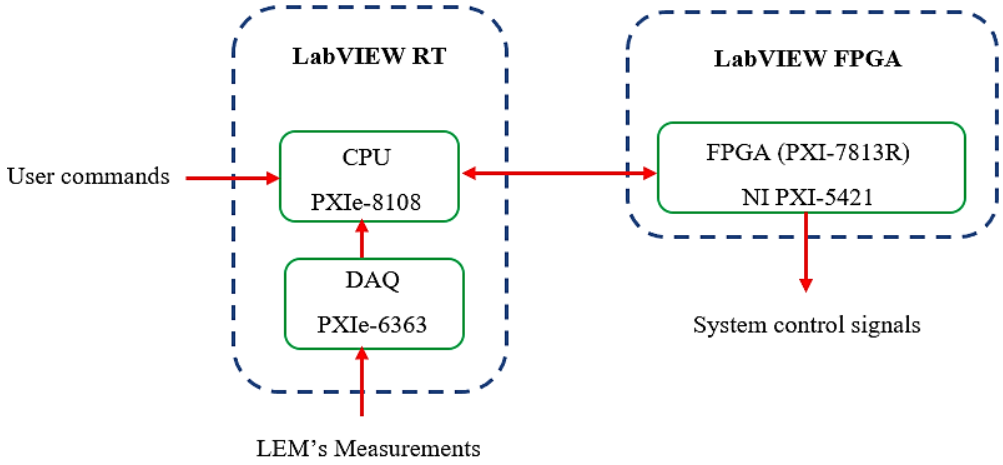

Figure 4. 15: Data flow between PXI hardware and software packages

The system control and converter switching tasks are carried out using the *PXI-7813R* FPGA card which has 160 configurable digital lines and a maximum logic rate of 40MHz. The measurements obtained using the transducers (LEM modules) are sent to the PXI DAQ card. The processing unit (*PXIe-8108*) is programmed to extract the sampled data from the DAQ card using LabVIEW RT. The measured data is then sent to the FPGA card for control processing. The codes for all system controllers and the converter modulation algorithms are implemented on the LabVIEW FPGA which has a graphical coding environment like Simulink. The control signals are then sent from the FPGA configurable digital I/Os to the converter drivers and the system protection circuits given in Fig. 4.12. All system controller and switching algorithm codes implemented in LabVIEW FPGA are given in *Appendix D.*

LabVIEW RT makes provision for graphical user interface (GUI) designs thereby enabling an operator with minimal knowledge of the system hardware to navigate through the system operations with ease. The several functionalities which have been included in the GUI are as follows:

- Monitoring the real-time operation of the system using LabVIEW scopes. The LabVIEW scopes contain a fixed number of samples that can be exported as images or data points for further analysis in other software packages such as MATLAB. In addition, the signals displayed on the scopes can be zoomed in/out.
- The indicators that are on the GUI signify the statuses of various components to the user.
- System settings can be altered before operations or when they system is in operation. These are such as system protection limits, controller gains, set points/reference values, and sampling rates of various functions.
- Run-time CPU usage monitoring has been included for the precipitation and prevention of software-related failures.
- Fail-safe system shut down can be performed.

The various parts of the DFIG system control user interface are presented in Appendix D

4.2.3 System Parameter Identification

To ensure an accurate controller design, a set of experiments have been conducted to determine the equivalent circuit parameters of the WRIM which are needed for the rotor current controller modeling. Moreover, the combined inertia of the WRIM and DC machines which is needed for the DFIG speed controller has also been determined.

4.2.3.1 DFIG Equivalent Circuit Parameters

To determine the system parameters such as the DFIG circuit parameters, the following standard tests were conducted, and the parameters were determined. The *YOKOGAWA WT1800* power analyzer has been used to conduct the measurements.

4.2.3.1.1 No Load Test

A standard IEEE no-load test discussed in [114] has been conducted to obtain information regarding the no-load impedance. The no-load test is performed by applying the rated three-phase stator voltage at the rated frequency to the stator windings while the rotor windings are shorted together. The rotor is kept uncoupled from any mechanical load. The single-phase no-load equivalent circuit for a WRIM is presented in Fig. 4.16.

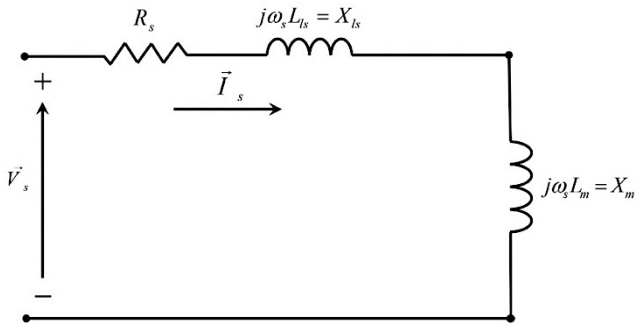

Figure 4. 16: Steady-state per-phase no-load equivalent circuit of the WRIM

The no-load test measurements are presented in Table 4.3.

Table 4. 3: No Load test results

	Phase A	**Phase B**	**Phase C**
$V_s^{rms}(V)$	20.63	19.91	19.18
$I_s^{rms}(A)$	16.18	16.34	15.92
$P_{NL}(W)$	184.65	179.61	168.41
$Q_{NL}(Var)$	290.43	293.31	288.08

The total three-phase no-load active and reactive power can be obtained from the per-phase values as follow:

$$P_{NL}^{total} = 532.67W \qquad and \qquad Q_{NL}^{total} = 871.85Var$$

The per-phase no-load resistance $R_{NL}$and reactance $X_{NL}$are calculated using (4.3) and (4.4), respectively:

$$R_{NL} = \frac{3P_{NL}^{total}}{\sum I_{sj}^2} = 0.699\Omega \tag{4.3}$$

$$X_{NL} = \frac{3Q_{NL}^{total}}{\sum I_{sj}^2} = X_m + X_{ls} = 1.14\Omega \tag{4.4}$$

The stator resistance is determined by performing a DC test on the induction machine. This is carried out using the *QPX1200SP* DC power supply whereby the DC power is supplied to the stator winding at the rated current of 20A. The DC voltage and current measurements are recorded as shown in Table 4.4, and the stator resistance is calculated using Ohm's law.

Table 4. 4: Measured values from the DC test

Phases	**V-W**	**U-W**	**U-V**
DC Voltage (V)	6.67	6.55	6.58
Current (A)	19.62	19.60	19.60
Resistance(Ω)	0.339	0.334	0.336

The average phase to phase resistance is 0.337Ω and hence the per-phase stator resistance is:

$$R_s = \frac{0.337}{2} = 0.169\Omega\ .$$

4.2.3.1.2 Blocked Rotor Test

The blocked rotor test is performed to obtain information regarding the leakage impedances and the rotor resistance of the machine. The test is done by mechanically clamping the rotor to remain stationary, the rotor windings are shorted together, and a three-phase voltage is applied to the stator terminals while making sure that the stator current does not exceed the rated value of 20A, specific to this investigation. The per-phase blocked rotor equivalent circuit for the WRIM is presented in Fig. 4.17.

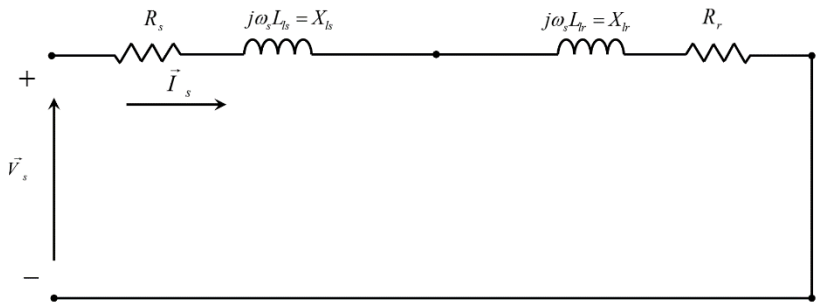

Figure 4. 17: Steady-state per-phase blocked rotor equivalent circuit of the WRIM

All circuit parameters of the rotor are referred to the stator. The blocked rotor test measurements shown in Table 4.5 were obtained using the *YOKOGAWA WT1800* Power Analyzer.

Table 4. 5: Measured results for the blocked rotor test

	Phase A	**Phase B**	**Phase C**
$V_s^{rms}(V)$	10.39	10.39	9.78
$I_s^{rms}(A)$	18.9	19.06	18.94
$P_{BL}(W)$	169.17	174.24	171.56
$Q_{BL}(Var)$	81.73	94.16	75.95

The total three-phase blocked rotor active and reactive power are obtained from the per phase power values as follow:

$$P_{BL}^{total} = 514.97W \quad and \quad Q_{BL}^{total} = 251.84Var$$

The per-phase blocked rotor resistance $R_{BL}$and reactance $X_{BL}$are calculated using (4.5) and (4.6), respectively:

$$R_{BL} = \frac{3P_{BL}^{total}}{\sum I_{sj}^2} = 0.477\Omega \tag{4.5}$$

$$X_{BL} = \frac{3Q_{BL}^{total}}{\sum I_{sj}^2} = X_{ls} + X_{lr} = 0.233\Omega \tag{4.6}$$

For smaller machines, the stator and rotor reactances can be assumed to be the same [52]. Therefore, the per-phase stator, rotor, and magnetizing reactance and their corresponding inductances for a $50Hz$ stator supply are computed as follow:

$$X_{ls} = \frac{X_{BL}}{2} = 0.117\Omega$$

$$X'_{lr} = 0.331\Omega$$

$$X_m = X_{NL} - X_{ls} = 1.028\Omega$$

$$X = 2\pi fL$$

$$\therefore L_{ls} = \frac{X_{BL}}{4\pi f} = 0.371mH$$

$$\therefore L'_{lr} = \frac{X'_{lr}}{2\pi f} = 1.05mH$$

$$\therefore L_m = \frac{X_m}{2\pi f} = 3.27mH$$

The per-phase rotor resistance is the calculated using (4.7).

$$R_r = \left(\frac{X_{lr}+X_m}{X_m}\right)^2 (R_{BL} - R_s) = 0.116\Omega \tag{4.7}$$

4.2.3.1.3 Open Rotor Test

The open rotor test provides the stator-rotor effective turns ratio for the induction machine. The test is conducted by applying a three-phase voltage to the stator windings in small increments while keeping the rotor windings open. The single-phase open rotor equivalent circuit for the WRIM is presented in Fig. 6.18.

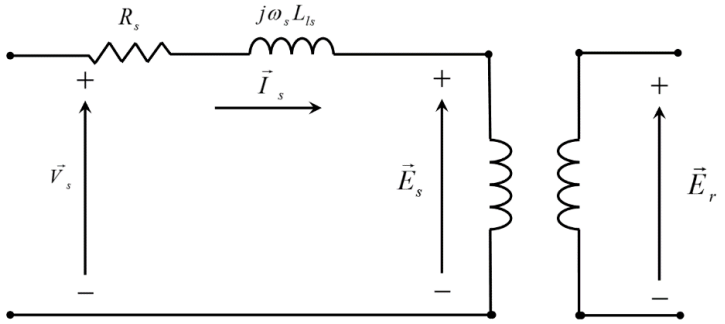

Figure 4. 18: Steady-state per-phase open rotor equivalent circuit

The stator winding losses can be considered negligible for the small voltages supplied. Therefore, the ratio between the stator supply voltage and the induced voltage at the open rotor terminals can be considered a close representation of the effective-turns-ratio [8]. The open rotor voltage measurements corresponding to the different stator voltages applied were measured using the *YOKOGAWA WT1800* power analyzer and are recorded in Table 4.6.

Table 4. 6: Measurement results for the WRIM open rotor test

Supplied stator RMS voltage (V)	**Induced rotor RMS voltage (V)**	**Ratio ($\frac{V_s}{V_r}$)**
2.96	10.60	0.28
4.95	17.77	0.28
7.02	20.32	0.35
9.52	31.22	0.30
13.05	46.89	0.28
16.06	57.74	0.28
19.09	68.63	0.28
21.51	77.31	0.28
Average effective-turns-ratio		***0.29***

Table 4.7 summarizes the DFIG circuit parameters obtained from the standard IEEE induction machine tests. These parameters are used to obtain the desired parameters of the rotor current controller.

Table 4. 7: Summary of the DFIG circuit parameters

Circuit parameter	Value
Stator Resistance	$R_s = 0.169\Omega$
Stator leakage inductance	$L_{ls} = 0.373mH$
Magnetizing inductance	$L_m = 3.27mH$
Rotor leakage inductance	$L_{lr}{}' = 1.05mH$
Rotor resistance	$R_r = 0.116$
Effective-turns-ratio	$n = \frac{N_s}{N_r} = 0.29$

4.2.3.1.4 Combined machine set inertia

The inertia of the WRIM and the DC machines that is needed for the DFIG speed controller design can be obtained by performing a machine retardation test following the procedure outlined in [8, 115]. To carry out the test, the machine needs to be accelerated above its no-load speed and then the electrical supply to the machine is abruptly cut-off [8]. As a result, the machine set freely slows down to standstill. When there is no electrical supply to the stator winding of the WRIM, the dynamic model for the DFIG mechanical drive train is given by (4.8):

$$J\frac{d\omega_m}{dt} = -T_m \tag{4.8}$$

If the rotor is not loaded, T_m in (4.8) can be described as a retarding torque that is imposed on the drive train due to the inertia and friction of the rotor [8]. Figure 4.19 presents the generic deceleration curve of a first-order differential equation given in (4.8) [8].

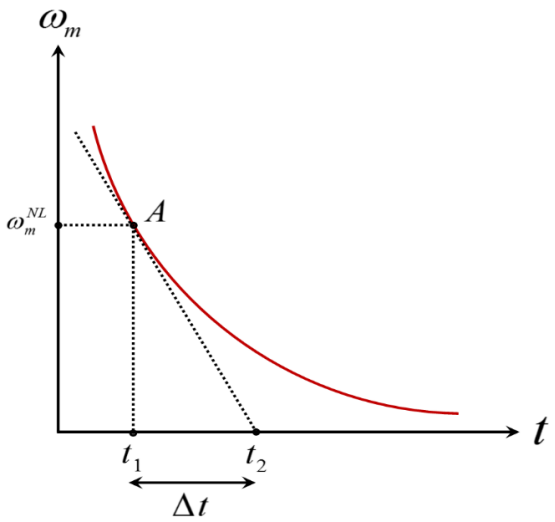

Figure 4. 19: Machine deceleration curve [8]

Consider point A in Fig. 4.19 as the point where the machine has reached the no-load speed ω_m^{NL}, then (4.8) can be deduced relative to this operating point as [8]:

$$J = \frac{d\omega_m}{dt}\Big|_{\omega_m=\omega_m^{NL}} = -T_m^{NL} \tag{4.9}$$

The value of the rotor inertia J in (4.9) can be determined if the following variables are known:

- The tangent $\frac{d\omega_m}{dt}\Big|_{\omega_m=\omega_m^{NL}}$ of the deceleration curve at $t = t_1$corresponding to the no load speed.
- The no load torque T_m^{NL}.

The first variable can easily be determined from the deceleration curve, whereas the no-load torque is quite challenging to obtain. Therefore, to determine the latter variable, its relationship with the mechanical power losses at the no-load speed should be considered and it is presented in (4.10) [8]:

$$P_m^{NL} = \omega_m^{NL} T_m^{NL} \tag{4.10}$$

Substituting (4.10) into (4.9) results in (4.11) which are used to compute the combined machine set inertia.

$$J = -\frac{P_m^{NL}}{\omega_m^{NL}\frac{d\omega_m}{dt}\Big|_{\omega_m=\omega_m^{NL}}} \tag{4.11}$$

The mechanical losses P_m^{NL} at the no-load speed ω_m^{NL} can be obtained using the segregation of losses method presented in [116] by considering the power balance within an induction machine operating at ω_m^{NL} as given in (4.12) [8]:

$$P_{in} = P_{cu} + P_{iron} + P_m^{NL} \tag{4.12}$$

If the operating voltages and currents are known, the total input power P_{in} and machine copper losses P_{cu} can be determined. The iron losses P_{iron} are segregated from the no-load mechanical losses P_m^{NL}, by using their linear relationship with respect to the square of the supply voltage expressed as [8, 115]:

$$P_{iron} + P_m^{NL} = f(V_s^2) = P_{in} - P_{cu}$$

$$P_{in} = 3V_s I_s \tag{4.13}$$

$$P_{cu} = I_s^2 R_s$$

Therefore, after performing the no-load test as discussed in *subsection 4.2.3.1.1*, the voltage that is supplied to the stator should be slowly decreased while concurrently taking the stator voltage, stator current, and power measurements to allow the computation of $P_{in} - P_{cu}$ for each decrement in the stator supply voltage.

The characteristic $P_{iron} + P_m^{NL} = f(V_s^2)$ is then plotted as shown in Fig. 4.20.

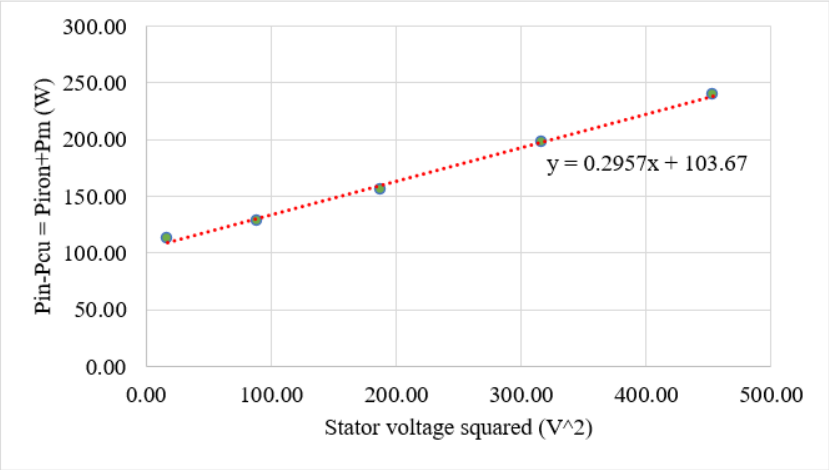

Figure 4. 20: Segregation of $P_{iron} + P_m^{NL} = f(V_s^2)$

The characteristic equation $y = 0.2957x + 103.67$ shown in Fig. 4.20 is a direct reflection of $P_{iron} + P_m^{NL} = f(V_s^2)$. Considering that the no-load mechanical losses are not dependent on the variations in the stator voltage, the *y-axis* intercept *103.67* of the characteristic equation represents the no-load mechanical losses P_m^{NL}. Fig. 4.21 presents the deceleration curve which is obtained by performing a retardation test on the machine set.

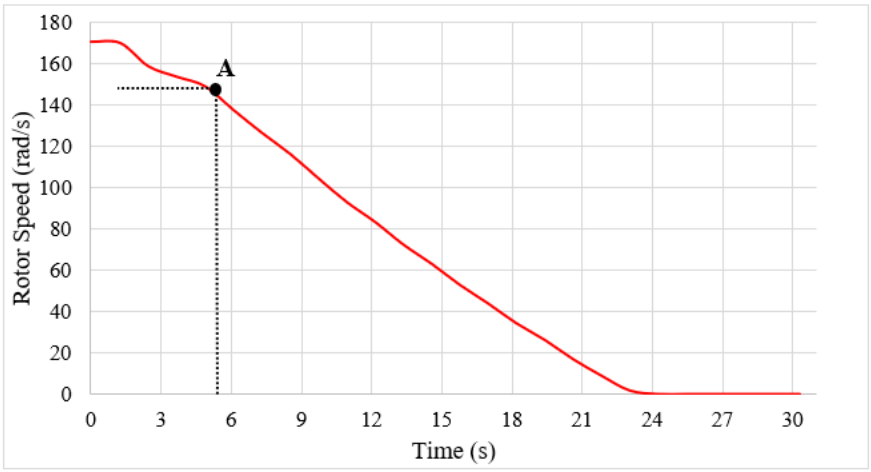

Figure 4. 21: Experimental deceleration curve for the WRIM and the DC machine set

The no-load speed of the machine is determined as$152.05 rad/s$ and the tangent at point A is calculated to be $\left.\frac{d\omega_m}{dt}\right|_{\omega_m=\omega_m^{NL}} = -7.67 m/s^2$. The combined machine set inertia is thus determined by substituting the numerical values of $\left.\frac{d\omega_m}{dt}\right|_{\omega_m=\omega_m^{NL}}$ and P_m^{NL}into (4.11):

$$J = 0.0889 kg.m^2$$

4.3 Experimental Validation and Performance Analysis of the DFIG's Control System

4.3.1 Experimental Validation of the Modulation Algorithms

Before implementing the rotor-side converter (RSC) and the grid-side converter (GSC) control systems, the converter modulation algorithms of both the 2-level and 3-level NPC VSC were first validated. The experimental test conditions are identical to the simulations. Therefore, the DC-bus is pre-charged to 100V by a single-phase variac while the output terminals of the converters are connected to a three-phase RL load with a resistance and an inductance of 47Ω and 47mH per-phase, respectively. The algorithms for the 2-level space vector PWM (SVPWM) technique, the 3-level SVPWM technique, and the DC-link neutral point voltage balancing have been implemented on the FPGA module in LabVIEW to provide the switching signals of the IGBTs in the 2-level and 3-level VSCs, respectively.

4.3.1.1 Two-level VSC Modulation

To validate the 2-level SVPWM technique, the testing modulation index was set to 0.8 and the resultant line-to-line and line-to-neutral converter PWM output voltage waveforms are displayed on an oscilloscope as presented in Fig. 4.22. The experimental results correspond to the simulation results presented in Fig. 3.7.

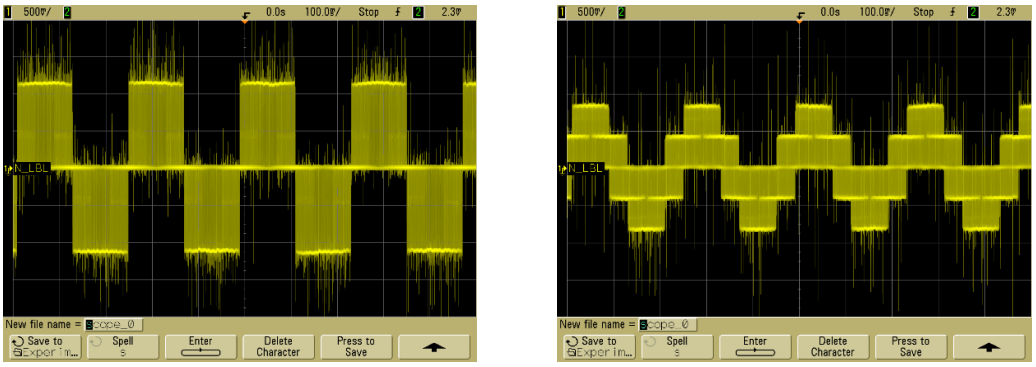

(a) (b)

Figure 4. 22: Two-level VSC PWM Output Voltages: (a) Line-Line, (b) Line-Neutral

4.3.1.2 Three-level VSC Modulation

To validate the 3-level SVPWM technique, the testing modulation index has initially been set to 0.4 and then to 0.8. The rms voltage values are observed to correspond to the theoretical computations carried out using (2.66) as follow:

$$V_{out_{peak}} = \frac{mV_{dc}}{\sqrt{3}}$$

$$for\ m = 0.4 \longrightarrow V_{out_{peak}} = 23.09V, V_{rms} = 16.33V$$

$$for\ m = 0.8 \longrightarrow V_{out_{peak}} = 46.19V, V_{rms} = 33.2V$$

The resultant line-to-line converter PWM output voltage waveforms are displayed on an oscilloscope as shown in Fig. 4.23.

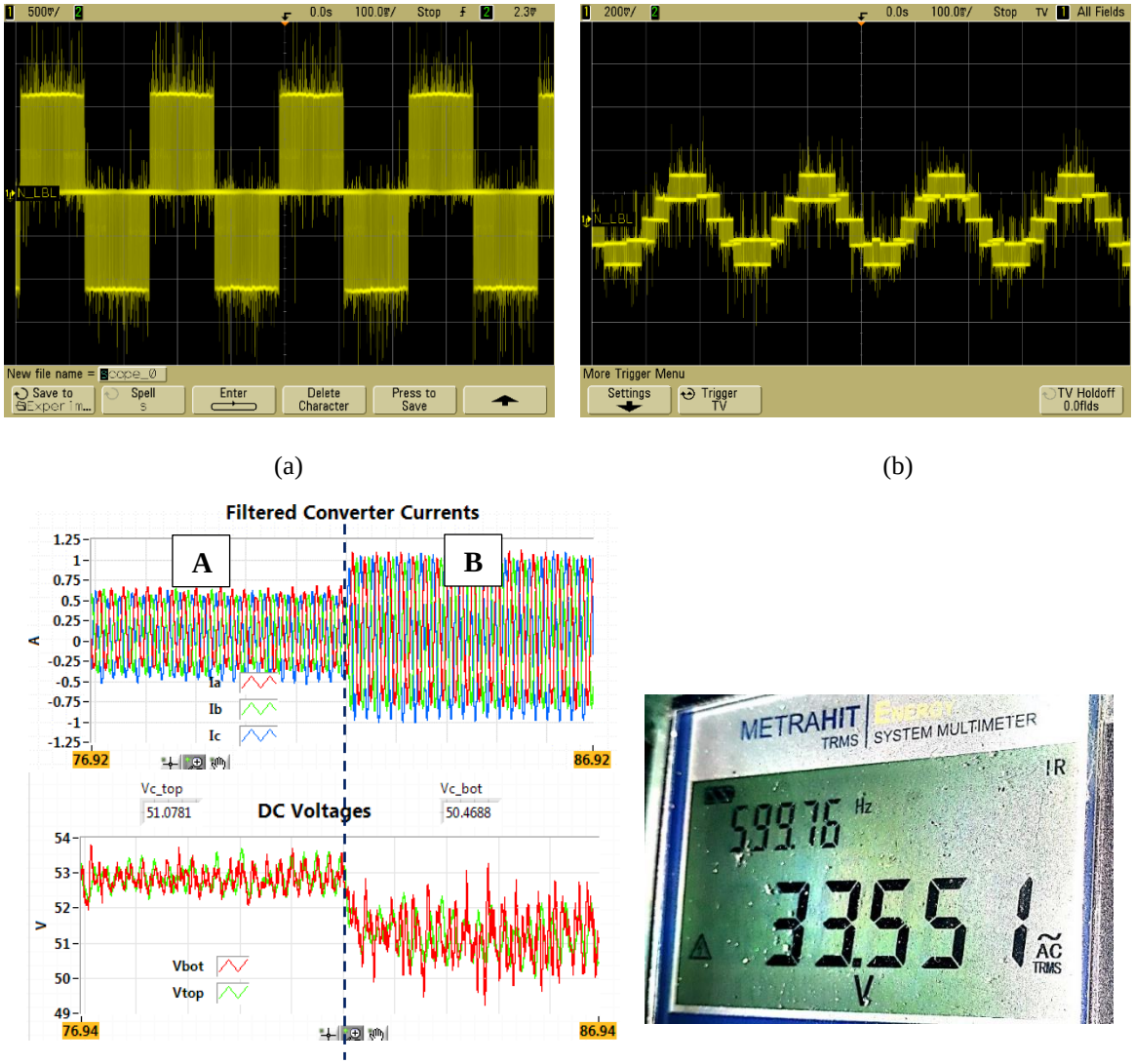

Figure 4. 23: Three-level VSC Modulation Experimental Results: (a) LL Voltage at *m=0.4*, (b) LL Voltage at *m=0.8*, (c) Converter Current and DC-link Capacitor Voltages, (d) Converter RMS output voltage at *m=0.8*, measured with a Digital Multi Meter (DMM)

It is seen from Fig. 4.23, that for smaller modulation indices, the converter output voltage in Fig. 4.23 (a) is the same as that of a two-level VSC depicted in Fig. 4.22(a), which corresponds to what was observed in the simulation results. Figure 4.23 (c) shows the three-phase converter output current waveforms, depicting the change in the amplitude as the modulation index changes from 0.4 (*region A*) to 0.8 (*region B*). Moreover, the DC-capacitor voltages are illustrated in Fig. 4.23 (c). It is observed that the DC-bus capacitor voltages contain high ripples due to the measurement noises associated with the practical system. However, the DC-link neutral point balance is still achieved. Moreover, higher ripples are observed during the 0.8 modulation index, which corresponds to what was observed in the simulation results presented in Fig. 3.11.

4.3.2 Experimental Validation of the DFIG-based WECS Controller System

4.3.2.1 Grid-side Converter Controller Responses

The experimental validation of the GSC controllers has been conducted under the same testing conditions as the simulations presented in *subsection 3.7.3*.

4.3.2.1.1 Independent Inner Current Controller Responses

For the independent inner current controller testing, the DC bus has been pre-charged to 200V using a single-phase variac. The experimental results which demonstrate the grid current control dynamics are presented in Fig. 4.24 and are compared to the simulation results presented in Fig. 3.16.

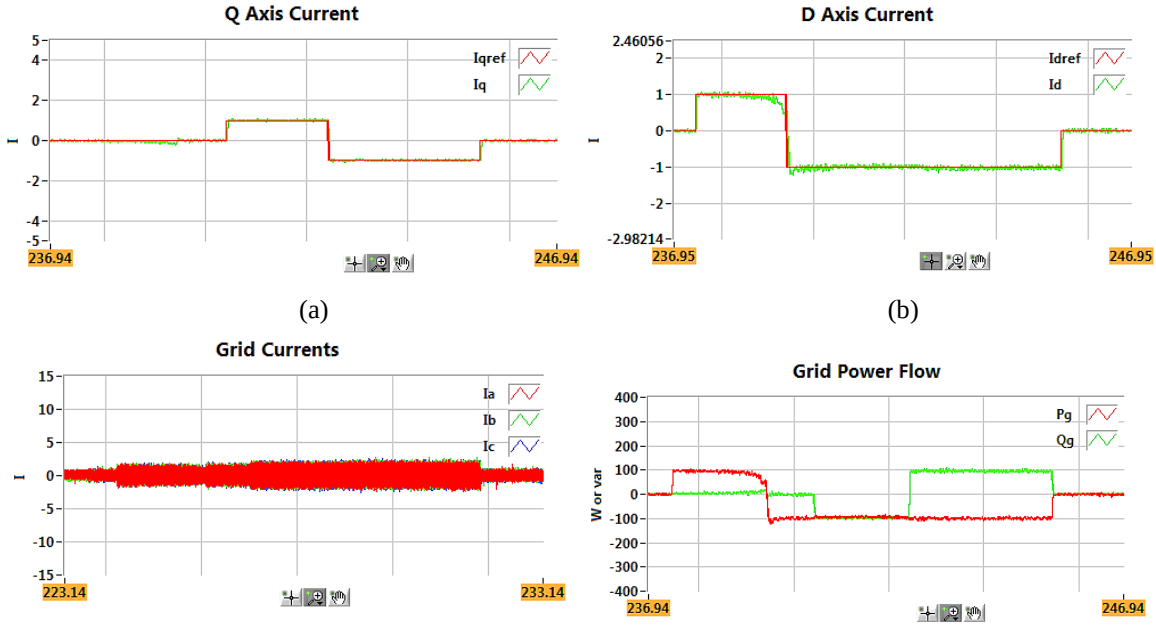

Figure 4. 24: Experimental grid current controller dynamics

It is observed from Fig. 4.24 (a) and (b) that the measured *d*- and *q*- axis currents closely follow the reference currents perfectly well, which demonstrates the effectiveness of the current controllers. Figure 4.24 (c) presents the corresponding active and reactive powers, and it is observed that the polarity of the grid active and reactive power flow changes due to the change in the *dq*-axis currents which depicts identical dynamics as was observed in the simulation results. The amplitude of the grid three-phase currents shown in Fig. 4.24 (d) is equal to the *dq*-axis currents, as expected. The changing polarities of the power flow demonstrate that the three-level VSC can operate in both rectifying and inverting modes. The correlation of the simulated results to the experimental results indicates the correctness of the grid filter model as well as the controller design.

4.3.2.1.2 DC-link Voltage Controller Response

The experimental results which demonstrate the practical DC-link controller dynamics are presented in Fig. 4.25 and are compared to the simulation results presented in Fig. 3.17.

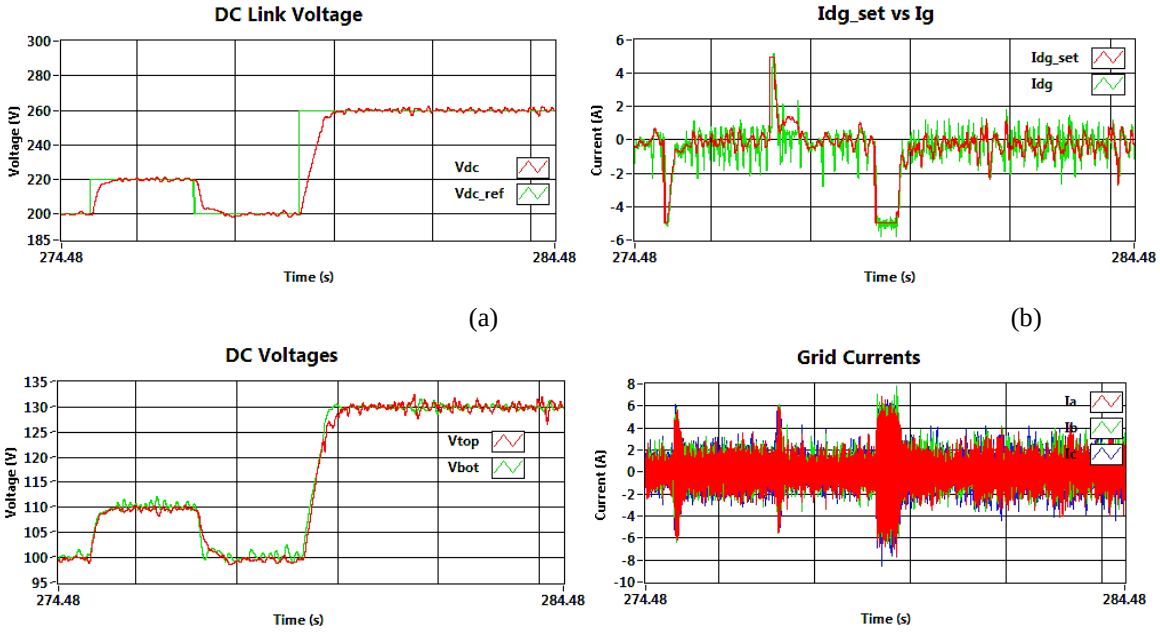

Figure 4. 25: Experimental DC-bus voltage control dynamics

It is observed in Fig. 4.25 (a) that the measured DC-link voltage follows the setpoints accordingly. The settling time of the DC-bus voltage steps is within 0.5s which corresponds to the designed settling time specification. Figure 4.25 (c) indicates that the voltage across the top and bottom capacitors are equal, and the DC-link neutral point is balanced. Figures 4.25 (b) and (d) present the corresponding grid currents whose response is like what was observed in the simulation results. Therefore, it is observed that the experimental results correlate to the simulation results presented earlier which validates the accuracy in the modeling of the DC-bus voltage controller.

4.3.2.2 Rotor-side Converter Controller Responses

The experimental validation of the RSC controllers has been conducted under the same test conditions as the corresponding simulations presented in *subsections 3.7.1 and 3.7.2*.

4.3.2.2.1 Experimental validation of the DFIG soft synchronization

The DFIG soft synchronization process has been implemented and experimental tests have been conducted under the same operating conditions as the corresponding simulation presented in *subsection 3.7.1* to validate the practical system. The experimental results which demonstrate the practical DFIG soft synchronization dynamics are presented in Fig. 4.26 and are compared to the simulation results presented in Fig. 3.13.

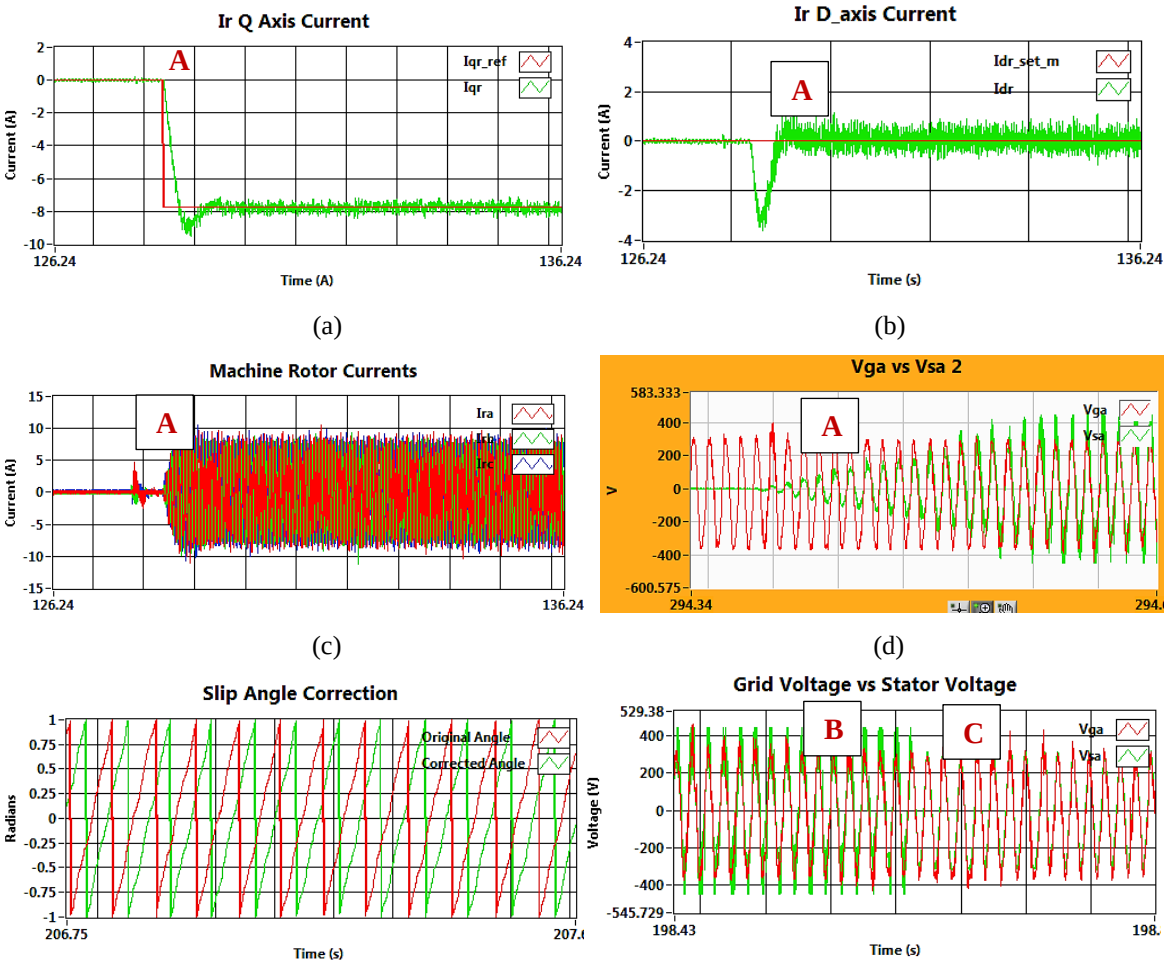

Figure 4. 26: Experimental DFIG soft synchronization dynamics

From Fig. 4.26 (a) and (b), it is indicated that the rotor current's *d*- and *q*-axis components were set to the references obtained using (2.126) at point ***A***. As a result, the stator voltage is induced to have the same amplitude and frequency as the grid voltage as shown in Fig. 4.26 (d). The rotor angle before and after correction are given in Fig. 4.26 (e). The slip angle correction ensures that there is no phase shift between the induced stator voltage and grid voltage as shown at point ***B*** in Fig. 4.26 (f). The stator contactor is closed at point ***C*** hence fully synchronizing the DFIG to the grid. The experimental results presented in Fig. 4.26 correlate to the simulation results presented in Fig. 3.13 which validates that the modeled synchronization controller and further validates that the parameters of the machine have been accurately determined.

4.3.2.2.2 Independent Inner Current Controller Responses

After successfully synchronizing the DFIG and the GSC to the grid, the experimental tests for the RSC controllers are conducted under the same operating conditions as the corresponding simulations presented in *subsection 3.7.2*. The experimental results presented in Fig. 4.27 demonstrate the practical rotor current controller dynamics and they are compared to the simulation results presented in Fig. 3.14.

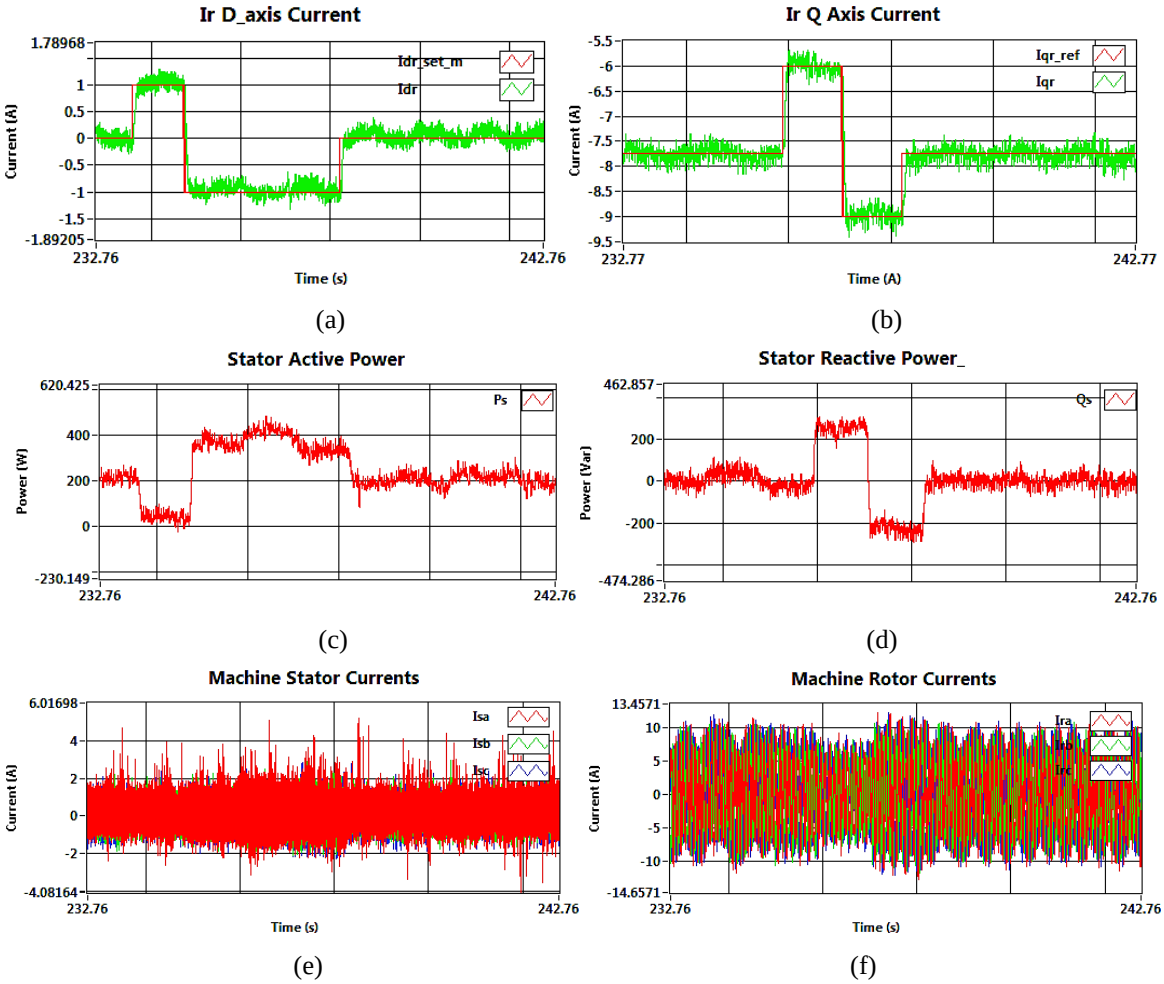

Figure 4. 27: Experimental rotor current control dynamics

During this test, the machine speed is maintained at a slip of *20%* by the DC machine drive, corresponding to a speed of *1210rpm*. From Fig. 4.27 (a) and (b), it is observed that the *d*- and *q*-axis currents follow the setpoints, as in the simulated results. Moreover, the changes in the stator's active and reactive power flow [Fig. 4.27 (c) and (d)] due to the changes in the rotor *dq*-axis currents depict dynamics that are identical to the corresponding simulation results. The changing polarities in the active power flow are an indication that the DFIG can operate in the motoring and generating mode. The three-phase stator and rotor currents are presented in Fig. 4.27 (e) and (f), respectively, and it is observed that their frequencies depict the same difference that was observed in the corresponding simulation results, as the stator and rotor currents operate at the grid and slip frequencies, respectively. The experimental results presented in Fig. 4.27 correlate to the simulated rotor current controller dynamics which validates the accuracy in the DFIG controller modeling and equivalent circuit parameter determination.

4.3.2.2.3 Speed Controller Response

The experimental results which demonstrate the practical DFIG speed controller dynamics are presented in Fig. 4.28 and are compared to the simulation results presented in Fig. 3.15.

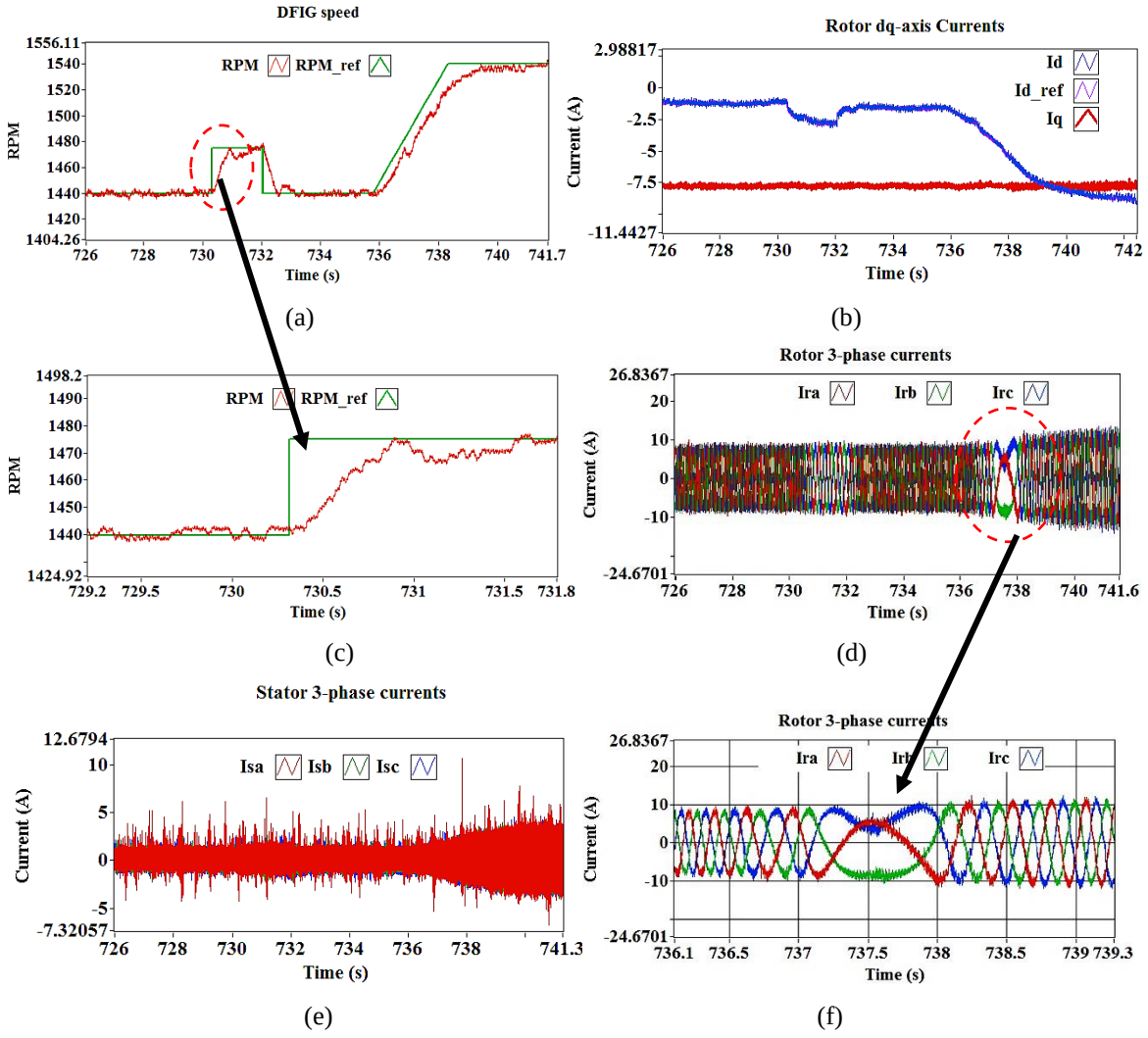

Figure 4. 28: Experimental DFIG speed control dynamics

For this test, the machine was initially operated at a steady-state speed of 1440rpm, after which the reference speed was stepped up by 35rpm at *t=730s* and returned to the original speed at *t=732s*. Thereafter, the machine speed was accelerated from *1440rpm* to *1540rpm* between *t=736s* to *t=738s*. It is observed in Fig. 4.28 (a) and (c) that the measured DFIG speed follows the setpoints instantly, with no overshoots and within the desired settling time specifications. From Fig. 4.28 (b), the *q*-axis current is seen to be maintained at -7.75A, whereas the *d*-axis current depicts negative non-zero values during the steady-state operating conditions of the machine which implies that the power is drawn from the grid to the rotor circuit. Moreover, the rotor *d*-axis current tracks the references from the speed controller instantly, and the corresponding stator current transients caused by variations can be observed in Fig. 4.28 (e), which depicts a similar behavior as observed in the simulation results. Likewise, the three-phase rotor currents shown in Fig. 4.28 (f) correspond to the simulation results whereby the rotor frequency became zero as the machine approaches the synchronous speed. Moreover, the rotor currents have a reversed sequence during the super-synchronous operation which indicates a change in the polarity of the rotor active power.

Therefore, the experimental results presented in Fig. 4.28 depict dynamics identical to the corresponding simulation results thereby validating the accuracy of the speed controller modeling and the combined machine-set inertia determination.

4.3.3 Experimental Validation of the Overall DFIG System

The dynamics of the overall DFIG-based WECS have been conducted under similar operating conditions as the simulations discussed in *subsection 3.7.4*. However, since the DC-drive that is used in the test rig is controlled manually, the experimental tests are performed slightly different from the simulations. Therefore, the dynamic tests are conducted under the following scenarios:

- ***Scenario 1***: Variation of the input torque from the DC-motor (prime mover) while keeping the DFIG speed regulated by the closed-loop speed controller.
- ***Scenario 2***: Variation of the DFIG speed using the closed-loop speed controller while keeping the input torque from the DC-motor constant.

4.3.3.1 DFIG system dynamics under scenario 1

The experimental results which demonstrate the dynamics of the practical complete system operating at a regulated DFIG speed with variable input torque are presented in Fig. 4.29. The results are compared to the simulation results illustrated in Fig. 3.18.

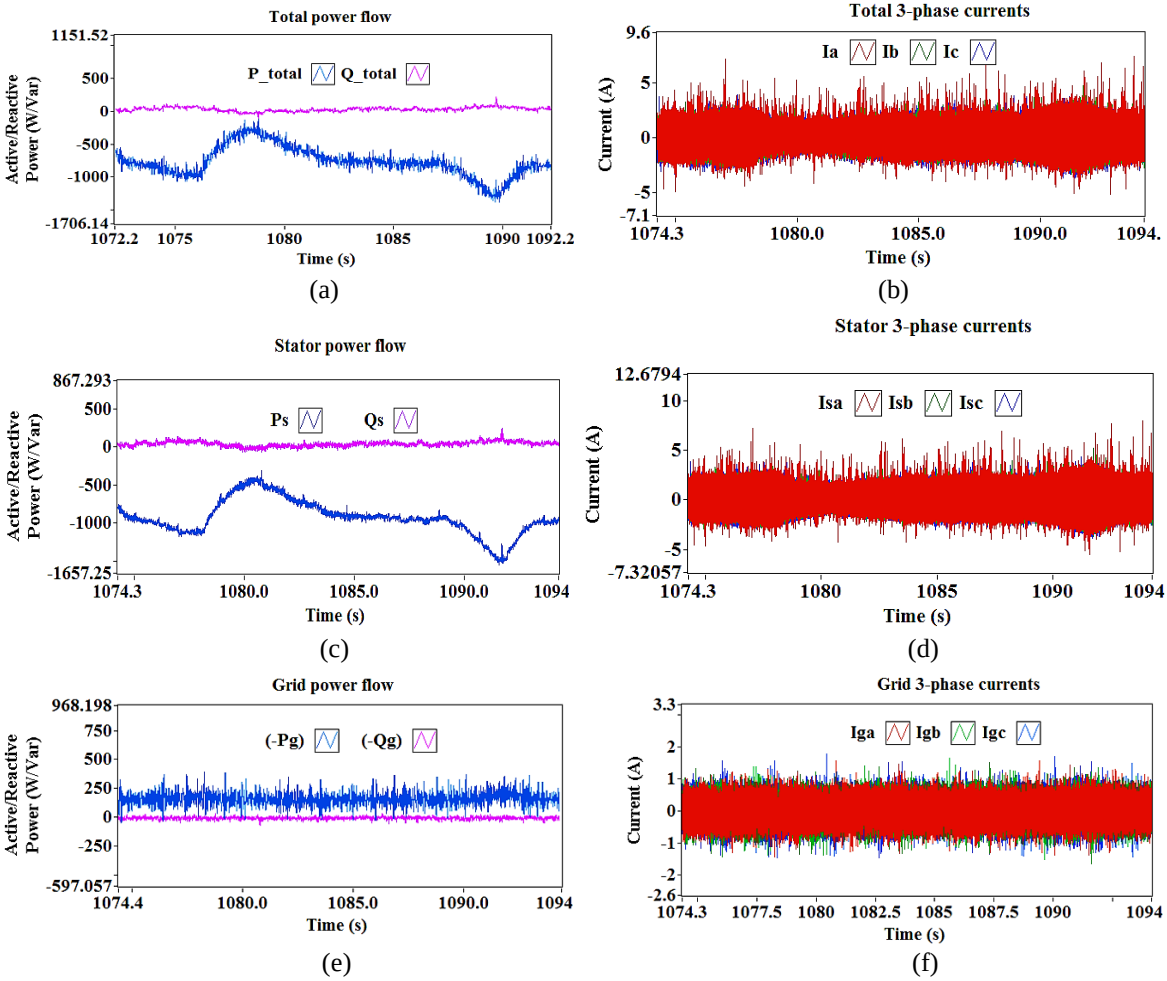

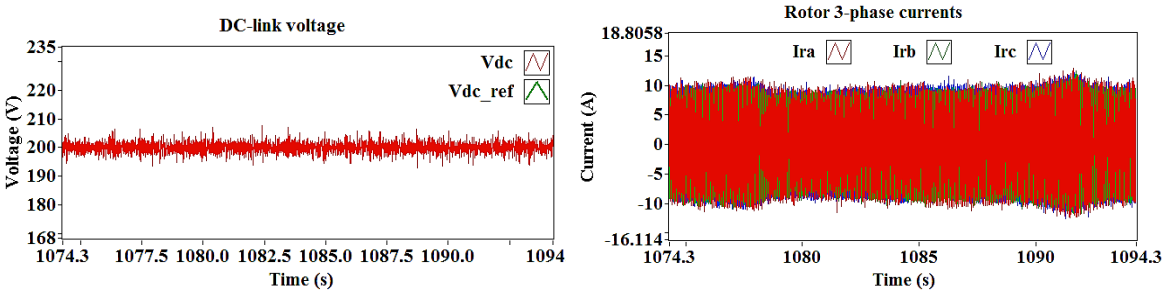

(g) (h)

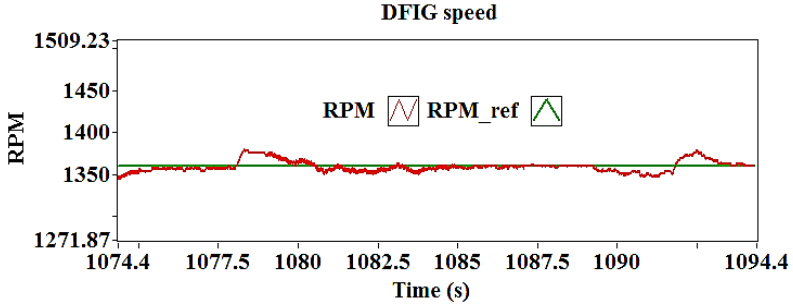

(i)

Figure 4. 29: Dynamic performance of the overall DFIG system operating at a constant speed and variable input torque

During this test, the machine speed is regulated at *1360rpm*. Whereas the input torque from the DC motor is varied by changing the armature voltage of the DC machine. The input torque T_a is varied in a ramp trend, from 0.37Nm at *t=1072.2s*, to 0.81Nm at *t=1075s*, and back to 0.221Nm at *t=1080s*, while the shaft speed was fixed at a 10% slip. Another ramp variation in the input torque was implemented at *t=1088s* and *t=1092s*, a change from 0.59Nm to 1.18Nm, respectively. It is shown in Fig. 4.29 (a) that the total active power output P_{total} depicts the changes in accordance with the variation in the input torque, as per the relationship given by expressions (3.7). The trend is similar to what was observed in Fig. 3.18 (a); hence, the experimental results depict dynamics that are identical to the simulation results presented in Fig. 3.18. The reactive power flowing in the system is maintained at zero for unity power factor operations. The stator and total active power are negative, indicating a power flow from the machine to the grid as expected in a DFIG-based WECS. It is observed in Fig. 4.29 (e) that the grid active power is positive, which indicates a directional flow from the grid to the rotor of the DFIG, as expected for DFIG sub synchronous operations. It is observed from Fig. 4.29 (g) and (i) that the DC-link voltage and DFIG speed are maintained at their respective setpoints regardless of the variation in the input torque, further validating the accuracy of the modeled control system.

4.3.3.2 DFIG system dynamics under scenario 2

The experimental results which demonstrate the dynamics of the practical complete system operating at a constant input torque while varying the DFIG speed are presented in Fig. 4.30. These results are compared to the simulation results presented in Fig. 3.18.

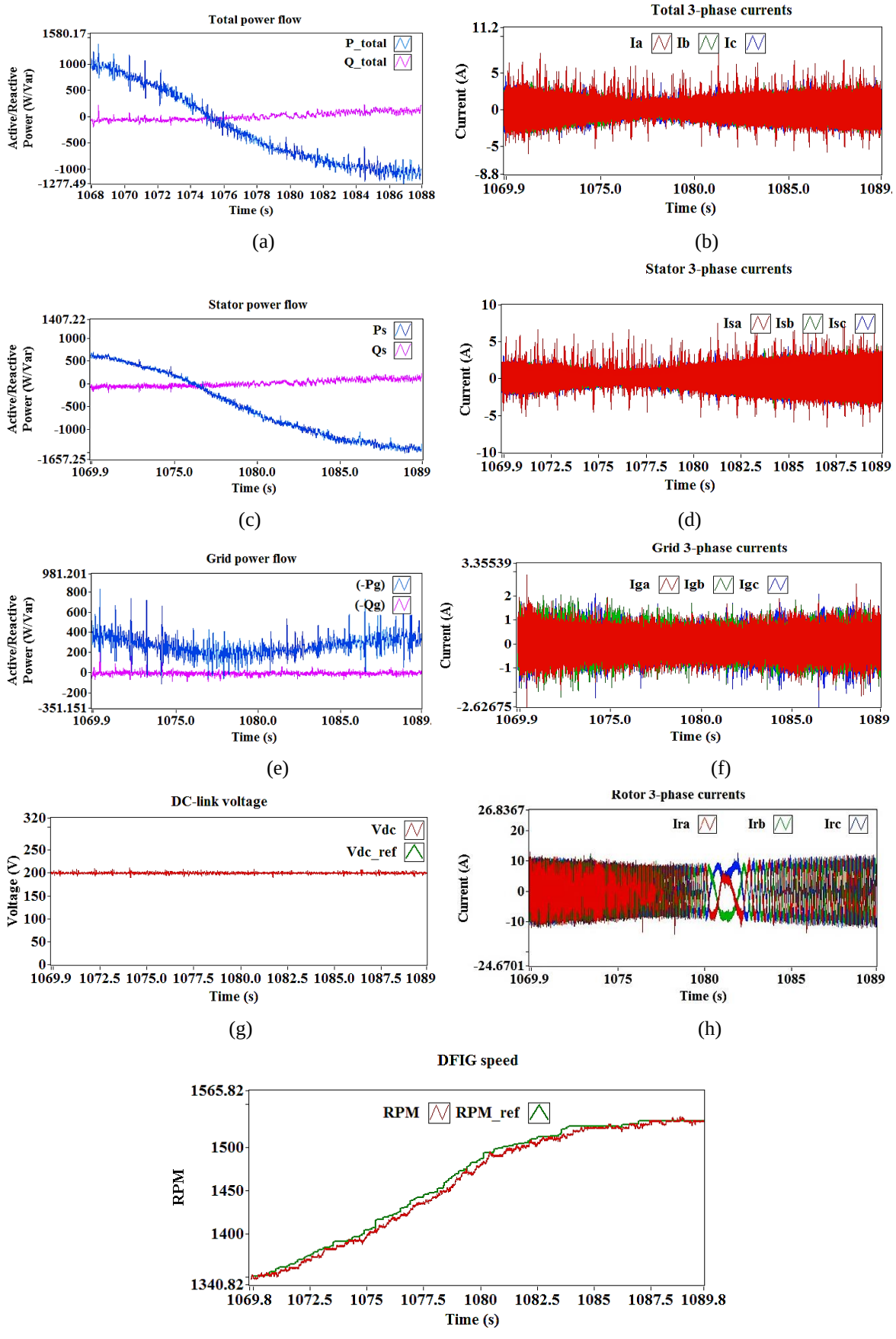

Figure 4. 30: Dynamic performance of the overall DFIG system at constant input torque and variable DFIG speed

During this test, the machine speed is accelerated from *1340rpm* to *1560rpm*, which corresponds to a slip range of 10% to -10%. The input torque from the DC motor is kept constant by the DC drive. The experimental results depict the same dynamics as seen in the simulated results presented in Fig. 3.18. It is observed that the total active power from the DFIG increases linearly with the speed whereas the reactive power is maintained at zero for unity power factor operations. The grid active power is observed to be moving towards the negative region as the machine approaches the super synchronous speed operating region. However, the power does not change its polarity as observed in the experimental results, this is due to the losses in the converters.

4.4 Chapter Summary

4.4.1 Development of the Experimental Test Rig

This subsection focused on the implementation of the experimental DFIG-based WECS test rig in the Machines Laboratory. The hardware and software components of the test rig have been discussed with emphasis put on their operating principles. The WRIM equivalent circuit parameters have been determined using the standard IEEE no-load, blocked rotor, and open rotor tests. These parameters are needed for the design of a robust controller system and have been summarized in Table 4.7.

4.4.2 Experimental Validation and Performance Analysis of the DFIG's Control System

This subsection focused on the practical implementation of the DFIG's control system in LabVIEW FPGA. Experimental tests have been performed on the DFIG-based laboratory setup, whereby the experimental results have been compared to the simulation results presented in *Chapter 3* to validate the performance of the control system's subcomponents. The experimental results presented in this chapter demonstrate a correlation between the developed test rig and the simulation model. Therefore, it is fully verified that the developed DFIG system is capable of operating in variable speed conditions which corresponds to a typical DFIG-based WECS. In this regard, the developed test rig can be used for further investigations on DFIG-based WECSs such as fault studies.

Chapter 5: A Case for Micromachines in Laboratory-based Test Rigs and Customization of the Scaled-down WRIM for Fault Implementation

5.1 Introduction

This chapter begins with an investigation into the correlation between the dimensional parameters and the electrical asymmetry indicators for large-scale wind generators and laboratory-based generators. For the latter, a comparison is made between using a standard small-scale off-the-shelf wound rotor induction machine (WRIM) and a micromachine to explore whether there is a need for micromachines in the context of studying faults in laboratory-based test rigs, or whether standard small-scale off-the-shelf IMs would suffice. After making a case for micromachines, the chapter goes on to give a detailed discussion on the customization of the scaled-down WRIM (micromachine) to enable the practical implementation of the stator inter-turn, rotor inter-turn, and the static eccentricity (SE) fault conditions in the laboratory environment. The chapter also sheds light on the signal processing techniques which are explored in this study to detect the machine faults during steady-state and transient operating conditions.

5.2 A Case for Micromachines in Laboratory-based DFIG Wind Turbine Systems

5.2.1 Orientation of the Investigation

Prior to the present time, the studies which were proposed to develop techniques for improving the performance of wind energy systems have been based on numerical modeling and the simulation of these systems. However, according to Dehnavifard *et al* [34], the complexity and sometimes, the inaccuracy of the simulation models reduce the quality of these simulation-based investigations, hence, highly accurate investigations can be achieved through experimental analysis. Therefore, in most investigations, researchers have adopted the use of small-scale induction machines (IM) for the development of experimental test rigs to perform several lab-based studies [117].

The two classes of small-scale IMs that can be used in laboratory-based test rigs are standard small-scale off-the-shelf IMs and micromachines. The standard small-scale off-the-shelf IMs are those that are ready-made and can be sourced from manufacturers. Such machines ranging in sizes from 4kW to 50kW have been adopted in many laboratory-based test rigs to perform a wide range of studies, mainly focusing on condition monitoring and fault diagnosis in IMs as presented in [118, 119]. Micromachines are scaled-down versions of the actual machines, and their development began in the 1950s to generate empirical data [117]. Micromachines are designed to mimic specific dynamic responses of the large-scale machines, which is ensured through dimensional analysis techniques [34]. Micromachines can be used in many applications as outlined in [113, 117, 120].

Under the concept of condition monitoring and fault diagnosis, the MCSA technique has been widely used for signal processing and fault-feature extraction, particularly for machines operating under steady-state conditions, whereby it is cost-effective, easy to implement, and non-invasive [30, 85, 86]. However, there is an increasing need to explore and develop novel techniques for processing both steady-state and transient signals, which would require rigorous testing in laboratory environments before these techniques can be standardized and applied to large-scale machines in the industry. As such, it is crucial to be strategic in selecting a small-scale machine that would ensure that the experimental results obtained from laboratory-based studies are an accurate reflection of what is expected in an in-service large-scale machine. Despite the popularity of using standard small-scale off-the-shelf IMs in laboratory-based test rigs to conduct fault studies, there are no reports in literature validating its applicability in comparison to using the actual machine. Therefore, this is an area that remains of considerable interest, and hence, it is the focal point of this subsection. From this perspective, this subsection delivers a comprehensive study of the correlation in the dimensional parameters, winding factors, and the evolution of specific electrical asymmetry indicators for an in-service large-scale DFIG, its micromachine, and a standard small-scale off-the-shelf WRIM. This is done to explore whether there is a need for micromachines in the context of studying faults in laboratory-based test rigs, or whether standard small-scale off-the-shelf IMs would suffice.

5.2.2 Conceptualization of the Study

To facilitate the comparative study, an in-service 850kW, 690V, 4-pole, 1500rpm DFIG that is presented in a case study by Artigao *et al* [23] has been adopted to serve as a benchmark for a large-scale machine. Whereas the micromachine used in this work is a 5kW WRIM that was modeled, verified in the Finite Element Method, and built in the university laboratory by Dehnavifard [113] as a scaled-down version of a 2.5MW DFIG using Berchten's scaling methodology discussed in [121], whereby the results were attained through experimentation. For the standard small-scale off-the-shelf IM, data has been collected from a research article where the authors conducted fault-related studies on a test rig that was developed using a standard small-scale off-the-shelf WRIM.

5.2.2.1 The In-service Large-scale DFIG

In the case studies by Artigao *et al* [23, 122], the stator current of an in-service wind turbine DFIG has been captured and analyzed using the MCSA technique during the steady-state period under healthy and faulty conditions. This was done to give a realistic representation of using this technique for fault diagnosis in an in-service large-scale DFIG. The test cases which represent different wind turbine operating conditions have been presented to illustrate the analysis which was conducted.

For this study, the results obtained from the test case in which the large-scale DFIG was operated at a sub-synchronous speed of 1350rpm (*slip = 0.1*) under the health condition will be used as a basis for comparison with the results obtained from the experimental analysis carried out on the micromachine-based test rig when the micromachine is in a healthy state and operated at 1350rpm. Concurrently, the results of the large-scale DFIG are also compared to those obtained from the experimental study from literature which used the standard small-scale off-the-shelf WRIM, also in a healthy state and operated at the speed of 1350rpm.

5.2.2.2 Modelling and Development of the Scaled-down WRIM

This section discusses the scaling methodology which is presented in more detail by Dehnavifard *et al* in [34] to develop the micromachine. The scaling methodology identifies several scaling factors that link the dimensions and physical properties of the 2.5MW DFIG (to be referred to as the *reference machine* from hereon) and that of the 5kW micromachine [13]. Berchten's scaling methodology discussed in [123] presents the scaling factors which link the dimension properties of the micromachine to the reference machine by taking into account the identical dynamic responses of the two machines. The scaling factors considered are presented in Table 5.1.

Table 5. 1: Scaling Factors [34]

Scaling factors	Physical Properties
k	Internal stator diameter (D), core length (L), and slot depth (h_s)
α	Current density (J)
β	Flux density (B)
γ	Slot width (b_{ss})
Δ	Air gap (δ)

The numerical values of the scaling factors are determined using the ratios of the reference DFIG parameters to the micromachine's parameters, presented by the equations in Table 5.2.

Table 5. 2: Scaling Formulas [13, 34]

Quantity	Relation	Equation No.
Power Rating (VA)	$S/S^* = k^3\alpha\beta\gamma$	(5. 1)
Winding Resistance (p.u.)	$R/R^* = {}^{\alpha}/_{k\beta}$	(5. 2)
Leakage Reactance (p.u.)	$X/X^* = {}^{\alpha\gamma^2}/_{k\beta}$	(5. 3)
Magnetizing Reactance (p.u.)	$X_m/X_m^* = {}^{k\alpha\gamma}/_{\Delta\beta}$	(5. 4)

It is deduced from Table 5.2 that the unknown dimension x of the micromachine is determined by multiplying the reference machine's dimension x^* by the scaling factor (5.5) [13]:

$$x = (scaling\ factor) \times x^* \tag{5.5}$$

According to [113], the transient and steady-state responses of the large-scale machines and their micromachine counterparts are expected to be the same if the resistances and the reactance of the two machines are equal in the per-unit system. Therefore, the following ratios are assumed: $\frac{R}{R^*} = 1$; $\frac{X_s}{X_s^*} = 1$, $\frac{X_m}{X_m^*} = 1$. Substituting these ratios into (5.1) – (5.4), the scaling factors are determined as follows:

$$S/_{S^*} = 5000/_{2.5 \times 10^6} = 0.002 = k^3\alpha\beta\gamma$$

$$\gamma = 1, \Delta = k^2, \alpha = 0.044/_k \; and \; \beta = 0.044/_{k^2}$$

The scaling factors are required to be positive ($\alpha > 0, \beta > 0, \gamma > 0, \Delta > 0$) and real ($\alpha, \beta, \gamma, \Delta \in R$) [34]. The minimum geometrical scaling factor *k* is determined as 0.25 and the voltage rating of the micromachine is related to that of the reference DFIG by (5.6) [13, 34]:

$$\frac{V}{V^*} = k^2\beta \tag{5. 6}$$

$$V_{s_{ll}} = 0.25^2 * \frac{0.044}{0.25^2} * 690 = 30.36V$$

In most cases, the design of micromachines which accurately emulate the dynamic behaviors of practical machines is not always possible due to the basic laws and limitations of the physical models. According to [121], the fundamental problem is concerning the time constants of the micromachines. In this case, time constant regulators may be required and have been developed in the literature to extend the usefulness of micromachines and ensure that they accurately emulate the transient and steady-state responses of the actual large-scale machines [13, 117]. For this study, the time constant of the micromachine is related to that of the large-scale / reference DFIG by (5.7) [13]:

$$\frac{T}{T^*} = \gamma^2 \tag{5. 7}$$

$$T = 1^2 * 0.0512 = 0.0512$$

It is observed from (5.7) that the time constants of the large-scale machine and the micromachine are the same which will ensure an identical dynamic response. Table 5.3 presents the parameters of the reference and the scaled-down DFIG.

Table 5. 3: Parameters of the Reference and Scaled-down DFIGs [13, 113]

Parameter	**Value**	
	Reference	***Scaled-DFIG***
Power [W]	2.5×10^6	5000
Voltage (line to line) [V]	690	30
Stator current [A]	1673.5	20
Rated speed	1500	1500
Torque [N.m]	13270	8.16
Number of poles	4	4
Number of slots: stator/rotor	60/48	30/24
Number of slots/phase: stator/rotor	30/16	10/8
Number of turns/phase: stator/rotor	80/160	80/320
Stator resistance R_s [p.u.]	0.018	0.019
Stator leakage reactance X_s [p.u.]	0.35	0.33
Stator time constant [s]	0.051	0.049
Referred rotor resistance R_r [p.u.]	0.03	0.02
Rotor leakage reactance X_r [p.u.]	0.4	0.43
Magnetizing reactance X_m [p.u.]	10.85	12.7

The developed micromachine is shown in Fig. 5.1. The winding profiles of the stator and rotor of the micromachine are given in Appendix B.

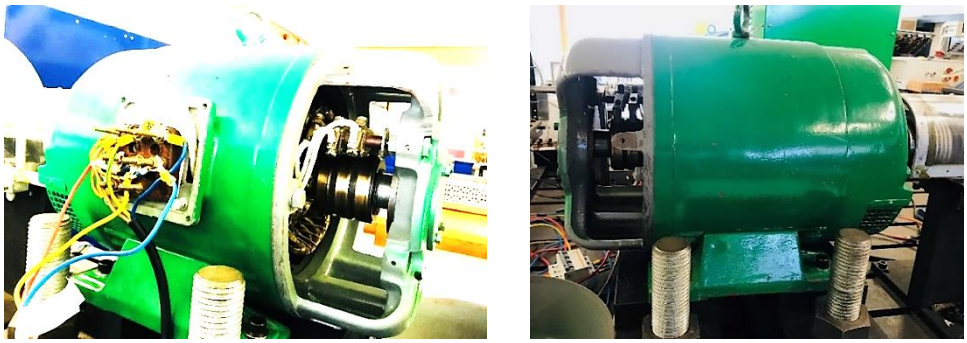

Figure 5. 1: The 5kW micro-WRIM

To evaluate the similarities in the evolution of the harmonic frequency components in the stator current spectrum of the micromachine in comparison to that of the large-scale DFIG, the stator current signal of the micromachine in a healthy state has been extracted from a test rig that has been discussed in more details in *Chapter 4*, for when the micromachine is operating at a sub-synchronous speed of 1350rpm. A total of 200 000 samples were captured at a sampling frequency of 5000 samples/s, for an acquisition period of 40 seconds.

5.2.2.3 Standard Small-scale off-the-shelf Induction Machines

The article of interest is by Faiz *et al* [119], in which an experimental test rig was set up comprising of a standard small-scale off-the-shelf WRIM rated at 4kW, 400V, 50Hz, 4-pole, and 1420rpm, driven by an induction motor and directly connected to the grid on the stator side while the rotor is connected to the grid via the power electronic converter system.

The windings of the standard small-scale WRIM have been modified by connecting tappings on the stator and rotor windings to make it possible to implement inter-turn faults in a controllable manner. Experiments were conducted to assess the standard small-scale WRIM under the health condition and when it is subjected to a rotor inter-turn short circuit fault. In each condition, the WRIM was operated at a sub-synchronous speed of 1350 rpm (*s = 0.1*). Considering the slip value from the test case which was performed on the in-service large-scale DFIG presented in *subsection 5.2.2.1*, this test case resembles the sub-synchronous speed condition at which the standard small-scale WRIM has been operated. Therefore, the results obtained from the spectral analysis of the stator current which was captured when the standard small-scale WRIM is in a healthy state are gathered to compare the location of the harmonic frequency components in the current spectrum of the standard machine to those of the large-scale DFIG.

5.2.3 Winding Configurations of the Large-scale, Micromachine, and Standard Small-scale Off-the-shelf Induction Machines

This section presents the dimensional parameters, winding configurations, and the determination of the distribution, pitch, and winding factors of the three machines under study. This is done to evaluate the link between the parameters of the small-scale machines to those of the large-scale DFIG. Fundamentally, the winding factors of a specific machine are dependent on the following factors which are determined by the winding layout and the number of slots per pole of a specific machine [114]:

- Pole pitch,
- The ratio of coil span to pole pitch (if short-pitched),
- The distribution and pitch factor.

For every induction machine, there is a flux density distribution in the air gap which is the same as the airgap MMF. The winding layout of the machine affects the MMF distribution and ultimately, its performance [114]. The fundamental & odd harmonics of the flux density are given by (5.8) [114]:

$$\left.\begin{aligned} B(\theta) &= B_{1(\max)} sin\theta + B_{3(\max)} sin3\theta + B_{5(\max)} sin5\theta + \cdots \\ B(\theta) &= \sum_{h=1,3,5,\ldots} \frac{4B_{h(\max)}}{\pi h} \sin(h\theta) \end{aligned}\right\} \quad (5.8)$$

Where h is the harmonic order and $B_{h(\max)}$ is the amplitude of the hth harmonic flux density wave.

The odd/space harmonics in the flux density wave in (5.8) induce time-harmonic voltages in the machine's windings. The distribution and pitching of the coils in a machine influence the magnitude of the voltages that are induced in the coils and their respective odd harmonics. Since the flux density distribution is usually non-sinusoidal, the induced voltages are also non-sinusoidal and hence, the distribution (k_d), pitch (k_p) and winding (k_w) factors are usually different for each harmonic voltage. The distribution, pitch, and winding factors of the hth harmonics are given by (5.9) [114]:

$$k_{dh} = \frac{\sin(nh\alpha/2)}{nsin(h\alpha/2)}$$

$$k_{ph} = \cos(h\gamma/2) \tag{5.9}$$

$$k_{wh} = k_{dh} \times k_{ph}$$

Where n is the number of slots/pole/phase, α is the angle between two adjacent slots (slot angle) and γ is the coil pitch.

Table 5.4 presents the k_d, k_p, and k_w factors of the first three odd harmonics in the stator voltage of the large-scale DFIG, the micromachine, and the standard small-scale WRIM.

Table 5. 4: Parameters and Winding Factors of the Large-Scale DFIG, Micromachine & Standard Small-Scale Off-the-Shelf WRIM

Parameter	**Large-scale DFIG**		**Micromachine/micro-WRIM**		**Standard small-scale WRIM**	
Slots/pole: sta./rot.	15/12		8/6		9/6	
Number of poles	4		4		4	
Slots/pole/phase: sta./rot.	5/4		3/2		3/2	
Slot angle α: sta./rot.	12/15		23/30		20/30	
Coil pitch γ: sta./rot.	36/45		69/90		60/90	
Factors	***Stator***	***Rotor***	***Stator***	***Rotor***	***Stator***	***Rotor***
Distribution k_{d1}, k_{d2}, k_{d3}	0.96	0.96	0.96	0.97	0.96	0.97
	0.65	0.7	0.68	0.71	0.67	0.71
	0.2	0.21	0.23	0.26	0.22	0.26
Pitch k_{p1}, k_{p2}, k_{p3}	0.951	0.966	0.951	0.966	0.866	0.87
	0.588	0.707	0.588	0.707	0	0
	0	0.259	0	0.258	-0.866	-0.87
Winding k_{w1}, k_{w2}, k_{w3}	0.910	0.93	0.91	0.93	0.83	0.84
	0.40	0.46	0.40	0.49	0	0
	0	0.053	0	0.05	-0.189	-0.22

Since the aforementioned factors of the large-scale DFIG and micromachine are usually directly linked to each other by a scaling factor through a scaling methodology, the winding factors of the large-scale DFIG are observed to be the same as the winding factors of its micromachine counterpart. However, since the dimensional parameters of a standard small-scale off-the-shelf WRIM are not linked to those of the large-scale DFIG, their distribution, pitch, and winding factors are not the same. According to [114], choosing a pitch for the coils that makes the pitch factor zero for a particular harmonic can result in the elimination of that harmonic from the winding voltage. This is what is observed for the 5^{th} harmonic of the large-scale DFIG and micromachine.

In the case of the standard small-scale machine, it is the 3^{rd} harmonic that is eliminated. Taking this concept into consideration, it further emphasizes the close link between the micromachine and the large-scale DFIG, in comparison to the standard small-scale WRIM. Based on the winding factors presented in Table 5.4, the rms voltage that is expected to be induced in the machine's windings can be determined. For the *h*th harmonic flux, the induced voltage is given by (5.10) [114]:

$$E_h \propto B_{h(\max)} k_{wh} \tag{5.10}$$

The rms voltage induced in the winding is given by (5.11) [114]:

$$E = \sqrt{E_1^2 + E_3^2 + E_5^2 + \cdots} = \sqrt{\sum_{h=1,3,5,\ldots} E_h^2} \tag{5.11}$$

To illustrate the procedure of calculating the induced rms voltages, given the amplitudes of the odd harmonics and the winding factors for a specific machine, the stator current spectrum of the micromachine is presented in Fig. 5.2.

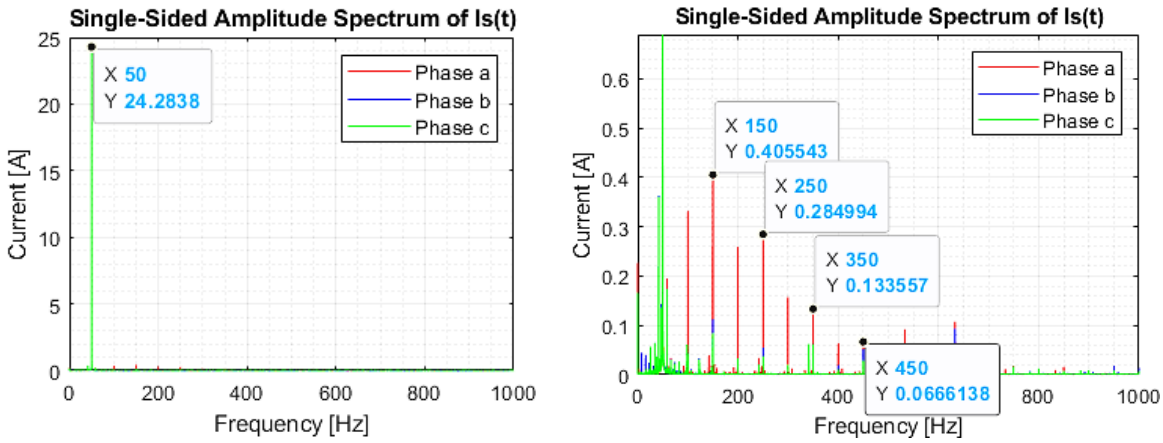

(a) (b)

Figure 5. 2: FFT Spectrum of the stator Current of the Micromachine, (a) un-zoomed, (b) zoomed in

From Fig. 5.2 (a), the amplitude $B_{1(\max)}$ of the first order harmonic (*fundamental component*) is 24.28. From (5.10), considering k_{w1} for the micromachine from Table 5.4, the rms voltage induced due to this harmonic is calculated as follows:

$$\boldsymbol{E_1} \propto B_{1(\max)} k_{w1} = 24.28 \times 0.910 \approx 22.09V$$

From Fig. 5.2(b), the amplitudes of the 3rd and 5th harmonic components are 0.4055 and 0.285, respectively. This corresponds to a ratio of 1.67% and 0.23% for the amplitude of the fundamental. The 3rd and 5th rms voltages are:

$$\boldsymbol{E_3} \propto B_{3(\max)} k_{w3} = (r_{E1:E3}) \times B_{3(\max)} \times k_{w3} = 0.0167 \times 24.28 \times 0.40 = 0.162V$$

$$\boldsymbol{E_5} \propto B_{5(\max)} k_{w5} = (r_{E1:E5}) \times B_{5(\max)} \times k_{w5}$$

$$= 0.0023 \times 24.28 \times 0 = 0V$$

Where, $r_{E1:E3}$ & $r_{E1:E5}$ are the ratios of the amplitude of the 3rd and 5th harmonics to that of the fundamental, respectively.

Based on (5.11), the total rms voltage induced in the stator winding of the scaled-down machine due to the 1st, 3rd and 5th harmonic flux density waves is determined to be 22.09V. It is observed that the obtained rms voltage is approximately equal to the micromachine's rated rms value of 21.4V (*see Table 5.3*)**.** This demonstrates that the amplitudes of the odd harmonic components present in the stator current spectrum of the machine and the winding factors, determine the resultant rms voltage that is induced in the windings of that specific machine and its respective harmonic components of different orders. The same concept can be used to calculate the rms voltages induced in the windings of the large-scale and the standard small-scale off-the-shelf IMs. It is worth noting that harmonic components of different orders will be induced in the rotor and stator currents of the machine due to the space and time harmonics, whether the machine is in a faulty state or a healthy state.

5.2.4 Identification of the frequency components in the stator current spectrum during the healthy state

This section focuses on the MCSA of the stator current signal of the three machines, all in their healthy states, to identify the harmonic frequency components in the stator current spectrum due to the inherent asymmetry in these machines, as well as the odd harmonics that are normally present in the spectra of IMs in a healthy state. This is done to ascertain the correlation in the evolution and location of these odd and asymmetry-related indicators in the large-scale machine and the small-scale machines considered.

5.2.4.1 Formulae for Calculating the Healthy and Asymmetry-related Frequency Components

Under a healthy operating condition, i.e., balanced supply and winding resistances, several inter-harmonic frequency components can appear in the spectra of the stator and rotor current signals.

These frequency components result from the distribution of the air-gap harmonic field and are related to multiple machine factors such as the physical characteristics, operating speed, supply frequency and its orders, and air-gap magnetic field pole-pair number [124, 125]. The possible frequency components that can appear in the stator current spectrum of a healthy machine due to the supply time harmonics are given by (5.12) [122]. In the same vein, the possible frequency components in the rotor current spectrum are given by (5.13) [118, 124-126]:

$$f_{Is}^{H} = |6k(1-s) \pm j|f_s \tag{5.12}$$

$$f_{Ir}^{H} = |6k(1-s) \pm s|f_s \tag{5.13}$$

Where *k* is an air-gap field space harmonic constant (*k=0,1,2, 3..*) and *j* is the supply time-harmonic one ($l = \pm 1$).

It is noted from the literature that the inherent construction asymmetry in practical induction machines results in several inter-harmonic frequency components that would appear on a stator current spectrum of a machine in a healthy state [23], but with much lower amplitudes which would then represent the threshold values/fingerprint for fault detection to avoid false alarms.

The even harmonic frequency components which serve as indicators of the inherent asymmetry and specific faults may be located by formulae indicative of these faults [23, 126]. Therefore, in the aspect of fault detection and quantification, it is the presence of more harmonics and the increase in the amplitude of these frequency components that indicate the presence of a fault [12]. Equation (5.14) determines the harmonic components related to an unbalance that may exist in the machine either due to the inherent asymmetry produced during the manufacturing stage or due to the occurrence of a fault [122]:

$$f_{FRU} = f_s\left(\frac{k}{p}(1-s) \pm l\right) \tag{5.14}$$

From [122], it is noted that the machine's configuration and the operating conditions highly influence the frequency components given by (5.12) – (5.14). Moreover, these frequency components also depend on the operating speed and the power injected into the grid which varies significantly due to the intermittent nature of practical wind turbine systems [23].

5.2.4.2 MCSA of the Stator Current Signal of a Large-scale DFIG in a Healthy State

To date, there is limited literature that focuses on applying stator current signature analysis specifically to in-service wind turbine DFIGs to identify faults in large-scale machines. However, Artigao *et al* [127] has addressed the issue by presenting a case study on using MCSA to detect faults in an in-service wind turbine DFIG. The case study also focused on identifying which harmonic frequency components are most suitable to monitor the health condition as well as the inherent asymmetry of the large-scale machine.

The results presented in [23], when the large-scale machine is in a healthy state have been presented in this section to form a basis for comparison with the developed micromachine and the standard small-scale machine. The stator current signal of the large-scale machine has been captured when the DFIG is operated at a sub-synchronous speed of 1350rpm. The MCSA has been applied to the stator current signal, and the peak search and identification were carried out as shown in Fig. 5.3.

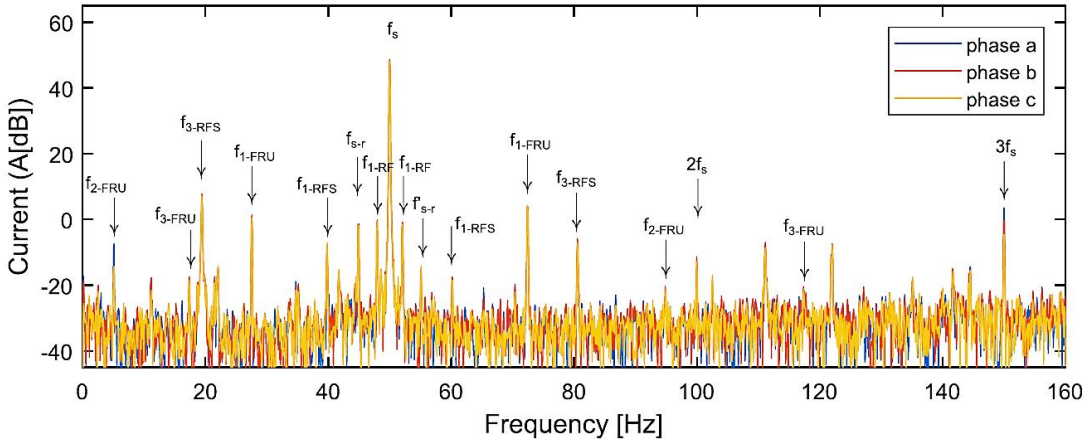

(a)

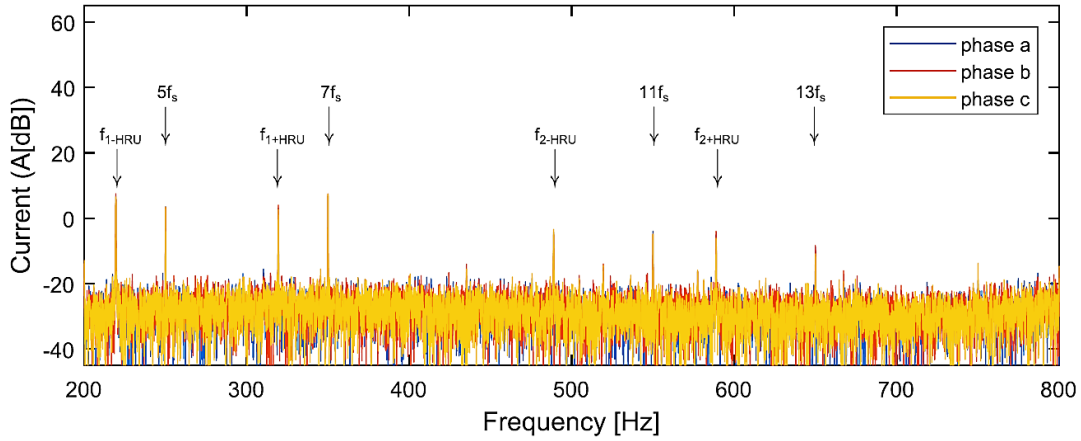

(b)

Figure 5. 3: Stator Current Spectrum for the large-scale DFIG operated at 1350rpm under the healthy state condition: (a) Low-frequency range; (b) High-frequency range [122]

The healthy state (f_{IS}^{H}) and the asymmetry-related frequency components (f_{FRU}) indicated in Fig. 5.3 have been calculated using (5.12) and (5.14) and are given in Table 5.5.

Table 5. 5: Calculated Frequency Components in the Stator Current Spectrum of Induction Machines operated at slip = 0.1

Frequency Components	**Frequencies**		
	***k* = 1**	***k* = 2**	***k* = 3**
f_{IS}^{H}	219.2	488.4	757.6
	319.2	588.4	857.6
	27.57	5.13	17.3
	72.43	94.87	117.3
f_{FRU}	219.2	488.4	757.6
	319.2	588.4	857.6
	27.57	5.13	17.3
	72.43	94.87	117.3

It is observed from Fig. 5.3 that the odd sub-harmonics have higher amplitudes than the even ones, specifically, sub-harmonic *k=1* (i.e.,f_{1+FRU}) has the highest amplitude, followed by sub-harmonic *k=3*.

5.2.4.3 MCSA of the Stator Current Signal of the Micromachine in a Healthy State

This section presents the stator current spectral analysis of the micromachine in the healthy state and operated at a sub-synchronous speed of 1350rpm. Since the micromachine has been operated at a speed equivalent to that of the large-scale DFIG presented earlier, the asymmetry-related frequency components indicated in Fig.5.4 are the same as those given in Table 5.5.

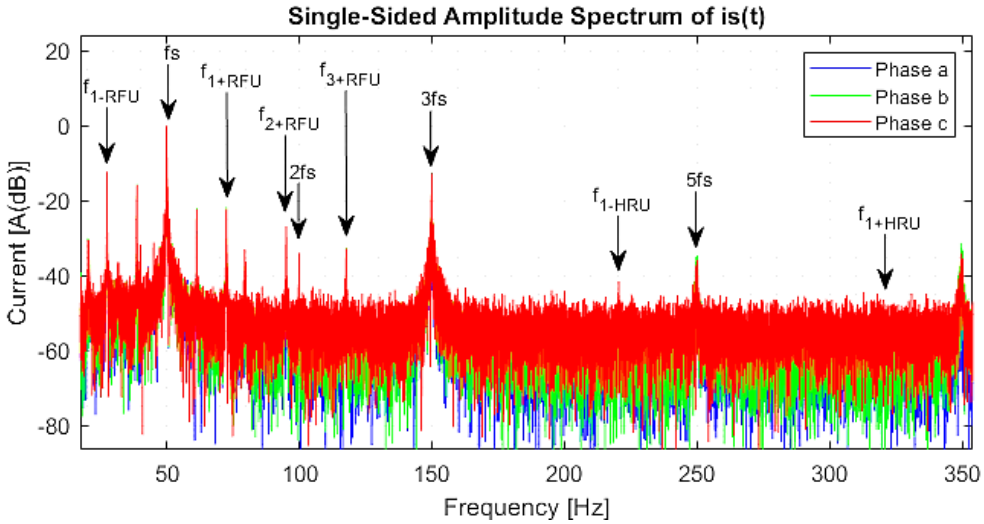

Figure 5. 4: Stator current spectrum for the micromachine operated at a sub-synchronous speed of 1350rpm, under the healthy state condition

From the stator current spectral analysis of the large-scale DFIG and the micromachine presented in Fig. 5.3 and Fig. 5.4, respectively, it has been observed that the possible harmonic frequencies in a healthy machine (f_{Is}^{H}) and those due to the inherent asymmetry (f_{FRU}) present in the respective machines, have detectable amplitudes and are located at approximately the same positions in the spectral plots of the two machines under the operating condition considered in this work. Moreover, like in the case of the large-scale machine, the odd sub-harmonics in the FFT spectrum of the micromachine presented in Fig. 5.4 have higher amplitudes than the even ones, specifically, sub-harmonic *k=1* (left sideband f_{1-FRU} and right sideband f_{1+FRU}) has the highest amplitude. Furthermore, the 3^{rd} harmonic ($3f_s$) for both the large-scale and micromachine has a higher amplitude than the other multiples. Conversely, the amplitude of the 5^{th} harmonic ($5f_s$) is very small for both machines, this ties up with the observation that the pitch and winding factors of the 5^{th} harmonic are zero as depicted in Table 5.4, which is dependent on the configuration of these machines.

5.2.4.4 MCSA of the Stator Current Signal of the Standard Small-scale Off-the-shelf Induction Machine in a Healthy State

To evaluate the similarities in the evolution and location of the harmonic frequency components in the spectrum of the standard small-scale WRIM in comparison to the large-scale DFIG presented earlier, a research article by Faiz *et al* [119] has been reviewed.

Figure 5.5 presents the FFT spectrum of the stator current which is captured when the standard machine is in a healthy state and operated at a sub-synchronous speed of 1350rpm.

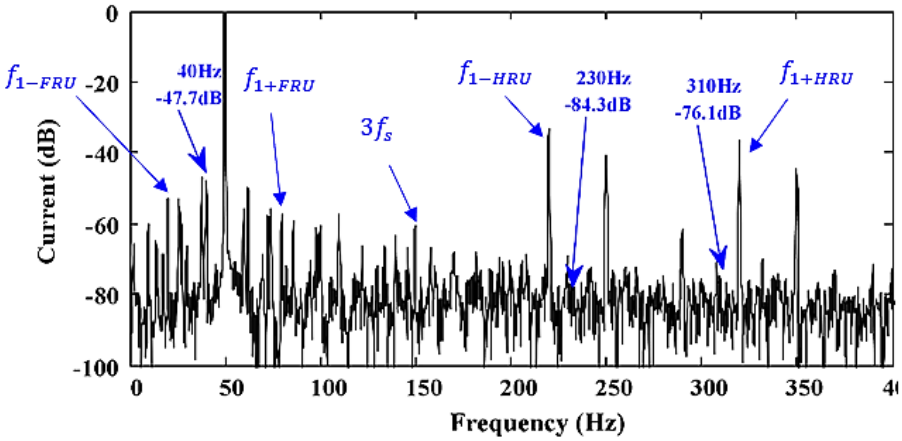

Figure 5. 5: Stator current spectrum of a standard small-scale WRIM in a healthy state and operating at a speed of 1350rpm [119]

Comparing the stator current spectral plot of the large-scale DFIG presented in Fig. 5.3 and that of the standard small-scale WRIM presented in Fig. 5.5, it is observed that the healthy state (f_{IS}^{H}) and the asymmetry-related frequency components (f_{FRU}) are located at approximately the same positions in the spectral plots of the two machines, just like in the case of the micromachine spectrum presented in Fig. 5.4. This demonstrates that the standard machine provides the same insight regarding the location of the expected frequency components, under the same slip conditions. However, it is worth noting that there will be a distinction in the amplitudes of the harmonic frequency components that are in the FFT spectrum of different machines due to the direct relationship between the amplitudes of these sub-harmonics and the winding factors of each specific machine. Moreover, each machine has a different configuration which highly influences the existence of certain frequency components in the spectral plots as recited in [122].

For the stator current spectrum of the standard small-scale IM presented in Fig. 5.5, it is observed that the sub-harmonic *k=1* does not have an amplitude that is higher than other odd sub-harmonics in the spectrum as opposed to what was observed for the large-scale machine and the micromachine. Moreover, the amplitude of the 3^{rd} harmonic is small, compared to what was observed in the spectral plots of the large-scale and micromachine. This ties up with the fact that the pitch & winding factors of the 3rd harmonic are zero for the standard small-scale off-the-shelf IM as depicted in Table 5.4.

5.2.5 Summary: A Case for Micromachines in Laboratory-based Test Rigs

From the investigations conducted in this subsection, it has been observed that the dimensional analysis technique that is adopted when scaling down a large-scale machine to reproduce a smaller version of it, i.e., the micromachine, ensures that the winding factors of the two machines are directly related by a scaling variable and hence, they are the same as demonstrated in Table 5.4.

However, this is not the case between a standard small-sized machine and a large-scale machine because the winding distribution, the pitching, and the number of slots per pole of the standard machine will rarely be the same as that of a large-scale machine. Therefore, it would require a researcher to do in-depth sourcing of a standard machine that would closely resemble a large-scale machine of interest before conducting a particular study. On the other hand, using a micromachine means that the equivalent circuit parameters and the time constants would have already been confirmed to emulate those of a large-scale machine, as demonstrated in this subsection. Therefore, the dynamic performance of the micromachine and the results obtained from such a test rig are expected to be an accurate reflection of what would be expected in an in-service large-scale machine.

Considering that the field of condition monitoring has shifted to include the process of tracking the evolution of fault-related frequency components under the transient operating conditions by using time-frequency analysis technique, the time constants are of utmost importance. In this context, the availability of a micromachine whose time constants resemble those of a large-scale machine ensures an identical transient response of the two machines. Ultimately, this would enable the experimental validation and testing of non-stationary signal analysis techniques such as Wavelets before these techniques can be implemented on in-service large-scale systems in the industry. It also brings attention to the precise selection of small-scale machines for laboratory systems based on the application required. Specific to this research investigation, the micromachine will assist in the development of condition monitoring strategies that are closely suited to the actual system.

5.3 Customization of the micro-WRIM to Implement the SE, and Stator & Rotor ITSCFs

In this investigation, the micromachine has been customized by modifying the stator and rotor windings to make provision for emulating inter-turn winding fault conditions at different severity levels. Moreover, the machine has also been customized to enable the implementation of a static eccentricity fault. Generally, the stator and rotor windings may be modified by connecting tappings to several numbers of turns of the coil of the machine [13]. This is the approach used in this study. The tappings that are connected to the windings of the micro-WRIM have been brought out of the machine to two patch-boards that are mounted on the exterior of the machine as shown in Fig. 5.6 (b). The specific turn on the coil on which the tappings are connected is determined by the fault severity level that ought to be achieved. The severity of the inter-turn short circuit faults that are considered in this study is 2%, 4%, 6%, and 8%. The corresponding number of turns shorted out per phase is computed in the following sections using the generic expression (5.15), taking into consideration the number of turns/phase for the stator and rotor stipulated in Table 5.3.

$$No.of\ shorted\ \frac{turns}{phase} = \frac{\%\ of\ shorted \frac{turns}{phase} \times total\ no.of \frac{turns}{phase}}{100} \quad (5.\ 15)$$

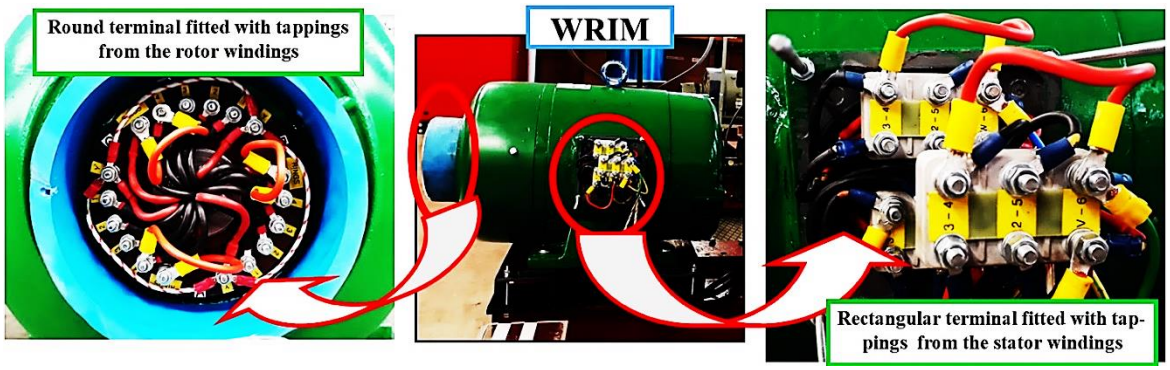

(a) (b) (c)

Figure 5. 6: Location of the terminal boxes on the micro-WRIM (a) rotor round terminal box, (b) overall view of the micro-WRIM with both terminal boxes, (b) stator terminal box

This arrangement allows the operator to have access to the stator and rotor winding turns and implement the desired fault severity levels by short-circuiting any of the taps externally.

5.3.1 Stator Inter-turn Winding Fault Implementation

The number of turns per phase to be shorted in the stator winding corresponding to the 2%, 4%, 6% and 8% of shorted turns/phase are computed using (5.16) as follow:

$$2\%\ shorted\ turns \rightarrow No.of\ shorted\ \frac{turns}{phase} = \frac{2\% \times 80}{100\%} = 1.6\ turns \approx 2\ turns$$

$$4\%\ shorted\ turns \rightarrow\ No.of\ shorted\ \frac{turns}{phase} = \frac{4\% \times 80}{100\%} = 3.2\ turns \approx 3\ turns$$

$$6\%\ shorted\ turns \rightarrow\ No.of\ shorted\ \frac{turns}{phase} = \frac{6\% \times 80}{100\%} = 4.8\ turns \approx 5\ turns$$

$$8\%\ shorted\ turns \rightarrow\ No.of\ shorted\ \frac{turns}{phase} = \frac{8\% \times 80}{100\%} = 6.4\ turns \approx 6\ turns$$

Following the procedure for modifying the windings as previously explained, a total of 12 tappings (4 per phase) have been brought out of the machine, from the stator winding, onto the terminal box as shown in Fig. 5.6 (c), to allow the operator to emulate stator inter-turn faults at different fault severities by shorting the desired external taps. That is, connecting the tap that corresponds to the desired percentage to the reference point as illustrated in Fig. 5.7.

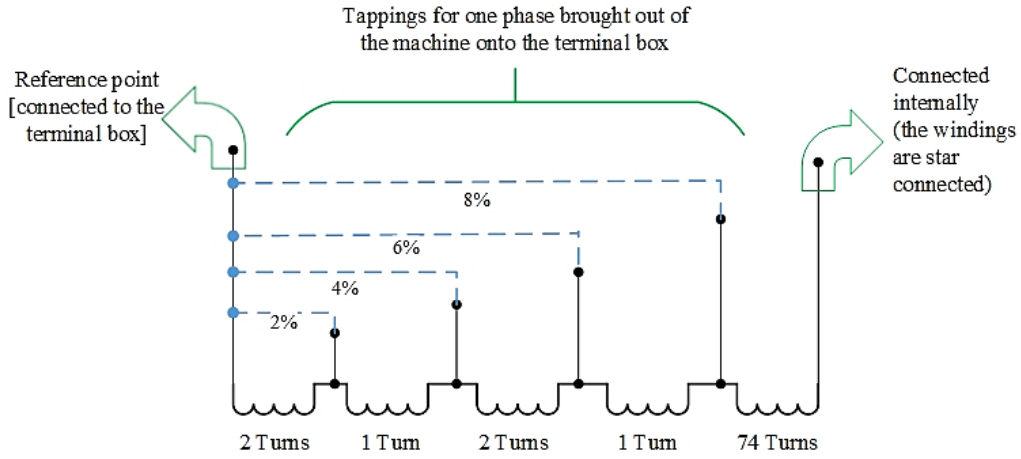

Figure 5. 7: Overview of tapping implementation on the stator winding

5.3.2 Rotor Inter-turn Winding Fault Implementation

The number of turns per phase to be shorted in the rotor winding corresponding to the 2%, 4%, 6% and 8% of shorted turns/phase are computed using (5.15) as follow:

$$2\%\ shorted\ turns \rightarrow No.of\ shorted\ \frac{turns}{phase} = \frac{2\% \times 320}{100\%} = 6.4\ turns \approx 6\ turns$$

$$4\%\ shorted\ turns \rightarrow\ No.of\ shorted\ \frac{turns}{phase} = \frac{4\% \times 80}{100\%} = 12.8\ turns \approx 13\ turns$$

$$6\%\ shorted\ turns \rightarrow\ No.of\ shorted\ \frac{turns}{phase} = \frac{6\% \times 80}{100\%} = 19.2\ turns \approx 19\ turns$$

$$8\%\ shorted\ turns \rightarrow\ No.of\ shorted\ \frac{turns}{phase} = \frac{8\% \times 80}{100\%} = 25.6\ turns \approx 26\ turns$$

A total of 12 tappings (4 for each phase) have been brought out of the machine, from the rotor winding, onto the round terminal box shown in Fig. 5.6 (a). In the case of the rotor, these tappings could be brought out of the machine through slip rings to an enlarged machine terminal box. However, because there are currently only 3 slip rings (1 for each phase), and hence this option will require additional slip rings to be added to the shaft. This will also require the shaft to be extended to make room for the additional slip rings. Considering the voltage drop associated with each brush/ slip ring as well as other challenges associated with extending the shaft, this option is not recommended. Therefore, the option of connecting leads/ small terminals on the rotor overhang has been explored instead. This has been implemented by using leads to attach to the rotor overhang: the small terminals have been attached to a round ring, which is placed around the shaft, outside of the machine casing as shown in Fig. 5.6 (a). The layout outlining how the different inter-turn fault severities are to be emulated in the laboratory environment by short-circuiting the external tapping points is provided in Appendix C. To implement the rotor inter-turn winding faults, the operator makes short-circuit connections on the leads that are placed on the round terminal as illustrated in Fig. 5.8. It is worth noting that each time a short-circuit connection is made on the leads, the machine had to be at a standstill for safety reasons.

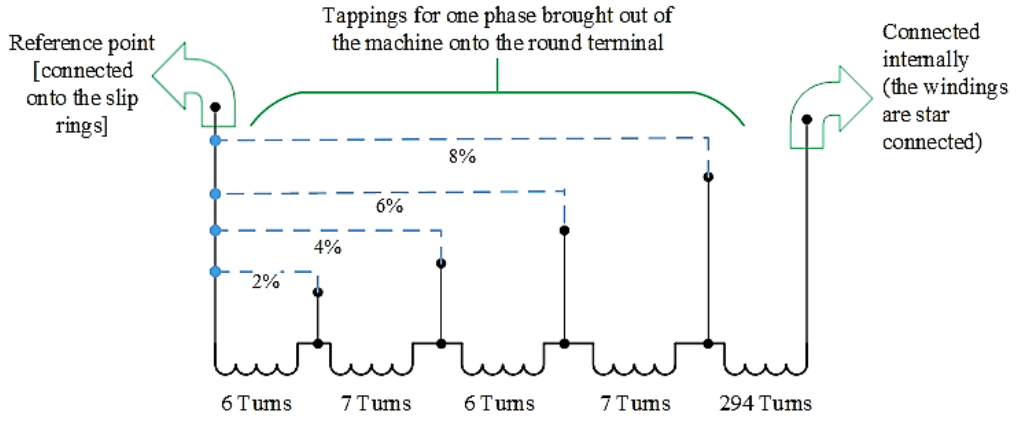

Figure 5. 8: Overview of tapping implementation on the rotor winding

5.3.3 Static Eccentricity Fault Implementation

Static eccentricity (SE) is a condition whereby the axis of rotation of the machine coincides with the axis of the rotor, but it is displaced from the axis of the stator [13, 15]. Therefore, to realize this fault in this study, the rotor shaft was pushed away from the center point, i.e., the stator axis by 1mm, towards the left side of the machine using screws on both sides of the shaft as illustrated in Fig. 5.9. This results in the axis of rotation getting displaced from the stator axis.

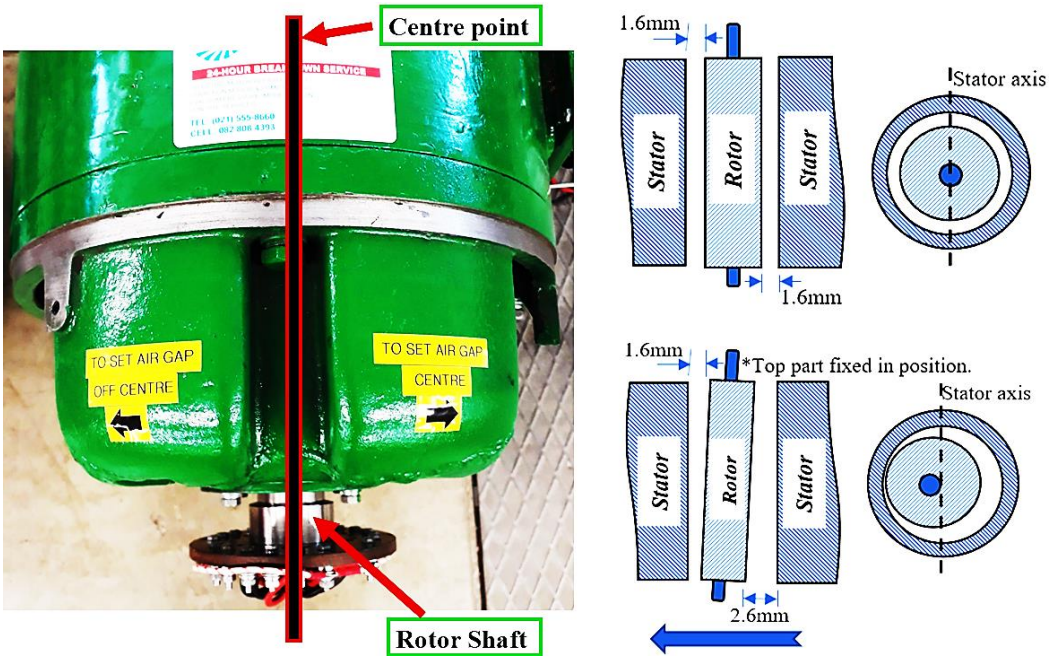

Figure 5. 9: Customization of the micro-WRIM to Implement the Static Eccentricity Fault

5.4 Signal Processing Techniques for Fault Feature Extraction and Fault Diagnosis in the micro-WRIM

In this study, two separate investigations have been conducted to diagnose the afore-mentioned faults when the micromachine is operating in two modes:

i) **Motor mode of operation**: the micromachine is assessed in the absence of the converter system. In this scenario, the stator windings are supplied with a balanced three-phase voltage using a programmable power supply while the rotor output terminals are shorted together, thus operating as a wound rotor induction machine (WRIM).

ii) **Generator mode of operation**: the micromachine is assessed when a converter system is incorporated into the rotor circuit, which then corresponds to a micro-DFIG that is in a complete wind energy conversion system (WECS).

For a micromachine operating in motor mode, the signal processing and fault-feature extraction techniques explored in this study to assess the micromachine for fault diagnosis are:

- The motor current signature analysis (MCSA) technique to perform the Fast Fourier Transform (FFT) analysis of the captured stator and rotor current signals under the steady-state operating condition.
- The Discrete Wavelet Transform (DWT) analysis technique is applied to the stator and rotor current signals during the starting (transient) operating condition.
    - But firstly, the Hilbert Huang Transform (HHT) technique was applied to the captured transient stator and rotor current signals to remove the fundamental component that masks the evolution of fault-related frequency components due to its higher magnitude. Thereby improving the DWT fault diagnosis technique under the transient operating region. Therefore, the DWT analysis has been applied to the resultant Hilbert modulus of the stator and rotor currents to diagnose the stator ITSCFs, rotor ITSCFs and the static eccentricity (SE) fault.
- The Short-term Fourier Transform (STFT) spectrogram plots of the Hilbert Modulus; to track the evolution of the fault-related frequency components during the starting transient.

For a micromachine operating in generator mode, the signal processing techniques explored for fault feature extraction and fault diagnosis are:

- The MCSA is applied to the stator current, rotor current, and the DFIG's controller signals during the steady-state period.
- The Discrete Wavelet Transform (DWT) analysis technique is applied to the resultant modulus of the stator and rotor current signals during a speed-varying condition.

5.4.1 Data Acquisition and Processing Rates

According to [128], for an induction machine, the significant information in the stator current signal is focused on the 0 - 400Hz band. In this regard, applying the Nyquist's theorem gives a minimum sampling frequency of 800Hz. In the case of the FFT analysis, it is crucial to have an adequate frequency resolution. Therefore, in this study, when the micromachine is operating in motor mode, the DAQ assistant has been set up to capture 66660 samples at a sampling frequency of 2222samples/s, for an acquisition period of 30 seconds, giving a frequency resolution of 0.03Hz. Whereas, when the micromachine is operating in the generator mode, a total of 200 000 samples were captured at a sampling frequency of 5000 samples/s, for an acquisition period of 40 seconds. The real-time current signals (raw data) are stored on the PXI embedded controller (PXIe-8108) and then extracted for further analysis in MATLAB.

5.4.2 Motor Current Signature Analysis Technique

5.4.2.1 Formulae for Calculating the Stator ITSCF-related Frequency Components in the Stator and Rotor Current Signals

For a machine in its healthy state, both the stator and rotor are balanced three-phase systems. In this ideal condition, only the stator frequency f_s, rotor frequency sf_s, and the corresponding natural time-space harmonics exist in the stator and rotor current signals, respectively [20, 129]. When an asymmetry occurs on the stator side, there will be frequency components appearing in the rotor-current spectrum due to the stator electrical asymmetry given by (5.16) [130-132]:

$$f_{I_r}^{SITSCF} = (2k \pm s)f_s \tag{5.16}$$

Where $k = 1,2,3, \ldots$, s is the slip, and f_s is the fundamental/stator frequency.

The inter-turn short-circuit faults in the stator induces harmonic frequencies in the stator current spectrum given by (5.17) [81, 89]:

$$f_{I_s}^{SITSCF} = f_s(\frac{k(1-s)}{p} \pm n) \tag{5.17}$$

Where $k = 0,1,2,3, \ldots, n = 1,2,3 \ldots$, s is the slip, and f_s is the fundamental frequency.

5.4.2.2 Formulae for Calculating the Rotor ITSCF-related Frequency Components in the Stator and Rotor Current Signals

The rotor inter-turn winding fault changes the symmetry of the rotor currents and thus induces frequency components in the rotor current spectrum given by (5.18) [110, 130-132]:

$$f_{I_r}^{RITSCF} = \pm ksf_s \tag{5.18}$$

In the same vein, the fault-related harmonics induced in the stator current spectrum due to the rotor inter-turn fault are given by (5.19) [119, 126, 133]:

$$f_{I_s}^{RITSCF} = (n \pm \frac{k(1-s)}{p})f_s \tag{5.19}$$

Whereas, the possible frequency components induced in the DFIG controller signals are given by (5.20) [9, 126]:

$$f_C^{RITSCF} = (n \pm \frac{k(1-s)}{p} \pm 1) f_s \tag{5.20}$$

Where $k = 0,1,2,3, \ldots, n = 1,2,3 \ldots, s$ is the slip, p is the number of pole pairs and f_s is the fundamental frequency.

5.4.2.3 Formulae for Calculating the Static Eccentricity Fault-related Frequency Components in the Stator and Rotor Current Signals

The non-uniformity in the air gap due to the static eccentricity fault modifies the inductance and flux paths of the induction machine which leads to the appearance of harmonic components in the spectra plots of the stator and rotor current signals [20, 134]. The frequency components resulting from the eccentricity fault conditions may be characterized as high frequency (HF) or low frequency (LF) components. The high-frequency components are the sideband harmonics around the principal slot harmonic (PSH) and are given by (5.21) [21-23, 78]

$$f_{ecc_{HF}} = f_s \left[(kR \pm n_d) \frac{1-s}{p} \pm v \right] \tag{5.21}$$

Where k = 1, 2, 3,.., R is the number of rotor slots, n_d is the eccentricity order (n_d = 0 for static eccentricity and n_d = 1, 2, 3… for dynamic eccentricity), v is the order of the stator time harmonics that are present in the power supply that is driving the machine (v = $\pm$1, $\pm$3, $\pm$5….).

The HF components are independent of the load torque oscillations and are rarely influenced by load variations [21, 23, 135]. However, these components can be changed by other factors such as noise and interferences by the switches in the power electronic converters that are in the rotor circuit thereby introducing HF components in the current spectrum which masks the fault-related harmonic components [21, 135]. Therefore, according to [21], using the LF components to detect eccentricity faults is more justifiable. Eccentricity faults result in low harmonic frequencies (f_{ecc}) in the stator current spectrum, around the supply frequency (f_s) given by (5.22), these components become intensified if a mixed eccentricity occurs [20-23, 78, 134]:

$$f_{ecc_{LF}} = f_s \pm k f_r = f_s \left[1 \pm \frac{k}{p}(1-s) \right] \tag{5.22}$$

Where, $k = 1,2,3 \ldots, p$ *is the number of pole pairs and* s *is the slip.*

The drawback of using the LF components is that they coincide with oscillating torque effects. It is worth noting that certain defects will most certainly give rise to other component faults. For instance, the change in the airgap flux due to a fault in the stator (5.17) or rotor (5.19) will lead to an airgap eccentricity given by (5.22).

5.4.3 Discrete Wavelet Transform Analysis Technique

The DWT analysis whose steps were discussed in more detail in *Chapter 2, section 2.7.2.3.2* is applied to the stator and rotor current signals during the starting transient to indicate the evolution of the fault features associated with the static eccentricity and inter-turn winding faults in both the stator and rotor windings. As mentioned previously, selecting the mother wavelet, and specifying the number of decomposition levels play a key role in the DWT analysis process.

5.4.3.1 Selection of the mother wavelet

Daubechies wavelets are frequently used as mother wavelets and the investigation in [109] justified that the Daubechies wavelet of the 44th order (*db44*) is the best suitable mother wavelet for the detection of inter-turn faults in induction motors, hence it has been used as the mother wavelet in this study.

5.4.3.2 Specification of the Number of Decomposition Levels

Considering the sampling frequency $F_s = 2222\ samples/sec, f_s = 50Hz,$ the number of decomposition levels is determined as follows:

$$n_f = integer\left[\frac{\log\left(\frac{F_s}{f_s}\right)}{\log(2)}\right] = 5.50 \approx 6 \tag{5.23}$$

The DWT decomposes the sampled current signals into approximation a_n and n detail signals d_j [103], which fall within the frequency bands computed using expressions (2.153) and (2.154) as given in Table 5.6.

Table 5. 6: Frequency Bands of the Wavelet Signals

Coefficient	***Frequency Band (Hz)***
D1	$555.5 - 1111$
D2	$277.75 - 555.5$
D3	$138.88 - 277.75$
D4	$69.44 - 138.88$
D5	$34.72 - 69.44$
D6	$17.36 - 34.72$
A6	$0 - 34.72$

Since the mother wavelet and the number of decomposition levels have been determined, the DWT analysis of the stator and rotor current signals can then be carried out to diagnose the inter-turn winding and static eccentricity faults. However, according to Ogidi [32], the presence of the fundamental frequency f_s (50Hz) in the stator current signal and the movement of this component within the rotor current signal as the speed increases presents a challenge in tracking the evolution of the fault indicators in the decomposition bands during the startup transient. This is due to its larger magnitude which overshadows the evolution of the fault indicators.

Other studies have also presented the difficulty encountered in detecting broken rotor bar (BRB) faults at very low slip values using MCSA due to the masking effect of the fundamental component [136]. In search of a solution, Puche-Panadero *et al* [136], and Xu *et al* [137] made use of the Hilbert Huang Transform (HHT) technique, as a means of improving the MCSA method to diagnose rotor asymmetries at low slip values. The highlight of the HHT technique is that it allows suppressing/removing the fundamental frequency component, thus only leaving room to work with the fault indicators thereby improving the fault diagnosis process [138]. Antonino-Daviu *et al* [139] presented a comparison between using DWT and HHT to analyze the startup stator current signal and diagnose BRBs in IMs. It was concluded that the HHT had more positive aspects in comparison with the DWT, although the patterns arising from HHT did not seem to be any clearer than those with the DWT technique. Furthermore, both techniques constituted some equivalent tools for extracting the left sideband harmonic fault indicator.

Ogidi [32] presented a novel technique of combining HHT and DWT to analyze the startup stator current signal to diagnose short-circuit faults in a permanent magnet machine. This procedure constituted applying HHT to the start-up stator current signals and then applying DWT to the resultant Hilbert modulus to extract the characteristic patterns of the fault indicators in the decomposition bands. The analysis results showed an improvement in the fault diagnosis process, and hence, the same technique is proposed for use in this study, but specific to fault diagnosis in the micromachine/ micro-WRIM. Therefore, for this study, the HHT technique, which is extensively discussed in [136], is proposed to be applied to the stator and rotor current to improve the detection of the stator ITSCF, rotor ITSCF, and SE fault by removing the fundamental frequency component from the current signals and applying the DWT on the resultant Hilbert modulus signals. The HHT signal analysis technique has frequently been used in different industrial applications and the detailed procedures of implementing this technique are discussed in more detail in [32, 136, 140].

5.5 Chapter Summary

5.5.1 A Case for Micromachines in Laboratory-based DFIG Wind Turbine Systems

This subsection presented a comprehensive study on the correlation in the dimensional parameters, winding factors, and the evolution of specific electrical asymmetry indicators for a large-scale DFIG, its micromachine/scaled-down version, and in a standard small-scale off-the-shelf WRIM. This was motivated by the importance of being strategic in selecting a small-scale machine that would ensure that the experimental results obtained from lab-based test rigs are an accurate reflection of what is expected in an actual system. In this context, it was deduced that the availability of a micromachine whose dimensional parameters, winding factors, and time constants resemble those of a large-scale machine ensures an identical transient response of the two machines.

5.5.2 Customization of the micro-WRIM to Implement the SE, and Stator & Rotor ITSCFs

This subsection presented the customization of the micromachine to enable the practical implementation of the stator inter-turn, rotor inter-turn, and the static eccentricity (SE) fault conditions in the laboratory environment. The scaled-down WRIM machine that is used in this work has been designed and built in the university laboratory by Dehnavifard using Berchten's scaling methodology. The parameters of the reference DFIG and the scaled-down DFIG have been presented in Table 5.3. The micromachine has been customized by modifying the stator and rotor windings to achieve inter-turn winding fault conditions at different severities, which are, 2%, 4%, 6%, and 8%. The corresponding number of turns shorted out per phase on the stator and rotor have been computed as presented in *subsections 5.3.1* and *5.3.2*, respectively. The machine has also been modified to make it possible to implement a static eccentricity fault as illustrated in Fig. 5.9.

5.5.3 Signal Processing Techniques for Fault Feature Extraction and Fault Diagnosis in the micro-WRIM

This subsection shed light on the signal processing techniques which will be used in *Chapters 6 and 7* to detect the ITSCFs in the rotor and stator of the WRIM, as well as the SE fault, during steady-state and transient operating conditions. As mentioned earlier, two separate investigations will be conducted to diagnose the machine faults when the micromachine is operating in two modes: in the absence of the power electronic (PE) converter system and after the PE converter has been incorporated into the rotor circuit.

The signal processing techniques that will be used for fault-feature extraction and fault diagnosis under each scenario are outlined in *subsection 5.4*. The formulae for computing the fault-related frequency components expected to emerge in the spectral plots of the captured signal due to the occurrence of the stator inter-turn, rotor inter-turn and the static eccentricity faults have been presented in *subsection 5.4.2*. The detailed signals analysis for fault-feature extraction and Fault Diagnosis in the scaled-down WRIM using the MCSA, DWT, HHT, and the STFT Spectrogram techniques is presented in *Chapter 6* (in the absence of the power electronic converter system) and in *Chapter 7* (in the presence of the power electronic converter system).

Chapter 6: Detection of the Inter-turn Winding and Static Eccentricity Faults in the micro-WRIM in Isolation of the Power Electronic Converter System

6.1 Introduction

This chapter gives a detailed discussion on the analysis of the captured stator and rotor current signals to detect the inter-turn short-circuit fault (ITSCF) and the static eccentricity (SE) fault conditions in a 5kW micro-WRIM operating in the motoring mode, i.e., in the absence of the power electronic converter system. Currently, the knowledge base is limited to fault detection in controlled DFIGs, mainly because previous works focus more on laboratory-based systems which are made up of standard off-the-shelf induction machines / DFIGs with back-to-back converters. However, the converter's switching harmonics and the dynamics of the control loops in such a system suppress the fault signatures in the terminal current signals thereby compromising the DFIG fault diagnosis process, like in the case of the inverter-fed squirrel cage induction machines (SCIMs). Therefore, to have a better understanding of the inherent fault signatures associated with WRIMs, it is crucial to investigate the diagnosis of machine faults in isolation of the converter, which is the focal point of this chapter. Considering that this is an area that has not been explored in literature, particularly in the diagnosis of inter-turn and air-gap eccentricity faults, it gives this work an edge. Therefore, the analysis in this chapter aims to plug a gap in the literature by taking a more fundamental approach to identifying fault-related components, but more importantly, stressing the factors that need to be considered when conducting fault diagnosis at a system level, especially when using harmonics under transient operating conditions. In this regard, the analysis of both the stator and rotor currents is conducted in this chapter, to detect the ITSCF and SE fault conditions using the MCSA, HHT, and DWT, under the steady-state and transient operating conditions, respectively. Additionally, a comparative study of using the stator and rotor current signals for fault detection has been presented, to identify which current signal is best suited for diagnosing the inter-turn winding and static eccentricity faults. Finally, the spectrogram plots of the rotor current signal have been presented to illustrate the evolution of the fault indicator(s) during the starting transient region.

6.2 Results and Discussions: Fault Feature Extraction and Fault Diagnosis

The experimental tests have been performed on the micro-WRIM under the following scenarios:

1. ***Scenario 1***: micro-WRIM in a healthy state.
2. ***Scenario 2***: micro-WRIM with a 2% and 4% stator inter-turn fault.
3. ***Scenario 3***: WRIM with a 2%, 4%, 6% and 8% rotor inter-turn fault.
4. ***Scenario 4***: WRIM with a static eccentricity fault.

The following loading conditions have been considered for each scenario under the steady-state condition:

1. ***No load condition***: slip = 0.027, no load stator current of 16A
2. ***Half load condition***: slip = 0.076, stator current of 18A
3. ***Full load condition***: slip = 0.106, full load current of 20A

To conduct the fault diagnosis process, the MCSA technique has been applied to both the stator and rotor current signals during the steady-state operating condition to detect the stator inter-turn, rotor inter-turn, and SE faults under different loading conditions. Whereas the DWT analysis technique has been applied to the resultant stator and rotor Hilbert modulus signals over the start-up/ transient region to detect the same machine faults.

6.2.1 Motor Current Signature Analysis Technique

This section presents the spectral analysis of the stator and rotor current signals in steady-state using MCSA to detect the stator ITSCF, rotor ITSCF, and SE faults implemented on the scaled-down WRIM, under different loading conditions.

6.2.1.1 Assessing the Micromachine under the Healthy State

6.2.1.1.1 No Load Condition

Under the no-load condition, the micromachine was operated at a sub-synchronous speed of 1458rpm, corresponding to a slip of 0.028. The waveforms of the stator and rotor currents for this case are presented in Fig. 6.1, captured when the machine has reached its steady state.

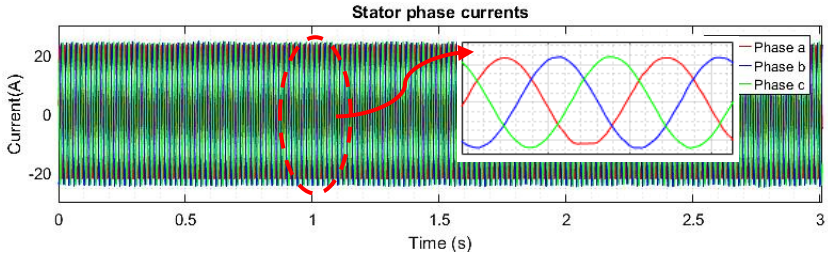

(a)

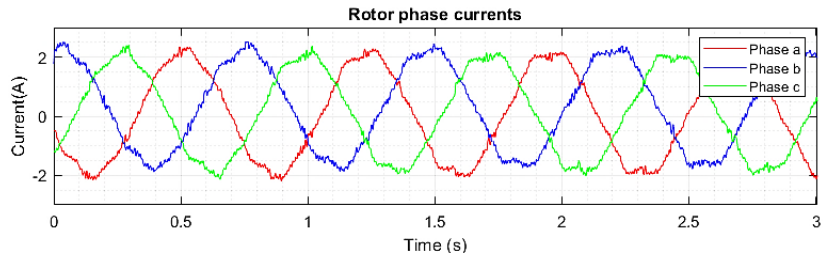

(b)

Figure 6. 1: (a) Stator and (b) rotor current waveforms for a micromachine in a healthy state under the no-load condition

Table 6.1 presents the parameters of the stator and rotor current signals for a micro-WRIM in healthy state under the no-load condition

Table 6. 1: Parameters of the stator and rotor current waveforms for a micro-WRIM in a healthy state at no-load condition

Phase	***Stator rms current [A]***	***Rotor rms current [A]***	***Stator frequency [Hz]***	***Rotor frequency [Hz]***	***Slip***
A	16.70	1.49	50	1.42	0.028
B	17.19	1.45			
C	17.19	1.43			

The MCSA has been applied to the captured stator and rotor current signals in MATLAB to obtain the FFT spectrum of the respective currents for a micromachine in a healthy state under the no-load condition. The spectral plots are presented in Fig. 6.2, where the supply frequency (f_s = 50Hz), its multiples, and the rotor current frequency (f_r) are indicated. The plots have been zoomed out to display the range of frequencies from 0 – 400Hz, which contains the significant frequency harmonics.

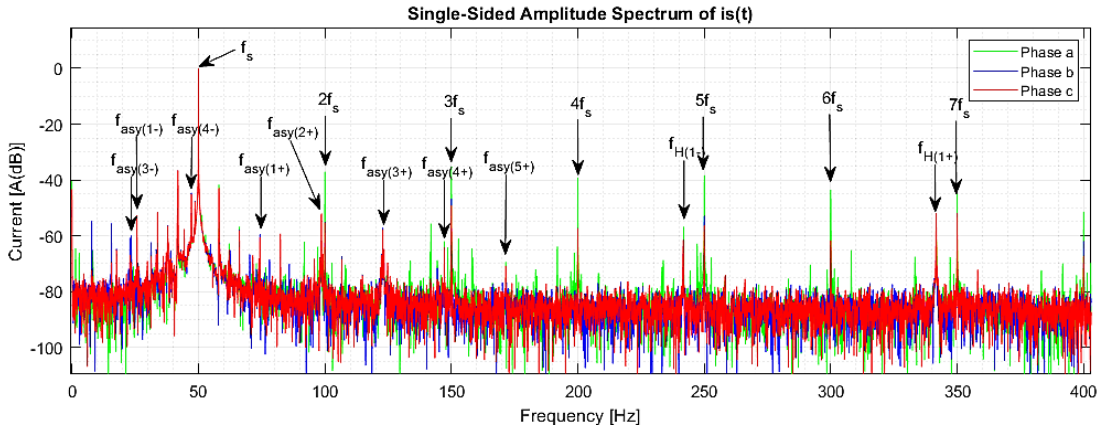

(a)

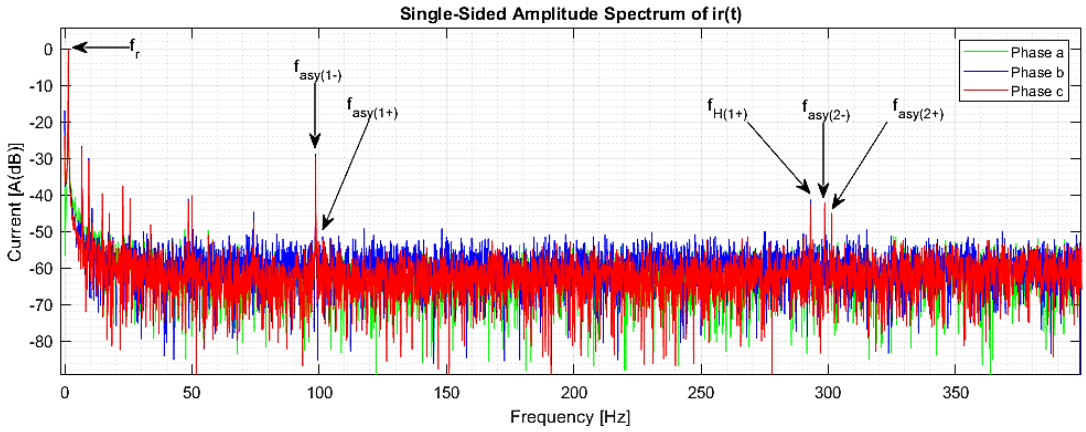

(b)

Figure 6. 2: (a) Stator and (b) rotor current FFT spectra plots for the micromachine operated at a sub-synchronous speed of 1458rpm, in a healthy state, under the no-load condition

The rest of the peaks indicated in the spectral plots are the healthy state and asymmetry-related frequency components calculated using (5.12) and (5.17), in the case of the stator current spectrum,

and using (5.13) and (5.19), in the case of the rotor current spectrum. The computed frequency components are summarized in Table 6.2, for different values of *k* (harmonic order).

Table 6. 2: Frequency components in the stator and rotor current spectrum of a micromachine in the healthy state under the no-load condition

	Stator Current Spectrum				**Rotor Current Spectrum**			
k	***Asymmetry-related components [Hz]***		***Healthy state-related components [Hz]***		***Asymmetry-related components [Hz]***		***Healthy state-related components [Hz]***	
	$f_{I_s}^{asy(+)}$	$f_{I_s}^{asy(-)}$	$f_{I_s}^{H(+)}$	$f_{I_s}^{H(-)}$	$f_{I_r}^{asy(+)}$	$f_{I_r}^{asy(-)}$	$f_{I_r}^{H(+)}$	$f_{I_r}^{H(-)}$
1	74.31	25.69	341.66	241.66	101.39	98.61	293.05	290.27
2	98.61	1.39	633.32	533.32	201.39	198.61	584.71	581.93
3	122.92	22.92	924.98	824.98	301.39	298.61	876.37	873.59
4	147.22	47.22	1216.64	1116.64	401.39	398.61	1168.03	1165.25
5	171.53	71.53	1508.3	1408.3	501.39	498.61	1459.69	1456.91
6	195.83	95.83	1799.96	1699.96	601.39	598.61	1751.35	1748.57
7	220.14	120.14	2091.62	1991.62	701.39	698.61	2043.01	2040.23
8	244.44	144.44	2383.28	2283.28	801.39	798.61	2334.67	2331.89

6.2.1.1.2 Half Load Condition

Under the half load condition, the micromachine was operated at a sub-synchronous speed of 1386rpm, corresponding to a machine slip of 0.076. The waveforms of the stator and rotor currents for this case are presented in Fig. 6.3.

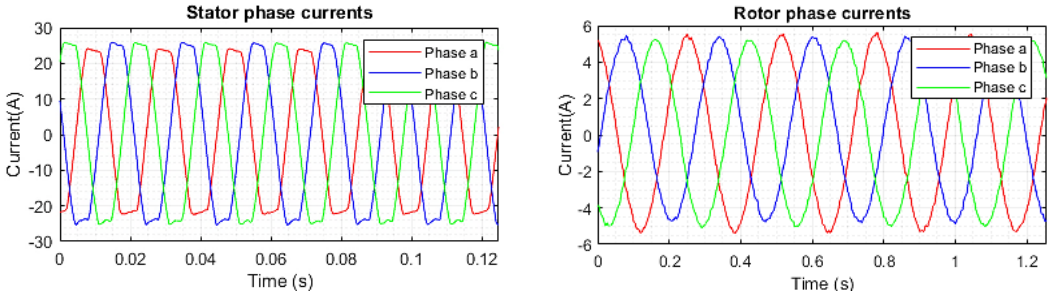

(a) (b)

Figure 6. 3: (a) Stator and (b) rotor currents for a micromachine in a healthy state under half load condition

Table 6.3 presents the parameters of the stator and rotor current signals for a micro-WRIM in healthy state under the half load condition.

Table 6. 3: Parameters of the stator and rotor current waveforms for a micro-WRIM in a healthy state at half load condition

Phase	***Stator rms current [A]***	***Rotor rms current [A]***	***Stator frequency [Hz]***	***Rotor frequency [Hz]***	***Slip***
A	18.27	3.74	50	3.8	0.076
B	19.40	3.59			
C	19.43	3.63			

Figure 6.4 indicates the healthy state and asymmetry-related frequency components in the spectral plots of a micromachine in healthy state under the half load condition.

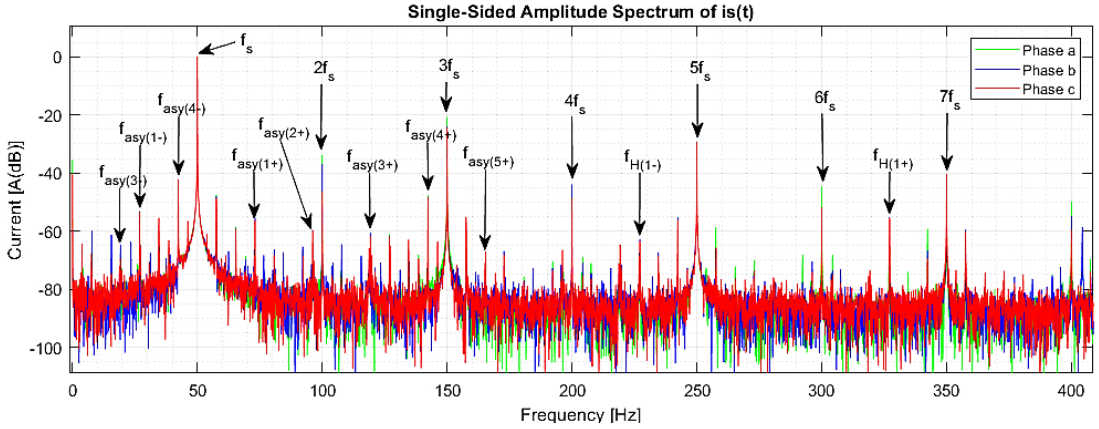

(a)

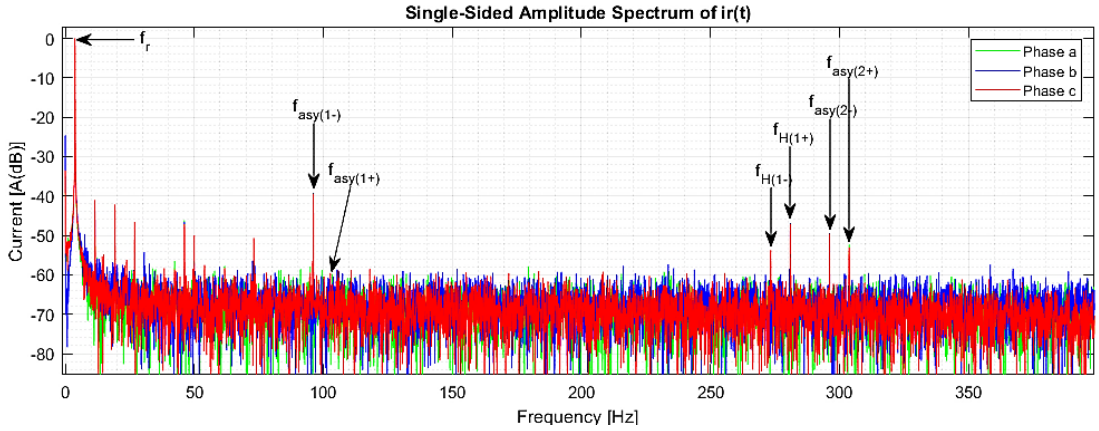

(b)

Figure 6. 4: (a) Stator and (b) rotor current FFT spectra plots for the micromachine operated at a sub-synchronous speed of 1386rpm, in a healthy state, under the half load condition

The computed frequency components for this scenario are summarized in Table 6.4, for different values of *k* (harmonic order).

Table 6. 4: Frequency components in the stator and rotor current spectrum of a WRIM in the healthy state under the half load condition

	Stator Current Spectrum				**Rotor Current Spectrum**			
k	***Asymmetry-related components [Hz]***		***Healthy state-related components [Hz]***		***Asymmetry-related components (Hz)***		***Healthy state-related components [Hz]***	
	$f_{I_s}^{asy(+)}$	$f_{I_s}^{asy(-)}$	$f_{I_s}^{H(+)}$	$f_{I_s}^{H(-)}$	$f_{I_r}^{asy(+)}$	$f_{I_r}^{asy(-)}$	$f_{I_r}^{H(+)}$	$f_{I_r}^{H(-)}$
1	73.1	26.9	327.2	227.2	103.8	96.2	281	273.4
2	96.2	3.8	604.4	504.4	203.8	196.2	558.2	550.6
3	119.3	19.3	881.6	781.6	303.8	296.2	835.4	827.8
4	142.4	42.4	1158.8	1058.8	403.8	396.2	1112.6	1105
5	165.5	65.5	1436	1336	503.8	496.2	1389.8	1382.2
6	188.6	88.6	1713.2	1613.2	603.8	596.2	1667	1659.4
7	211.7	111.7	1990.4	1890.4	703.8	696.2	1944.2	1936.6
8	234.8	134.8	2267.6	2167.6	803.8	796.2	2221.4	2213.8

6.2.1.1.3 Full Load Condition

Under the full load condition, the WRIM operates at a sub-synchronous speed of 1341rpm, resulting in a machine slip of 0.106. The waveforms of the stator and rotor currents for this case are presented in Fig. 6.5. It is observed that the waveform of the stator gets distorted due to the unbalance that is associated with loading the machine.

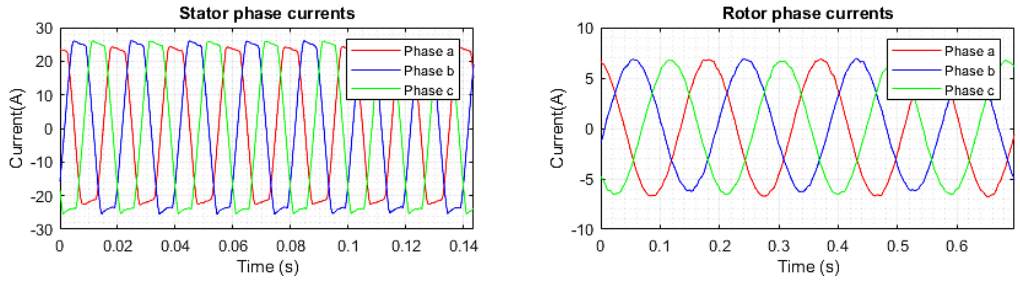

(a) (b)

Figure 6. 5: (a) Stator and (b) rotor current waveforms for a WRIM in a healthy state at full load condition

Table 6.5 presents the parameters of the stator and rotor current signals for a micro-WRIM in healthy state under the full load condition.

Table 6. 5: Parameters of the stator and rotor current waveforms for a micro-WRIM in a healthy state at full load condition

Phase	***Stator rms current [A]***	***Rotor rms current [A]***	***Stator frequency [Hz]***	***Rotor frequency [Hz]***	***Slip***
A	18.95	4.81	50	5.3	0.106
B	20.20	4.60			
C	20.22	4.68			

Figure 6.6 indicates the healthy state and asymmetry-related frequency components in the spectral plots of a WRIM in a healthy state under the full load condition

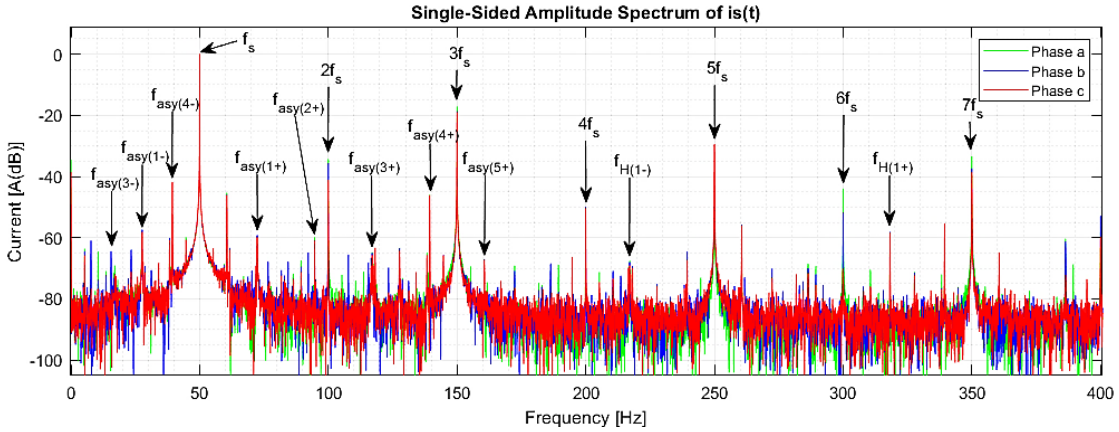

(a)

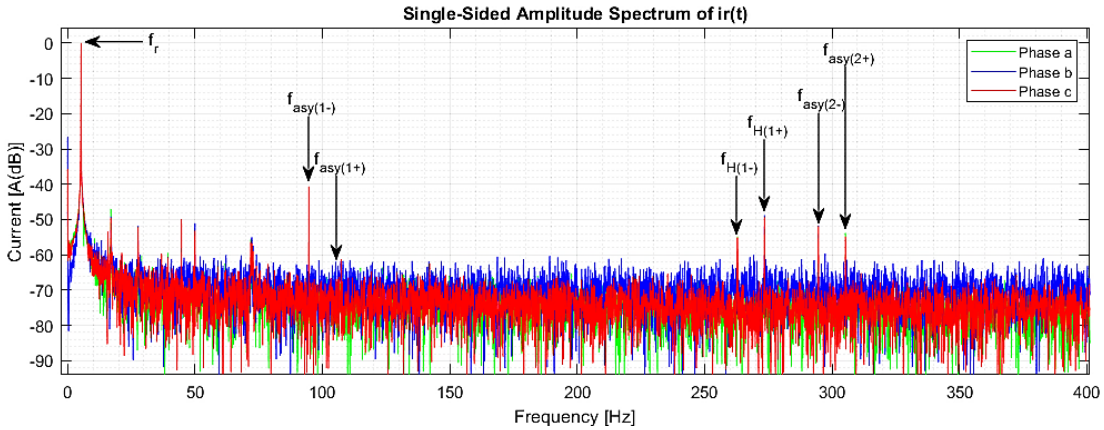

(b)

Figure 6. 6: (a) Stator and (b) rotor current FFT spectra plots for the micromachine operated at a sub-synchronous speed of 1341rpm, in a healthy state, under the full load condition

The computed frequency components for this scenario are summarized in Table 6.6.

Table 6. 6: Frequency components in the stator and rotor current spectrum of a WRIM in the healthy state under the full load condition

	Stator Current Spectrum				**Rotor Current Spectrum**			
k	***Asymmetry-related components [Hz]***		***Healthy state-related components [Hz]***		***Asymmetry-related components [Hz]***		***Healthy state-related components [Hz]***	
	$f_{I_s}^{asy(+)}$	$f_{I_s}^{asy(-)}$	$f_{I_s}^{H(+)}$	$f_{I_s}^{H(-)}$	$f_{I_r}^{asy(+)}$	$f_{I_r}^{asy(-)}$	$f_{I_r}^{H(+)}$	$f_{I_r}^{H(-)}$
1	72.35	27.66	318.14	218.14	105.31	94.69	273.45	262.83
2	94.69	5.31	586.28	486.28	205.31	194.69	541.59	530.97
3	117.04	17.04	854.42	754.42	305.31	294.69	809.73	799.11
4	139.38	39.38	1122.56	1022.56	405.31	394.69	1077.87	1067.25
5	161.73	61.73	1390.7	1290.7	505.31	494.69	1346.01	1335.39
6	184.07	84.07	1658.84	1558.84	605.31	594.69	1614.15	1603.53
7	206.42	106.42	1926.98	1826.98	705.31	694.69	1882.29	1871.67
8	228.76	128.76	2195.12	2095.12	805.31	794.69	2150.43	2139.81

6.2.1.2 Diagnosis of Stator Inter-turn Short-Circuit Faults in the micro-WRIM

This section presents the spectral analysis of the stator and rotor current signals of a 5kW micromachine subjected to the stator inter-turn short circuit fault (ITSCF) condition at different severity levels for the loading conditions considered in this study. In this investigation, the different stator ITSCF severities considered are the 2% and 4%, corresponding to 2 and 3 shorted turns/phase, respectively, implemented on phase B of the stator. As presented in subsection 5.4.2.1 of *Chapter 5*, the stator ITSCF induces harmonic frequencies in the stator and rotor current signals, which can be pre-determined using eq. (5.17) and eq. (5.16), respectively.

6.2.1.2.1 No Load Condition

Table 6.7 presents the rms values of the stator and rotor currents for the micromachine subjected to different stator ITSCF severity levels under the no-load condition.

Table 6. 7: Stator and rotor rms current values at different numbers of shorted turns under the no-load condition

Shorted turns	**Stator I_{rms} [A]**			**Rotor I_{rms} [A]**		
	A	***B***	***C***	***A***	***B***	***C***
0	16.70	17.19	17.19	1.49	1.45	1.43
2	16.86	18.18	17.81	1.57	1.53	1.49
3	17.03	18.85	18.18	1.59	1.55	1.52

From the results presented in Table 6.7, the rms values of the three-phase currents are approximately equal under the healthy condition. However, when a short circuit is introduced in *phase B* of the stator, the stator current in phase B increases significantly than in the other phases. On the contrary, the rms values of the rotor current remain the same despite the occurrence of the inter-turn fault on the stator.

The MCSA technique has initially been applied to the captured stator and rotor current signals, for all phases (A, B and C) to obtain the FFT spectrum of the respective currents and characterize the signatures when the machine is subjected to the stator interturn winding faults. During the analysis, it was observed that the signals of *phase B* (stator faulted phase) gave more distinctive fault indicators, and hence, the FFT spectra presented in this section and subsequent sections will be limited to those of the currents of the faulted phases, for both stator ITSCF and rotor ITSCF conditions, the same approach can be used in real industrial applications.

Therefore, the FFT spectral plots of the captured stator and rotor current signals of *phase* B currents as presented in Fig. 6.7 (a) and (b), respectively. The spectral plots presented are those of the healthy state *vs* 4% stator ITSCF only.

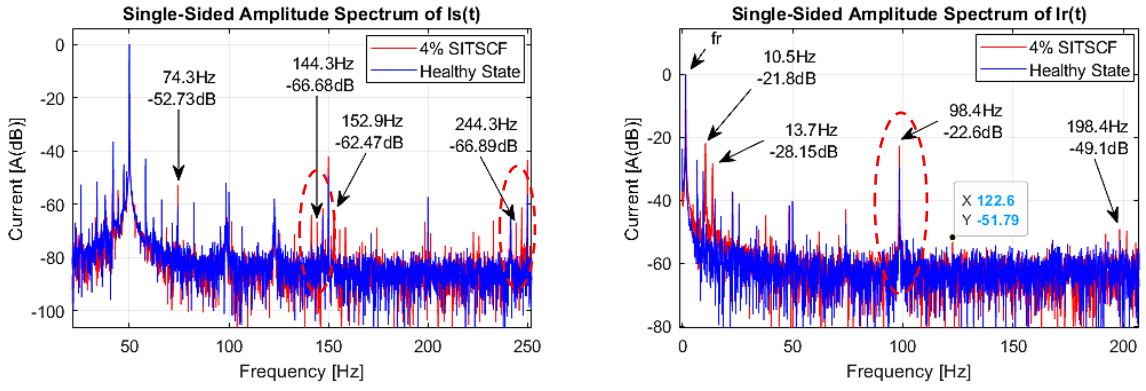

(a) (b)

Figure 6. 7: Current spectral plots of a micromachine with the stator ITSCF at no load; (a) stator, (b) rotor

The predicted frequency components presented in Table 6.2 are observed in the stator current spectrum in Fig. 6.7 (a) and in the rotor current spectrum (Fig. 6.7 (b)), whereby the amplitudes of specific components increase as the stator inter-turn fault occurs. The increase in the stator inter-turn fault severity can be quantitatively presented by analyzing the change in the magnitudes of the

specific fault-related frequency components. A summary of the changes in the magnitudes of the fault-related frequency components observed in the stator and rotor current spectral plots under the no-load condition is graphically illustrated in Fig. 6.8.

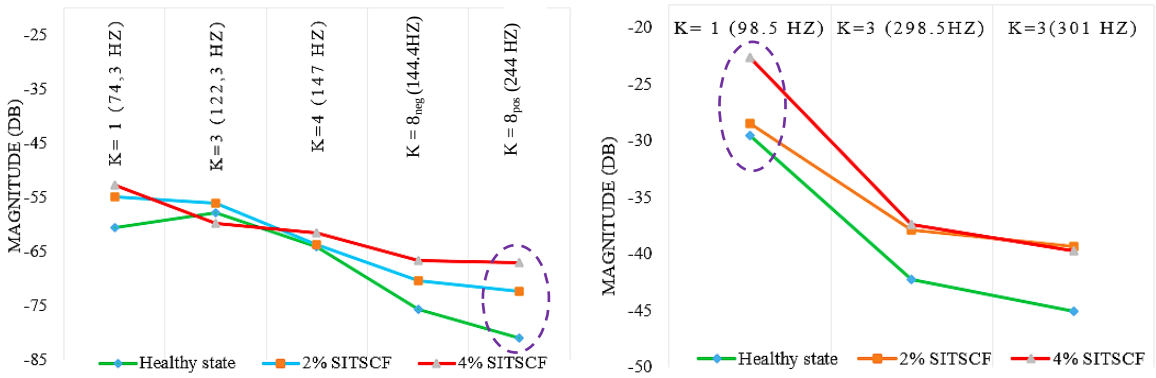

Figure 6. 8: Summary of the fault-related harmonics in the (a) stator and (b) rotor current spectrum at different stator ITSCF fault severities under the no-load condition

From Fig. 6.8 (a), it is observed that increasing the stator inter-turn fault severity level results in a consistent increase in the magnitude of the 144.4 and 244Hz components, whereby the 244.4Hz component corresponding to (k_{1+} = 8) increased the most with 14.11dB [*from -81dB in healthy state to -66.89dB at 4% stator ITSCF*]. In the case of the rotor current spectrum, the consistent magnitude increase is observed in the 98.5Hz component (k_{1-} = *1*), an increase of 6.96dB [*from -29.56dB in a healthy state to -22.6dB at 4% stator ITSCF*] as presented in Fig. 6.8 (b). Therefore, the 244.4Hz and 98.5Hz components are the good stator inter-turn fault indicators in the stator and rotor current signals, respectively, under the no-load condition.

6.2.1.2.2 Half Load Condition

Table 6.8 presents the rms values of the stator and rotor currents for the micromachine subjected to different stator ITSCF severity levels under the half load condition.

Table 6. 8: Stator and rotor rms current values at different numbers of shorted turns under the half load condition

Shorted turns	**Stator I_{rms} [A]**			**Rotor I_{rms} [A]**		
	A	**B**	**C**	**A**	**B**	**C**
0	18.27	19.40	19.43	3.74	3.59	3.63
2	17.95	19.48	19.18	3.17	3.04	3.07
3	18.08	19.86	19.28	3.17	3.02	3.06

It is observed in Table 6.8 that when a short circuit is introduced in *phase B* of the stator, the stator current in phase B increases significantly than in the other phases. The MCSA of the stator and rotor current signals has been conducted and the spectral plots are presented in Fig. 6.9 (a) and (b), respectively.

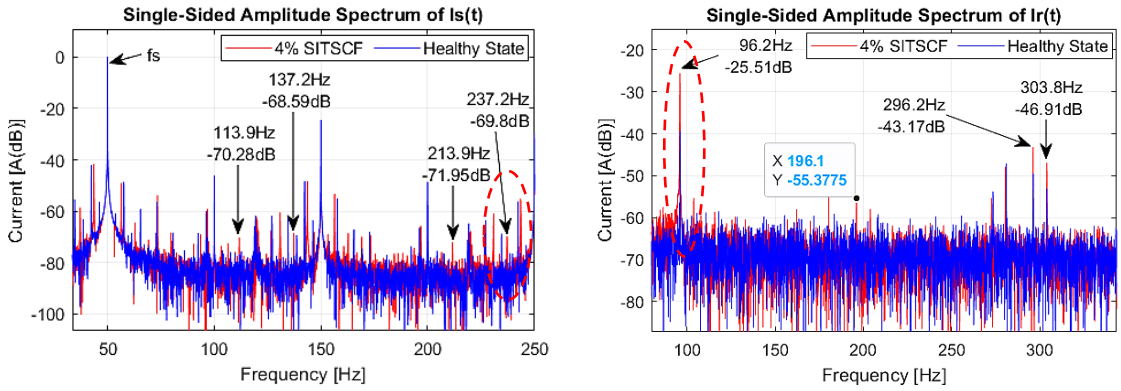

(a) (b)

Figure 6. 9: Current spectral plots for a micromachine with a stator ITSCF at half load; (a) Stator and (b) Rotor

Likewise, the spectral plots presented are those of the healthy state *vs* 4% stator ITSCF only. Figure 6.10 summarizes the changes in the magnitudes of the fault-related frequency components observed in Fig. 6.9 (a) and (b) as the stator ITSCF severity is increased, under the half load condition.

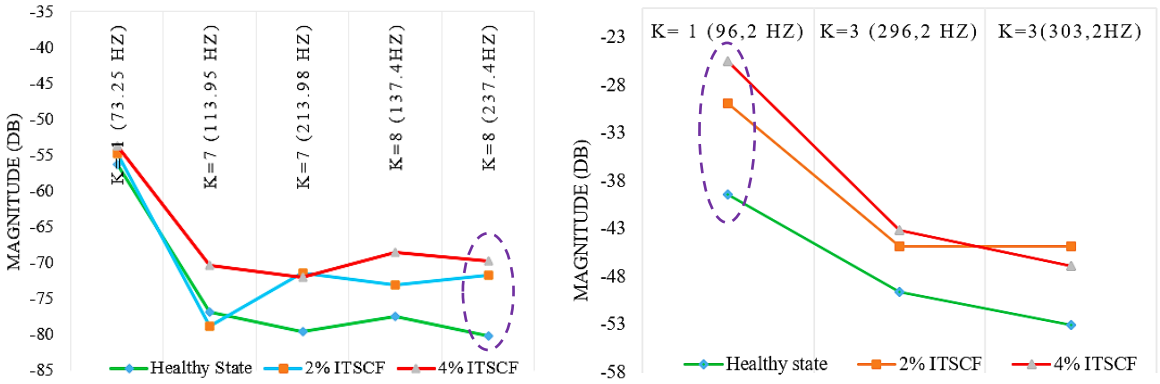

(a) (b)

Figure 6. 10: Summary of the fault-related harmonics in the (a) stator and (b) rotor current spectrum at different stator ITSCF fault severities under the half load condition

From Fig. 6.10 (a), it is observed that increasing the stator inter-turn fault severity results in a consistent increase in the magnitude of the 137.4 and 237.4Hz components, whereby the 237.4Hz component (k_{1+} = 8) increased the most, with 10.37dB. For the rotor current spectrum (Fig. 6.10(b)), a consistent magnitude increase is observed in the 96.2Hz component (k_{1-} = *1*), with an increase of 13.86dB.

6.2.1.2.3 Full Load Condition

Table 6.9 presents the rms values of the stator and rotor currents for the micromachine subjected to different stator ITSCF severity levels under the full load condition.

Table 6. 9: Stator and rotor rms current values at different numbers of shorted turns under the full load condition

Shorted turns	**Stator I_{rms} [A]**			**Rotor I_{rms} [A]**		
	A	***B***	***C***	***A***	***B***	***C***
0	18.95	20.20	20.22	4.81	4.60	4.68
2	18.77	20.31	20.06	4.36	4.18	4.27
3	18.78	20.51	20.03	4.25	4.06	4.14

From Table 6.9, the stator current in phase B increased significantly more than in the other phases when an inter-turn fault was introduced in phase B of the stator. Figure 6.11 (a) and (b), present the spectral plots of the stator and rotor current signals, respectively.

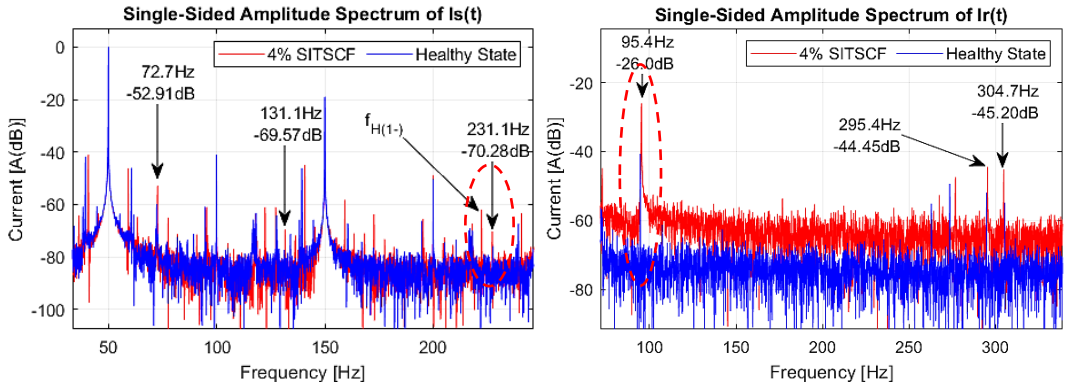

(a) (b)

Figure 6. 11: Current spectral plots for a micromachine with a stator ITSCF at full load; (a) Stator and (b) Rotor

Figure 6.12 summarizes the changes in the magnitudes of the fault-related frequency components observed in Fig. 6.11 (a) and (b) as the stator ITSCF severity increases, under the full load condition.

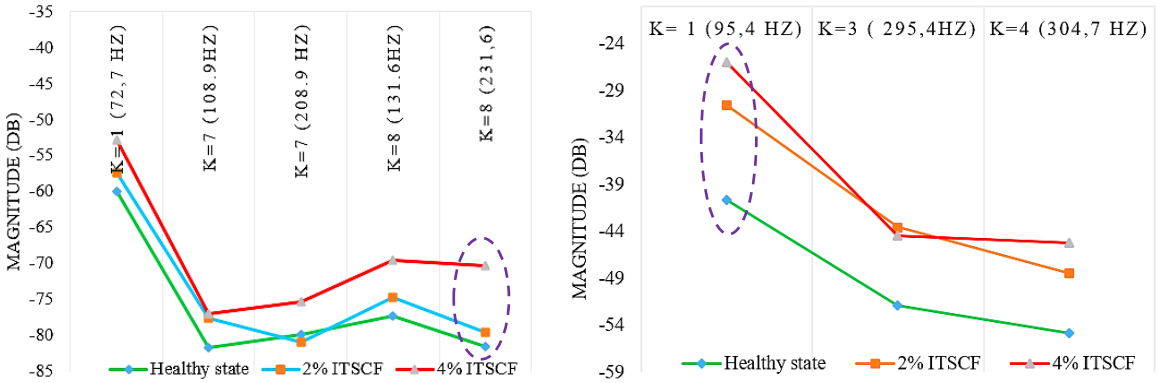

(a) (b)

Figure 6. 12: Summary of the fault-related harmonics in the (a) stator and (b) rotor current spectrum at different stator ITSCF fault severities under the full load condition

From, Fig. 6.12 (a), it is observed that an increase in the fault severity of the stator inter-turn fault results in a consistent increase in the magnitude of the 131.6 and 231.6Hz components, whereby the 231.6Hz component (k_{1+} = 8) increased the most with 11.33dB.

For the rotor current spectrum, the consistent magnitude increase is observed in the 95.4Hz component ($k_{1-} = 1$), an increase of 14.65dB.

6.2.1.2.4 Summary: Dominant Stator ITSCF Indicators in the Stator & Rotor Current Signals

Table 6.10 summarizes the dominant stator inter-turn fault indicators in the stator and rotor current signals under the different loading conditions considered.

Table 6. 10: Main stator inter-turn fault indicators in the stator and rotor current signals

Load Condition	**Stator Inter-turn Short Circuit Fault Indicators**	
	In the stator current spectrum	***In the rotor current spectrum***
No Load (s = 0.027)	244.4 Hz ($k_{1+} = 8$)	98.5 Hz ($k_{1-} = 1$)
Half Load (s = 0.076)	237.4 Hz ($k_{1+} = 8$)	96.2 Hz ($k_{1-} = 1$)
Full Load (s = 0.103)	231.6 Hz ($k_{1+} = 8$)	95.4 Hz ($k_{1-} = 1$)

From the results presented in the subsequent sections, it has been determined that the stator inter-turn fault indicators in the rotor current spectrum were more sensitive to the changes in the severity of the stator ITSCF as compared to the fault indicators in the stator current spectrum. This has been demonstrated by the significant changes which were observed in the amplitudes of the fault indicators that are in the rotor current spectral plots, especially under the medium and full load conditions. This makes the rotor current signal best suited for diagnosing the stator ITSCFs, compared to using the stator current signal. The changes in the magnitudes of the main stator inter-turn fault indicators in the stator and rotor current spectra at different loading conditions are illustrated in Fig. 6.13.

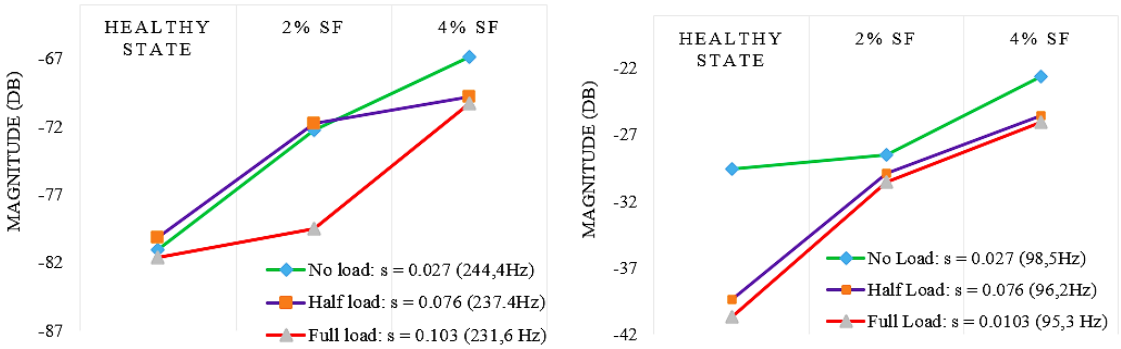

(a) (b)

Figure 6. 13: Changes in the magnitudes of the main stator ITSCF indicators in the (a) stator and (b) rotor current spectrum at the different loading conditions

It is observed that, for each load condition, as the stator inter-turn fault severity is increased, the magnitude of the main fault indicators increases accordingly.

6.2.1.3 Diagnosis of Rotor Inter-turn Short Circuit Faults in the micro-WRIM

This section presents the spectral analysis of the stator and rotor current signals of a micromachine subjected to a rotor inter-turn short circuit fault (ITSCF) condition at different severity levels under the loading conditions considered. In this investigation, the rotor ITSCF severity levels considered are 2%, 4%, and 6%, corresponding to 6, 13, and 19 shorted turns/phase, respectively. The inter-turn short circuits have been implemented on phase C of the rotor. As presented in *subsection 5.4.2.2 of Chapter 5*, the rotor ITSCF induces harmonic frequencies in the stator and rotor current signals, which can be pre-determined using eq. (5.19) and eq. (5.18), respectively.

6.2.1.3.1 No Load Condition

Table 6.11 presents the rms values of the stator and rotor currents for the micromachine subjected to different rotor ITSCF severity levels under the no-load condition.

Table 6. 11: Stator and rotor rms current values at different numbers of shorted turns under the no-load condition

Shorted turns	**Stator I_{rms} [A]**			**Rotor I_{rms} [A]**		
	A	***B***	***C***	***A***	***B***	***C***
0	16.70	17.19	17.19	1.49	1.45	1.43
6	16.79	17.20	17.19	1.51	1.48	1.45
13	16.67	17.11	17.21	1.57	1.53	1.53
19	16.70	17.22	17.32	1.75	1.71	1.71

Based on the results presented in Table 6.11, the rms values of the stator current do not change drastically despite the occurrence of the inter-turn fault on the rotor. On the contrary, the rms values of the rotor currents increase as the rotor inter-turn fault severity increases. The spectral analysis of the stator and rotor current signals has been conducted and the plots are as presented in Fig. 6.14(a) and (b), respectively.

The spectral plots presented are those of the healthy state *vs* 6% rotor ITSCF only. The peaks of the fault-related frequency components in the stator current spectrum have already been presented in Table 6.2, while those in the rotor current spectrum are determined using eq. (5.18) and presented in Table 6.12.

Table 6. 12: Calculated fault-related frequency components in the rotor current spectrum of a micromachine subjected to a rotor ITSCF under the no-load condition

	Fault-related Freq components [Hz]		**Fault-related Freq components [Hz]**		**Fault-related Freq components [Hz]**
k	$f_{I_r}^{RITSCF(\pm)}$	***k***	$f_{I_r}^{RITSCF(\pm)}$	***k***	$f_{I_r}^{RITSCF(\pm)}$
1	1.36	11	14.96	21	28.56
3	4.08	13	17.68	23	31.28
5	6.8	15	20.4	25	34
7	9.52	17	23.12	27	36.72
9	12.24	19	25.84	29	39.44

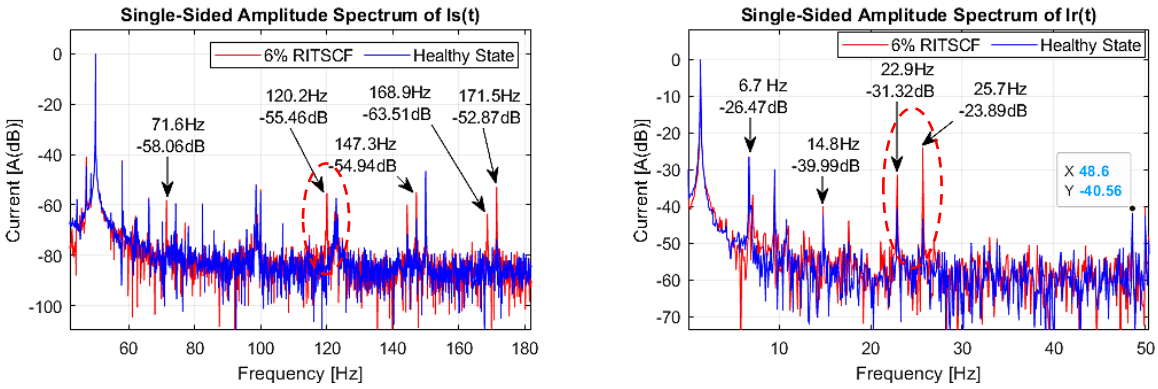

(a) (b)

Figure 6. 14: Current spectral plots for a micromachine with a rotor ITSCF at no load, (a) Stator (b) Rotor

The predicted harmonic components are observed in the stator current spectrum in Fig. 6.14(a) and in the rotor current spectrum presented in Fig. 6.14(b), whereby the amplitudes of specific components increase when the rotor inter-turn fault occurs. A summary of the changes in the magnitudes of the dominant harmonic components as the fault severity increases is graphically illustrated in Fig. 6.15.

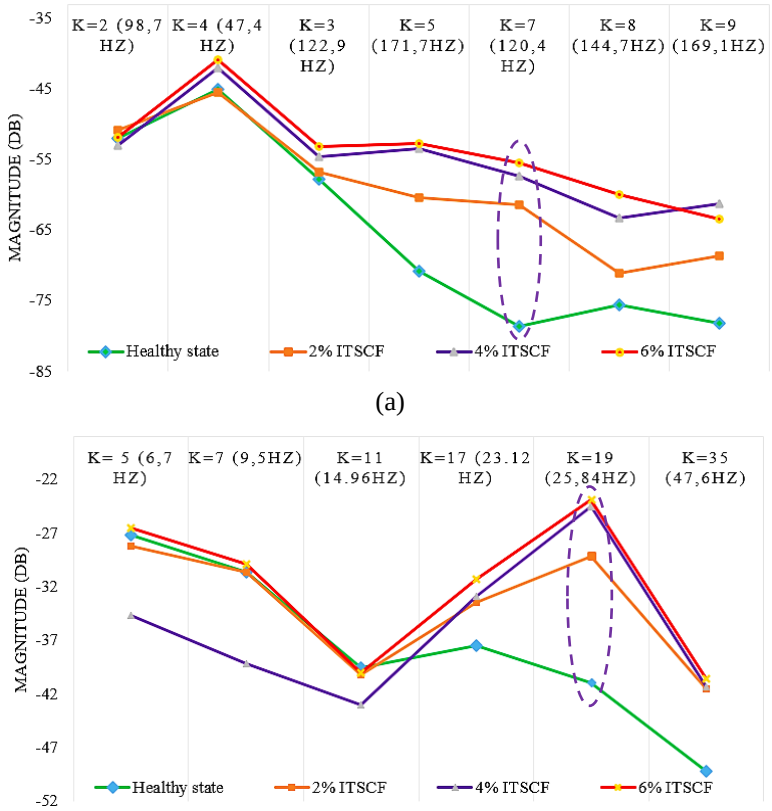

(a)

(b)

Figure 6. 15: Summary of the fault-related harmonics in the (a) stator and (b) rotor current spectrum at different rotor ITSCF fault severities under the no-load condition

It is observed from Fig. 6.15 (a) that increasing the rotor inter-turn fault severity results in a significant increase in the magnitudes of the 144.7, 120.4, and 171 Hz components, whereby the 120.4 Hz component (i = 1, k = 7) increased the most, by 23.12dB**.** For the rotor current spectrum, the consistent increase in magnitude is observed in the 23.12 and 25.7 Hz components, whereby the 25.7 Hz component (i = 1, k = *19*) increased the most, with 17.05dB as illustrated in Fig. 6.15 (b). Therefore, the 120.4Hz and 25.7Hz components are the good rotor inter-turn fault indicators in the stator and rotor current signals, respectively, under the no-load condition.

6.2.1.3.2 Half Load Condition

Table 6.13 presents the rms values of the stator and rotor currents for the micromachine subjected to different rotor ITSCF severity levels under the half load condition.

Table 6. 13: Stator and rotor rms current values at different numbers of rotor shorted turns under the half load condition

Shorted turns	**Stator I_{rms} [A]**			**Rotor I_{rms} [A]**		
	A	***B***	***C***	***A***	***B***	***C***
0	18.27	19.40	19.43	3.74	3.59	3.63
6	18.31	19.40	19.44	3.72	3.59	3.64
13	18.26	19.39	19.46	3.70	3.56	3.65
19	18.27	19.40	19.48	3.71	3.55	3.69

It is observed from Table 6.13 that the rotor current in *phase C* increases significantly more than in the other two phases as the rotor inter-turn fault severity is increased. Figure 6.16 (a) and (b), present the spectral plots of the stator and rotor current signals, respectively. The fault-related frequency components in the stator current spectrum at half load have already been presented in Table 6.4, while those in the rotor current spectrum are presented in Table 6.14.

Table 6. 14: Calculated fault-related frequency components in the rotor current spectrum of a micromachine subjected to a RITSCF at half load condition

	Fault-related Freq components [Hz]		**Fault-related Freq components [Hz]**		**Fault-related Freq components [Hz]**
k	$f_{I_r}^{RITSCF(\pm)}$	***k***	$f_{I_r}^{RITSCF(\pm)}$	***k***	$f_{I_r}^{RITSCF(\pm)}$
1	3.81	11	41.91	21	80.01
3	11.43	13	49.53	23	87.63
5	19.05	15	57.15	25	95.25
7	26.67	17	64.77	27	102.87
9	34.29	19	72.39	29	110.49

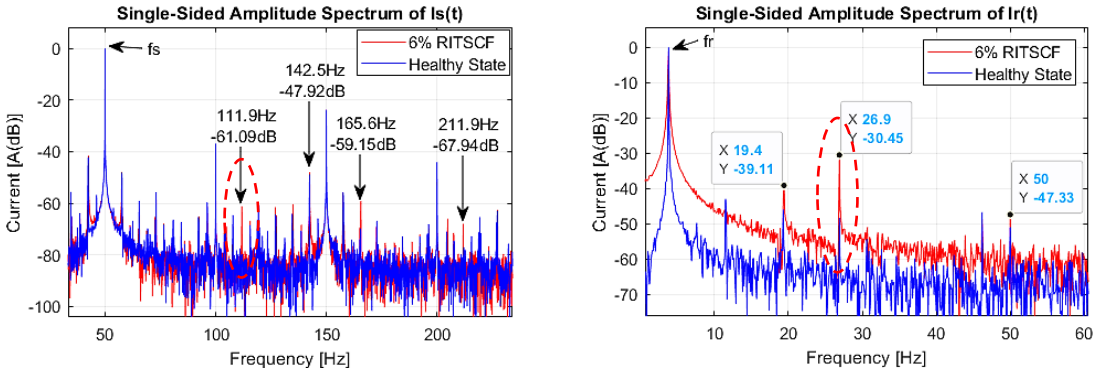

(a) (b)

Figure 6. 16: Current spectral plots for a micromachine with a rotor ITSCF at half load, (a) Stator, (b) Rotor

Figure 6.17 summarizes the changes in the magnitudes of the harmonics observed in the stator and rotor current spectral plots under the half load condition.

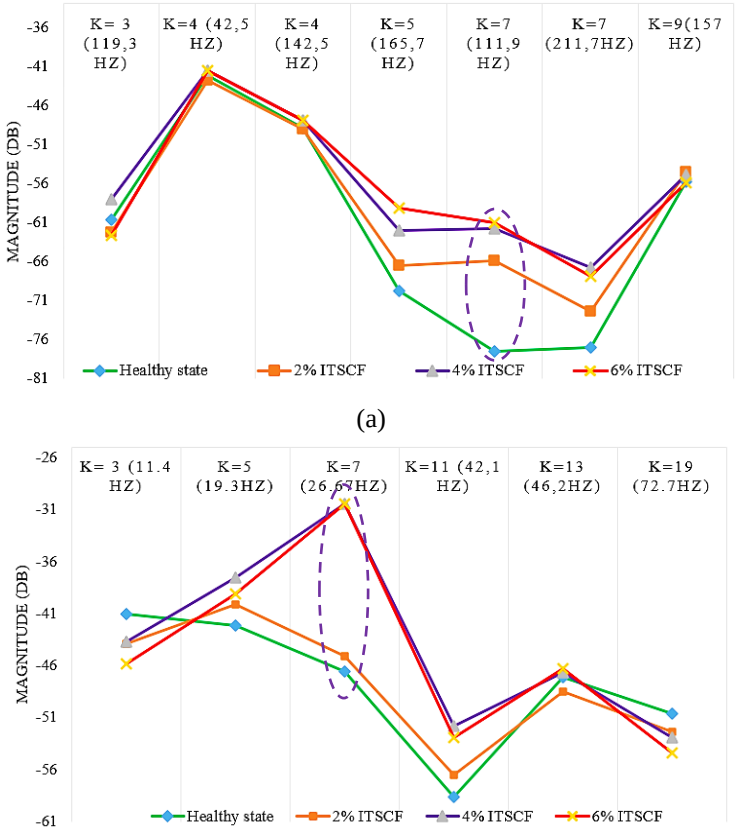

(a)

(b)

Figure 6. 17: Summary of the fault-related harmonics in the (a) stator and (b) rotor current spectrum at different rotor ITSCF fault severities under the half load condition

It is observed from Fig. 6.17 (a) that increasing the rotor ITSCF severity level results in a consistent increase in the amplitude of the 165.7, 111.9, and 211.9 Hz components, whereby the 111.9Hz component, which corresponds to k = 7, increased the most, with 16.38dB. For the rotor current spectrum, the increase in magnitude is observed in the 19.3 and 26.7 Hz components, whereby the 26.7 Hz component (i = 1, k = 7) increased the most, with 16.13dB as illustrated in Fig. 6.17 (b).

6.2.1.3.3 Full Load Condition

Table 6.15 presents the rms values of the stator and rotor currents for the micromachine subjected to different rotor ITSCF severity levels under the full load condition.

Table 6. 15: Stator and rotor rms current values at different numbers of rotor shorted turns under the full load condition

Shorted turns	**Stator I_{rms} [A]**			**Rotor I_{rms} [A]**		
	A	***B***	***C***	***A***	***B***	***C***
0	18.95	20.20	20.22	4.81	4.60	4.68
6	19.01	20.23	20.26	4.82	4.64	4.73
13	18.98	20.22	20.26	4.79	4.61	4.75
19	19.01	20.26	20.31	4.83	4.64	4.82

From the results presented in Table 6.15, the rotor current in *phase C* increases more consistently than in the other phases as the rotor inter-turn fault severity is increased. The FFT spectral plots of the stator and rotor currents are presented in Fig. 6.18 (a) and (b), respectively. The peaks of the fault-related frequency components in the stator current spectrum at full load have already been presented in Table 6.6, while those in the rotor current spectrum are presented in Table 6.16.

Table 6. 16: Calculated fault-related frequency components in the rotor current spectrum of a micromachine subjected to a RITSCF under the full load condition

	Fault-related Freq components [Hz]		**Fault-related Freq components [Hz]**		**Fault-related Freq components [Hz]**
k	$f_{I_r}^{RITSCF(\pm)}$	***k***	$f_{I_r}^{RITSCF(\pm)}$	***k***	$f_{I_r}^{RITSCF(\pm)}$
1	5.23	11	57.53	21	109.83
3	15.69	13	67.99	23	120.29
5	26.15	15	78.45	25	130.75
7	36.61	17	88.91	27	141.21
9	47.07	19	99.37	29	151.67

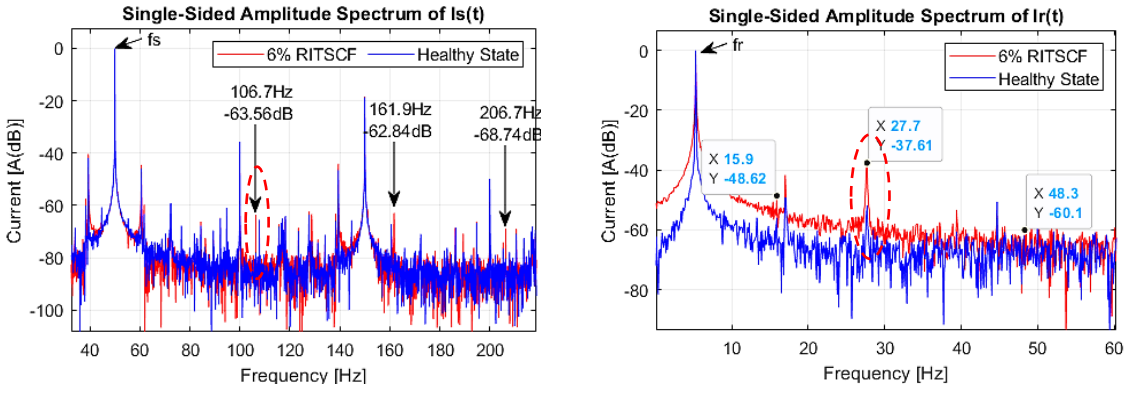

(a) (b)

Figure 6. 18: Current spectral plots of a micromachine with a rotor ITSCF at full load; (a) Stator, (b) Rotor,

Figure 6.19 summarizes the changes in the magnitudes of the fault-related frequency components observed in Fig. 6.18 (a) and (b), as the rotor ITSCF severity is increased.

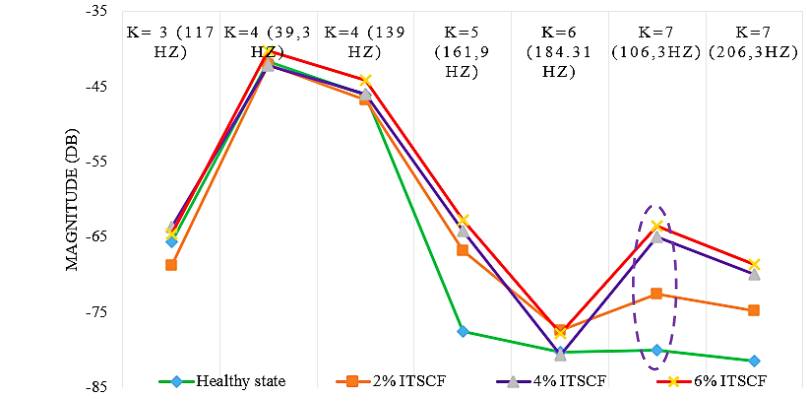

(a)

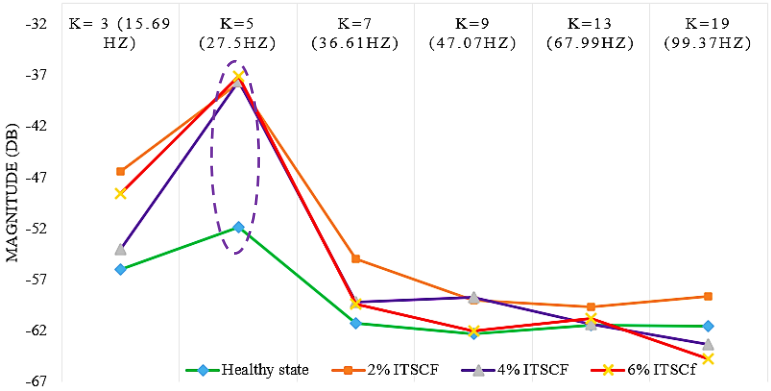

(b)

Figure 6. 19: Summary of the fault-related harmonics in the (a) stator and (b) rotor current spectrum at different rotor ITSCF fault severities under the full load condition

From Fig. 6.19 (a), it is observed that increasing the rotor ITSCF severity resulted in a consistent increase in the amplitudes of the 106.3, 161.9, and 206.3 Hz components, whereby the 106.3Hz component ($i = 1$, $k = 7$) increased the most, with 13.49dB. For the rotor current spectrum, the increase in magnitude is observed in the 27.5Hz component, ($i = 1$, $k = 7$), with an increase of 14.69dB as illustrated in Fig. 6.19 (b).

6.2.1.3.4 Summary: Dominant Rotor ITSCF Indicators in the Stator and Rotor Current Signals

Table 6.17 summarizes the dominant rotor inter-turn fault indicators in the stator and rotor current signals under the different loading conditions considered.

Table 6. 17: Main rotor inter-turn fault indicators in the stator and rotor current signals

Load Condition	**Rotor Inter-turn Short Circuit Fault Indicators**	
	In the stator current spectrum	***In the rotor current spectrum***
No Load (s = 0.027)	120.4 Hz ($i = 1$, $k = 7$)	25.33 Hz
Half Load (s = 0.076)	111.9 Hz ($i = 1$, $k = 7$)	26.9 Hz
Full Load (s = 0.103)	106.3 Hz ($i = 1$, $k = 7$)	27.5 Hz

From the analyses presented in this section, it has been observed that the sensitivity of the rotor inter-turn fault indicators in the rotor current spectrum, i.e., 25.33Hz (*at no load*), 26.9Hz (*at half load*), and 27.2Hz (*at full load*) is slightly above that on the indicators in the stator current spectrum, for the different loading conditions considered. This has been demonstrated by the slightly higher change in the magnitudes of the indicators in the rotor current spectrum, compared to those in the stator current spectrum. This makes the rotor current signal best suited for diagnosing the rotor ITSCFs, compared to using the stator current signal. The changes in the magnitudes of the main rotor inter-turn fault indicators in the stator and rotor current spectra at different loading conditions are illustrated in Fig. 6.20.

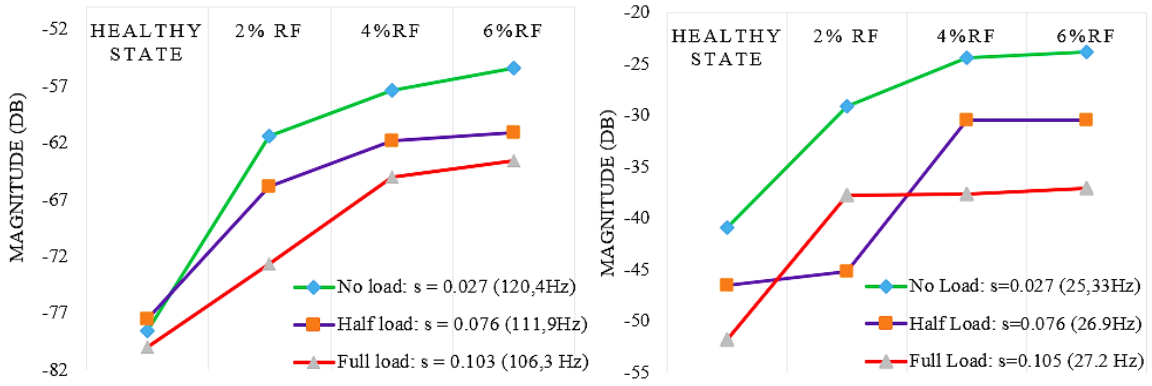

(a) (b)

Figure 6. 20: Magnitudes of the main rotor ITSCF indicators in the (a) stator and (b) rotor current spectrum at the different load conditions

From Fig. 6.20, it is observed that, for each load condition, as the rotor inter-turn fault severity is increased, the magnitude of the main fault-related frequency component increases accordingly.

6.2.1.4 Diagnosis of the Static Eccentricity Fault in the micro-WRIM

This section presents the spectral analysis of the stator and rotor current signals of a micromachine subjected to a static eccentricity fault condition under the different loading conditions. In this investigation, the static eccentricity (SE) fault has been implemented by pushing the rotor shaft away from the center point by 1mm, towards the left side of the machine to displace the rotating axis from the stator axis. As presented in subsection 5.4.2.3 of *Chapter 5*, the SE fault induces harmonic frequencies in the stator and rotor current signals, which can be pre-determined using eq. (5.22).

6.2.1.4.1 No Load Condition

Table 6.18 presents the rms values of the stator and rotor currents for the micromachine in a healthy state and when subjected to an SE fault under the no-load condition.

Table 6. 18: Stator and rotor rms current values for the micromachine in a healthy state and with an SE fault, under the no-load condition

State	Stator I_{rms} [A]			Rotor I_{rms} [A]		
	A	***B***	***C***	***A***	***B***	***C***
Healthy	16.70	17.19	17.19	1.49	1.45	1.43
SE fault	15.60	15.76	15.82	1.50	1.42	1.47

Figure 6.21 (a) and (b) present the spectral plots of the stator and rotor current signals, respectively.

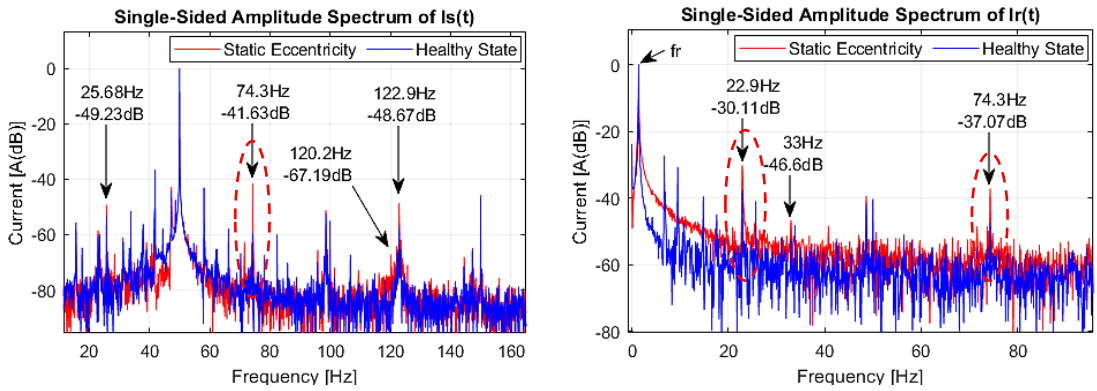

(a) (b)

Figure 6. 21: (a) Stator and (b) rotor current spectrum of a micromachine subjected to a static eccentricity fault under the no-load condition

From Fig. 6.21 (a) and (b), it is observed that the frequency components due to the static eccentricity fault overlap with those due to the stator inter-turn and rotor inter-turn faults. This means that one type of fault could lead to another fault. Figure 6.22 summarizes the changes in the magnitudes of the fault-related frequency components in the stator and rotor current spectral plots when the SE fault occurs under the no-load condition.

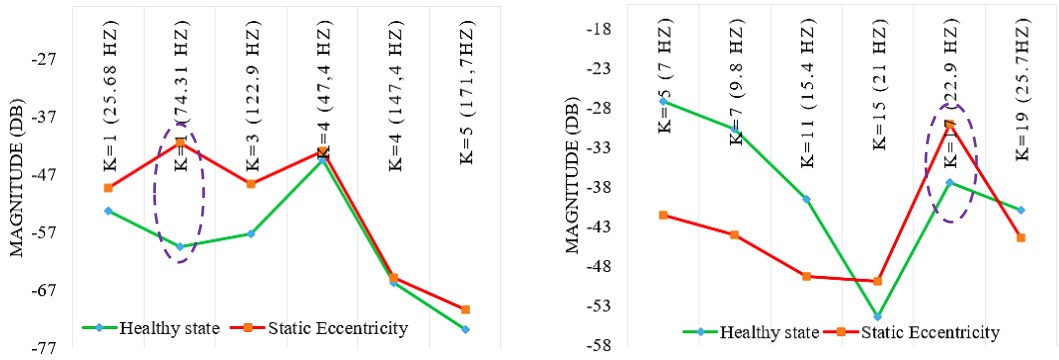

(a) (b)

Figure 6. 22: Summary of the fault-related harmonics in the (a) stator and (b) rotor currents of a machine with an SE fault under the no-load condition

From Fig. 6.22 (a), a significant increase in amplitude is observed in the 74.31Hz component which corresponds to k = 1, with an increase of 17.74dB, followed by the 122.9Hz component (k = *3*). For the rotor current spectrum, a significant magnitude increase is observed in the 22.9Hz component (k = 17) as observed in Fig. 6.22 (b). It is further observed that the amplitude of the 7Hz component (k = 5) decreased significantly.

6.2.1.4.2 Half Load Condition

Table 6.19 presents the rms values of the stator and rotor currents for the micromachine in a healthy state and when subjected to an SE fault under the half load condition.

Table 6. 19: Stator and rotor rms current values for the micromachine in a healthy state and with an SE fault, under the half load condition

State	Stator I_{rms} [A]			Rotor I_{rms} [A]		
	A	***B***	***C***	***A***	***B***	***C***
Healthy	18.27	19.40	19.43	3.74	3.59	3.63
SE fault	17.95	19.01	19.08	3.72	3.54	3.65

The FFT spectral plots of the stator and rotor currents are presented in Fig. 6.23 (a) and (b), respectively.

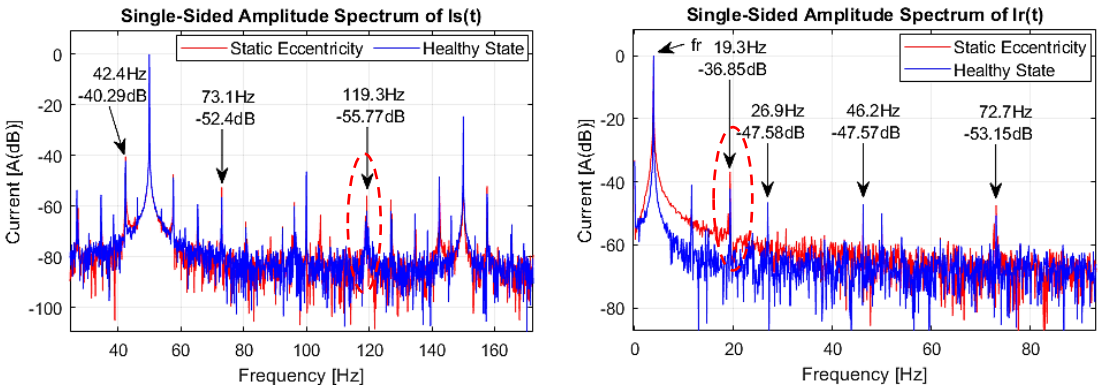

(a) (b)

Figure 6. 23: (a) Stator and (b) rotor current spectrum of a micromachine subjected to a static eccentricity fault under the no-load condition

Figure 6.24 summarizes the changes in the magnitudes of the fault-related frequency components in the stator and rotor current spectral plots when the SE fault occurs under the half-load condition.

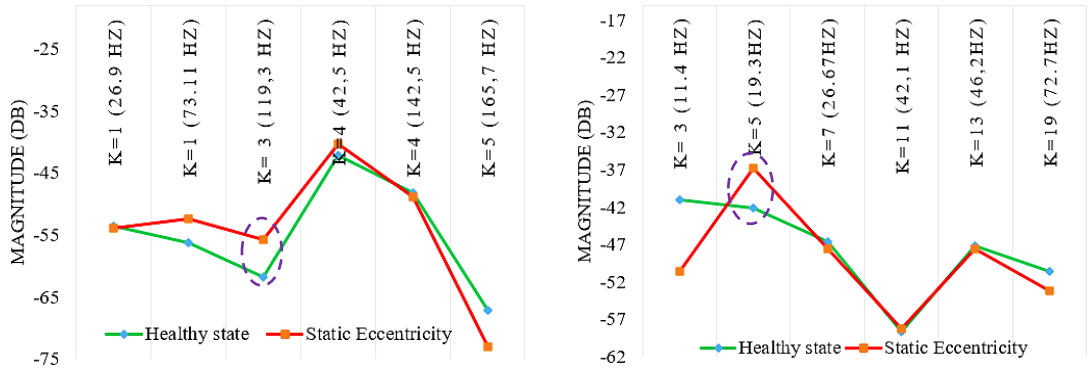

(a) (b)

Figure 6. 24: Summary of the fault-related harmonics in the (a) stator and (b) rotor currents of a machine with an SE fault under the half load condition

From Fig. 6.24 (a), a significant increase in amplitude is observed in the 119.3Hz component which corresponds to k = 3. For the rotor current spectrum, a significant magnitude increase is observed in the 19.3Hz component (k = 5) as illustrated in Fig. 6.24 (b).

6.2.1.4.3 Full Load Condition

Table 6.20 presents the rms values of the stator and rotor currents for the micromachine in a healthy state and when subjected to an SE fault under the full load condition.

Table 6. 20: Stator and rotor rms current values for the micromachine in a healthy state and with an SE fault, under the full load condition

State	Stator I_{rms} [A]			Rotor I_{rms} [A]		
	A	***B***	***C***	***A***	***B***	***C***
Healthy	18.95	20.20	20.22	4.81	4.60	4.68
SE fault	18.83	20.05	20.11	4.87	4.62	4.78

The spectral plots of the stator and rotor currents are presented in Fig. 6.25 (a) and (b), respectively.

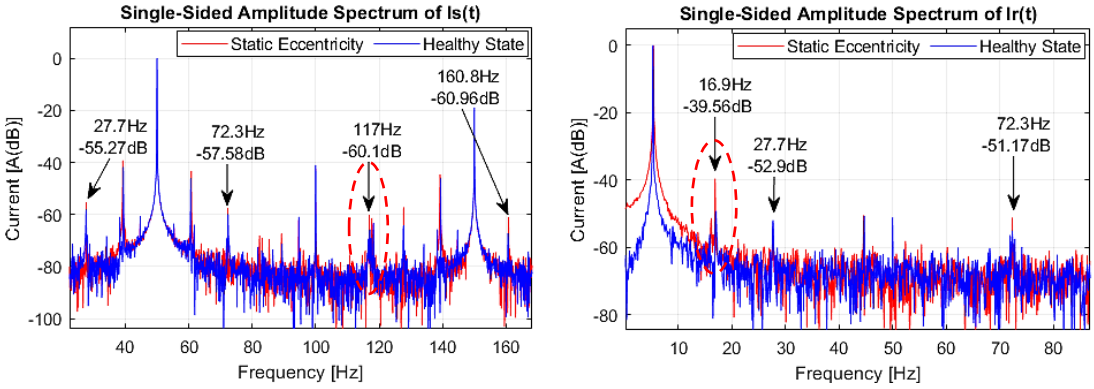

(a) (b)

Figure 6. 25: (a) Stator and (b) rotor current spectrum of a micromachine subjected to a static eccentricity fault under the full load condition

Figure 6.26 summarizes the changes in the magnitudes of the fault-related frequency components in the stator and rotor current spectral plots when the SE fault occurs under the full-load condition.

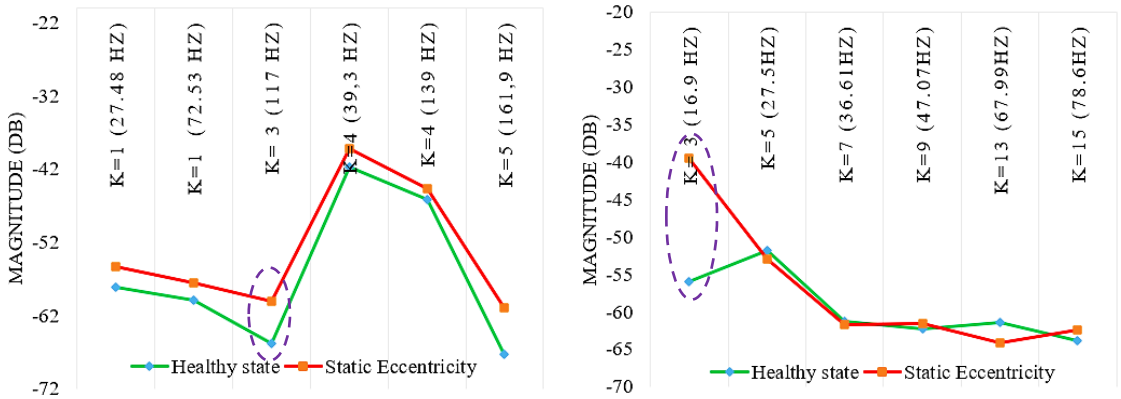

(a) (b)

Figure 6. 26: Summary of the fault-related harmonics in the (a) stator and (b) rotor currents of a machine with an SE fault under the full load condition

From Fig. 6.26 (a), a significant increase in amplitude is observed in the 117.6Hz component in the stator current spectrum, which corresponds to k = 3. For the rotor current spectrum, a significant magnitude increase is observed in the 16.9Hz component (k = 3) as illustrated in Fig. 6.26 (b).

6.2.1.4.4 Summary: Dominant SE Fault Indicators in the Stator and Rotor Current Signals

Table 6.21 summarizes the main static eccentricity fault indicators in the stator and rotor current signals under the different loading conditions considered.

Table 6. 21: Main static eccentricity fault indicators in the stator and rotor current signals

Load Condition	**Static Eccentricity Fault Indicators**	
	In the stator current spectrum	***In the rotor current spectrum***
No Load (s = 0.027)	74.31 Hz ($i = 1, k = 1$)	22.9 Hz
Half Load (s = 0.076)	119.3 Hz ($i = 1, k = 3$)	19.3 Hz
Full Load (s = 0.103)	117.6 Hz ($i = 1, k = 3$)	16.9 Hz

The changes in the magnitudes of the main static eccentricity fault indicators in the stator and rotor current spectra at different loading conditions are illustrated in Fig. 6.27.

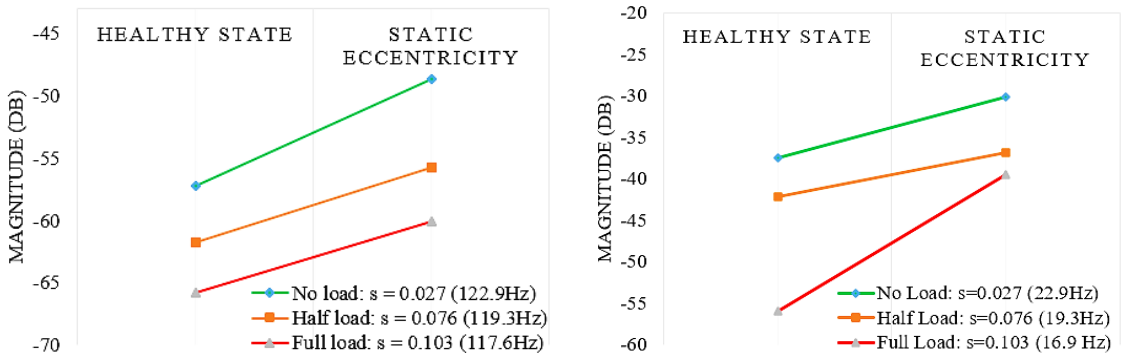

(a) (b)

Figure 6. 27: Magnitudes of the main static eccentricity fault indicators at the different load conditions

It is observed that, for each load condition, the magnitude of the main fault-related frequency component increases accordingly.

6.2.2 Discrete Wavelet Transform Analysis

This section presents the Discrete Wavelet Transform (DWT) analysis of the stator and rotor current signals to detect the stator ITSCF, rotor ITSCF, and SE faults implemented on the scaled-down WRIM, during the starting transient operating region.

6.2.2.1 Assessment of the Micromachine in the Healthy State at Start-up

Figure 6.28 (a) presents the change in the machine speed, while (b) and (c) shows the resultant Hilbert modulus of the sampled starting current signal (***s***, at the top) and the signals resulting from the DWT of the Hilbert Modulus of the stator and rotor currents of the micromachine in the healthy state, respectively.

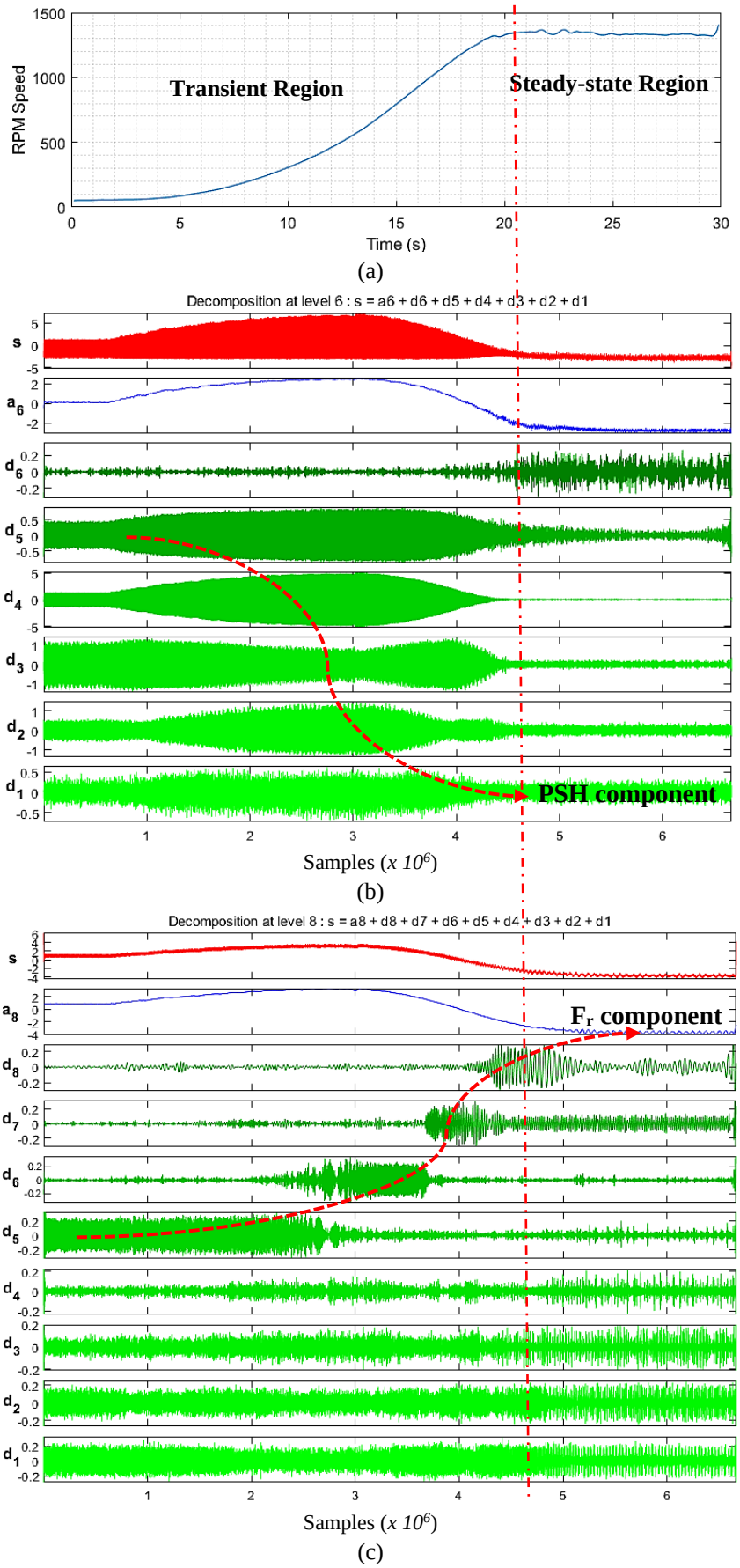

Figure 6. 28: (a) Speed, start-up (b) stator, and (c) rotor currents, and the DWT of the resultant Hilbert Modulus of the sampled signals for a machine in a healthy state condition

A pattern is observed in Fig. 6.28 (b) which is the evolution of the Principal Slot Harmonic (PSH), this is a harmonic component that is always present in every machine regardless of its condition. This harmonic frequency evolves in the stator current during the start-up transient from an initial value of 50Hz (*s = 1*) and it increases as the slip decreases and settles at a frequency of 633.8Hz (in *d1*) when the machine reaches a steady state (*s = 0.027*). From Fig. 6.28 (c), there is a clear pattern observed across the *d5 – a8* coefficients which is the evolution of the $f_r = sf_s$ frequency component as the slip changes from 1 (*at rest*) to 0.027 (*at steady state*). Therefore, the f_r component starts in *d5* ($s \approx 1$) and as time (or rotor speed) increases as shown in Fig. 6.28 (a), f_r increases and crosses into *d6* and further increases, ending up in *a8* at a steady state. Detail *d4 – d1* envelope the high-frequency components of the signal and hence, no unique frequency information/ response is observed in these bands.

6.2.2.2 Diagnosis of the Stator Inter-turn Short-circuit Fault at Start-up

6.2.2.2.1 Stator Current Signal Decomposition

Figure 6.29 shows the resultant Hilbert modulus of the stator current, and the signals resulting from the DWT of the Hilbert modulus of the stator current signal of a micromachine with a 2%, 4%, 6%, and 8% stator ITSCFs. Additional decomposition levels have been considered for better analysis. The evolution of the main fault indicator (244.4Hz) which has been identified from the spectral analysis presented in Fig. 6. 7 (a) for the stator ITSCF is observed in Fig. 6.29, for different levels of fault severity.

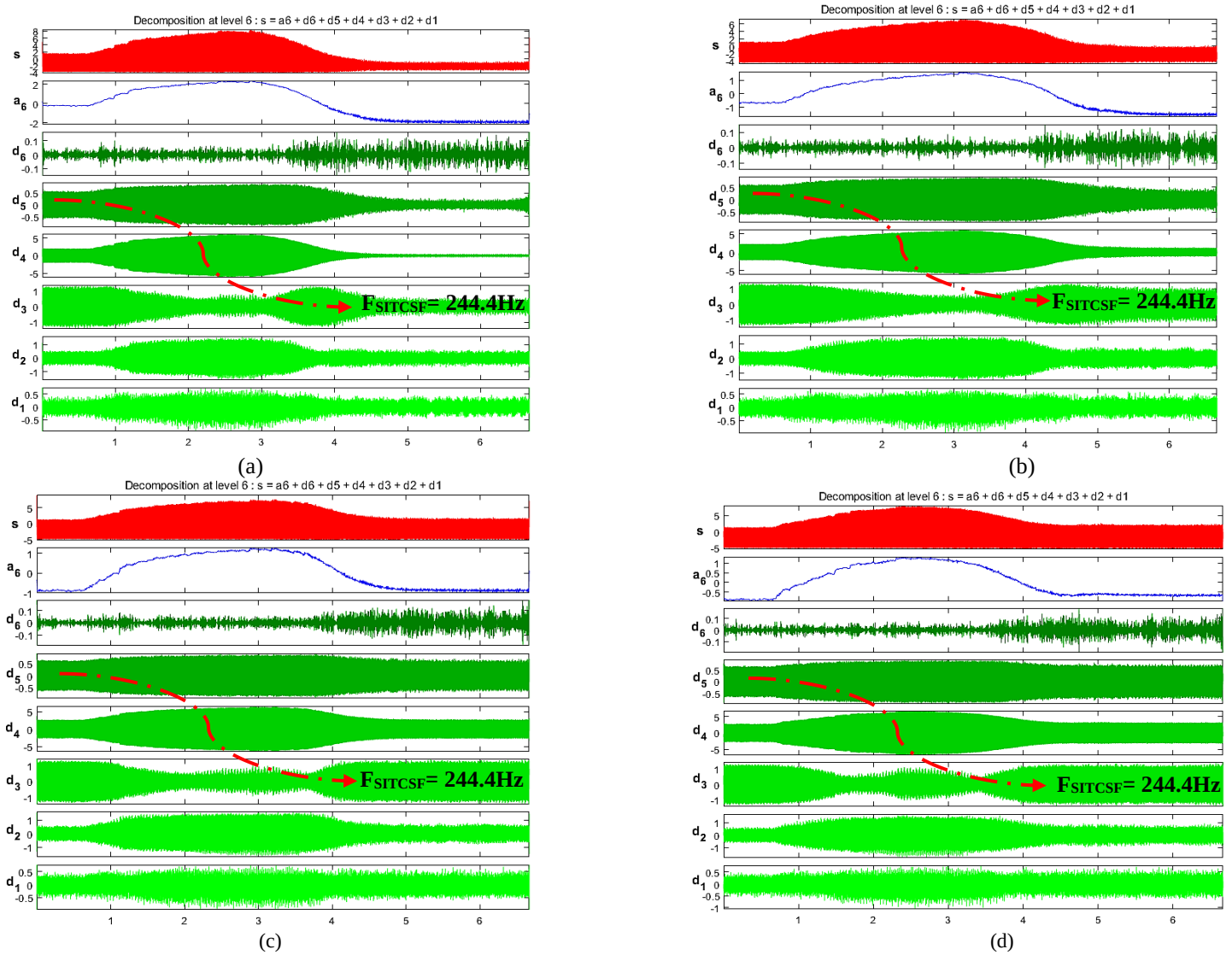

Figure 6. 29: Start-up stator current and DWT of the Hilbert modulus of the signal for a machine with a stator ITSCF at the severity of; (a) 2%, (b) 4%, (c) 6%, and (d) 8%

From Fig. 6.29, it is observed that the dominant fault frequency component moves from the *d5* frequency band to *d4* and settles in *d3* at 244.4Hz. It is observed in plots *(a)* - *(d)* that an increase in the fault severity level is associated with an increase in the harmonic content of detail band *d3* at a steady state. To quantitatively evaluate this observation, the concept of determining the energy content of the *d3* frequency band has been explored, using the equations given in (2.156). Figure. 6.30 illustrates the change in the energy of the *d3* frequency band.

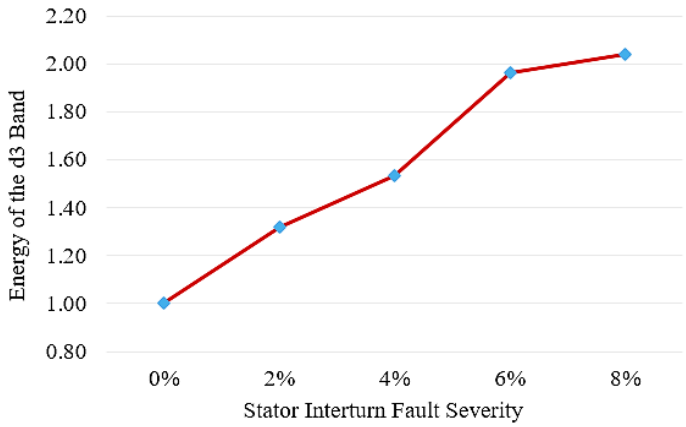

Figure 6. 30: The energy concentrated in detail band d3 of the stator current at different stator ITSCF severity levels

It is observed from Fig. 6.30 that the energy of the *d3* bands increases as the fault severity increases. This is due to the amplification of the stator inter-turn fault indicator (244.4Hz) that is enveloped in this band when the machine reaches its steady-state condition. This is a clear indication that a stator ITSCF is detectable during the transient and steady-state condition using the discrete wavelet transform and the fault severity level can be demonstrated through the evaluation of the energy content in the detail band of interest.

6.2.2.2.2 Rotor Current Signal Decomposition

Figure 6.31 shows the resultant Hilbert modulus of the rotor current, and the signals resulting from the DWT of the Hilbert modulus of the rotor current signal of a micromachine with a 2%, 4%, 6%, and 8% stator ITSCFs. The evolution of the main fault indicator (98.5Hz) has been identified from the spectral analysis presented in Fig. 6. 7 (b) for the stator ITSCF is observed in Fig. 6.31, for different stator inter-turn fault severities.

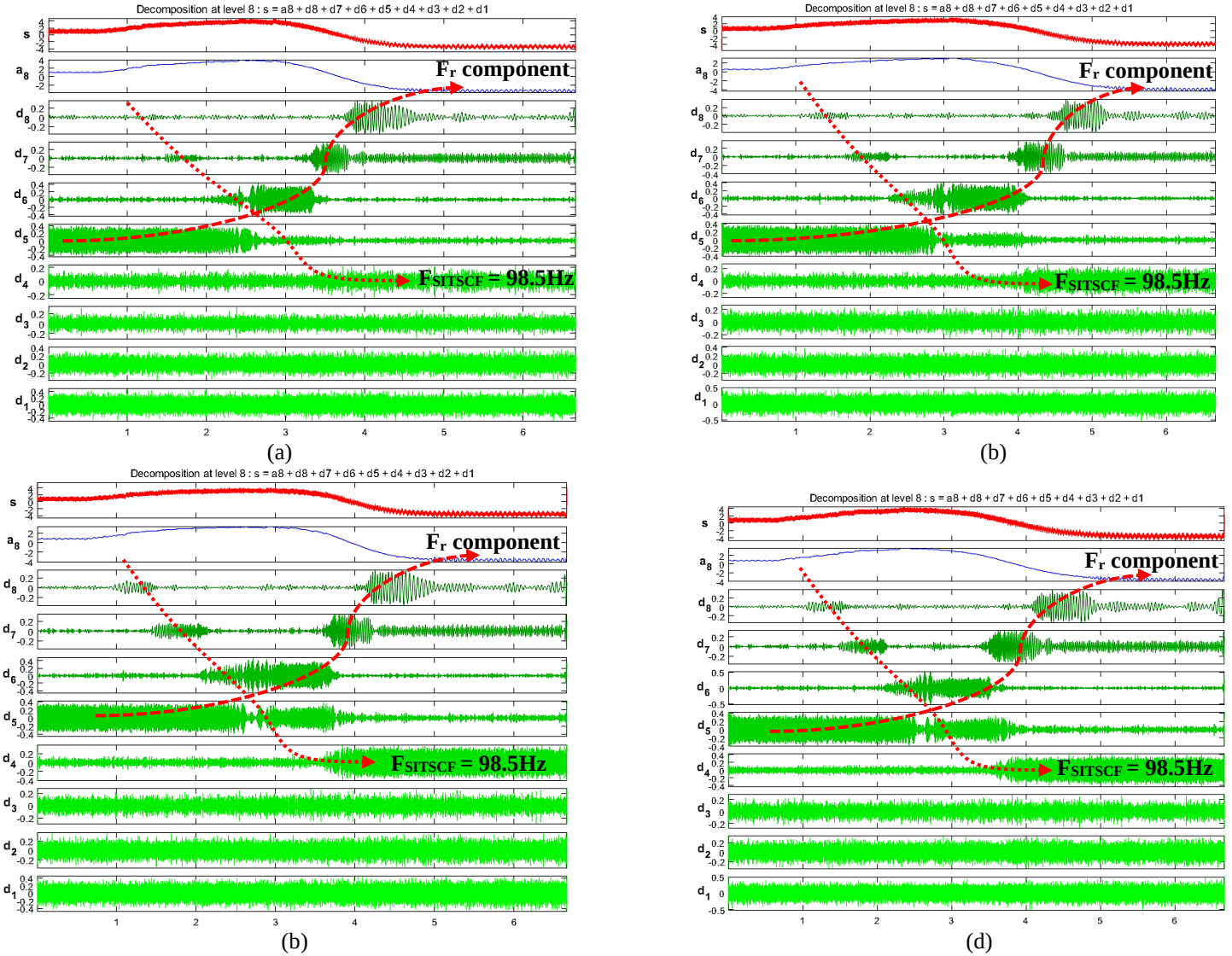

Figure 6. 31: Start-up rotor current and DWT of the Hilbert modulus of the signal for a machine with a stator ITSCF at a severity level of; (a) 2%, (b) 4%, (c) 6%, and (d) 8%

From the plots in Fig. 6.31, the evolution of the fault frequency component is observed from very low-frequency values (dependent on the slip) and evolves from *d8* through *d7*, *d6*, *d5* and settles in *d4* at 98.5Hz. Likewise, a quantitative analysis is carried out to demonstrate the effect of increasing the stator inter-turn fault severity level on the detail band where the fault indicator settles.

Figure. 6.32 illustrates the change in the energy of the *d4* frequency band where the stator inter-turn fault indicator (98.5Hz) settles when the machine reaches its steady state.

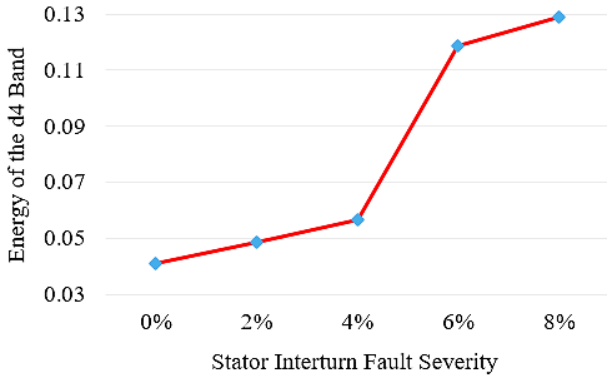

Figure 6. 32: The energy concentrated in detail band d4 of the rotor current at different stator ITSCF severities

Likewise, it is observed that, as the fault severity level is increased, the energy content of *d4* increases due to the amplification of the 98.5Hz component that is enveloped in this band, and thus, the evolution of the fault frequency components becomes more evident.

6.2.2.3 Diagnosis of the Rotor Inter-turn Short-circuit Fault at Start-Up

6.2.2.3.1 Stator Current Signal Decomposition

Figure 6.33 shows the resultant Hilbert modulus of the stator current, and the signals resulting from the DWT of the Hilbert modulus of the stator current signal of a machine with a 2%, 4%, 6%, and 8% rotor ITSCFs. The evolution of the dominant fault frequency component identified as 120.4Hz is not visible in the plots presented in Fig. 6.33, despite the increase in the fault severity level. However, there is also an evolution of low-frequency components from *d5* to *d6* as the machine reaches the steady-state condition. This means that the DWT of the stator current signal does not provide a clear diagnosis of the rotor ITSCF.

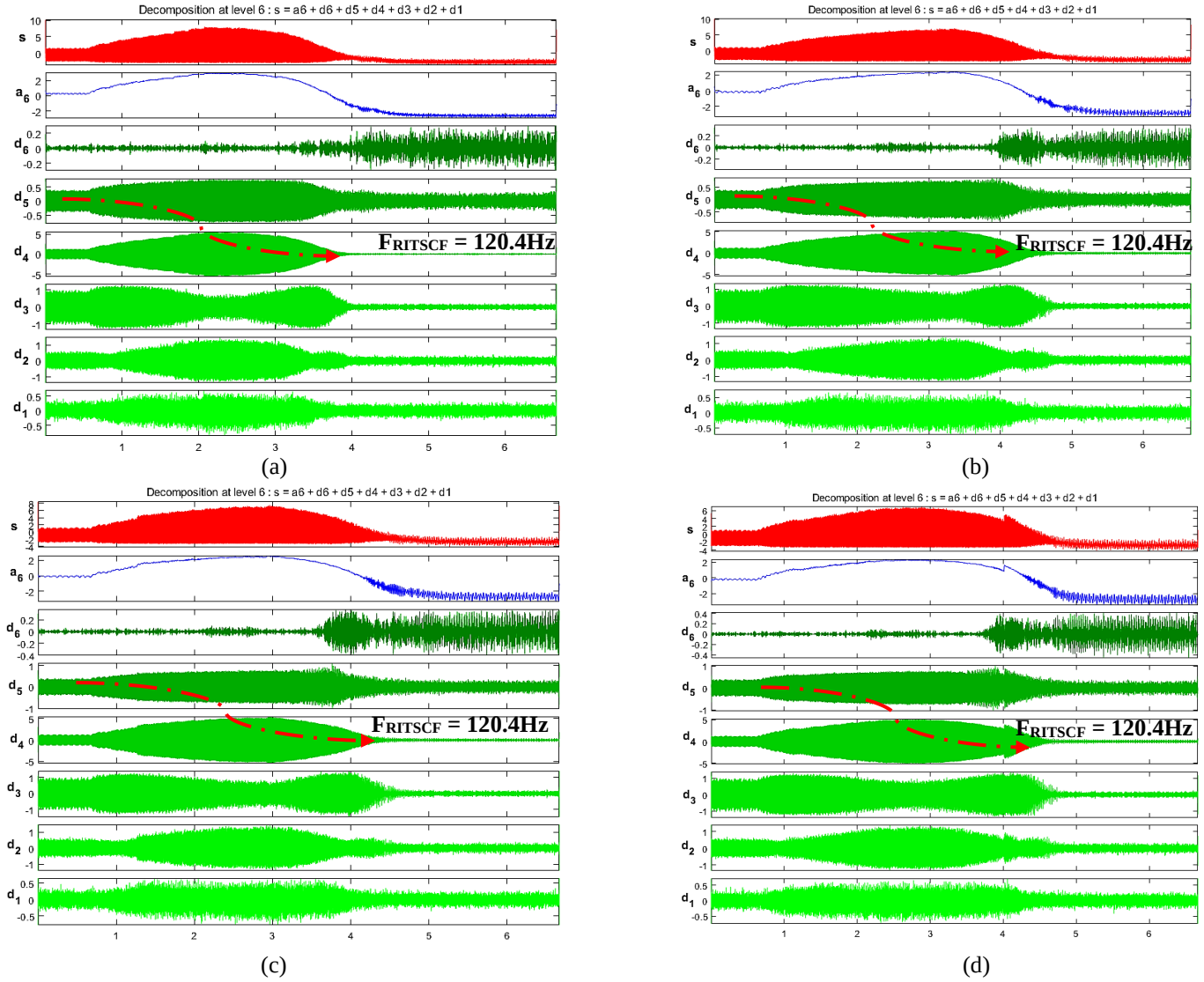

Figure 6. 33: Start-up stator current and DWT of the Hilbert modulus of the signal for a machine with a rotor ITSCF at a severity level of; (a) 2%, (b) 4%, (c) 6%, and (d) 8%

A quantitative analysis is carried out to demonstrate the effect of increasing the rotor inter-turn fault severity level on the detail band *d4* where the fault indicator settles, and it is observed in Fig. 6.34 that the energy concentrated in *d4* at steady-state increases with the fault severity level.

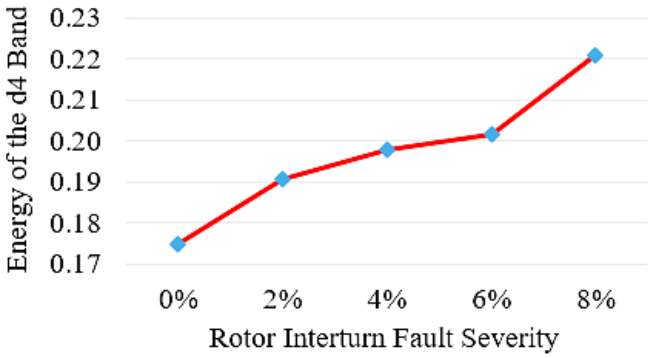

Figure 6. 34: The energy concentrated in detail band d4 of the stator current at different rotor ITSCF severities

6.2.2.3.2 Rotor Current Signal Decomposition

Figure 6.35 shows the resultant Hilbert modulus of the rotor current, and the signals resulting from the DWT of the Hilbert modulus of the rotor current signal of a micromachine with a 2%, 4%, 6%, and 8% rotor ITSCFs. The evolution of the main fault indicator (25.84Hz) which has been identified from the spectral analysis presented in Figure 6. 15 (b) for the rotor ITSCF is observed in Fig. 6.35, for different rotor inter-turn fault severities. The fault frequency component is observed to evolve from *d5* and settles in *d6* at 25.33Hz. It is observed that as the fault severity level was increased, the harmonic content of the detail band *d6* increased as well, and hence, the evolution of the fault frequency component becomes more evident.

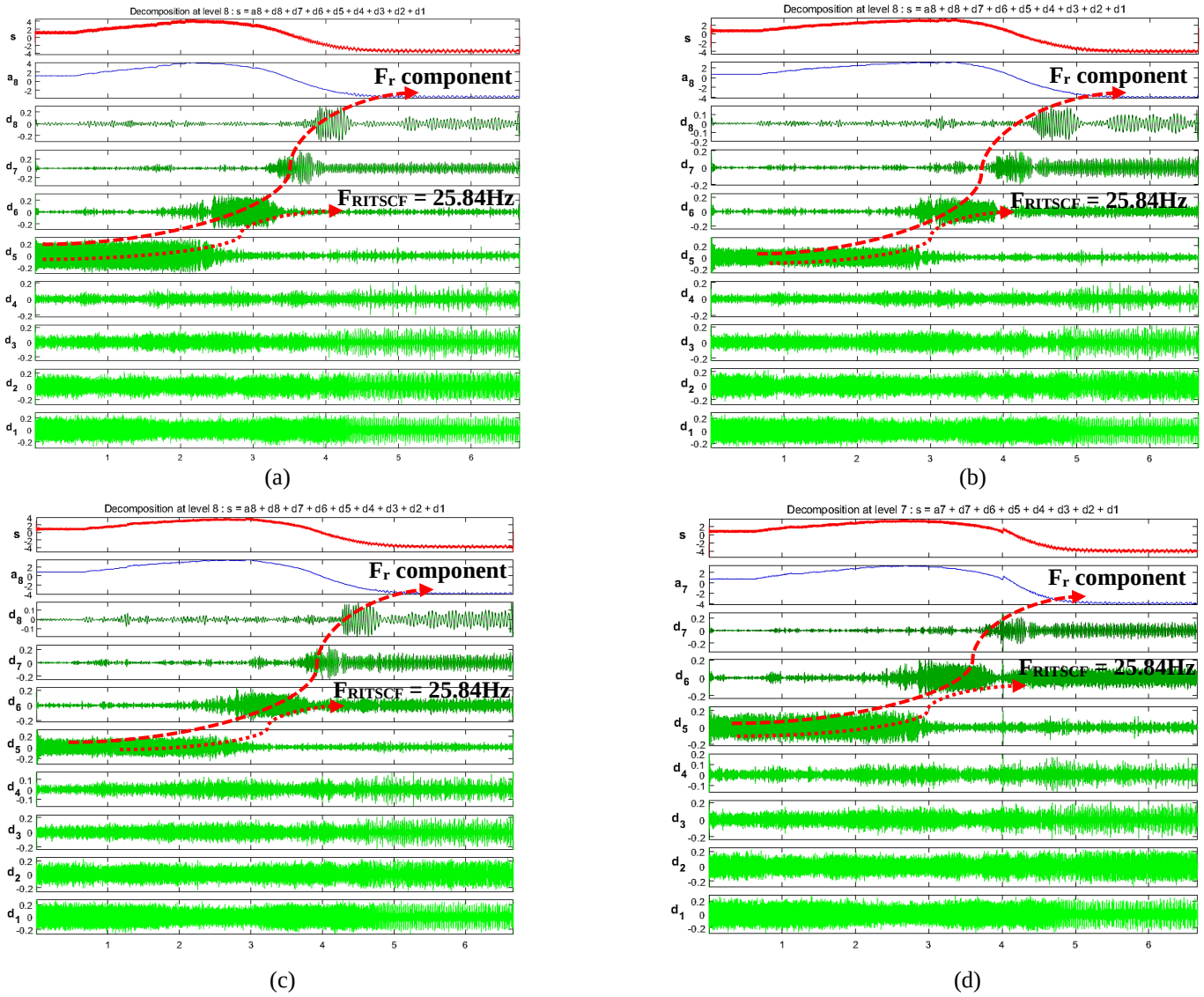

Figure 6. 35: Start-up rotor current and DWT of the Hilbert modulus of the signal for a machine with a rotor ITSCF at a severity level of; (a) 2%, (b) 4%, (c) 6%, and (d) 8%

Figure. 6.36 illustrates the change in the energy of the *d6* frequency band where the stator inter-turn fault indicator (25.33Hz) settles when the machine reaches its steady state.

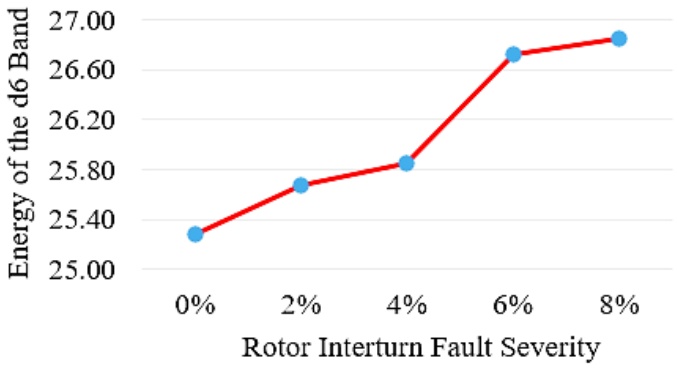

Figure 6. 36: The energy concentrated in detail band d6 of the rotor current at different rotor ITSCF severities

It is observed that the energy concentrated in *d6* at steady-state increases with the fault severity, due to the amplification of the fault indicator that is enveloped in this band.

It is evident from Fig. 6.33 and Fig. 6.35 that the decomposition of the rotor current signal reflects the evolution of the rotor ITSCF indicator much clearer than the decomposition of the stator current signal presented. Therefore, it is established that the rotor current signal is better suited for diagnosing the stator and rotor ITSCFs in the micromachine during the starting transient condition.

6.2.2.4 Diagnosis of the Static Eccentricity Fault at Start-Up

Figure 6.37 shows the resultant Hilbert modulus of the sampled stator & rotor current signals and the corresponding decomposition bands of a micromachine with a static eccentricity fault.

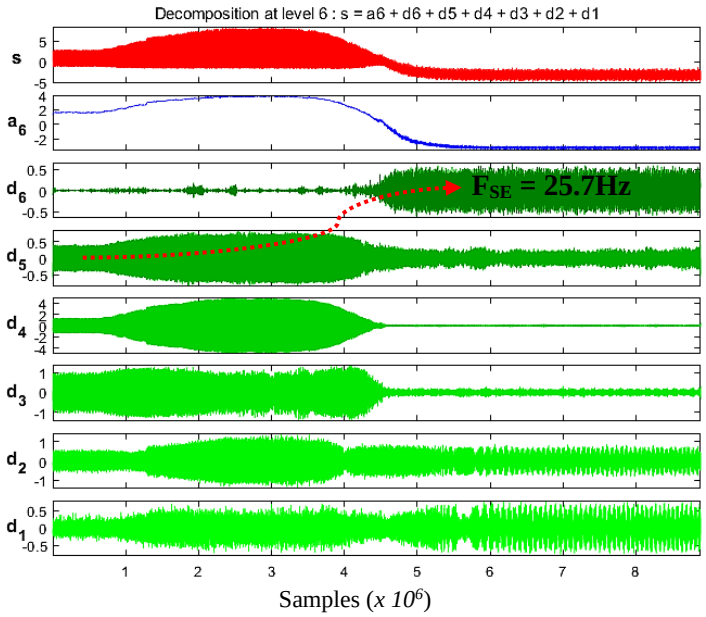

(a)

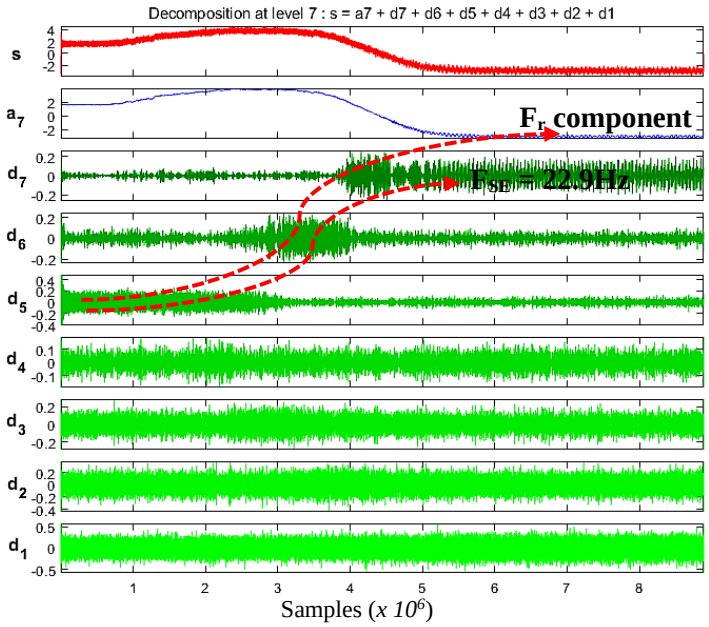

(b)

Figure 6. 37: Start-up (a) stator and (b) rotor currents, and the DWT of the resultant Hilbert Modulus of the sampled signals for a machine with a Static Eccentricity Fault

Fundamentally, during the starting transient, as the slip decreases from $s = 1$ to almost zero (when the machine reaches the steady-state condition), two components associated with an eccentricity fault are expected to evolve in the DWT of the stator current. The first component starts equal to 50Hz and decreases, reaching almost $f_s/2$ (25Hz) when the steady-state is reached. Whereas the second component starts off being equal to f_s and increases towards $3f_s/2$ when the steady-state is reached. From Fig. 6.37 (a), the evolution of the first fault component is observed to start in *d5* and settles in *d6* at 25.7Hz. However, the evolution of the second fault component is not observed. Nonetheless, the 25.7Hz component is sufficient to indicate the presence of an eccentricity fault in the machine. It is noted that the static eccentricity fault indicator stands out more in the stator current spectrum compared to the indicator in the rotor current spectrum.

6.2.3 Identification of Fault-related Frequency Components in Spectrogram Plots of the Rotor Current Signal

Since it has been established from the MCSA and DWT analyses that have been conducted earlier that the rotor current signal is better suited for diagnosing the stator and rotor ITSCFs, the spectrogram plots presented in this section are those of the rotor currents only. This is done for a machine in a healthy state condition and when it is subjected to the stator inter-turn and rotor inter-turn fault conditions.

Figure 6.38 presents the spectrogram plot of the rotor current for a machine in a healthy state, and when subjected to the stator and rotor inter-turn faults at a severity level of 8%.

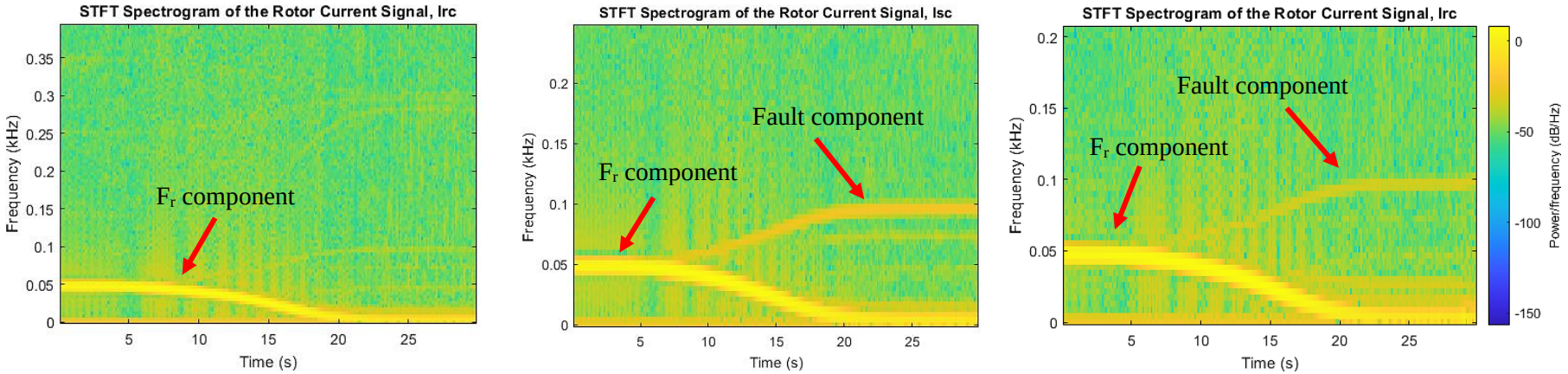

(a) (b) (c)

Figure 6. 38: Spectrogram Plot of the rotor current for the micromachine in different states: (a) in a healthy state condition, (b) with an 8% Stator ITSCF, (c) with an 8% rotor ITSCF

The evolution of the F_r component is observed in all spectrogram plots and the fault components are observed in Fig. 6.38 (b) and (c), when the machine is subjected to the stator inter-turn and rotor inter-turn faults, respectively. It is observed from Fig. 6.38 that the fault indicators evolve in a characteristic way, which is in the opposite direction of the f_r component. Therefore, observing this trend can be used to diagnose the presence of a fault in the machine. It would be possible to make use of the gradient of the positive slope of this pattern or use the y-axis to identify the value of the frequency. Furthermore, observing how recognizable/distinct the pattern becomes could be used to validate an increase in the fault severity as this corresponds to the intensification of the fault-related harmonics

6.3 Chapter Summary

This chapter focused on the analysis of the stator and rotor current signals to detect the stator inter-turn, rotor inter-turn, and the static eccentricity fault conditions in a 5kW micro-WRIM operating in the motoring mode, i.e., in the absence of the power electronic converter system, which is a fundamental approach that has not been explored in literature. The analysis was done under both steady-state and transient operating conditions. The experimental tests were performed on the micro-WRIM under four scenarios: in a healthy state; with a 2% and 4% stator inter-turn fault; with a 2%, 4%, 6%, and 8% rotor inter-turn fault, and with a static eccentricity fault. Different loading conditions have been considered for each scenario under the steady-state condition: no load (*slip* = 0.027, I_s = 16A); half load (*slip* = 0.076, I_s = 18A) and full load (*slip* = 0.106, I_s = 20A). It is worth noting that the 8% interturn fault severity level could not be emulated in the laboratory experiments during the direct on-line starting of the micro-WRIM (for MCSA analysis) because it resulted in very high short-circuit currents in addition to the high inrush currents. However, it was possible to emulate this severity level under the variable speed experiment, i.e., when the WRIM was soft-started WRIM (for DWT analysis) because the inrush and short circuit currents did not shoot up at start-up.

The classical MCSA technique has been used to detect the dominant fault-related harmonic frequency components associated with different faults on a WRIM during the steady-state operating condition. Tables 6.10, 6.17 and 6.21 summarized the dominant fault-related indicators which were identified in the spectral plots of the stator and rotor current signals for a micromachine subjected to the stator inter-turn, rotor inter-turn and the SE faults, respectively, under the different loading conditions.

A distinct novel exercise of this analytical study was to compare the use of the stator and rotor current signals to identify which current signal is best suited for diagnosing the faults in the micro-WRIM in isolation of the converter. This has been done by identifying the dominant fault frequency components in the rotor and stator current signals and observing which dominant fault indicator has significantly been influenced, in magnitude (dB), by the occurrence of the fault, or by the increase of the fault severity level. In this regard, the following conclusions are drawn:

- ***Stator inter-turn fault***: the stator inter-turn fault indicators in the rotor current spectrum, i.e., 98.5Hz (*at no load*), 96.2Hz (*at half load*), and 95.3Hz (*at full load*), corresponding to *k = 1*, were more sensitive to the changes in the severity of the stator inter-turn fault compared to the fault indicators in the stator current spectrum, for the loading conditions considered. Therefore, the rotor current signal has been identified to be better suited for diagnosing the stator ITSCFs in steady state, compared to using the stator current signal.

- ***Rotor inter-turn fault***: the sensitivity of the rotor inter-turn fault indicators in the rotor current spectrum, i.e., 25.33Hz (*at no load*), 26.9Hz (*at half load*), and 27.2Hz (*at full load*) is slightly above that on the indicators in the stator current spectrum. This has been demonstrated by the slightly higher change in the magnitudes of the indicators in the rotor current spectrum, compared to those in the stator current spectrum, as the fault severity is increased. Likewise, the rotor current signal proves to be better suited for diagnosing the rotor ITSCFs, compared to using the stator current signal.
- ***Static Eccentricity fault***: The same trend has been observed for the static eccentricity fault condition, i.e., a larger change in the magnitudes of the indicators in the rotor current spectrum, compared to those in the stator current spectrum, especially under the medium and full load conditions.

For the transient operating condition, the Hilbert Huang Transform (HHT) and Discrete Wavelet Transform (DWT) analysis techniques have been used to analyze the stator and rotor current signals to monitor the evolution of the identified dominant fault-related frequency components during the transient (*starting*) operating condition. The analysis results presented earlier, regarding the starting transient, have illustrated that the identified dominant fault indicators, under the no-load condition, evolved within the decomposition bands and settled at the frequency values given in Tables 6.10, 6.17 and 6.21, as expected. This has proven the effectiveness of using the HHT and the DWT analysis techniques to diagnose the stator inter-turn, rotor inter-turn, and the SE faults using the start-up stator and rotor current signals.

A quantitative analysis has been conducted to evaluate the changes in the wavelet energy of the frequency/decomposition bands of interest, i.e., the band that envelops the fault indicator at a steady state. It was observed that as the stator inter-turn faulty severity increased, the energy concentrated in the *d3* band of the stator current and the *d4* band of the rotor current increased accordingly. This is due to the amplification of the stator inter-turn fault indicators that are enveloped in these bands when the machine reaches its steady-state condition. For the rotor inter-turn fault condition, it was observed that the energy concentrated in the *d4* band of the stator current and the *d6* band of the rotor current increased as the fault severity was increased. Lastly, the spectrogram plots of the rotor current signal were presented and the evolution of the fault indicator(s) during the starting transient was illustrated.

In summary, the highlight of this chapter lies in the exercise of assessing the micro-WRIM in isolation of the converter system to diagnose the inter-turn winding and the eccentricity faults. This analysis constituted a fundamental approach to fault-feature extraction and fault diagnosis, which has not been explored in the literature, thus giving this study an edge in the body of knowledge.

In this regard, the approach enabled the fault signatures to be characterized independent of the harmonics which result from the switching mechanism of the converter switches thus ensuring clarity in the fault diagnosis process before moving on to complicated closed-loop controlled DFIGs. Therefore, the analysis presented in this chapter enabled the development of a systematic fault diagnosis approach that would be applied to a controlled DFIG, which will be the focal point of the next chapter, i.e., Chapter 7.

Chapter 7: Detection of the Inter-turn and Static Eccentricity Faults in the micro-WRIM in the presence of the Power Electronic Converter System

7.1 Introduction

This chapter focuses on the diagnosis of the stator inter-turn short circuit fault (ITSCF), rotor ITSCF and static eccentricity (SE) faults in the scaled-down WRIM in the presence of the power electronic (PE) converter system. Likewise, two analysis techniques have been explored in this chapter to analyze the stator current, rotor current, and the DFIG controller signals during the steady-state and transient operating conditions. The steady-state signal analysis process is aimed at evaluating the fault diagnosis capability of the stator current and rotor current signals, and from the controller point of view, determining which DFIG controller signal is best suited for fault diagnosis in a closed-loop controlled DFIG. Whereas the transient signal analysis is aimed at monitoring the evolution of the fault-related frequency components during the speed-varying condition.

7.2 Results and Discussions: Fault Feature Extraction and Fault Diagnosis

The experimental tests have been conducted on the complete DFIG-based WECS under four scenarios, with the WRIM fully synchronized to the power utility grid:

5. ***Scenario 1***: micro-WRIM in a healthy state,
6. ***Scenario 2***: micro-WRIM with a 2%, 4% and 6% stator inter-turn fault.
7. ***Scenario 3***: micro-WRIM with a 2%, 4% and 6% rotor inter-turn fault.
8. ***Scenario 4***: micro-WRIM with a static eccentricity fault.

Different loading conditions have been considered for each scenario under the steady-state region. The loading condition, in this case, is classified based on the amount of active power that is delivered to the power utility grid.

1. ***High load and super-synchronous speed***: 4kW, 0VAR and operating at a speed of 1600rpm, i.e., a machine slip=-0.067
2. ***Medium load and sub-synchronous speed***: 2kW, 0VAR, and operating at a speed of 1374rpm, i.e., a machine slip = 0.087.
3. ***Low load and sub-synchronous speed***: 800W, 0VAR, and operating at a speed of 1230rpm, i.e., a machine slip = 0.17.

Until recently, the research studies on the detection of stator ITSCFs, and air gap eccentricities have mainly utilized the MCSA of the terminal stator current signal for diagnosis [3, 30] and made less use of the terminal rotor currents and the DFIG's direct and quadrature (*dq)* controller signals.

However, considering that a generator in a typical DFIG-based WECS is controlled through a closed-loop system, the diagnostic signatures in the terminal current signals can get suppressed to a certain extent in the process, which is worse for the rotor current signal [10]. These effects have been demonstrated in several research studies carried out on DFIGs, and inverter-fed squirrel cage induction machines [141, 142]. The high harmonic content originating from the switching mechanism of the rotor-side converter also diminishes the fault signatures in the terminal current signals, thereby making the fault diagnosis process more challenging [13, 142]. As such, the use of the DFIG controller signals to detect generator faults has been gaining momentum lately [9, 10]. Different controller signals have been utilized in several studies to detect stator winding inter-turn faults in conventional DFIGs in laboratory environments [9, 10, 119, 130]. However, it has been noted that the detection of the static eccentricity fault using the DFIG controller signals has not been thoroughly explored in the literature. Therefore, this chapter has not only focused on using the stator and rotor current signal for analysis, but also includes analyzing the DFIG controller signals to study and diagnose the stator inter-turn, rotor inter-turn, and the SE faults in micro-DFIG. The DFIG controller signals considered in this work are the rotor *dq* currents, rotor current error signals, and the rotor *dq* modulating voltages.

7.2.1 Motor Current Signature Analysis Technique

This section presents the spectral analysis of the stator current, rotor current, and the DFIG controller signals in steady-state to detect the stator ITSCF, rotor ITSCF, and SE faults implemented on the micro-DFIG, under different speed and power delivery conditions.

7.2.1.1 Computation of the Asymmetry-related Harmonic Frequency Components

This section focuses on determining the asymmetry-related frequency components that are expected to appear in the FFT spectral plots of the stator current, rotor current, and the DFIG controller signals when the 5kW micromachine is operating at different speed and loading conditions, i.e., feeding different amounts of active power into the grid.

7.2.1.1.1 High Load and Super-synchronous Speed Operating Condition

Under this operating condition, the micromachine is operated at a super-synchronous speed of 1600rpm (slip = -0.067), with a power demand of P_s = -4kW and Q_s = 0Var. For this scenario, the asymmetry-related frequency components calculated using (5.17) in the case of the stator current spectrum, using (5.16) in the case of the rotor current spectrum, and using (5.20) in the case of the DFIG controller signals are summarized in Table 7.1, for different values of *k* (harmonic order).

Table 7. 1: Frequency components in the spectrum of the stator current, rotor current, and DFIG controller signals of a micro-DFIG in the healthy state under the high load and super-synchronous speed of 1600rpm

	Stator current		***Rotor current***		***DFIG Controller Signals***		
k	***Asymmetry-related components [Hz]***		***Asymmetry-related components [Hz]***		***Asymmetry-related components [Hz]***		
	$f_{I_s}^{asy(+)}$	$f_{I_s}^{asy(-)}$	$f_{I_r}^{asy(+)}$	$f_{I_r}^{asy(-)}$	$f_C^{asy(-,+)}$	$f_C^{asy(-,-)}$	$f_C^{asy(+,+)}$
0	50.00	50.00	-3.33	3.33	100.00	0.00	100.00
1	76.67	23.33	96.67	103.33	73.33	-26.67	126.67
2	103.33	-3.33	196.67	203.33	46.67	-53.33	153.33
3	130.00	-30.00	296.67	303.33	20.00	-80.00	180.00
4	156.67	-56.67	396.67	403.33	-6.67	-106.67	206.67
5	183.33	-83.33	496.67	503.33	-33.33	-133.33	233.33
6	210.00	-110.00	596.67	603.33	-60.00	-160.00	260.00
7	236.67	-136.67	696.67	703.33	-86.67	-186.67	286.67
8	263.33	-163.33	796.67	803.33	-113.33	-213.33	313.33

7.2.1.1.2 Medium Load and Sub-synchronous Speed Operating Condition

Under this operating condition, the micromachine is operated at a sub-synchronous speed of 1374rpm (slip = 0.087), with a power demand of P_s = -2kW and Q_s = 0Var. Likewise, the computed frequency components for this scenario are summarized in Table 7.2, for different values of *k*.

Table 7. 2: Frequency components in the spectrum of the stator current, rotor current, and DFIG controller signals of a micro-DFIG in the healthy state under the medium load and sub-synchronous speed of 1374rpm

	Stator current		***Rotor current***		***DFIG Controller Signals***		
k	***Asymmetry-related components [Hz]***		***Asymmetry-related components [Hz]***		***Asymmetry-related components [Hz]***		
	$f_{I_s}^{asy(+)}$	$f_{I_s}^{asy(-)}$	$f_{I_r}^{asy(+)}$	$f_{I_r}^{asy(-)}$	$f_C^{asy(-,+)}$	$f_C^{asy(-,-)}$	$f_C^{asy(+,+)}$
0	50	50	4.2	-4.2	100	0	100
1	72.9	27.1	104.2	95.8	77.1	-22.9	122.9
2	95.8	4.2	204.2	195.8	54.2	-45.8	145.8
3	118.7	-18.7	304.2	295.8	31.3	-68.7	168.7
4	141.6	-41.6	404.2	395.8	8.4	-91.6	191.6
5	164.5	-64.5	504.2	495.8	-14.5	-114.5	214.5
6	187.4	-87.4	604.2	595.8	-37.4	-137.4	237.4
7	210.3	-110.3	704.2	695.8	-60.3	-160.3	260.3
8	233.2	-133.2	804.2	795.8	-83.2	-183.2	283.2

7.2.1.1.3 Low Load and Sub-synchronous Speed Operating Condition

Under this operating condition, the micromachine is operated at a sub-synchronous speed of 1230rpm (slip = 0.17), with a power demand of P_s = -800W and Q_s = 0Var. The computed frequency components for this scenario are summarized in Table 7.3, for different values of *k*.

Table 7. 3: Frequency components in the spectrum of the stator current, rotor current, and DFIG controller signals of a micromachine in the healthy state under the low load and sub-synchronous speed of 1230 rpm

	Stator current		***Rotor current***		***DFIG Controller Signals***		
k	***Asymmetry-related components [Hz]***		***Asymmetry-related components [Hz]***		***Asymmetry-related components [Hz]***		
	$f_{I_s}^{asy(+)}$	$f_{I_s}^{asy(-)}$	$f_{I_r}^{asy(+)}$	$f_{I_r}^{asy(-)}$	$f_C^{asy(-,+)}$	$f_C^{asy(-,-)}$	$f_C^{asy(+,+)}$
0	50	50	9	-9	100	0	100
1	70.5	29.5	109	91	79.5	-20.5	120.5
2	91	9	209	191	59	-41	141
3	111.5	-11.5	309	291	38.5	-61.5	161.5
4	132	-32	409	391	18	-82	182
5	152.5	-52.5	509	491	-2.5	-102.5	202.5
6	173	-73	609	591	-23	-123	223
7	193.5	-93.5	709	691	-43.5	-143.5	243.5
8	214	-114	809	791	-64	-164	264

7.2.1.2 Diagnosis of Stator Inter-turn Short-Circuit Faults in the micro-DFIG

This section presents the spectral analysis of the stator current, rotor current, and the DFIG controller signals of a 5kW micro-DFIG subjected to the stator inter-turn short circuit fault (ITSCF) condition at different severity levels while delivering different amounts of power to the grid. In this investigation, the different Stator ITSCF severities considered are the 2%, 4%, and 6%, corresponding to 2, 3, and 5 shorted turns/phase, respectively. These short circuits have been implemented in phase B of the stator.

7.2.1.2.1 High Load and Super-Synchronous Speed Operating Condition

The spectral analysis of the stator and rotor current signals captured at a steady-state has been conducted and the spectral plots are presented in Fig. 7.1 (a), and (b), respectively. The spectral plots presented are those of the healthy state *vs* 6% stator ITSCF only. The peaks of the fundamental frequency, the time and space harmonics, and the fault-related frequency components presented in Table 7.1 are observed in the spectral plots.

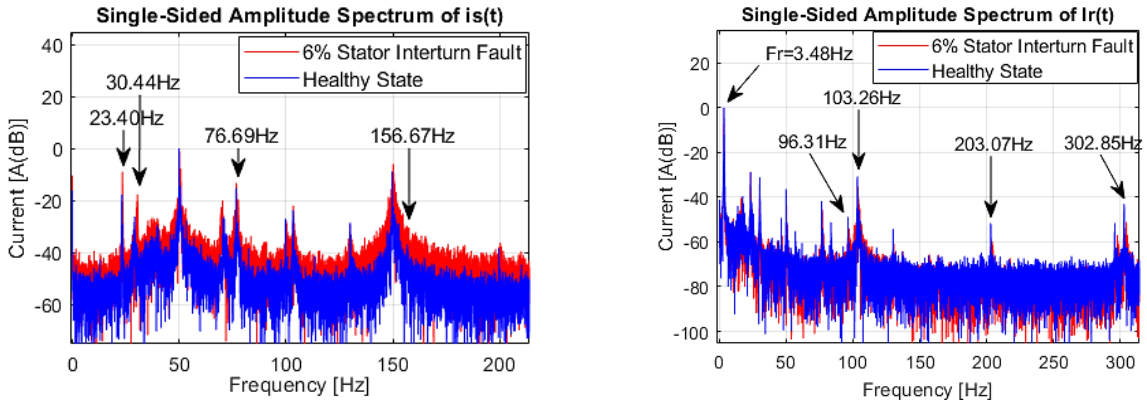

(a) (b)

Figure 7. 1: MCSA of the current signals for a micromachine with a stator ITSCF, at *high load*; (a) stator, (b) rotor

From Fig. 7.1, an increase in the amplitude of some spectral components is observed when the stator inter-turn fault occurred; this is particularly seen in Fig. 7.1*(a)*, i.e., the stator current spectrum. A summary of the changes in the magnitudes of the dominant harmonic frequency components as the stator inter-turn fault severity increases is provided in Fig. 7.2 (a), and (b), for the stator and rotor current signals, respectively.

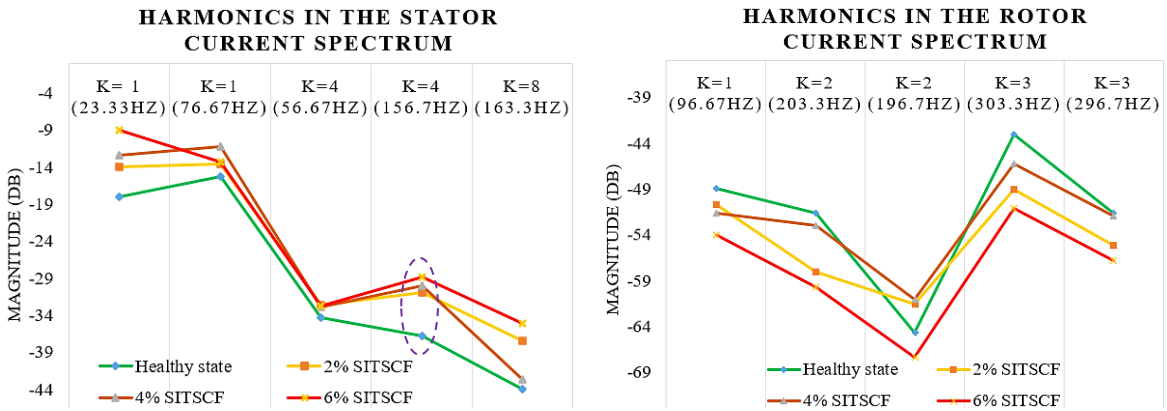

(a) (b)

Figure 7. 2: Summary of the dominant stator inter-turn fault-related harmonics in the (a) stator and (b) rotor current spectral plots for a micromachine at *high load*

From Fig. 7.2 (a), it is observed that increasing the stator ITSCF severity results in a consistent increase in the amplitudes of the 23.33Hz and 156.7Hz components, whereby the 156.67Hz (*k=4)* increased the most with 8.01dB, (22% increase). However, unlike in the stator current spectrum, there is no consistent increase observed in the amplitudes of the fault-related harmonic components that are in the rotor current spectrum, as shown in Fig. 7. 2(b). This can be attributed to the masking effect of the closed-loop control of the DFIG and the switching mechanism of the electronic converter that is in the rotor circuit, which suppresses the fault-related harmonics thus making them undetectable.

Therefore, as mentioned earlier, it is worth exploring the use of the DFIG controller signals to detect the stator inter-turn fault that is implemented on the micromachine. In this regard, Fig. 7. 3 presents the spectral plots of the rotor *dq* currents (*a & b*), the rotor current error signals (*c & d*), and the rotor *dq* modulating voltage signals (*e & f*), showing the possible frequency components that emerge due to the stator ITSCF.

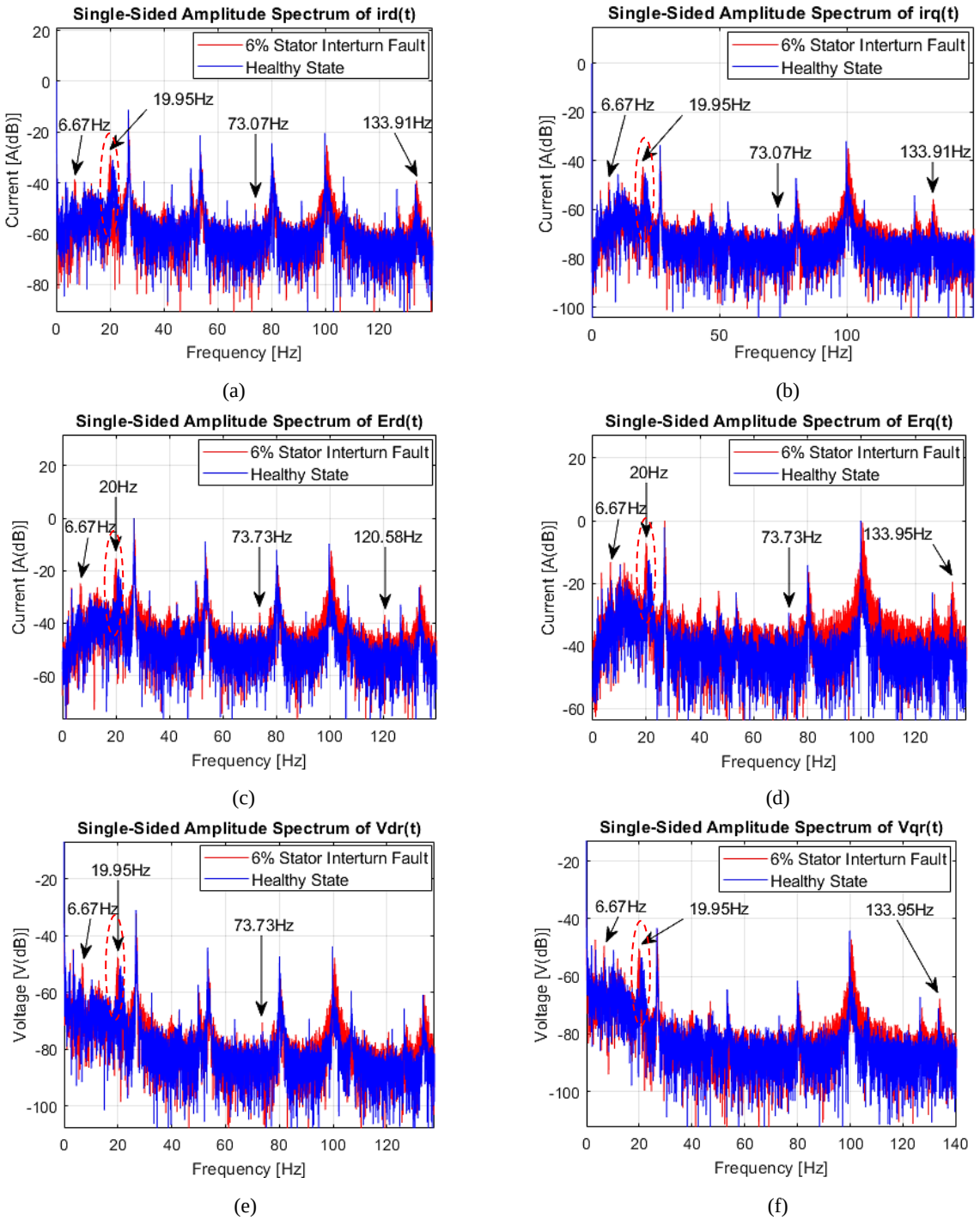

Figure 7. 3: MCSA of the DFIG controller signals for a micromachine with a Stator ITSCF, at *high load*; (a) & (b) rotor *dq* currents, (c) & (d) rotor current error signals, (e) & (f) rotor *dq* modulating voltage signals

From *Fig. 7.3(a)-(f)*, the amplitudes of some frequency components increased when the stator inter-turn fault occurred. To evaluate the fault detection potential of the individual fault indicators that are in the DFIG controller signals, a sensitivity study has been conducted to examine the percentage increase in the amplitudes of the fault-related harmonic components when a fault occurs. As a result, the fault-related frequency component which consistently portrays a good fault detection potential in all controller signals is identified.

Additionally, conclusions can be drawn as to which controller signal gets significantly impacted by the occurrence of a fault. In this investigation, the sensitivity study is realized by adopting a technique that was previously used by Sarma *et al* in [9, 10], which is based on determining a sensitivity index using (7.1):

$$Sensitivity\ [\%] = \frac{M_{Faulty} - M_{Healthy}}{M_{Healthy}} \times 100 \qquad (7.1)$$

Where, M_{Faulty} and $M_{Healthy}$ are the magnitudes of a specific fault-related frequency component in the spectrum of a faulty and a healthy machine, respectively.

Figure. 7.4 illustrates the sensitivity analysis results of the fault-related components in the DFIG controller signals when the stator ITSCF occurs at a 6% fault severity level.

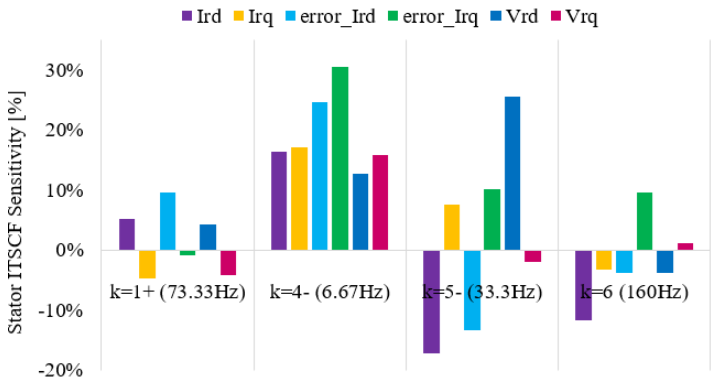

Figure 7. 4: Sensitivity study results of the Stator ITSCF-related frequency components in the DFIG controller signals, for a micromachine at *high load*

It is observed from Fig. 7.4 that the substantial increase occurs in the 6.67Hz component *(i.e., the $2sf_s$, k=4)* for all the DFIG controller signals considered. Table 7.4 presents the numerical percentage increase in the amplitude of the dominant fault index (i.e., 6.67Hz) in the respective DFIG controller signals when a 6% stator inter-turn fault occurs.

Table 7. 4: Percentage increase in the amplitude of the dominant stator ITSCF indicator in the respective DFIG controller signals, for a micromachine at *high load*

DFIG Controller Signal	***Percentage Increase in Magnitude***
Rotor d-axis current, I_{rd}	17%
Rotor q-axis current, I_{rq}	17%
D-axis rotor current error signal, *error_* I_{rd}	25%
Q-axis rotor current error signal, *error_* I_{rq}	31%
Rotor d-axis modulating voltage, V_{rd}	13%
Rotor q-axis modulating voltage, V_{rq}	16%

Therefore, from Table 7.4, it is observed that the stator inter-turn fault has a significant impact on the amplitude of the 6.67Hz (*k=4-), i.e., the $2sf_s$* component that is in the *error_*I_{rq} signal, which increased with 31%. Second to this, is the *k=4-* component that is in the *error_*I_{rd} signal, a 25% increase, compared to the other DFIG controller signals.

7.2.1.2.2 Medium Load and Sub-synchronous Speed Operating Condition

Like in the scenario presented earlier, the spectral analysis of the stator and rotor current signals has been carried out and the spectral plots are presented in Fig. 7.5 (a) and (b), respectively, for the healthy state (*blue*) *vs* 6% stator ITSCF (*red*).

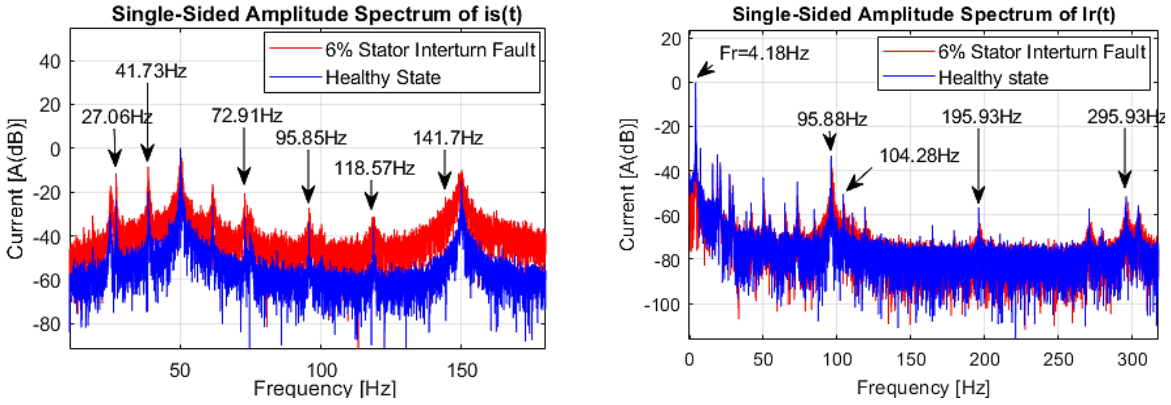

(a) (b)

Figure 7. 5: MCSA of the current signals for a micromachine with a stator ITSCF, at *medium load*; (a) stator, (b) rotor

From Fig. 7.5, the amplitudes of some frequency components increased when the stator inter-turn fault occurred, particularly in Fig. 7.5(a). Figures 7.6 (a) and (b) summarize the changes in the magnitudes of the dominant harmonic components in the stator current and rotor current spectral plots, respectively, as the stator inter-turn fault severity level is increased.

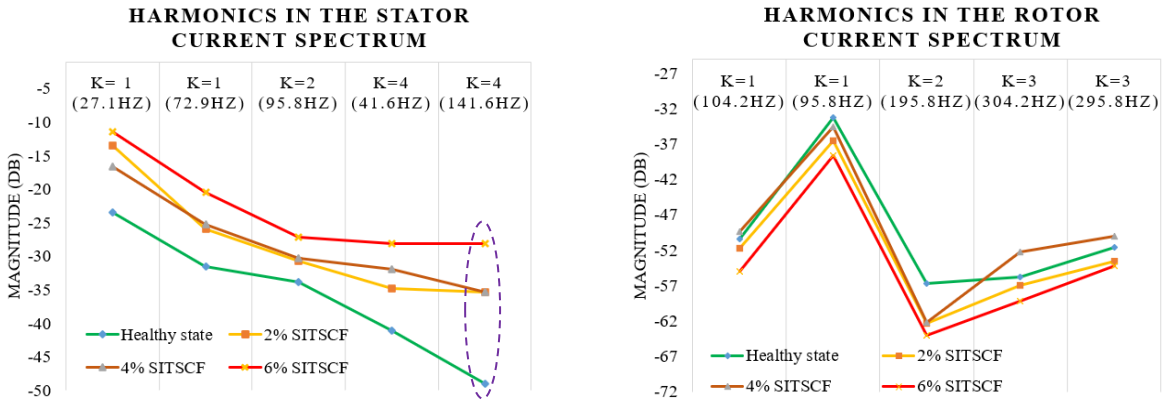

(a) (b)

Figure 7. 6: Summary of the dominant stator inter-turn fault-related harmonics in the (a) stator and (b) rotor current spectral plots for a micromachine at *medium load*

From Fig. 7.6 (a), it is observed that increasing the stator ITSCF severity results in a consistent increase in the amplitudes of the 27.1, 41.6, and 141.6Hz components, whereby the 141.6Hz (*k=4)*, component, increased the most with 20.87dB, (43%increase). However, there is no consistent amplitude increase observed in any of the fault-related harmonic components that are in the rotor current spectrum. This can be attributed to the masking effect of the closed-loop control of the DFIG and the switching mechanism of the electronic converter that is in the rotor circuit.

Hence, the MCSA of the DFIG controller signals has been carried out to detect the stator inter-turn fault implemented on the micromachine under this scenario. Fig. 7.7 presents the spectral plots of the rotor *dq* currents (*a* & *b*), the rotor *dq* current error signals (*c* & *d*) and the rotor *dq* modulating voltage signals (*e* & *f*).

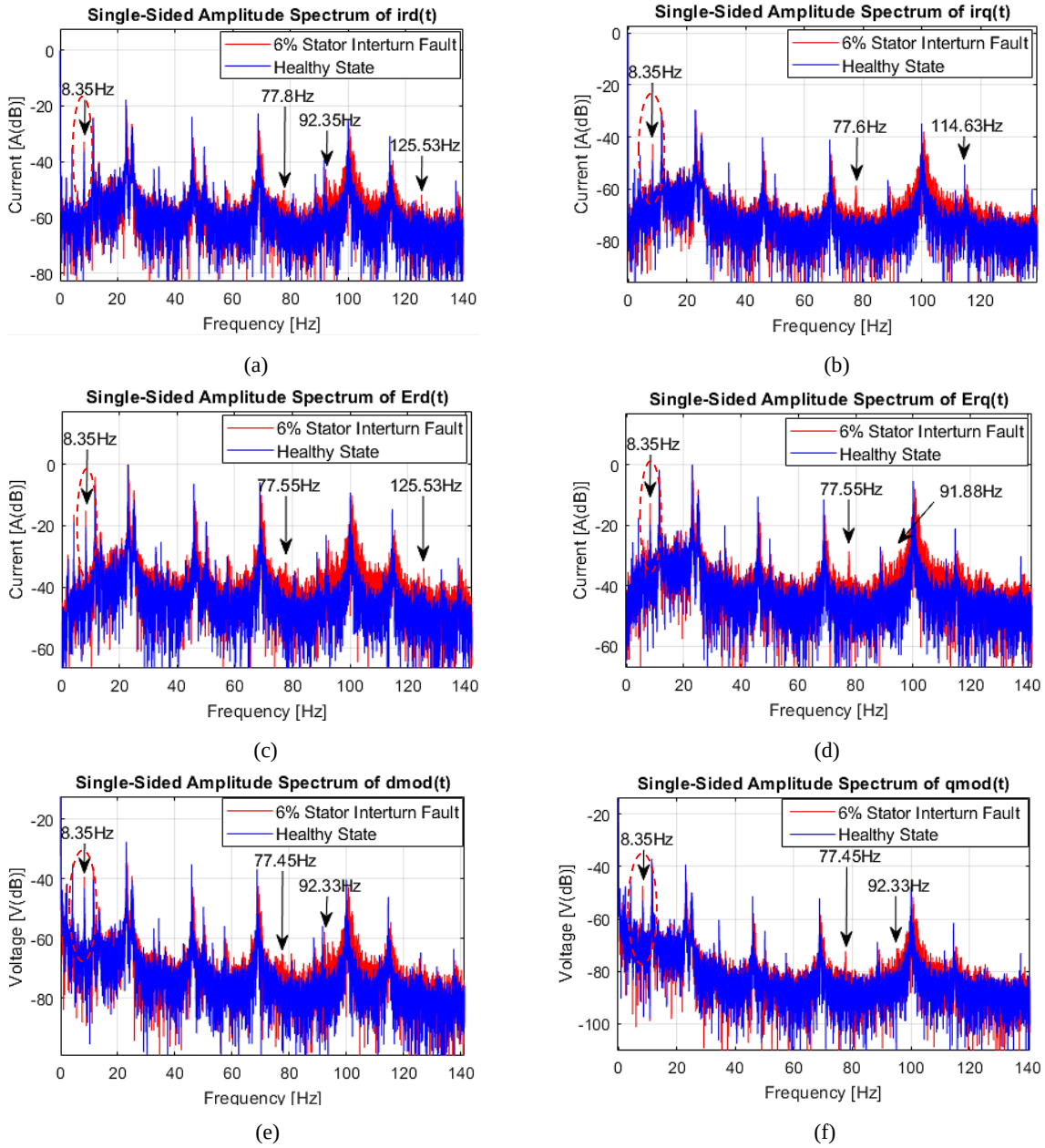

Figure 7. 7: MCSA of the DFIG controller signals for a micro-DFIG with a Stator ITSCF, at *medium load*; (a) & (b) rotor *dq* currents, (c) & (d) rotor current error signals, (e) & (f) rotor *dq* modulating voltage signals

From *Fig. 7.7(a)-(f)*, the amplitudes of some frequency components increased when the stator inter-turn fault occurred. Likewise, a sensitivity study has been conducted to compare the stator inter-turn fault detection potential of the different fault indicators that are in the spectrum plots of the DFIG controller signals when the fault occurs at a 6% fault severity level. Fig. 7.8 illustrates the sensitivity analysis results.

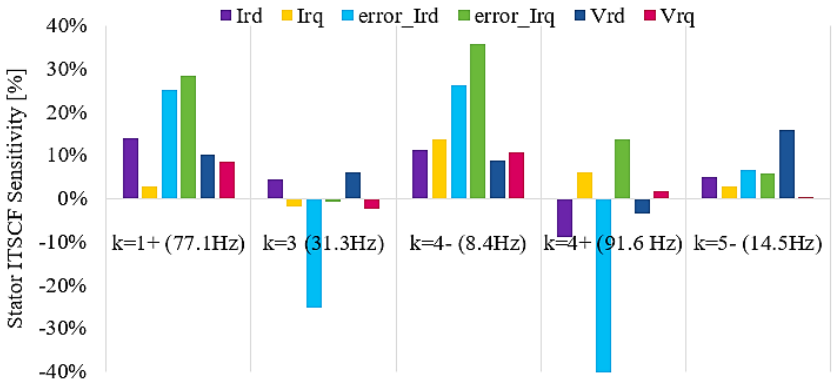

Figure 7. 8: Sensitivity study results of the Stator ITSCF-related frequency components in the DFIG controller signals, for a micromachine at *medium load*

It is observed from Fig. 7.8 that a significant increase occurs in the 8.4Hz component *(i.e., the 2sf$_s$, k=4)* for all the DFIG controller signals considered. This index is equivalent to what was observed in the first scenario, i.e., these indices both correspond to *k=4* (*the 2sf$_s$ components).* Quantitatively, Table 7. 5 presents the percentage increase in the amplitude of the dominant fault index (i.e., 8.4Hz) in the respective DFIG controller signals when a 6% stator inter-turn fault occurs.

Table 7. 5. Percentage increase in the amplitude of the dominant stator ITSCF indicator in the respective DFIG controller signals, for a micromachine at *medium load*

DFIG Controller Signal	***Percentage Increase in Magnitude***
Rotor d-axis current, I_{rd}	11%
Rotor q-axis current, I_{rq}	14%
D-axis rotor current error signal, *error_* I_{rd}	26%
Q-axis rotor current error signal, *error_* I_{rq}	36%
Rotor d-axis modulating voltage, V_{rd}	9%
Rotor q-axis modulating voltage, V_{rq}	11%

Therefore, from Table 7.5, it is observed that the stator inter-turn fault has a significant impact on the amplitude of the *k=4-, i.e., the 2sf$_s$* component that is in the *error_*I_{rq} signal, which increased by 36%. Second to this, is the *k=4-* component that is in the *error_*I_{rd} signal, compared to the other DFIG controller signals. It is worth noting that this is the same observation seen in the first scenario.

7.2.1.2.3 Low Load and Sub-synchronous Speed Operating Condition

The spectral analysis of the stator and rotor current signals under this scenario has been conducted and the spectral plots are presented in Fig. 7.9 (a) and (b), respectively, for the healthy state (*blue*) *vs* 6% stator ITSCF (*red*).

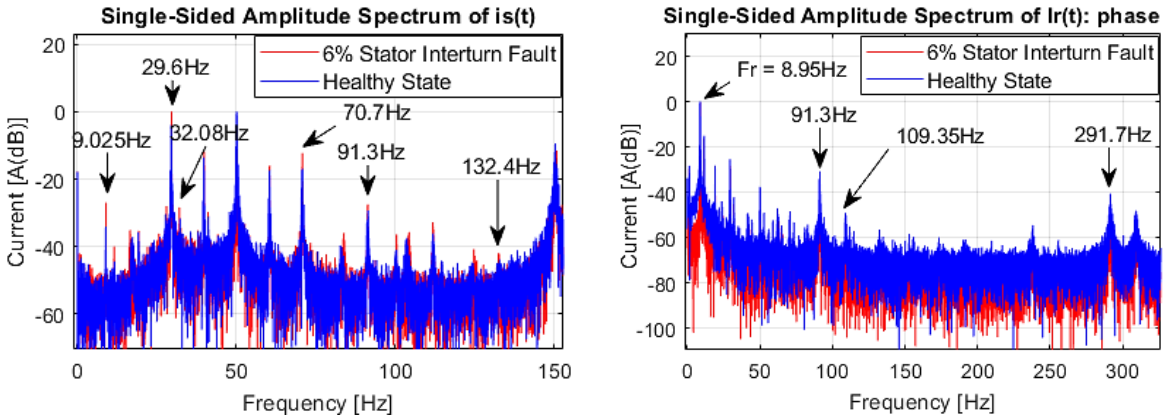

(a) (b)

Figure 7. 9: MCSA of the current signals for a micromachine with a stator ITSCF, at *low load*; (a) stator, (b) rotor

The amplitudes of some spectral components increased particularly in Fig. 7.9 (a), in comparison with the healthy case. Figures 7.10 (a) and (b) summarize the changes in the magnitudes of the dominant harmonic components in the stator current and rotor current spectral plots, respectively, as the stator inter-turn fault severity level is increased.

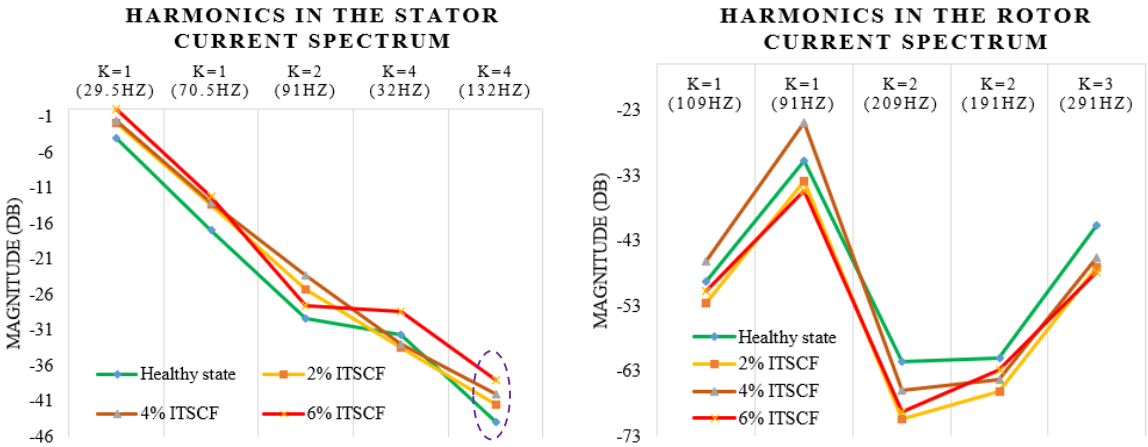

(a) (b)

Figure 7. 10: Summary of the dominant stator inter-turn fault-related harmonics in the (a) stator and (b) rotor current spectral plots for a micromachine at *low load*

From Fig. 7.10 (a), it is observed that increasing the stator ITSCF severity results in a consistent increase in the amplitudes of the 29.1, 70.5, and 132Hz components, whereby the 132Hz (*k=4)*, component, increased the most with 5.9dB, (13% increase). However, like in the two scenarios presented earlier, there is no consistent increase observed in the amplitude of the fault-related harmonic components that are in the rotor current spectrum presented in Fig. 7. 10(b).

The MCSA of the DFIG controller signals has been conducted and the spectral plots are presented in Fig. 7.11, for the rotor *dq* currents (*a* & *b*), the rotor current error signals (*c* & *d*), and the rotor *dq* modulating voltage signals (*e* & *f*).

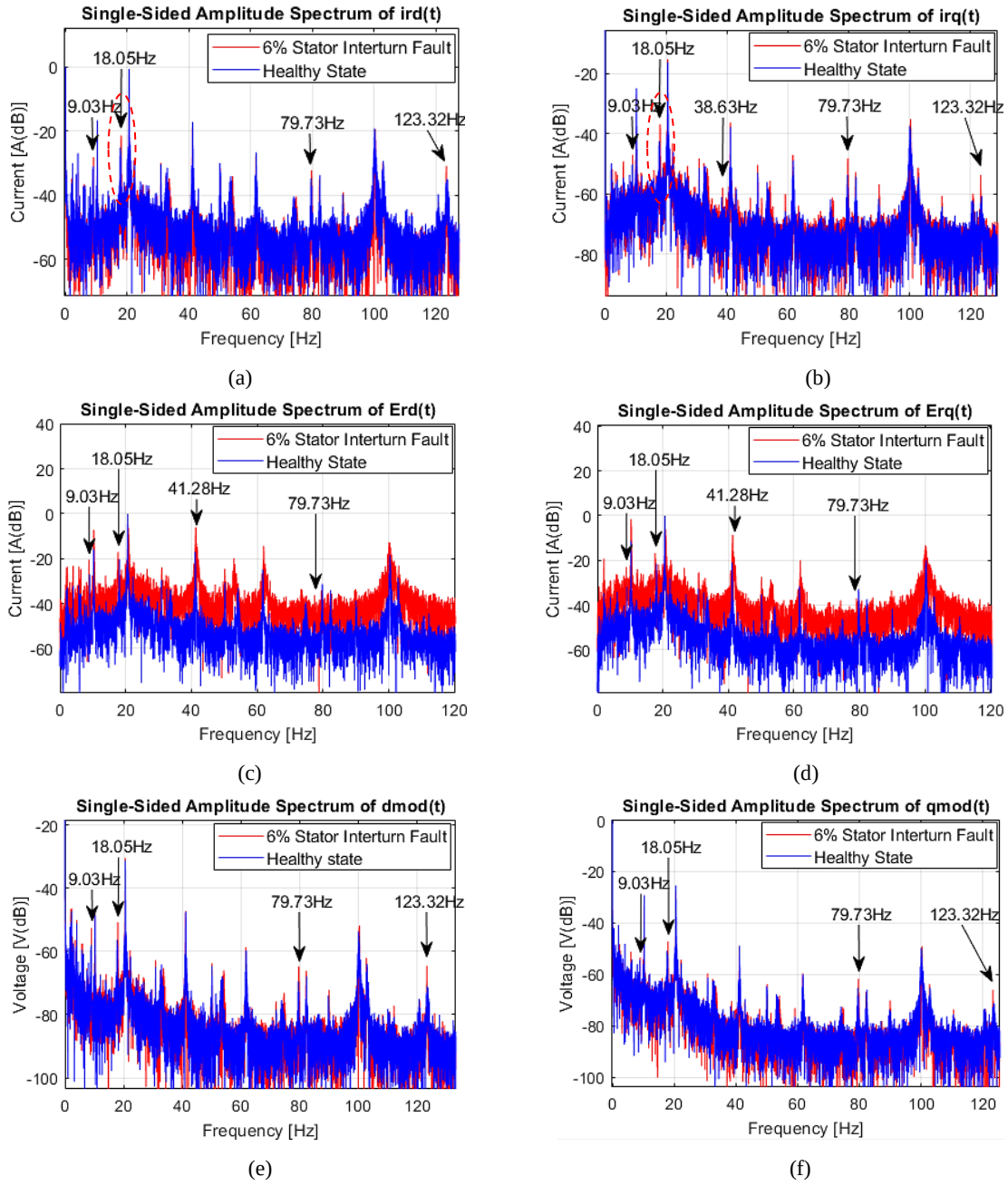

Figure 7. 11: MCSA of the DFIG controller signals for a micromachine with a Stator ITSCF, at *low load*; (a) & (b) rotor *dq* currents, (c) & (d) rotor current error signals, (e) & (f) rotor *dq* modulating voltage signals

From *Fig. 7.11(a)-(f)*, the amplitudes of some frequency components increased when the stator inter-turn fault occurred. Likewise, a sensitivity study has been conducted to compare the stator inter-turn fault detection potential of the different fault indicators that are in the spectrum plots of the DFIG controller signals when the fault occurs at a 6% severity level. Fig. 7.12 illustrates the sensitivity analysis results.

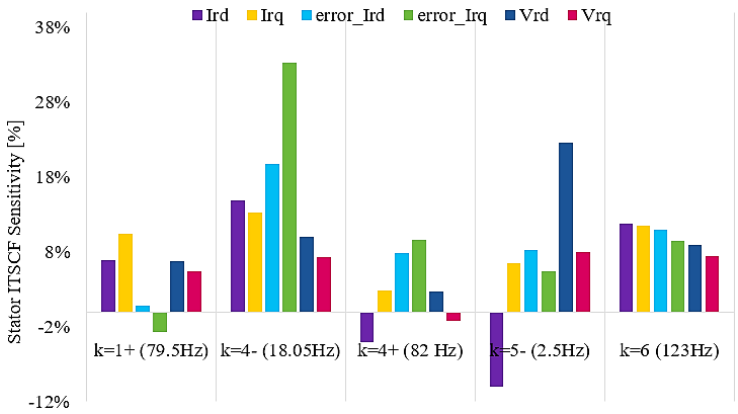

Figure 7. 12: Sensitivity study results of the Stator ITSCF-related frequency components in the DFIG controller signals, for a micromachine at *low load*

It is observed from Fig. 7.12 that a significant increase occurs in the 18.05Hz component *(i.e., the $2sf_s$, k=4)* for all the DFIG controller signals considered. This index is equivalent to what was observed in the scenarios presented earlier, i.e., these indices both correspond to *k=4* (*the $2sf_s$ components)*. Quantitatively, Table 7. 6 presents the percentage increase in the amplitude of the dominant fault index (i.e., the 18.05Hz) in the respective DFIG controller signals when a 6% stator inter-turn fault occurs.

Table 7. 6: Percentage increase in the amplitude of the dominant stator ITSCF indicator in the respective DFIG controller signals, for a micromachine at *low load*

DFIG Controller Signal	***Percentage Increase in Magnitude***
Rotor d-axis current, I_{rd}	15%
Rotor q-axis current, I_{rq}	13%
D-axis rotor current error signal, *error_* I_{rd}	20%
Q-axis rotor current error signal, *error_* I_{rq}	33%
Rotor d-axis modulating voltage, V_{rd}	10%
Rotor q-axis modulating voltage, V_{rq}	7%

Therefore, from Table 7.6, it is observed that the stator inter-turn fault has a significant impact on the amplitude of the *k=4-, i.e., the $2sf_s$* component that is in the *error_*I_{rq} signal, which increased by 33%. Second to this, is the *k=4-* component that is in the *error_*I_{rd} signal, compared to the other DFIG controller signals. It is worth noting that this is the same observation as the one in the two scenarios presented earlier.

7.2.1.2.4 Summary: Dominant Stator ITSCF Indicators in the Stator Current, Rotor Current, and the DFIG Controller Signals

Table 7.7 summarizes the main stator inter-turn fault indicators in the stator current, rotor current, and in the DFIG controller signals, for different amounts of power injected into the grid.

Table 7. 7: Dominant Stator ITSCF Indicators in the Stator Current, Rotor Current, and the DFIG Controller Signals for different operating conditions

Signals	**Power injected into the grid | shaft speeds**		
	P_s = -4kW, Q_s = 0Var, ω_r = 1600rpm	***P_s = -2kW, Q_s = 0Var, ω_r = 1374rpm***	***P_s = -800W, Q_s = 0Var, ω_r = 1230rpm***
Stator current I_s	156.67Hz ($k = 4_+$)	141.6Hz ($k = 4_+$)	132Hz ($k = 4_+$)
Rotor current I_r	none	none	none
I_{rd}	6.67Hz ($k = 4_-$)	8.35Hz ($k = 4_-$)	18.05Hz ($k = 4_-$)
I_{rq}	6.67Hz ($k = 4_-$)	8.35Hz ($k = 4_-$)	18.05Hz ($k = 4_-$)
E_{rd}	6.67Hz ($k = 4_-$)	8.35Hz ($k = 4_-$)	18.05Hz ($k = 4_-$)
E_{rq}	6.67Hz ($k = 4_-$)	8.35Hz ($k = 4_-$)	18.05Hz ($k = 4_-$)
V_{rd}	6.67Hz ($k = 4_-$)	8.35Hz ($k = 4_-$)	18.05Hz ($k = 4_-$)
V_{rq}	6.67Hz ($k = 4_-$)	8.35Hz ($k = 4_-$)	18.05Hz ($k = 4_-$)

From the analyses presented in this section, it has been determined that the $k=4_+$, i.e., the *(1+2s) fs* component in the stator current spectrum was significantly affected by the stator inter-turn fault, irrespective of the amount of power injected into the grid. Therefore, it had a sufficient amplitude and could effectively be used for fault diagnosis using the stator current signal. On the other hand, it has been observed that the rotor current signal is not adequate for diagnosing the stator inter-turn fault. From the controller point of view, the sensitivity study has illustrated that the $k=4_-$ component in the respective controller signals was the most sensitive to the stator ITSCF compared to other harmonic components. Specifically, it is noted that the stator inter-turn fault has a significant impact on the fault indices corresponding to $k=4_-$ in the *q-axis* of the rotor error signal (*error_I_{rq})* compared to other controller signals, and thus, this component serves as a good indicator of the stator ITSCF when using the DFIG controller signals.

7.2.1.3 Diagnosis of Rotor Inter-turn Short-Circuit Winding Faults in the micro-DFIG

This section presents the spectral analysis of the stator current, rotor current, and the DFIG controller signals of a micromachine subjected to a rotor inter-turn short circuit fault (ITSCF) condition at different severity levels while delivering different amounts of power to the grid. In this investigation, the rotor ITSCF severity levels considered are 2%, 4%, and 6%, corresponding to 6, 13, and 19 shorted turns/phase, respectively. These short circuits have been implemented in phase C of the rotor.

7.2.1.3.1 High Load and Super-synchronous Speed Operating Condition

The MCSA of the stator and rotor current signals under this scenario has been conducted and the respective spectral plots are presented in Fig. 7. 13(a), and (b), respectively, for the healthy state *vs* 6% rotor ITSCF.

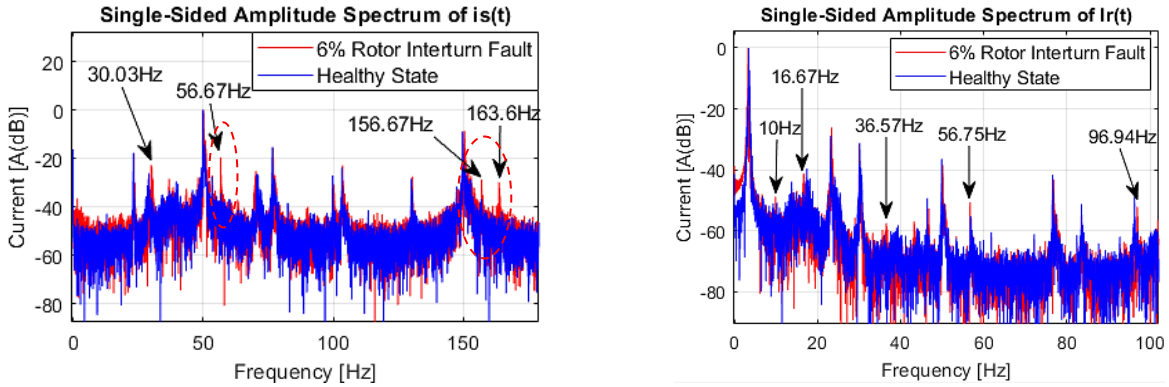

(a) (b)

Figure 7. 13: MCSA of the current signals for a micromachine with a rotor ITSCF, at *high load*; (a) stator, (b) rotor

From Fig. 7.13, the amplitudes of some frequency components increased when the rotor inter-turn fault occurred. A summary of the changes in the magnitudes of the dominant harmonic components as the rotor inter-turn fault severity increases is provided in Fig. 7. 14 (a), and (b), for the stator and rotor current signals, respectively.

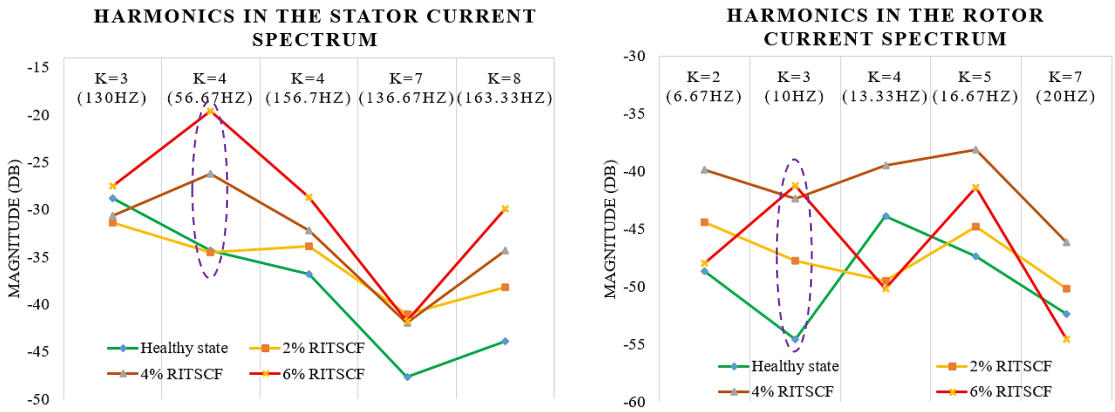

(a) (b)

Figure 7. 14: Summary of the dominant Rotor ITSCF fault-related harmonics in the (a) stator and (b) rotor current spectral plots for a micromachine at *high load*

From Fig. 7.14 (a), it is observed that, increasing the rotor ITSCF severity results in a consistent increase in the amplitudes of the 56.67, 156.67, and 163.6Hz components, whereby the 56.67Hz (*k=4), i.e.,* the *(1-2s) fs* component, increased the most with 14.71dB, (43% increase). In the case of the rotor current spectrum shown in Fig. 7. 14 (b), a consistent amplitude increase is observed in the 10Hz component (*k = 3)*, with a change of 13.38dB. This shows that these are good indicators of the rotor ITSCFs.

However, it is noted that the change in the amplitudes of the fault indicators in the stator current spectrum is more significant compared to those in the rotor current spectrum. This can be attributed to the diminishing effect of the closed-loop control of the DFIG and the switching of the electronic converter that is in the rotor circuit. This effect is more significant on the terminal rotor current signal compared to the terminal stator current signals.

Therefore, DFIG controller signals have been analyzed to detect the rotor ITSCF and investigate their capability in detecting the rotor inter-turn fault implemented on the micromachine in this experimental study. Fig. 7. 15 presents the spectral plots of the rotor *dq* currents (*a* & *b*), for the rotor current error signals (*c* & *d*) and the rotor *dq* modulating voltage signals (*e* & *f*), showing the possible frequency components that emerge due to the rotor ITSCF.

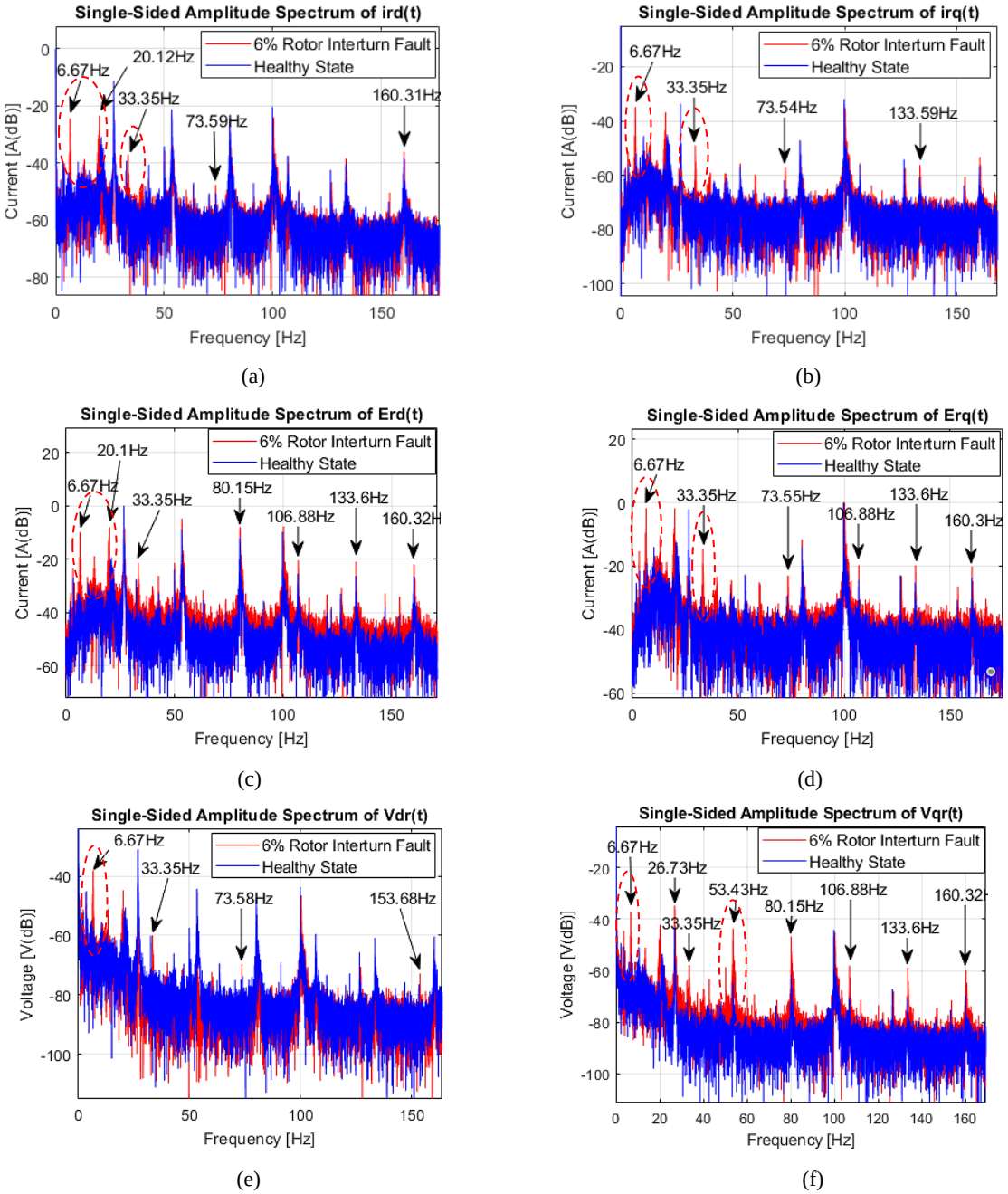

Figure 7. 15: MCSA of the DFIG controller signals for a micromachine with a Rotor ITSCF, at *high load*; (a) & (b) rotor *dq* currents, (c) & (d) rotor current error signals, (e) & (f) rotor *dq* modulating signals

An increase in the amplitude of some spectral components is observed in *Fig. 7.15(a)-(f)*, in comparison to the healthy case.

Likewise, a sensitivity study has been conducted to compare the rotor inter-turn fault detection potential of the different fault indicators that are in the spectrum plots of the DFIG controller signals when the fault occurs at a 6% severity level. Figure 7. 16 illustrates the sensitivity analysis results.

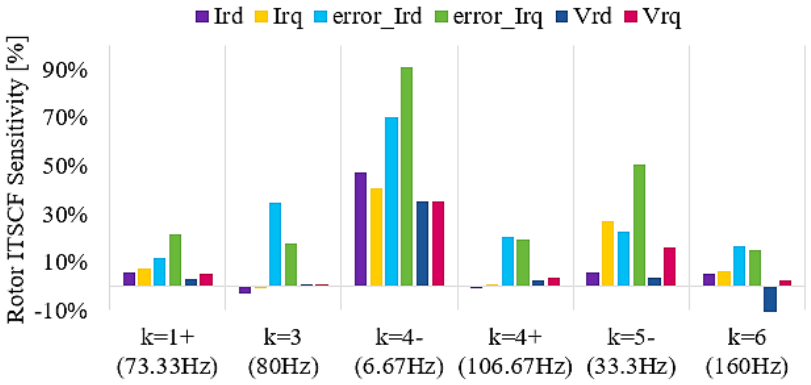

Figure 7. 16: Sensitivity study results of the Rotor ITSCF-related frequency components in the DFIG controller signals, for a micromachine at *high load*

It is observed from Fig. 7. 16 that a substantial increase occurs in the 6.67Hz component *(i.e., the $2sf_s$, k=4)* for all the DFIG controller signals. Table 7. 8 presents the percentage increase in the amplitude of the dominant fault index (i.e., 6.67Hz) in the respective DFIG controller signals when a 6% rotor inter-turn fault occurs.

Table 7. 8: Percentage increase in the amplitude of the dominant Rotor ITSCF indicator in the respective DFIG controller signals, for a micromachine at **high load**

DFIG Controller Signal	***Percentage Increase in Magnitude***
Rotor d-axis current, I_{rd}	47%
Rotor q-axis current, I_{rq}	41%
D-axis rotor current error signal, *error_* I_{rd}	70%
Q-axis rotor current error signal, *error_* I_{rq}	91%
Rotor d-axis modulating voltage, V_{rd}	35%
Rotor q-axis modulating voltage, V_{rq}	35%

Overall, it is observed that the rotor inter-turn fault has a significant impact on the amplitude of the *k=4., i.e., the $2sf_s$* component that is in the *error_*I_{rq} signal, with an increase of 91%, followed by the same fault component in the *error_*I_{rd} signal, compared to the other DFIG controller signals.

7.2.1.3.2 Medium Load and Sub-synchronous Speed Operating Condition

The spectral analysis of the stator and rotor current signals under this scenario has been conducted and the spectral plots are presented in Fig. 7.17 (a) and (b), respectively. The spectral plots presented are those of the healthy state *vs* 6% rotor ITSCF only.

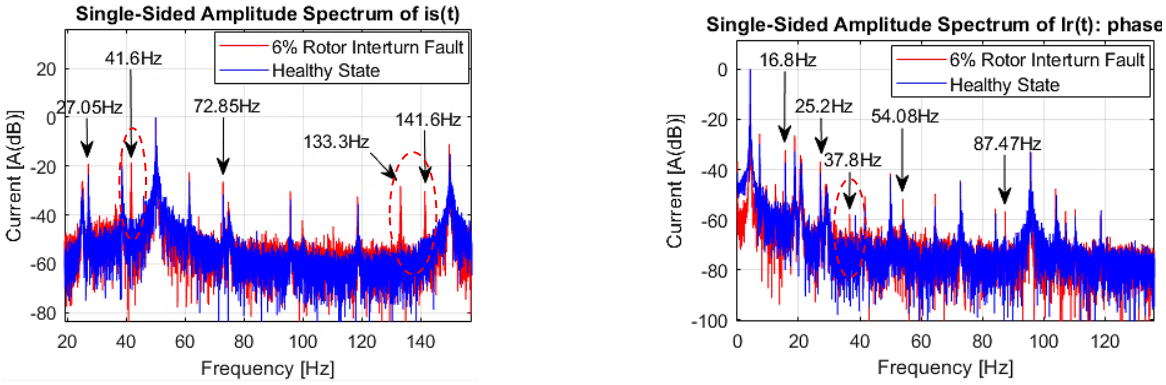

(a) (b)

Figure 7. 17: MCSA of the current signals for a micromachine with a Rotor ITSCF, at *medium load*; (a) stator, (b) rotor

A summary of the changes in the magnitudes of the dominant harmonic components as the rotor inter-turn fault severity increases is provided in Fig. 7.18 (a) and (b), for the stator and rotor current signals, respectively.

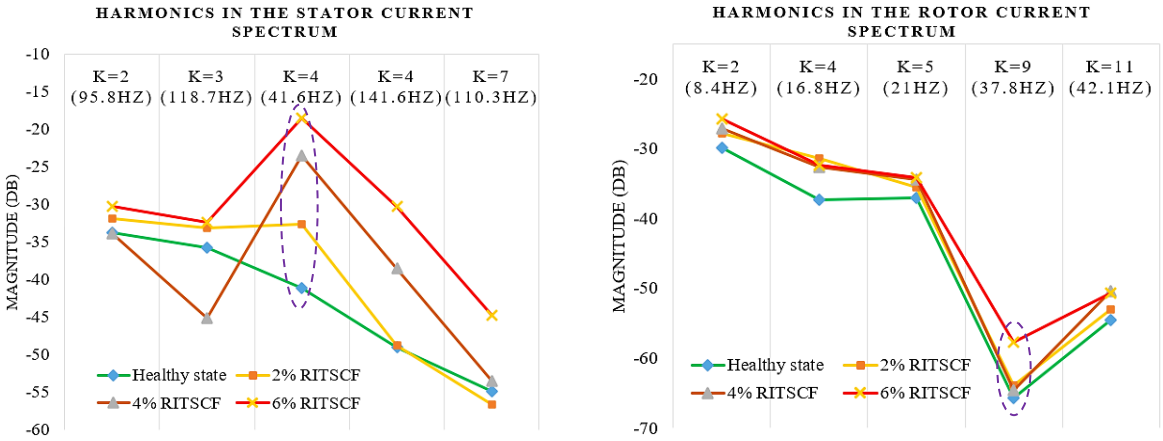

(a) (b)

Figure 7. 18: Summary of the dominant Rotor ITSCF fault-related harmonics in the (a) stator and (b) rotor current spectral plots for a micromachine at *medium load*

From Fig. 7. 18 (a), it is observed that, increasing the rotor ITSCF severity results in a consistent increase in the amplitudes of the 41.6, 141.6 & 110.3Hz components, whereby the 41.6Hz (*k=4)*, *i.e.*, the *(1-2s) fs* component, increased the most with 22.64dB, (55% increase). In the case of the rotor current spectrum shown in Fig. 7. 18 (b), a consistent amplitude increase is observed in the 37.8Hz component (*k = 9)*, with a change of 7.89dB. However, it is noted that the change in the amplitudes of the fault indicators in the stator current spectrum is more significant compared to those in the rotor current spectrum.

The MCSA of the DFIG controller signals has been conducted to detect the rotor ITSCF in the micromachine. Fig. 7. 19 presents the spectral plots of the rotor *dq* currents (*a & b*), for the rotor current error signals (*c & d*) and the rotor *dq* modulating voltage signals (*e & f*), showing the possible frequency components that emerge due to the rotor ITSCF.

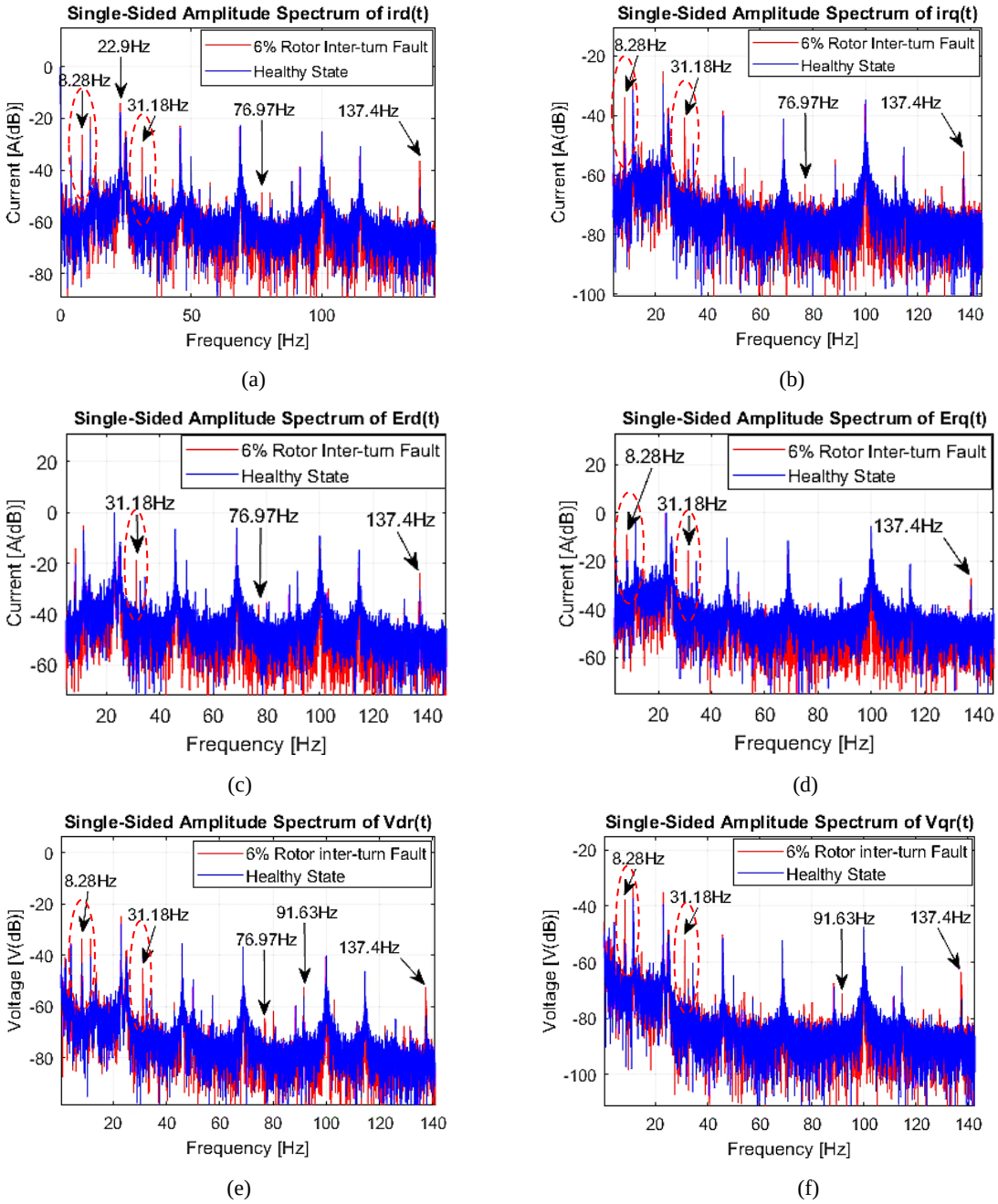

Figure 7. 19: MCSA of the DFIG controller signals for a micromachine with a Rotor ITSCF, at *medium load*; (a) & (b) rotor *dq* currents, (c) & (d) rotor current error signals, (e) & (f) rotor *dq* modulating signals

From *Fig. 7.19 (a)-(f)*, the amplitudes of some frequency components increased when the rotor inter-turn fault occurred. Likewise, the sensitivity study has been conducted to compare the rotor inter-turn fault detection potential of the different fault indicators that are in the spectrum plots of the DFIG controller signals when the fault occurs at a 6% severity level. Figure 7. 20 illustrates the sensitivity analysis results.

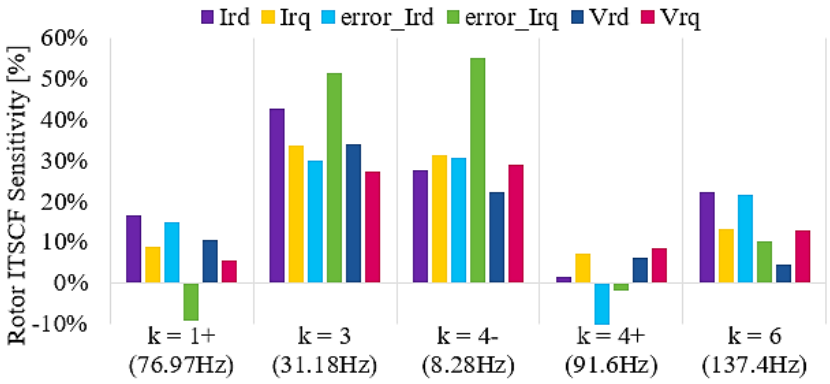

Figure 7. 20: Sensitivity study results of the Rotor ITSCF-related frequency components in the DFIG controller signals, for a micromachine at *medium load*

From Fig. 7.20, a significant increase in amplitude is observed to occur in the 8.28Hz component *(i.e., the $2sf_s$, k=4)* for all the DFIG controller signals, as well as in the 31.18Hz component (*k=3)* for some controller signals. Table 7. 9 summarizes the percentage increase in the amplitude of the dominant fault index (i.e., 8.28Hz) in the respective DFIG controller signals when a 6% rotor ITSCF occurs.

Table 7. 9: Percentage increase in the amplitude of the dominant rotor ITSCF indicator in the respective DFIG controller signals, for a micromachine at *medium load*

DFIG Controller Signal	***Percentage Increase in Magnitude***
Rotor d-axis current, I_{rd}	27%
Rotor q-axis current, I_{rq}	31%
D-axis rotor current error signal, *error_* I_{rd}	31%
Q-axis rotor current error signal, *error_* I_{rq}	55%
Rotor d-axis modulating voltage, V_{rd}	22%
Rotor q-axis modulating voltage, V_{rq}	29%

Overall, it is observed that the rotor inter-turn fault has a significant impact on the amplitude of the *k=4*. (*i.e., the $2sf_s$)* component in the *error_*I_{rq} signal, the same observation as the one in the high load scenario. Second to this, is the *k=3* component in the I_{rd} signal, compared to the other DFIG controller signals.

7.2.1.3.3 Low Load and Sub-synchronous Speed Operating Condition

The spectral analysis of the stator and rotor current signals has been conducted and the spectral plots are presented in Fig. 7.21 (a) and (b), respectively. Likewise, the spectral plots presented are those of the healthy state *vs* 6% rotor ITSCF only.

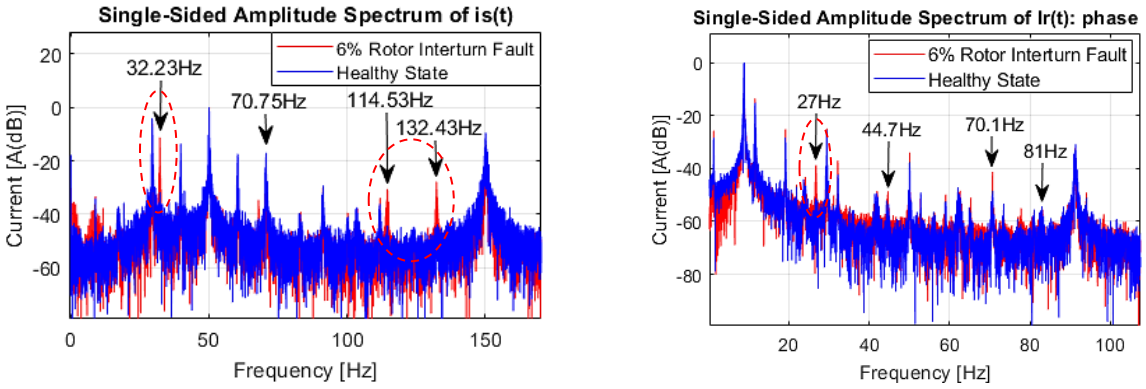

(a) (b)

Figure 7. 21: MCSA of the current signals for a micromachine with a Rotor ITSCF, at *low load*; (a) stator, (b) rotor

A summary of the changes in the magnitudes of the dominant harmonic components as the rotor inter-turn fault severity increases is provided in Fig. 7. 22 (a) and (b), for the stator and rotor current signals, respectively.

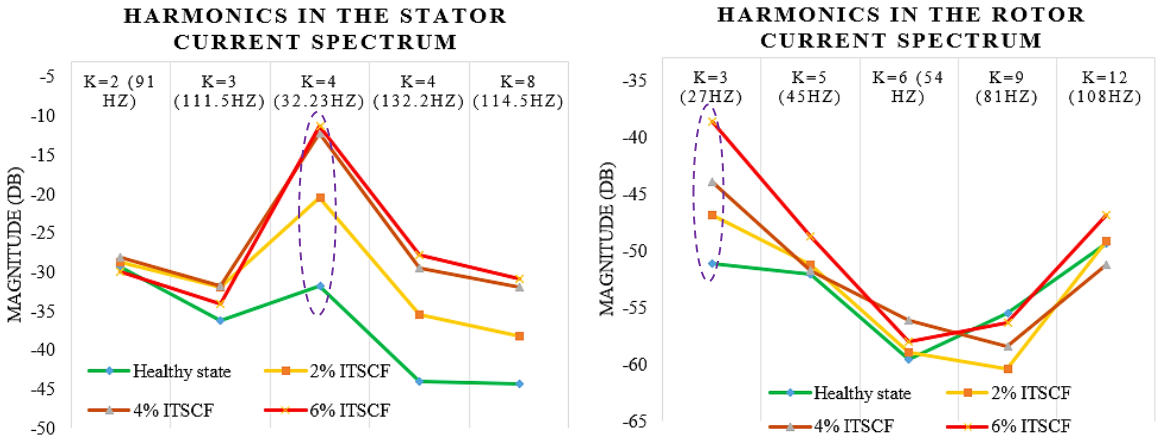

(a) (b)

Figure 7. 22: Summary of the dominant Rotor ITSCF fault-related harmonics in the (a) stator and (b) rotor current spectral plots for a micromachine at *low load*

From Fig. 7. 22 (a), It is observed that, increasing the rotor ITSCF severity results in a consistent increase in the amplitudes of the 32.23, 114.53, and 132.43 Hz components, whereby the 32.23Hz (*k=4), i.e.,* the *(1-2s) fs* component, increased the most with 20.47dB, (65% increase). In the case of the rotor current spectrum shown in Fig. 7.22 (b), a consistent amplitude increase is observed in the 27Hz component (*k = 3)*, with a change of 12.49dB. Like in the scenarios presented earlier, it is noted that the change in the amplitudes of the fault indicators in the stator current spectrum is more significant compared to those in the rotor current spectrum.

Fig. 7. 23. presents the spectral plots of the rotor *dq* currents (*a & b*), for the rotor current error signals (*c & d*) and the rotor *dq* modulating voltage signals (*e & f*), showing the possible frequency components that emerge due to the rotor ITSCF.

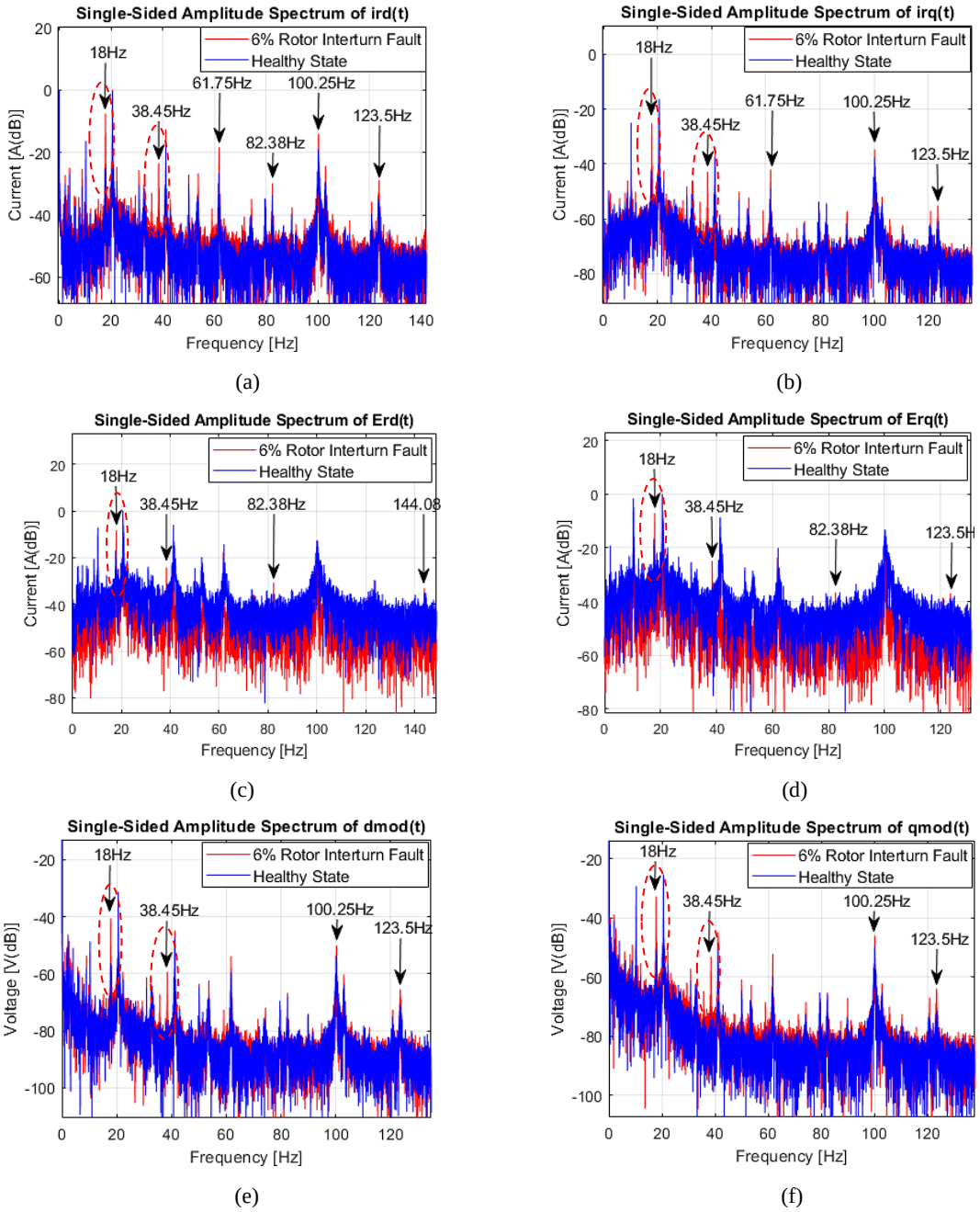

Figure 7. 23: MCSA of the DFIG controller signals for a micromachine with a Rotor ITSCF, at *low load*; (a) & (b) rotor *dq* currents, (c) & (d) rotor current error signals, (e) & (f) rotor *dq* modulating signals

An increase in the amplitude of some spectral components is observed in *Fig. 7.23(a)-(f)* when the rotor inter-turn fault occurred. Likewise, a sensitivity study has been conducted to compare the rotor inter-turn fault detection potential of the different fault indicators that are in the spectrum plots of the DFIG controller signals when the fault occurs at a 6% fault severity level. Figure 7.24 illustrates the sensitivity analysis results.

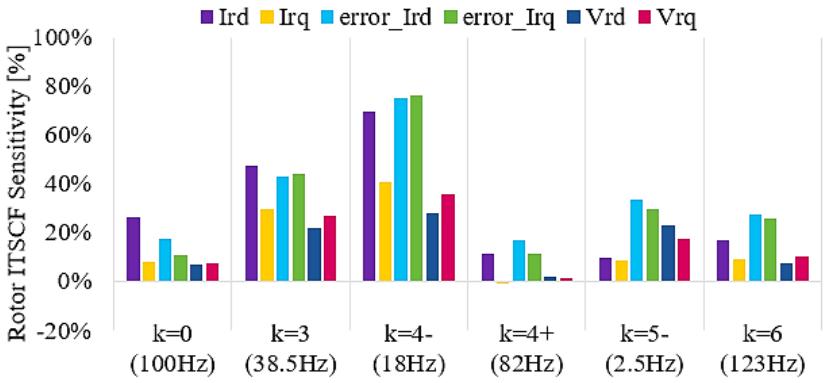

Figure 7. 24: Sensitivity study results of the Rotor ITSCF-related frequency components in the DFIG controller signals, for a micromachine at *low load*

It is observed from Fig. 7.24 that a substantial increase occurs in the 18Hz component *(k=4-)*, followed by the 38.5Hz component *(k=3)* for all the DFIG controller signals. Table 7. 10 summarizes the percentage increase in the amplitude of the dominant fault index (i.e., 18Hz) in the respective DFIG controller signals when a 6% rotor ITSCF occurs.

Table 7. 10: Percentage increase in the amplitude of the dominant rotor ITSCF indicator in the respective DFIG controller signals, for a micromachine at *low load*

DFIG Controller Signal	***Percentage Increase in Magnitude***
Rotor d-axis current, I_{rd}	70%
Rotor q-axis current, I_{rq}	41%
D-axis rotor current error signal, *error_* I_{rd}	75%
Q-axis rotor current error signal, *error_* I_{rq}	76%
Rotor d-axis modulating voltage, V_{rd}	28%
Rotor q-axis modulating voltage, V_{rq}	36%

Overall, it is observed that the rotor inter-turn fault has a significant impact on the amplitude of the *k=4-*, *i.e.*, *the* $2sf_s$ component in the *error_*I_{rq} signal, whereby an increase of 76% is observed. Second to this, is the *k=4-* component in the *error_*I_{rd} signal, having increased in amplitude by 75%.

7.2.1.3.4 Summary: Dominant Rotor ITSCF Indicators in the Stator Current, Rotor Current, and the DFIG Controller Signals

Table 7. 11 summarizes the main rotor inter-turn fault indicators in the stator current, rotor current, and the DFIG controller signals, for different amounts of power injected into the grid.

Table 7. 11: Dominant Rotor ITSCF Indicators in the Stator Current, Rotor Current, and the DFIG Controller Signals for different operating conditions

Signals	**Power injected into the grid | shaft speeds**		
	P_s = -4kW, Q_s = 0Var, ω_r = 1600rpm	***P_s = -2kW, Q_s = 0Var, ω_r = 1374rpm***	***P_s = -800W, Q_s = 0Var, ω_r = 1230rpm***
Stator current I_s	56.67Hz (k = 4.)	41.6Hz (k = 4.)	32.23Hz (k = 4.)
Rotor current I_r	10Hz (k = 3)	37.8Hz (k = 9)	27Hz (k = 3)
I_{rd}	6.67Hz (k = 4.)	8.28Hz (k = 4.)	18Hz (k = 4.)
I_{rq}	6.67Hz (k = 4.)	8.28Hz (k = 4.)	18Hz (k = 4.)
E_{rd}	6.67Hz (k = 4.)	8.28Hz (k = 4.)	18Hz (k = 4.)
E_{rq}	6.67Hz (k = 4.)	8.28Hz (k = 4.)	18Hz (k = 4.)
V_{rd}	6.67Hz (k = 4.)	8.28Hz (k = 4.)	18Hz (k = 4.)
V_{rq}	6.67Hz (k = 4.)	8.28Hz (k = 4.)	18Hz (k = 4.)

Therefore, it has been determined from the analyses that the *k=4.*, i.e., the *(1-2s) fs* component in the stator current spectrum was significantly affected by the rotor inter-turn fault, irrespective of the amount of power injected into the grid. It had a sufficient amplitude and could effectively be used for fault diagnosis. From the controller point of view, the sensitivity study has illustrated that the *k=4.* component in the controller signals was the most sensitive to the rotor ITSCF compared to other harmonic components. Specifically, it is noted that the rotor inter-turn fault has a significant impact on the fault indices corresponding to *k=4.* in the *q-axis* of the rotor error signal (*error_I_{rq})* compared to other controller signals, and thus, this component serves as a good indicator of the rotor ITSCF when using the DFIG controller signals.

7.2.1.4 Diagnosis of the Static Eccentricity Fault in the micro-DFIG

This section presents the spectral analysis of the stator current, rotor current, and the DFIG controller signals of a micromachine subjected to a static eccentricity fault condition while delivering different amounts of power to the grid. In this investigation, the static eccentricity (SE) fault has been implemented by pushing the rotor shaft away from the center point by 1mm, towards the left side of the machine to displace the rotating axis from the stator axis.

The detailed analysis of the stator current, rotor current, and the DFG controller signals for fault feature extraction and fault diagnosis under the medium load and sub-synchronous speed operation condition is presented in the following sections. The MCSA of the stator and rotor current signals under this scenario has been conducted and the respective spectral plots are presented in Fig. 7. 25(a), and (b), respectively, for the healthy state *vs* the static eccentricity fault.

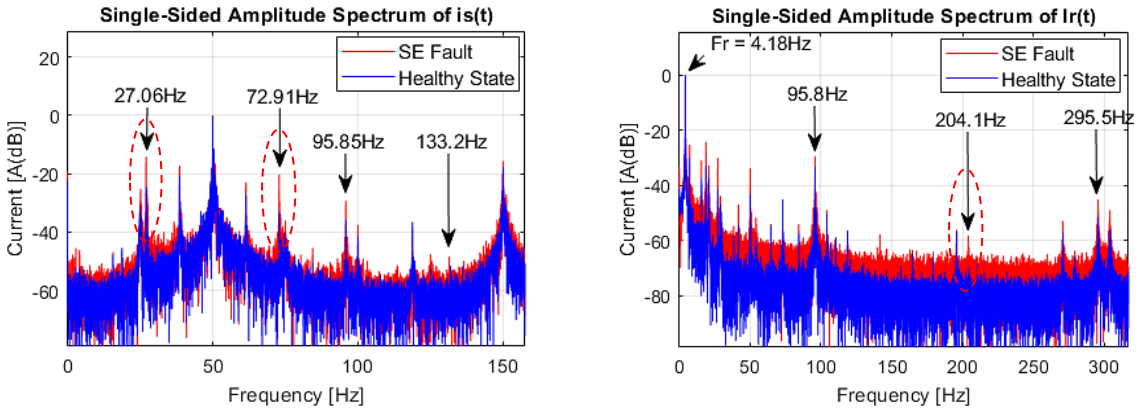

(a) (b)

Figure 7. 25: MCSA of the current signals for a micromachine with an SE fault, at *medium load*; (a) stator, (b) rotor

A summary of the changes in the magnitudes of the dominant fault harmonic components observed in Fig. 7.25 as the SE fault occurs, is provided in Fig. 7. 26 (a), and (b), for the stator and rotor current signals, respectively.

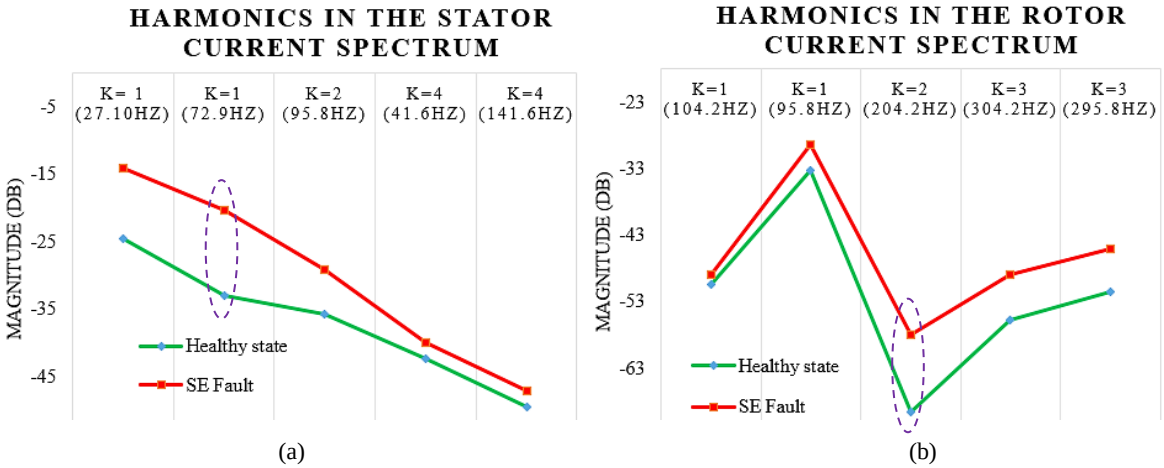

(a) (b)

Figure 7. 26: Summary of the dominant SE fault-related harmonics in the (a) stator and (b) rotor current spectral plots for a micromachine at *medium load*

It is observed in Fig. 7.26 (a) that the occurrence of the SE fault results in a significant increase in the amplitudes of the 27.10 and 72.9Hz components in the stator current spectrum, whereby the 72.9Hz (*k=1)* increased the most with 12.68dB, (38% increase). In the case of the rotor current spectrum shown in Fig. 7. 26 (b), a large amplitude increase is observed in the 204.2Hz component (*k = 2)*, with a change of 11.45dB. This shows that these are good indicators of the SE fault.

The use of the DFIG controller signals has also been explored in this section to investigate their capability in detecting the SE fault implemented on the micromachine in this experimental study. Fig. 7. 27 presents the spectral plots of the rotor *dq* currents (*a & b*), for the rotor current error signals (*c & d*) and the rotor *dq* modulating voltage signals (*e & f*), showing the possible frequency components that emerge due to the SE fault condition.

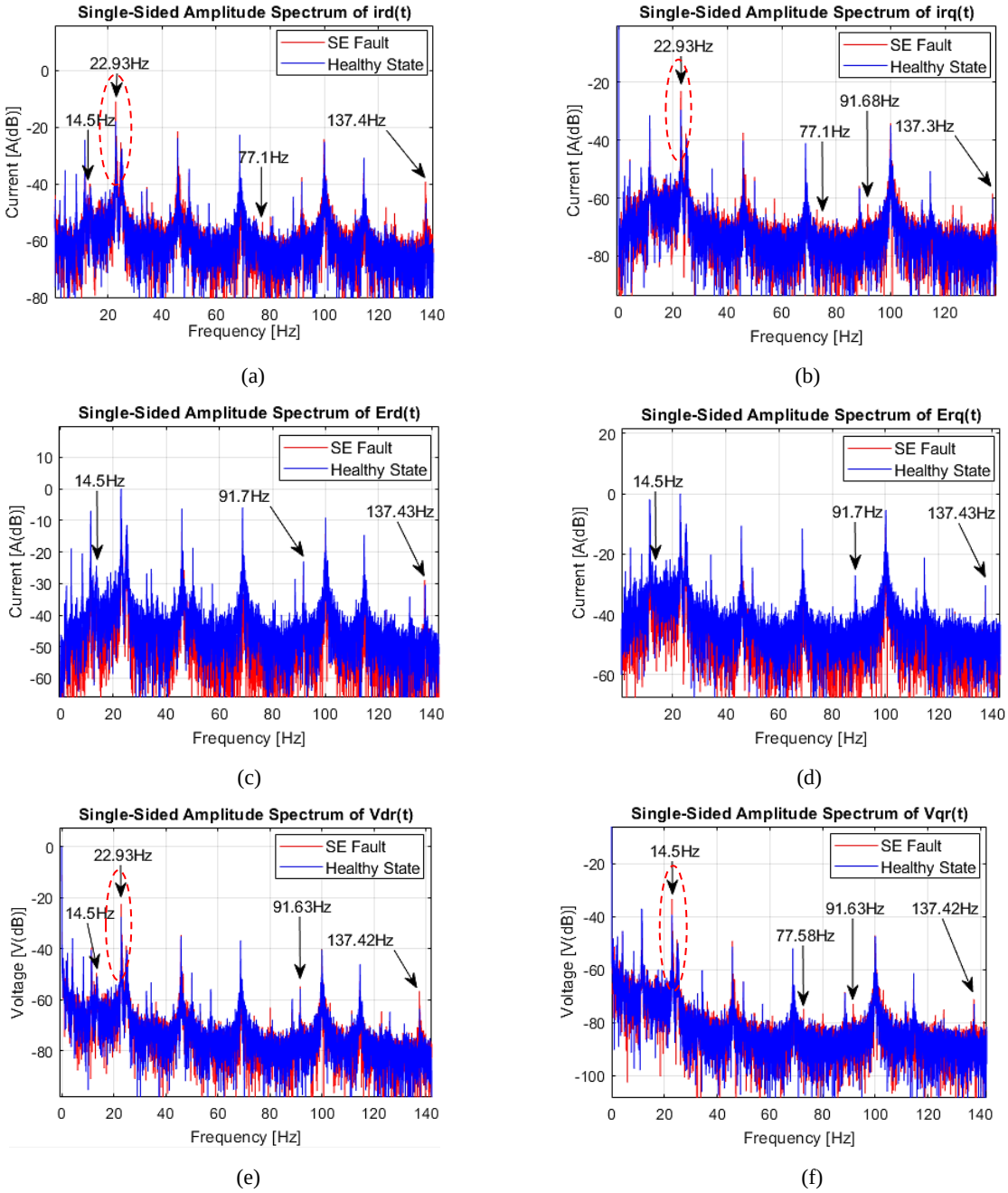

Figure 7. 27: MCSA of the DFIG controller signals for a micromachine with an SE fault, at *medium load*; (a) & (b) rotor *dq* currents, (c) & (d) rotor current error signals, (e) & (f) rotor *dq* modulating signals

An increase in the amplitude of some spectral components is observed in *Fig. 7.27(a)-(f)*, in comparison to the healthy case. Likewise, a sensitivity study has been conducted to compare the static eccentricity fault detection potential of the different fault indicators that are in the spectrum plots of the DFIG controller signals. Figure 7. 28 illustrates the sensitivity analysis results.

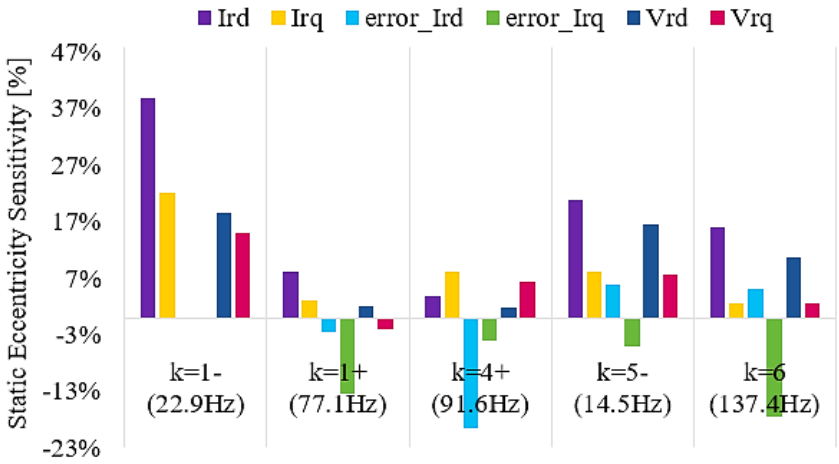

Figure 7. 28: Sensitivity study results of the SE fault-related frequency components in the DFIG controller signals, for a micromachine at *medium load*

It is observed from Fig. 7. 28 that a substantial increase occurs in the 22.9Hz component *(k=1)* for a majority of the DFIG controller signals, except the *error signals*. Table 7. 12 presents the percentage increase in the amplitude of the dominant fault index (i.e., 14.5Hz) in the respective DFIG controller signals.

Table 7. 12: Percentage increase in the amplitude of the dominant static eccentricity indicator in the respective DFIG controller signals, for a micromachine at *medium load*

DFIG Controller Signal	***Percentage Increase in Magnitude***
Rotor d-axis current, I_{rd}	39%
Rotor q-axis current, I_{rq}	22%
D-axis rotor current error signal, *error_* I_{rd}	0%
Q-axis rotor current error signal, *error_* I_{rq}	0%
Rotor d-axis modulating voltage, V_{rd}	19%
Rotor q-axis modulating voltage, V_{rq}	15%

Overall, it is observed that the static eccentricity fault has a significant impact on the amplitude of the *k=1-* component that is in the I_{rd} signal, with an increase of 39%, followed by the same fault component in the I_{rq} signal, compared to the other DFIG controller signals.

7.2.1.4.1 Summary: Dominant SE Fault Indicators in the Stator Current, Rotor Current, and the DFIG Controller Signals

Table 7. 13 summarizes the main static eccentricity fault indicators in the stator current, rotor current, and the DFIG controller signals, for the medium power injected into the grid.

Table 7. 13: Dominant SE fault Indicators in the Stator Current, Rotor Current, and the DFIG Controller Signals

Signals	**Power injected into the grid | shaft speeds**
	P_s = -2kW, Q_s = 0Var, ω_r = 1374rpm
Stator current I_s	72.9Hz (k = 1)
Rotor current I_r	204.2Hz (k = 2)
I_{rd}	22.9Hz (k = 1-)
I_{rq}	22.9Hz (k = 1-)
E_{rd}	22.9Hz (k = 5)
E_{rq}	*Insignificant*
V_{rd}	22.9Hz (k = 1-)
V_{rq}	22.9Hz (k = 1-)

Therefore, it has been determined from the analyses that the *k=1,* component in the stator current spectrum was significantly affected by the static eccentricity fault and thus, it had a sufficient amplitude and could effectively be used for fault diagnosis. For the rotor current signal, the component corresponding to *k=2* was also significantly affected by the SE fault. From the controller point of view, the sensitivity study has illustrated that the *k=1-* component in the controller signals was the most sensitive to the SE faults compared to other harmonic components. Specifically, it is noted that the static eccentricity fault has a significant impact on the fault indices corresponding to *k=1-* in the *d-axis* rotor current signal (I_{rd}) compared to other controller signals, and thus, this component serves as a good indicator of the SE fault when using the DFIG controller signals.

7.2.2 Hilbert and Discrete Wavelet Transform Analysis

This section presents the Hilbert Transform (HT) and the Discrete Wavelet Transform (DWT) analysis of the stator and rotor current signals to detect the stator and rotor inter-turn faults implemented on the micro-DFIG during the speed-varying conditions. For this investigation, experiments have been conducted on the micro-DFIG that has been synchronized to the utility grid. The micro-DFIG has been assessed under the healthy state and when subjected to the inter-turn fault conditions during an accelerating speed transient, from 1200rpm to 1325rpm, corresponding to a slip range of $s = 0.2$ to $s = 0.117$. Figure 7.29 illustrates the change in the instantaneous micro-DFIG speed.

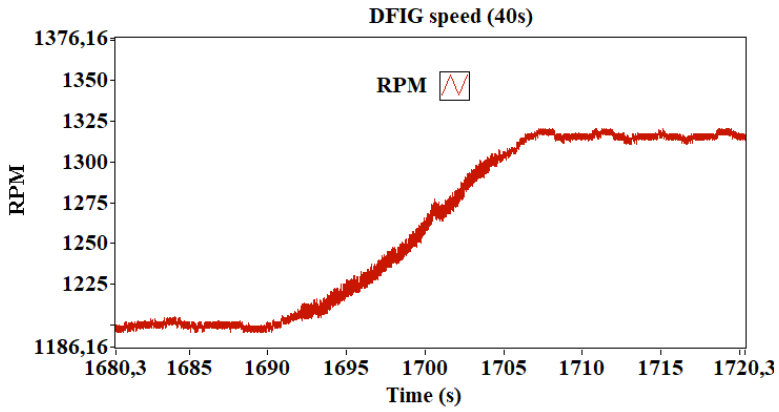

Figure 7. 29: Instantaneous micro-DFIG Speed

Considering the sampling frequency F_s = 5000 samples/s, the application of the expression in (2.154) leads to an 8th level decomposition (n_f = 8). The frequency bands have been computed and are presented in Table 7.14. Likewise, the Daubechies wavelet of the 44th order (*db44*) has been used as the mother wavelet.

Table 7. 14: Frequency Bands of the Wavelet Signals for a micromachine operating in generator mode

Coefficient	***Frequency Band (Hz)***
D1	1250 – 2500
D2	625 – 1250
D3	312.5 – 625
D4	156.25 – 312.5
D5	78.13 – 156.25
D6	39.06 – 78.13
D7	19.53 – 39.06
D8	9.77 – 19.53
D9	4.88 – 9.77
A9	0 – 9.77

In this investigation, the wavelet decomposition of the resultant Hilbert modulus of the stator and rotor current signals for the micro-DFIG in the healthy state has been used as a reference in comparison with the inter-turn faulty case.

7.2.2.1 Rotor Current Signal Decomposition

Figures 7.30 (a), (b), and (c) shows the signals resulting from the DWT of the Hilbert Modulus of the rotor current signal for the micro-DFIG in the healthy state, and when it is subjected to a 6% rotor inter-turn fault and a 6% stator inter-turn fault, respectively.

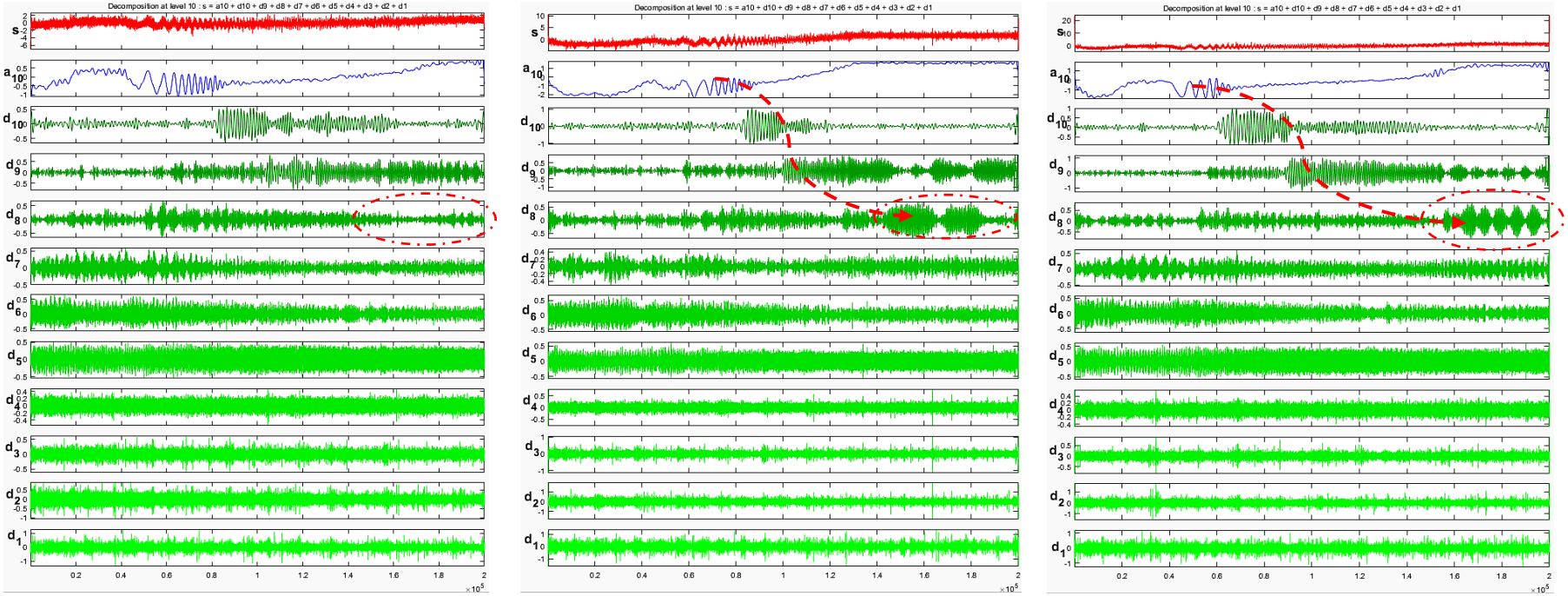

(a) (b) (c)

Figure 7. 30: DWT the Hilbert modulus of the rotor current signal for the micro-DFIG at different states: (a) the healthy state, (b) with a 6% rotor ITSCF and (c) with a 6% stator ITSCF

The contribution of the rotor and stator inter-turn fault frequencies [at sf_s, *(2-s) fs* & *(2+s) fs*] in the rotor current signals is to be observed in detail *d8*. From Fig. 7.30 (a), it is observed that the wavelet decomposition of the rotor current signal's Hilbert modulus is not affected in the *d8* frequency band. However, a change in harmonic content is observed in Fig. 7.30 (b) and (c) when the micro-DFIG is subjected to a rotor and stator inter-turn fault conditions, respectively.

7.2.2.2 Stator Current Signal Decomposition

Figures 7.31 (a), (b), and (c) shows the signals resulting from the DWT of the Hilbert Modulus of the stator current signal for the micro-DFIG in the healthy state, and when it is subjected to a 6% rotor inter-turn fault and a 6% stator inter-turn fault, respectively.

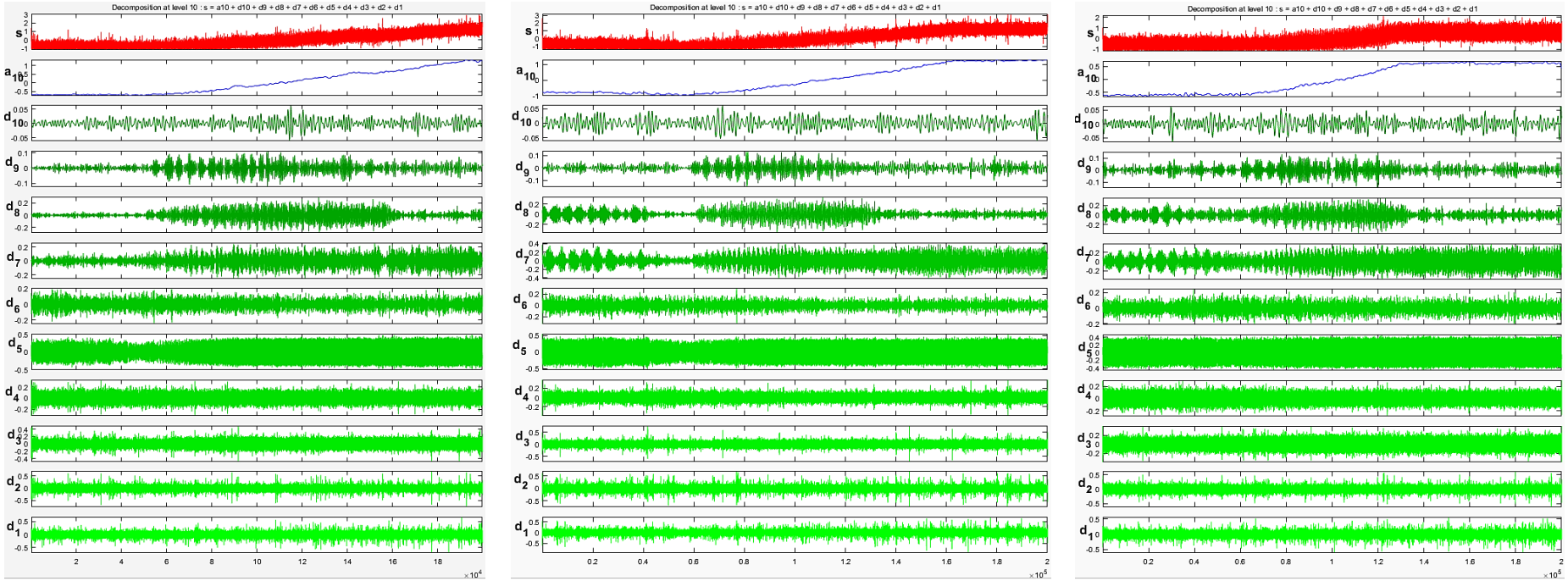

(a) (b) (c)

Figure 7. 31: DWT the Hilbert modulus of the stator current signal for the micro-DFIG at different states: (a) the healthy state, (b) with a 6% rotor ITSCF and (c) with a 6% stator ITSCF

The contribution of the rotor and stator inter-turn fault frequencies [at *(1-2s) fs* & *(1+2s) f_s*] in the stator current signals is to be observed in detail *d6.* However, it is observed in Fig. 7.31 that there is no distinct change observed in the decomposition bands of the stator current's Hilbert modulus despite the inter-turn faults that occurred in the micro-DFIG. This further illustrates that the rotor current signal is better suited to diagnose the stator and rotor inter-turn faults under the transient operating condition, as opposed to using the stator current signal.

7.3 Chapter Summary

This chapter focused on analyzing the stator current, rotor current, and the DFIG controller signals to diagnose the stator inter-turn short circuit fault (ITSCF), rotor ITSCF and static eccentricity (SE) faults in the scaled-down WRIM in the presence of the power electronic (PE) converter system. The analysis was done under both steady-state and transient operating conditions. The experimental tests were performed on the micro-WRIM under 4 scenarios: in a healthy state; with a 2%, 4%, and 6% stator inter-turn fault; with a 2%, 4%, and 6% rotor inter-turn fault and with a static eccentricity fault. Different loading conditions have been considered for each scenario under the steady-state condition. The loading condition in this case is classified based on the amount of active power that is delivered to the power utility grid: high load (*-4kW, 0Var, ω_r=1600rpm, slip = -0.067*); medium load (*-2kW, 0Var, ω_r=1374rpm, slip = 0.087*); low load (*-800W, 0Var, ω_r=1230rpm, slip = 0.17*). It is worth noting that the systematic fault diagnosis approach that was developed in the preceding chapter has been applied to the controlled micro-DFIG and has made the fault diagnosis process comprehensible.

The classical MCSA technique has been used to analyze the captured signals and detect the dominant fault-related harmonic frequency components associated with different faults in the micro-WRIM during the steady-state operating condition. Tables 7.7, 7.11 and 7.13 summarized the dominant fault-related indicators which were identified in the spectral plots of the stator current, rotor current, and the DFIG controller signals, for a micromachine subjected to a stator inter-turn, rotor inter-turn and the SE faults, under the different power delivery conditions.

The novel exercise of this analytical study was to compare the use of the stator current, rotor current, and the DFIG controller signals to identify which signal is best suited for diagnosing the faults in the micro-DFIG. In this regard, the following conclusions are drawn:

- ***Stator inter-turn fault***: it has been determined that the $k=4_+$, i.e., the *(1+2s) fs* component in the stator current spectrum was significantly affected by the stator inter-turn fault, irrespective of the amount of power injected into the grid. On the other hand, it has been observed that the rotor current signal is not adequate for diagnosing the stator inter-turn fault. This can be attributed to the masking effect of the closed-loop control of the DFIG and the switching mechanism of the electronic converter that is in the rotor circuit, which suppresses the fault-related harmonics thus making them undetectable. From the controller point of view, the sensitivity study has illustrated that the stator inter-turn fault has a significant impact on the fault indices corresponding to $k=4_-$ in the *q-axis* of the rotor error signal (*error_I_{rq}*) compared to other controller signals, and thus, this component serves as a good indicator of the stator ITSCF when using the DFIG controller signals.

- ***Rotor inter-turn fault***: the *k=4*., i.e., the *(1-2s) fs* component in the stator current spectrum was significantly affected by the rotor inter-turn fault, irrespective of the amount of power injected into the grid. It had a sufficient amplitude and could effectively be used for fault diagnosis. Although there are some dominant fault indicators identified in the rotor current spectrum, it is noted that the change in the amplitudes of the fault indicators in the stator current spectrum is more significant compared to those in the rotor current spectrum. Similar to the stator inter-turn fault scenario, the sensitivity study has illustrated that the rotor inter-turn fault has a significant impact on the fault indices corresponding to *k=4*. in the *q-axis* of the rotor error signal (*error_*I_{rq}*)* compared to other controller signals and thus, this component serves as a good indicator of the rotor ITSCF when using the DFIG controller signals.

- ***Static Eccentricity fault***: it has been determined that the *k=1* component in the stator current spectrum was significantly affected by the static eccentricity fault and thus, it had a sufficient amplitude and could effectively be used for fault diagnosis. For the rotor current signal, the component corresponding to *k=2* was also significantly affected by the SE fault. The sensitivity study has illustrated that the SE fault had a significant impact on the fault indices corresponding to *k=1*. in the *d-axis* rotor current signal (I_{rd}*)* compared to other controller signals.

For the transient operating condition, the Hilbert Transform (HT) and Discrete Wavelet Transform (DWT) analysis techniques have been used to analyze the stator and rotor current signals to monitor the evolution of the identified dominant inter-turn fault-related frequency components during the speed-varying operating condition. Based on the analysis results presented earlier, a change in harmonic content was observed in the detail band *d8* of the rotor current's Hilbert modulus when the micro-DFIG was subjected to the rotor and stator inter-turn fault conditions. However, no distinct change was observed in the decomposition bands of the stator current's Hilbert modulus despite the inter-turn faults that occurred in the micro-DFIG. This further illustrates that the rotor current signal is better suited to diagnose the stator and rotor inter-turn faults in a micro-DFIG under the speed-varying operating condition, as opposed to using the stator current signal.

In summary, the highlight of this chapter lies in using the various DFIG controller signals in addition to the terminal stator and rotor current signals, to diagnose the stator and rotor inter-turn faults, while delivering different amounts of active power to the utility grid. Furthermore, the static eccentricity fault condition has also been diagnosed, which, based on the literature review, has not been thoroughly explored using the DFIG controller signals.

In essence, it is observed that the DFIG controller signals are best suited to diagnose faults in the micro-DFIG under the steady-state operating condition, compared to the terminal stator and rotor current signals. Even so, it is noted that the terminal stator current signal still does possess some good fault diagnostic potential, unlike the rotor current signals. Under the speed-varying condition, it has been illustrated that use of the Hilbert transform technique to suppress the fundamental frequency component has improved the detectability of the evolution of fault indicators in the rotor current signal, despite the diminishing effects of the converters' switching mechanism.

Chapter 8: Assessing the Behaviour of the Micro-DFIG due to Undervoltage Conditions and Inter-turn Short-Circuit Faults

8.1 Introduction

The focal point of this chapter is twofold. Firstly, the focus is on evaluating the impact of having a low voltage level at the point of common coupling (PCC), i.e., a voltage dip, on the behavior of the micro-DFIG that is in its healthy state. The root-mean-square (RMS) value of the stator and rotor currents are observed as the voltage at the PCC changes from the rated grid voltage (380 V_{LL}) to 85% of the rated voltage. Secondly, the chapter aims to evaluate the asymmetry/unbalance that occurs in the stator and rotor currents due to the occurrence of the inter-turn faults in the micro-DFIG, with the emphasis on the impact that this asymmetry is envisaged to have on the entire system. The second exercise is realized by determining the negative sequence component (NSC) of the stator and rotor currents and observing how this component is affected when the inter-turn short circuit faults occur in the stator and rotor windings, at different severity levels. In this aspect, the ratio of the negative-sequence to the positive-sequence component for each current signal also referred to as the current unbalance factor, has been determined and used to quantify the unbalance as the inter-turn fault severity level is increased. Subsequently, a comparison has been carried out to investigate how reducing the voltage at the PCC affects the fault diagnosis capability of the NSC. Moreover, the impact of the combination of scenarios, i.e., the inter-turn fault and the low grid voltage condition, on the operation of the micro-DFIG has been presented, taking into consideration the changes observed in the rms currents of the faulted phase winding as well as the negative-sequence current component as the fault severity level is increased.

8.2 Assessing the micro-DFIG in its healthy state under the Rated and Low Grid Voltage Conditions

This section focuses on evaluating the impact of a low voltage level at the PCC on the operation and behaviour of the micro-DFIG while in its healthy state, i.e., without inter-turn faults on either the stator or rotor windings. In this assessment, the rms values of the stator and rotor currents are used as a means of investigating the machine's sensitivity to a steady-state voltage dip. This is done by observing their trend as the voltage at the PCC was changed from the rated grid voltage to a lower grid voltage level i.e., 85% of the rated voltage, which is characterized as an under-voltage condition. The under-voltage condition explored in this study is of the symmetrical type. The micro-DFIG was operated at a speed of 1230rpm (s = 0.18), under the two grid voltage conditions considered in this investigation.

8.2.1 Overview

Voltage distortions and amplitude variations are common phenomena in power systems. Harmonics, notches, impulses, etc., are considered as voltage distortions, whereas amplitude variations are the voltage sags, voltage swells, overvoltages, and undervoltages [143]. Voltage sags have become of considerable interest because they pose detrimental consequences to the supplied equipment depending on their sensitivity [144]. According to [145], a voltage sag/dip is referred to as a momentary reduction of the voltage in a node of an electrical network under a specific threshold, which lasts for a particular duration. Specifically, according to IEEE standard 1159-1995, the threshold is 90% to 10% of the nominal/rated voltage for a time between 0.5 cycles to less than or equal to one minute [146]. If the duration of the voltage dip exceeds one minute, then it becomes an undervoltage condition. Voltage dips can be characterized as symmetrical or asymmetrical, depending on the causes [144]. A symmetrical voltage dip is when the individual phase voltages are equal and the phase relationship is 120°, else, the sag is asymmetrical [144].

Grid disturbances in form of under- and over-voltages may lead to the disconnection of renewable power plants (RPPs) from the grid which may result in grid instability and other power quality issues. According to the South African Grid Code (SAGC) requirements stipulated in [147], RPPs are required to remain connected to the network and operate continuously within the voltage range of -15% to 10% of the nominal voltage at the point of common coupling (PCC). Moreover, to fulfill the low voltage ride-through requirements for RPPs, it is recommended that, regardless of the type of fault, the RPP should remain in operation within the range of 0.9 p.u. (U_{min}) to 1.1 p.u. (U_{max}) at the PCC [148]. In addition, after the voltage at the PCC has been recovered, the RPP is required to increase its active power production to at least 90% of the pre-fault level within one second [149].

In this study, the focus is on exploring the behavior of the micro-DFIG under a steady-state low grid voltage condition. This scenario is similar to a voltage sag condition in the sense that the voltage at the PCC has been dropped below the standard threshold value, i.e., to 85% of the rated grid voltage. However, unlike the voltage sag condition which is characterized by a dip in the voltage that lasts for a particular duration and considers the transient response, in this investigation, the grid voltage is maintained at a steady-state low voltage level for an unlimited period. Emulating a steady-state low grid voltage condition is of particular importance in this study, to examine the behavior of the micro-DFIG when it is subjected to inter-turn fault conditions, while also considering the scenario of having a low voltage at the PCC. However, before examining the impact of these combined scenarios on the behavior of the micro-DFIG, it is vital to investigate how having a steady-state low voltage at the PCC would influence the operation of the micro-DFIG.

Therefore, this exercise forms a foundation for understanding the behavior of this specific machine under the low grid voltage conditions, independent of the faults, before exploring the impact of both conditions, which is deemed as the worst-case scenario in this investigation.

According to Gnacincki *et al* [150] and Chauhan *et al* [151], induction machines (IMs), which are the workhorse of the industry are often exposed to over-or undervoltage conditions which may lead to an increase in winding temperatures thereby accelerating the aging of the insulation system and significantly shortening the lifespan of the IM and worsening its reliability and durability. Additionally, the impacts of undervoltage conditions on the induction machine behavior are speed reduction, coupled with torque and current peaks [144, 152]. Prolonged undervoltage conditions could lead to equipment failure which results in the halting of operations which is associated with significant economic consequences [143].

8.2.2 Results and Discussions

Table 8.1 presents the rms values of the stator and rotor phase currents, as well as the average/total rms currents for the micro-DFIG in a healthy state under the rated and low grid voltage conditions.

Table 8. 1: Stator and rotor rms currents for a micro-DFIG in a healthy state under the rated and low grid voltage conditions.

Voltage at PCC (V_{LL})	***Stator*** I_{rms} ***[A]***				***Rotor*** I_{rms} ***[A]***			
	I_{sa}	I_{sb}	I_{sc}	$I_{average}$	I_{ra}	I_{rb}	I_{rc}	$I_{average}$
Rated (380)	0.79	0.7	0.7	0.73	5.76	5.49	5.64	5.63
85% of the rated (323)	1.11	1.01	1.01	1.04	5.79	5.81	5.76	5.79

From the rms values of the stator and rotor currents presented in Table 8.1, it is observed that the rms values under the low grid voltage condition are slightly higher than those under the rated grid voltage condition. A significant increase or peak in current is observed in the stator current, compared to the rotor current, that is, an average increase of 42.5% compared to a 2.84% increase in the rotor current. This is expected, as per the findings from the literature [144, 152], and also considering that despite a low voltage at the PCC, the micro-DFIG in this experiment was still operated in a way that ensured that the same amount of power was delivered to the grid, as in the case of the rated grid voltage condition. Therefore, to achieve this, the stator current had to increase to cater for the drop in the voltage to obtain the same amount of power that was fed into the grid under the rated voltage condition, according to the power equation $P = VI$. This behavior also ensures that the low voltage ride-through capability of the micro-DFIG is achieved since keeping the machine connected to the supply during voltage dips is advantageous from the system's stability point of view [143].

Nonetheless, the significant increase in the stator current could pose a risk of overheating the stator windings thereby accelerating the aging of the insulations, reducing the efficiency of the machine, and significantly shortening its lifespan as recited by Gnacinski *et al* [150]. However, if the current remains within the rated threshold during the undervoltage condition, as observed in this investigation, the micro-DFIG's health state will be retained.

8.3 Assessing the micro-DFIG subjected to the Stator ITSCFs under the Rated and Low Grid Voltage Conditions

This section focuses on evaluating the unbalance/asymmetry that occurs in the stator and rotor of the micro-DFIG due to the stator inter-turn short-circuit fault (ITSCF) condition. The analysis is done under both the rated and low grid voltage conditions. The average stator and rotor rms currents as well as the rms current of the faulted stator phase winding, i.e., *phase B*, have been presented. The evaluation of the asymmetry is conducted by determining the positive-sequence and the negative-sequence components of the stator and rotor current signals when the micro-DFIG is subjected to stator inter-turn faults at different severity levels. The severity levels considered are the 2%, 4%, and 6%, corresponding to 2, 3, and 5 shorted turns/phase, respectively. The ratio of the negative-sequence to the positive-sequence component has also been determined and used as the fault index to observe the variation of this parameter as the stator fault severity level is increased.

8.3.1 Review of the Current Sequence Components

According to [153], the three-phase currents $\dot{I}_A, \dot{I}_B$ and $\dot{I}_C$, can be decomposed into three components, i.e., the positive-sequence current component $\dot{I}_P$, the negative-sequence current component $\dot{I}_N$, and the zero-sequence current component $\dot{I}_0$ as illustrated in (8.1):

$$\dot{I}_P = \frac{1}{3}(\dot{I}_A + a\dot{I}_B + a^2\dot{I}_C)$$

$$\dot{I}_N = \frac{1}{3}(\dot{I}_A + a^2\dot{I}_B + a\dot{I}_C) \tag{8.1}$$

$$\dot{I}_0 = \frac{1}{3}(\dot{I}_A + \dot{I}_B + \dot{I}_C)$$

Where a=$1\angle 120° = e^{j120°}$

It is observed from (8.1) that each sequence component can be calculated using the instantaneous values of the three-phase currents, although the computation process may be complex. For this investigation, the positive- and negative sequence components are of particular interest. The determination of these components has been simplified in [153], whereby the following expressions are adopted: Suppose $\dot{I}_A = I_A e^{j0}$, $\dot{I}_B = I_B e^{j\varphi_b}$, and $\dot{I}_C = I_C e^{j\varphi_c}$ and presuming that $I_B = xI_A, I_C = yI_A$, then:

$$\dot{I}_A + \dot{I}_B + \dot{I}_C = 0 \tag{8.2}$$

According to the sine and cosine theorem, the following expressions can be obtained:

$$\left.\begin{aligned} \cos\alpha_1 &= \frac{I_B^2+I_C^2-I_A^2}{2I_BI_C} = \frac{x^2+y^2-1}{2xy} \\ \cos\alpha_2 &= \frac{I_A^2+I_C^2-I_B^2}{2I_AI_C} = \frac{1+y^2-x^2}{2y} \\ \cos\alpha_3 &= \frac{I_A^2+I_B^2-I_C^2}{2I_AI_B} = \frac{1+x^2-y^2}{2x} \end{aligned}\right\} \tag{8.3}$$

$$\frac{\sin\alpha_1}{I_A} = \frac{\sin\alpha_2}{I_B} = \frac{\sin\alpha_3}{I_C} \tag{8.4}$$

According to the basic theorem of trigonometric functions, the expressions for the positive-sequence current component I_P and the negative-sequence current component I_N can be deduced as follow:

$$\left.\begin{aligned} I_{Px} &= \frac{I_A}{2}\left\{1+\frac{1}{\sqrt{3}}\sqrt{[(x+y)^2-1][(1+y)^2-x^2]}\right\} \\ I_{Py} &= \frac{I_A}{2\sqrt{3}}(y^2-x^2) \\ \boldsymbol{I_P} &= \sqrt{I_{Px}^2+I_{Py}^2} \end{aligned}\right\} \tag{8.5}$$

$$\left.\begin{aligned} I_{Nx} &= \frac{I_A}{2}\left\{1-\frac{1}{\sqrt{3}}\sqrt{[(x+y)^2-1][(1+y)^2-x^2]}\right\} \\ I_{Ny} &= \frac{I_A}{2\sqrt{3}}(x^2-y^2) \\ \boldsymbol{I_N} &= \sqrt{I_{Nx}^2+I_{Ny}^2} \end{aligned}\right\} \tag{8.6}$$

The positive-sequence and negative-sequence components can be used to deduce the status of the generator as explored by Chen *et al* [153]. In this regard, when a generator is operating under a healthy state, the three-phase current signal is expected to only have a positive-sequence component [153]. Whereas for a generator in the faulty state, there is expected to be a level of asymmetry in the machine which would introduce a negative-sequence component in the three-phase currents. Subsequently, there would be a negative sequence injection into the grid at the point of common coupling. Therefore, under the aspect of fault diagnosis, the negative sequence component can be used to diagnose the occurrence of a fault in the generator. Moreover, this component can be used to evaluate the severity of the unbalance/asymmetry resulting from the occurrence of the fault condition in the generator.

8.3.2 Results and Discussions

Table 8.2 presents the average stator and rotor rms currents, as well as the rms current of the faulted stator phase winding, i.e., *phase B*. The sequence components of the stator and rotor current signals have also been presented, for a micro-DFIG subjected to the stator ITSCF at different severity levels under the rated grid voltage condition.

Table 8. 2: Current Sequence Components for different stator ITSCF severity levels under the rated grid voltage condition

Number of Shorted turns	***Stator I_{rms} [A]***					***Rotor I_{rms} [A]***			
	$I_{sb(faulty\ phase)}$	I_{s_avr}	I_{s_P}	I_{s_N}	I_{s_N} / I_{s_P} *(%)*	I_{r_avr}	I_{r_P}	I_{r_N}	I_{r_N} / I_{r_P} *(%)*
0	0.7	0.73	0.95	0.16	16.86	5.63	5.70	0.11	1.85
2	0.93	0.79	0.97	0.24	24.33	5.6	5.67	0.09	1.66
3	0.98	0.80	0.93	0.24	25.94	5.72	5.78	0.10	1.75
5	1.19	0.84	0.85	0.41	48.09	5.67	5.75	0.11	1.91

Whereas Table 8.3 presents the average stator and rotor rms currents, the rms current of the stator faulted phase, and the sequence components of the stator and rotor current signals, for a micro-DFIG with a stator ITSCF at different severity levels under the low grid voltage condition.

Table 8. 3: Current Sequence Components for different stator ITSCF severity levels under the low grid voltage condition

Number of Shorted turns	***Stator I_{rms} [A]***					***Rotor I_{rms} [A]***			
	$I_{sb(faulty\ phase)}$	I_{s_avr}	I_{s_P}	I_{s_N}	I_{s_N} / I_{s_P} *(%)*	I_{r_avr}	I_{r_P}	I_{r_N}	I_{r_N} / I_{r_P} *(%)*
0	1.01	0.91	1.05	0.16	15.09	5.79	5.75	0.03	0.54
2	1.09	0.92	1.01	0.24	23.89	5.79	5.76	0.07	1.17
3	1.33	1.03	1.10	0.36	32.26	6.08	6.02	0.09	1.42
5	1.35	1.05	1.00	0.46	45.98	5.98	5.95	0.04	0.70

It is observed from Table 8.2 and Table 8.3 that the three-phase stator and rotor currents have a large value of the positive-sequence component I_P when the micro-DFIG is in the healthy state, i.e., with zero shorted turns. Moreover, there is a small value of the negative-sequence component I_N in the current signals, which is attributed to the inherent asymmetry that is in the micro-DFIG. When a stator inter-turn occurs in phase B, it is observed that the rms current I_{sb} of the faulted phase increases significantly with the fault severity level and a minimal increase is also observed in the average rms current I_{s_avr}. The positive-sequence component I_{s_P} of the stator current is observed to be decreasing, while the negative-sequence current component I_{s_N} increases consistently with the fault severity level. In this regard, the stator ITSCF is associated with an increase in an unwanted component, i.e., the negative-sequence current component I_{s_N}, which could potentially result in increased stator power losses and reduced machine efficiency.

On the other hand, there is no consistent increase observed in the average rotor rms current I_{r_avr} and the positive- and negative-sequence components of the rotor current, i.e., I_{r_P} and I_{r_N}. This is attributed to the control associated with the power electronic converter that is in the rotor circuit, whereby the controllers come into play to keep the rotor currents stable despite the occurrence of the stator inter-turn fault. Consequently, the fault on the stator side does not significantly influence the sequence components of the rotor current.

Examining the rms currents and the sequence components under the rated and low grid voltage conditions, it is observed that the values of the average rms currents as well as that of the faulted phase, i.e., *phase B*, under the low grid voltage level (*see Table 8.3*) are higher than those under the rated grid voltage condition in Table 8.2. A significant increase in the rms currents under the low grid voltage condition is expected, as was observed, and discussed in *subsection 8.2.2*. Specifically, for the stator inter-turn fault condition under the rated grid voltage condition, the stator rms current of the faulted phase increased by 70% for 5 shorted turns and by 92.9% when considering both the low grid voltage and 5 shorted turns conditions. Therefore, under the low grid voltage condition, the faulted phase carries a much higher current compared to the rated grid voltage condition.

Likewise, the values of the positive-sequence current components under the low grid voltage condition are also slightly higher than those under the rated grid voltage condition. Whereas the negative-sequence component is fairly consistent across the two voltage conditions. Overall, it is evident that the stator ITSCF has a significant impact on the negative-sequence component of the stator current, under either voltage condition compared to that of the rotor current. This results in a significant unbalance in the stator windings which could potentially lead to overheating of these windings, particularly those of the faulted phase, given the significant increase in the rms current in this phase as the fault severity level is increased, especially under the low grid voltage condition.

From the fault quantification point of view, it is shown in Table 8.2 and Table 8.3 that the ratio of the negative-sequence to the positive-sequence components in the stator current increases consistently with the fault severity level. Figure 8.1 (a) and (b) present the plots of the ratio I_N / I_P *(%),* for the stator and rotor current signals, respectively, under the rated grid voltage condition.

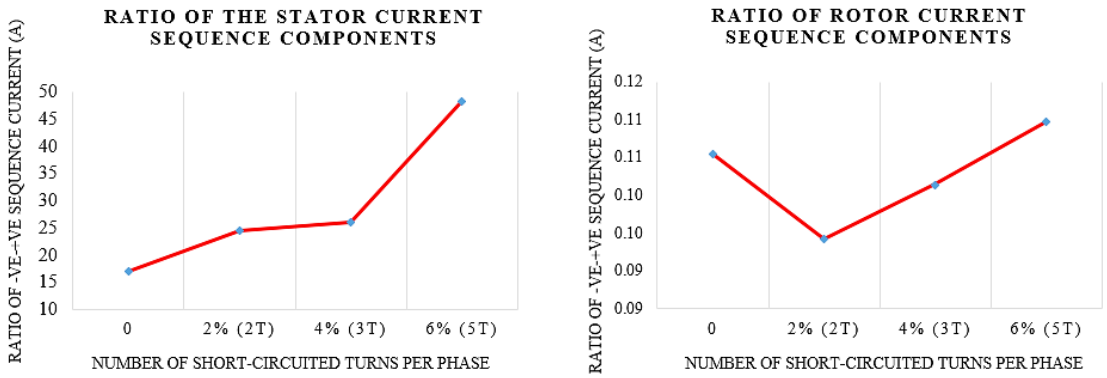

(a) (b)

Figure 8. 1: Comparison of the ratio of sequence components for different stator ITSCF severity levels under the rated grid voltage condition, (a) stator current (b) rotor current

Whereas Fig. 8.2 (a) and (b) present the plots of the ratio I_N / I_P *(%)*, for the stator and rotor current signals, respectively, under the low grid voltage condition.

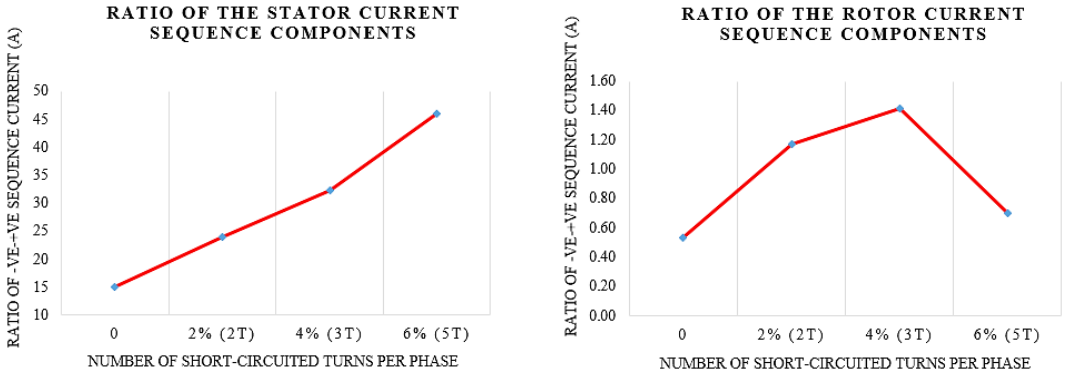

(a) (b)

Figure 8. 2: Comparison of the ratio of sequence components for different stator ITSCF severity levels under the low grid voltage condition, (a) stator current (b) rotor current

Therefore, from Fig 8.1 and Fig. 8.2, it is deduced that the ratio of the negative-sequence to positive-sequence components portrays a similar trend under both rated and low grid voltage conditions. As such, the asymmetry in the stator and rotor of the micro-DFIG due to the stator inter-turn fault is evident, despite the different voltage levels at the PCC, and the following conclusions can be drawn:

- The increase in the fault severity level is associated with a decrease in the positive-sequence component and an increase in the negative-sequence component of the stator current. As such,
  - A low negative-sequence component of the stator current corresponds to a low number of shorted turns on the stator.
  - A high value of the negative sequence component of the stator current corresponds to a high number of shorted turns on the stator.

  ∴ The negative sequence component is directly proportional to the fault severity level.

- The increase in the fault severity level is associated with an increase in the ratio of the negative-sequence to the positive-sequence component of the stator current. Hence, the unbalance in the stator winding of the micro-DFIG increases as the fault severity increases.
- It is observed that the presence of the stator inter-turn fault does not influence the negative-sequence component of the rotor current signal. This is due to the control effect of the power electronic converter that is in the rotor circuit.
- The rms currents and the current sequence components under the low grid voltage condition are slightly higher than those under the rated grid voltage condition, and so is the ratio of the negative- to positive-sequence components.
- The combination of scenarios, i.e., the stator inter-turn fault and the low grid voltage condition, which, in this study, is deemed as the worst-case scenario, could be detrimental to the operation of the micro-DFIG, particularly the faulted stator phase winding, should the currents exceed the rated values. This is considering that the rms current of the faulted stator phase increases consistently with the fault severity level, and so does the negative-sequence component of the stator current, and these values are much higher under the low grid voltage condition in comparison to the rated grid voltage condition as recited previously.

8.4 Assessing the micro-DFIG subjected to the Rotor ITSCF under the Rated and Low Grid Voltage Conditions

This section focuses on evaluating the unbalance/asymmetry that occurs in the stator and rotor of the micro-DFIG due to the rotor inter-turn short-circuit fault (ITSCF), under the rated and low grid voltage conditions. The average stator and rotor rms currents as well as the rms current of the faulted rotor phase winding, i.e., *phase B*, have been presented. Likewise, the positive-sequence and negative-sequence components of the stator and rotor current signals have been determined, for the micro-DFIG subjected to the rotor inter-turn faults at different severity levels. The fault severity levels considered are the 2%, 4%, and 6%, corresponding to 6, 13, and 19 shorted turns/phase, respectively. Ultimately, the ratio of the negative-sequence to the positive-sequence component has been determined and used as the fault index to observe how this parameter changes as the rotor fault severity level is increased.

Table 8.4 presents the average stator and rotor rms currents, as well as the rms current of the faulted rotor phase winding, i.e., *phase B*. The sequence components of the stator and rotor current signals have also been presented, for a micro-DFIG subjected to the rotor ITSCF at different severity levels under the rated grid voltage condition.

Table 8. 4: Current Sequence Components for different rotor ITSCF severity levels under the rated grid voltage condition

Number of Shorted turns	***Stator I_{rms} [A]***				***Rotor I_{rms} [A]***				
	I_{s_avr}	I_{s_P}	I_{s_N}	I_{s_N} / I_{s_P} *(%)*	$I_{rb(faulty\ phase)}$	I_{r_avr}	I_{r_P}	I_{r_N}	I_{r_N} / I_{r_P} *(%)*
0	0.73	0.95	0.16	16.86	5.49	5.55	5.70	0.11	1.85
6	0.77	0.96	0.11	11.92	5.66	5.57	5.47	0.14	2.48
13	0.78	0.98	0.11	11.43	5.8	5.58	5.31	0.37	7.00
19	0.82	1.04	0.11	10.26	5.82	5.59	5.17	0.43	8.34

Whereas Table 8.5 presents the average stator and rotor rms currents, the rms current of the rotor faulted phase, and the sequence components of the stator and rotor current signals, for a micro-DFIG with a rotor ITSCF at different severity levels under the low grid voltage condition.

Table 8. 5: Current Sequence Components for different rotor ITSCF severity levels under the low grid voltage condition

Number of Shorted turns	***Stator I_{rms} [A]***				***Rotor I_{rms} [A]***				
	I_{s_avr}	I_{s_P}	I_{s_N}	I_{s_N} / I_{s_P} *(%)*	$I_{rb(faulty\ phase)}$	I_{r_avr}	I_{r_P}	I_{r_N}	I_{r_N} / I_{r_P} *(%)*
0	0.93	1.05	0.16	15.09	5.81	5.78	5.75	0.03	0.54
6	0.88	1.00	0.15	15.31	6.06	5.84	5.62	0.26	4.71
13	0.85	0.95	0.14	14.75	6.09	5.85	5.46	0.46	8.45
19	0.98	1.12	0.14	12.88	6.23	5.88	5.35	0.56	10.51

Like in the case presented in *subsection 8.3*, it is observed from Table 8.4 and Table 8.5 that the three-phase stator and rotor currents have a large value of the positive-sequence component I_P when the micro-WRIM is in the healthy state, i.e., with zero shorted turns on the rotor. Moreover, there is a small value of the negative-sequence component I_N in the current signals, which is attributed to the inherent asymmetry that is in the micro-DFIG.

When the rotor inter-turn occurs in *phase B*, it is observed that the rms current I_{rb} of the faulted phase increases significantly with the fault severity level and a minimal increase is also observed in the average rms current I_{r_avr}. The positive-sequence component I_{r_P} of the rotor current is observed to decrease while the negative-sequence current component I_{r_N} increases consistently with the fault severity level. In this regard, the rotor ITSCF is associated with an increase in an unwanted component, i.e., the negative-sequence component I_{r_N}, and hence, the unbalance in the rotor winding becomes more adverse with the increase in the fault severity level. Consequently, this could result in overheating of the rotor windings and potentially cause damage to the power electronic (PE) converter that is in the rotor circuit of the machine. On the other hand, there is no consistent increase observed in the positive- and negative-sequence components of the stator current, i.e., I_{s_P} and I_{s_N}.

This, as mentioned earlier, is attributed to the control effect of the power electronic converter that is in the rotor circuit. Therefore, the fault on the rotor side does not significantly influence the sequence components of the stator current signal.

Like in the case of the stator inter-turn fault scenario, it is observed that the average rms currents, the rms current of the faulted phase, and the sequence components under the low grid voltage condition have higher values (*see Table 8.4*) compared to those under the rated grid voltage condition stipulated in Table 8.5. Specifically, for the rotor inter-turn fault condition under the rated grid voltage condition, the rotor rms current of the faulted phase increased by 6.01% for 19 shorted turns and by 13.48% when considering both the low grid voltage and shorted turn fault conditions. Therefore, under the low grid voltage condition, the faulted phase carries a much higher current compared to the rated voltage condition. Furthermore, the rotor ITSCF has a significant impact on the negative-sequence component of the rotor current under either voltage condition, compared to that of the stator current. Given this observation and considering the increase in the rms current of the faulted rotor phase winding as the fault severity increases, a rotor inter-turn fault would result in the increased stator and rotor power losses, pose a potential burnout of the machine, or risk damaging the PE converter. This effect would become worse under both the rotor inter-turn fault and the low grid voltage conditions, should the rms currents end up exceeding the rated values of the machine and the PE converter system.

From the fault quantification point of view, it is observed in Table 8.4 and Table 8.5 that the ratio of the negative-sequence to the positive-sequence components in the rotor current increases consistently with the fault severity level. Whereas an opposite trend is observed in the stator current signal. Figure 8.3 (a) and (b) present the plots of the ratio I_N / I_P *(%)*, for the stator and rotor current signals, respectively, under the rated grid voltage condition:

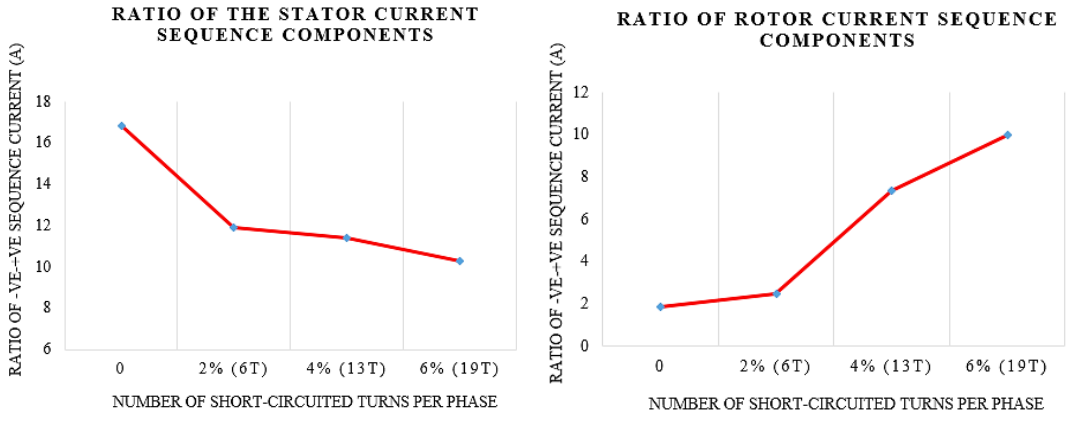

(a) (b)

Figure 8. 3: Comparison of the ratio of sequence components for different rotor ITSCF severity levels under the rated grid voltage condition, (a) stator current (b) rotor current

Whereas Fig. 8.4 (a) and (b) present the plots of the ratio I_N / I_P *(%)*, for the stator and rotor current signals, respectively, under the low grid voltage condition.

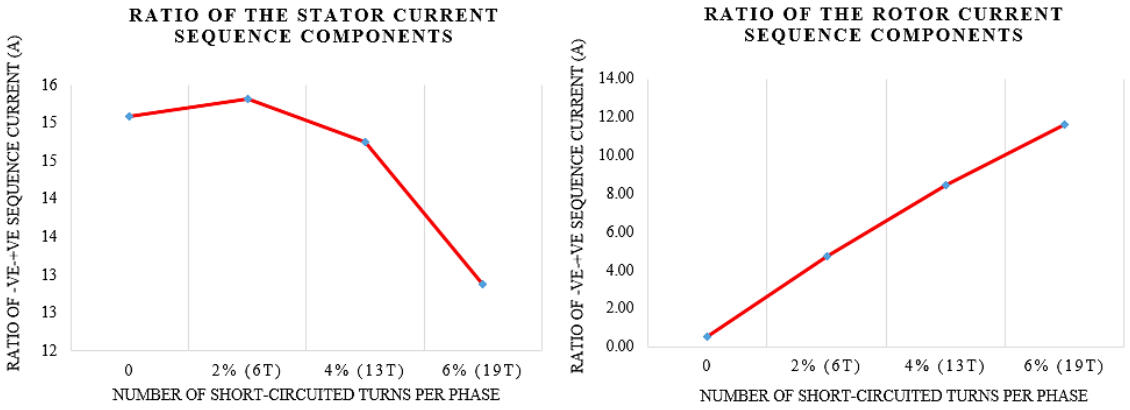

(a) (b)

Figure 8. 4: Comparison of the ratio of sequence components for different rotor ITSCF severity levels under the low grid voltage condition, (a) stator current (b) rotor current

Therefore, from Fig 8.3 and Fig. 8.4, it is deduced that the ratio of the negative-to-positive sequence components portrays a similar trend under both rated and low grid voltage conditions. Therefore, the following conclusions can be drawn:

- The increase in the rotor fault severity level is associated with a decrease in the positive-sequence component and an increase in the negative-sequence component of the rotor current signal. As such,
  - A low negative-sequence component of the rotor current corresponds to a low number of shorted turns on the rotor.
  - A high value of the negative sequence component of the rotor current corresponds to a high number of shorted turns on the rotor.
- The increase in the rotor inter-turn fault severity level is associated with an increase in the ratio of the negative sequence to the positive sequence component of the rotor current signal.
  Hence, the unbalance in the rotor winding of the micro-DFIG becomes more adverse as the fault severity increases.
- It is observed that the presence of the rotor inter-turn fault does not influence the negative-sequence component of the stator current signal. This is due to the decoupling between the rotor winding and the stator winding.
- In the same vein, the ratio of the negative sequence to the positive sequence component of the stator current signal does not follow the rising trend but it is rather inversely proportional to the increase in the rotor inter-turn fault severity.

- The current sequence components under the low grid voltage condition are slightly higher than those under the rated grid voltage condition, and so is the ratio of the negative- to positive-sequence components.
- Likewise, the worst-case scenario, i.e., the combination of the rotor inter-turn fault and the low grid voltage conditions could be detrimental to the operation of the micro-DFIG, particularly the faulted rotor phase winding, and the power electronic converter that is in the rotor circuit, should the currents exceed the rated values. This is considering that the rms current of the faulted rotor phase increases consistently with the fault severity level, and so does the negative-sequence component of the rotor current, and these values are much higher under the low grid voltage condition in comparison to the rated grid voltage condition as discussed earlier.

8.5 Chapter Summary

This chapter focused on assessing the impact of a low voltage level at the point of common coupling (PCC) on the behavior of the micro-DFIG that is in its healthy state and operated at a speed of 1230rpm (s = 0.18). The assessment was realized by determining the root-mean-square (RMS) values of the stator and rotor currents and observing their trend as the voltage at the PCC changes from the rated grid voltage (380 V_{LL}) to a slightly lower grid voltage level. i.e., 85% of the rated voltage. From the analysis presented in this section, it is observed that the current rms values under the low grid voltage condition are higher than those under the rated grid voltage condition. Whereby a significant increase or peak in current was observed in the stator current, compared to the rotor current. This is expected, considering that despite a low voltage at the PCC, the micro-DFIG was still operated in a way that ensured that the same amount of power is delivered to the grid, as in the case of the rated grid voltage condition. This behaviour means that the low voltage ride-through capability of the micro-DFIG was achieved, thus making it advantageous from the system's stability point of view. However, it is worth noting that a significant increase in the stator current could potentially run the risk of overheating the stator windings thereby accelerating the aging of the insulations, increasing power losses, and reducing the efficiency of the machine, and significantly shortening its lifespan. However, if the current remains within the rated value during the undervoltage condition, the micro-DFIG's health state will be retained.

The second focal point of this chapter was to evaluate the unbalance/asymmetry that occurs in the stator and rotor of the micro-DFIG due to the occurrence of the inter-turn winding faults in this machine. To conduct this investigation, the negative sequence components (NSC) of the stator and rotor currents were obtained, for the micro-DFIG in a healthy state and when subjected to the stator inter-turn and rotor inter-turn faults at the 2%, 4%, and 6% severity levels. The micro-DFIG was operated at a speed of 1230rpm (s = 0.18), under two grid voltage levels at the PCC.

A comparative study was carried out to investigate how reducing the voltage at the PCC affects the fault diagnosis capability of the NSC. Furthermore, the average stator and rotor rms currents, as well as the rms currents of the faulted phases on both the stator and rotor of the micro-DFIG, were presented to observe their trend as the fault severity level was increased, in addition to the change resulting from the drop in the voltage level at the PCC.

From the analyses presented earlier, the following conclusions are drawn:

- ***Stator inter-turn fault***: the stator rms current of the faulted phase increased significantly with the fault severity level, and a minimal increase was also observed in the average stator rms current. The positive-sequence component of the stator current decreased while the negative-sequence current component increased consistently with the fault severity level. On the other hand, there is no notable change observed in the average rotor rms current and the positive- and negative-sequence components of the rotor current. This is attributed to the control effect of the power electronic converter that is in the rotor circuit whereby the controllers could be coming into play to keep the rotor currents stable despite the occurrence of the stator inter-turn fault. From the fault index point of view, it has been observed that the ratio of the negative-sequence to the positive-sequence components in the stator current increases consistently with the fault severity level.

- ***Rotor Inter-turn fault***: the rotor rms current of the faulted phase increased with the fault severity level, and a minimal increase was also observed in the average rotor rms current. The positive-sequence component of the rotor current decreased while the negative-sequence current component increased consistently with the fault severity level. On the other hand, there is no notable change observed in the positive- and negative-sequence components of the stator current. This, as mentioned earlier, is attributed to the control effect of the power electronic converter. Likewise, it was observed that the ratio of the negative-sequence to the positive-sequence components in the rotor current increases consistently with the fault severity level. Whereas an opposite trend is observed in the stator current signal.

It is deduced that evaluating the impacts of the inter-turn faults on the system by assessing the negative sequence components of the captured current signals yields identical trends, under both rated and low grid voltage conditions. Therefore, the fault quantifying capability of the NSC is not diminished by the decrease in the voltage level at the PCC. It is noted that the values of the positive-sequence current components under the low grid voltage condition are slightly higher than those under the rated grid voltage condition.

The same observation has also been made for the rotor and stator rms currents for the faulted phases, most particularly the stator rms currents, whereby it was observed that the faulty stator current increased by 92.7% compared to an increase of 13.48% in the rotor rms current when a shorted turn occurred in the rotor phase winding. Overall, it is worth mentioning that this significant increase in the rms currents would result in increased stator and rotor power losses, pose a potential burnout of the machine, or risk damaging the PE converter. This could become worse under the faulty case in combination with the low grid voltage condition which is associated with a significant increase in the rms currents, should these currents end up exceeding the rated values of the machine and the PE converter system.

Examining the unbalance resulting from the inter-turn fault conditions by taking note of the ratio of the negative- to the positive-sequence component, also referred to as the current unbalance factor, it is observed that an inter-turn fault in the stator winding is associated with higher values of this component under either grid voltage conditions, compared to the rotor inter-turn fault condition. Specifically, for a 6% stator inter-turn fault, i.e., 5 shorted turns on the stator phase winding, the ratios of the stator current components are 48.09% under the rated grid voltage and 45.98% under the low grid voltage condition. On the other hand, for a 6% rotor inter-turn fault, i.e., 19 shorted turns on the rotor phase winding, the ratios of the rotor current components are 8.34% and 10.51%, under the rated and low grid voltage conditions, respectively. Given this observation, it is evident that the stator inter-turn fault condition would be more detrimental to the grid considering the high unbalance coupled with a high negative sequence injection into the grid at the PCC because of this fault, in comparison to the rotor inter-turn fault condition. The minimal unbalance from the rotor inter-turn fault is attributed to the decoupling offered by the dc-link component and the control effect of the power electronic converter that is in the rotor circuit.

Chapter 9: Conclusions and Recommendations

9.1 Conclusion

The study focused on the development of a micro-based doubly fed induction generator (DFIG) test rig for fault studies. The 5kW wound rotor induction machine (WRIM) that was used in the test rig was based on a scaled-down version of a 2.5MW DFIG. Based on the investigations conducted in this study, the following conclusions can be drawn:

9.1.1 Implementation and Testing of the DFIG's Control System through Simulations

To ensure that the operating principles of the different components of the DFIG-based WECS are thoroughly understood before implementing the DFIG system in the laboratory, the complete system was modeled and implemented in MATLAB/Simulink. The model parameters were derived from the actual hardware parameters, i.e., extracted from supplier datasheets or determined experimentally, to ensure that the simulation model resembles the practical system. The desired controller specifications that ensure a robust control system have been determined and the values have been used in the model. The dynamic testing of the complete DFIG-based WECS was carried out and it was observed that the results fully verify the expected system behaviors, hence, it was concluded that the developed control architecture can be implemented in the laboratory for practical verification and testing.

9.1.2 Development and Testing of the Laboratory-scale DFIG-based WECS

The complete experimental test rig was developed and built in the Machines Laboratory, whereby the DFIG's control system was implemented in LabVIEW FPGA. The hardware and software components of the test rig have been discussed with emphasis put on their operating principles. Experimental tests were performed on the DFIG-based laboratory test rig to validate the dynamic performance of the control system by comparing the experimental results to the simulation results presented earlier. The experimental results demonstrated a good correlation between the developed test rig and the simulation model. Therefore, it was concluded that the developed test rig can be used for further investigations such as fault studies on the micro-DFIG which was the main goal of this research investigation.

9.1.3 A Case for Micromachines in Lab-based Test Rigs and Customization of the Micromachine for Fault Implementation

An investigation was conducted to ascertain the correlation in the dimensional parameters, winding factors, and the evolution of specific electrical asymmetry indicators for an in-service large-scale DFIG, its micromachine/scaled-down version, and in a standard small-scale off-the-shelf WRIM. Based on the results presented, it has been observed that the availability of a micromachine whose dimensional parameters, winding factors, and time constants resemble those of a large-scale machine ensures an identical transient

response of the two machines. Specific to this research investigation, the micromachine assists in the development of fault detection strategies that are closely suited to the actual system. The micromachine in this study was customized by modifying the stator and rotor windings to be able to emulate interturn winding faults at different severity levels in the laboratory environment. The micromachine was also modified to make it possible to implement a static eccentricity fault.

9.1.4 Fault Diagnosis in the micro-WRIM in the absence of the Converter System

The stator and rotor current signals were captured and analyzed using the MCSA, DWT and HHT techniques to detect faults in the 5kW micro-WRIM in isolation of the converter system. Assessing the micro-WRIM in isolation of the converter constitutes a fundamental approach to fault diagnosis, which facilitates characterizing the fault signature independent of the converter's switching harmonics thus ensuring clarity in the fault diagnosis process before moving on to the more advanced closed-loop controlled DFIG. In this investigation, experimental tests were performed on the micro-WRIM under 4 scenarios: healthy state; with stator inter-turn, rotor inter-turn, and static eccentricity fault conditions. Different loading conditions have been considered for each scenario under the steady-state condition: *no load, half load and, full load*. The analysis was done under both steady-state and transient (starting) operating conditions.

Comparing the use of the stator and rotor current signals to identify which signal is better suited to diagnose the different faults in the micro-WRIM, the following deductions have been made, for each fault scenario: The stator inter-turn fault indicators in the rotor current spectrum, i.e., 98.5Hz (*no load*), 96.2Hz (*half load*), and 95.3Hz (*full load*), corresponding to $k = 1$, were more sensitive to the changes in the severity of the stator inter-turn fault compared to the fault indicators in the stator current spectrum at the different loading conditions. Therefore, the rotor current signal has been identified to be better suited for diagnosing the stator ITSCFs, compared to using the stator current signal. The same trend has been observed for the rotor interturn and the static eccentricity fault conditions, i.e., a larger change in the magnitudes of the indicators in the rotor current spectrum, compared to those in the stator current spectrum, for all loading conditions.
Under the starting transient condition, the dominant fault indicators identified evolved within the decomposition bands and settled at the frequency values, as expected. This has proven the effectiveness of using the DWT analysis techniques for inter-turn and SE fault diagnosis using the start-up stator and rotor current signals. The quantitative analysis which was carried out by determining the energy content of the frequency band(s) where the fault indicators settled at steady state has demonstrated that increasing the inter-turn fault severity resulted in increasing the energy concentrated in the frequency bands of interest. Lastly, the spectrogram plots of the rotor current signal were presented and the evolution of the fault indicator (s) during the starting transient was also observed.

9.1.5 Fault Diagnosis in the micro-DFIG in the presence of the Converter System

The stator current, rotor current, and the DFIG controller signals were captured and analyzed to detect faults in the 5kW micro-WRIM in the presence of the converter system, under both steady-state and transient operating conditions. The experimental tests were performed on the micro-DFIG under the same 4 scenarios mentioned in subsection 9.1.4. Likewise, different loading conditions have been considered for each scenario under the steady-state condition. The loading condition in this case is classified based on the amount of active power that is delivered to the power utility grid: *high load, medium load, and low load.*

The highlight of this chapter was focused on using the various DFIG controller signals in addition to the terminal stator and rotor current signals, to diagnose inter-turn faults, while delivering different amounts of active power to the utility grid. Furthermore, the static eccentricity fault condition has also been diagnosed, which has not been thoroughly explored using DFIG controller signals in literature. Based on the comparative analysis presented in this section, it has been deduced that the DFIG controller signals (specifically the *k=4*- component in the *q-axis* of the rotor error signal (*error_*I_{rq}*)*) are, by far, best suited to diagnose faults in the controlled micro-DFIG under the steady-state operating condition, compared to using the terminal stator and rotor current signals. However, it is worth noting that the stator current signal still does have a good fault diagnostic potential (specifically, the *k=4*, i.e., the *(1*$\pm$*2s) fs* component), unlike the terminal rotor current signal, under the steady-state operating condition. Under the speed-varying condition, the analysis results presented have illustrated a change in harmonic content in the detail band *d8* of the rotor current's Hilbert modulus when the micro-DFIG was subjected to the rotor and stator inter-turn fault conditions. However, no distinct change was observed in the decomposition bands of the stator current's Hilbert modulus despite the inter-turn faults that occurred in the micro-DFIG. This illustrates that the rotor current signal is better suited to diagnose the stator and rotor inter-turn faults in a micro-DFIG under the speed-varying operating condition, as opposed to using the stator current signal.

9.1.6 The Behaviour of the Micro-DFIG due to Undervoltage Conditions and Inter-turn Faults

The impact of a low voltage level at the point of common coupling (PCC) on the behavior of the micro-DFIG that is in its healthy state was assessed by determining the rms values of the stator and rotor currents and observing their trend as the voltage at the PCC was changed to 85% of the rated voltage. It was observed that the current rms values under the low grid voltage conditions are higher than those under the rated grid voltage condition, whereby a significant increase in current was observed in the stator current, compared to the rotor current. Furthermore, the study evaluated the asymmetry that occurs in the stator and rotor of the micro-DFIG due to the occurrence of the inter-turn winding faults under both the rated and low grid voltage conditions. In this regard, the negative sequence components of the stator and rotor currents were obtained when the stator and rotor inter-turn faults occur at 2%, 4%, and 6% severity levels.

It was observed that the positive-sequence components of the stator and rotor currents decreased while their negative-sequence current components increased consistently with the fault severity level. From the fault index point of view, the ratio of the negative-sequence to the positive-sequence components in the stator and rotor currents increased consistently with the fault severity level.

Overall, considering the worst-case scenario, i.e., the combination of the inter-turn fault and the low grid voltage conditions caused a significant rise in the faulted currents in comparison to the faulted cases under the rated grid voltage condition. Therefore, this scenario could become detrimental to the operation of the micro-DFIG, particularly the faulted phase windings, and the power electronic converter that is in the rotor circuit, should the currents exceed the rated values for extended periods. Examining the unbalance due to the inter-turn fault conditions by taking note of the ratio of the negative- to the positive-sequence component, it has been observed that, the stator inter-turn fault condition would be more detrimental to the grid. This is considering the high unbalance coupled with a high negative sequence injection into the grid at the PCC due to this fault, in comparison to the rotor inter-turn fault condition.

9.2 Recommendations and Future Work

Having a functioning test rig in place, potential future research investigations may be conducted by upgrading the current test rig to expand on the concept of condition monitoring, fault diagnosis, and mitigation. Moreover, further investigations may also be conducted relating to the power quality issues associated with the micromachine-based test rig. The investigations that can be considered in the upgraded test rig are stated as follow:

- For this research investigation, the focus has been on emulating the inter-turn faults as well as the static eccentricity fault condition in isolation from each other. It would be insightful to explore a scenario where these fault conditions are emulated/implemented in combination, i.e., implementation of these faults on the micromachine at the same time and diagnosed accordingly.
- Extending the usefulness of the micromachine by further customizing it to enable the practical implementation of the dynamic and mixed eccentricity fault conditions.
- Expanding the functionality of the developed experimental test rig to incorporate an appropriate fault mitigation and system maintenance strategy.
- Evaluating the impacts of the inter-turn faults on the stability of the wind energy conversion system, from a power systems perspective.
- Conducting experimental investigations on the upgraded test rig concerning power quality (PQ) and grid integration issues, when the micromachine is driven by a variable-speed wind turbine emulator (WTE).

REFERENCES

[1] Statistica. (2021, 06 Nov). *Installed Wind Power Capacity Worldwide 2001-2020*. Available: : https://www.statista.com/statistics/268363/installed-wind-power-capacity-worldwide/

[2] Global Wind Energy Council. (2018, 03 June). *Global Statistics*. Available: https://gwec.net/global-figures/graphs/

[3] D. Shah, S. Nandi, and P. Neti, "Stator-interturn-fault detection of doubly fed induction generators using rotor-current and search-coil-voltage signature analysis," *IEEE Transactions on Industry Applications*, vol. 45, pp. 1831-1842, 2009.

[4] A. Balasubramanian and R. Muthu, "Model Based Fault Detection and Diagnosis of Doubly Fed Induction Generators–A Review," *Energy Procedia*, vol. 117, pp. 935-942, 2017.

[5] E. Hamatwi and P. Barendse, "Condition monitoring and fault diagnosis of stator and rotor interturn winding faults in a DFIG-based wind turbine system: A Review," in *2020 International SAUPEC/RobMech/PRASA Conference*, Cape Town, South Africa, 2020, pp. 1-6.

[6] Q. Lu, T. Breikin, and H. Wang, "Modelling and fault diagnosis of stator inter-turn short circuit in doubly fed induction generators," in *18th IFAC World Congress*, Milano, Italy, 2011, pp. 1013-1018.

[7] M. Hossain, A. Abu-Siada, and M.-S. Energies, "Methods for advanced wind turbine condition monitoring and early diagnosis: A literature review," *Energies*, vol. 11, 2018.

[8] X. M. Hu, "Development of a System for Testing Grid-Connected Doubly Fed Induction Generators with implementation of a Three-Level Neutral-Point-Clamped Converter," Masters, Electrical Engineering, University of Cape Town, 2017.

[9] N. Sarma, P. M. Tuohy, A. Mohammed, and S. Djurović, "Rotor Electrical Fault Detection in DFIGs Using Wide-Band Controller Signals," *IEEE Transactions on Sustainable Energy*, vol. 12, pp. 623-633, 2021.

[10] N. Sarma, P. M. Tuohy, and S. Djurović, "Stator Electrical Fault Detection in DFIGs Using Wide-Band Analysis of the Embedded Signals From the Controllers," *IEEE Transactions on Energy Conversion*, vol. 36, pp. 800-811, 2021.

[11] W. Qiao and D. Lu, "A survey on wind turbine condition monitoring and fault diagnosis—Part I: Components and subsystems," *IEEE Transactions on Industrial Electronics*, vol. 62, pp. 6536-6545, 2015.

[12] P. Gangsar and R. Tiwari, "Signal based condition monitoring techniques for fault detection and diagnosis of induction motors: A state-of-the-art review," *Mechanical systems and signal processing*, vol. 144, pp. 1-37, 2020.

[13] E. Hamatwi, P. S. Barendse, and A. Khan, "Development of a Test Rig for Fault Studies on a scaled-down DFIG," in *IEEE Energy Conversion Congress and Exposition (ECCE)*, Vancover, Canada, 2021, pp. 3805-3812.

[14] E. Swana and W. Doorsamy, "Investigation of combined electrical modalities for fault diagnosis on a wound-rotor induction generator," *IEEE Access*, vol. 7, pp. 32333-32342, 2019.

[15] J. Petryna, A. Duda, and M. Sułowicz, "Eccentricity in Induction Machines—A Useful Tool for Assessing Its Level," *Energies*, vol. 14, pp. 1-26, 2021.

[16] S. Nandi, S. Ahmed, and H. A. Toliyat, "Detection of rotor slot and other eccentricity related harmonics in a three phase induction motor with different rotor cages," *IEEE Transactions on Energy Conversion*, vol. 16, pp. 253-260, 2001.

[17] J. Faiz and S. Moosavi, "Eccentricity fault detection–From induction machines to DFIG—A review," *Renewable and Sustainable Energy Reviews,* vol. 55, pp. 169-179, 2016.

[18] G. Jagadanand, L. Gopi, S. George, and J. Jacob, "Inter-turn fault detection in induction motor using stator current wavelet decomposition," *International Journal of Electrical Engineering and Technology (IJEET),* vol. 3, pp. 103-122, 2012.

[19] O. Imoru, M. A. Bhaskar, A. A. Jimoh, Y. Hama, A. T. Bolanle, and J. Tsado, "Detection of Stator Shorted-Turns Faults in Induction Machines using DC-Centered Periodogram," in *World Congress on Engineering*, London, UK, 2017.

[20] E. Hamatwi, P. S. Barendse, and A. Khan, "An Investigation into the Diagnosis of Interturn Winding Faults in a Scaled-down DFIG using the MCSA and DWT of the Stator and Rotor Current," in *IEEE Energy Congress and Exposition (ECCE)*, Vancover, Canada, 2021, pp. 3797-3804.

[21] J. Fiaz and S. M. M. Moosavi, "Eccentricity Fault Detection- from Induction Machines to DFIG - A review," *Renewable and Sustainable Energy Reviews,* vol. 55, pp. 169-179, 2016.

[22] K. Yahia, A. Cardoso, A. Ghoggal, and S. Zouzou, "Induction motors airgap-eccentricity detection through the discrete wavelet transform of the apparent power signal under non-stationary operating conditions," *ISA Transactions,* vol. 53, pp. 603-611, 2014.

[23] E. Artigao, A. Honrubia-Escribano, and E. Gomez-Lazaro, "Current signature analysis to monitor DFIG wind turbine generators: A case study," *Renewable Energy,* vol. 116, pp. 1-23, 2018.

[24] J. Thomas. (June 2017, Wind Turbine Reliability. 1-5.

[25] C. A. Walford, "Wind turbine reliability: understanding and minimizing wind turbine operation and maintenance costs," Sandia National Laboratories2006.

[26] V. Fernandez-Cavero, D. Morinigo-Sotelo, O. Duque-Perez, and J. Pons-Llinares, "A comparison of techniques for fault detection in inverter-fed induction motors in transient regime," *IEEE Access,* vol. 5, pp. 8048-8063, 2017.

[27] S. K. Yadav and P. K. Kalra, "Condition monitoring of internal combustion engine using EMD and HMM," in *Intelligent autonomous systems*, ed Berlin, Heidelberg: Springer, 2010, pp. 167-185.

[28] M. Mauntz and J. Peuser, "Identification of Critical Operation Conditions of Industrial Gearboxes by 24/7 Monitoring of Oil Quality, Oil Aging, and Additive Consumption," *Journal of Physics: Conference Series*, vol. 843, pp. 1-8, 2017.

[29] L. M. Popa, B.-B. Jensen, E. Ritchie, and I. Boldea, "Condition monitoring of wind generators," in *38th IAS Annual Meeting on Conference Record of the Industry Applications Conference, 2003.*, 2003, pp. 1839-1846.

[30] H. Douglas, P. Pillay, and P. Barendse, "Detection of interturn stator faults in doubly-fed induction generators," in *14th IAS Annual Meeting: Industry Applications Conference*, 2005, pp. 1097-1102.

[31] W. Qiao and D. Lu, "A survey on wind turbine condition monitoring and fault diagnosis—Part II: Signals and signal processing methods," *IEEE Transactions on Industrial Electronics,* vol. 62, pp. 6546-6557, 2015.

[32] O. O. Ogidi, "Modelling anf Detection of Faults in Axial-Flux Permanent Magnet Machines," PhD, Department of Electrical Engineering, University of Cape Town, Cape Town, Dec 2015.

[33] G. C. Stone, "Condition Monitoring and Diagnostics of Motor and Stator Windings – A Review," *IEEE Transactions on Industrial Informatics,* vol. 20, pp. 2073-2080, 2013.

[34] H. Dehnavifard, M. A. Khan, and P. S. Barendse, "Development of a 5kW Scaled Prototype of a 2.5MW Doubly-fed Induction Generator," *IEEE Transactions on Industry Applications,* vol. 52, pp. 4688-4698, 2016.

[35] T. Lei, "Doubly-fed Induction Generator Wind Turbine Modelling, Control and Reliability," PhD, Electrical and Electronic Engineering, University of Manchester, 2014.

[36] O. Anaya-Lara, D. Campos-Gaona, E. Moreno-Goytia, and G. Adam, *Offshore wind energy generation: control, protection, and integration to electrical systems*: John Wiley & Sons, 2014.

[37] M. Zaggout, P. Tavner, C. Crabtree, and L. Ran, "Detection of rotor electrical asymmetry in wind turbine doubly-fed induction generators," *IET Renewable Power Generation,* vol. 8, pp. 878-886, 2014.

[38] A. A. Salah and D. G. Dorrell, "Operating Induction Machine in DFIG Mode Including Rotor Asymmetry," presented at the 27th SAUPEC/RobMech/PRASA Conference, Bloemfontein, South Africa, 2019.

[39] B. B. R. Anita and B. Babypriya, "Modelling, simulation and analysis of doubly fed induction generator for wind turbines," *Journal of electrical engineering,* vol. 60, pp. 79-85, 2009.

[40] G. Mokryani, P. Siano, A. Piccolo, V. Calderaro, and C. Cecati, "A novel fuzzy system for wind turbines reactive power control," in *2011 IEEE International Conference on Fuzzy Systems (FUZZ-IEEE 2011)*, 2011, pp. 231-235.

[41] G. Abad, J. Lopez, A. M. Rodriguez, L. Marroyo, and G. Iwanski, *Doubly Fed Induction Machine: Modeling and Control for Wind Energy Generation*. Hoboken, New Jersey: John Wiley & Sons Inc., 2011.

[42] L. Lopes, J. Lhuilier, M. Khokar, and A. Mukherjee, "A wind turbine emulator that represents the dynamics of the wind turbine rotor and drive train," in *2005 IEEE 36th Power Electronics Specialists Conference*, Recife, Brazil, 2005, pp. 2092-2097.

[43] E. Hamatwi, I. E. Davidson, and M. N. Gitau, "Rotor Speed Control of a Direct-Driven Permanent Magnet Synchronous Generator-Based Wind Turbine Using Phase-Lag Compensators to Optimize Wind Power Extraction," *Journal of Control Science and Engineering,* vol. 2017, pp. 1-17, 2017.

[44] E. Hamatwi, "Control of a Permanent Magnet Synchronous Generator-based Wind Energy Conversion System," Masters of Science, Electrical, Electronic and Computer Engineering, University of KwaZulu-Natal, 2016.

[45] S. Muyeen, M. H. Ali, R. Takahashi, T. Murata, J. Tamura, Y. Tomaki, *et al.*, "Comparative study on transient stability analysis of wind turbine generator system using different drive train models," *IET Renewable Power Generation,* vol. 1, pp. 131-141, 2007.

[46] R. Araneo and M. Mitolo, *Electrical Safety Engineering of Renewable Energy Systems*: John Wiley & Sons, 2021.

[47] J. M. Kharade and D. N. G. Savagave, "A Review of HVDC Converter Topologies," *International Journal of Innovative Research in Science, Engineering and Technology,* vol. 6, pp. 1822-1830, 2017.

[48] S. Tripathi, A. Tiwari, and D. Singh, "Grid-integrated permanent magnet synchronous generator based wind energy conversion systems: A technology review," *Renewable and Sustainable Energy Reviews,* vol. 51, pp. 1288-1305, 2015.

[49] M. R. Islam, Y. Guo, and J. Zhu, "Power converters for wind turbines: Current and future development," *Materials and processes for energy: communicating current research and technological developments,* vol. 1, pp. 559-571, 2013.

[50] G. P. Adam, *Voltage Source Converter: Modulation, Modelling, Control and Applications in power Systems*. Charleston, SC, USA: CreateSpace Independent Publishing Platform, 2014.

[51] A. Antonopoulos, L. Angquist, and H.-P. Nee, "On dynamics and voltage control of the modular multilevel converter," in *2009 13th European Conference on Power Electronics and Applications*, 2009, pp. 1-10.

[52] W. Li, L.-A. Gregoire, and J. Bélanger, "Control and performance of a modular multilevel converter system," in *CIGRÉ Canada, Conference on Power Systems, Halifax*, 2011, pp. 1-8.

[53] S. S. Fazel, S. Bernet, D. Krug, and K. Jalili, "Design and comparison of 4-kV neutral-point-clamped, flying-capacitor, and series-connected H-bridge multilevel converters," *IEEE Transactions on Industry Applications*, vol. 43, pp. 1032-1040, 2007.

[54] O. Anaya-Lara, D. Campos-Gaona, E. Moreno-Goytia, and G. P. Adam, "Voltage Source Converter Topologies," in *Offshore Wind Energy Generation: Control, Protection and Integration to Electrical Systems*

[55] R. Ottersten, *On control of back-to-back converters and sensorless induction machine drives*: Chalmers University of Technology, 2003.

[56] R. Aleksandr, G. S. Marcelo, A.-D. Ahmed, and S. Muyeen, "LCL filter design and performance analysis for grid-interconnected systems," *IEEE Transactions on Industry Applications*, vol. 50, pp. 1225 - 1232, 2013.

[57] A. Belkheiri, S. Aoughellanet, and M. Belkheiri, "FPGA implementation of a space vector pulse width modulation technique for a two-level inverter," *Elektrotehniski Vestnik*, vol. 85, pp. 77-83, 2018.

[58] D. Rathnakumar, J. LakshmanaPerumal, and T. Srinivasan, "A new software implementation of space vector PWM," in *Proceedings. IEEE SoutheastCon, 2005.*, 2005, pp. 131-136.

[59] Y. Boukadida, F. Marignetti, V. Fiengo, R. Di Stefano, and C. Ungaro, "Labview FPGA-based Space Vector Modulation Control of 3-Phase Voltage Source Inverter," in *2019 Fourteenth International Conference on Ecological Vehicles and Renewable Energies (EVER)*, 2019, pp. 1-7.

[60] S. Busquets-Monge, J. Bordonau, D. Boroyevich, and S. Somavilla, "The nearest three virtual space vector PWM-a modulation for the comprehensive neutral-point balancing in the three-level NPC inverter," *IEEE power electronics letters*, vol. 2, pp. 11-15, 2004.

[61] B. Tolunay, "Space Vector Pulse Width Modulationfor Three-Level Converters: a LabVIEW Implementation," masters, Department of Electrical Engineering, Uppsala University, 2012.

[62] J. Lopez-Sarabia, G. Escobar, P. R. Martinez-Rodriguez, S. Iturriaga-Medina, J. Mayo-Maldonado, and D. Del Puerto-Flores, "DC-Link capacitors voltage balance in an HB-NPC five-level grid-tied inverter via the common-mode control component," *IEEE Journal of Emerging and Selected Topics in Power Electronics*, 2021.

[63] J. Pou, D. Boroyevich, and R. Pindado, "New feedforward space-vector PWM method to obtain balanced AC output voltages in a three-level neutral-point-clamped converter," *IEEE transactions on industrial electronics*, vol. 49, pp. 1026-1034, 2002.

[64] N. Celanovic and D. J. I. t. o. i. a. Boroyevich, "A fast space-vector modulation algorithm for multilevel three-phase converters," vol. 37, pp. 637-641, 2001.

[65] A. Petersson, *Analysis, modeling and control of doubly-fed induction generators for wind turbines*: Chalmers University of Technology, 2005.

[66] G. Tapia, A. Tapia, and J. X. Ostolaza, "Two alternative modeling approaches for the evaluation of wind farm active and reactive power performances," *IEEE transactions on energy conversion*, vol. 21, pp. 909-920, 2006.

[67] N. S. Nise, *CONTROL SYSTEMS ENGINEERING*, 6th ed.: John Wiley & Sons, 2011.

[68] M. Morari and E. Zafiriou, *Robust process control*. Englewood Cliffs: Prentice Hall, 1989.

[69] L. Harnefors and H.-P. Nee, "Model-based current control of AC machines using the internal model control method," *IEEE Transactions on Industry Applications,* vol. 34, pp. 133-141, 1998.

[70] L. Harnefors and H.-P. Nee, "Robust current control of AC machines using the internal model control method," in *Conference Record of the 1995 IEEE Industry Applications Conference Thirtieth IAS Annual Meeting*, Orlando, FL, USA, 1995, pp. 303-309.

[71] R. Ottersten, "On control of back-to-back converters and sensorless induction machine drives," PhD, Department of Electric Power Enginering, Chalmers University of Technology, 2003.

[72] D. Campos-Gaona, E. L. Moreno-Goytia, and O. Anaya-Lara, "Fault ride-through improvement of DFIG-WT by integrating a two-degrees-of-freedom internal model control," *IEEE Transactions on Industrial Electronics,* vol. 60, pp. 1133-1145, 2012.

[73] S. K. Senapati and A. K. Swain, "Modeling and simulation of AC/DC grid side voltage source converter used in wind power generation system," in *2014 International Conference on Circuits, Power and Computing Technologies [ICCPCT-2014]*, 2014, pp. 484-489.

[74] S. Li, R. Challoo, and M. J. Nemmers, "Comparative study of DFIG power control using stator-voltage and stator-flux oriented frames," in *IEEE Power & Energy Society General Meeting*, 2009, pp. 1-8.

[75] G. Tapia, G. Santamaria, M. Telleria, and A. Susperregui, "Methodology for smooth connection of doubly fed induction generators to the grid," *IEEE transactions on energy conversion,* vol. 24, pp. 959-971, 2009.

[76] J. Cortajarena, J. De Marcos, P. Alvarez, F. Vicandi, and P. Alkorta, "Start up and control of a DFIG wind turbine test rig," in *IECON 2011-37th Annual Conference of the IEEE Industrial Electronics Society*, 2011, pp. 2030-2035.

[77] I. S. 493-2007, "Recommended Practice for the Design of Reliable Industrial and Commercial Power Systems," ed, 2007, pp. 272-273.

[78] S. Nandi, H. A. Toliyat, and X. Li, "Condition monitoring and fault diagnosis of electrical motors—A review," *IEEE transactions on energy conversion,* vol. 20, pp. 719-729, 2005.

[79] S. Nandi, T. C. Ilamparithi, S. B. Lee, and D. Hyun, "Detection of eccentricity faults in induction machines based on nameplate parameters," *IEEE Transactions on Industrial Electronics,* vol. 58, pp. 1673-1683, 2010.

[80] S. Nandi, R. M. Bharadwaj, and H. A. Toliyat, "Performance analysis of a three-phase induction motor under mixed eccentricity condition," *IEEE Transactions on Energy Conversion,* vol. 17, pp. 392-399, 2002.

[81] J. Antonino-Daviu, P. J. Rodriguez, M. Riera-Guasp, M. Pineda-Sanchez, and A. Arkkio, "Detection of combined faults in induction machines with stator parallel branches through the DWT of the startup current," *Mechanical Systems and Signal Processing,* vol. 23, pp. 2336-2351, 2009.

[82] O. Imoru, M. A. Bhaskar, A. A. Jimoh, and Y. Hamam, "Ealry Diagnosis of Induction Machine Stator Winding Faults by Discrete Wavelet Transform," *International Jounral of Emerging Electric Power Systems,* pp. 1-12, 2017.

[83] O. Imoru, M. A. Bhaskar, A. A. Jimoh, and Y. Hamam, "Diagnosis of Stator Shorted-turn faults in Induction Machines using discrete wavelet transform," *African Journal of Science, Technology, Innovation and Development,* vol. 9, pp. 349-355, 2017.

[84] W. Yang, P. Tavner, and M. Wilkinson, "Condition monitoring and fault diagnosis of a wind turbine synchronous generator drive train," *IET Renewable Power Generation,* vol. 3, pp. 1-11, 2009.

[85] S. Bindu and V. V. Thomas, "Diagnoses of internal faults of three phase squirrel cage induction motor—A review," in *International Conference on Advances in Energy Conversion Technologies (ICAECT)*, Manipal, India, 2014, pp. 48-54.

[86] W. T. Thomson and M. Fenger, "Case histories of current signature analysis to detect faults in induction motor drives," in *IEEE International Electric Machines and Drives Conference, 2003. IEMDC'03.*, 2003, pp. 1459-1465.

[87] K. Prakasam and S. Ramesh, "Investigation of Induction Motor Stator Faults Using Motor Current Signature Analysis and Multisim," *Middle-East Journal of Scientific Research,* vol. 23, pp. 277-284, 2015.

[88] D. Miljković, "Brief review of motor current signature analysis," *HDKBR Info magazin,* vol. 5, pp. 14-26, 2015.

[89] T. Thomson, "On-line MCSA to Diagnose Shorted Turns in Low Voltage Stator Windings of 3-phase Induction Motors Prior to Failure," in *IEEE Conference on Electrical Machines and Drives (IEMDC)*, Boston Massachusetts, 2001, pp. 891-898.

[90] W. T. Thomson and R. J. Gilmore, "Motor Current Signature Analysis to Detect Faults in Induction Motor Drives- Fundamentals, Data Interpretation, and Industrial Case Histories," in *32nd Turbomachinery Symposium*, Houston, Texas, September 2003, pp. 146-156.

[91] J. Cusido, L. Romeral, J. A. Ortega, J. Rosero, and A. G. Espinosa, "Fault Detection in Induction Machines using Power Spectral Density in Wavelet Decomposition," *IEEE Transactions on Industrial Electronics,* vol. 55, pp. 633-643, February 2008.

[92] H. H and R. Dahiya, "Condition monitoring of wind turbine for rotor fault detection under non stationary conditions," *Ain Shams Engineering Journal*, pp. 2441–2452, 2017.

[93] Y. Gritli, C. Rossi, D. Casadei, F. Filippetti, and G. A. Capolino, "A Diagnostic Space Vector-based Index for Rotor Electrical Fault Detection in Wound-Rotor Induction Machines Under Speed Transient," *IEEE Transactions on Industrial Electronics,* vol. 64, pp. 3892-3902, 2017.

[94] M. Dlamini, P. Barendse, and A. Khan, "Detecting faults in inverter-fed induction motors during startup transient conditions," in *2014 IEEE Energy Conversion Congress and Exposition (ECCE)*, 2014, pp. 3131-3138.

[95] H. Douglas, P. Pillay, and A. Ziarani, "Detection of broken rotor bars in induction motors using wavelet analysis," in *IEEE International Electric Machines and Drives Conference,* Madison, WI, USA,, 2003, pp. 923-928.

[96] M. A. S. A. Tobi, G. Bevan, P. Wallace, D. Harrison, and P. K. Ramachandran, "A review on applications of wavelet transform and artificial intelligence systems in fault diagnosis of rotating machinery," *International Journal of Industrial Electronics and Electrical Engineering,* vol. 4, pp. 70-82, Sept 2016.

[97] O. Imoru, "Detection and Diagnosis of Faults in Electrical Machines," PhD, Electrical Engineering, Tshwane University of Technology, Tshwane, South Africa, 2017.

[98] Y. Gritli, A. Stefani, F. Filippetti, and A. Chatti, "Stator fault analysis based on wavelet technique for wind turbines equipped with DFIG," in *2009 International Conference on Clean Electrical Power*, Capri, Italy, 2009, pp. 485-491.

[99] M. E. H. Benbouzid and G. B. Kliman, "What stator current processing-based technique to use for induction motor rotor faults diagnosis?," *IEEE Transactions on Energy Conversion*, vol. 18, pp. 238-244, 2003.

[100] R. N. Dash, B. Subudhi, and S. Das, "Induction motor stator inter-turn fault detection using wavelet transform technique," in *2010 5th International Conference on Industrial and Information Systems*, 2010, pp. 436-441.

[101] H. H. Eldeeb, H. Zhao, and O. Mohammed, "Wavelet transformation-based diagnosis of turn-to-turn faults in vector control drive system," in *IEEE Energy Conversion Congress and Exposition (ECCE)*, 2019, pp. 339-344.

[102] R. Yan, R. X. Gao, and X. Chen, "Wavelets for fault diagnosis of rotary machines: A review with applications," *Signal processing*, pp. 1-15, 2014.

[103] M. Riera-Guasp, J. A. Antonino-Daviu, M. Pineda-Sanchez, R. Puche-Panadero, and J. Pérez-Cruz, "A general approach for the transient detection of slip-dependent fault components based on the discrete wavelet transform," *IEEE transactions on Industrial electronics*, vol. 55, pp. 4167-4180, Dec 2008.

[104] M. J. Gómez, C. Castejón, and J. C. García-Prada, "Review of recent advances in the application of the wavelet transform to diagnose cracked rotors," *Algorithms*, vol. 9, pp. 1-13, 2016.

[105] M. Dlamini, "Development of an Induction Motor Condition Monitoring Test Rig and Fault Detection Strategies," Masters in Electrical Engineering, Electrical Engineering, University of Cape Town, 2014.

[106] J. Cusido, L. Romeral, J. Ortega, A. Garcia, and J. Riba, "Wavelet and PDD as fault detection techniques," *Electric Power Systems Research*, vol. 80, pp. 915-924, 2010.

[107] D. Jiang and C. Liu, "Machine condition classification using deterioration feature extraction and anomaly determination," *IEEE Transactions on Reliability*, vol. 60, pp. 41-48, March 2011.

[108] J. C. Hernández, J. Antonino-Daviu, F. Martínez-Giménez, and A. Peris, "Comparison of different wavelet families for broken bar detection in induction motors," in *2015 IEEE International Conference on Industrial Technology (ICIT)*, Seville, Spain, 2015, pp. 3220-3225.

[109] D. Sonje, P. Kundu, and A. Chowdhury, "A Novel Approach for Sensitive Interturn Fault Detection in Induction Motor Under Various Operating Conditions," *Arabian Jounral of Science and Engineering*, vol. 44, pp. 6887-6900, 2019.

[110] A. U. Rehman, Y. Chen, M. Zhang, Y. Zhao, L. Wang, Y. Liu, *et al.*, "Fault detection and fault severity calculation for rotor windings based on spectral, wavelet and ratio computation analyses of rotor current signals for a doubly fed induction generator in wind turbines," *Electrical Engineering*, pp. 1-12, 2020.

[111] G. Bin, J. Gao, X. Li, and B. Dhillon, "Early fault diagnosis of rotating machinery based on wavelet packets—Empirical mode decomposition feature extraction and neural network," *Mechanical Systems and Signal Processing*, vol. 27, pp. 696-711, 2012.

[112] C. Shen, D. Wang, F. Kong, and W. T. Peter, "Fault diagnosis of rotating machinery based on the statistical parameters of wavelet packet paving and a generic support vector regressive classifier," *Measurements*, vol. 46, pp. 1551-1564, 2013.

[113] H. Dehnavifard, "Development of a Scaled Doubly-Fed Induction Generator for Assessment of Wind Power Integration Issues," PhD, Electrical Engineering, University of Cape Town, 2016.

[114] P. C. Sen, *Principles of Electric Machines and Power Electronics*, 3rd ed. Canada: John Wiley & Sons, 2014.

[115] I. D. Ilina, "Experimental determination of moment to inertia and mechanical losses vs. speed, in electrical machines," in *2011 7th International Symposium on Advanced Topics in Electrical Engineering (ATEE)*, 2011, pp. 1-4.

[116] R. Babau, I. Boldea, T. Miller, and N. Muntean, "Complete parameter identification of large induction machines from no-load acceleration–deceleration tests," *IEEE Transactions on Industrial Electronics,* vol. 54, pp. 1962-1972, 2007.

[117] R. Solomon, M. Khan, P. Barendse, P. Pillay, and K. Folly, "Review and application of micromachines for wind energy integration," in *2012 XXth International Conference on Electrical Machines*, 2012, pp. 2151-2157.

[118] S. Williamson and S. Djurovic, "Origins of stator current spectra in DFIGs with winding faults and excitation asymmetries," in *2009 IEEE International Electric Machines and Drives Conference*, 2009, pp. 563-570.

[119] J. Faiz, S. M. Moosavi, M. B. Abadi, and S. M. Cruz, "Magnetic equivalent circuit modelling of doubly-fed induction generator with assessment of rotor inter-turn short-circuit fault indices," *IET Renewable Power Generation,* vol. 10, pp. 1431-1440, 2016.

[120] D. Limebeer, R. Harley, M. Lahoud, and H. Nattrass, "Laboratory measurements of subsynchronous resonance," *IFAC Proceedings Volumes,* vol. 13, pp. 327-340, 1980.

[121] S. Berchen, K. Reichert, and E. Thaler, "Micromachine for Real-Time Generator Simulation Design Limits and a Novel Solution with Adjustable Parameters," *IEEE Transactions on Energy Conversion,* vol. 9, pp. 624-634, 1989.

[122] E. Artigao, A. Honrubia-Escribano, and E. Gómez-Lázaro, "In-service wind turbine DFIG diagnosis using current signature analysis," *IEEE Transactions on Industrial Electronics,* vol. 67, pp. 2262-2271, 2020.

[123] S. Berchten, K. Reichert, and E. Thaler, "Micromachine for real-time generator simulation design limits and a novel solution with adjustable parameters," *IEEE Power Engineering Review,* vol. 9, pp. 38-39, 1989.

[124] N. Sarma, P. M. Tuohy, and S. Djurovic, "Stator Electrical Fault Detection in DFIGs using Wide-band Analysis of the Embedded Signals from the Controllers," *IEEE Transactions on Energy Conversion,* 2020.

[125] N. Sarma, P. M. Tuohy, A. Mohammed, and S. Djurovic, "Rotor Electrical Fault Detection in DFIGs using Wide-band Controller Signals," *IEEE Transactions on Sustainable Energy,* 2020.

[126] S. Djurovic, C. J. Crabtree, P. J. Tavner, and A. Smith, "Condition monitoring of wind turbine induction generators with rotor electrical asymmetry," *IET Renewable Power Generation,* vol. 6, pp. 207-216, 2012.

[127] E. Artigao Andicoberry, "Current signature analysis to diagnose doubly-fed induction generators of in-service wind turbines," PhD: Industrial Engineering, University of Castilla-La Mancha, Spain, Electrical Engineering, 2018.

[128] J. C. Roura and J. L. R. Martinez, "Transient Analysis and Motor Fault Detection using the Wavelet Transform," in *Discrete Wavelet Transforms- Theory and Applications*, J. T. Olkkonen, Ed., ed Rijeka, Croatia: InTech Europe, 2011.

[129] Y. Gritli, L. Zarri, C. Rossi, F. Filippetti, G.-A. Capolino, and D. Casadei, "Advanced diagnosis of electrical faults in wound-rotor induction machines," *IEEE Transactions on Industrial Electronics,* vol. 60, pp. 4012-4024, 2012.

[130] A. Stefani, A. Yazidi, C. Rossi, F. Filippetti, D. Casadei, and G.-A. Capolino, "Doubly fed induction machines diagnosis based on signature analysis of rotor modulating signals," *IEEE Transactions on industry applications,* vol. 44, pp. 1711-1721, 2008.

[131] Y. Gritli, A. Stefani, C. Rossi, F. Filippetti, and A. Chatti, "Experimental validation of doubly fed induction machine electrical faults diagnosis under time-varying conditions," *Electric Power Systems Research,* vol. 81, pp. 751-766, 2011.

[132] Y. Gritli, A. Stefani, A. Chatti, C. Rossi, and F. Filippetti, "The combined use of the instantaneous fault frequency evolution and frequency sliding for advanced rotor fault diagnosis in DFIM under time-varying condition," in *2009 35th Annual Conference of IEEE Industrial Electronics*, 2009, pp. 3471-3476.

[133] R. K. Ibrahim, S. J. Watson, S. Djurović, and C. J. Crabtree, "An effective approach for rotor electrical asymmetry detection in wind turbine DFIGs," *IEEE Transactions on Industrial Electronics,* vol. 65, pp. 8872-8881, 2018.

[134] H. Hooshmandi Safa, M. Ebrahimi, A. Davoudi, and A. Pouramin, "Analytical derivation of induction motors inductances under eccentricity conditions," *Progress In Electromagnetics Research,* vol. 60, pp. 95-110, 2014.

[135] J. Faiz and S. Moosavi, "Review of eccentricity fault detection techniques in IMs focusing on DFIG," in *2015 IEEE 5th International Conference on Power Engineering, Energy and Electrical Drives (POWERENG)*, Riga, Latvia, 2015, pp. 513-520.

[136] Puche-Panadero, M. Pineda-Sanchez, M. Riera-Guasp, J. Roger-Folch, E. Hurtado-Perez, and J. Perez-Cruz, "Improved Resolution of the MCSA Method Via Hilbert Transform, Enabling the Diagnosis of Rotor Asymmetries at Very Low Slip," *IEEE Transactions on Energy Conversion,* vol. 24, pp. 52-59, 2009.

[137] B. Xu, L. Sun, L. Xu, and G. Xu, "Improvement of the Hilbert method via ESPRIT for detecting rotor fault in induction motors at low slip," *IEEE Transactions on Energy Conversion,* vol. 28, pp. 225-233, 2013.

[138] M. Sahraoui, A. Ghoggal, S. Guedidi, and S. E. Zouzou, "Detection of inter-turn short-circuit in induction motors using Park–Hilbert method," *International Journal of System Assurance Engineering and Management,* vol. 5, pp. 337-351, 2014.

[139] J. A. Antonino-Daviu, M. Riera-Guasp, M. Pineda-Sanchez, and R. B. Perez, "A critical comparison between DWT and Hilbert–Huang-based methods for the diagnosis of rotor bar failures in induction machines," *IEEE Transactions on Industry Applications,* vol. 45, pp. 1794-1803, 2009.

[140] M. Sahraoui, S. E. Zouzou, A. Ghoggal, and S. Guedidi, "A New Method to Detect Inter-turn Short-Circuit in Induction Motors," presented at the XIX International Conference on Electrical Machines (ICEM), Rome, Italy, 2003.

[141] B. Akin, U. Orguner, H. A. Toliyat, and M. Rayner, "Low order PWM inverter harmonics contributions to the inverter-fed induction machine fault diagnosis," *IEEE Transactions on Industrial Electronics,* vol. 55, pp. 610-619, 2008.

[142] A. Bellini, F. Filippetti, G. Franceschini, and C. Tassoni, "Closed-loop control impact on the diagnosis of induction motors faults," *IEEE transactions on Industry Applications,* vol. 36, pp. 1318-1329, 2000.

[143] J. C. Gomez, M. M. Morcos, C. A. Reineri, and G. N. Campetelli, "Behavior of induction motor due to voltage sags and short interruptions," *IEEE Transactions on Power Delivery,* vol. 17, pp. 434-440, 2002.

[144] L. Guasch, F. Córcoles, and J. Pedra, "Effects of symmetrical and unsymmetrical voltage sags on induction machines," *IEEE Transactions on power delivery*, vol. 19, pp. 774-782, 2004.

[145] H. Elena, L. Ionel, and C. Anca, "Impact of three-phase voltage dips on the induction motors-An experimental study," in *4th International Symposium on Electrical and Electronics Engineering (ISEEE)*, Galati, Romania, 2013, pp. 1-6.

[146] S. Kamble and C. Thorat, "Voltage sag characterization in a distribution systems: A case study," *Journal of Power and Energy Engineering*, vol. 2, pp. 546-553, 2014.

[147] NERSA, "Grid Connection Code for Renewable Power Plants (RPPs) Connected to the Electricity Transmission System (TS) of the Distribution System (DS) in South Africa," ed, 2014.

[148] B. Nhlapo and K. Awodele, "Review and comparison of the South African grid code requirements for wind generation with the European countries' grid codes," in *2020 International SAUPEC/RobMech/PRASA Conference*, 2020, pp. 1-6.

[149] S. Ncwane and K. A. Folly, "A review of the impact of integrating wind generation on transient stability," in *2020 International SAUPEC/RobMech/PRASA Conference*, 2020, pp. 1-6.

[150] P. Gnacinski, "Windings temperature and loss of life of an induction machine under voltage unbalance combined with over-or undervoltages," *IEEE Transactions on Energy Conversion*, vol. 23, pp. 363-371, 2008.

[151] S. Chauhan and S. B. Singh, "Effects of voltage unbalance and harmonics on 3-Phase induction motor during the condition of undervoltage and overvoltage," in *2019 6th International Conference on Signal Processing and Integrated Networks (SPIN)*, 2019, pp. 1141-1146.

[152] G. Yaleinkaya, M. H. Bollen, and P. A. Crossley, "Characterization of voltage sags in industrial distribution systems," *IEEE transactions on industry applications*, vol. 34, pp. 682-688, 1998.

[153] Y. Chen, A. U. Rehman, Y. Zhao, L. Wang, S. Wang, M. Zhang, *et al.*, "Numerical Modeling, Electrical Characteristics Analysis and Experimental Validation of Severe Inter-Turn Short Circuit Fault Conditions on Stator Winding in DFIG of Wind Turbines," *IEEE Access*, vol. 9, pp. 13149-13158, 2021.

APPENDINCES

APPENDIX A: Datasheets of the Hardware Components and Schematic Diagrams

A.1 PXI Controller Datasheets

- **Chassis***: PXIe-1062Q*: https://www.ni.com/pdf/manuals/371843d.pdf
- **DAQ card***: PXIe -6363*: https://www.ni.com/pdf/manuals/377776a.pdf
- **CPU card***: PXIe-8108*: https://www.ni.com/pdf/manuals/372810b.pdf
- **FPGA card***: PXI-7813R*: https://www.ni.com/pdf/manuals/370489g.pdf
- **Shielded Connector boards***: SCB-68*: https://www.ni.com/pdf/manuals/371745c.pdf

A.2 Voltage Source Converter-related Datasheets

- **2-Level VSC IGBTs***: SKM200GB12V*: https://www.semikron.com/products/product-classes/igbt-modules/detail/skm200gb12v-22892064.html
- **3-Level NPC VSC IGBTs***: SKiM201MLI12E4*: https://www.semikron.com/products/product-classes/igbt-modules/detail/skim201mli12e4-23918890.html
- **Gate Drivers***: SKHI22B12*: https://www.semikron.com/products/product-classes/igbt-driver/detail/skhi-22-ab-h4-r-l501252l5012524.html
- **Signal Level-shifter AND gates***: MN74HC08*: https://assets.nexperia.com/documents/data-sheet/74HC_HCT08.pdf

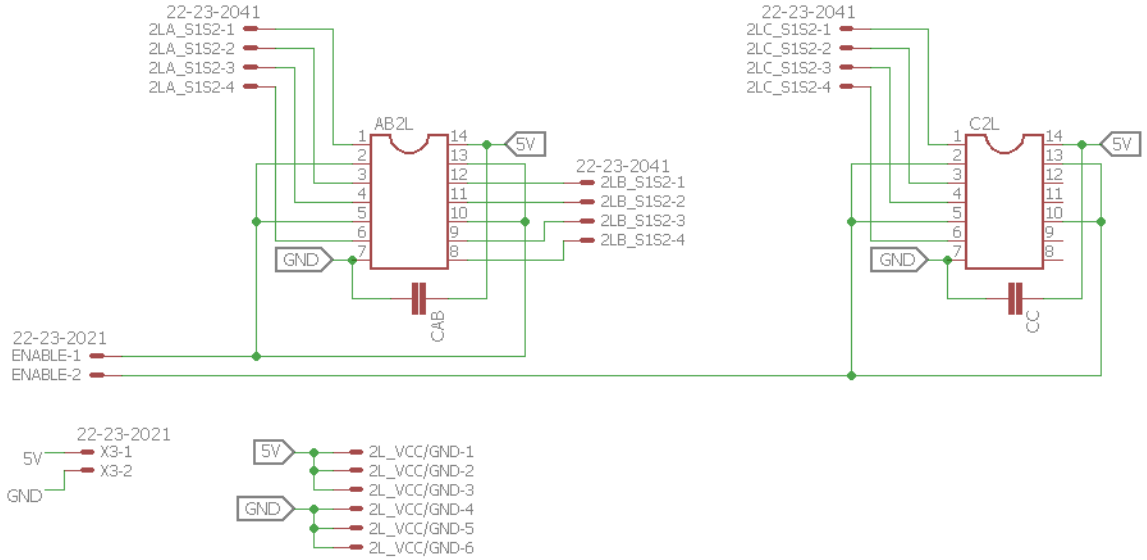

(a)

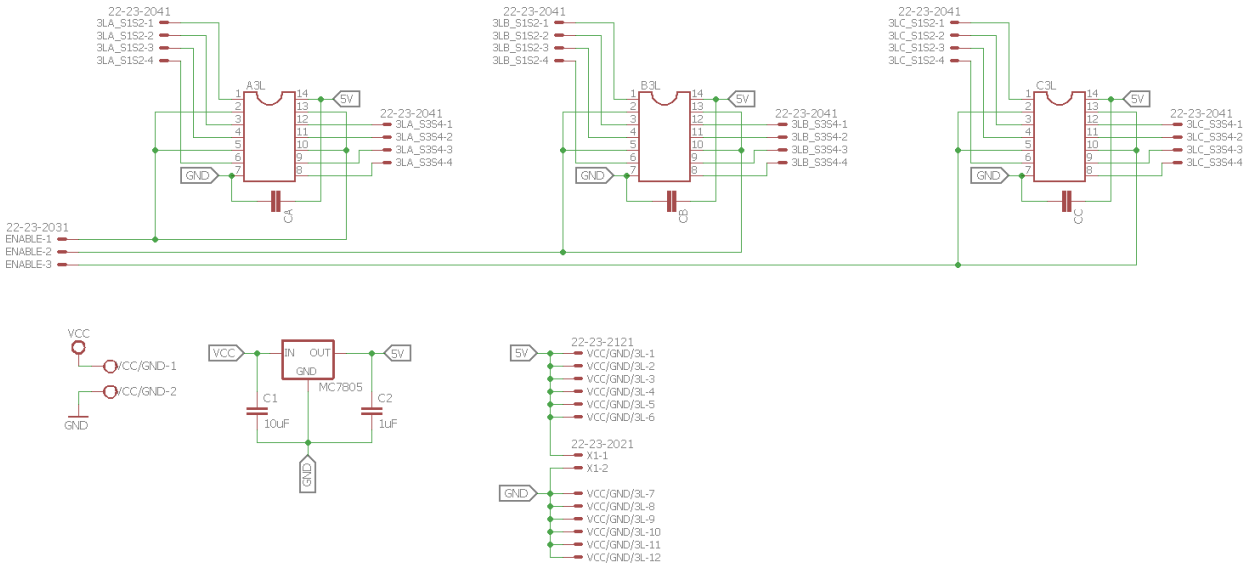

(b)

Figure A. 1: Schematic diagram of the FPGA level shifter: (a) for the 2-level VSC, (b) for the 3-level VSC

A.3 Voltage and Current Transducers' Datasheets

- **Voltage**: *LEM LV 25-P*: https://www.lem.com/sites/default/files/products_datasheets/lv_25-p.pdf
- **Current**: *LEM LA 100-A*: https://www.lem.com/sites/default/files/products_datasheets/la_100-p_e_.pdf

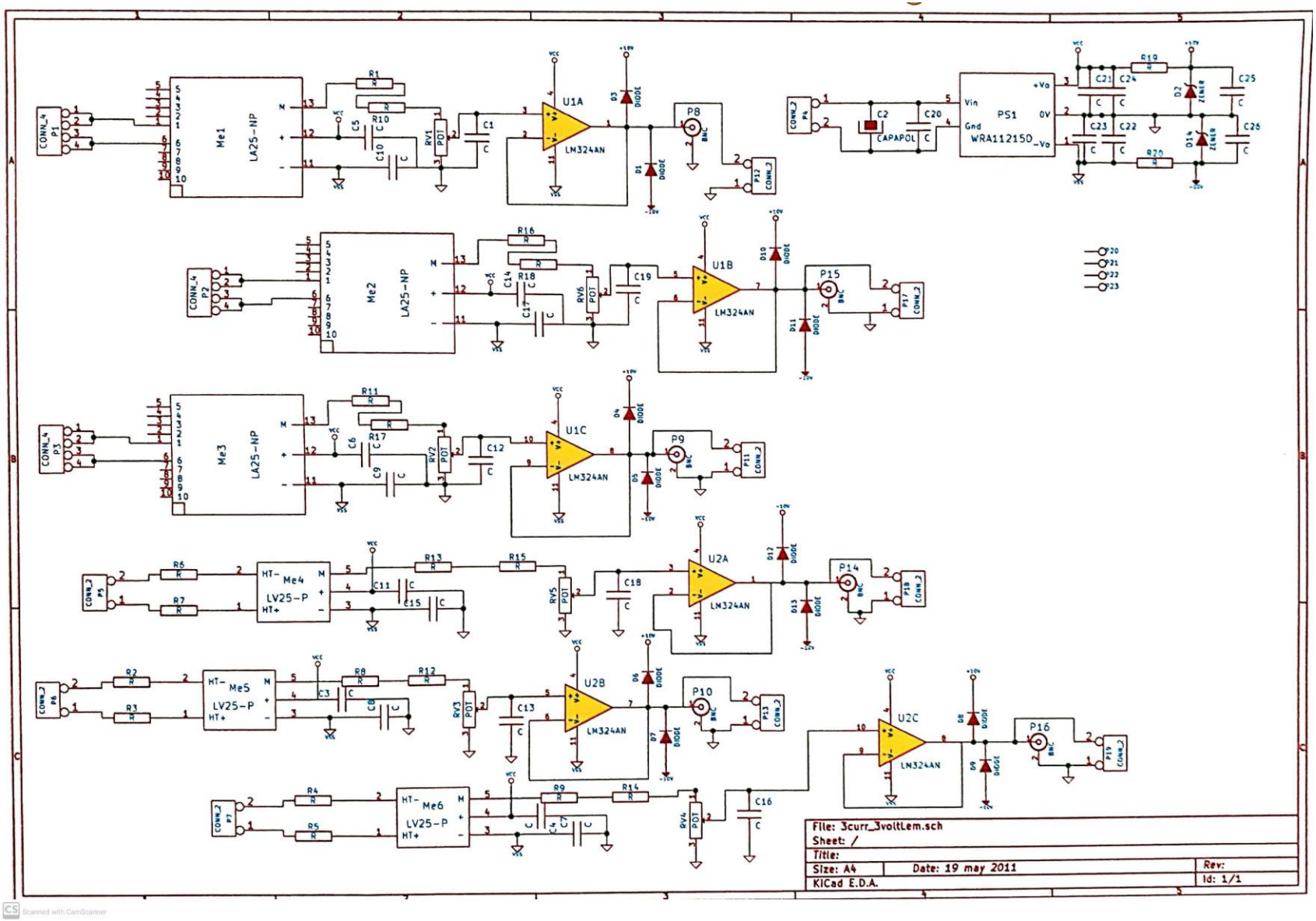

Figure A. 2: Schematic diagram of the LEM integrated circuit board

A.4 Incremental Encoder related Datasheets

- **Encoder**: *RS58-0/1000*: https://www.hengstler.de/gfx/file/shop/encoder/RI58/datasheet_ri58-o_2020_en.pdf
- **Differential Driver**: *AM26LS31CN*: https://www.ti.com/document viewer/AM26LS31/datasheet/device-images-dv#dv
- **Differential Receiver**: *AM26LS31ACN*: https://www.ti.com/lit/ds/symlink/am26ls32ac.pdf?ts=1624609200894&ref_url=https%253A%252F%252Fwww.ti.com%252Fstore%252Fti%252Fen%252Fp%252Fproduct%252F%253Fp%253DAM26LS32ACPWR

A.5 Schematic Diagrams of the protection circuitry

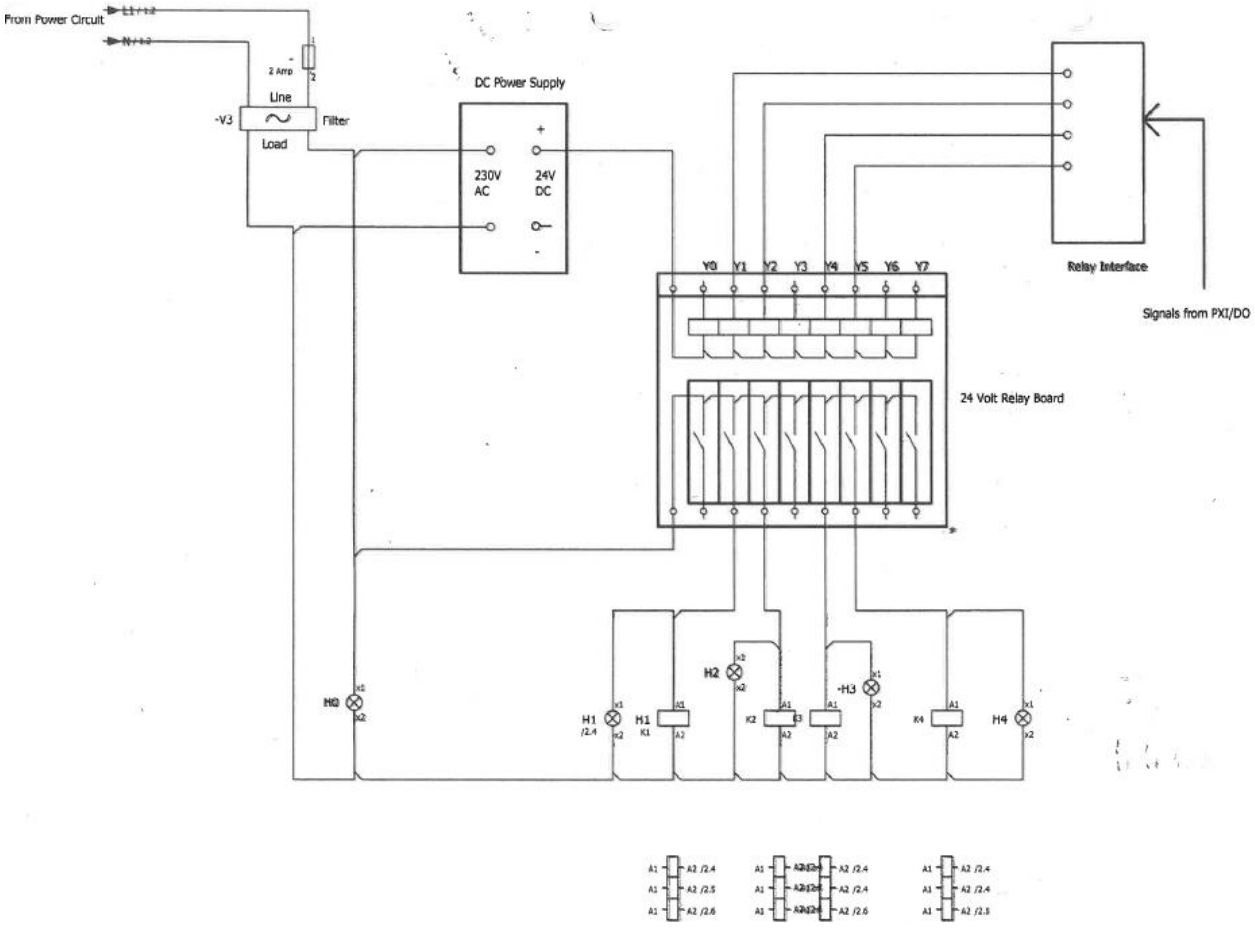

(a)

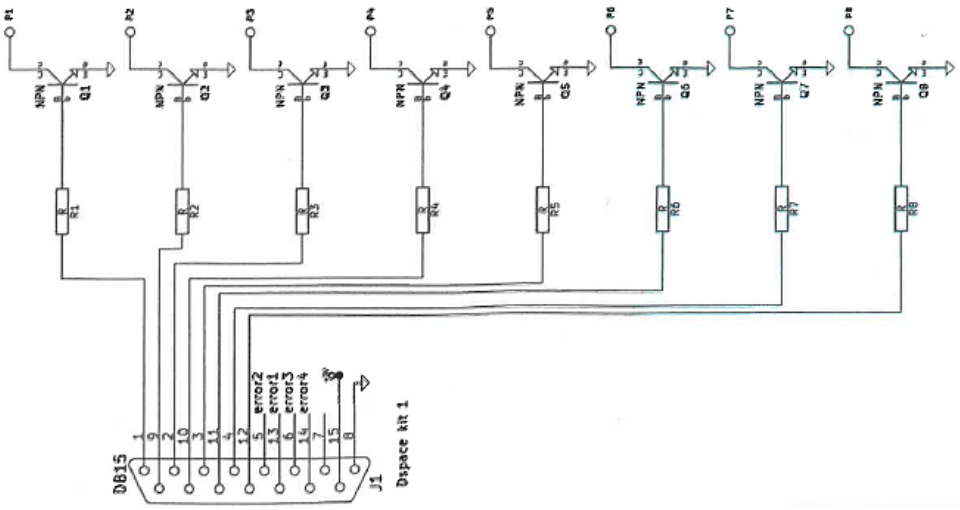

(b)

Figure A. 3: Schematic diagram of the protection circuitry: (a): Overall, (b) Buffer circuit/relay interface

APPENDIX B: The Winding Profiles of the Stator and Rotor of the 5kW WRIM

Table B. 1: The micro-DFIG winding details

Parameter	Stator	Rotor
Turn per coil	4	4
Winding Layers	2	2
Parallel Branches	2	1
Coil Pitch	7	5
Number of Strands	2	3
Wire diameter range [mm]	1.829	0.724

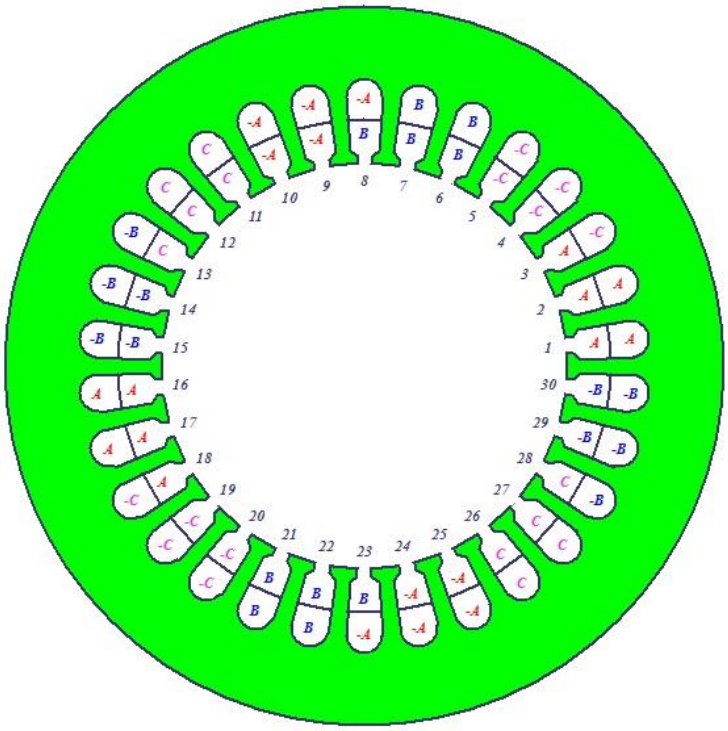

	Phase	Turns	In Slot	Out Slot
Coil_1	A	4	1T	8B
Coil_2	A	4	2T	9B
Coil_3	A	4	3T	10B
Coil_4	-C	4	4T	11B
Coil_5	-C	4	5T	12B
Coil_6	B	4	6T	13B
Coil_7	B	4	7T	14B
Coil_8	B	4	8T	15B
Coil_9	-A	4	9T	16B
Coil_10	-A	4	10T	17B
Coil_11	C	4	11T	18B
Coil_12	C	4	12T	19B
Coil_13	C	4	13T	20B
Coil_14	-B	4	14T	21B
Coil_15	-B	4	15T	22B

(a)

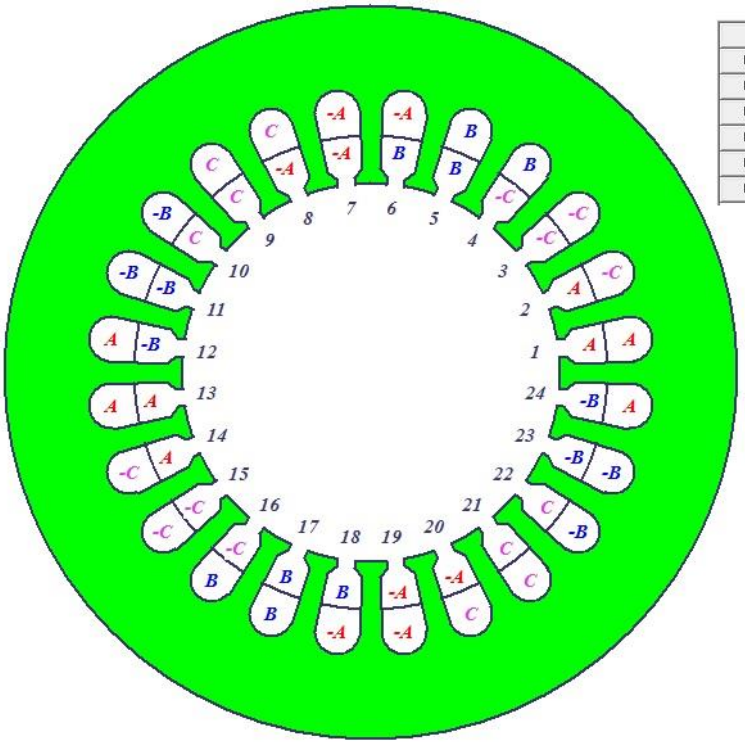

	Phase	Turns	In Slot	Out Slot
Coil_1	A	20	1T	6B
Coil_2	A	20	2T	7B
Coil_3	-C	20	3T	8B
Coil_4	-C	20	4T	9B
Coil_5	B	20	5T	10B
Coil_6	B	20	6T	11B

(b)

Figure B. 1: The micro-DFIG's Winding Profile for: (a) the stator, (b) the rotor

APPENDIX C: Layout of Short-Circuiting the External Tapping Points to Emulate the Stator and Rotor Inter-turn Short-Circuit Winding Faults

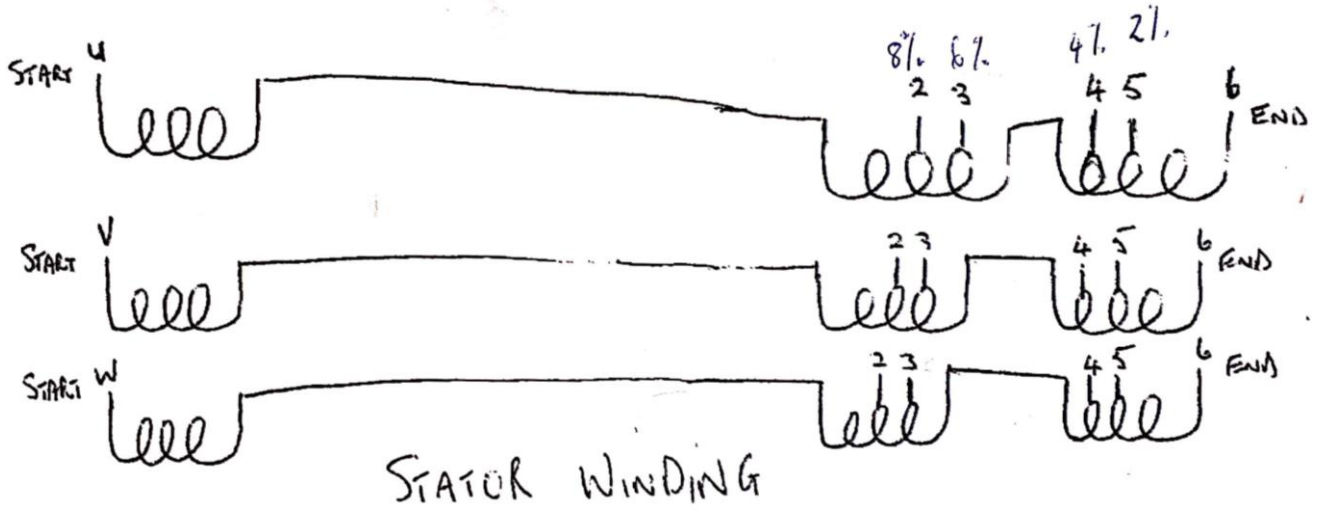

(a)

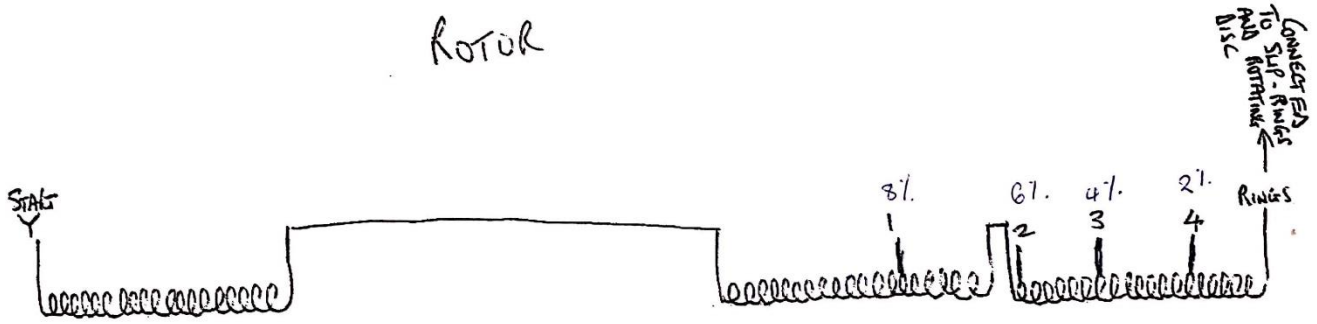

(b)

Figure C. 1: Layout of Short-Circuiting the External Tapping Points to Implement the Inter-turn Faults on the (a) stator winding (b) rotor winding

APPENDIX D: LabVIEW GUI and Codes

D.1 Labview RT Graphical User Interface (GUI)

(a)

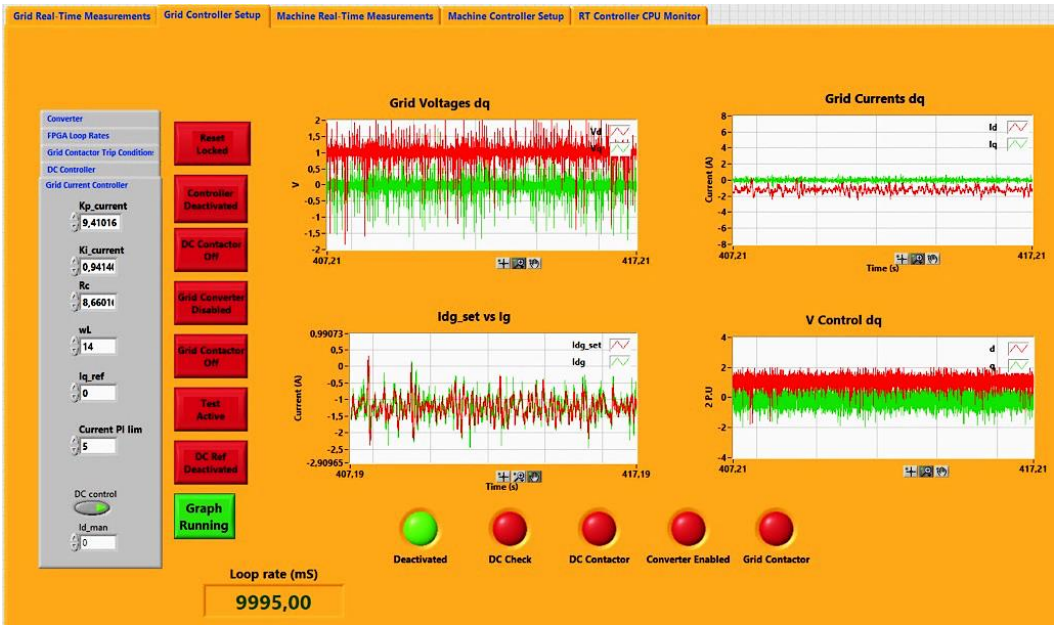

(b)

Figure D. 1: Grid-side GUI (a) grid real-time measurements, (b) Grid controller setup

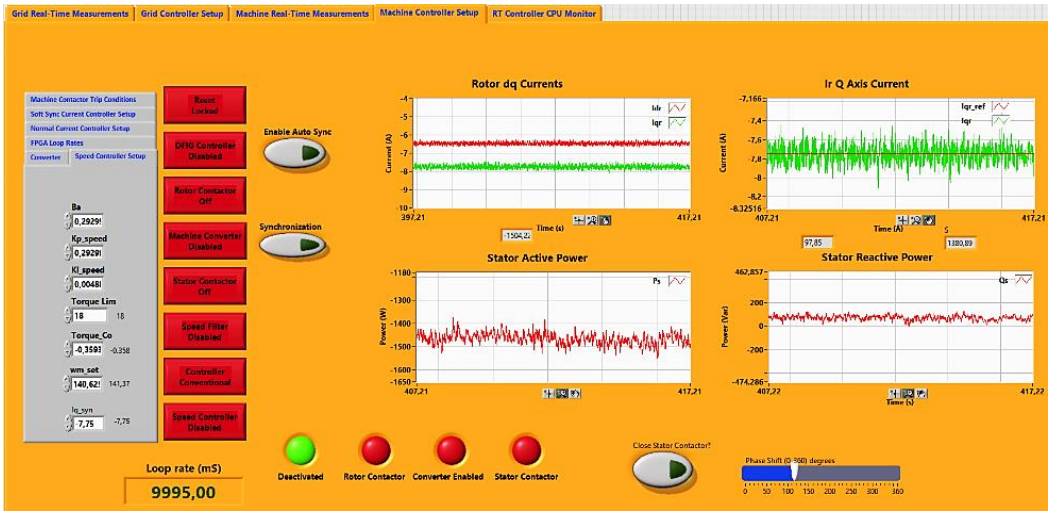

(a)

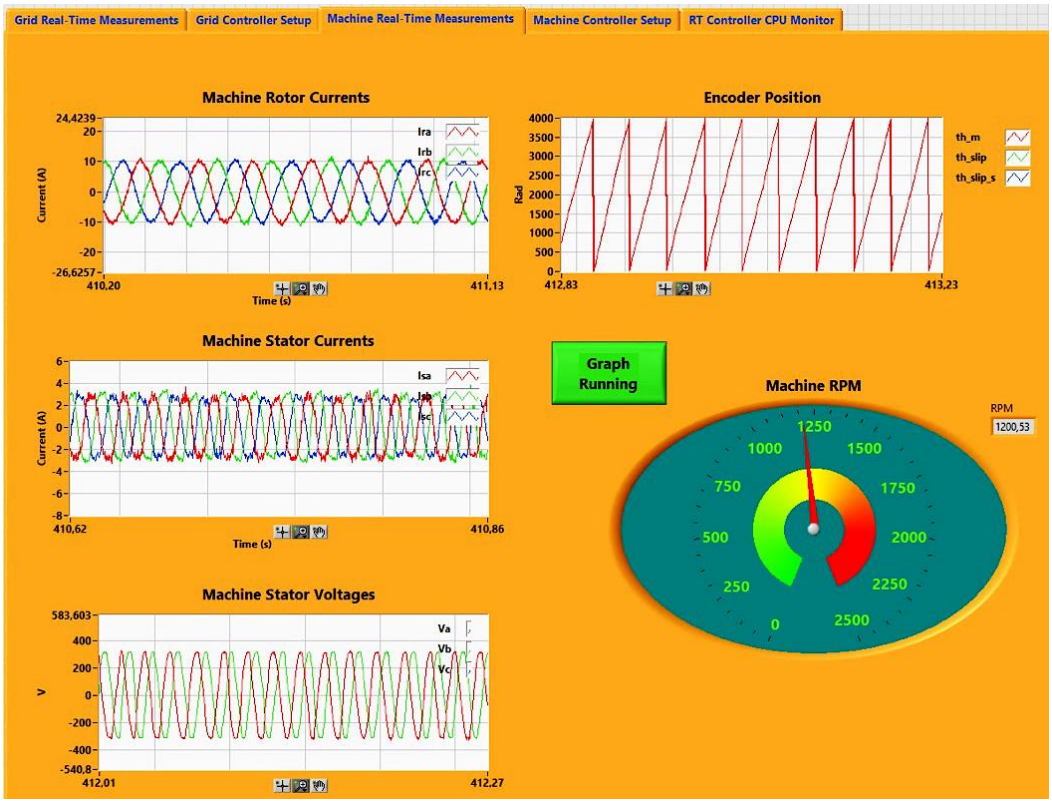

(b)

Figure D. 2: Machine-side GUI (a) Machine controller setup, (b) Machine

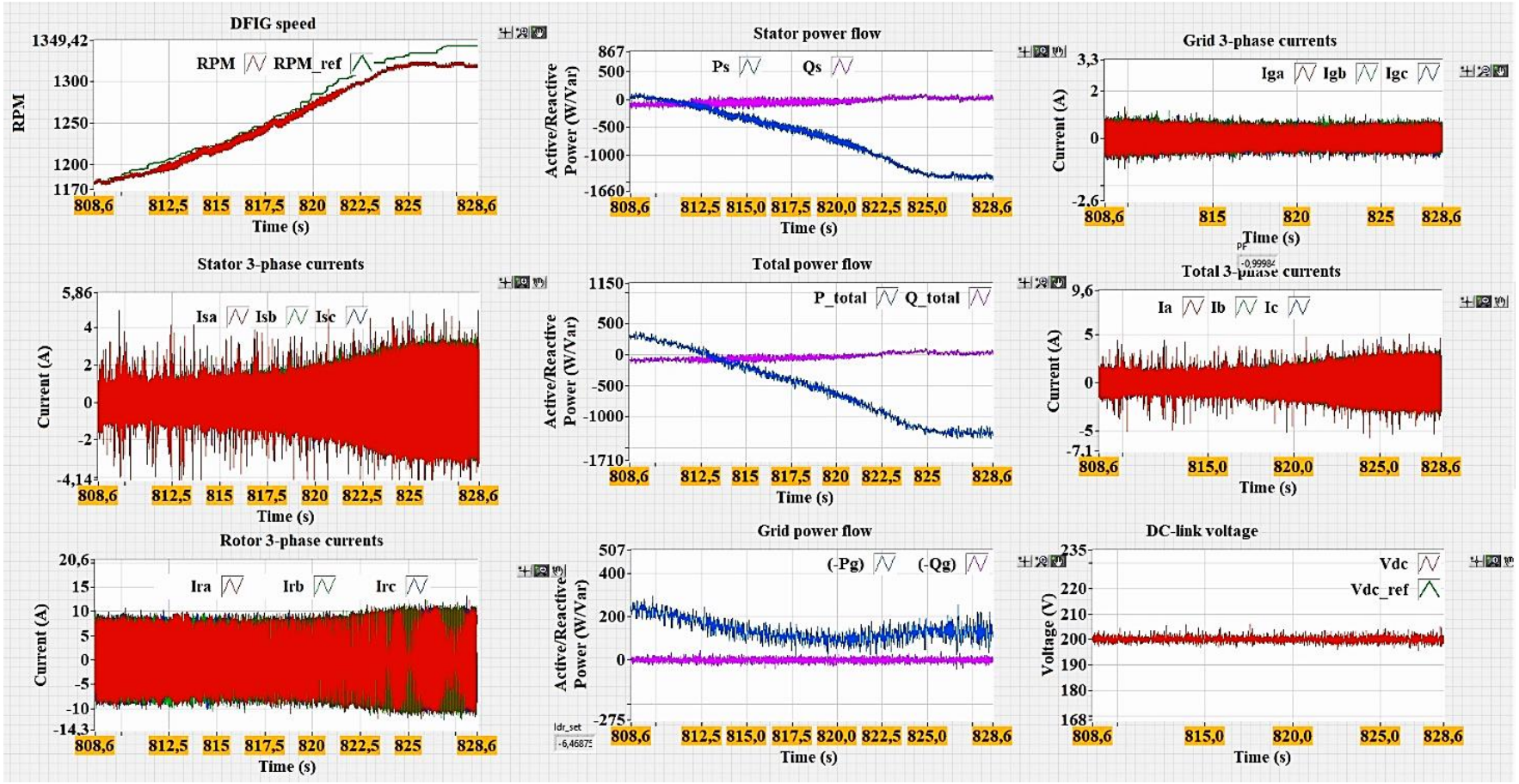

Figure D. 3: DFIG real-time speed, current and power flow measurements

D.2 LabVIEW Block Diagram Environment

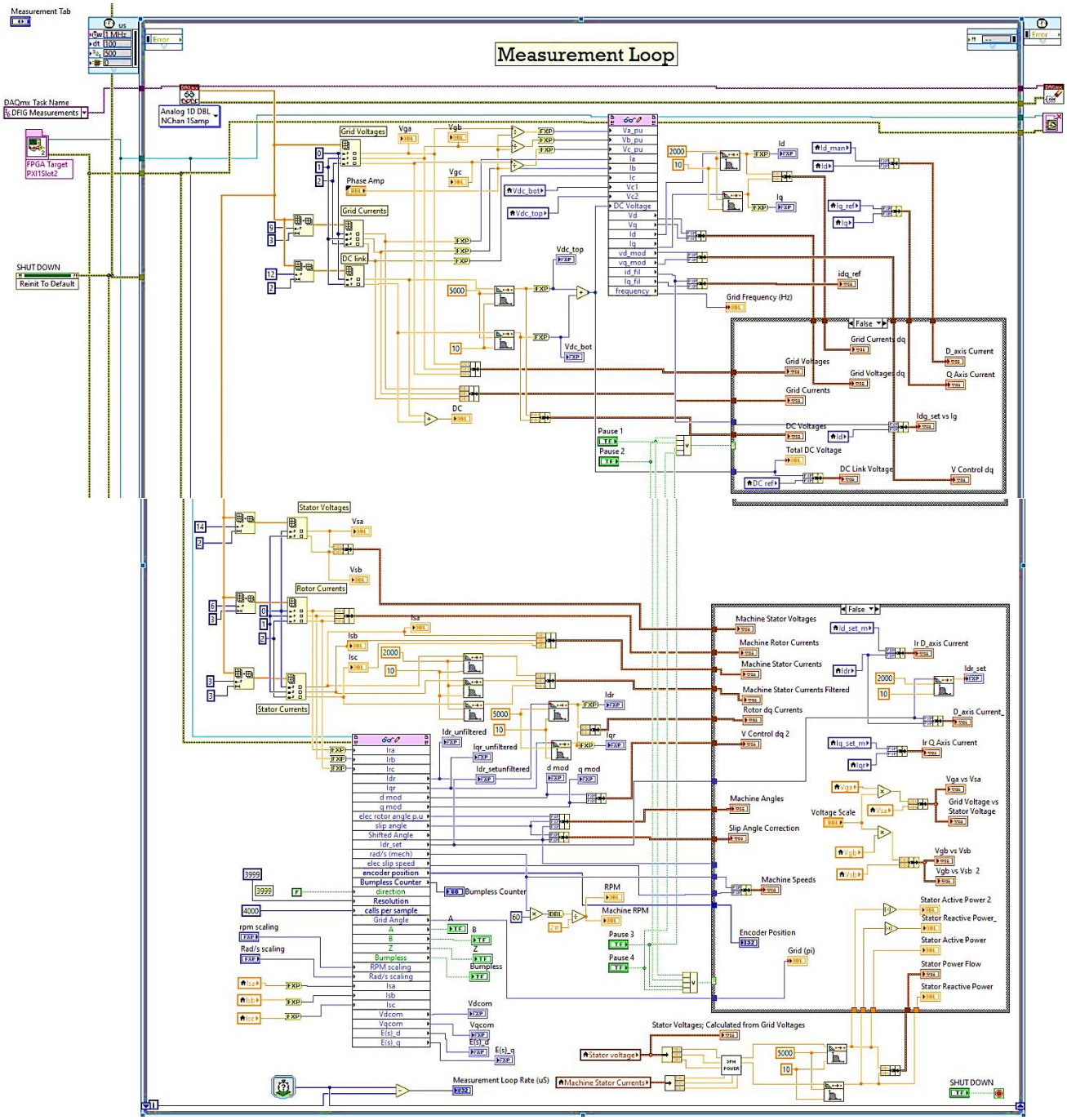

Figure D. 4: LabVIEW block diagram environment: Measurement Loop

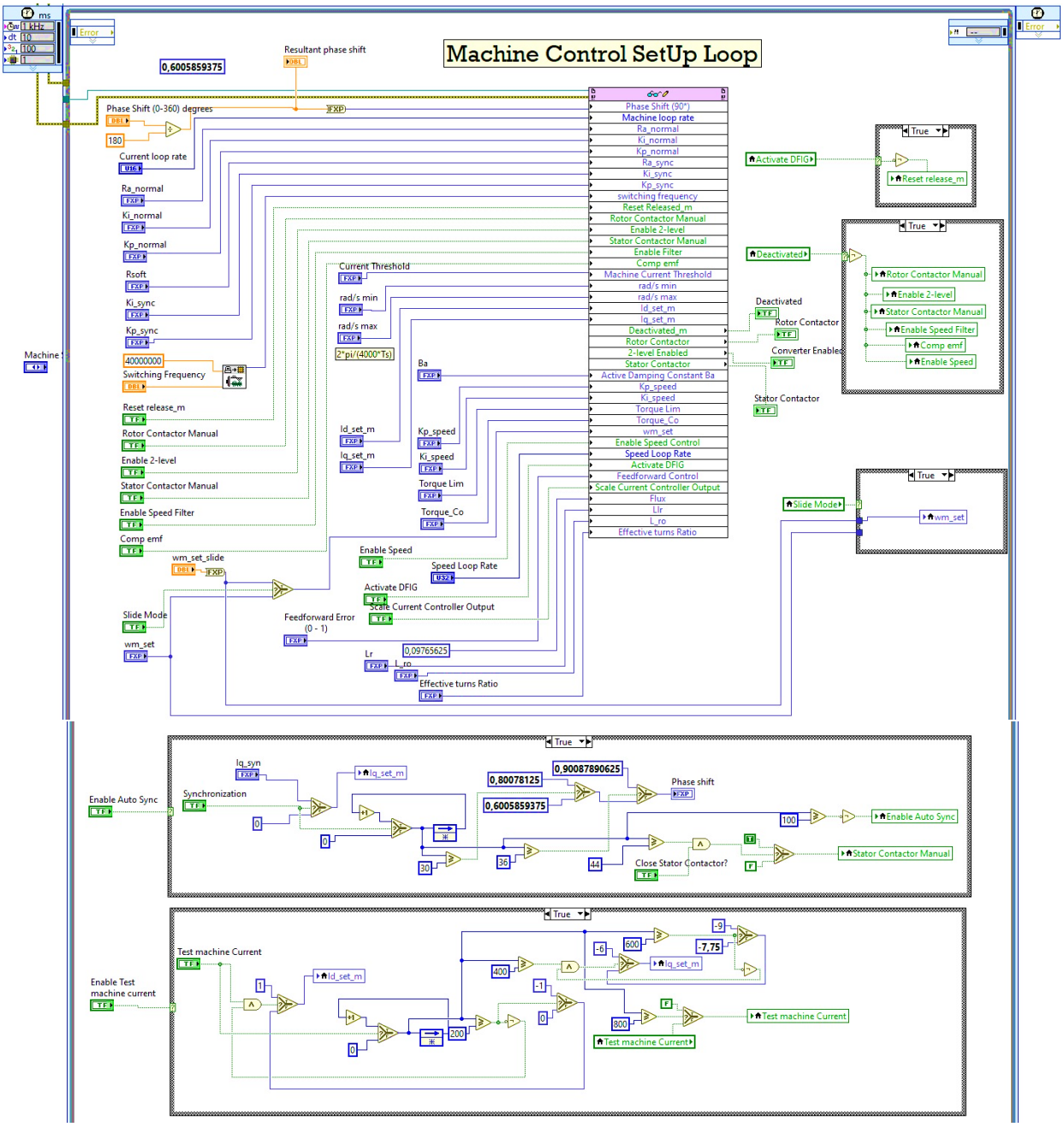
Machine Control SetUp Loop
Resultant phase shift
0,6005859375
Phase Shift (0-360) degrees
180
Current loop rate
Ra_normal
Ki_normal
Kp_normal
Rsoft
Ki_sync
Kp_sync
40000000
Switching Frequency
Reset release_m
Rotor Contactor Manual
Enable 2-level
Stator Contactor Manual
Enable Speed Filter
Comp emf
wm_set_slide
Slide Mode
wm_set
Current Threshold
rad/s min
rad/s max
2*pi/(4000*Ts)
Id_set_m
Iq_set_m
Ba
Kp_speed
Ki_speed
Torque Lim
Torque_Co
Enable Speed
Speed Loop Rate
Activate DFIG
Scale Current Controller Output
Feedforward Error (0 - 1)
Lr
0,09765625
L_ro
Effective turns Ratio
Machine
Phase Shift (90°)
Machine loop rate
Ra_normal
Ki_normal
Kp_normal
Ra_sync
Ki_sync
Kp_sync
switching frequency
Reset Released_m
Rotor Contactor Manual
Enable 2-level
Stator Contactor Manual
Enable Filter
Comp emf
Machine Current Threshold
rad/s min
rad/s max
Id_set_m
Iq_set_m
Deactivated_m
Rotor Contactor
2-level Enabled
Stator Contactor
Active Damping Constant Ba
Kp_speed
Ki_speed
Torque Lim
Torque_Co
wm_set
Enable Speed Control
Speed Loop Rate
Activate DFIG
Feedforward Control
Scale Current Controller Output
Flux
Llr
L_ro
Effective turns Ratio
Activate DFIG
Reset release_m
Deactivated
Rotor Contactor Manual
Enable 2-level
Stator Contactor Manual
Enable Speed Filter
Comp emf
Enable Speed
Deactivated
Rotor Contactor
Converter Enabled
Stator Contactor
Slide Mode
wm_set
Enable Auto Sync
Synchronization
Iq_syn
Iq_set_m
0,80078125
0,90087890625
0,6005859375
Phase shift
Close Stator Contactor?
Enable Auto Sync
Stator Contactor Manual
Enable Test machine current
Test machine Current
Id_set_m
Iq_set_m
-7,75
Test machine Current

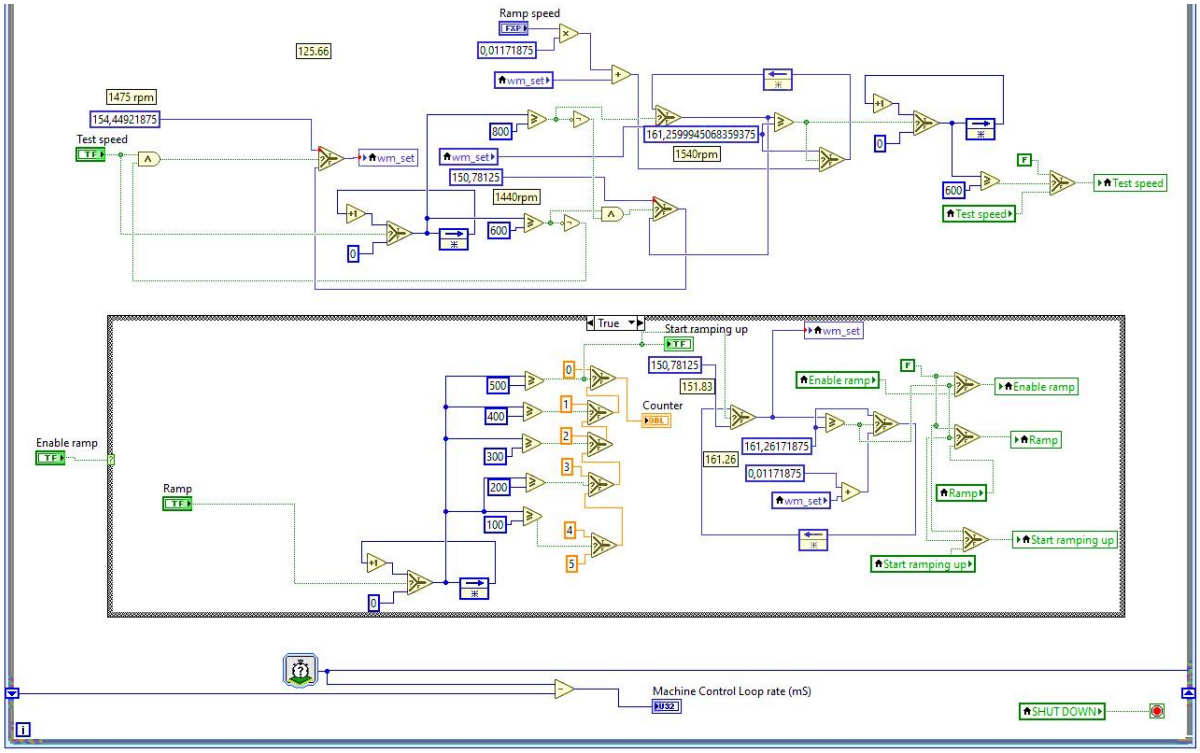

Figure D. 5: LabVIEW block diagram environment: Machine Control Setup Loop

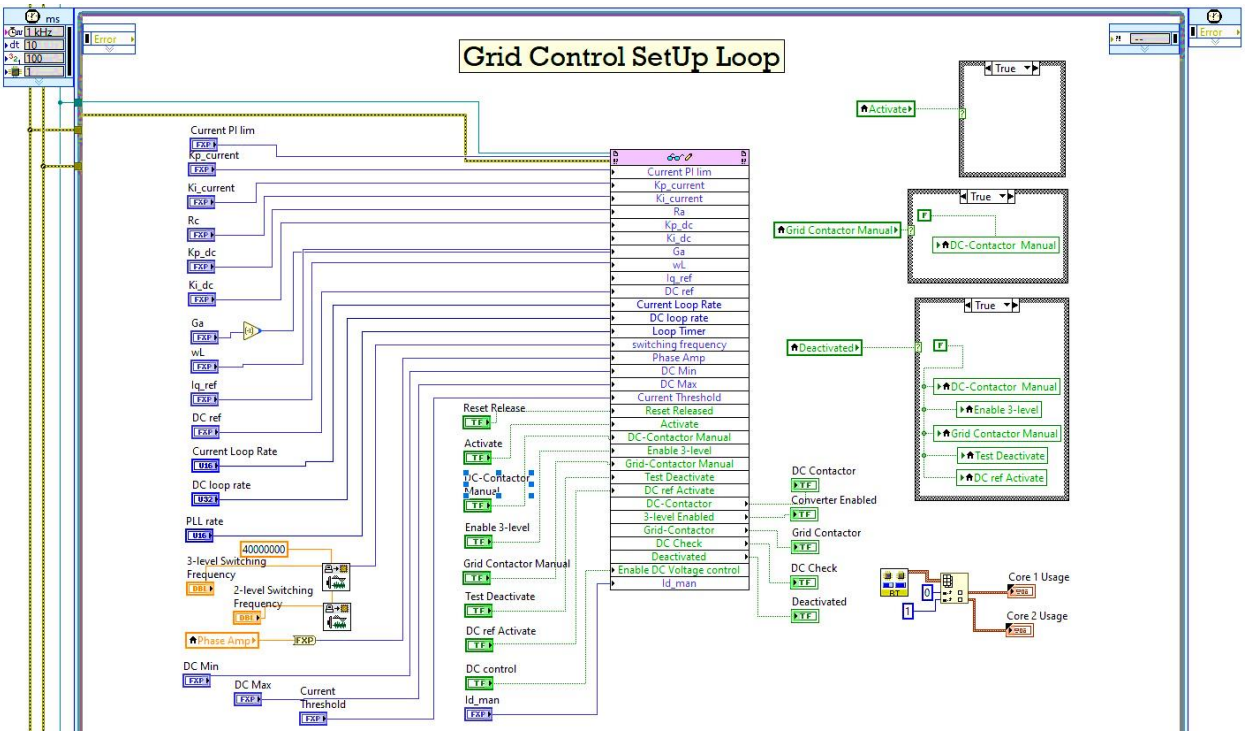

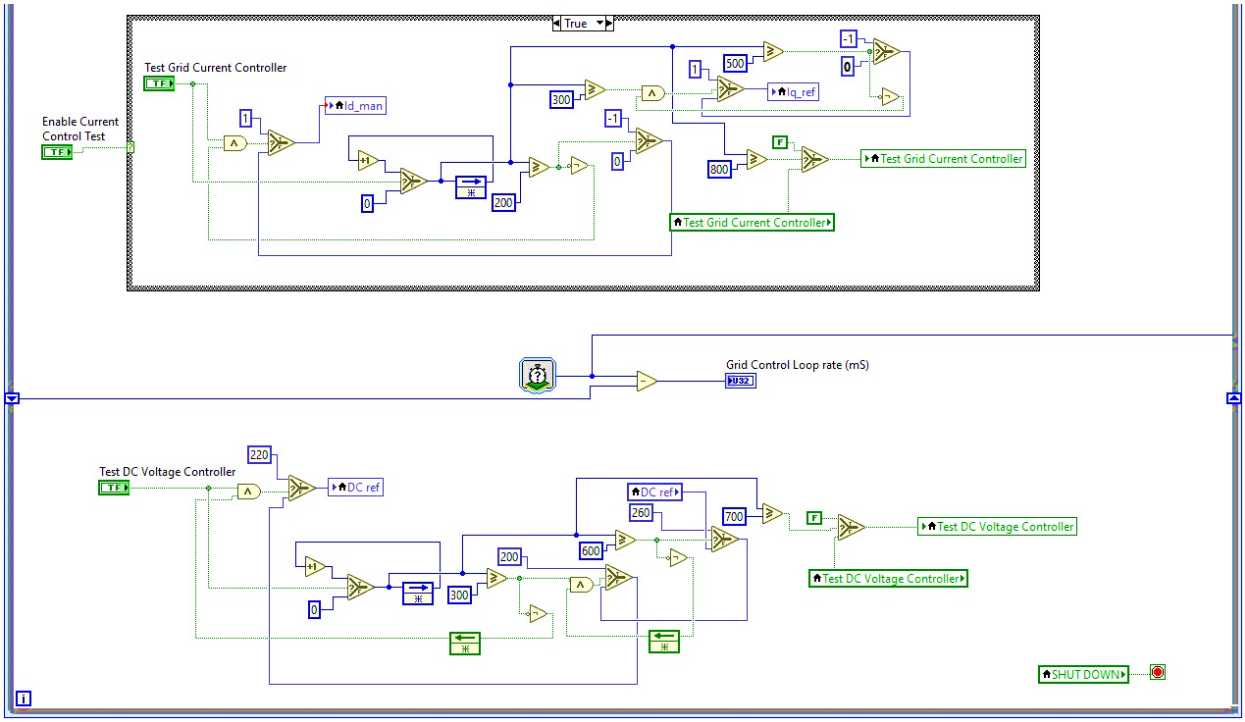

Figure D. 6: LabVIEW block diagram environment: Grid Control Setup Loop

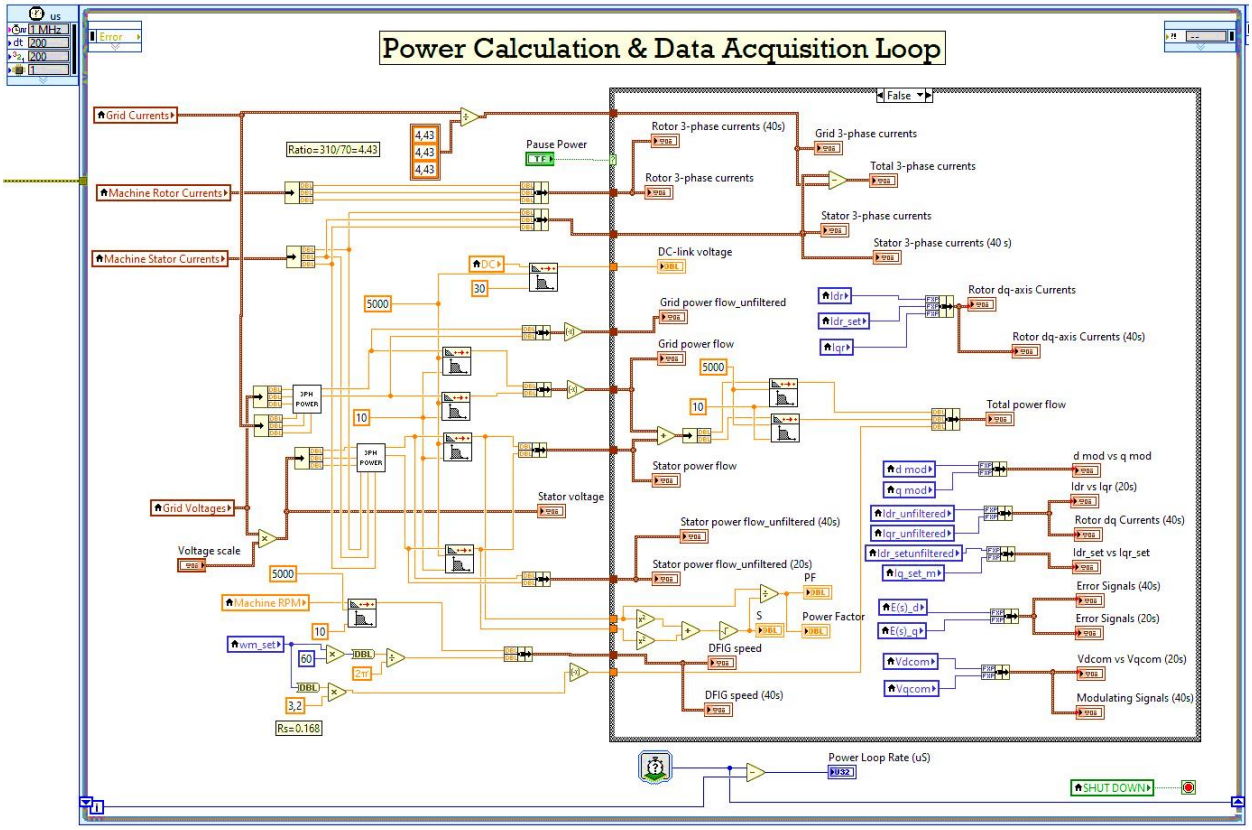

Figure D. 7: LabVIEW block diagram environment: Power Calculation and DAQ Loop

D.3 LabVIEW FPGA CODES

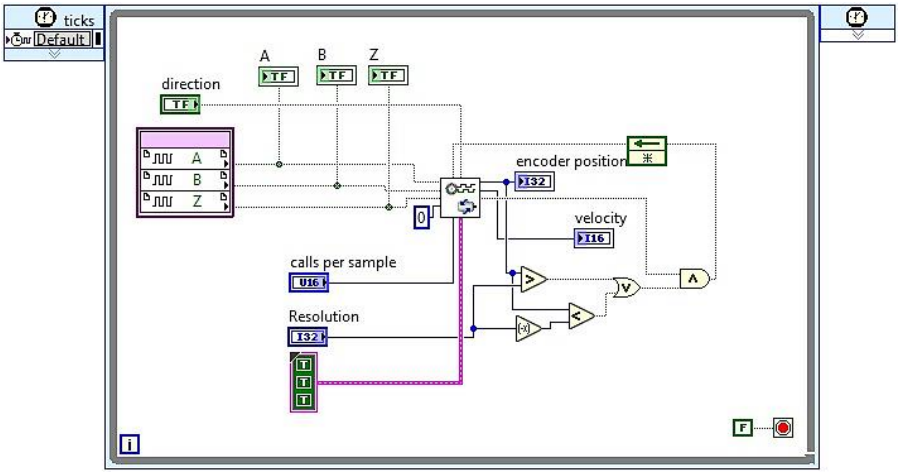

Figure D. 8: Incremental Encoder position determination

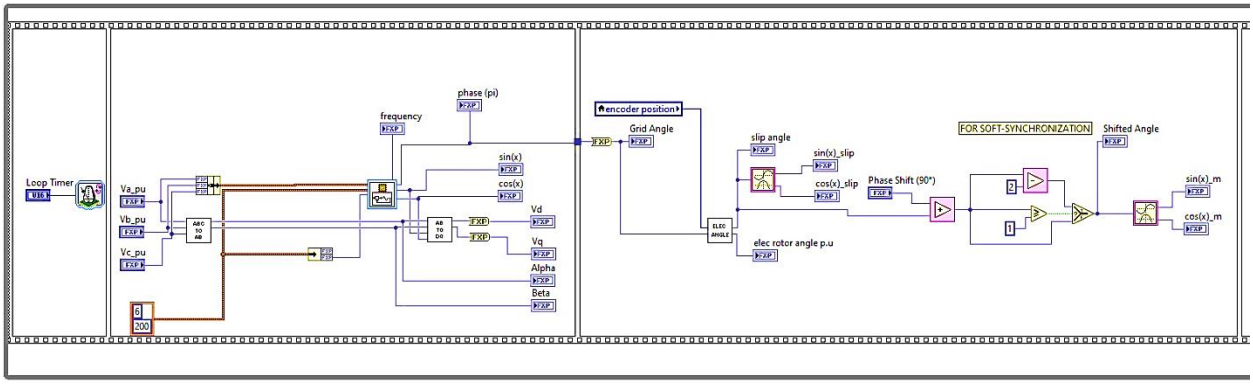

Figure D. 9: Grid (PLL) and Machine/slip angle calculation

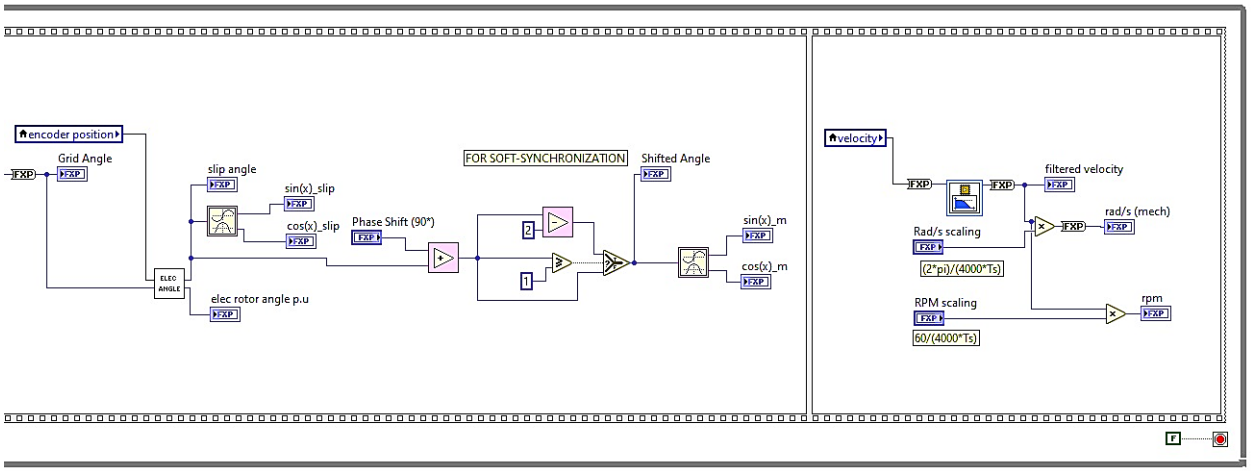

Figure D. 10: Slip angle and DFIG Speed Calculation

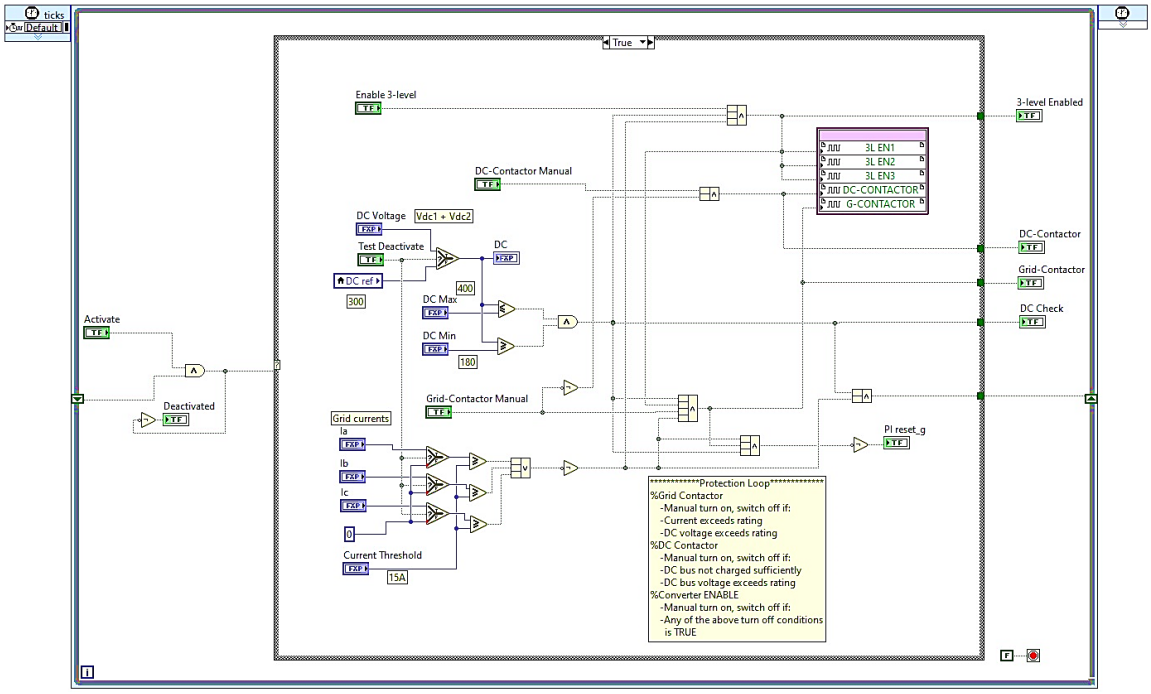

Figure D. 11: Grid-side VSC Protection

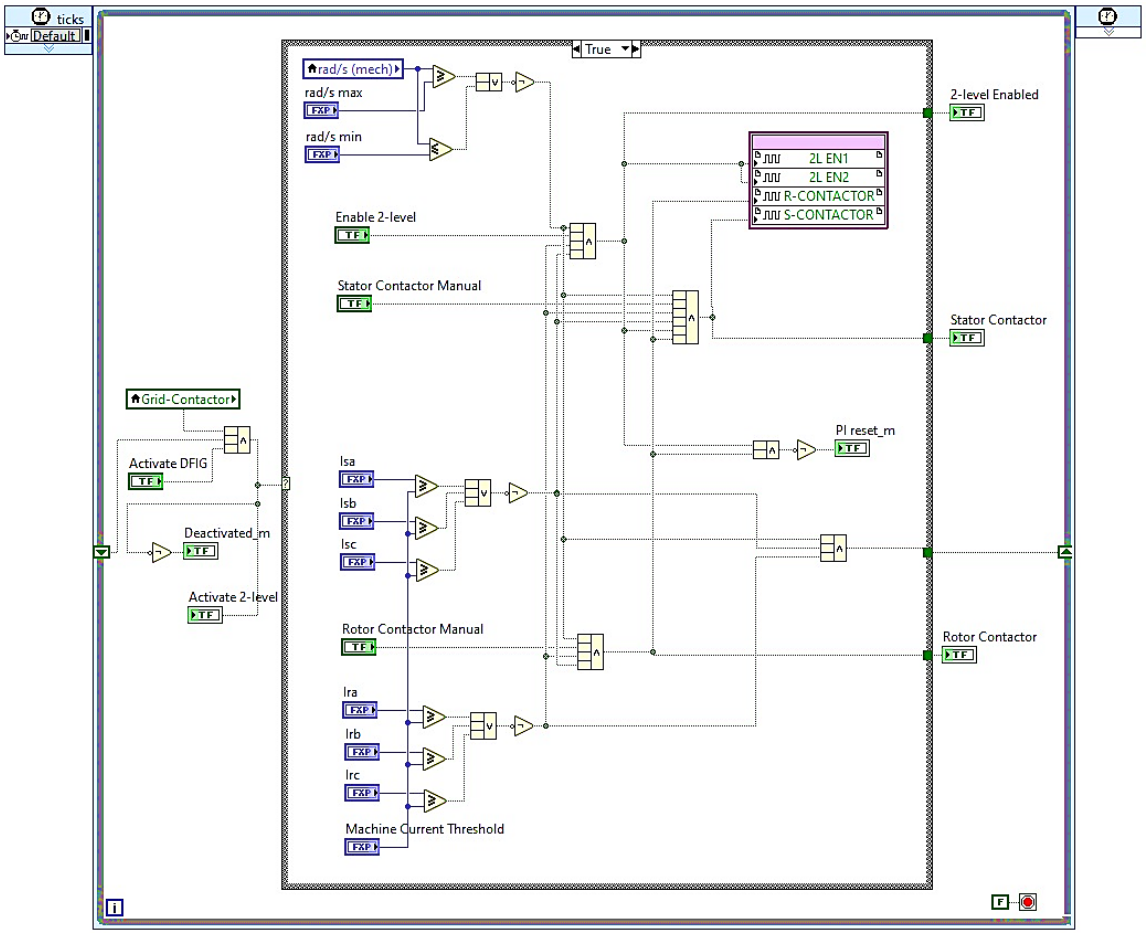

Figure D. 12: Machine -side VSC Protection

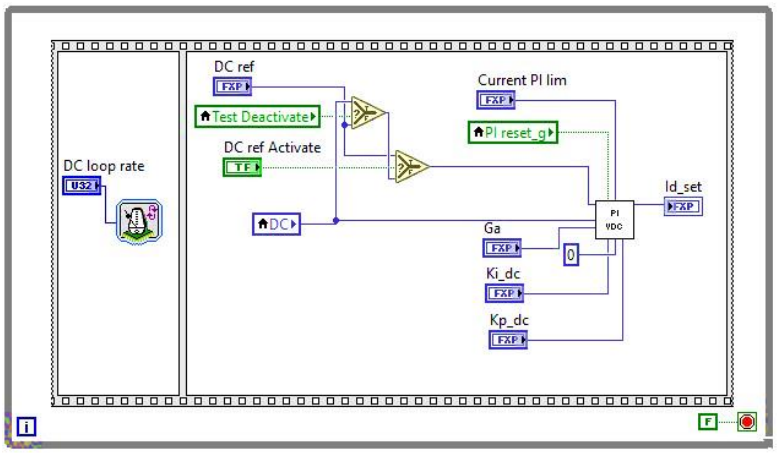

(a)

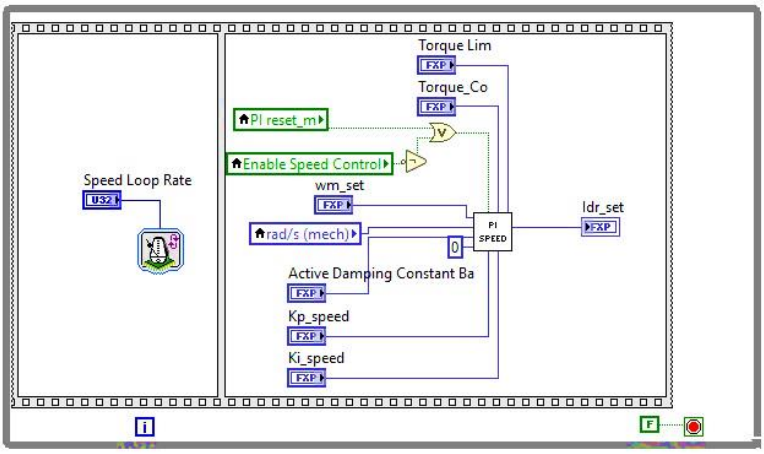

(b)

Figure D. 13: Outer Control Loops: (a) DC-link Voltage, (b) DFIG Speed

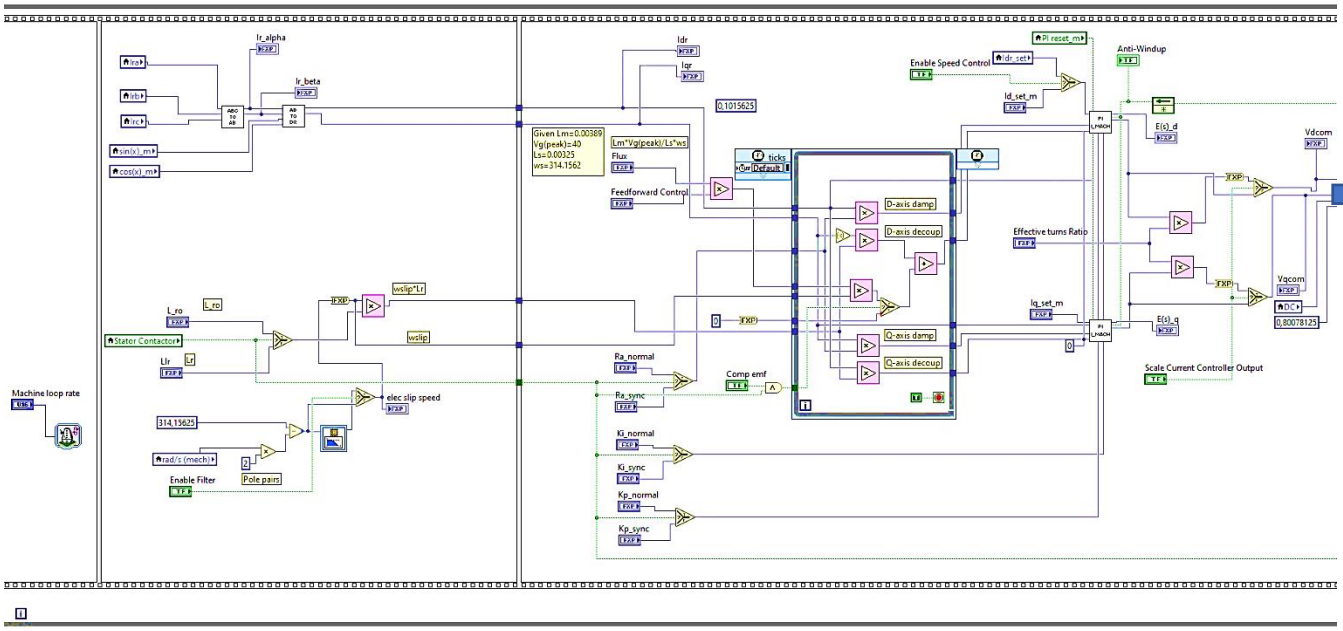

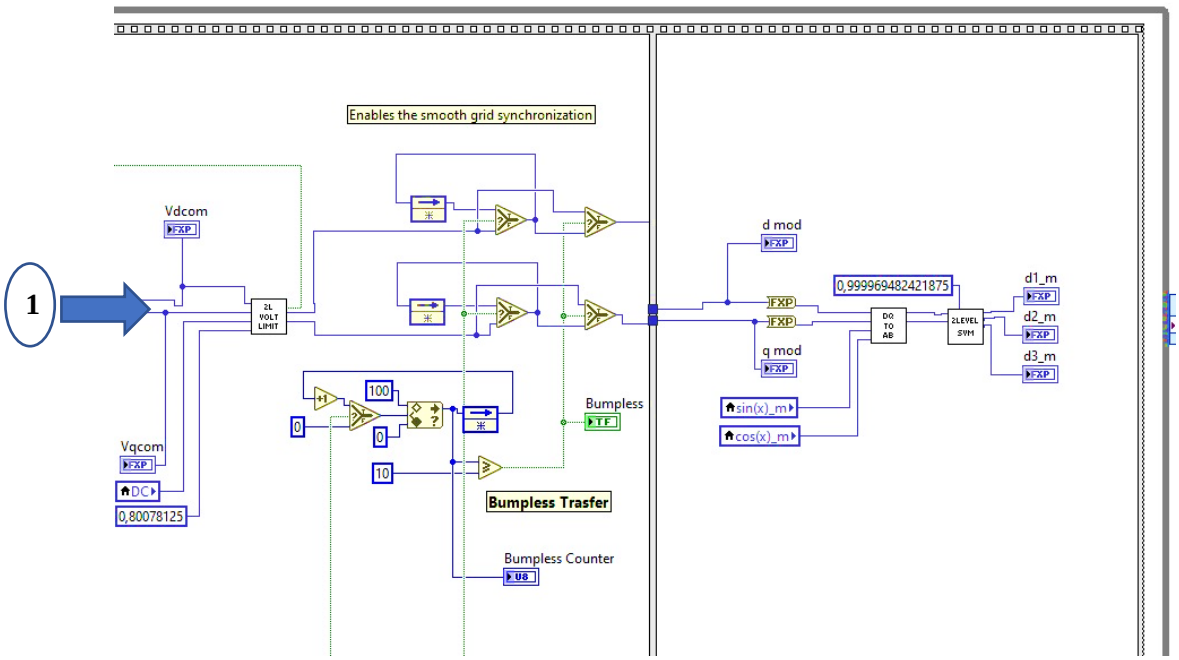

Figure D. 14: Rotor-side Converter Current Control Loop

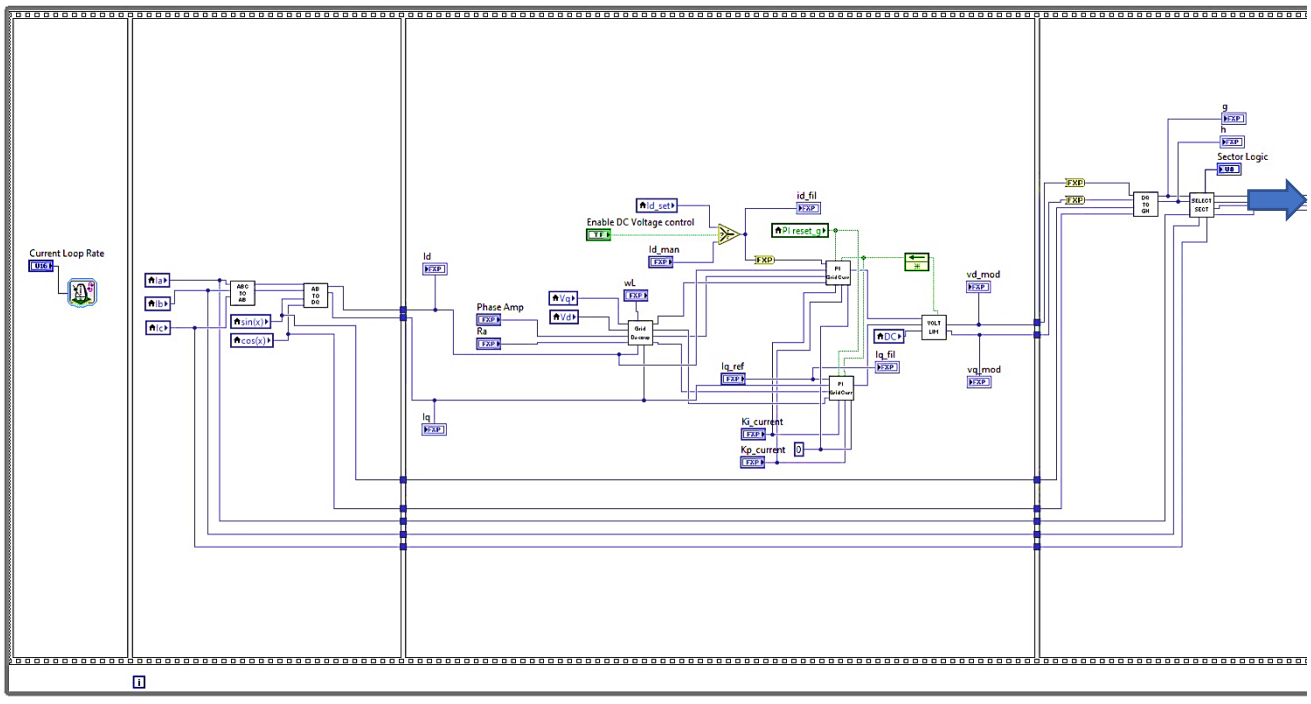

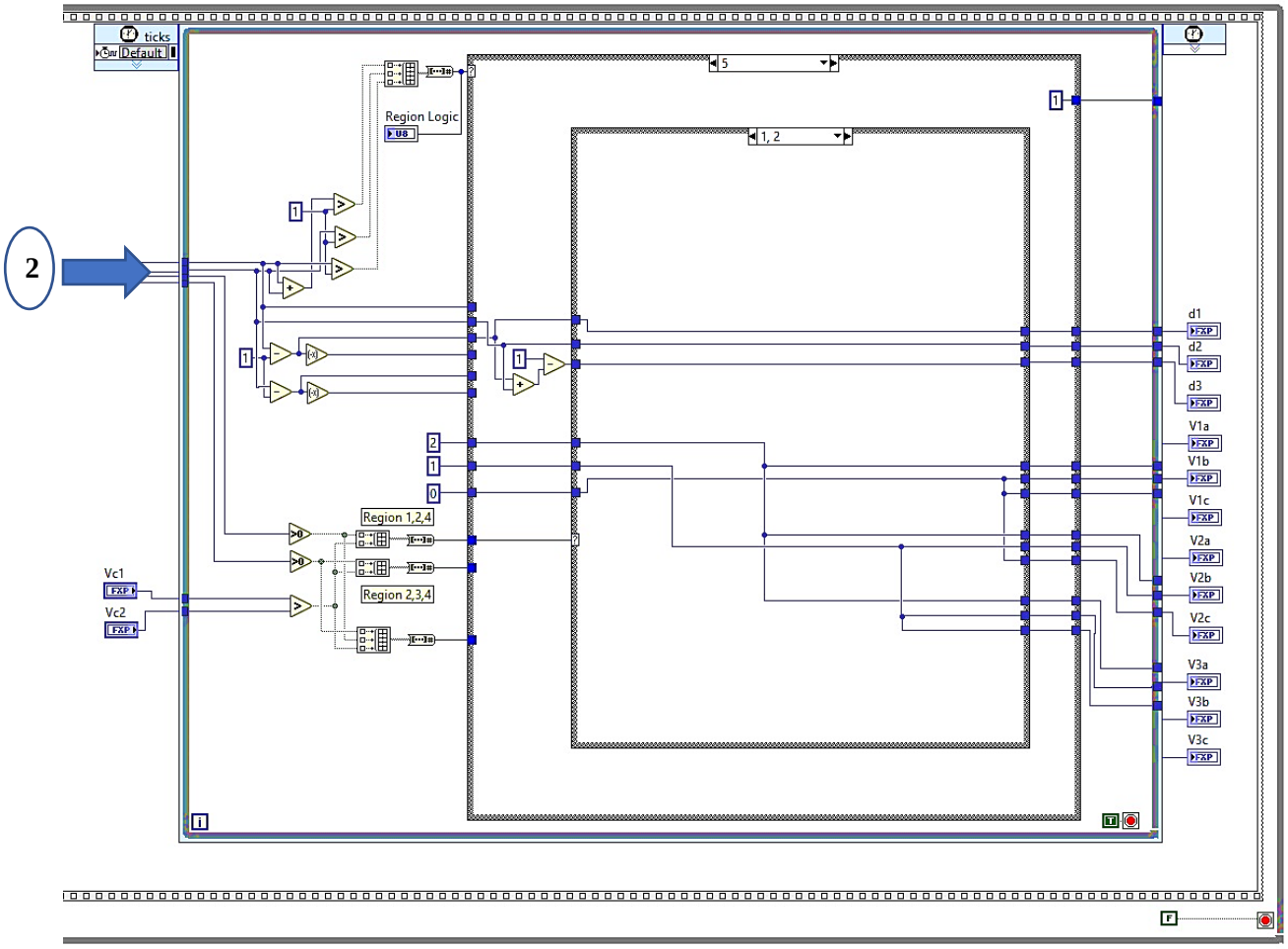

Figure D. 15: Grid-side Converter Current Control Loop

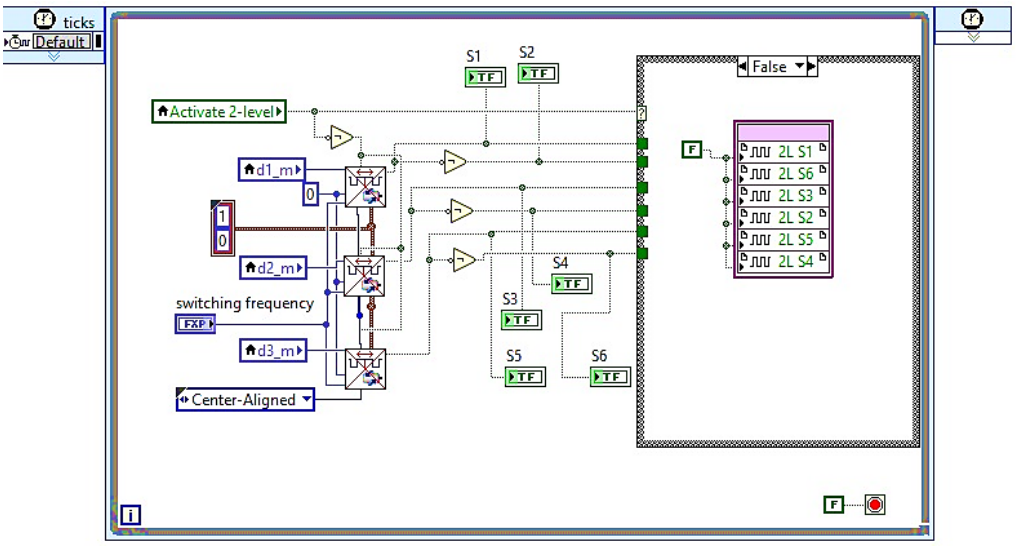

(a)

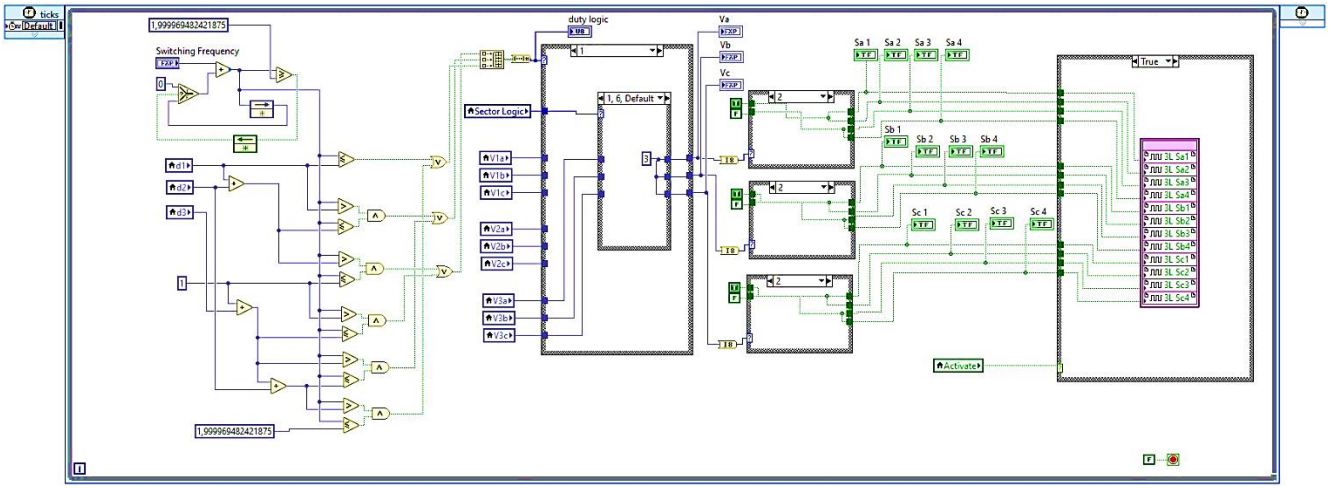

(b)

Figure D. 16: Switching Algorithms: (a) 2-Level VSC, (b) 3-Level VSC